Differentiation regimes in the Central Andean magma systems: case studies of Taapaca and Parinacota volcanoes, Northern Chile

DISSERTATION

zur Erlangung des mathematisch-naturwissenschaftlichen Doktorgrades
"Doctor rerum naturalium"
der Georg-August-Universität Göttingen

im Promotionsprogramm Geowissenschaften / Geographie
der Georg-August University School of Science (GAUSS)

vorgelegt von

Magdalena Banaszak

aus Poznań/Polen

Göttingen 2014

Betreuungsausschuss:

Prof. Dr. Gerhard Wörner
Abteilung Geochemie, Geowissenschaftliches Zentrum, Universität Göttingen

Prof. Dr. François Holtz
Institut für Mineralogie, Leibniz Universität Hannover

Mitglieder der Prüfungskommission

Referent:
Prof. Dr. Gerhard Wörner
Abteilung Geochemie, Geowissenschaftliches Zentrum, Universität Göttingen

Korreferent:
Prof. Dr. François Holtz
Institut für Mineralogie, Leibniz Universität Hannover

weitere Mitglieder der Prüfungskommission:

Prof. Dr. Sharon Webb
Abteilung Experimentelle und Angewandte Mineralogie, Geowissenschaftliches Zentrum, Universität Göttingen

Prof. Dr. Andreas Pack
Abteilung Isotopengeologie, Geowissenschaftliches Zentrum, Universität Göttingen

Dr. Andreas Kronz
Abteilung Geochemie, Geowissenschaftliches Zentrum, Universität Göttingen

Dr. Klaus Simon
Abteilung Geochemie, Geowissenschaftliches Zentrum, Universität Göttingen

Tag der mündlichen Prüfung: 23. April 2014

DEDICATION

TO HANNAH AND NILS.

ACKNOWLEDGEMENTS

This PhD thesis would not have been possible without the never-ending support and patience of my Doctor Father Gerhard Wörner. The enthusiasm he has for magmatism was contagious and motivational for me even during tough times in the PhD pursuit. I appreciate all his contributions of time and ideas funding to my experience in research and understanding andesites and dacites.

I especially want to thank
François Holtz
Roman Botcharnikov
Andreas Kronz
Klaus Simon
John Hora
André Stechern
Nils Blum-Oeste
for help and jewel suggestions which immensely contributed to this thesis.

THE MANTLE PROPOSES; THE CRUST DISPOSES.

Wes Hildreth (2007)

ABSTRACT

Volcanoes have shaped the Earth's surface and are nature's most awesome manifestation of the power within our planet (Rosaly M. Lopes). Compositional and mineralogical diversity of erupted lavas reflects distinct magma differentiation paths, resulting from magmatic processes controlled by magma sources and architecture of the Earth's crust. A differentiation regime is a concept encompassing different magmatic conditions and mechanisms operating in subvolcanic plumbing systems during magma evolution. This study addresses the compositional and mineralogical variability of magmas erupted in the Andean Central Volcanic Zone (14°-27°S).

Taapaca and Parinacota located in the Central Andes (18°S), are composite stratovolcanoes distinctive in their morphology: Taapaca represents a dacitic dome complex; Parinacota forms a symmetrical stratocone. These two characteristic effusive end-member types of the arc volcanism reflect two different magma evolutionary paths. Taapaca has erupted compositionally and mineralogically uniform dacites. In contrast, Parinacota demonstrates a large compositional variability of the erupted lavas, from basaltic andesite to rhyolite. Moreover, Parinacota experienced an edifice sector collapse, which punctuates changes in the composition of prevailing Fe-Mg silicates in the andesite lavas. Although both volcanos appear to be completely different, Taapaca and Parinacota share several characteristics such as trace element and isotopic composition, mineral chemistry, and a range of physical parameter P-T-fO_2 during magma crystallization.

Geochemical, geochemical-statistical and petrological investigations presented in this study in a connection with experimental constraints reveal one principal mechanism operating in the subvolcanic Taapaca and Parinacota systems: two-stage magma mixing between magmas generated in the mantle wedge, lithospheric mantle and the continental crust is responsible for the varying compositions of the erupted Taapaca and Parinacota lavas. Proportions of the mafic and silicic magmas, simultaneously present in the subvolcanic plumbing system constitute mineralogy of the hybrid lavas.

This study shows that the proportions of the compositionally and physically contrasting magmas define the distinct differentiation regimes of the calc-alkaline magmas in the volcanic systems, controlled by input rates from the mantle and the deep crust.

TABLE OF CONTENTS

CHAPTER 1: A study of volcanic differentiation regimes – Introduction and Overview...................... 1

CHAPTER 2: End-member magma compositions from Taapaca Dome Complex and Parinacota Stratovolcano, 18°S, Central Volcanic Zone, N. Chile and their significance in the genesis of the Central Andean Quaternary magmas: Application of Polytopic Vector Analysis.. 7

ABSTRACT 7

1. INTRODUCTION 8

2. POLYTOPIC VECTOR ANALYSIS 12

3. VOLCANOLOGICAL BACKGROUND...13

4. SAMPLES AND METHODS 15

4.1. DATA SOURCES 15
4.2. GEOCHEMICAL AND PETROGRAPHIC CHARACTERISTICS OF THE SAMPLES..15
4.2.1. Taapaca Volcanic Complex (TVC) 15
4.2.2. Geochemical relationship of Taapaca and Parinacota mafic magmas 16
4.2.3. Parinacota Volcano...17
4.3. ANALYTICAL METHODS 18
4.4. STATISTICAL METHOD: THE PVA CALCULATION PROCEDURE..19
4.4.1. Data sets used in the PVA...19
4.4.2. PVA modules and calculation conditions 19

5. RESULTS..21

5.1. NUMBER OF END-MEMBERS 22
5.2. PVA END-MEMBER COMPOSITIONS 25
5.3. MIXING PROPORTIONS OF THE PVA END-MEMBERS..32
5.4. CONSTRAINED ISOTOPIC COMPOSITION OF THE PVA BASALTIC END-MEMBER.....................................36

6. DISCUSSION 40

6.1. GEOLOGICAL BACKGROUND OF PVA END-MEMBERS..40
6.2. GEOCHEMICAL CHARACTERS OF THE PVA END-MEMBERS 41
6.2.1. Geochemical character of the BEM...41
6.2.2. Geochemical character of the AEM...42
6.2.3. Geochemical character of the RDEM...43
6.3. PVA END-MEMBERS IN CONTEXT WITH THE QUATERNARY CVZ MAGMAS..46
6.3.1. Relationship of the PVA end-members to the regional Quaternary differentiation trends 46
6.3.2. Relationship of the PVA end-members to the entire Quaternary CVZ lavas 46
6.3.3. Frequency of the PVA compositions in the CVZ...47
6.4. PREVIOUS PETROGENESIS MODELS OF THE CVZ MAGMAS 49
6.4.1. MASH-dominated petrogenesis of the modern Andean magmas..49
6.4.2. Temporal changes in the Miocene-Holocene magma compositions in the CVZ..........................49
6.5. NOVEL PETROGENETIC MODEL OF THE CVZ MAGMAS BASED ON PVA RESULTS 50
6.5.1. Magmatic source of the BEM PVA end-member 51
6.5.2. Magmatic source of the AEM PVA end-member 53
6.5.3. Magmatic source of the RDEM PVA end-member 55
6.5.4. Novel petrogenetic model: sources instead processes...59
6.6. SPATIAL COMPOSITIONAL VARIABILITY OF THE QUATERNARY CVZ MAGMAS AND ROLE OF THE PVA END-MEMBERS 61
6.6.1. Spatial compositional variability of the Quaternary volcanics along the CVZ 61
6.6.2. Spatial compositional variability across the CVZ 63
6.7. PETROLOGICAL EVIDENCE FOR RDEM BASED ON FE IN PLAGIOCLASE 63
6.8. PETROLOGICAL EVIDENCE FOR BEM AND AEM BASED ON OLIVINE COMPOSITIONS 64
6.8.1. Relationship between Fo81 threshold-value and alkaline (shoshonitic) affinity of the parental magma...65
6.8.2. Connection between olivine compositions and textures in basaltic andesites from Parinacota...66
6.8.3. Examination of Fo and Ni contents in natural olivines with BEM and AEM PVA compositions .69
6.8.4. Magma mixing recorded in olivine trends form Parinacota...71

7. CONCLUSIONS **72**
8. REFERENCES **74**
APPENDIX **84**

CHAPTER 3: Differentiation regime of Taapaca dacitic complex, Central Volcanic Zone, N. Chile 90

ABSTRACT **90**
1. INTRODUCTION **91**
2. VOLCANOLOGICAL BACKGROUND **93**
2.1. GEOLOGICAL SETTING 93
2.2. ORIGIN OF THE CVZ QUATERNARY MAGMAS 93
2.3. ERUPTIVE HISTORY OF TAAPACA VOLCANIC COMPLEX 96
2.4. GEOCHEMICAL CHARACTERISTICS OF TAAPACA LAVAS 97
2.4.1. Taapaca hybrid dacites *97*
2.4.2. Comparison to other Andean dacitic complexes *98*
2.5. PREVIOUS WORK 100
3. METHODS **100**
3.1. SAMPLE SELECTION 100
3.2. ANALYTICAL METHODS 101
3.3. GEOTHERMO-OXY-BAROMETRY 102
3.3.1. Geothermometer *102*
3.3.2. Geothermo-oxy-barometer *103*
3.3.3. Amphibole Barometry *104*
3.3.4. Semiquantitative amphibole thermobarometer *104*
3.3.5. Amphibole Combi-P-T-fO_2-H_2O_{melt}-meter *105*
4. PETROGRAPHY AND MINERAL CHEMISTRY OF THE TVC **105**
4.1. PETROGRAPHY 105
4.1.1. Dacites *106*
4.1.2. Mafic enclaves *106*
4.2. MINERAL TEXTURES AND CHEMISTRY 108
4.2.1. Plagioclase *108*
4.2.2. Amphibole *110*
4.2.3. Biotite *113*
4.2.4. Fe-Ti oxide *113*
4.2.5. Accessory minerals *115*
4.2.6. Pyroxene *115*
4.2.7. Sanidine *115*
5. CONSTRAINTS ON CRYSTALLIZATION CONDITIONS **116**
5.1. COMPOSITIONS OF NATURAL AND EXPERIMENTAL AMPHIBOLE 117
5.2. AL-IN-HORNBLENDE GEOBAROMETRY 118
5.3. AMPHIBOLE THERMO-OXY-BAROMETER 121
5.3.1. Pressure *122*
5.3.2. Temperature *124*
5.3.3. Oxygen fugacity *125*
5.3.4. Melt water-contents H_2O_{melt} *126*
5.4. AMPHIBOLE-PLAGIOCLASE THERMOMETRY 128
5.4.1. Selection of amphibole-plagioclase pairs *128*
5.4.2. Amphibole-plagioclase crystallization temperatures of Taapaca rocks *128*
5.4.3. Comparison of temperature results from H&B94 and R&R2011 .... *129*
5.5. AMPHIBOLE TI-THERMOMETER 132
5.6. CA-AMPHIBOLE SEMI-QUANTITATIVE THERMOBAROMETRY 133
5.7. GEOTHERMO-OXY-BAROMETRY BASED ON Fe-TI OXIDE 134
6. SIMPLE MAGMA MIXING MODELING **135**

7. DIFFERENTIATION REGIME OF TVC **137**

7.1. MAGMA MIXING REGIME 138
7.1.1. Liquid line of descent (LLD) of Taapaca and Parinacota suite *138*
7.1.2. Evidence from mineral chemistry *139*
7.1.3. Petrology of magma mixing proportions obtained from the PVA study *144*
7.2. GEOTHERMO-OXY-BAROMETRY OF TVC MAGMAS 146
7.2.1. What does govern amphibole compositions *146*
7.2.2. Differentiation regime reflected by intensive parameter of crystallization *149*

8. LINK BETWEEN TVC AND PLUTONIC REALM **151**

8.1. COMPOSITIONAL LINK BETWEEN VOLCANIC AND PLUTONIC REALM RECOGNIZED IN TAAPACA (AND PARINACOTA) 151
8.2. SANIDINE MEGACRYSTS FIRST-ORDER LINK TO PLUTONIC REALM 152
8.3. INCREMENTAL MAGMA EMPLACEMENT AND EXTRUSION 153
8.4. REJUVENATION, COMMINGLING AND MOBILIZATION OF THE SILICIC TAAPACA MAGMAS 154

9. PLUMBING SYSTEM OF TAAPACA VOLCANIC COMPLEX **156**

10. SUMMARY AND CONCLUDING REMARKS **159**

11. REFERENCES **161**

CHAPTER 4: Petrological and geochemical changes in magmas of Parinacota Volcano, N. Chile, accompanied by edifice sector collapse **170**

ABSTRACT **170**

1. INTRODUCTION **171**

2. VOLCANOLOGICAL BACKGROUND **174**

2.1. PREVIOUS STUDIES 174
2.2. GEOLOGICAL SETTING 174
2.3. EVOLUTIONARY STAGES 176
2.3.1. Initial Eruptions Chungará Andesites (ca) *176*
2.3.2. Pre-collapse units of Old Cone (OC) and Rhyodacite Dome Plateau (dp) *176*
2.3.3. Edifice collapse and Debris Avalanche (dbf) *177*
2.3.4. Post-collapse units of Young Cone (YC) and Flank Eruptions – Ajata Flows (a) *178*

3. METHODS **181**

3.1. SAMPLING 181
3.2. ANALYTICAL METHODS 181
3.3. GEOTHERMO-OXY-BAROMETRY METHODS (GTOB) 182
3.3.1. Two-pyroxene thermometer and barometer *182*

4. WHOLE ROCK CHEMISTRY **183**

5. PETROGRAPHY AND MINERAL CHEMISTRY **189**

5.1. PETROGRAPHY 189
5.1.1. Pre-collapse units *189*
5.1.2. Post-collapse units *191*
5.2. MINERAL CHEMISTRY 193
5.2.1. Plagioclase *194*
5.2.2. Amphibole *195*
5.2.3. Pyroxene *198*
5.2.4. Olivine *200*
5.2.5. Fe-Ti Oxide *201*

6. GEOTHERMO-OXY-BAROMETRY (GTOB) - RESULTS **202**

6.1. BAROMETRY 205
6.1.1. Crystallization pressure of Parinacota amphiboles *205*
6.1.2. Crystallization pressure of Parinacota pyroxenes *207*

6.2. THERMOMETRY 212
6.2.1. Thermal conditions in Pre-collapse magmas 212
6.2.2. Thermal conditions in post-collapse magmas....................213
6.3. OXYGEN BAROMETRY....................214
6.4. MELT WATER CONTENTS....................214

7. DIFFERENTIATION REGIMES OF PARINACOTA VOLCANO....................219

7.1. DIFFERENTIATION REGIMES REFLECTED BY DIFFERENT VOLCANO MORPHOLOGIES AND MINERAL ASSEMBLAGES....................219
7.2. EVOLUTION OF MAGMA COMPOSITIONS ASSOCIATED WITH SECTOR COLLAPSE....................220
7.2.1. Parinacota 220
7.2.2. Clues from other arc volcanoes....................225
7.3. OCCURRENCE OF AMPHIBOLE VS. PYROXENE AND RELATION TO SECTOR COLLAPSE....................226
7.3.1. Amphibole crystallization - Insight from Taapaca basaltic andesite enclaves....................226
7.3.2. Insights from Parinacota 227
7.4. SUBVOLCANIC SYSTEM OF PARINACOTA VOLCANO 229

8. SUMMARY AND CONCLUDING REMARKS 230

9. REFERENCES....................232

CHAPTER 1

A study of volcanic differentiation regimes – Introduction and Overview

The most mafic compositions of Quaternary magmatism in the Andean Central Volcanic Zone (CVZ) encompass medium-K to high-K calc-alkaline basaltic andesites (52-55 SiO_2 wt%). These baseline compositions are geochemically variable and characterized by large ranges in major (3.6-9.4 wt% MgO, 4-7 wt% Na_2O+K_2O, 0.8-1.8 wt% TiO_2) and trace element concentrations (9-197 ppm Ni, 501-1944 ppm Sr, 95-257 ppm Zr), as well as trace element ratios (LILE/HFSE: 93>Sr/Y>24; LREE/HREE: 63>La/Yb>8). Such a remarkable variability of the parental lavas reflects distinct petrogenetic processes during ascent and evolution of mantle-derived melts traversing an exceptionally thick continental crust, reaching up to 70 km in the Central Andes. The geochemical nature of primary mantle input into the crustal magma systems is therefore poorly constrained in the Andean CVZ, due to an absence of erupted primitive basaltic lavas (<52 wt% SiO_2).

The geochemically variable baseline basaltic andesitic components affect magma systems of Taapaca and Parinacota volcanoes, both located at 18°S in the CVZ. The major and trace element compositions of both volcanoes fall on the same compositional trend, given that their magmatic regimes are quite distinct: Taapaca is a dome complex consisting of hybrid monotonous dacites hosting basaltic andesite enclaves; Parinacota is a compositionally complex stratocone comprising basaltic andesites to rhyolites. Thus, these volcanoes represent two distinct differentiation regimes, manifested by their different morphologies, monotonous vs. variable SiO_2 ranges, and additionally, amphibole- vs. pyroxene-bearing intermediate magmas.

This study addresses the rapidly developing research field of magmatic differentiation processes comprising magma generation, intracrustal ascent and storage. An integration of geochemical, statistical, and petrological approaches, the latter conducted by the Petrology Group of the Leibnitz University of Hannover headed by François Holtz, provides a consistent model of magmatic processes operating underneath Taapaca and Parinacota. The main outcomes of this work support numerous recent studies linking the volcanic and plutonic realm, as a key for understanding the formation evolution of magmatic systems (Reubi & Blundy, 2009) and the processes that lead to the observed petrologic diversity on our planet (Bachmann et al., 2007).

This work is divided in three main Chapters, presenting at first determination of the major and trace element compositions and geochemical character of magmas involved in the petrogenesis of Taapaca and Parinacota volcanic rocks (Chapter 2). Further Chapters trace the differentiation paths of these magmas, based on petrography, mineral chemistry, and intensive parameter of crystallization in Taapaca (Chapter 3) and Parinacota (Chapter 4) magmas.

Chapter 2

Searching for magmatic end-member compositions of mixed Taapaca magmas, comprising evidently more than two end-members, I applied a multivariate statistic procedure, a Polytopic Vector Analysis (PVA), designed for mixtures in geological environments where pure end-members themselves (can or) cannot be directly sampled (Johnson et al., 2002). PVA is a mathematical method that allows simultaneous application of the complete major and trace element datasets and determination of the number of magmatic end-members, their compositions, and their proportions in the hybrid magmas.

The statistical geochemical PVA modelling of Taapaca magmas reveals two distinct mafic mixing end-members and one uniform felsic magma composition: 1) a low-Mg high-Al calc-alkaline basaltic andesite (AEM), 2) an incompatible trace element enriched shoshonitic basalt (BEM), and 3) a high-K calc-alkaline, HREE-depleted rhyodacite (RDEM). The mixing proportions of each end-member in the Taapaca dacites and basaltic andesitic mafic enclaves reveal two-stage magma mixing. The first mixing stage produces hybrid baseline magmas consisting of the AEM and BEM. The second mixing stage represents shallow crustal magma mixing between the already mixed, mafic (AEM+BEM) and the silicic RDEM components. These compositions enclose nearly all Quaternary CVZ lavas in a mixing triangle and account for the entire compositional variability of the Quaternary volcanic rocks in the CVZ.

The PVA end-members represent distinct magma sources: the mantle wedge, enriched lithospheric mantle, and the continental crust, respectively. These end-members are expected to be ubiquitous in the central Andes and have uniform geochemical character. In Chapter 2, I propose a novel petrogenetic model for the Quaternary CVZ lavas.

This model shows that besides the paradigmatic type arc magma originating in the mantle wedge, two other components play a key role in the formation of highly enriched CVZ Quaternary volcanics. The highly enriched shoshonitic magma, reaching the surface as a clear component in the back arc setting, also strongly affect the volcanic arc lavas in the central Andes as a mixing component. The trace element characteristics of the rhyodacitic component, which is an equivalent of granodiorite, unravel geochemical signatures, which cannot be consistently explained by AFC processes of the arc basalt. This silicic component, termed the "*magic D"* by Gerhard Wörner (personal communication) shows, that generation of silicic magmas in the continental crust is obviously an essential process in the continental arcs, and links the volcanic and plutonic realms.

Chapter 3

The third Chapter deals with insights from geothermo-oxy-barometry (GTOB) results obtained from Taapaca rocks, examined in a connection with the experimental results carried out on a dacite composition from Taapaca, a basaltic andesite from Parinacota, and an andesite from Lascar volcano by Blum-Oeste (2014), Botcharnikov et al. (in prep.), and Stechern et al. (in prep.). The analysis of natural and experimental amphibole compositions allows an application of appropriate GTOB methods, which are available for amphibole crystallizing in the calc-alkaline magmas. Two distinct amphibole species, low-Al-Ti magnesiohornblende and high-Al-Ti magnesiohastingsite, which obviously crystallized from RDEM- and (BEM+AEM)-type magmas, respectively, yield surprisingly similar pressure range at 2-3 kbar, at different thermal conditions. This result is consistent with rejuvenation and remobilization mechanisms of cold and wet, crystal-rich silicic magmas, stagnating at shallow crustal depth by a hot mafic input, via magma mixing. Mafic magmas start to crystalize during underplating of the silicic magmas. Rapid cooling and mixing with the silicic material hinder olivine and pyroxene and promotes amphibole crystallization from the basaltic andesite recharge magma. Thus, the petrogenesis of monotonous Taapaca dacites represents a typical rejuvenation of small-volume proto-plutons.

Chapter 4

The fourth Chapter focuses on the chemical and petrographical variability of andesite lavas from Parinacota volcano, in relation to the edifice sector collapse. An occurrence of a debris avalanche deposit punctuates a shift toward less silicic magmas (mainly >60 wt% SiO_2) accompanied by a change in the prevailing Fe-Mg silicate phases in the Parinacota rocks, from amphibole to pyroxene. These changes have been previously connected to a mass unload affecting magmatic pressure in the volcanic plumbing system, thus, the differentiation path of post-collapse magmas (Wörner et al., 1988; Ginibre & Wörner, 2007). A study by Hora et al. (2009) presenting isotopic compositions of Parinacota magmas suggests that the changes in the plumbing system started before edifice sector collapse.

This study shows that both, major element compositions and mineral chemistry reveal progressive changes in the subvolcanic system, independent of the sector collapse. Moreover, other stratovolcanoes, which experienced edifice destruction, erupted - opposite to Parinacota - more silicic and amphibole-bearing lavas subsequently to the edifice collapse.

Adopting the model of Taapaca end-member magmas to Parinacota, we can explain observed changes in the SiO_2 content of the erupted lavas by a “cleaning “of the plumbing system form the silicic magmas. This is caused by an increasing mafic recharge, which has been recognized by Hora et al. (2009) in the pre-collapse lavas. Thus, the mixing proportions between the mafic and silicic magmas feeding simultaneously Parinacota plumbing system are responsible for the compositional variability of the erupted lavas.

The availability of the RDEM silicic magmas in subvolcanic systems determines also the mineralogy of the Fe-Mg phases in the intermediate magmas. Volcanic rocks from both neighboring Taapaca and Parinacota volcanoes show that amphibole and titanomagnetite are present in basaltic andesites, andesites and dacites that show geochemical evidence for mixing with a large proportion of the silicic RDEM magma. Other basaltic andesites and andesites of slightly different major element composition have ±olivine, pyroxene, titanomagnetite and ilmenite, while amphibole is absent. During magma mixing, a drop in temperature, an increase in the water content, and changes in the redox conditions of the (AEM+BEM) component destabilize olivine, pyroxene and ilmenite and promote amphibole + titanomagnetite crystallization in the hybrid magmas. Amphibole-bearing intermediate rocks thus form primarily by the hybridization of (AEM+BEM)+RDEM, whereas pyroxene-bearing rocks are differentiation products of dominantly AEM+BEM hybrids with minor RDEM admixture.

This model of “cleaning” of the plumbing system is consistent with experimental studies addressing the andesite petrogenesis in the subduction zones (e.g. Reubi & Blundy, 2009; Blatter et al. 2013). They emphasize the role of the silicic magmas - compositionally equivalent to our *magic D* - in the formation of the andesitic stratovolcanoes via magma mixing; fractionation-differentiation is not a dominant shallow crustal process leading to generation of intermediate magmas.

Lascar volcano

A comprehensive data set comprising P-T-fO_2-H_2O_{melt} conditions, obtained during this work from 15 samples of Lascar volcano, is included in Stechern et al. (in prep.).

Lascar is a young (<43 ka) composite volcano located in southern part of the CVZ (23°S), characterized by high-eruption rates (~0.8 km^3/ka) and andesitic to dacitic composition with prevailing two pyroxene assemblage (Gardeweg et al., 1998). Mineral chemistry and consequently physical conditions differ considerably from those of Taapaca and Parinacota. Plagioclase reaches An83, in contrast to the highest An63 found in Taapaca and Parinacota; amphibole is mainly high-Al low-Ti tschermakite, an amphibole species that do not occur at Taapaca and Parinacota. T-fO_2 conditions show generally slightly lower crystallization temperatures in more oxidized magmas; amphibole indicate higher water contents of the mafic component in comparison to Taapaca and Parinacota, and two pyroxene barometry reveals higher crystallization pressures.

The PVA results presented in Chapter 2 show that Lascar lavas are dominated by the AEM-type arc basaltic magmas, with a minor contribution of the BEM-type component. This observation suggests that compositional differences of the baseline lavas influence the mineral composition but the principal differentiation mechanisms are the same in all three investigated volcanoes.

References

Bachmann, O., Miller, C. F. & De Silva, S. L. (2007). The plutonic-volcanic connection as a stage for understanding crustal magmatism. *Journal of Volcanology and Geothermal Research* **167**, 1-23.

Blatter, D. L., Sisson, T. W. & Hankins, W. B. (2013). Crystallization of oxidized, moderately hydrous arc basalt at mid- to lower-crustal pressures: implications for andesite genesis. *Contributions to Mineralogy and Petrology* **166**, 861-886.

Blum-Oeste, N. (2014). Entgasung und Kristallisation beim Aufstieg dazitischer Magmen zur Erdoberfläche. *PhD Thesis*, *University of Göttingen*.

Botcharnikov, R., Stechern, A., Banaszak, M., Wörner, G. & Holtz, F. (**in prep.**). Experimental constraints on pre-eruptive conditions of Taapaca and Parinacota volcanoes, Central Andes.

Gardeweg, M. C., Sparks, R. J. S. & Matthews, S. J. (1998). Evolution of Lascar Volcano, Northern Chile. *Journal of Geological Society, London* **155**, 89-104.

Ginibre, C. & Wörner, G. (2007). Variable parent magmas and recharge regimes of the Parinacota magma system (N. Chile) revealed by Fe, Mg and Sr zoning in plagioclase. *Lithos* **98**, 118-140.

Hora, J. M., Singer, B. S., Wörner, G., Beard, B. L., Jicha, B. R. & Johnson, C. M. (2009). Shallow and deep crustal control on differentiation of calc-alkaline and tholeiitic magma. *Earth and Planetary Science Letters* **285**, 75-86.

Johnson, G. W. (2002). Principal components analysis and receptor models in environmental forensics, in: "An Introduction to Environmental Forensics", edited by B. L. Murphy and R.D. Morrison. *Academic, San Diego, California*, 461-515.

Reubi, O. & Blundy, J. (2009). A dearth of intermediate melts at subduction zone volcanoes and the petrogenesis of arc andesites. *Nature* **461**, 1269-1272.

Stechern, A., Banaszak, M., Botcharnikov, R., Holtz, F. & Wörner, G. (**in prep.**). Petrological and experimental constraints on the pre-eruptive conditions of 1993 Lascar andesites and the evolution of calc-alkaline intermediate lavas.

Wörner, G., Harmon, R. S., Davidson, J., Moorbath, S., Turner, D. L., McMillan, N., Nye, C., Lopez-Escobar, L. & Moreno, H. (1988). The Nevados de Payachata volcanic region (18°S/69°W, N. Chile) I. Geological, geochemical, and isotopic observations. *Bulletin of Volcanology* **50**, 287-303.

Dacite from Taapaca Volcanic Complex

Andean Central Volcanic Zone (18°S)

Photo: Nils Blum-Oeste

CHAPTER 2

End-member magma compositions from Taapaca Dome Complex and Parinacota Stratovolcano, 18°S, Central Volcanic Zone, N. Chile and their significance in the genesis of the Central Andean Quaternary magmas: Application of Polytopic Vector Analysis

ABSTRACT

The composition of primary mantle input into the crustal magma systems is poorly constrained in the Andean Central Volcanic Zone (CVZ) due to an absence of erupted basaltic lavas (<52 wt% SiO_2). The most mafic magmas found in Quaternary volcanic centers in the CVZ are rare basaltic andesite lavas (~52-54 wt% SiO_2 and ~4-9 wt% MgO), which constitute a set of "baseline" compositions.

Such baseline andesitic components affect the magma systems of Taapaca and Parinacota volcanoes, both located at 18°S in the CVZ. These compositions are variable in major and trace element contents, LILE/HFSE (Sr/Y: 20-160) and REE patterns (Sm/Yb: 2-12) given that their magmatic regimes are quite distinct: Taapaca is a dome complex consisting of hybrid monotonous dacites hosting basaltic andesite enclaves and Parinacota is a compositionally complex stratocone comprising basaltic andesite to rhyolite magmas. Taapaca dacites, however, fall on the same compositional trend formed by the broad range of Parinacota lavas.

Searching for magmatic end-member compositions in the mixed Taapaca magmas, comprising evidently more than two end-members, I applied a multivariate statistic procedure, a Polytopic Vector Analysis (PVA). This method is designed for mixtures in geological environments where pure end-members themselves (can or) cannot be directly sampled. PVA is a mathematical method that allows simultaneous application of the complete major and trace element datasets and determination of the number of magmatic end-members, their compositions, and their proportions in the hybrid magmas.

The PVA yields a nearly complete major and trace element compositions of basaltic (BEM), basaltic andesitic (AEM) and rhyodacitic (RDEM), three common end-member magmas involved in petrogenesis of Taapaca and Parinacota lavas. They represent shoshonitic, high-Al calc-alkaline and high-K calc-alkaline magmatic series, respectively. These geochemically distinct end-members represent near primary magma compositions, which require separate magma sources, representing three main subduction environments: lithospheric mantle, asthenospheric mantle and the crust, respectively.

Olivine compositions found in the baseline lavas of Parinacota volcano, contrasting in trace element signatures, form two distinct forsterite (Fo)-Ni trends with compositionally and texturally defined initial Fo contents. The initial Fo81 in olivines form high-LILE/HFSE lavas corresponds to calculated olivine Fo80 in equilibrium with high-LILE/HFSE shoshonitic PVA end-member; the

initial Fo76 in olivines from low-LILE/HFSE lavas corresponds to the same value obtained from low-LILE/HFSE high-Al calc-alkaline PVA end-member. Thus, the statistical end-members are confirmed by petrological observations in the natural rocks.

The PVA results provide a novel petrogenetic model for the CVZ lavas, including three distinct magma series, an alternative model to the broadly accepted MASH-model, involving only one mantle-derived arc magma, which undergoes extensive differentiation processes in the crust. This study shows that petrogenesis of the geochemically variable CVZ Quaternary arc lavas is mainly based on two-stage mixing processes: 1) a magma mixing between high-Al calc-alkaline and shoshonitic components producing the baseline mafic magmas; 2) a magma mixing between the mafic, hybrid baseline and crustal magmas generating the andesites and dacites, compositions which dominate the Quaternary CVZ arc volcanoes.

1. INTRODUCTION

The composition of primary arc magmas in the Andean Central Volcanic Zone (CVZ) is strongly affected by complex multi-stage differentiation processes, commonly connected to the enormous thickness of the crust (e.g. Davidson et al., 1990) reaching up to 70 km in the central part of the CVZ (e.g. James, 1971a; Isacks, 1988; Allmendinger et al., 1997; Prezzi et al., 2009). The volumetrically dominant compositions of the Central Andean lavas are highly differentiated andesites to rhyodacites (Thorpe et al., 1984; Stern et al., 2004 and references therein). Primitive basalts (SiO_2<50 wt%, MgO>8 wt%) have not been found in the Quaternary Central Andean volcanic arc (Davidson & de Silva, 1995; Kay et al., 1999). Consequently, identification of the primary melts involved in the generation of the intermediate magmas in the CVZ is particularly complicated.

Several examples of the most mafic Quaternary eruptive products in the CVZ comprise: minor eruptive centers close to Puntas Negras (23.5°S) volcano (50.5 wt% SiO_2, Déruelle, 1994), monogenetic cones adjacent to Cerro Galan (25.5°S) caldera (52.3 wt% SiO_2, Thorpe et al., 1984), San-Francisco-Incahuasi (27°S) cinder cones (53.5 wt% SiO_2, Kay et al., 1996a), Cerro Overo (23°S) maar eruption (54.2 wt% SiO_2, Thorpe et al., 1984), as well as flank lava flows at Parinacota volcano (53 wt% SiO_2, Wörner et al., 1988) and mafic enclaves found e.g. in the Taapaca dacites (52 wt% SiO_2, Clavero et al., 2004). These basaltic andesite magmas are considered to be parental magmas, evolved from the Andean mantle-derived primary melts, overprinted by crustal components. As broadly accepted, according to a MASH (Melting-Assimilation-Storage-Homogenization) concept described by Hildreth & Moorbath (1988), these magmas underwent extensive modification by the MASH-processes in the deep crust or crust-mantle boundary where they reach the *baseline* - the same parental composition from which further differentiation takes place. However, these parental magmas and their differentiation in the shallow crust cannot account for the variability of the intermediate magmas in the Central Andes (Davidson et al., 1990, 1991).

The large compositional variability is a typical feature of the subduction-zone magmatism. A broad spectrum of magmas erupted in the volcanic arcs worldwide represent three major magma series, tholeiitic, calc-alkaline and alkaline (Wilson, 1989). Each of these series can comprise compositions ranging from basalt to rhyolite, showing generally poor correlation with the isotopic compositions (Hildreth, 2007). The striking geochemical diversity of the intermediate magmas produced in the subduction-zone environments led to distinct petrogenetic concepts, involving subducted oceanic lithosphere, mantle and/or continental lithospheric realms, as possible magma sources (e.g. Eichelberger, 1978; Kay, 1978; Gill, 1981; Thorpe et al., 1981, 1982, 1984; Hildreth & Moorbath, 1988; Defant & Drummond, 1990; Tatsumi & Eggins, 1995; Yagodzinski et al., 1995; Carmichael, 2002; Annen et al., 2006; Straub et al., 2008; Reubi & Blundy, 2009).

A generation model of intermediate beside basaltic melts presented by Straub et al. (2008, 2011, and 2013) involves infiltration of the sub-arc mantle by silicic slab components, forming compositional continuum from basalts to dacites, modified by shallow fractional crystallization and recharge magma mixing to produce a broad spectrum of andesitic and dacitic magmas.

An alternative model views the lower crust as a “second-order” source for intermediate and silicic magmas generated by MASH and AFC (assimilation and fractional crystallization, DePaolo, 1981b) processes in the “Deep Crustal Hot Zone” (DCHZ), proposed by Annen et al. (2006, 2008) and improved by Solano et al. (2012). In the Hot Zone, the evolved magmas develop from incomplete crystallization of the mantle-derived basaltic melts during stagnation in the lower crust or crust-mantle boundary, due to a rheological trap. The residual melts from the mafic magmas interact with crustal partial melts in different proportions, depending on fertility of the mantle-derived melts and crust composition, emplacement rates and emplacement geometry of the mafic magmas (Annen et al., 2008).

Lithospheric magmagenesis based on partial melting of the crustal and/or underplated basaltic material related to an elevated thermal gradient in the crust, caused by long-term injections of the hot mantle-derived magma is considered to be a primary mechanism responsible for a generation of intermediate to silicic crustal melts. The partial melting of the crust explains occurrence of high-volume monotonous intermediate magmas forming crystal-rich ignimbrite eruptions (Hildreth, 1981, 2004; Wolff & Gardner, 1995; Bachmann et al., 2002). Moreover, dehydration-melting of amphibole-bearing lower arc crust is postulated as a common chemical and physical differentiation mechanism generating primary silicic (granitic) melts and is related to compression and reheating during crustal thickening (Brown, 1994; Petford & Atherton, 1996; Petford et al., 2000; Corney et al., 2001 and references therein). The release of silicic melts, their addition to the upper crust and formation of dense crustal roots of the lower arc crust presents an important process in the maturing subduction zones. Rejuvenation and remobilization processes of near-solidus silicic upper-crustal silicic magma bodies (crystal mush) by more mafic magma shortly before eruption are broadly discussed mechanisms of production of intermediate magmas by Bachmann et al. (2002), Bachmann & Berganz (2006), Huber et al. (2009), (2010a), (2010b), (2012), and Ruprecht et al. (2012).

Reviewing the compositions of melt inclusions trapped in phenocrysts together with host whole rock chemistry of arc magmas, Reubi & Blundy (2009) show that bimodal compositions recorded by the melt inclusions, separated by a remarkable gap between 55-71 wt% SiO_2, imply bimodality of the primary arc melts ascending from the lower crust. Hence, the effective and common mingling and mixing processes of mafic and evolved melts within the upper crust are responsible for generation of erupted intermediate compositions. They also emphasize the role of the MASH-derived silicic melts (≥66 wt% SiO_2) beneath intermediate arc volcanoes, which is obscured by the abundance of mingled andesite magmas (Eichelberger, 1978).

Looking at the Quaternary magmatism in the Cascades (Hildreth, 2007), the distinctive types of relatively primitive erupted magmas indicate coexistence of large- and small-degree partial melts from different depths and varied source materials and ascent paths in subduction zones. Therefore, the identification of end-member compositions involved in the evolution of the magmatic systems is of prime importance for tracing the magma differentiation paths generally. The Neogene magmas erupted in the Central Andes occur: 1) in the volcanic arc as high-K and medium-K calc-alkaline stratovolcanoes and 2) in the back-arc setting as high-K calc-alkaline, shoshonitic and OIB-type minor centers. An increasing alkalinity of magmas away from the trench observed in island arcs (Dickinson, 1975) is also apparent in the Andean CVZ (Kay et al., 1994, 1999; Matteini et al., 2002; Acocella et al., 2011); however, low-K (tholeiitic) magmas are absent, as commonly observed in mature arcs (Wilson, 1989).

The differentiation and magma mixing processes operating simultaneously or successively on different magma stagnation levels and geochemical environments overprint the final eruptive products with a range of geochemical signatures. Consequently, the identification of the primary magma composition using traditional quantitative two (mafic and silicic) end-member mass balance or AFC (assimilation fractional crystallization) procedures cannot account for the pronounced geochemical variability observed often within individual petrographic units. Even in the case of the simplest binary magma mixing, a number of assumptions are required. In most cases, the modeling gives inconsistent results obtained for different geochemical variables. The classical mass balance models rather examine compositional relations using presumed end-member compositions or end-member proportions, instead of precise mathematical estimation of the magmatic end-member compositions and their proportions in the differentiated magmas. Use of geochemical modeling to validate petrologic processes commonly involves only a subset of whole rock analyses: bivariate plots of selected elements, element ratios or isotopic ratios. Thus, by performing simple mixing calculations using least squares method, the question arises ‘is it possible to use all measured elements in one calculation algorithm without making any prior assumptions about the compositions of the end-members?’ This question leads to the use of multivariate statistical methods, involving all measured chemical variables simultaneously.

Polytopic Vector Analysis (PVA) is based on initial works of Imbrie (1963), Klovan & Imbrie (1971), Klovan & Miesch (1976), Miesch (1976a, 1976b) and improved by Full et al. (1982), Ehrlich & Full (1987) and Johnson et al. (2002). The PVA is an oblique factor analysis procedure that allows determination of a number of end-members, their compositions, and proportions from geochemical data sets representing mixtures. The unique advance of the PVA algorithm is the applicability to geological environments where the pure end-members themselves can or cannot be directly sampled, i.e. the compositions of end-members are not required. Further improvement of the PVA procedure presented by Vogel et al. (2008) and applied by Tefend et al. (2007) and Deering et al. (2008) allows evaluation of magma mixing and fractional crystallization in volcanic systems.

The PVA algorithm provides an appropriate statistical approach for intermediate rocks that result mainly from the magma mixing processes. The Taapaca Volcanic Complex located in the Andean Central Volcanic Zone (CVZ) offers an opportunity to investigate the end-member compositions involved in the mixing process using the PVA method, because petrographic and mineral chemical features clearly indicate simple binary mixing between mafic and silicic components, characterized by only negligible role of fractional crystallization (details in Chapter 3). However, geochemical properties of the Taapaca mafic enclaves, contrasting in LILE and HFSE contents suggest more than two mixing components. Furthermore, a compositional sub-trend identified in the Taapaca dacites suggests also a second silicic end-member, which cannot be identified from the classical mass balance. The primary melt composition(s) producing the geochemically distinct basaltic andesite enclaves were heretofore unidentified, since the primitive magmas do not occur in the CVZ. Thus, these basaltic andesite enclaves serve as mixing end-members in the mass balance modeling. Nonetheless, they represent themselves, to a certain extent, differentiated or hybrid magmas. In this case, the PVA method, which does not require any end-member composition in the calculation algorithm or any other assumptions, provides a remarkable improvement of the geochemical modeling of the magmatic system, where the mixing end-member magmas have never erupted. The purpose of the PVA study presented here are: 1) to determine the number, compositions, and mixing proportions of the end-member magmas involved in the petrogenesis of Taapaca rocks and 2) to explain the origin of these end-member compositions.

The most mafic compositions found at Taapaca, distinct with respect to variable trace element signatures, are also present at neighboring Parinacota volcano as single flank eruptions. They have been also recognized as parental magmas recorded in plagioclase zoning found in Parinacota lavas (Ginibre & Wörner, 2007). Both volcanoes form markedly overlying whole rock compositional trends supported by similar amphibole and plagioclase chemistry. A broad compositional range of Parinacota lavas, overprinted distinctly by fractionation, would require extensive PVA study, which is beyond the scope of this study. For this reasons, I have involved only olivine from the most mafic Parinacota lavas to this statistical-geochemical study, to trace the early petrological evolution of the distinct mafic magmas and to validate the calculated end-member compositions from olivine-free Taapaca rocks.

The results of the multivariate statistical geochemical modeling presented in this study reveal, for the first time ever, entire major and a majority of the trace element compositions of magmas that most probably account for the complete compositional variability occurring in the Quaternary volcanic centers in the CVZ. Because primary magma compositions had not previously been clearly identified for the Central Andean magmatic systems, these results are a significant step toward an understanding of the petrogenesis of the Central Andean magmatic systems.

2. POLYTOPIC VECTOR ANALYSIS

Polytopic Vector Analysis (PVA) is a multivariate statistical technique developed explicitly for analyzing mixed species in geological systems. The PVA is based on Q-Mode factor analysis and Principal Component Analysis (PCA), which enable the information preserved in a large number of variables to aid interpretation of the behavior of multivariate data. The purpose of this method used in geochemistry and petrology is to utilize a comprehensive whole rock database into a model wherein each analyzed rock sample is viewed as a mixture of a possibly small number of potential end-members. Johnson et al. (2002) outlined the entire PVA algorithm based on numerous modules explained in detail in a series of publications (Klovan & Imbrie, 1971; Full et al., 1981, 1982). On the basis of major and trace element contents, where the samples tend to have constant row sums (problem described by Miesch, 1976), the PVA method generates three basic parameters which are satisfactory for description of any mixed system: 1) the number of end-members (sources), 2) the composition of each end-member (signature of each source), and 3) the relative proportions of each end-member (source) in every sample (the proportions of the end-members sum to 1.0 within each sample).

The calculation algorithm of the polytopic *vector analysis* involves the eigenvector decomposition models, resolved in terms of oblique vectors, in contrast to the *factor analysis*, which uses orthogonal axes. The oblique vectors resolve the number of end-members (sources) for mixed species, giving the name “Vector Analysis”. Considering that the end-members form a set of oblique axes, the relationship of these axes is visualized by a relation to orthogonal axes generated by the VARIMAX solution presented by Full et al. (1981). The VARIMAX space provides a framework, a geometric figure termed as *polytope* (geometric object which exists in any number of dimensions, giving the name “polytopic”), for examining the relationships of the end-members. The vertices of the polytope represent the end-members in the *k*-1 dimensions (*k* determine the number of end-members). Thus, three-dimensional space forming three end-members system requires a two-dimensional polytope, the triangle. Accordingly, the PVA can evaluate systems that require more than three dimensions, where all data are constrained to *k*-1 dimensional space within *k*-space.

In the factor analysis, the extraction of the factor-number (end-members in the PVA) is based on the evaluation of eigenvalues of the eigenvectors, representing the factors/end-members, using different criteria for determining their number. For instance, the *Kaiser-criterion* drops all factors with eigenvalues below 1.0; the *scree*-plot, showing the eigenvalues in their decreasing order, recommends selection of the number of factors above the “elbow” in the plot. The PVA algorithm provides an essential improvement of the factors/end-members extraction in comparison to the Q-mode and PCA. It includes *coefficients of determination (CDs)* developed by Miesch (1976) and Klovan & Miesch (1976) that evaluate goodness-of-fit on a variable-by-variable basis, rather than for the whole data set in one step as by the *Kaiser* or *scree* tests. The *CDs*, called also Klovan/Miesch Coefficients of Determination (KMCD) calculated for each variable represent the ratio between the variance associated with a specific variable (measured concentrations of an oxide/element) and the back-calculated equivalent-value (concentrations) using *k*-end-member solution. Hence, the KMCDs evaluate the consistency of a *k*-end-member model by presenting the back-calculated versus measured values of each variable (oxide or element) so that they provide a measure similar to the conventional r^2 as defined by least squares linear regression. The KMCD-values are based on the variation associated with the diagonal function f(x)=x and not on the best-fit function of the measured and back-calculated values.

A unique feature of the PVA is the DENEG operation integrated into the PVA. Developed by Full et al. (1981), this operation allows the end-members to be resolved without a priori knowledge of their composition. Using iterative systematic enlargement and rotation of the polytope axes, the DENEG operation moves the edges of the initial polytope, parallel to the original edge orientation to enclose all data points. This leads to the determination of new vertices representing the expected, unknown end-member compositions, which are not represented in the database.

3. VOLCANOLOGICAL BACKGROUND

Taapaca Volcanic Complex (TVC) is a dacitic dome complex (35 km³) located on the western edge of the Altiplano, in the Andean Central Volcanic Zone, Northern Chile (Figure 1). This potentially active volcano lies west of the main volcanic chain, 30 km west of Parinacota volcano at 18°S (Wörner et al., 1988; Davidson et al., 1990; Bourdon et al., 2000; Ginibre & Wörner, 2007; Hora et al., 2007, 2009). The eruptive history of the TVC is presented by Kohlbach & Lohnert (1999) and refined by Clavero et al. (2004).

The Taapaca dome complex started its eruptive history ~1.5 Ma ago with an initial andesitic phase (stage 1) which formed shield-like stratocone. Since 1.46 ±0.07 Ma, the oldest $^{40}Ar/^{39}Ar$ age obtained from dacite samples (Clavero et al. 2004), Taapaca has generated exclusively monotonous dacites characterized by uniform petrography and mineral chemistry. The morphological evolution of TVC in stages 2 to 4 started with the construction of a stratovolcano of steeply-dipping flanks (stage 2) which changed at 0.5 Ma ago to small-volume lava domes and block-and-ash flow deposits (stage 3). The eruptive activity of TVC culminated by the extrusion of voluminous domes and associated block-and-ash flows. Since 0.47 Ma Taapaca has formed the modern morphologically composite part of the TVC edifice, characterized by frequent edifice collapse events marked by numerous debris avalanche deposits (stage 4).

The dacites are highly crystalline rocks containing mainly >20 vol% of plagioclase, amphibole, biotite and Fe-Ti oxides and host up to 5 vol% microcrystalline basaltic andesite enclaves and up to 4 vol% sanidine megacrysts (Clavero, 2002). Although the dacites show homogeneity at the millimeter scale, textural and mineral chemical evidence for magma mixing indicate mixing as a main petrogenetic process operating in the TVC.

Taapaca and Parinacota are two morphologically distinct volcanoes showing remarkably overlapping trends for major and trace elements, isotopic composition and mineral chemistry (Figure 2). In contrast to monotonous intermediate eruptive products of Taapaca, Parinacota erupted a broad compositional and petrographic variety of lavas during its 163 ka eruptive history. Parinacota volcano (46 km³) is a younger of two stratovolcanoes forming the Nevados de Payachata volcanic region located on the western Altiplano (18°S), on the North Chile-Bolivia border area. The detailed study of Parinacota eruptive chronology and geochemical studies are presented by Wörner et al. (1988), Davidson et al. (1990), Clavero et al. (2004), and Hora et al. (2007, 2009). A striking change from amphibole-bearing to generally amphibole-free Parinacota eruptive products is punctuated by voluminous edifice sector collapse, accompanied by compositional shift to more mafic lavas.

The initial eruptive phase consists of effusion of Chungara andesites (163-117 ka) forming the base of the modern Parinacota edifice. After ~60 ka hiatus, Parinacota built an "Old Cone", a unit consisting of a complex of stratocone and coulees accompanied by simultaneous emplacement of a rhyodacite-rhyolite unit, the Dome Plateau (47-40 ka). The pre-collapse units show a compositional range from mafic andesite to rhyolite; the post-collapse lavas are restricted to basaltic andesite and andesite. The stratocone failed 20-15 ka ago by a single gravitational edifice sector collapse, which produced a ~6 km³ debris avalanche deposit. A minor basaltic andesite amphibole-free lava flow found in the youngest unit of the Old Cone, akin to post-collapse "Young Cone" lavas, suggests the reconfiguration of the plumbing system starting already before the edifice collapse (see Chapter 4 for details). The recent conical shaped stratocone results from a rapid reconstruction of the edifice, forming the andesitic Young Cone unit (~8 ka-recent), accompanied by andesite (Middle and High Ajata Flows) and basaltic andesite (Lower and Upper Ajata Flows) flank eruptions. The latter, basaltic andesite units erupted from a line of flank vents, together with the Old Cone basaltic andesite lavas represent the most mafic lavas found in the Parinacota region. These olivine-bearing rocks of contrasting Sr, Ba concentrations, REE patterns, and isotopic compositions relate in composition to the olivine-free Taapaca mafic enclaves (Figure 2).

Figure 1.
Topographic map showing location of Taapaca and Parinacota volcanoes at 18°S and some other volcanic centers of the CVZ. Inset to the left presents the position of the CVZ relative to the Northern, Southern and Austral Volcanic Zones. The most mafic lava compositions found in the CVZ are marked by black triangles (Chiar Kkollu, Porunita, Cerro Overo, Incahuasi).

4. SAMPLES AND METHODS

4.1. DATA SOURCES

The major and trace element analyses of Taapaca volcano used for the PVA calculations comprise different data sets: 1) CAL-sample series presented by Clavero (2002), and 2) TAP-samples series representing a data compilation of numerous studies carried out at the Geoscience Centre Göttingen. The latter include unpublished data of Kohlbach (1999), Banaszak (2007), Kiebala (2008) and analyses carried out in this study. The whole rock data set of Parinacota volcano includes CAL-samples analyses of Clavero (2002), PAR-samples of Hora et al. (2007) and unpublished whole rock data PAR-samples of Entenmann (1994), Table A (Appendix) presents the whole rock compositions used in PVA calculation procedures.

4.2. GEOCHEMICAL AND PETROGRAPHIC CHARACTERISTICS OF THE SAMPLES

4.2.1. TAAPACA VOLCANIC COMPLEX (TVC)

Clavero et al. (2004) present the detailed stratigraphy and basic geochemical characteristics of Taapaca volcano. A comprehensive petrological and geochemical study of the TVC is presented in Chapter 3 of this work and is summarized below.

Taapaca started its eruptive history with porphyritic, two-pyroxene andesites. After the initial phase, Taapaca generated petrographically uniform dacites in the range of 62-67 wt% SiO_2. The mineral assemblage of the dacites comprises two populations of plagioclase (An22-49, Fe<2000 ppm and An30-57, Fe 1800-4200 ppm), two amphibole populations (low-Al-Ti magnesiohornblende and high-Al-Ti magnesiohastingsite), biotite, Fe-Ti oxides, apatite, titanite, zircon, and sanidine megacrysts, reaching up to 12 cm in length. The sanidine hosts only one population of plagioclase and one population of amphibole inclusions: low-Fe plagioclase and low-Al-Ti magnesiohornblende. All Taapaca dacites contain fine-grained basaltic andesitic mafic enclaves (MEs) ranging from 52 to 60 wt% SiO_2, composed of titanomagnetite and single populations of the high-Fe plagioclase and high-Al-Ti magnesiohastingsite. Besides a number of textural disequilibrium features found in the dacites, the distinct plagioclase and amphibole populations implicate magma mixing between sanidine bearing silicic and basaltic andesitic end-members.

The compositions of the Taapaca dacites show characteristic scatter for numerous elements such as Al, Na, K, Ti, P, Sr, Ba, Zr as well as compatible elements Cr, Ni, Co (Figure 4 and Figure 5) There is a main-trend and a sub-trend (*subgroup*) recognized in the dacites from the whole rock composition. The basaltic andesite enclaves form either an uniform mixing trend for Sr, Ni, Zr or separate groups in Ti, P, Na, Al, Ba, Cr vs. SiO_2 plots. Based on the variable Sr concentrations and Sr/Y ratios, the mafic enclaves are divided into three groups: 1) >1200 ppm and 2) 800-1200 ppm Sr, both termed as *high-Sr MEs*; 3) <800 ppm, termed as *low-Sr MEs*.

Examining the REE patterns (Figure 2d), the high- and low-Sr MEs show distinct Sm/Yb ratios, which must reflect different parental magmas. The LREE of the dacites plot between compositions of the high- and low-Sr MEs but HREE of the dacites show markedly lower values than all the Taapaca MEs (Figure 2). Thus, the marked HREE depletion of the dacites suggests magma mixing between the mafic magmas and the silicic end-member, which must be strongly depleted in HREE, and having high Sm/Yb ratios.

Based only on the geochemical, petrographic and mineral chemical observations, Taapaca samples indicate that the dacites result from mixing between two mafic and the silicic end-member. The simple mixing modeling presented in Chapter 3, based on a connection between basaltic andesite enclaves and their host dacites reveal an array of mixing lines, which converge to a rhyodacitic composition identified as the silicic magma mixing end-member. However, the simple mixing modeling shows broad compositional range for some elements, suggesting more than one silicic end-member. Therefore, the application of the multivariate statistical method that uses simultaneously all available major and trace element compositions is expected to reveal an existence of end-members, which cannot be obtained from the classical method.

4.2.2. GEOCHEMICAL RELATIONSHIP OF TAAPACA AND PARINACOTA MAFIC MAGMAS

The mafic enclaves hosted in the Taapaca dacites show a range of geochemical signatures related to two geochemically distinct basaltic andesite flank vents eruptions of Parinacota. These Parinacota most mafic lavas are characterized by contrasting TiO_2, P_2O_5, Sr, Ba, and Zr concentrations, REE patterns, LILE/HFSE, LREE/HREE, MREE/HREE and isotopic composition (e.g. Davidson et al., 1990; Hora et al., 2009). It is necessary to mention that the extreme geochemical differences observed for the Taapaca basaltic andesite MEs are significantly more pronounced in the Taapaca basaltic andesite enclaves compared to the Parinacota basaltic andesite lavas, especially for HFSE

(TiO_2, Zr, Hf), LILE (Sr, Ba, Na_2O, K_2O), HREE and Al_2O_3, Ni and Cr (Figure 2 and Figure 4). Moreover, Taapaca mafic enclaves show a range of compositions that suggest mixing trend between these two mafic end-members, particularly visible for Sr, Ba, Ni and Zr as well as in the continuous REE patterns.

4.2.3. PARINACOTA VOLCANO

The stratigraphic, geochemical and petrographic characteristics of Parinacota Volcano are described in detail by Wörner et al. (1988), Davidson et al. (1990), Ginibre & Wörner (2007), Hora et al. (2007, 2009) as well as presented in detail in Chapter 4 of this work.

A marked geochemical similarity of the Parinacota basaltic andesite lavas with the Taapaca mafic enclaves (Figure 2, Figure 4 and Figure 5) is assumed to result from similar magmatic sources. Therefore, in this study we use the textural and chemical characteristics of olivines found in Parinacota basaltic andesite lavas to evaluate and test the end-member compositions obtained from PVA for Taapaca volcano, which lacks olivine in its eruptive products. Here, we adopt the term “high-Sr” and “low-Sr” basaltic andesites for magmas showing distinct trace element signatures, high- and low-LILE/HFSE and high- and low-LREE/HREE ratios, respectively, following the description by Wörner et al. (1988) and Ginibre & Wörner (2007).

The olivine compositions are taken from basaltic andesites representing three Parinacota units: 1) pre-collapse Old Cone low-Sr basaltic andesites (unit OCba, introduced additionally in Chapter 4 to the stratigraphic units of Hora et al., 2007), 2) post-collapse low-Sr Lower Ajata flow (unit a2), and 3) post-collapse high-Sr Upper Ajata (unit a3).

The fine-grained and glomerophyric (OCba)-lavas (56.5 wt% SiO_2) consist mainly of plagioclase, clinopyroxene, orthopyroxene and magnetite phenocrysts. Olivine is a minor phenocrystic phase, and it occurs also as anhedral inclusions in clinopyroxenes, altered cores with complex sequences of peritectic rims, and olivine-agglomerates mantling orthopyroxene. The fine-grained Lower Ajata (a2) lavas (56.4 wt% SiO_2) contain olivine and clinopyroxene as main pheno- and microcrysts phases. Plagioclase occurs only as microcrysts and microlites. Orthopyroxene, resorbed large plagioclase, and quartz are rare and represent xenocrystic assemblage. The (a2) lavas show a significant amount of amphibole microcrystic remnants, completely replaced by its breakdown products. Although (OCba) and (a2) low-Sr lavas differ petrographically by higher crystallinity, more pronounced disequilibrium features in olivines and higher abundance of the orthopyroxene in the pre-collapse (OCba) unit, both units overlap exactly in their olivine compositions for trace elements in a range of Fo81-65. In contrast, the high-Sr Upper Ajata lavas (a3), (53.3 wt% SiO_2), which erupted from the same flank vent as in the Lower Ajata (a2) unit, are fine grained olivine-clinopyroxene-phyric. They contain euhedral olivines and clinopyroxenes in a continuous crystal size-range. Plagioclase occurs only as microlites. The composition of the large olivine phenocrysts overlap with those found in the low-Sr lavas, but the rims of the phenocrysts and smaller olivine crystals in the (a3) are limited to Fo74, forming separate trends for all trace elements in olivine.

The two distinct compositional olivine trends for major and trace elements related to the low- and high-Sr Parinacota lavas comprising all morphological types of olivine (Figure 16) are the most spectacular feature found in the Parinacota basaltic andesite lavas.

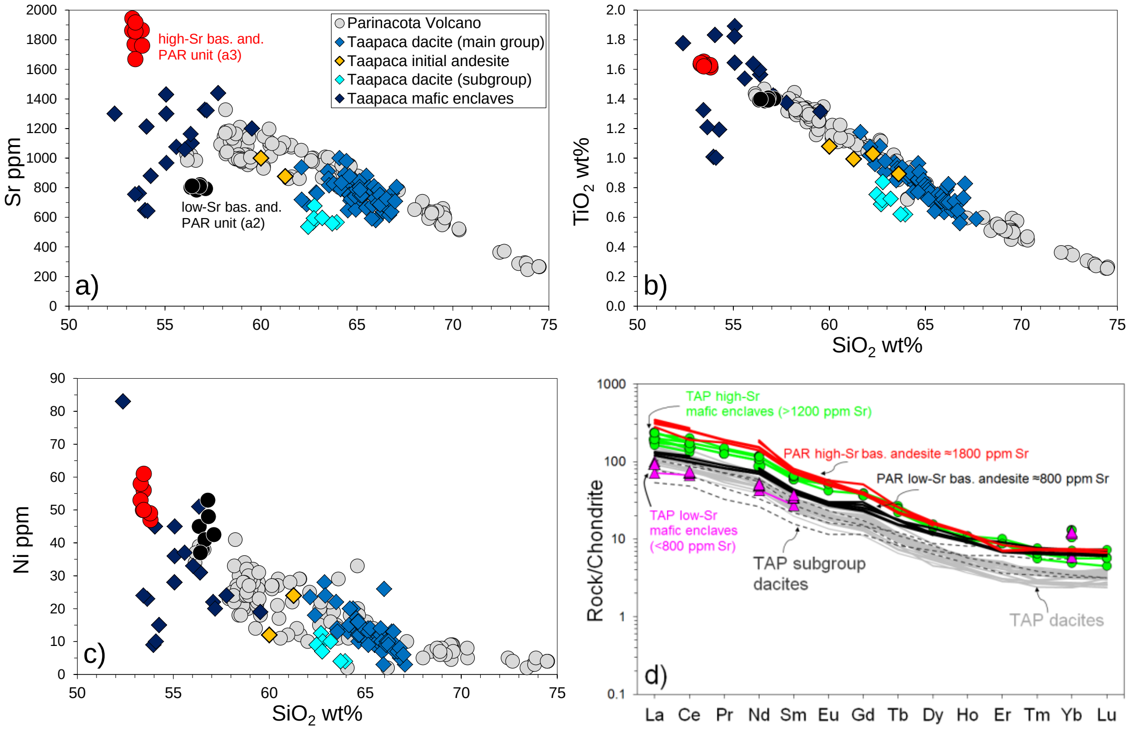

Figure 2. *Representative major and trace element compositions in* ***a)-c)*** *and rare earth element (REE) patterns in* ***d)*** *of Taapaca and Parinacota eruptive products show almost overlapping compositional trends in the* SiO_2 *range >58 wt%. The basaltic andesites (<57* SiO_2 *wt%) from both volcanoes reveal analogous geochemical variations, assumed to result from similar magmatic sources. TAP – Taapaca, PAR – Parinacota.*

4.3. ANALYTICAL METHODS

Major and trace element compositions of the TAP samples were determined by X-ray fluorescence spectroscopy (XRF) and inductively coupled plasma mass spectrometry (ICPMS) at Geoscience Centre Göttingen using standard measurement procedures, described by Kohlbach (1999), Banaszak (2007), and Kiebala (2008). Whole rock analyses of the CAL-samples presented by Clavero (2002) were carried out at the Chilean Geological Survey laboratories: absorption spectrometry (AAS) was used for major elements and inductively coupled plasma-atomic emission spectrometry (ICP-AES) were used for trace elements. The Taapaca whole rock compositions representing five studies and two different analytical methods do not show any systematic deviation for any analyzed element. Furthermore, a comparison of two samples, PAR-15 (Parinacota dataset Chapter 4) and CAL-164B, demonstrating one characteristic eruption, a white ash fall deposit from Parinacota volcano, show differences in whole rock composition ± 0.6 wt% for SiO_2 and <0.2 wt% for other major elements. Consequently, both TAP- and CAL-series can be simultaneously used in the statistical PVA modeling.

Measurements of olivine compositions were performed by wavelength-dispersive X-ray spectroscopy (WDS) electron microanalysis using a five-spectrometer JEOL JXA 8900 Superprobe at Geoscience Centre Göttingen. A standard quantitative silicate analysis program comprising Si, Ti, Al, Fe, Mn, Mg, Ca, Na, K, extended by Cr and Ni was used at 15 kV, 15 nA at 10 µm probe diameter. The olivine compositions were determined during several measurement sessions, therefore the analyses vary with respect to the number of determined elements. Selected elements (Na, K, Ti, Cr, Ni) were excluded from the measuring program depending on a main phase analyzed during a measurement session. The peak/background counting times were 15/5 s for major elements and 30 /15 s, for trace elements. During exclusive olivine measuring sessions Ti, K and Na were excluded and the peak counting times were 15 s for major elements (Mg, Fe, Si) and 30 s for trace element (Mn, Ca, Ni, Cr, Al); 5s and 15 s counting times for background, respectively. The calibrations were conducted on olivine (San Carlos) for Mg and Si, hematite for Fe, rhodonite for Mn, wollastonite for Ca, garnet (KAK) for Al, NiO for Ni, Cr_2O_3 for Cr, TiO_2 for Ti, albite for Na and sanidine for K. Resulting analysis have a statistical precision of ±1%. Variations in the peak counting times used during different measurement sessions do not result in any compositional deviations. Phi-rho-Z matrix correction procedure of Armstrong (1995) was used. The Backscattered electron (BSE) images were taken at the same voltage and initial probe current conditions as the quantitative measurement conditions.

4.4. STATISTICAL METHOD: THE PVA CALCULATION PROCEDURE

4.4.1. DATA SETS USED IN THE PVA

The available whole rock data for Taapaca are not complete for all elements. For this reason, the PVA calculations were carried out on three different data compilations giving basis for three different calculation models: 1) PVA model (43e-36s) comprises the highest number of geochemically relevant record of 43 elements for 36 samples, 2) PVA model (25e-8p) is based on eight available dacite – mafic enclave pairs for 25 elements, and 3) PVA model (23e-73s) represents the highest number of samples, comprising 23 elements available for 73 samples. It is worth noting, that the first model has a higher number of variables than samples, the second model has nearly equal number of variables and samples, and the third model has much lower number of variables than samples.

The whole rock analysis for the PVA were used in weight percent (wt%) for all major, minor and trace elements, due to normalization to the sum of 100 performed by the PVA. Fe was used as FeO^{TOT} (measured FeO + measured Fe_2O_3 converted to FeO).

4.4.2. PVA MODULES AND CALCULATION CONDITIONS

The polytopic vector analysis was performed using a PVA software package version 8.06 (2003) by R. Ehrlich, C&E Associates, Salt Lake City, Utah. The PVA software is composed of two modules: I) the **VSPACE** (*vector space*) module used to estimate the number of the end-members, and II) the **PVA** module used to calculate the compositions and relative proportions of the end-members.

4.4.2.1. The VSPACE module

The VSPACE module performs the Q-MODE factor analysis of the (whole rock) data. The data input consists of ASCII files in which each column carries a variable (analyte = oxide or element) and each row represented the whole rock data for a given sample.

The output provides: 1) general statistics such the mean, the standard deviation, the maximum and minimum values of the variables (analytes) of the raw and transformed data, 2) mathematical criteria for estimation of the number of end-members such eigenvectors and eigenvalues as well as the Klovan/Miesch Coefficients of Determination (KMCD), and 3) prepares appropriate matrix that are used as input to the main PVA module.

The essential part of the VSPACE is an estimation of the number of end-members. The first procedure was an examination of the eigenvectors associated with meaningful and non-random variability of the data, which were inspected graphically using the conventional scree-plots. The main procedure of the end-member extraction was based on the inspection of the KMCD-values presented as *Johnson CD (JCD) plots* in the VSPACE panel. The JCD-plots show original (measured) versus by *k* end-member solution predicted (calculated) compositions of the analytes. If all points represent perfectly back-calculated values, they lie on a diagonal of the plot and indicate the KMCD values equal 1. A point scatter results in KMCD<1 and indicate lower precision of a given *k* end-member model for a particular analyte. This graphic tool allows efficient variable-by-variable (analyte-by-analyte) assessment of the “pro and contra” of choosing a certain number of end-members. Moreover, the JCD-plots allow identification of outlying samples. In this way, it is possible to eliminate from the analysis any anomalous samples representing analytical errors or mistakes in a data entry. In this study, a table-bar chart of the KMCD-values, including the number of factors/end-members and variables (analytes), was created to simplify the graphic visualization of the KMCDs (Table 2).

4.4.2.2. The PVA module

The PVA module is the proper polytopic vector analysis. It consists of a complex algorithm to determine the size and to fit the orientation of the polytope that encloses the data cloud at the given number *k* of end-members estimated in the VSPACE module, where the input file to the PVA module is created. The PVA module requires a setting of starting parameters for: A) an initialization algorithm, which creates an initial polytope and B) the DENEG procedure to determine non-negative values of the analyte-contents and mixing-proportions.

The number of end-members *k* determines the number of vertices and *k*-1 dimension of the polytope. The PVA software package includes seven options for choosing the initial size and the orientation of the initial polytope. A detailed discussion about the initial polytope options is given by Johnson et al. (2002) and references cited therein. In this study, the EXTENDED- and VARIMAX-initialization options were used as recommended for extreme (not included in the data set, or rather not erupted) end-member compositions expected from the analyzed samples suite. The “EXTENDED” is a default option in the PVA which selects the most extreme samples in the *k* end-member solution as the initial trial vertices of the initial polytope. The "VARIMAX" sets the reference axes of the initial polytope on the maximum variance of the squared loadings of the *k* end-member (factor in the factor analysis) solution. The VARIMAX initialization for the model (25e-8p) and (23e-73s) converged more rapidly than EXTENDED and resulted in more extreme end-member compositions. The model (43e-36s), where the number of variables is higher than the number of the samples, the VARIMAX initialization resulted in a lack of convergence therefore an EXTENDED initialization was chosen.

The polytope in the *k* end-member space must meet three criteria which are performed by the "DENEG"-operation in the PVA module: 1) the polytope vertices (end-members) are non-negative (non-negative concentrations), 2) all of the sample vectors are enclosed by the polytope (non-negative mixing proportions), and 3) some sample vectors must plot on edges, faces or vertices of the polytope. The DENEG is an iterative procedure. In each iteration, it moves the polytope edges outward in chosen length values to define new vertices, and rotates them to change negative values to zero. It enlarges and rotates the initial polytope until the criteria 1) to 3) are fulfilled, that is, the analysis converge all negative values to zero. If the DENEG operation does not converge, the DENEG-values can be changed. These values define how far the polytope can expand in a single iteration and can be modified as long as the program announces that the convergence occurred. The DENEG-values are generally >0 and <1, but may also be as larger, if required for convergence. In this study a default value of 0.25 were used in the model (23e-73s) and (25e-8p) which reached convergence in 449 and 166 iterations, respectively. The model (43e-36s) required smaller DENEG-value of 0.01 to converge in iteration 453. Three additional adjustable parameters in the DENEG panel allow specification of the conditions to terminate the iterations because of slow convergence: COMC – greatest allowable negative value in end-member composition, DENC – greatest negative value allowed in the mixing proportions, and VACUT – VARIMAX iteration cutoff. In this study, the lowest in the PVA software allowable value of 0.0001 was used for the COMC, DENC and VACUT.

The final output data of the PVA panel comprise the end-member compositions and the mixing proportions in each sample.

5. RESULTS

The presented results comprise the number, compositions of the end-members and their mixing proportions in each sample. Due to the incomplete whole rock data set for Taapaca samples, the PVA modeling has been performed on three data sets: 1) model (43e-36s), 2) model (25e-8p) and 3) model (23e-73s), as described in the section 4.1.

5.1. NUMBER OF END-MEMBERS

The extraction of the end-member number involved in the magma mixing process is based on both previous geochemical-petrological study and multivariate statistical methods. The petrographic features reveal one mafic and one silicic end-member. The geochemical data indicates two mafic and apparently more than one silicic end-member.

Mathematically, the common approach to extract the number of factors/end-members in multivariate statistics is to generate *eigenvalues* by Principal Component Analysis (PCA) that represent the variance accounted for each underlying factor/end-member. The *eigenvalues* for the selected data sets used in three PVA models for Taapaca samples (Table 1) show that the first three *eigenvalues* account for >90% of the variance. Additional factors/end-members have relatively small *eigenvalues* and can be related to further components but do not represent principal end-members accounting for the main variability in the mixing system.

Table 2 provides the Klovan-Miesch coefficients of determination (KMCDs) for each analyte, relatively to the number of end-members in the PVA models. The KMCDs increase for each variable with increasing *k*-number of end-members in the models. The most significant increase of the KMCDs for most variables is observed by addition of the third end-member. An addition of more than three end-members to the model causes generally only a small increase of the KMCDs and significant increase for only few elements (Nb, Ta, Th, and U). As explained by Miesch (1976), in the conventional factor analysis, *common factors/end-members* responsible for main processes or effects, cause variability in more than one variable. In contrast, *oblique factor/end-members* cause a large increase in only one variable. The addition of an end-member to satisfy whole variability in the system (all KMCDs above any satisfactory value) would lead to a creation of inexistent end-members (oblique factor). Due to a general rule of the satisfactory KMCD-values (Deering et al., 2008), the KMCD values >0.5 for an analyte support a certain end-member solution, >0.7 values give a strong support, and >0.9 a very strong support. The variability of the KMCDs for particular elements such Na_2O, MnO and Zr observed in the Taapaca data set, are also reported in other PVA-studies (Miesch, 1976; Deering et al., 2008; Vogel et al., 2008). The low KMCD-values for these elements may be explained by e.g. a compositional variability of these elements between samples depending on the variable amounts of the particular minerals in the single samples (Deering et al., 2008).

As presented in Table 2, the KMCD-values obtained in this study for the three end-member solution provide strong to very strong support for 70% of the elements in the model (43e-36s), 84% elements in the model (25e-8p) and 74% elements in the model (23e-73s). The elements showing KMCD>0.7 are labeled yellow in the Table 2. The three end-member solution is also supported by *Kaiser-criterion* accepting eigenvalues >1.

Table 1. *Number of eigenvectors and eigenvalues for three selected data sets. Model 43e-36s is based on 43 elements and 36 samples; Model 25-8p is based on 25 elements and 8 dacite – mafic enclave pairs; and Model 23e-73s is based on 23 elements, 73 samples.*

No. Eigenvector (PVA EM)	Model 43e-36s		Model 25e-8p		Model 23e-73s	
	Eigenvalue	Cum. Variance %	Eigenvalue	Cum. Variance %	Eigenvalue	Cum. Variance %
1	30.2553	84.04	15.3974	73.32	60.8484	83.35
2	2.6803	91.49	3.4221	89.62	7.6572	93.84
3	0.9388	94.1	1.3975	96.27	2.0763	96.69
4	0.4786	95.43	0.251	97.47	0.655	97.58
5	0.3975	96.53	0.1463	98.16	0.4424	98.19
6	0.2639	97.26	0.1077	98.68	0.2663	98.56
7	0.2386	97.93	0.0806	99.06	0.2065	98.84
8	0.185	98.44	0.0483	99.29	0.1654	99.07
9	0.1109	98.75	0.0442	99.5	0.1519	99.27
10	0.0816	98.97	0.0338	99.66	0.1028	99.41
11	0.0781	99.19	0.024	99.78	0.0981	99.55
12	0.058	99.35	0.0157	99.85	0.0767	99.65
13	0.0507	99.49	0.0108	99.9	0.0624	99.74
14	0.0376	99.6	0.0066	99.93	0.0492	99.81
15	0.0281	99.67	0.0062	99.96	0.0384	99.86
16	0.0236	99.74	0.0029	99.98	0.0316	99.9
17	0.0195	99.79	0.0024	99.99	0.0205	99.93
18	0.016	99.84	0.0012	100	0.0167	99.95
19	0.0132	99.88	0.0007	100	0.0121	99.97
20	0.0125	99.91	0.0002	100	0.0104	99.98
21	0.0093	99.94	0	100	0.0055	99.99
22	0.0066	99.95			0.0039	100
23	0.0044	99.97			0.0024	100
24	0.0033	99.98				
25	0.0027	99.98				
26	0.0019	99.99				
27	0.0013	99.99				
28	0.0009	99.99				
29	0.0006	100				
30	0.0005	100				
31	0.0003	100				

Table 2. *Coefficients of determination (KMCDs) of the model (25e-8p), (23e-73s) and (43e-36s) based on Klovan/Miesch principle. The KMCD-values are similar to the conventional r² known from the least squares linear regression and represent ratios between the variance associated with the measured and by PVA back-calculated concentrations. The blue bars are scaled from 0 to 1. Yellow labeling selects KMCD≥0.7, which give strong support to the three-end-member solution in the PVA.*

Model 25-8p	Number of end-members								
Analyte	2	3	4	5	6	7	8	9	10
SiO2	0.88	0.99	0.99	0.99	0.99	0.99	1	1	1
TiO2	0.35	0.98	0.98	0.98	0.99	1	1	1	1
Al2O3	0.52	0.84	0.87	0.91	0.97	0.97	0.97	0.97	0.97
FeO	0.91	0.99	0.99	0.99	0.99	0.99	1	1	1
MnO	0.81	0.92	0.96	0.96	0.99	0.99	0.99	0.99	0.99
MgO	0.82	0.95	0.96	0.96	0.97	0.97	0.99	0.99	1
CaO	0.96	0.96	0.97	0.98	0.98	0.98	0.98	0.98	0.98
Na2O	0.75	0.92	0.92	0.93	0.97	0.98	0.98	0.97	0.98
K2O	0.78	0.93	0.95	0.95	0.98	0.98	0.98	0.98	0.99
P2O5	0.09	0.79	0.91	0.93	0.95	0.96	0.98	0.98	0.98
Nb	-0.01	0.37	0.46	0.93	0.92	0.96	0.97	0.99	1
Zr	-0.02	0.44	0.66	0.77	0.78	0.93	0.96	0.99	0.99
Y	0.75	0.73	0.92	0.92	0.96	0.96	0.96	0.96	0.99
Sr	0.05	0.92	0.96	0.98	0.98	0.99	1	1	1
Rb	0.76	0.92	0.94	0.96	0.96	0.97	0.99	0.99	0.99
Zn	0.5	0.87	0.86	0.87	0.87	0.92	0.93	0.99	0.99
Ni	0.14	0.63	0.81	0.8	0.81	0.82	0.95	0.95	0.98
Co	0.72	0.86	0.86	0.87	0.87	0.87	0.95	0.95	0.99
Cr	0.13	0.28	0.89	0.9	0.92	0.92	0.98	0.98	0.98
V	0.54	0.91	0.93	0.93	0.94	0.97	0.98	0.99	0.99
Ba	0.03	0.81	0.94	0.94	0.94	0.95	0.97	0.97	0.98
Sc	0.76	0.84	0.9	0.9	0.91	0.92	0.96	0.97	0.98
La	-0.02	0.8	0.92	0.93	0.98	0.98	0.98	0.98	0.98
Ce	-0.02	0.77	0.91	0.93	0.97	0.97	0.99	0.99	0.99
Nd	0.04	0.85	0.9	0.92	0.97	0.97	0.98	0.99	0.99

Model 23-73	Number of end-members								
Analyte	2	3	4	5	6	7	8	9	10
SiO2	0.93	0.99	0.99	0.99	0.99	0.99	0.99	0.99	1
TiO2	0.6	0.94	0.95	0.96	0.97	0.97	0.97	0.98	0.98
Al2O3	0.37	0.54	0.6	0.91	0.91	0.96	0.96	0.99	0.99
FeO	0.95	0.99	0.99	0.99	0.99	0.99	0.99	0.99	0.99
MnO	0.84	0.85	0.85	0.86	0.94	0.94	0.95	0.96	0.97
MgO	0.91	0.94	0.94	0.98	0.98	0.98	0.98	0.98	0.98
CaO	0.95	0.95	0.95	0.96	0.98	0.98	0.98	0.99	0.99
Na2O	0.5	0.66	0.92	0.94	0.97	0.97	0.98	0.98	0.98
K2O	0.81	0.9	0.97	0.97	0.97	0.97	0.97	0.97	0.97
P2O5	0.36	0.83	0.86	0.95	0.95	0.95	0.95	0.96	0.97
Nb	0.09	0.37	0.37	0.5	0.74	0.75	0.8	0.93	0.93
Zr	0.02	0.59	0.59	0.69	0.69	0.86	0.89	0.9	0.89
Y	0.74	0.74	0.81	0.84	0.87	0.88	0.9	0.91	0.94
Sr	0.22	0.92	0.93	0.94	0.94	0.94	0.97	0.97	0.97
Rb	0.81	0.86	0.89	0.89	0.9	0.9	0.91	0.91	0.93
Ni	0.37	0.66	0.75	0.73	0.79	0.87	0.88	0.88	0.9
Co	0.76	0.84	0.85	0.87	0.87	0.88	0.94	0.97	0.99
Cr	0.32	0.42	0.42	0.56	0.72	0.78	0.85	0.85	0.91
V	0.81	0.89	0.89	0.9	0.91	0.94	0.94	0.98	0.98
Ba	0.01	0.75	0.84	0.89	0.89	0.9	0.9	0.91	0.95
La	0.02	0.78	0.93	0.93	0.95	0.96	0.97	0.97	0.97
Ce	0.05	0.86	0.93	0.94	0.95	0.95	0.96	0.98	0.98
Nd	0.16	0.91	0.95	0.95	0.96	0.98	0.98	0.98	0.98

Continued Table 2

Model 43-36	Number of end-members								
Analyte	2	3	4	5	6	7	8	9	10
SiO2	0.93	0.95	0.97	0.97	0.98	0.99	0.99	0.99	0.99
TiO2	0.64	0.95	0.96	0.97	0.98	0.98	0.99	0.99	0.99
Al2O3	0.35	0.7	0.72	0.74	0.73	0.87	0.92	0.92	0.94
FeO	0.94	0.95	0.97	0.98	0.98	0.98	0.99	0.99	0.99
MnO	0.67	0.66	0.7	0.7	0.74	0.84	0.93	0.94	0.94
MgO	0.82	0.81	0.84	0.86	0.86	0.97	0.98	0.98	0.98
CaO	0.9	0.85	0.89	0.9	0.9	0.96	0.98	0.99	0.99
Na2O	0.41	0.78	0.79	0.79	0.79	0.82	0.89	0.9	0.91
K2O	0.71	0.75	0.87	0.89	0.93	0.93	0.95	0.95	0.95
P2O5	0.49	0.97	0.97	0.97	0.97	0.98	0.98	0.98	0.98
Nb	0.37	0.56	0.71	0.72	0.74	0.79	0.79	0.82	0.89
Zr	0.23	0.81	0.86	0.86	0.87	0.88	0.92	0.95	0.95
Y	0.62	0.68	0.73	0.77	0.77	0.77	0.78	0.79	0.79
Sr	0.32	0.82	0.87	0.87	0.89	0.9	0.9	0.96	0.97
Rb	0.73	0.86	0.92	0.92	0.94	0.94	0.94	0.94	0.95
Zn	0.67	0.72	0.74	0.77	0.78	0.81	0.89	0.91	0.92
Ni	0.33	0.74	0.78	0.8	0.83	0.84	0.86	0.86	0.88
Co	0.66	0.76	0.76	0.79	0.82	0.82	0.86	0.88	0.9
Cr	0.5	0.6	0.64	0.66	0.72	0.72	0.81	0.88	0.89
V	0.67	0.79	0.79	0.82	0.89	0.91	0.92	0.95	0.95
Ba	0.03	0.58	0.81	0.82	0.84	0.84	0.86	0.9	0.92
Sc	0.67	0.73	0.77	0.89	0.91	0.95	0.96	0.96	0.97
Li	0.05	0.26	0.54	0.55	0.73	0.88	0.96	0.97	0.97
Cu	0.09	0.1	0.35	0.71	0.8	0.93	0.97	0.97	0.97
La	0.13	0.65	0.72	0.86	0.88	0.92	0.92	0.94	0.97
Ce	0.23	0.7	0.79	0.88	0.91	0.94	0.95	0.96	0.97
Pr	0.28	0.79	0.85	0.92	0.95	0.97	0.97	0.97	0.98
Nd	0.31	0.81	0.86	0.91	0.95	0.97	0.97	0.97	0.98
Sm	0.44	0.88	0.91	0.94	0.97	0.97	0.97	0.97	0.98
Eu	0.48	0.87	0.94	0.94	0.96	0.96	0.96	0.98	0.98
Gd	0.54	0.75	0.85	0.92	0.92	0.93	0.94	0.94	0.94
Tb	0.7	0.84	0.94	0.95	0.96	0.96	0.96	0.97	0.97
Dy	0.87	0.88	0.91	0.91	0.97	0.98	0.98	0.99	0.99
Ho	0.81	0.84	0.9	0.9	0.96	0.96	0.97	0.97	0.97
Er	0.79	0.87	0.93	0.93	0.97	0.98	0.98	0.98	0.98
Tm	0.68	0.81	0.84	0.83	0.95	0.95	0.97	0.97	0.98
Yb	0.59	0.86	0.89	0.88	0.97	0.97	0.98	0.98	0.99
Lu	0.53	0.78	0.86	0.86	0.95	0.95	0.96	0.96	0.98
Hf	0.21	0.51	0.57	0.78	0.82	0.81	0.88	0.9	0.9
Ta	0	0.05	0.06	0.68	0.74	0.74	0.75	0.9	0.95
Pb	0.57	0.62	0.66	0.67	0.69	0.72	0.75	0.81	0.89
Th	-0.02	0	0.08	0.4	0.66	0.78	0.92	0.95	0.96
U	0.19	0.19	0.18	0.28	0.55	0.8	0.86	0.86	0.87

5.2. PVA END-MEMBER COMPOSITIONS

The major and trace element compositions of three Taapaca end-members obtained from the three calculation models based on three different sample- and analyte-numbers are given in the Table 3 and are presented in Figure 4, Figure 5, and Figure 6, together with the whole rock data available from the studies of Taapaca and Parinacota mentioned in 4.1 of this study.

The PVA yields end-members of basaltic (BEM), basaltic andesitic (AEM) and rhyodacitic (RDEM) compositions. There are noticeable differences in the PVA outcome depending on the selective data sets used for the calculations in the three models, as presented for instance in the Sr-SiO_2 space in Figure 3. The SiO_2 contents of the PVA end-members show 3 to 4 wt% difference in a range of 45 to 48 wt% for BEM, 55 to 58 wt% for AEM and 69 to 73 wt% for RDEM. Sr concentrations vary from 1700 to 2390 ppm for BEM, 244 to 716 ppm for AEM and 438 to 858 for RDEM. Different shapes of the triangles formed by the PVA end-members result simply from the chosen plotting parameters. These compositional differences of the PVA end-members indicate that the sample selection and/or an availability of the samples, providing representative compositional spectrum of the natural mixing system, is obviously superimposed on the precision of the determination of the mixing end-members in the PVA, expressed by the KMCD-values. For these reason, the PVA results achieved from the Taapaca mixing system provide a compositional approximation of the real magmas, not absolute major and trace element contents.

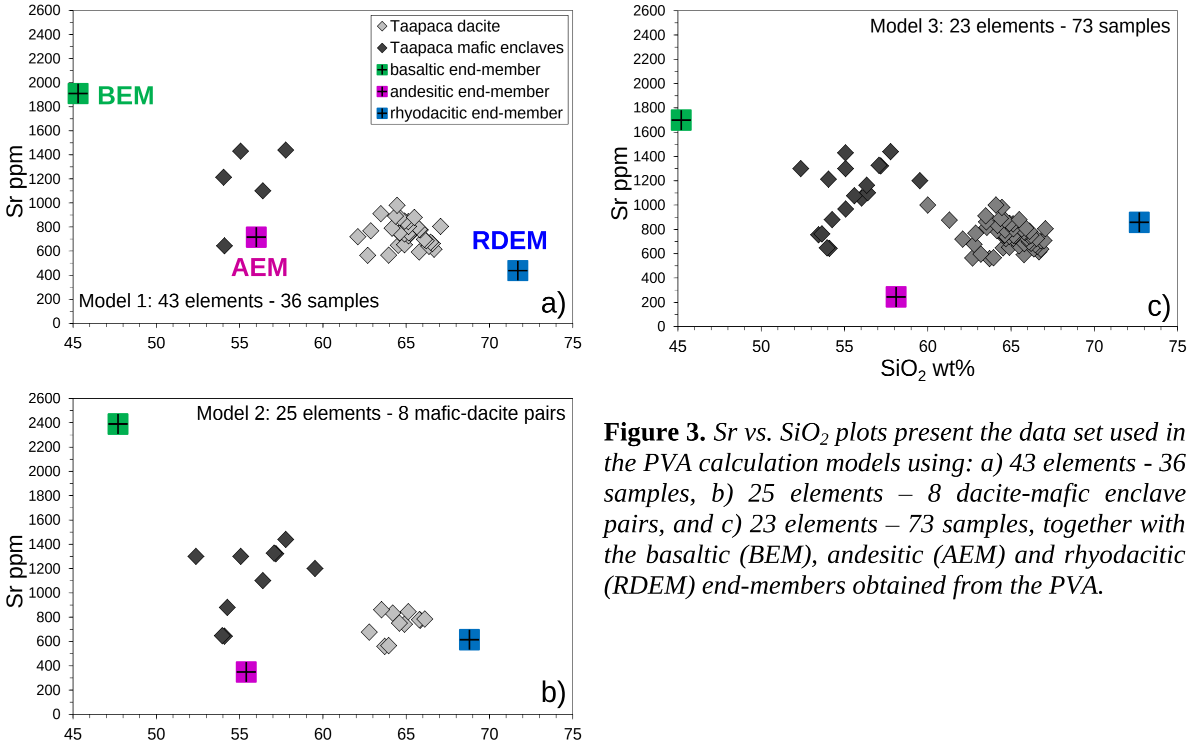

Figure 3. *Sr vs. SiO$_2$ plots present the data set used in the PVA calculation models using: a) 43 elements - 36 samples, b) 25 elements – 8 dacite-mafic enclave pairs, and c) 23 elements – 73 samples, together with the basaltic (BEM), andesitic (AEM) and rhyodacitic (RDEM) end-members obtained from the PVA.*

It has to be mentioned, that the modeling based on the Taapaca whole rock data carried out for more than three end-members does not always converge to geologically reliable end-member compositions. An addition of further end-members improve the KMDC-values (Table 2); nonetheless, the PVA models for *k*=4 yield consistently the same rhyodacitic RDEM end-member at about 70 to 74 wt% SiO$_2$ and separates the mafic compositions into diverse andesitic, basaltic andesitic, basaltic end-members which show zero-concentrations for numerous elements. At *k*>4, the PVA reveals rather extreme silicic (>75 wt% SiO$_2$) or very low SiO$_2$ and even SiO$_2$-free compositions. While SiO$_2$ contents decrease in some models to 35 wt% and Sr and Ba exceed 4000 ppm, the MgO contents of some mafic PVA end-members do not exceed ~9 wt%, which would be rather expected for more mafic compositions. Some PVA models, (not presented in this work), contain mainly Si, Al, Na, K, Ba, Rb - compositions corresponding to feldspars. Such end-members suggest possible sanidine accumulation in some samples. The PVA calculations carried out for a high number of end-members (k>5), which results in satisfactory KMCD values >0.8 for all oxides/elements, reveal compositions, which cannot be related to any minerals or rocks. Therefore, the end-members in *k*>4 PVA models for Taapaca samples do not represent realistic compositions.

Hence, the PVA results give statistical evidence that Taapaca is fed by only three principal end-members responsible for the generation of the monotonous dacite lavas through nearly entire eruptive history of this volcano. By viewing the PVA end-members with regard to the whole Taapaca and Parinacota data set, presented in the Figure 4 and Figure 5, the model (25e-8p) including only the dacite samples and their basaltic andesite enclaves, comprises in a mixing triangle the most extreme high-Sr basaltic andesite Parinacota lavas as well as the most extreme low-Sr Taapaca mafic enclaves. Therefore, the model (25e-8p) may provide the most reliable results, which represent magma compositions involved in the petrogenesis of Taapaca and Parinacota rocks.

The RDEM represents a rhyodacite in the composition range between 68 to 72 wt% SiO_2, depending on the used volume of the database. The array of mixing lines used in the simple mixing modeling, presented in the Chapter 3 of this work in Figure 18 converges at the same SiO_2-range. For comparison, the results of the simple mixing modeling based on a linear regression analysis (SiO_2 independent variable) are given in Table 3. It should be noted, that the simple mixing modeling yields the composition of the rhyodacitic end-member if the basaltic andesitic enclaves are assumed as mafic end-members in the mixing system.

Inferring from previous petrographic and geochemical studies of the Taapaca dacites, that the RDEM composition corresponds to the highly differentiated sanidine-bearing magma characterized by very low concentrations of $MgO<1$ wt%, $FeO<3$ wt%, $CaO<3$ wt%, $TiO_2<0.6$ wt%, $P_2O_5<0.3$ $Ni<10$ ppm and $Cr<20$ ppm. This composition generally meets the Parinacota rhyodacite-rhyolite trend. The RDEM composition obtained from the PVA model (25e-8p) shows the best fit to the natural rhyodacite samples. Compositional divergence observed between the model (43e-36s) and (23e-73s) and the natural compositions may reflect either the small differences between Taapaca and Parinacota whole rock trends or may result from lower KMCD-values in comparison to the model (25e-8p).

The REE pattern of the RDEM, illustrated in Figure 6, overlaps with the most depleted Taapaca light REE (LREE) patterns from La to Nd and shows a strong depletion in the middle (MREE) and heavy REE (HREE) range, from Sm to Lu, relatively to the natural Taapaca samples. REEs of the RDEM form a pattern similar to some most evolved Parinacota rocks of 72-74 wt% SiO_2 (Figure 6b). However, the RDEM is characterized by a stronger depletion in HREE from Tb to Lu in comparison to the mentioned samples.

The BEM and AEM represent end-members, which are considerably distinct from the natural lavas sampled in the Taapaca-Parinacota region. The BEM reveals an alkali-rich basalt of ~47 wt% SiO_2 characterized by low MgO ~6.5 wt% and marked by enrichment in selective LILE (Sr, Ba), HFSE (Ti, Zr, Hf) and LREE relatively to AEM and RDEM. The AEM is a basaltic andesite to mafic andesite of 55-58 SiO_2 wt% which differs significantly from the basaltic andesite and andesite in Taapaca and Parinacota whole rock trends, especially for Al_2O_3, Na_2O, K_2O, TiO_2, P_2O_5, Sr, Ba, Ni and Zr concentrations (Figure 4 and Figure 5). The AEM shows the lowest contents of the LILEs, HFSEs and LREEs in the Taapaca mixing system. The REE pattern of the AEM is nearly unfractionated. The BEM and AEM end-members meet at the HREEs where the AEM even shows slight enrichment in Yb and Lu relatively to the BEM (Figure 6). These contrasting REE patterns of BEM and AEM generally mimic the high-Sr and low-Sr Taapaca mafic enclaves, respectively.

The geochemical characteristics and geological significance of the PVA end-members is discussed in section 6 of this study.

Table 3. *End-member (EM) compositions obtained from the PVA using different data sets for modeling. Compositions of the rhyodacitic end-member obtained from the simple mixing modeling, presented for comparison, are based on 8 mafic-dacite pairs or 79 samples. RDEM – rhyodacite end-member; BEM – basaltic end-member; AEM – basaltic andesitic end-member. * - denotes assumed SiO_2 contents in the simple mixing modeling.*

	Model 43-36			Model 25-8p			Model 23-73			*Simple mixing modeling*			*Simple mixing modeling*		
	43 analyte 36 samples			25 analyte 8 mafic silicic pairs			23 analyte 73 samples			*8 dacite-mafic enclaves pairs*			*79 samples*		
analyt	RDEM	BEM	AEM	RDEM	BEM	AEM	RDEM	BEM	AEM	*rhyodacite end-member*			*rhyodacite end-member*		
SiO2 wt%	717	45.3	56.0	68.8	47.7	55.4	72.7	45.2	58.1	68*	69*	70*	68*	70*	72*
TiO2	0.23	2.57	109	0.53	2.77	0.72	0.53	2.43	0.65	0.59	0.53	0.47	0.54	0.37	0.19
Al2O3	15.9	17.1	19.0	16.0	15.1	19.1	14.8	17.2	18.7	16.1	16.0	15.9	16.1	16.0	15.9
FeO	14	11.1	7.8	2.7	9.8	8.2	0.7	11.5	7.2	2.9	2.5	2.2	2.8	2.1	13
MnO	0.04	0.14	0.12	0.05	0.08	0.17	0.00	0.15	0.14	0.05	0.05	0.04	0.05	0.04	0.03
MgO	0.2	6.5	3.6	0.8	6.6	4.3	0.0	6.8	3.7	0.9	0.6	0.4	10	0.6	0.1
CaO	19	10.0	6.8	2.8	8.7	7.7	11	10.0	6.8	3.0	2.7	2.3	3.1	2.5	2.0
Na2O	4.8	4.0	3.2	4.6	4.5	2.9	5.2	3.8	3.1	4.6	4.6	4.7	4.5	4.5	4.6
K2O	3.6	18	19	3.4	3.0	14	4.5	16	15	3.4	3.5	3.6	3.5	3.7	3.8
P2O5	0.05	104	0.31	0.17	102	0.10	0.22	0.87	0	0.20	0.19	0.17	0.15	0.08	0.01
Nb ppm	3	17	10	7	12	5	7	12	5	6.9	6.9	6.8	5.4	4.6	3.9
Zr	130	304	145	156	314	92	193	246	86	161	161	161	154	147	139
Y	4.2	22.6	22.7	7.4	17.2	23.6	0.0	25.5	20.9	7.9	7.1	6.4	6.6	5.0	3.4
Sr	438	1910	716	615	2390	349	858	1700	244	667	639	610	647	564	481
Rb	120	0	68	109	0	62	122	0.00	69	107	111	115	103	111	120
Zn	53	149	105	61	181	82				60	56	52	65	57	49
Ni	0	60	16	3	78	0	6	61	5	3	1	-2	6	1	-3
Co	0	47	27	6	34	22	0	41	22	7	5	4	7	5	2
Cr	0	100	52	12	124	45	0	114	38	8	3	-1	11	2	-7
V	36	282	163	67	322	143	32	300	151	76	67	59	71	53	36
Ba	852	1670	762	976	2270	204	1420	1440	170	985	986	986	990	961	932
Li	35	25	0							5	4	3	4	3	1
Sc	0	16	15	5	11.4	30.1				26	26	26	32	33	34
Cu	26	59	43							6.7	7.0	7.2	6.8	7.4	8.1
La	17	69	20	24	96	0.5	42.3	62.1	0	25	25	24	28	26	24
Ce	30	154	49	49	189	7	78	126	0.408	50	48	46	53	48	43
Pr	3.1	19.5	5.7							5.2	5.0	4.8	5.3	4.5	3.6
Nd	10.8	77.5	218	19.8	98.1	5.2	33	68.8	0.341	20.5	19.2	17.9	22.6	19.1	15.6
Sm	160	13.50	4.62							3.2	3.0	2.7	3.2	2.3	15
Eu	0.30	4.01	131							0.87	0.81	0.75	0.80	0.55	0.31
Gd	0.99	11.20	5.30							2.6	2.4	2.2	2.5	19	12
Tb	0.07	129	0.68							0.27	0.24	0.22	0.25	0.16	0.07
Dy	0.43	5.46	3.68							127	113	0.98	116	0.79	0.42
Ho	0.11	0.80	0.70							0.22	0.20	0.17	0.21	0.15	0.10
Er	0.15	2.18	2.20							0.49	0.39	0.30	0.47	0.30	0.13
Tm	0.03	0.23	0.26							0.07	0.06	0.05	0.06	0.05	0.03
Yb	0.23	136	192							0.32	0.21	0.10	0.33	0.15	-0.02
Lu	0.04	0.19	0.27							0.07	0.06	0.05	0.07	0.05	0.04
Hf	2.31	6.76	2.76							2.9	2.8	2.7	2.7	2.4	2.0
Ta	0.25	0.86	148							0.46	0.47	0.48	0.36	0.33	0.30
Pb	214	7.7	13.0							18	18	18	19	20	22
Th	5.28	8.93	9.56							6.2	6.3	6.3	6.4	6.5	6.6
U	2.66	153	142							2.5	2.6	2.7	2.6	2.8	3.0

Figure 4. ***Next page:*** *Major element compositions of the Taapaca end-member magmas obtained from the PVA. In blue RDEM (rhyodacitic end-member), in green BEM (basaltic end-member) and in violet AEM (bas. andesitic end-member) presented with the complete whole rock data set of Taapaca and Parinacota volcano. (43e-36s), (25e-8p) and (23e-73s) denote calculation models based on 1) 43 elements and 36 samples; 2) 25 elements and 8 dacite-mafic enclave pairs, and 3) 23 elements and 73 samples.*

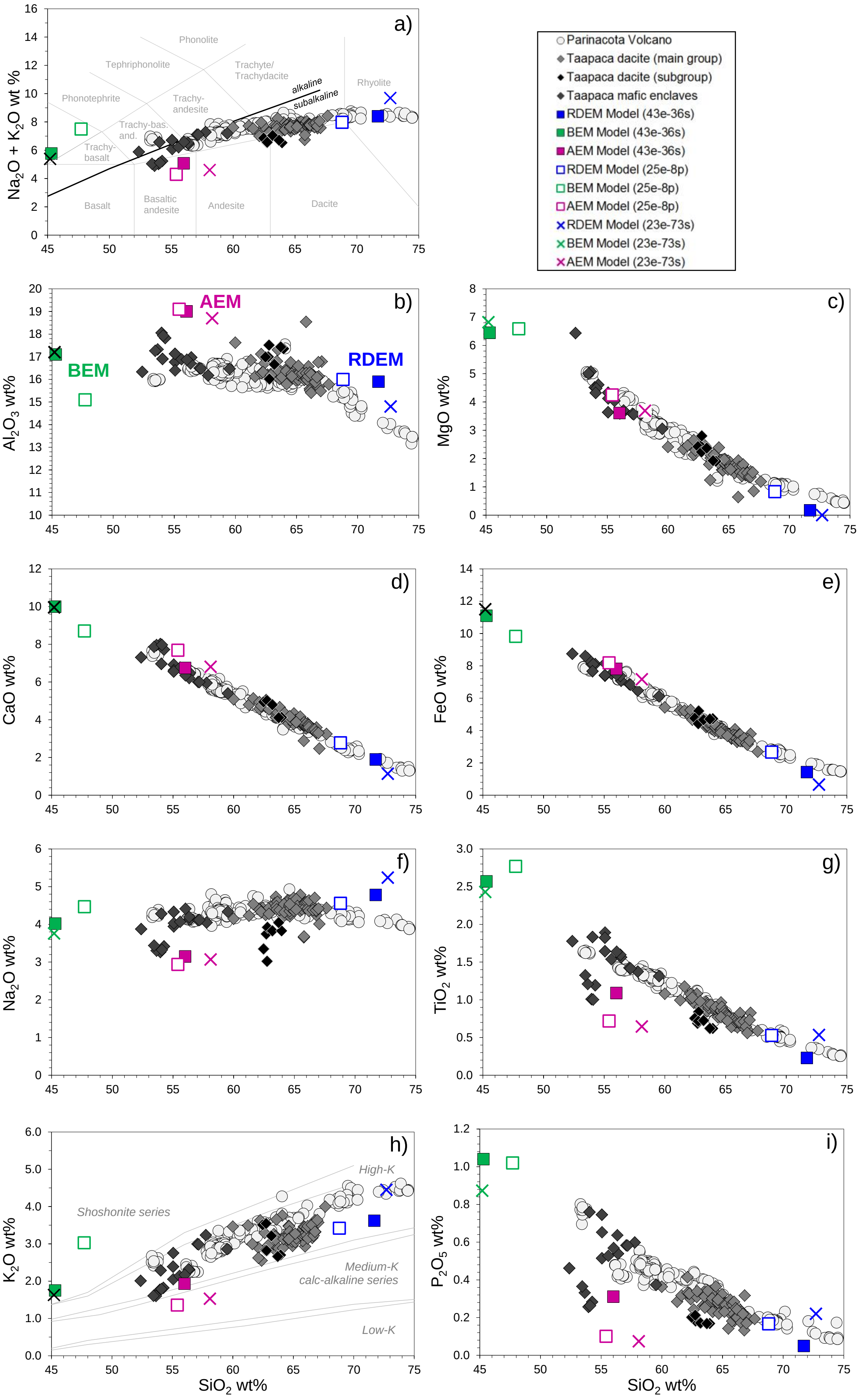
a)
Na2O + K2O wt %
Phonolite
Tephriphonolite
Trachyte/ Trachydacite
Phonotephrite
Trachy-andesite
Trachy-bas. and.
Trachy-basalt
Rhyolite
alkaline
subalkaline
Basalt
Basaltic andesite
Andesite
Dacite
○ Parinacota Volcano
◆ Taapaca dacite (main group)
◆ Taapaca dacite (subgroup)
◆ Taapaca mafic enclaves
■ RDEM Model (43e-36s)
■ BEM Model (43e-36s)
■ AEM Model (43e-36s)
□ RDEM Model (25e-8p)
□ BEM Model (25e-8p)
□ AEM Model (25e-8p)
× RDEM Model (23e-73s)
× BEM Model (23e-73s)
× AEM Model (23e-73s)
b)
Al2O3 wt%
AEM
BEM
RDEM
c)
MgO wt%
d)
CaO wt%
e)
FeO wt%
f)
Na2O wt%
g)
TiO2 wt%
h)
K2O wt%
Shoshonite series
High-K
Medium-K calc-alkaline series
Low-K
i)
P2O5 wt%
SiO2 wt%
45 50 55 60 65 70 75

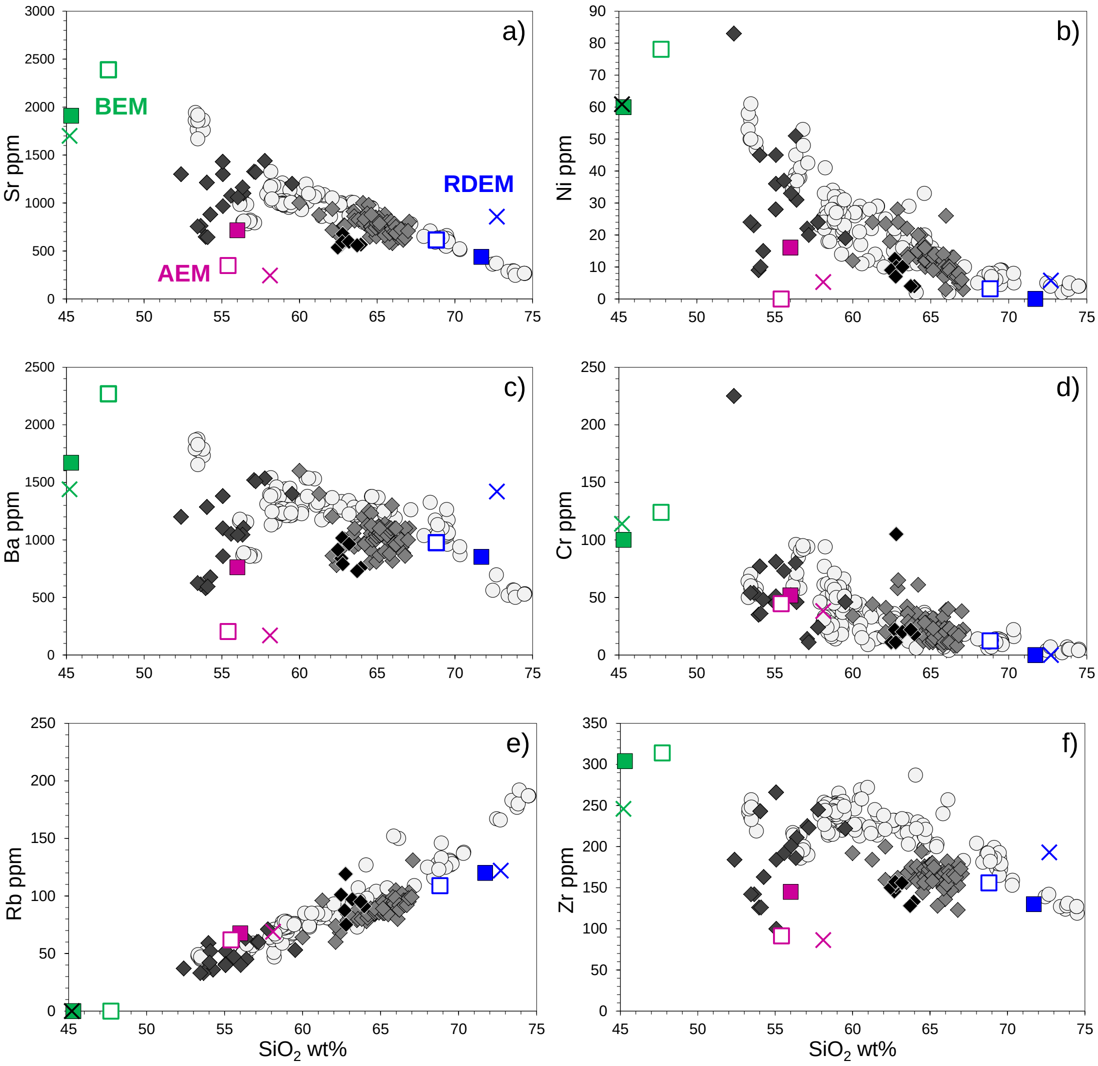

Figure 5. *Selected trace element compositions of the PVA end-members presented with the complete whole rock dataset of Taapaca and Parinacota. Symbols are the same as used in Figure 4.*

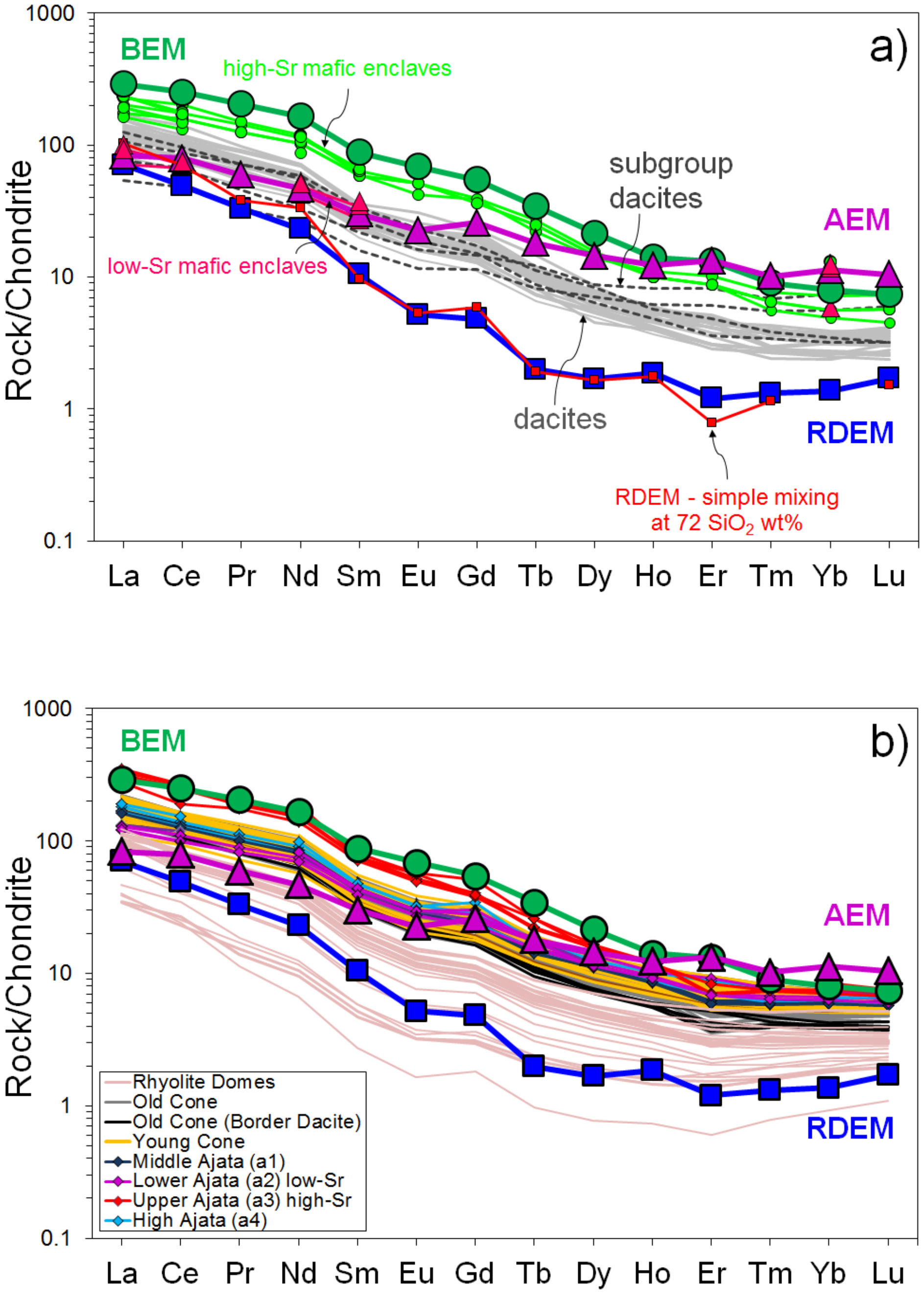

Figure 6. *Chondrite-normalized REE patterns of the PVA end-members obtained from the PVA model (43e-36s) including 36 samples and 43 elements, presented in comparison with:* ***a)*** *Taapaca main group dacites (light gray), subgroup dacites (dashed gray), high-Sr (light green), low-Sr (pink) mafic enclaves, and the rhyodacitic end-member (red) obtained from the simple mixing modeling (Chapter 3);* ***b)*** *Parinacota lavas, the stratigraphic units are listed in the legend.*

5.3. MIXING PROPORTIONS OF THE PVA END-MEMBERS

Mixing proportions of the end-members in each sample obtained from the PVA and normalized mixing relations between the mafic components (BEM+AEM) are given in Table 4. Additionally, SiO_2 and Sr contents in each sample are presented to demonstrate a correlation between the end-member proportions and the whole rock composition. If the BEM, AEM and RDEM occupy the corners of the mixing triangle oriented in the same way as the end-members plot in the Sr-SiO_2 space (Figure 2 and Figure 3), the mixing proportions mimic the Sr-SiO_2 trend. Ternary diagrams showing variations of the end-member mixing proportions for the three PVA calculation models are presented in Figure 7 and Figure 8.

The three PVA models presented show considerably different absolute mixing proportions of the end-members in the Taapaca samples depending on the number of samples and analytes included in the calculation models (Figure 7). As mentioned in section 4.4.2.2, one of the PVA condition says that some samples must plot on edges, faces or vertices of the polytope. The PVA does not need an occupancy of the vertices because pure end-members are not required to be present in the data set as samples. Nonetheless, the PVA algorithm needs at least one sample in which one end-member must be absent, that is, at least one sample must lie on the edge of the triangle in the three end-members model. The PVA calculations based on the selected Taapaca data sets locate different samples on the edges of the mixing triangle (Table 4, “0.0” values marked in red font) in the presented models. This leads to dissimilar polytope rotations of the data clouds in the (43e-36s), (25e-8p) and (23e-73s) calculation models. For instance, the model (43e-36s) characterized by much lower number of samples than variables, assigns a low-Sr mafic enclave (sample TAP 97-37/1) on a vertices, so that the PVA defines it as a pure AEM end-member. This basaltic andesite sample, as observed in the thin section, contains quartz and feldspar crystals incorporated form the silicic magma, which clearly indicates that this sample cannot be a pure mafic end-member. This observation shows that the mixing proportions obtained by PVA must be evaluated in connection to the petrographic features. Furthermore, in the same model several samples fall outside the polytope showing negative mixing proportions. The negative values indicate that the actual end-member located on the vertices (in this case the sample TAP 97-37/1) cannot account for a pure end-member and all samples in the mixing system can be considered as mixtures of a set of more extreme end-member compositions (Full, 1981).

In the simple mixing modeling, the mafic enclaves act themselves as mafic end-members. In the PVA, the mafic enclaves are mixtures of the three end-members. This result is in accordance with feldspars and quartz observed in the enclaves, assimilated from the silicic magma. Regardless of the calculation model, the mixing proportions of the mafic enclaves (MEs) plot as two separate low-Sr (<880 ppm Sr) and high-Sr (>880 ppm Sr) groups (Figure 7). The high-Sr MEs contain 20 to 50% of an incorporated RDEM material, with an exception to the most mafic sample found at Taapaca volcano (CAL-138B, 6.4 wt% MgO, 83 ppm Ni). This sample shows only 1.5 % of the RDEM in the model (25e-8p) and 15 % in the model (23e-73s). The portions of the AEM do not exceed 50%

of the mafic component in the high-Sr mafic enclaves. In contrast, the low-Sr MEs contain >60% of the AEM mafic component and other than the high-Sr mafic enclaves, very low portions <10% of the RDEM.

The dacites consists of 47 to 82 % RDEM in the model (43e-36s), 59 to 86 % in the model (25e-8p) and 40 to 68 % in the model (23e-73s). The values obtained from the model (25e-8p) show the most consistent results in comparison to the simple mixing modeling resulting in the range of 60 to 80% of the rhyodacitic end-member in the Taapaca dacites. Owing to compositional differences between the recognized main group and the dacite subgroup (see section 4.2.1), the latter has both higher AEM and markedly lower RDEM proportions. The rhyodacitic component does not exceed 60% in the subgroup dacites and these proportions correspond to lower SiO_2 contents of the subgroup dacites.

Figure 8 presents connecting lines between the dacites and their mafic enclaves, available for each PVA calculation model from the selected data sets. There are significant differences in the direction of these lines, which reflect distinct courses of the magma mixing processes. Such inconsistent results require further considerations based on the petrographic and mineral chemical observations.

Due to the location of some samples on the vertices or edges of the polytope in the PVA, the dacites in the model (43e-36s), presented in Figure 8a, are generated by mixing between the RDEM and only BEM or AEM. However, the dacites plot within the mixing triangle. This suggests mixing of mafic end-members with already hybrid silicic magma affected by former mafic recharge(s). The subgroup dacites in the model (23e-73s) show lower BEM/AEM ratios of the calculated proportions than their mafic enclaves do, whereas the main dacite group contains higher portions of the AEM relatively to their mafic enclaves (Figure 8c). The latter tendency suggests again that the rhyodacite component RDEM must have mixed with the AEM end-member before the high-Sr recharge took place. In the case that all dacites have the same BEM/AEM ratio of the mixing proportions in the MEs and in the dacites, a single magma recharge and mixing event could produce the hybrid dacites. This is observed in the model (25e-8p), (Figure 8b), where the ratios of BEM/AEM proportions show nearly constant values in the MEs and their host dacites.

The petrographic and mineral chemical features found in the Taapaca dacites, e.g. invariable trace element and isotope composition of the sanidine megacrysts and their compositionally uniform plagioclase and amphibole inclusions are clear evidence for crystallization in a chemically closed system (see Chapter 3). This means that an erupted part the rhyodacitic reservoir have not experienced multiple mafic recharges before the eruption triggering mafic input. Moreover, nearly indistinguishable compositions of the mafic enclaves found in a single eruption (mafic enclave samples TAP 07-04, 07-05M, and 02-02b found in the TAP 97-28 dacite) indicate that compositionally uniform mafic recharges have affected Taapaca magmatic system and single recharge events have led to a mobilization and an extrusion of parts of the rhyodacite reservoir. This petrological evidence strongly supports the correctness of the (25e-8p) model.

Considering the fact that the MEs are insufficiently represented and most dacite samples are represented in the database without their MEs, the most reliable results for the mixing proportions can be expected from the model based on the mafic-dacite pairs included in the model (25e-8p). The PVA program iterates, (enlarges the vertices and rotates the polytope), as long as the extreme compositions are enclosed in the polytope or located on its edges. The position of all samples in the polytope is then influenced by the overrepresented dacites that may distort the position of the polytope. Nevertheless, for the whole Taapaca system, the outlier compositions are presumed to play an important role in analyzing the entire system.

Assuming that the model (25e-8p) reflects the magma mixing processes at Taapaca correctly, two stages of magma mixing can be defined. The first stage, marked as (1) in the Figure 8b, comprises two mafic components BEM and AEM forming mafic recharge magma. This already hybrid magma (BEM+AEM) injects into the rhyodacitic RDEM component and induces the second magma mixing stage (2). In the second stage, two distinct magma mixing and mingling processes can be defined: 1) mingling of the hybrid mafic magma with the rhyodacitic component (BEM+AEM)+RDEM, producing the mafic enclaves, and 2) mixing of the rhyodacite with the hybrid mafic recharge RDEM+(BEM+AEM), resulting in homogenous dacites.

Petrological interpretation of the magma mixing proportions determined by the PVA for Taapaca volcanic system is discussed in Chapter 3, section 7.1.3 of this work.

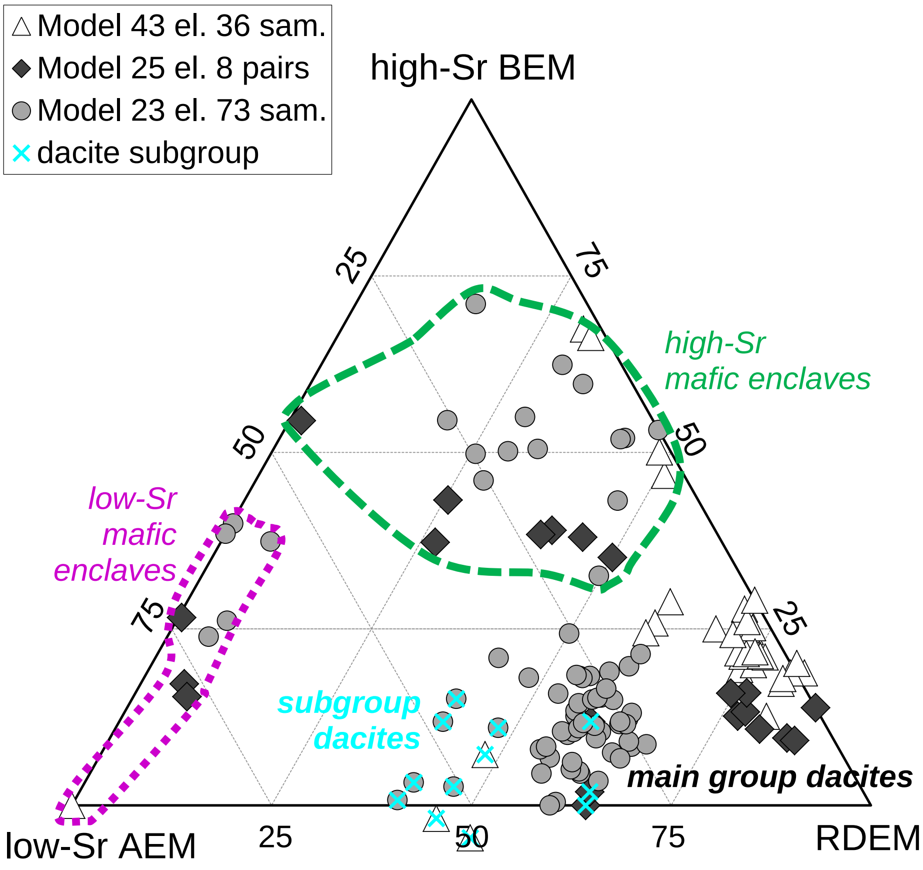

Figure 7. *Proportions of end-members for Taapaca samples plotted on triangular diagram due to three end-member space obtained from the PVA models using 43 elements and 36 samples in model 1, 25 elements and 8 dacites-mafic enclaves pairs in model 2, and 23 elements and 73 samples in model 3.*

Table 4. *Mixing proportions of the PVA end-members in samples used in three calculation models carried out for 43 analyte und 36 samples, 25 analyte and 8 mafic enclaves-dacite pairs (several samples have double analyses), and 23 analyte and 73 samples. The samples are presented in order with increasing Sr contents for mafic enclaves and dacites. The bars are scaled from the lowest to the highest values in each column. The values in brackets represent the SiO_2 wt% calculated for each end-member in each model presented in the Table 3. The colors of the bars correspond to EM symbols presented in the Figure 4 and Figure 5. The red font marks proportions ≤ 0, which indicate samples placed on the edges or vertices of the polytope (mixing-triangle in the three end-members model) in the PVA.*

			Model 43 analyte -36samples			Model 25 analyte-8 mafic-dacite pairs			Model 23 analyte - 73 samples			Model 43e-36s		Model 25e-8p		Model 23e-73s	
Sample	SiO_2 wt%	Sr ppm	Proportions of end-members (EM) in each sample									Portions of the mafic end-members BEM and AEM					
Mafic enclaves			RDEM (72)	BEM (45)	AEM (56)	RDEM (69)	BEM (48)	AEM (55)	RDEM (73)	BEM (45)	AEM (58)	BEM (45)	AEM (56)	BEM (48)	AEM (55)	BEM (45)	AEM (58)
TAP 97-37/1	54.1	643	0.000	0.000	1000	0.055	0.172	0.773	0.052	0.239	0.709	0.000	1000	0.182	0.818	0.252	0.748
TAP-97-37-1	54.0	647				0.067	0.154	0.779	0.064	0.261	0.675			0.165	0.835	0.279	0.721
TAP 97-36/1	53.4	755							0.003	0.399	0.598					0.400	0.600
TAP 97-36	53.6	762							0.000	0.385	0.615					0.385	0.615
CAL-147	54.3	880				0.005	0.266	0.730	0.062	0.374	0.564			0.267	0.733	0.399	0.601
TAP 97-25/1	55.1	967							0.197	0.545	0.257					0.680	0.320
TAP 97-8	56.0	1058							0.295	0.502	0.203					0.712	0.288
TAP 97-27/1	55.6	1076							0.257	0.498	0.246					0.670	0.330
TAP 97-29/1	56.4	1101	0.508	0.467	0.025	0.268	0.373	0.359	0.285	0.460	0.255	0.950	0.050	0.509	0.491	0.644	0.356
TAP 97-38/1	56.3	1163							0.331	0.505	0.165					0.754	0.246
CAL-148A	59.5	1200				0.501	0.351	0.148	0.467	0.432	0.101			0.703	0.297	0.810	0.190
TAP-003	54.0	1213	0.303	0.675	0.022				0.302	0.624	0.074	0.968	0.032			0.894	0.106
CAL-138B	52.4	1300				0.015	0.545	0.440	0.151	0.710	0.139			0.553	0.447	0.836	0.164
CAL-116B	55.1	1300				0.254	0.433	0.313	0.292	0.550	0.158			0.580	0.420	0.777	0.223
TAP 07-05	57.2	1322				0.406	0.390	0.204	0.432	0.520	0.048			0.656	0.344	0.916	0.084
TAP 07-04 M	57.1	1327				0.395	0.384	0.221	0.428	0.519	0.054			0.634	0.366	0.906	0.094
TAP-002	55.1	1430	0.318	0.663	0.019				0.342	0.597	0.062	0.972	0.028			0.906	0.094
TAP-02-02-b	57.8	1439	0.485	0.501	0.014	0.449	0.380	0.171	0.469	0.532	0.000	0.972	0.028	0.690	0.310	1000	0.000
Dacite																	
TAP-97-37	63.7	559				0.643	0.000	0.357	0.412	0.033	0.556			0.000	1000	0.055	0.945
TAP 97-02	62.7	564	0.481	0.072	0.447				0.405	0.118	0.476	0.139	0.861			0.199	0.801
TAP 97-37	64.0	566	0.522	-0.046	0.525	0.639	0.019	0.342	0.404	0.007	0.589	-0.096	1096	0.053	0.947	0.012	0.988
TAP-97-10	65.8	592	0.465	-0.018	0.553				0.465	0.026	0.509	-0.034	1034			0.049	0.951
CAL-141	63.2	596							0.479	0.110	0.412					0.210	0.790
TAP 97-35	66.7	615	0.823	0.188	-0.011				0.642	0.034	0.324	1060	-0.060			0.096	0.904
CAL-117	66.8	637							0.603	0.005	0.392					0.012	0.988
TAP 97-30	66.4	639	0.806	0.126	0.068				0.598	0.000	0.402	0.652	0.348			0.000	1000
TAP 97-11	64.5	647	0.740	0.192	0.068				0.565	0.068	0.368	0.739	0.261			0.155	0.845
TAP-97-11	64.9	652	0.753	0.199	0.047				0.546	0.079	0.374	0.808	0.192			0.175	0.825
TAP-97-34	66.6	662	0.801	0.173	0.026				0.614	0.045	0.341	0.869	0.131			0.116	0.884
CAL-136	65.5	664							0.565	0.045	0.390					0.104	0.896
TAP 97-34	66.5	673	0.806	0.188	0.007				0.611	0.048	0.341	0.965	0.035			0.124	0.876
CAL-147A	62.8	677				0.590	0.119	0.291	0.406	0.151	0.444			0.290	0.710	0.254	0.746
CAL-124E	65.8	682							0.552	0.083	0.365					0.186	0.814
TAP-97-01	66.2	686	0.800	0.180	0.020				0.599	0.051	0.350	0.898	0.102			0.127	0.873
TAP 97-01	66.1	697	0.807	0.201	-0.008				0.596	0.061	0.343	1041	-0.041			0.151	0.849
CAL-149	66.8	706							0.659	0.083	0.258					0.244	0.756
CAL-150	67.0	708							0.676	0.086	0.238					0.266	0.734
TAP 97-06	62.1	719	0.605	0.288	0.107				0.430	0.209	0.361	0.730	0.270			0.366	0.634
CAL-124C	64.7	724							0.567	0.126	0.306					0.292	0.708
CAL-128C	66.5	725							0.639	0.075	0.286					0.207	0.793
TAP 97-07	65.1	726	0.736	0.216	0.049				0.571	0.100	0.330	0.816	0.184			0.232	0.768
CAL-13	66.0	728							0.652	0.090	0.258					0.260	0.740
TAP 97-29	64.9	742	0.726	0.246	0.028	0.770	0.126	0.104	0.564	0.134	0.303	0.898	0.102	0.549	0.451	0.307	0.693
CAL-143	66.1	744							0.628	0.115	0.257					0.309	0.691
TAP 87-002	65.3	748	0.746	0.220	0.034				0.576	0.104	0.320	0.866	0.134			0.245	0.755
TAP 97-29	64.6	751	0.720	0.250	0.031	0.777	0.132	0.091	0.562	0.145	0.293	0.891	0.109	0.593	0.407	0.330	0.670
TAP-87-002	65.2	751	0.733	0.211	0.056				0.561	0.105	0.334	0.792	0.208			0.239	0.761
CAL-152	66.2	751							0.635	0.123	0.242					0.336	0.664
TAP-001	64.6	752	0.703	0.278	0.019				0.578	0.189	0.233	0.936	0.064			0.449	0.551
CAL-139	64.6	753							0.577	0.150	0.274					0.354	0.646
TAP-97-22	62.9	768	0.601	0.258	0.141				0.482	0.181	0.338	0.647	0.353			0.349	0.651
TAP-97-28	65.9	775	0.763	0.210	0.027	0.847	0.095	0.057	0.610	0.104	0.286	0.886	0.114	0.625	0.375	0.268	0.732
TAP 97-28	65.8	779	0.756	0.212	0.032	0.859	0.092	0.050	0.609	0.095	0.296	0.868	0.132	0.650	0.350	0.243	0.757
CAL-148	66.1	784				0.862	0.138	0.000	0.635	0.131	0.234			1000	0.000	0.359	0.641
TAP-02-03	64.2	790	0.681	0.250	0.069				0.530	0.158	0.312	0.784	0.216			0.336	0.664
CAL-140	64.6	794							0.586	0.153	0.261					0.369	0.631
TAP-97-48	65.6	803	0.730	0.234	0.037				0.598	0.113	0.289	0.865	0.135			0.280	0.720
CAL-142	67.1	805							0.653	0.067	0.281					0.192	0.808
TAP-97-45	65.1	805	0.726	0.216	0.059				0.579	0.109	0.311	0.787	0.213			0.260	0.740
CAL-124A	65.9	810							0.636	0.115	0.249					0.316	0.684
CAL-131	63.6	816							0.544	0.183	0.273					0.402	0.598
CAL-138A	64.2	833				0.765	0.159	0.076	0.557	0.183	0.260			0.678	0.322	0.413	0.587
TAP-02-02-a	65.1	845	0.736	0.215	0.049	0.807	0.108	0.085	0.582	0.117	0.302	0.816	0.184	0.559	0.441	0.279	0.721
TAP 97-45	64.9	849	0.726	0.252	0.022				0.603	0.149	0.248	0.919	0.081			0.376	0.624
CAL-116A	63.5	861				0.745	0.159	0.096	0.549	0.180	0.271			0.623	0.377	0.400	0.600
CAL-121	61.3	876							0.501	0.243	0.256					0.488	0.512
TAP-97-18	64.6	878	0.707	0.242	0.052				0.582	0.152	0.266	0.825	0.175			0.364	0.636
TAP-97-13	65.5	880	0.746	0.217	0.036				0.627	0.118	0.255	0.857	0.143			0.317	0.683
TAP 97-18	64.4	890	0.715	0.260	0.025				0.586	0.165	0.249	0.913	0.087			0.399	0.601
TAP 97-41	63.5	911	0.596	0.244	0.159				0.539	0.185	0.276	0.605	0.395			0.401	0.599
TAP-97-17	64.5	980	0.709	0.291	0.000				0.599	0.197	0.204	1000	0.000			0.491	0.509
CAL-123	60.0	1000							0.497	0.325	0.178					0.646	0.354
CAL-120	64.1	1000							0.605	0.214	0.181					0.542	0.458

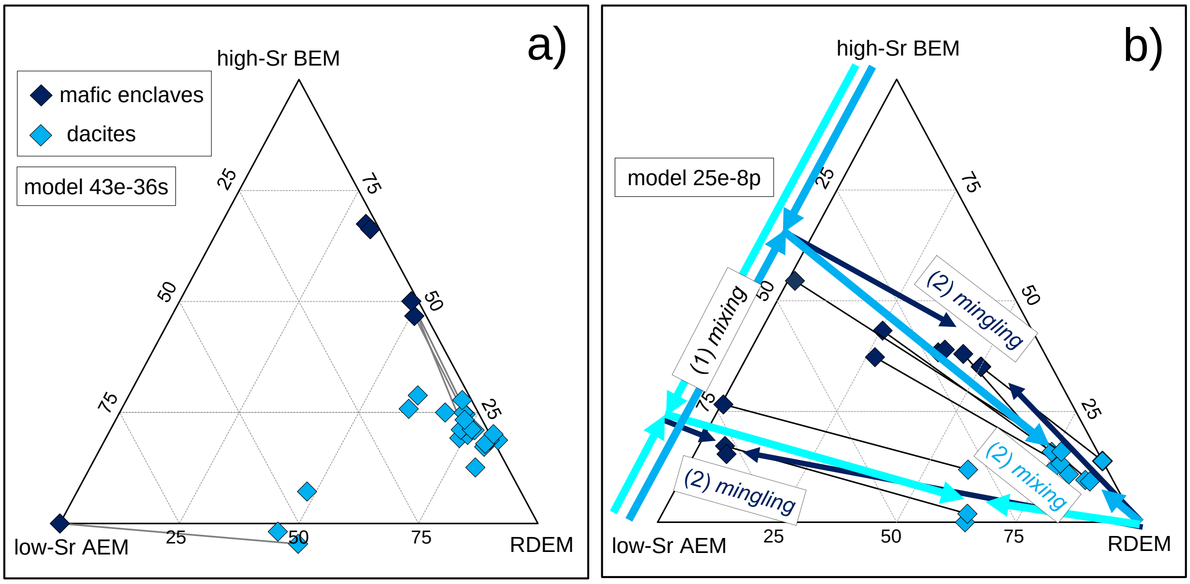

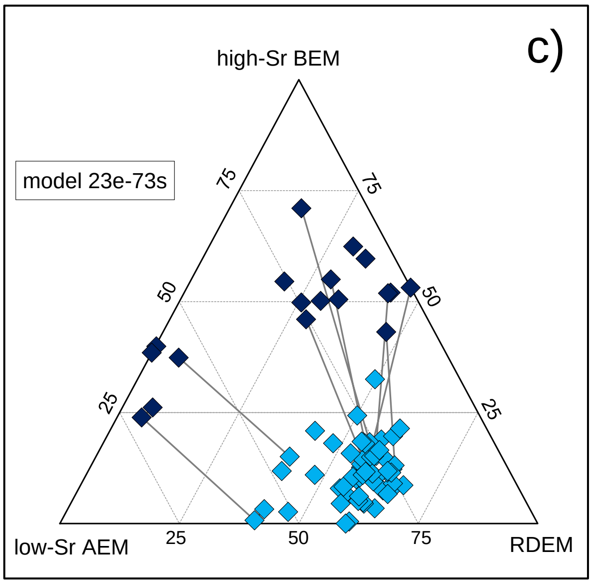

Figure 8. *Proportions of end-members for single Taapaca samples plotted on a triangular diagram due to three end-members space obtained from three PVA models using in **a)** model (43e-36s), **b)** model (25e-8p) and **c)** model (23e-73s) as described in the section 4.4.1. Additionally, **b)** demonstrates two mixing stages: (1) mixing between the mafic components forming hybrid (BEM+AEM) recharge magma, and (2) mixing between the rhyodacite and hybrid mafic component RDEM+(BEM+AEM) generating homogenous dacites, and mingling between hybrid mafic component and rhyodacite (BEM+AEM)+RDEM resulting in mafic enclaves hosted in the dacites. Light blue and cyan lines illustrate magma mixing; dark blue line illustrates magma mingling.*

5.4. CONSTRAINED ISOTOPIC COMPOSITION OF THE PVA BASALTIC END-MEMBER

The PVA technique is applicable for normalized datasets (Miesch, 1976; Johnson et al., 2002). Consequently, the isotope compositions cannot be directly assessed. However, the results obtained from the PVA provide the element contents of the end-members and their mixing proportions, which are essential parameters required in the mass balance. A three-component simple mixing relation integrating isotopic signatures is expressed by equation presented by Myers et al. (1986):

$$\varepsilon_{hm}C'_{hm} = X\varepsilon_1 C'_1 + Y\varepsilon_2 C'_2 + Z\varepsilon_3 C'_3 \qquad \text{(equation E1),}$$

where ε represents isotopic ratio of the end-members indicated by (1)-, (2)- and (3)-components in the hybrid magma (hm), equally to the natural hybrid samples; C’ is the concentration of the denominator isotope in the indicated components; X, Y, Z are mixing proportions of the end-members. A collection of linear equations based on the measured isotopic ratios and element concentrations in the natural samples combined with C’ and X, Y, Z obtained from the PVA should reveal the isotopic characteristics of the estimated RDEM, BEM and AEM end-members.

The significant differences in the Sr and Nd concentrations of the PVA end-members in the presented PVA calculation models depending on the data set used, account for very imprecise C'_{hm} values in the equation E1. Likewise, the proportions of the end-members provide inaccurate values.

Systems of three simultaneous linear equations were solved using Cramer's third order determinant method. The PVA results applied, for example, to low-Sr mafic enclave TAP 97-37-1, high-Sr mafic enclave TAP 97-29/1 and dacite TAP 97-37 yield $^{87}Sr/^{86}Sr$ ratios of 0.720605 for the RDEM, 0.642692 for the BEM, and 0.690588 for AEM, using the Sr concentrations and mixing proportions from the model (25e-8p). Further PVA models show $^{87}Sr/^{86}Sr$ in a range from 0.63 to 0.93 for the same samples. Other samples involved in the equation systems reveal values $^{87}Sr/^{86}Sr>1$ or $^{87}Sr/^{86}Sr<0.6$. For these reasons, the application of the PVA outcomes in the simple mixing mass balance equations, which are very sensitive to all input parameters, results in geologically unreliable results.

Despite of the wide variation in the major and trace element composition, Sr and Nd isotopic ratios of Taapaca and Parinacota vary in a remarkably narrow range (Wörner et al., 1988, Davidson et al., 1990) in comparison to other volcanic centers in the CVZ, e.g. Ollagüe volcano (22°S) and its satellite Porunita mafic lavas. Figure 9 presents Sr and Nd isotopic composition of Taapaca and Parinacota compared to several Central Andean Quaternary volcanic arc lavas erupted along 15° to 26° S (data taken from Mamani et al., 2010). The high-Sr Upper Ajata (a3) lava and low-Sr Taapaca mafic enclave (TAP 97-37-1) differ in Sr and Nd isotopic composition from the main Parinacota and Taapaca range, showing lower Sr- and higher Nd-ratios, respectively. These values determine the baseline isotopic composition erupted at 18°S (Figure 9a, b). Other analyzed Taapaca (high-Sr) mafic enclaves, showing higher $^{87}Sr/^{86}Sr$ ratios, yield significantly higher proportions of the incorporated silicic RDEM PVA end-member, as shown in Figure 8. The higher $^{87}Sr/^{86}Sr$ ratios observed in the low-Sr Lower Ajata (a2) are related to higher amounts of incorporated xenocrysts from the former rhyolitic lavas of the (rd) stage through which (a2) erupted (Hora et al., 2009), compared to the later (a3) eruption. These observations suggest that the differences in Sr and Nd ratios in the basaltic andesitic Taapaca and Parinacota samples result from distinct proportions of the incorporated shallow silicic material and are not necessarily connected to the deeper, MASH processes. Hence, a compositional gap observed in the MgO-$^{87}Sr/^{86}Sr$ space between (a3) and TAP 97-37-1 and the main $^{87}Sr/^{86}Sr$ and $^{143}Nd/^{144}Nd$ trends define a differentiation step between baseline parental compositions and compositions modified by shallow differentiation.

Assuming that the changes of $^{87}Sr/^{86}Sr$, $^{143}Nd/^{144}Nd$, and MgO follow one specific trend during differentiation, we extrapolate the observed trend connecting the small compositional gap between the variably differentiated basaltic andesite (Figure 9) to higher MgO values. The best fit curves ($R^2=0.99$ for MgO vs. $^{87}Sr/^{86}Sr$ and 0.97 for MgO vs. $^{143}Nd/^{144}Nd$, equations presented in Figure 9) including Taapaca mafic enclaves reveal $^{87}Sr/^{86}Sr=0.70\mathbf{517}-0.70\mathbf{523}$ and $^{143}Nd/^{144}Nd=0.512\mathbf{489}-0.512\mathbf{502}$ for 6.4-6.6 wt% MgO obtained from the PVA BEM, slightly different from the analyzed parental baseline values (0.70**588** and 0.512**379** at 4.5 wt% MgO).

The mathematically constructed curves differ for both volcanoes and show a shift to higher Sr and Nd isotope ratios at given MgO contents in Parinacota lavas compared to Taapaca. This divergence may be caused by 1) different source characteristics, which may also explain certain differences in the major and trace element contents between the most mafic Taapaca and Parinacota magmas; or 2) different differentiation regimes affecting the correlation between Sr isotopic ratios and MgO contents. Although the Taapaca sample CAL-138 B shows exceptionally high compatible elements contents (MgO, Ni, Cr), this most mafic magma does not reach extremely high Sr and Ba contents as observed in the Upper Ajata (a3). This CAL-138 confirms the slight differences in the magma evolution. Unfortunately, we do not dispose of REE and isotope composition of this sample.

The extrapolation of the mafic recharge magmas trends at the investigated two volcanoes, points toward the most mafic samples collected in the Altiplano region at 19°S, Chiar Kkollu alkali basalt from monogenetic volcanic center (^{87}Sr/^{86}Sr=0.70**405** and ^{143}Nd/^{144}Nd=0.512**801**, Davidson & de Silva, 1995), dated at 22.5 Ma (Thorpe et al. 1984) and Neogene (<2 Ma) parasitic cones located between San Francisco and Incahuasi volcanoes in the southern CVZ at 27°S (^{87}Sr/^{86}Sr=0.70**523-**0.70**580** and ^{143}Nd/^{144}Nd=0.512**538-**0.512**544**, Kay et al., 1999). The estimated Sr-Nd isotopic composition of the BEM plots directly next to the Incahuasi basaltic andesite; however, the Incahuasi lavas reveal important differences in major element chemistry (section 6.8.1, Figure 12).

The isotopic composition of the silicic RDEM and andesitic AEM is difficult to evaluate, due to the low number of the analyzed mafic samples. However, in major and trace element compositions, Taapaca samples reveal two isotopic trends linked to the main group and subgroup recognized in the Taapaca dacites, described in the section 4.2.1. Samples identified as the low-Sr subgroup (low LILE, HFSE, and Ni) yield lower ^{87}Sr/^{86}Sr and higher ^{143}Nd/^{144}Nd values in comparison to the high-Sr mafic enclaves and Taapaca main group. As described in the previous section, these samples show also lower amounts of the incorporated silicic end-member relative to the high-Sr mafic enclaves and main dacite group, and only up to ~30% mixed BEM end-member in the mafic enclave. These observations indicate that the isotopic composition of the AEM must fall between BEM and the more evolved RDEM, in the range displayed in Figure 9a for 3.6-4.3 MgO wt%, as obtained from the PVA. Furthermore, a low compositional contrast in the Sr-Nd isotopic ratios observed in the low-Sr mafic enclave (TAP 97-37-1) and its dacite host (TAP 97-37), which contain 40-64 % of the silicic RDEM, point to an isotopic composition of RDEM which must be similar to those found in the Taapaca dacites and sanidine megacrysts (0.70**6728**±6-0.70**6795**±5, Kiebala, unpublished data), reaching a maximum of approximately ^{87}Sr/^{86}Sr ~0.70**70** and 143Nd/^{144}Nd ~0.512**22**.

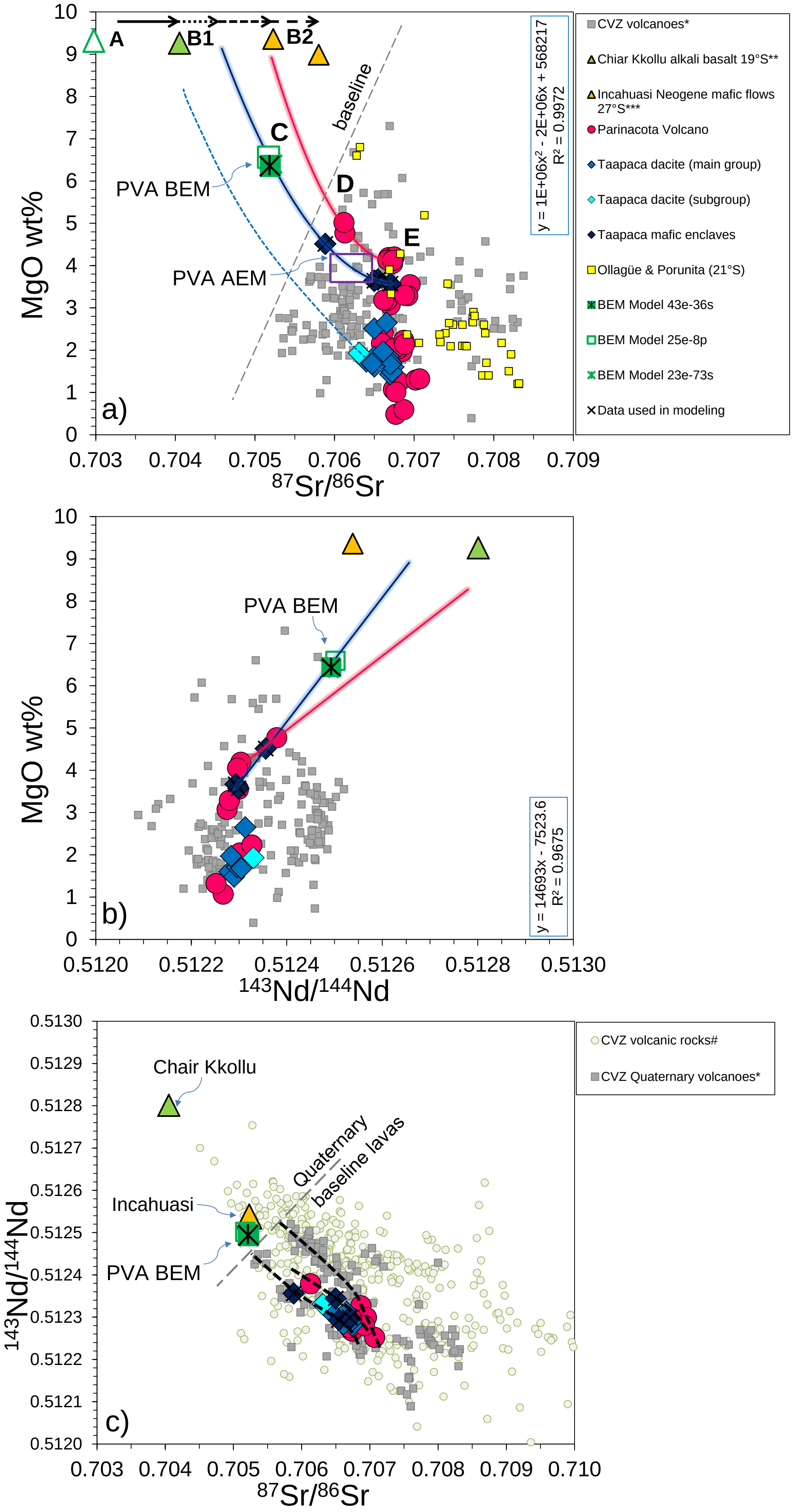

Figure 9: description on the next page.

Figure 9. ***Previous page****: Modeled isotopic ratios in* ***a)*** ^{87}*Sr/*^{86}*Sr and* ***b)*** ^{143}*Nd/*^{144}*Nd for the PVA end-members constrained from an assumption of a connection between isotopic ratios and MgO content in the melt due to differentiation processes. Compositions of arc lavas form selected volcanic canters in the CVZ (15-26°S) are presented for comparison (data taken from Mamani et al., 2010). Additionally, isotopic composition of the most mafic samples collected in the Altiplano region (19°S), Miocene Chiar Kkollu alkali basalt (Davidson & de Silva, 1995) and Puna region (27°S), the Neogene (<2 Ma) Incahuasi parasitic cone lavas (Kay et al., 1999) show relation of the natural lavas to mathematically constructed BEM. The gray dashed lines signify "baseline"- threshold values found in the CVZ lavas. Solid blue and red lines are the best-fit curves resulting from the presented equations, including Taapaca mafic enclaves (blue) and low-Sr (a2) and high-Sr (a3) Parinacota basaltic andesite lavas (red). In a), black arrows connecting A-B1-B2 illustrates possible diversification of the mantle-derived magmas occurring in the source region (Wörner, pers. com.); C-D-E account for differentiation/mixing processes occurring in the crust.* ***c)*** *Nd vs. Sr plot presents constructed Sr-Nd isotopic composition of the basaltic PVA basaltic BEM end-member from a) and b) in comparison with isotopic compositions found in the CVZ. Black dashed lines suggest possible separate trends for Taapaca and Parinacota.*

6. DISCUSSION

6.1. GEOLOGICAL BACKGROUND OF PVA END-MEMBERS

Wörner et al. (1988) recognize that at least three distinct components must be involved in the petrogenesis of lavas erupted in the volcanic region at 18°S. For the first time these three end-member compositions, which have not been observed as erupted magma compositions in the CVZ, are defined using multivariate statistical method. The PVA resolves hybrid intermediate magmas into three geochemically distinct end-members: rhyodacitic (RDEM), basaltic andesitic (AEM) and basaltic (BEM) components. During the long eruptive history of the TVC, all three end-members must have obviously been involved over 1.3 Ma in the volcanic system, with remarkably similar silicic to mafic proportions. Statistically, the system does not require more than three end-members to explain the geochemical variability in the Taapaca dataset. However, with respect to the long activity of the system, some minor temporal variability, which cannot be resolved by PVA, may have existed in the mafic and silicic end-members, and may have contributed to the compositional variability of Taapaca dacites.

A similar scenario for multicomponent mixing and thus validation of the Taapaca PVA end-member compositions is provided by a study by Vogel et al. (2008). They applied PVA at Unzen volcano, a dacitic dome complex located 70 km behind the Japanese volcanic front. The Unzen example shows remarkable similarities to Taapaca with respect to monotonous dacite erupted over a long time (550 ka), containing also two populations of compositionally distinct mafic enclaves (Browne et al., 2006). The PVA results carried out on Unzen samples similarly identify three end-members. Their SiO_2 contents (70, 52 and 54 wt%) correspond geochemically to the Taapaca end-members with similar REE patterns. The highest Sr/Y ratio is again found in the silicic and the lowest in the andesitic end-member.

The study by Hildreth (2007) presents distinct primary and parental members found in the Quaternary eruptive products in the Cascades, with a wide and continuous range of chemical compositions differing in alkalinity, Fe/Mg, LILE/HFSE and LREE/HREE. These distinct magma types exist close together in space and time and can contribute simultaneously in one volcanic system. The major and trace element composition of the Taapaca PVA end-members strikingly reflects a variety of primary and parental magmas generated in the continental arcs, and therefore, this magma mixing scenario presented here may be of general applicability in many arcs worldwide.

6.2. GEOCHEMICAL CHARACTERS OF THE PVA END-MEMBERS

To classify the PVA end-members, TAS (Figure 4a and Figure 10a) and K_2O vs. silica diagrams (Figure 4h and Figure 10b) in connection with trace element characteristics and natural examples (Figure 11 and Figure 12) are used. Trace element contents are compared conventionally with N-MORB (Figure 12). Following the discrimination of Irvine & Baragar (1971) in the TAS diagram, the RDEM and AEM are members of sub-alkaline rock series; the BEM plots in the alkaline field. The discrimination for shoshonite/sub-alkaline rocks of Rickwood (1989) based on K_2O and SiO_2 concentrations shows that the RDEM represents high-K calc-alkaline, the AEM medium-K calc-alkaline, and BEM shoshonitic magmatic series.

6.2.1. GEOCHEMICAL CHARACTER OF THE BEM

The BEM (47 wt% SiO_2) basaltic end-member shows high total alkali content of $Na_2O+K_2O=7.5$ wt%, an enrichment in incompatible elements with exception to Y and HREE relative to N-MORB (Figure 12). The BEM basaltic composition has particularly high Sr and Ba contents exceeding 2000 ppm, which are justified by the high concentrations of these elements found in the high-Sr (a3) lavas form Parinacota, reaching up to 1944 ppm Sr (Figure 5). Surprisingly, other LILE, Rb and Cs contents are very low but consistent with the Taapaca-Parinacota differentiation trend (Figure 5). Furthermore, the BEM shows high LILE/HFSE ratios, steep REE pattern resulting in high LREE/HREE. The Nb-Ta anomaly is smaller in comparison to sub-alkaline AEM and RDEM end-members (Figure 12). Estimated Sr and Nd isotope values ($^{87}Sr/^{86}Sr=0.70517-0.70523$, $^{143}Nd/^{144}Nd=0.512489-0.512502$) are substantially more radiogenic compared to MORB or even NVZ and SVZ lavas ($^{87}Sr/^{86}Sr<0.705$, $^{143}Nd/^{144}Nd>0.51265$). At low basaltic SiO_2 content this Sr-Nd isotopic ratios cannot result from crustal contribution and suggest enriched magma source. These geochemical characteristics impart a shoshonitic character of the BEM; however, the BEM composition does not meet all shoshonite characteristics presented by Morrison (1980), such *low-TiO_2 contents <1.3 wt%.*

The BEM shows a great resemblance to shoshonite lavas found in the central Andean back-arc. For instance, 2390 ppm Sr, 78 ppm Ni, Sr/Y=84.5 and 139.0, Nb/Ta=19.9, Sm/Yb=9.9, values estimated for BEM are in accordance with absarokite lava flow from Oroscocha volcano at Quinsachata back-arc in Peru (14°S), showing 2564 ppm Sr, 79.4 ppm Ni, Sr/Y=88.4, Nb/Ta=20.3, Sm/Yb=7.9 at 50 wt% SiO_2. However, there is a discrepancy between $K_2O/Na_2O=0.6$ and Mg#=54 in BEM and 1.7 and 66 found in the absarokite, respectively. Despite the minor differences in major and trace element composition presented in the spider diagram (Figure 12), the REE pattern of the BEM mimics well the shoshonitic lava (Figure 11) and confirms its shoshonite-type signature.

6.2.2. GEOCHEMICAL CHARACTER OF THE AEM

In view of the SiO_2 and alkali content of the AEM (55 wt% SiO_2), this mafic end-member represents composition that is to some extent evolved in comparison to the BEM. On the basis of major elements and moderate K_2O content (1.4 wt%) at the given silica, the AEM is classified as medium-K calc-alkali basaltic andesite (Figure 4a, h and Figure 10a, b); in the AFM diagram (not presented) the basaltic andesitic PVA end-member falls also below the discrimination lines of Irvine & Baragar (1971) into the calc-alkaline field. The subdivision between tholeiite and high-Al basalts after Middlemost (1975) based on alkaline index A.I.=(Na_2O+K_2O)/((SiO_2-43)*0.17) vs. Al_2O_3 reveals an affiliation to the high-Al basalt (calc-alkaline) suite. This calc-alkaline basalt (CAB) is referred as an “arc basalt” or high-Al basalt (HAB); however, it must be distinguished between high-Al olivine tholeiite (HAOT) and HAB that represent two distinct magmatic lineages (Hildreth, 2007). Beside the characteristic high Al_2O_3 content of 19 wt%, also low CaO/Al_2O_3=0.4, low MgO contents (4.5 wt%) and low Mg-number of 48 are referred to high-Al basalts – basaltic andesites (e.g. Marsh, 1979a, 1979b; Tatsumi et al., 1983, 2003; Brophy & Marsh, 1986; Sisson & Groove, 1993; Grove et al., 2003, 2006).

Despite the apparently evolved character of the AEM, its HFSE contents meet the CAB characteristics. In the classifications based on (Ti/100, Zr, Y*3), Ti vs. Zr and (Ti/100, Zr, Sr/2) by Pearce & Cann (1973), the AEM plots in a field of Sr-enriched calc-alkaline basalt (not presented). The AEM end-member shows the typical arc hallmarks of slab contribution: moderate LILE enrichment, Nb-Ta through (Figure 12) and nearly unfractionated REE pattern with a minor LREE-enrichment (Figure 6 and Figure 11).

Looking at the Quaternary magma compositions in the CVZ, the whole rock composition of the AEM is comparable to basaltic andesites from Lascar volcano. Lascar erupted lavas, which are characterized by the lowest LILE contents as well as LILE/HFSE: Sr/Y (11-41), LREE/HREE: La/Yb (5-19) and MREE/HREE: Sm/Yb (1.3-3.5) among the Quaternary volcanoes in the CVZ (own unpublished data, and Figure 11 in Mamani et al., 2010). These values are in accordance with 14.8, 10.3 and 2.4 of the AEM, respectively. Comparing the REE patterns to the natural samples, the AEM closely follows the Lascar basaltic andesite composition (58 wt% SiO_2) included in Mamani et al. (2010), (Figure 11).

Regarding the basaltic magmas occurring in the Southern Volcanic Zone (SVZ), the major element composition of the AEM presents strong similarity to the high-Al basalts from the Quaternary volcanic centers (37-42°S) of the SVZ, presented by e.g. Lopez-Escobar et al. (1977). The REE pattern (Figure 11) of the AEM overlaps with the basalts of Lanin volcano at 39.5°S (49.7-51.4 wt% SiO_2, 19.2-22 wt % Al_2O_3) characterized by the same Mg# of 48.

6.2.3. GEOCHEMICAL CHARACTER OF THE RDEM

The RDEM (69 wt% SiO_2) shows high-K calc-alkaline affinity with a total alkali content of (Na_2O+K_2O)=8 wt% (Figure 4a, h and Figure 10a, b). In terms of the Al-saturation (A/CNK=molar Al_2O_3/(CaO+Na_2O+K_2O) the RDEM is metaluminous or weakly peraluminous (A/CNK=0.98). N-MORB normalized trace element diagram (Figure 12) shows the highest enrichment in K, Pb and U, strongly pronounced Nb-Ta anomaly and HREE depletion.

Petrological and geochemical study of Taapaca dacites (Chapter 3) shows that the rhyodacite RDEM end-member represents a voluminous, long-lasting rhyodacite reservoir, located in the shallow crust at mainly depth of 7 to 10 km. The RDEM is characterized by a wide number of petrological features (high crystallinity, near-solidus crystallization temperatures and mineral assemblages, presence of mafic enclaves) and geochemical signatures (SiO_2>56 wt%, MgO<3 wt%, Sr/Y>20, Y<15 ppm, Yb<1.9 ppm, absence of Eu anomaly, strongly fractionated REE patterns with LREE enrichment and HREE depletion), which qualify the RDEM to a particular group of crystal-rich intermediate magmas. These magmas, characterized by very high Sr/Y signature, have been identified worldwide in subduction settings (Zellmer, 2009), also in all Andean volcanic zones (NVZ, Samaniego et al., 2005; CVZ, Goss et al., 2010; SVZ, Rodriguez et al., 2007). Some authors have denoted these compositions as “adakitic” or adakite-like in contrast to the “true” adakite defined by Defant & Durmmond (1990). Depending on the PVA calculation model, the RDEM reveals Sr/Y ratios of 104 and 84, values nearly as high as these obtained for the BEM shoshonitic end-member.

Figure 10. ***Next page**: **a)** TAS, **b)** K_2O vs. SiO_2 and **c)** Sr vs. SiO_2 diagrams showing compositions of the PVA end-members with exposed Taapaca and Parinacota samples and Quaternary CVZ lavas (data compilation of Mamani et al. 2010) for comparison. The latter are divided into volcanic centers of the northern Altiplano arc sector (14-19°S) and the southern Puna arc sector (20-28°S), (see section 6.3.2). Additionally, the extreme lava compositions from Lascar volcano located at the southern sector are highlighted (Matthews et al., 1999 and own data). Blue solid lines connecting the PVA end-members demonstrate magma mixing lines. The mixing triangle, comprising BEM, AEM and RDEM as “corner” compositions, encloses all Quaternary lavas found at 15-19°S and the most part of the Puna region (20-28°S). Lava compositions from Lascar (23°S) diverge from the main trend suggesting contribution of different silicic end-member or contribution of the AFC processes. A majority of the most mafic baseline lavas (<54 wt% SiO_2) plot on the BEM-AEM mixing line. The PVA magmatic end-members may account for the compositional variability found in the Quaternary eruptive products of the CVZ. Apparently, the northern volcanoes have a somewhat stronger influence of the enriched (shoshonitic) component. Trace element patterns for these three components derived from the PVA show even more distinct geochemical character of the end-members (Figure 11 and Figure 15).*

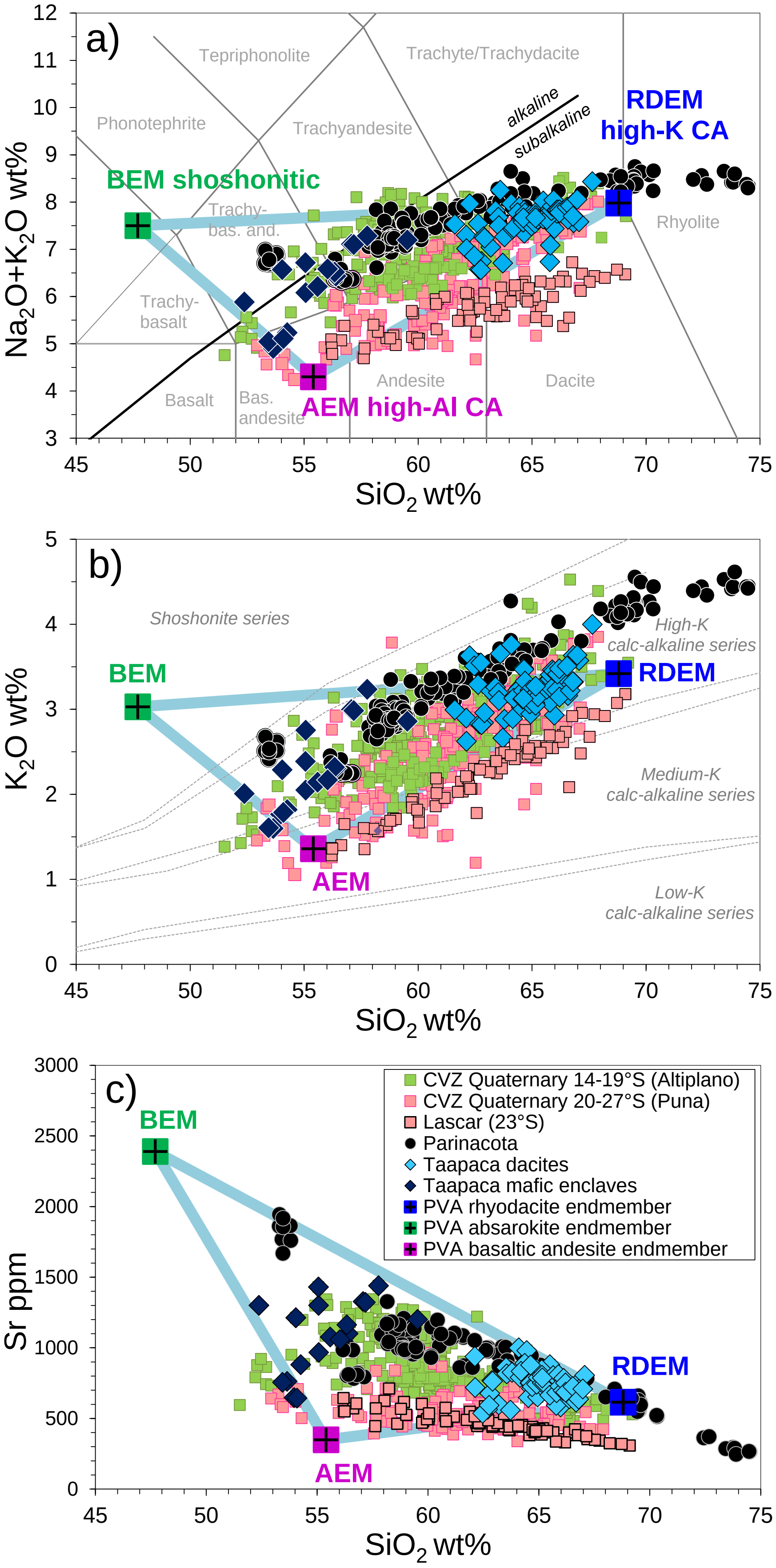
a)
Tepriphonolite
Trachyte/Trachydacite
Phonotephrite
Trachyandesite
alkaline
subalkaline
RDEM
high-K CA
BEM shoshonitic
Trachy-
bas. and.
Rhyolite
Trachy-
basalt
Basalt
Bas.
andesite
Andesite
Dacite
AEM high-Al CA
Na$_2$O+K$_2$O wt%
SiO$_2$ wt%
12
11
10
9
8
7
6
5
4
3
45
50
55
60
65
70
75
b)
Shoshonite series
High-K
calc-alkaline series
BEM
RDEM
AEM
Medium-K
calc-alkaline series
Low-K
calc-alkaline series
K$_2$O wt%
SiO$_2$ wt%
5
4
3
2
1
0
45
50
55
60
65
70
75
c)
BEM
RDEM
AEM
Sr ppm
SiO$_2$ wt%
3000
2500
2000
1500
1000
500
0
45
50
55
60
65
70
75
🟩 CVZ Quaternary 14-19°S (Altiplano)
🟥 CVZ Quaternary 20-27°S (Puna)
☐ Lascar (23°S)
● Parinacota
◇ Taapaca dacites
◆ Taapaca mafic enclaves
⊞ PVA rhyodacite endmember
⊞ PVA absarokite endmember
⊞ PVA basaltic andesite endmember

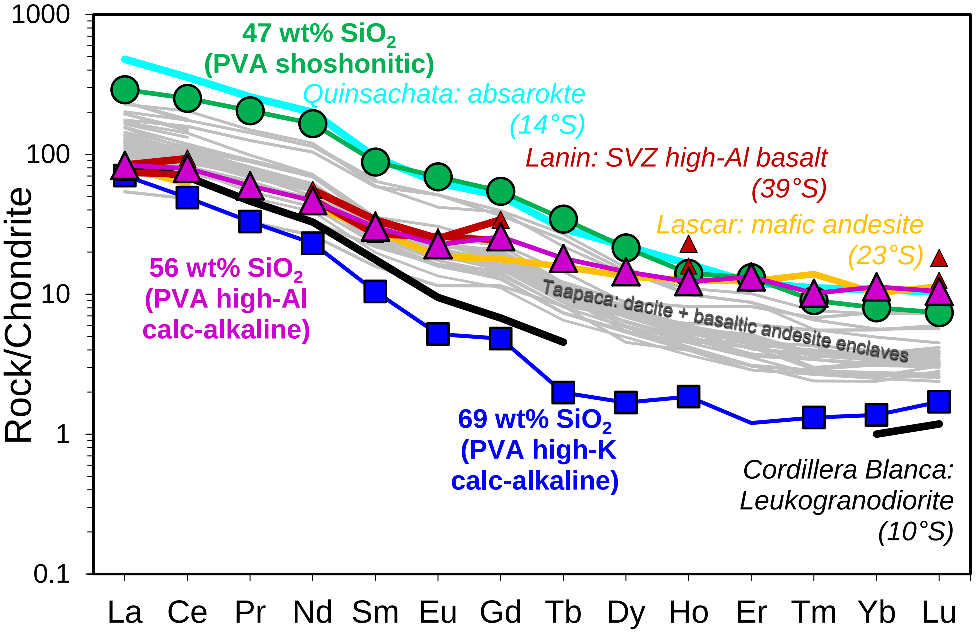

Figure 11. *REE-patterns of the PVA Taapaca end-members: High REE contents and high LREE/HREE are typical for shoshonites. The BEM end-member (green) mimics the absarokite composition from Quinsachata (Peru). Minor LREE enrichment characterizes high-Al calc-alkaline mafic lavas. The AEM end-member (violet) meets Quaternary mafic andesite (58 wt% SiO_2) from Lascar volcano and high-Al basalts from Lanin volcano (39.5°S) SVZ. Strong spoon-like HREE-depletion is a common signature of crustal melts generated in matured continental arcs in presence of garnet and/or amphibole. The RDEM end-member (dark-blue) follows the REE patter of leukogranodiorite from Cordillera Blanca (10 °S), interpreted to be a crustal melt. Reference data are taken from the compilation of Mamani et al. (2010) for Quinsachata and Lascar, Petford & Atherton (1996) for Cordillera Blanca, and Lopez-Escobar et al. (1977) for Lanin.*

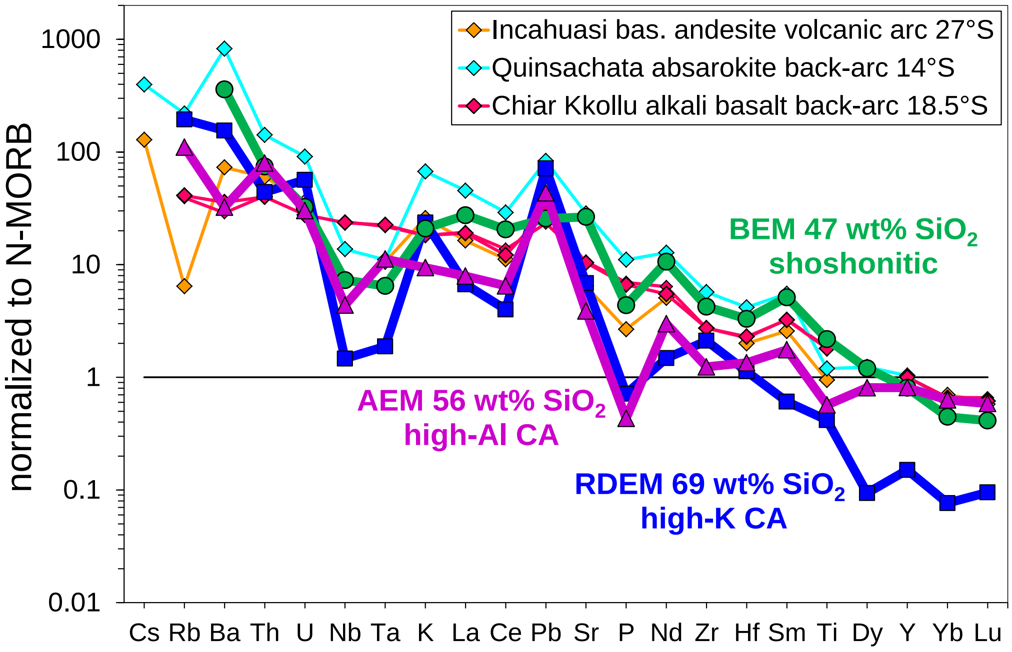

Figure 12. *N-MORB normalized trace element diagram showing the PVA end-members in comparison to: Incahuasi basaltic andesite – the most mafic lava found in the Quaternary CVZ volcanic arc (Kay et al., 1999); Quinsachata absarokite back-arc lava (Mamani et al., 2010), and Chiar Kkollu alkali basaltic back-arc lava (Davidson & de Silva, 1995).*

6.3. PVA END-MEMBERS IN CONTEXT WITH THE QUATERNARY CVZ MAGMAS

6.3.1. RELATIONSHIP OF THE PVA END-MEMBERS TO THE REGIONAL QUATERNARY DIFFERENTIATION TRENDS

The BEM and AEM, two geochemically contrasting mafic compositions identified as mixing components in the Taapaca dacites, correspond to the most mafic magmas of two distinctive suites, which have been recognized by Wörner et al. (1988) and described as two discrete chemical groups occurring at 18°S by Davidson et al. (1990) and McMillan et al. (1993). These suites are defined by distinct major- and incompatible trace element compositions alternating with time; however, both trends reveal almost uniform Sr-Nd-O and Pb isotopic characteristics. The basaltic and andesitic end-members obtained from the PVA may be parental compositions for these suites: 1) The basaltic high-Sr (shoshonitic) BEM lies above the most mafic basaltic andesite lavas in the differentiation trend and is enriched in certain LILE (Sr, Ba), HFSE (Ti, Zr, Hf, Th) and LREE, akin to the Quaternary (<1 Ma) **PP-**suite (**P**omerape-**P**arinacota). 2) The andesitic low-Sr (calc-alkaline) AEM meets exactly the most mafic composition of the Neogene **N-**suite (56 wt% SiO_2, 3.5 wt% MgO), represented by Miocene samples (10-6.5 Ma, Wörner et al., 1988) found in the Parinacota region. The N-suite does not have compositions <55 wt% SiO_2 in the Parinacota region (Davidson et al. 1990). This is also observed for other CVZ Quaternary magmas, compositionally corresponding to the N-suite.

The low-Sr Taapaca mafic enclaves show a chemical affinity to the N-suite more clearly than the low-Sr Parinacota basaltic andesite (a2) lavas. This is expressed by both low Sr/Y ratios of ~40 that are typical for N-suite (Figure 15), but also an entire major and trace element composition matching the Miocene N-suite rocks found at 18°S and at other Quaternary volcanic centers in the CVZ (Figure 10). The N- and PP-trends converge to one rhyodacitic composition at ~70 wt % SiO_2 that meets the silicic RDEM PVA end-member. More evolved volcanic rocks are very rare (Figure 13) in the recent stratovolcanoes located in the CVZ (Wörner et al., 1988; Hora et al., 2007; Mamani et al., 2010).

6.3.2. RELATIONSHIP OF THE PVA END-MEMBERS TO THE ENTIRE QUATERNARY CVZ LAVAS

Taking into account all available whole rock compositions of the CVZ Quaternary volcanic rocks, we can recognize that the PVA end-members appear to play an important role in the modern Andean magmas. Figure 10 illustrates the relationship of the BEM, AEM and RDEM end-members with the Quaternary volcanic rocks found in the CVZ volcanic arc (data compilation Mamani et al., 2010). These Quaternary CVZ volcanics are divided in this study into two main compositional sectors: 1) northern Altiplano-sector (14-19°S) and southern Puna-sector (20-28°S). The presented division meets a borderline at 19/20°S correlating with the boundary between Arequipa and Antofalla crustal domains, identified on the base of distinct isotopic compositions and Sr/Y and Sm/Yb signatures in the Quaternary volcanic rocks (Wörner at al., 1992; Mamani et al., 2008). Moreover, this division is also consistent with a borderline between Altiplano Plateau and Puna

Plateau trending NW-SE across Chile, Bolivia and Argentina, corresponding to a variety of lateral paleo-geographic features, as proposed by Allmendinger et al. (1997).

The whole rock compositions of the northern and southern CVZ sectors form two compositional groups. With exception to the rhyolites, the PVA end-members encompass the compositions of the most samples in a mixing triangle (blue lines, Figure 10) and define "corner" compositions. The enriched lavas of the northern sector lie on the mixing line between the shoshonitic BEM and rhyodacitic RDEM end-members; the most lavas of the southern sector lie on the mixing line between the high-Al calc-alkaline AEM and RDEM end-members.

The most mafic Quaternary CVZ lavas (52-54 wt% SiO_2), the baseline compositions, lie on the mixing line between BEM and AEM, suggesting their hybrid character. This magma mixing scenario corresponds to the Taapaca magma mixing course producing hybrid (BEM+AEM) mafic enclaves, presented in Figure 8. These baseline compositions, which plot on the BEM-AEM mixing line, may represent hybrid parental magmas resulting from distinct mixing proportions between BEM and AEM. They undergo further AFC processes and/or further magma mixing with silicic end-members producing the compositional variability of the Quaternary CVZ volcanics. However, fractionation may play negligible role in the CVZ volcanic systems, as can be concluded from a very rare occurrence of highly fractionated rhyolite lavas.

Both the northern and the southern sector lavas converge to silicic compositions at about 69-70 wt% SiO_2, corresponding to the RDEM. Lascar volcano (highlighted in Figure 10) shows a deviation from the main convergence trend to a slightly different rhyodacitic composition. Hence, volcanoes from the southern CVZ arc segment reveal an existence of another, alkali poorer calc-alkaline silicic end-member.

The PVA end-members presented as the "corner" compositions may be considered as parental magmas involved in the petrogenesis of the CVZ lavas. In comparison to the baseline compositions demonstrated by Davidson et al., (1991), the PVA compositions show more pristine, near-primary compositions.

6.3.3. FREQUENCY OF THE PVA COMPOSITIONS IN THE CVZ

From Figure 10 it can be noticed, that the "corner" end-member compositions plot at SiO_2 values, which are rarely or even not represented by natural Quaternary CVZ volcanics. Figure 13, presenting the SiO_2-frequency of the Quaternary CVZ lavas, demonstrates that there are marked rarities of natural samples at SiO_2 values of 54-56, 68.5 and 71-72 wt%, related to the AEM and RDEM. The BEM represent the lowest SiO_2-value that does not occur as an erupted composition in the CVZ volcanic arc at all. The AEM falls close before the small gap present in the PP-trend (Parinacota trend, Figure 10) and Taapaca trend at 57 wt% SiO_2, which separates Parinacota basaltic andesite lavas and Taapaca MEs from the most erupted CVZ lavas >57 and <68 wt % SiO_2. The RDEM corresponds to the gap observed between the dacites and rhyolites.

In connection with the entire Quaternary CVZ volcanics our PVA results show that the characteristic courses in the differentiation trends of the Quaternary CVZ lavas advocate for two magma mixing steps between three end-member magmas involved in generation of basaltic andesite and andesite - dacite lavas, rather than for typical fractionation curves, as interpreted by Davidson et al. (1991) for PP-trend. Therefore, the characteristic compositional gaps and the existence of the PVA end-members only as not-erupting mixing components, indicate specific physical conditions during magma mixing as well as thermal-rheological evolution of the end-members before mixing takes place.

The BEM and AEM mix and generate the baseline compositions lying on the (BEM+AEM) mixing line. These compositions range from 52 to ~56 wt% SiO_2 and erupt rare. Their highest SiO_2 content is limited by the highest value represented by the AEM end-member. If these hybrid magmas mix with more silicic crustal components, it is probable that the mixed composition skip over the closest SiO_2 values. It is interesting to note, that this compositional gap runs parallel to the (BEM+AEM) mixing line (Figure 10) and not for one defined SiO_2 composition. Therefore, there is not any obvious gap visible in the frequency diagram (Figure 13).

Based on petrological study of the Taapaca dacites, the RDEM is supposed to represent upper crustal rhyodacitic magma reservoir, comparable to large intermediate to silicic reservoirs, growing by incremental addition of crustal, compositionally similar melts (Huber et al. 2009). High crystallinity of the Taapaca dacites, in average of 25 vol% suggests that the rhyodacite reaches the rheological locking point at (sub)solidus temperatures at 700-760°C (Chapter 3). The intermediate-silicic melts undergo “mushification”; they became high crystalline crystal mushes, the most viscous magmas on Earth, as described by e.g. Scaillet et al. (1998) or Huber et al. (2009, 2012). Due to compositional and thermal-rheological properties of the silicic crustal magmas, they cannot erupt as pure lavas and can be only found as mixing components remobilized by rejuvenation by more mafic, hotter and water-richer melts (Bachmann & Berganz, 2006; Huber et al., 2009, 2010, 2011, 2012) or as plutons.

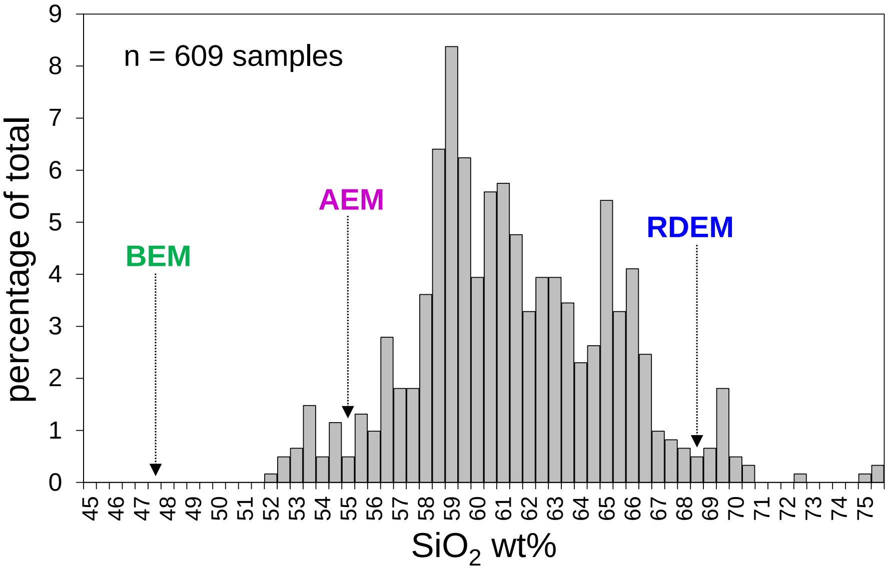

Figure 13. *SiO_2 contents of the Quaternary volcanic rocks in the CVZ including whole rock analyses (n = 609 samples) from data compilation of Mamani et al. (2010) used also in Figure 10. The AEM and RDEM PVA end-members fall into compositional minima at 55.4 and 68.8 wt% SiO_2, values obtained from the PVA calculation model (25e-8p).*

6.4. PREVIOUS PETROGENESIS MODELS OF THE CVZ MAGMAS

6.4.1. MASH-DOMINATED PETROGENESIS OF THE MODERN ANDEAN MAGMAS

So far, the broadly accepted explanation of the compositional variability of the Quaternary CVZ lavas is based, in general, on the MASH-model (Hildreth & Moorbath, 1988), involving mantle-derived melts, which undergo intra-crustal MASH processes at different crustal levels. The significance and commonness of the MASH zones in the crust and complex MASH processes (Hildreth & Moorbath, 1988; Annen et al., 2006; Hildreth, 2007) is emphasized by, in fact, lack of primitive arc basalts erupted in the Central Andean volcanic arc and their remarkable scarcity in the continental arc settings worldwide (Nye & Reid, 1986).

The MASH concept of Hildreth & Moorbath (1988), which has been extended to the “Deep Hot Zone” (DHZ) model by Annen et al. (2006) and Solano et al. (2012), offers a plausible explanation of compositional fluctuations observed in the mature Andean arc. It incorporates the AFC and MASH processes, allows random injection of mantle-derived melts into entire lower crust forming a series of layers (sills) at different emplacement levels. The exceptionally thick crust exceeding 70 km beneath the Altiplano (e.g. Prezzi et al., 2009 and references therein) provides a development of multi-level MASH zones (Ginibre & Wörner, 2007; Mamani et al., 2010). Interactions between such layers provide chemical mixing between more and less evolved magmas, leading to a wide spectrum of melt compositions extracted from the DHZ. Furthermore, the magmatic diversification can proceed at the mantle-crust boundary where heterogeneities on a small scale can develop (e.g. Griffin & O`Reilly, 1986; Hildreth & Moorbath, 1988). Hildreth (2007) suggests that each volcanic center has its own focal MASH zone with peripheral areas to such foci, where primitive magma batches are not intercepted and hybridized and can ascent to produce monogenetic volcanoes as in the case of the Cascades.

Magmas erupted in the modern central Andean volcanic arc demonstrate compositional correlation with the crustal thickness along and across the arc and in temporal sequences (e.g. James, 1982; Hildreth & Moorbath, 1988; Kay et al., 1991, 1994, 2005; Wörner et al., 1988, 1992; Haschke et al., 2002, Haschke & Günther, 2003; Mamani et al. 2008, 2010). These previous studies assumed that the geochemical and isotopic variations in the Quaternary CVZ lavas result from equilibration of the mantle-derived melts in the crust-mantle boundary or in the deep lower crust according to the MASH processes. These lavas are supposed to reflect altering residual mineral assemblages in the lower crust, leading to the occurrence of a “garnet signature”, as well as increasing extend of assimilation, leading to more radiogenic Sr-Nd isotopic compositions in the thickening Andean crust.

6.4.2. TEMPORAL CHANGES IN THE MIOCENE-HOLOCENE MAGMA COMPOSITIONS IN THE CVZ

Haschke et al. (2002) and Mamani et al. (2010) demonstrated different episodes of crustal thickening in the CVZ using trace element ratios, determined for volcanic rocks as diagnostic tool describing changes in deep crustal mineral assemblages since Jurassic time (~200 Ma).

The major crustal thickening events in the Central Andes occurred at Oligocene time (~30 Ma) and continued in the Late Miocene (10-6 Ma), (Mamani et al., 2010 and references therein). These tectonic events are supposed by many authors to be reflected in: 1) successively increasing Sr/Y, coupled with destabilization of plagioclase and increasing proportions of garnet (e.g. Garrison & Davidson, 2003); 2) increasing Sm/Yb ratios, not affected by plagioclase but sensitive to pressure dependent changes from clinopyroxene to amphibole and finally to garnet (Kay & Mpodozis, 2001); and 3) increasing Dy/Yb, resolving changes form amphibole- to garnet-bearing facies in the lower crust, resulting from lower partition coefficients of Dy in the garnet (Macpherson et al., 2006; Davidson et al., 2007).

Ginibre & Wörner (2007) and Mamani et al. (2010) observed that magmas erupted after crustal thickening at regions of the thick crust may not always show the “thick crust” signatures, related to the stability of Al-phases. They conclude that MASH processes in a thick crust are not restricted to the deepest parts of the crust. Therefore, magmas traversing thick crust can be “MASH-ed” in different crustal levels characterized by varying mineral residues. This imparts distinct geochemical signatures (e.g. LILE/HREE or MREE/HREE) at similar Sr-Nd-O-Pb isotopic composition in lavas, which erupt even from the same vent, as observed by Parinacota flank vent eruptions.

Concentrating on the Neogene to recent volcanic rocks in the CVZ, McMillan et al. (1993) argue that Miocene N- and Holocene PP-suite magmas represent the same primary mantle-derived magma compositions affected by deep MASH processes operating under changing crustal thickness. Similar isotopic composition and distinct LREE/HFSE ratios observed in the N- and PP-suites imply the same source of crustal contamination at different pressures. Amphibolite mineral assemblage, at moderate-pressures, must have affected the N-suite lavas; the PP-suite encounters for high-pressure garnet-bearing assemblage. The time delay of the enrichment observed in the PP-suite can be connected to a long thermal relaxation time affecting geothermal gradient in the lower crust, in response to the crustal thickening and heat addition from the ascending mantle-derived magmas (McMillan et al., 1993; Mamani et al., 2010).

6.5. NOVEL PETROGENETIC MODEL OF THE CVZ MAGMAS BASED ON PVA RESULTS

The BEM, AEM and RDEM end-member compositions obtained from the PVA, conducted on Taapaca rocks, represent different magma series, as identified in the section 6.2. These compositions have individual geochemical signatures and cannot be related to each other via AFC. Therefore, by PVA determined magma compositions must have originated from different magmatic sources and represent three different primary magmas involved in the petrogenesis of the Taapaca magmas. As presented in the section 6.3, these Taapaca end-members may account for primary magmas, which generally occur in the Quaternary Central Andean Volcanic Zone. In the next sections, I discuss possible sources for the end-member magma compositions obtained by PVA and propose an alternative model to the previous, MASH-based interpretations of the genesis and evolution of the central Andean magmas.

6.5.1. MAGMATIC SOURCE OF THE BEM PVA END-MEMBER

The BEM PVA end-member is the most enriched, near primary composition identified in this study in the modern CVZ volcanic arc. The enriched trace element and isotopic signatures found in the Quaternary CVZ most mafic rocks are still subject of debate. Many researches consider different possible sources of the enrichment. As listed by Kay et al. (1999), the potential sources are: 1) enriched lithospheric mantle (Rogers & Hawkesworth, 1989), 2) subducted sediments and fluids (e.g. Stern, 1991; Kay et al., 1994), 3) subduction erosion (Stern, 1991; Kay et al. 2005) and 4) crustal contamination by MASH processes (Hildreth & Moorbath, 1989; Davidson et al., 1990; Mamani et al., 2010) or 5) complex combination of all of these processes (Kay et al., 1999).

Based on extensive study of trace element and Sr-Nd-Pb-O isotopic composition in the Central Andean volcanics, Mamani et al. (2010) exclude subducted sediments, tectonic erosion and contribution from enriched subcontinental lithosphere as possible sources for the observed enrichment and geochemical variations in the Quaternary CVZ lavas. Numerous authors (Mamani et al., 2010 and references therein) favor the mature and composite crust as a source of enrichment. Davidson et al. (1990) suggest that breakdown of amphibole in the crustal rocks in response to changing pressure and temperature conditions in the thickening crust and migration of the mineral stability phase-boundaries lead to release of incompatible elements. Field, petrographic and geochemical evidence confirm this phenomenon: the transformation from shallow amphibole-plagioclase-bearing arc plutonic rocks into anhydrous garnet-bearing granulite facies, related to compression during crust thickening, have been found in the exhumed sequences of the lower crust forming the Jijal complex of the Kohistan paleo-island arc in Pakistan (Yamamoto & Yoshino, 1998; Yoshino et al. 1998; Garrido et al. 2006). Beside high-pressure crystallization of garnet-bearing assemblages from mantle-derived melts, dehydration and dehydration-melting of the hornblende-rich crustal sources is suggested to be a common intra-crustal differentiation process, reflecting an important arc maturation process (e.g. Jamieson et al., 2011). Both dehydration processes lead to a breakdown of hydrous minerals with one significant difference, that the dehydration results in a release of H_2O-rich fluids and dehydration-melting generates H_2O-undersaturated granitic melts (e.g. Johannes & Holtz, 1996). As defined by Hermann et al. (2006), the aqueous fluids contain <30 wt% of total amount of dissolved solids and the hydrous melts contain <35 wt% H_2O.

The enrichment in incompatible elements, characterizing the BEM, may principally result from contamination with crustal fluids and/or melts. However, simultaneous enrichment in mobile and immobile trace elements rules out sole contribution of the fluid phases. Numerous petrological and experimental studies (e.g. Tatsumi et al. 1986; Brenan et al. 1995; Adam et al. 1997; Scambelluri & Philippot, 2001; Green & Adam 2003) show that fluids readily transport LILE, whereas REE and HFSE are rather retained in the residues. Only silica-rich melts, simultaneously enriched in mobile and immobile incompatible elements would significantly affect the LILE and HFSE budget of the basaltic BEM. Such melts, however, would also cause alteration toward more evolved (>47 wt%

SiO_2) magma composition. Therefore, an intra-crustal enrichment by contamination with H_2O-rich fluids and/or silicic deep crustal partial melts for BEM can be ruled out.

If the BEM would originate from a mantle-derived primitive arc basaltic melt, trapped at mantle crust boundary due to buoyancy barrier, it could be “MASH-ed” to gather its enriched signature in the lower crust. However, the BEM type magma must have escaped the deep crustal MASH to retain its primitive basaltic silica content. Observed Mg, Mg-number, Ni, and Cr contents of the BEM are relatively lower than expected values in basaltic mantle-derived melts. Such low concentrations of compatible elements would indeed require an early olivine and pyroxene fractionation leading at the same time to higher SiO_2 contents. Moreover, the significant overprint of the trace element budget and isotopic composition would require considerable assimilation/contamination. Thus, the BEM would have evolved at least to a basaltic andesite composition due to, for instance, thermal evolution of contaminated magmas triggering fractionation (Taylor, 1980; Hawkesworth, 1982).

All presented central Andean Quaternary magmas show isotopic composition significantly differing from MORBs or OIBs (0.7024-0.7035 and 0.7030-0.7050, respectively; Wilson, 1989, s.143). Sr, Nd, Pb and O isotope data are commonly presented as an essential indication for the deep crustal contamination and homogenization of mantle-derived basaltic magmas at Parinacota and Taapaca (Davidson et al., 1990, 1991; Wörner et al., 1992; Kiebala, 2008; Mamani, 2008; Hora et al., 2009). Lead isotope data of Parinacota lavas correlate with the composition of the local Proterozoic basement (e.g. Wörner et al., 1992; Mamani, 2006). $\delta^{18}O$ values determined for Taapaca and Parinacota (Entenmann, 1994; Banaszak, 2007; Chang, 2008) range from +6.7 to +7.4‰ and reflect enriched signature, displaced considerably from the typical mantle values (+5.7 to +6.2 ‰). The elevated Sr and low Nd isotopic ratios of Taapaca and Parinacota lavas (see section 5.4) exhibit only minor variations within a wide SiO_2 content, reflecting preserved isotopic baseline composition. The estimated Sr-Nd isotopic composition of the BEM (Figure 9) is less radiogenic than the Quaternary baseline CVZ lavas but still considerably evolved.

The isotopic composition of Miocene alkali basalt Chiar Kkollu from monogenetic back arc volcanic center, showing distinctively lower $^{87}Sr/^{86}Sr$ ratios (0.7041) than recent baseline CVZ lavas, is supposed to represent the sub-Andean mantle source (Davidson & De Silva, 1995). The difference in the isotopic composition between the Chiar Kkollu and BEM end-member is in accordance with the abrupt increase in the baseline Sr isotopic composition from ~0.7045 to 0.7055 and increase of Nd isotopic composition, accompanied by changes in the trace element characteristics (e.g. increasing La/Yb, Sm/Yb), due to the Miocene uplift and crustal thickening (Mamani, 2006 and references therein). Two opposite hypotheses have been postulated to explain the recent enrichment of the youngest CVZ lavas: 1) increased contribution of crustal material in the parental magmas, as discussed e.g. by Davidson et al. (1990) and Mamani et al. (2010), or 2) incorporation of an enriched subcontinental lithospheric mantle (SLM) proposed by Rogers & Hawkesworth (1989). Owing to the fact that the BEM is a basaltic composition, more primitive than the baseline magmas but enriched in nearly all incompatible elements with more radiogenic Sr-Nd isotopic composition in comparison to expected primitive mantle values, the origin from an enriched source is preferred over the crustal overprint of arc-like primitive melts derived from the asthenospheric mantle.

The SLM has been proposed in numerous studies as the source of basaltic magmas enriched in incompatible elements, characterized by elevated Sr and low Nd isotopic ratios (e.g. Hawkesworth & Vollmer, 1979; Hawkesworth et al., 1984; Halliday et al., 1985; Nelson et al., 1986; Dudás et al,. 1987; Rogers & Hawkesworth, 1989; Carmichael et al., 1996; Luhr, 1997; Conrey et al., 1997; Hesse & Grove, 2003). Mantle metasomatism processes may produce the enrichment of the SLM (Gill, 1981; Menzies & Hawkesworth, 1987). These processes involve aqueous liquids and silicate melts migrating upwards from underlying dehydrated slab and the asthenosphere. However, as discussed by Wilson (1989), the generation of the strongly enriched magmas cannot occur in response to the introduction of the fluids and partial melts into a “normal” mantle. Otherwise, they would occur in the majority of the volcanic arcs and as commonly observed they are present in the mature subduction zones. The strongly fractionated REE patterns, evolved Sr, and oxygen isotopic composition appear only in the Pleistocene to recent CVZ lavas.

Rogers & Hawkesworth (1989) connected the occurrence of enriched volcanics to the mobilization of an old, late Proterozoic mantle lithosphere due to migration of the volcanic front across the northern Chile to the east. According to this model, the BEM-type composition can represent near primary magma, derived from the enriched SLM, which may remain nearly unaffected by interaction with the continental crust. Hawkesworth et al. (1979) argue that elevated $\delta^{18}O$ values (>6‰), high Sr and low Nd isotopic ratios may be evidence that this Sr-Nd-O isotopic composition may exist in metasomatized upper mantle. Following this argument, the CVZ Quaternary volcanics do not require extensive crustal contamination.

Thus, the shoshonitic affinity of the BEM may be directly connected to the models of shoshonite generation in the back arc where these enriched magmas reach the surface as nearly pure shoshonite lavas. As broadly accepted, the generation of magmas with shoshonitic affinity requires little partial melting of metasomatized, garnet-bearing lithospheric mantle sources (Deruelle, 1991; Kay et al., 1996a, 1999; Petrinovic et al., 2006; Guzmán et al., 2006). The extensional regime of the back arc induces the eruption of the shoshonite as clear components. The volcanic arc represents then a distinct tectonic regime where the shoshonites erupt only as one component in the hybrid mafic magma.

6.5.2. MAGMATIC SOURCE OF THE AEM PVA END-MEMBER

The compositional resemblance of the AEM obtained from the PVA to the low-Mg high-Al basalts and basaltic andesites found in the most volcanic arcs worldwide (Chile SVZ, Cascades, Japan, and New Zealand) indicates that the AEM represents the most abundant primary magma type, characteristic for the subduction zones. These calc-alkaline basalts and basaltic andesites are regarded as the paradigmatic magmatic arc suite generated in the mantle wedge (e.g. Marsh, 1979a, 1979b; Tatsumi, 1983, 1986, 2003, Brophy & Marsh, 1986; Crawford et al., 1987; Sisson & Grove, 1993a, 1993b; Gaetani et al., 1993, 2003; Baker et al., 1994; Wagner et al., 1995; Yagodzinski et al., 1995; Gaetani & Grove, 1998, 2003; Grove et al. 2002, 2003, 2005, 2006).

The compositional similarities of the CABs worldwide suggest that this type of magma must be generated in the subduction zones by similar processes under similar conditions. It is generally accepted, that dehydration of H_2O-bearing minerals in subducted oceanic lithosphere liberates a flux of volatiles that rises upward into the overlying mantle wedge. It concerns the asthenospheric part of the mantle wedge. The aqueous fluid interacts chemically with mantle peridotite and lowers its melting point, resulting in partial melting of the mantle rocks. This process is known as a flux melting (e.g. Wyllie, 1982; Tatsumi, 1986, 1989; Grove et al., 2002; Gaetani & Grove, 2003). Emerging fluid-rich melt separates from its residue and ascends to the shallower part of the mantle wedge where it traverses the inverted thermal gradient. Along the upward melt trajectories in the mantle wedge, the water contents in the primary melt decreases and the melt fraction of the partial melting increases. As presented by Grove et al. (2006) the water content in the initial melts varies from 28% at the base of the mantle wedge and decreases to 5%. The melt fraction at the cold base of the mantle wedge reaches 2.5-3% and 10-15% in the mantle wedge “core”. These variations depend on mantle wedge geometry and temperature distribution, and are responsible for compositional differences in the primary asthenospheric melts, which are not directly CAB.

One of the specific features of many high-Al CAB magmas (~19 wt% Al_2O_3) is their low $Mg\#_{melt}$(1) <60, as well as low Ni and Cr contents, characteristics likewise represented by the AEM. The high-Al basalts and AEM compositions are therefore too evolved to be directly derived from the mantle peridotites. During ascent, the hydrous basaltic arc melts undergo extensive fractionation. The high H_2O-contents destabilize plagioclase as an early crystallization phase and promote crystallization of Fe-Mg-silicate and Fe-oxide phases. The fractionation is consequently dominated by olivine, clinopyroxene and magnetite (e.g. Sisson & Grove, 1993a; Crawford et al., 1987; Grove et al., 2003). Crystallization of Fe-Mg silicates depletes the residual melt in MgO and FeO, and increases SiO_2, Al_2O_3 and alkalis, producing high-Al basalts and andesites characterized by low Mg# and calc-alkaline affinity.

The AEM composition is in keeping with major element and Sr concentrations of melt inclusions hosted in olivines (Fo83-69) found in basaltic andesites (~52-53.5 wt% SiO_2) from Llaima volcano (SVZ, 39°S), presented by Bouvet de Maisonneuve et al. (2013). These melt inclusions form fractionation trends, which span from [~49 wt% SiO_2, 6.5-7 wt% MgO, 3-4 wt% Na_2O+K_2O and 500 ppm Sr] to [55-57 wt% SiO_2, ~3.5 wt% MgO, 3.5-5 wt% Na_2O+K_2O and 350-400 ppm Sr]. The AEM lies exactly on these melt inclusion trends with its 55.4 wt% SiO_2, 4.3 wt% MgO, 3.5 wt% Na_2O+K_2O and 349 ppm Sr in the PVA model (25e-8p). The compositional consistency of the statistically obtained AEM with the chemical trends of the natural olivine-hosted melt inclusions suggests that the AEM may well represent a certain fractionation stage from a basaltic composition, characterized by e.g. initially low MgO contents (<7 wt%), as determined in the melt inclusions.

---

[1] Mg-number, $Mg\#_{melt}$ equals the molar ratio of $Mg/[Mg+Fe^{TOT}]$ in the whole rock.

In spite of the fact that the AEM end-member shows depletion in LILE and HFSE relatively to the BEM – shoshonitic end-member, this composition is enriched in LILE and LREE and depleted in HFSE in comparison to N-MORB (Figure 12). This trace element characteristic is generally regarded to be caused by the fluid addition from the slab to the mantle wedge (e.g. Gill, 1981; Tatsumi et al., 1986) and enrichment during fractionation of the Fe-Mg phases (Wilson, 1989). Besides the HFSE-poor aqueous slab-fluids involved in the generation of the arc basalt, the depletion in HFSE is also linked to 1) higher degrees of partial melting of the mantle wedge, promoted by the water-rich fluid, 2) retention of the HFSE in accessory mantle mineral phases, and 3) re-melting of an already depleted mantle source (Wilson, 1989).

The AEM is characterized by stronger depletion of Nb in comparison to Ta (Figure 12). Due to the fact that Nb and Ta are not fractionated during slab dehydration (e.g. Rudnick et al., 2000), Nb/Ta>1 found in the AEM may result from the mantle melting or fractionation processes, due to distinct partition coefficients of these elements in pyroxene and amphibole(2) (e.g. Rudnick et al., 2000; Tiepolo et al., 2000; Blundy & Wood, 2003). Amphibole is regarded as an important early fractionating phase (Davidson et al., 2007). Sisson & Grove (1993a) report that with the appearance of amphibole in high-Al basalt, the abundance of olivine decreases. In some Parinacota lavas, olivine cores (Fo88-95) are preserved in high-Al-Ti amphiboles (Entenmann, 1994). Furthermore, the scarcity of olivine and commonness of amphibole in the CVZ lavas support the role of amphibole in the early evolution of the AEM-type magmas.

The compositional similarity of the AEM to the high-Al CAB lavas found in the SVZ, indicates, that the AEM represents the principal arc magma type involved in the petrogenesis of magmas produced in the entire Andean volcanic arc. Although this primary melts do not reach the surface as pure component in the Central Andes, the high-Al CAB is predominant and persistent in the CVZ. It occurs in the northern Altiplano- and southern Puna-sector of the CVZ volcanic arc and has been identified as the Miocene N-suite in the Altiplano sector (section 6.3.1).

6.5.3. *MAGMATIC SOURCE OF THE RDEM PVA END-MEMBER*

The most specific trace element signature of the RDEM end-member is its high Sr/Y ratio connected to the processes generating "adakitic" magmas. High Sr/Y=104 and 84 (depending on the PVA model) of the RDEM overlap with likewise high Sr/Y=139 and 85 of the BEM shoshonitic end-member. So far, this signature has been connected to the MASH processes of the mantle-derived arc basaltic magma and role of garnet in the thickening Andean crust, giving the characteristic "garnet signature", as mentioned in section 6.4. For the first time, the PVA study resolves this signature into two completely different magmatic components in the Quaternary volcanics of the CVZ.

In contrast to the true adakite, which are generated from young and hot subducted oceanic crust (e.g. Kay, 1978; Defant & Durmmond, 1990), various processes can produce the "adakitic" rocks.

---

[2] D(Nb) and D(Ta) partition coefficients in amphibole correlate with the size of M1-sites (Blundy & Wood, 2003), therefore Nb-Ta fractionation depends on amphibole composition.

These include: 1) high-pressure fractionation from mantle-derived basaltic magma, 2) partial melting of the thick crust where garnet and/or amphibole is a stable phase (e.g. Garrison & Davidson, 2003; Castillo et al., 1999; Macpherson et al., 2006; Barboni et al., 2011) or 3) combination of these both processes (Annen et al., 2006, 2008; Solano et al., 2012). Consequently, detailed geochemical studies are required to establish the source(s) and generation path(s) of the silicic RDEM end-member. This section presents some considerations of the possible source of the RDEM-type magma.

The model based on numerical simulations proposed by Annen et al. (2006, 2008) and Solano et al. (2012) involves fractionation of the mantle-derived melts in connection with partial crustal melting proceeding in a “Deep Hot Zone” (DHZ), analogue to the MASH zone (Hildreth & Moorbath, 1988; Hildreth, 2007). These processes lead to generation of intermediate and silicic magmas in the subduction zones.

A conception of the DHZ model is described as follows: The DHZ is generated by successively emplaced mantle-derived basalts. They form complex systems of sills, beginning at mantle-crust boundary and reach different lower crustal levels. Progressive intrusions of the hot mafic melts into the DHZ region in the crust 1) induce incomplete crystallization of the basalts and accumulation of its residual melts; 2) trigger re-melting of the formerly intruded and crystallized basalts and 3) activate partial melting of the surrounding crust. The residual melts are, however, volumetrically more significant than crustal melts in the DHZ model. The MASH processes including AFC and magma mixing, affecting the evolution of the residual and partial melts and interactions between them, are strongly controlled by chemical and physical properties of the mantle-derived melts and the crust, described by Annen et al. (2006, 2008) and Solano et al. (2012). Temperatures, H_2O-contents, and emplacement rates are critical parameter in this model. The variable differentiation path would then result from 1) various proportions of the crustal component incorporated by the MASH processes due to different thermal conditions, 2) different crystallization phases and crystallization sequences influenced by variable H_2O contents (e.g. Müntener et al., 2001), and also 3) different stagnation times at the deep crust.

Due to the high variability of the parameters involved in the modeling, it is not possible to predict the differentiation conditions, proportions of the residual basaltic and partial crustal melts involved in the generation of the RDEM, based solely on the approximation and comparison to the presented models of Annen et al. (2006) and Solano et al. (2012). Nevertheless, the DHZ model is broadly considered as an essential petrogenetic model of subduction-related intermediate and silicic magmas (Reubi & Blundy, 2009), hence also generation path of the RDEM-type magmas in the CVZ.

According to the DHZ model, strongly fractionated REE pattern and high Sr/Y imply a deep crustal overprint of the RDEM. These geochemical signatures of the RDEM, connected to the presence of residual garnet are similar to those of the BEM. However, partition coefficients of Y and Yb for garnet are significantly higher in the intermediate liquids in comparison to basalts (compilation Kd data from Rollinson, 1993). This means, that also small amount of residual garnet may lead to the strong depletion of Y and Yb in the silicic RDEM end-member. Consequently, similar high Sr/Y ratios found in the rhyodacitic RDEM and basaltic BEM do not require similar geochemical overprint processes and similar compositional (mineralogical) environment.

Experimental studies of Müntener et al. (2009), Alonso-Perez et al. (2009) demonstrate that garnet is stable also at relatively shallow crustal depth corresponding to pressures <0.8 GPa, coexisting with amphibole. They show that crystallization of hydrous calc-alkaline magmas at crustal levels generates “adakitic” signatures through the fractionation of garnet and amphibole. Therefore, the geochemical character of the RDEM must not be connected necessarily to the deep crust.

Furthermore, although both end-members, the BEM and the RDEM show depletion in MREE to HREE, the RDEM presents rather “spoon-like” REE pattern (Figure 11), which also suggests mineralogically different depletion milieu. Strong depletion in MREE and HREE observed in the REE pattern of the RDEM indicates substantial participation of amphibole in the fractionation process. An abrupt change in a slope of REE pattern in the RDEM at Gd (MREE), corresponds to an abrupt increase of partition coefficients D≥1 for the Gd-Lu in the amphibole and garnet (Fig. 1 in Davidson et al, 2007 and references therein). If only garnet would be involved in the fractionation as dominating phase, the REE pattern of the RDEM would show steady decrease to Lu, similarly to the BEM shoshonitic end-member, according to the steady increase of the $D^{(Gd\text{-}Lu)}$ values. Barboni et al. (2011) show that massive fractionation of amphibole without plagioclase accounts for sudden slope break of REE and additionally can produce adakitic signature. Due to the curved line of $D^{(Gd\text{-}Lu)}$ for amphibole, the amphibole fractionation induces spoon-like MREE-HREE pattern, which is apparent in the RDEM in comparison to the BEM.

Although the DHZ (MASH+AFC) model is currently favored by the scientific community, there are two arguments, which cast doubts on the DHZ model as plausible petrogenesis of the RDEM-type magma.

First, as discussed in previous two sections, magmas entering the crust are derived from lithospheric and asthenospheric mantle and have BEM and AEM compositions. The REE patterns of the PVA end-members suggest that the RDEM could not have evolved by high-pressure fractionation from BEM- or AEM-type magmas. Commonly, the concentrations of REEs, which are incompatible elements, increase with increasing SiO_2. Therefore, the significantly lower REEs in the RDEM in comparison to the BEM and AEM cannot result from fractionation of the basaltic BEM- or AEM-type magma or directly from their precursory primary melt.

Secondly, if garnet is a fractionation phase during high-pressure crystallization of the mantle-derived basaltic magma, why it has never been found in any single volcanic rock in the Central Andes? Even the enriched, high-LILE basaltic andesites from Parinacota volcano, showing pronounced “garnet signature” are garnet-free. These Parinacota lavas, which traversed the crust quickly (Hora et al., 2009), could have retained the early fractionating phases, at least as crystal remnants. There is an example of high-Fo(88-95) olivine remnants in Parinacota andesite (mentioned in section 6.5.2), indicating early olivine fractionation of arc basalts, producing the AEM composition.

Garnet is rare but present in subduction-related medium- and high-K alkaline basaltic andesite – rhyolite series, as reported by Bach et al. (2012) and references therein. The explanation of the presence or absence of garnet may result from differently proceeding fractionation vs. partial melting processes in the crust, although both processes lead to the garnet signature in magma. If the basaltic magma crystallizes under high-pressure conditions in the DHZ, garnet is present in the liquid and is successively withdrawn to form a residuum; some crystals may persist in the fractionated melt forming orthocrysts or antecrysts in the finally erupted lavas. During partial melting, garnet remains in the residuum and is absent in the generated melts.

The REE patterns of the Taapaca RDEM match those of e.g. leukogranodiorite of the Cordillera Blanca Batholith (10°S), (Petford & Atherton, 1996) presented in Figure 11, and intrusive granites found in the metaplutonic Jijal complex (Garrido et al, 2006). Both examples are interpreted to be produced by partial melting of deep (>30 km) metabasaltic sources with amphibole and garnet but not plagioclase as residual phases.

The geochemical characteristics of the RDEM are in agreement with magmas identified as crustal melts presented by e.g. Petford & Atherton (1996) and Garrido et al. (2006). The Taapaca rhyodacite reservoir, characterized by a granitic mineral assemblage (low-An plagioclase, alkali feldspar, biotite, hornblende, quartz, magnetite, titanite and zircon), displays petrological and geochemical characteristics that are reminiscent of granodioritic plutons (e.g. Petford & Atherton, 1996) and Monotonous Intermediates (e.g. Hildreth, 1981a; Bachmann et al., 2002). Therefore, the RDEM end-member represents in fact a granitic magma composition. This statement allows relation of the RDEM petrogenesis to generation, segregation, and ascent of granitic melts described in numerous studies. Many authors emphasize the role of dehydration-melting of hornblende-bearing crustal rocks as a common intra-crustal differentiation process in arcs and consequence of their maturation processes as thickening, leading to an addition of granitic partial melts to the upper arc crust and formation of dense garnet granulite lower crust (e.g. Brown, 1994, 2001, 2004, 2007; Solar et al., 1998; Vigneresse & Clemens, 2000; Chappell, 2004; Vigneresse, 2004; Garrido et al. 2006; Clark et al., 2011; Sawyer et al., 2011). A basaltic underplating of the Andean crust may serve as a heat source for generation of the silicic melts produced by dehydration-melting in the thickening crust.

Considering crustal melting as a process developing the RDEM end-member, it should be noted, that Cenozoic ignimbrite deposits of the CVZ are also interpreted to be a result of crustal melting, connected to the thickening of the CVZ crust (de Silva, 1989a,b; Francis et al., 1989). Generally, these dacitic to rhyolitic ignimbrites of the CVZ show more radiogenic Sr-Nd isotopic composition in the range of $0.706<{}^{87}Sr/{}^{86}Sr<0.711$ (e.g. Mamani, 2006) in comparison to the CVZ arc lavas. As mentioned in section 5.4, the Sr-isotopic ratio of the RDEM is most probably similar to Taapaca dacites (${}^{87}Sr/{}^{86}Sr< 0.707$). The ${}^{87}Sr/{}^{86}Sr$ ratios of Pliocene Lauca-Perez ignimbrites, which is a part of the volcanic basement in the Taapaca – Parinacota region at 18°S (Wörner et al., 2000) reveal values of 0.7067-0.7072 (Davidson et al., 1990), nearly overlapping with Taapaca dacites. This similar $^{87}Sr/^{86}Sr$-range of the ignimbrite deposit and Taapaca dacites supports the interpretation of the RDEM as crustal melt.

However, according to a study by Knesel & Davidson (2002), the isotopic composition of the partial melt may vary depending of melting temperature, and accordingly the mineral phases involved in the melting process. Consequently, different melting reactions may give rise to variable Sr-isotopic ratios in melts generated from one single crustal protolith. Furthermore, as reported by McLeod et al. (2013), xenoliths representing Central Andean basement reveal significant Sr-isotopic heterogeneity (0.7105-07368). This finding supports the variability of isotopic composition, which may occur in crustal melts. Regarding the investigation of the crustal partial melting processes, isotopic composition represents rather unreliable geochemical tool.

Referring to geophysical observations imaging the Andean crustal structures by different seismic methods (Ocola & Meyer, 1972; Wigger et al., 1994; Yuan et al., 2000; Babeyko et al., 2002; Schurr et al., 2003; Zandt et al., 2003; Kulakov et al., 2006), the recent volcanoes and ignimbrite fields in the CVZ are associated with low seismic velocities at the mid-crustal levels (15 to 25 km; Chmielowski et al., 1999; Yuan et al., 2000; Babeyko et al., 2002). This observation is i.a. interpreted as a zone of continuing metamorphism and partial melting which decouples upper-crustal brittle imbrication from ductile lower-crustal thickening (Yuan et al., 2000), forming the Andean-Low-Velocity-Zone (ALVZ). The low-velocity-zone extends through the entire Central Andes (Yuan et al., 2000; Beck & Zandt, 2002). Beck & Zandt (2002) relate the detected mid-crustal low-velocity-zone beneath the eastern wedge of the Western Cordillera to a region of partial melt linked to the active volcanic arc.

In light of the presented evidence, the RDEM silicic Taapaca end-member is likely to be generated by partial melting of the crust consisting of an old basement and underplating mantle-derived material Therefore, the RDEM can be regarded as a primary, unfractionated crustal melt.

6.5.4. NOVEL PETROGENETIC MODEL: SOURCES INSTEAD PROCESSES

The PVA results viewed in a general context, contradict previous MASH-based models, assuming that the baseline geochemical signature of erupted lavas is set by modification of mantle-derived arc basaltic magmas during entrapment at the mantle-crust boundary or in the deep crust (e.g. Hildreth, 2007; Mamani et al., 2010 and references therein). Here presented study reveals whole rock compositions of three distinct (near) primary magmas, which occur simultaneously in the central Andean volcanic arc. The PVA resolves the hybrid Taapaca dacites into three clear end-members. They are not generated via MASH and/or AFC. These magmas are produced by independent partial melting processes in different magmatic environments. Shoshonitic, high-Al calc-alkaline and high-K calc-alkaline magmas are *the components* that originate from three different sources: the lithospheric mantle, the asthenospheric mantle and the crust, respectively.

The widely established explanation for the compositional variability of the Quaternary CVZ lavas is so far based on three main conditions affecting the baseline signatures of the CVZ lavas: 1) the bulk composition of the underlying crust, 2) the crustal thickness, and 3) the depth of the magma-crust interaction as specified by Mamani et al. (2010). The first condition is responsible for variation in isotopic composition of the Quaternary CVZ lavas along the volcanic arc, which correlates with the boundaries of the crustal domains (Mamani et al., 2008, 2010 and references therein). All three conditions are supposed to affect the trace element patterns due to different residual, Al-bearing mineral phases and their variable proportions in the residuum. They are accepted as explanation for the simultaneous occurrence of the geochemically distinct lavas in single volcanic systems.

The PVA based model shows that the observed compositional variability in the quaternary CVZ lavas may be rather generated via mixing between three distinct magmatic components. An examination of the natural Taapaca and CVZ volcanic rocks and the statistically obtained end-member compositions suggests that the petrogenesis in the Central Andes proceeds probably analogue to the Taapaca volcanic system. The mineralogically uniform but geochemically contrasting Taapaca rocks indicate that uniform differentiation processes may produce a broad geochemical spectrum of CVZ lavas, as visible for Taapaca rocks in e.g. Figure 10. This is possible when geochemically different end-member magmas are involved. Taapaca rocks overlap with a broad range of volcanics found in the CVZ. Its end-members enclose nearly all CVZ Quaternary lavas. This system may reflect universal petrogenesis in the CVZ volcanic arc, and have general validity for the CVZ magmatism.

I propose a general two-stage magma mixing petrogenetic model for Quaternary CVZ lavas involving the BEM, AEM and RDEM-type components (Figure 14). This description is merely a basic model. It requires further studies to develop a detailed petrogenetic concept and validate its correctness.

The baseline mafic magmas, which occur in the Quaternary CVZ volcanic systems, are produced by magma mixing between the asthenospheric melts evolving to high-Al calc-alkaline basaltic andesite magmas (AEM), and shoshonitic basaltic magmas (BEM) generated in the lithospheric mantle. This hybrid (AEM+BEM) component can reach the surface as lavas identified as baseline compositions, or mix with silicic crustal magmas and produce {(AEM+BEM)+RDEM}. All of the hybrid components may undergo AFC processes; however, AFC seem to play a negligible role in the generation of the entire compositional variability in the Quaternary CVZ volcanics. The first stage magma mixing can proceed anywhere in the lithosphere, the second stage proceed in the upper crust due to middle crustal origin of the silicic component.

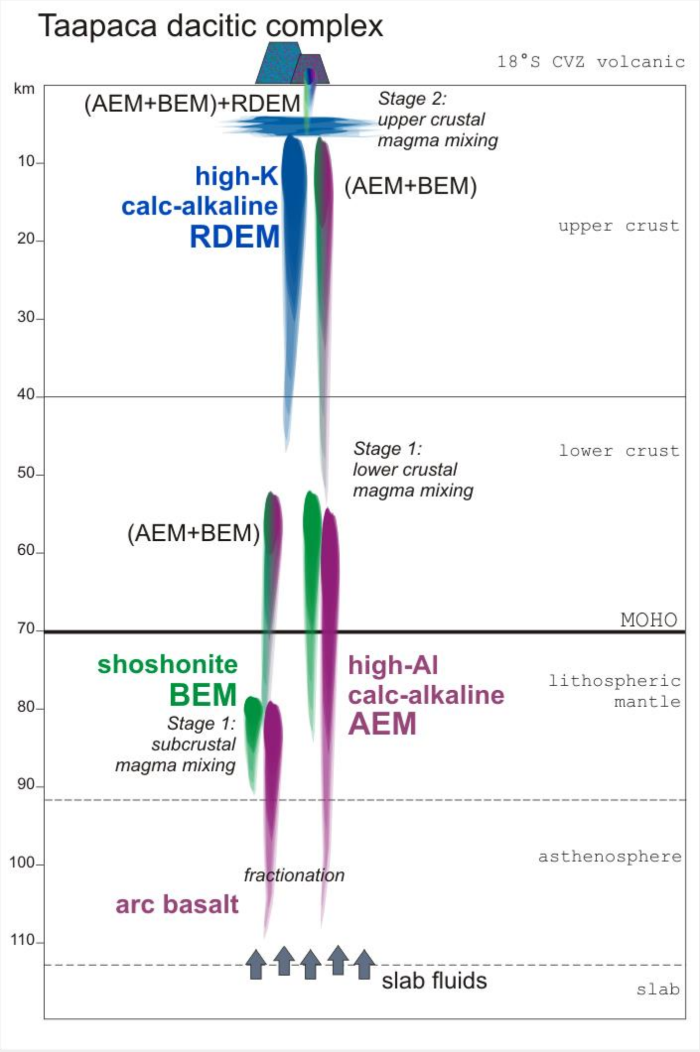

Figure 14. *Schematic illustration of a novel petrogenetic model of the Quaternary CVZ magmas based on multivariate statistical and petrological study of Taapaca volcano located at 18°S. AEM, BEM and RDEM are high-Al calc-alkaline, shoshonitic and high-K calc-alkaline components, respectively, which affect the volcanic systems in the northern CVZ volcanic arc, at the Altiplano-sector. According to geophysical and geochemical evidence (e.g. Kay et al., 1994, Schurr et al., 2006) the lithospheric mantle is missed in the southern Puna-sector of the CVZ (see section 6.6.1). The cross section of the subduction zone is inferred from geophysical studies mentioned in section 6.5.3. However, the thickness of the lithospheric mantle and mantle wedge below Taapaca are not given (dashed lines). Spatial variability of magma composition along and across the CVZ volcanic arc is discussed in section 6.6.*

6.6. SPATIAL COMPOSITIONAL VARIABILITY OF THE QUATERNARY CVZ MAGMAS AND ROLE OF THE PVA END-MEMBERS

6.6.1. SPATIAL COMPOSITIONAL VARIABILITY OF THE QUATERNARY VOLCANICS ALONG THE CVZ

The PVA results suggest that the compositional variability along the CVZ volcanic arc (Figure 10) results rather from a variable contribution of three distinct primary magmas representing three major magmatic series: 1) the enriched shoshonitic, 2) common high-Al calc-alkaline, and 3) high-K calc-alkaline. Sr/Y signature (Figure 15) separates the basaltic andesites and andesites into two groups of low- and high-Sr/Y, at a threshold value of about Sr/Y=50. In the northern Altiplano-sector (14-19°S) both groups (50<Sr/Y<50) occur, even in a single volcano, as observed at Taapaca and Parinacota. In contrast, in the southern Puna-sector (20-27°S) only Sr/Y<50 basaltic andesites and andesites are observed. Exceptional are three andesite samples from El Negrillar (24°S), which show Sr/Y>50, highlighted in Figure 15. This observation suggests general absence of the BEM-type magmas in the (20-23°S)-sector of the southern CVZ arc and possible existence of these magmas southwards of 23°S in the most southern CVZ volcanic arc.

A group of samples >65 wt% SiO_2 from the (20-24°S) Puna-sector is characterized by Sr/Y>50, significantly higher than that found in the more mafic southern lavas. These samples represent dacitic dome complexes (Aucanquilcha, Irrutupuncu, Olca, Socompa, location: see Figure 1). They overlap compositionally and mineralogically with the Taapaca dacites. As mentioned in previous sections, the PVA reveals high Sr/Y ratios in two end-members, the BEM and the RDEM. Therefore, the elevated Sr/Y ratios in the dacitic complexes may rather originate from RDEM-type end-member than from the enriched, shoshonitic component.

Available shoshonite data from the CVZ present shoshonitic activity at the back arc in the northern Altiplano (southern Peru 14-16°S, Carlier et al., 1996, 2005; Mamani et al. 2010) and central Puna (northern Chile 24 °S, Coira & Kay, 1993; Kay et al., 1994, 1999; Matteini et al., 2002; Guzmán et al. 2006; Acocella et al., 2011). The PVA results suggest the existence of the shoshonitic component in the volcanic arc also in two segments, similar to the back arc. The occurrence of these enriched magmas forms a belt along the Arica elbow, interrupted in the (20-23°S) CVZ sector.

The findings of this study support clearly geophysical studies by e.g. Schurr et al. (2006), formulated as follow: “The seismic properties of the Puna mantle point to dominantly asthenospheric conditions. This is in contrast to the apparently intact mantle lithosphere found beneath the northerly Altiplano (Whitman et al., 1992; Myers et al., 1998; Haberland et al., 2003)”. This study shows that the modern lavas erupted in the CVZ volcanic arc are dominated by asthenospheric AEM-type magmas at the Puna-sector; lavas of the northern Altiplano-sector are strongly affected by BEM-type magmas originated in the lithospheric mantle.

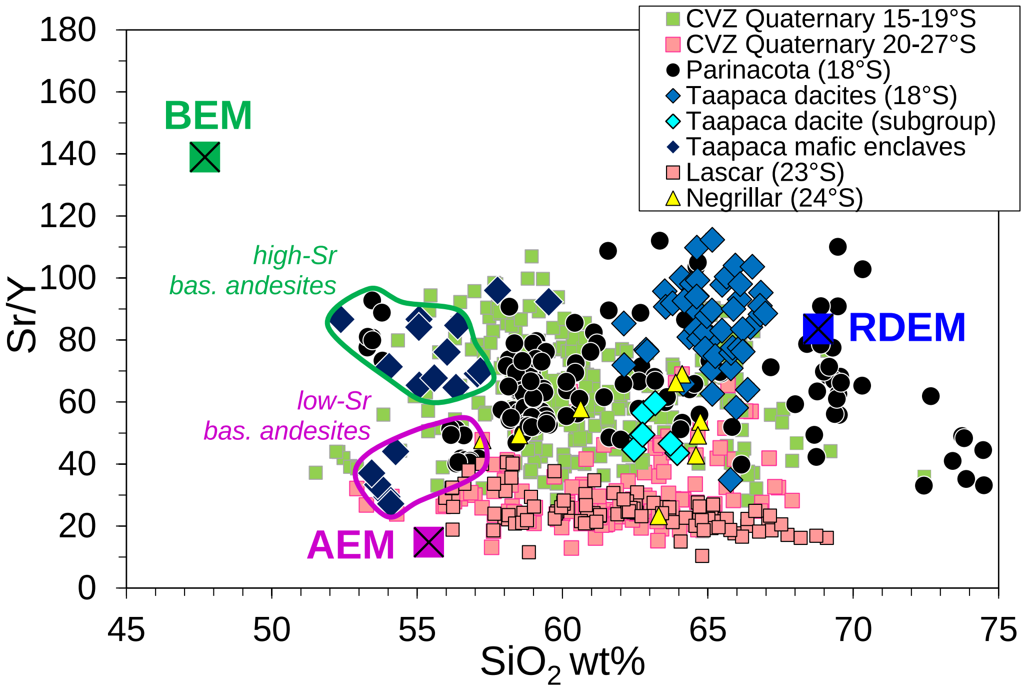

Figure 15. *Sr/Y vs. SiO_2 displays the contribution of the low- and high-Sr/Y Quaternary lavas in the northern (14-19°S) and southern (20-27°S) CVZ volcanic arc. Whole rock compositions represent data compilation of the Quaternary CVZ volcanics by Mamani et al. (2010) and own data. BEM, AEM and RDEM are the PVA shoshonitic, high-Al calc-alkaline and silicic high-K calc-alkaline PVA Taapaca end-members, respectively.*

6.6.2. SPATIAL COMPOSITIONAL VARIABILITY ACROSS THE CVZ

The Quaternary volcanism in the Central Andes comprises: 1) frontal volcanic arc located on the western edge of the Altiplano-Puna Plateau as well as 2) back arc volcanic centers within the Plateau, eastwards to the active CVZ volcanic chain. The voluminous silicic volcanism is omitted in this study. In contrast to the CVZ volcanic arc lavas, which are compositionally restricted to the erupted high-K and medium-K calc-alkaline series, considerable compositional variability occurs in the back arc. There are simultaneously present high-K calc-alkaline, shoshonitic and intraplate-type (OIB-like) eruptive products (e.g. Coira & Kay, 1993; Kay et al., 1994, 1999; Carlier at al. 1996, 2005; Davidson & De Silva, 1995; Matteini et al., 2002; Acocella et al., 2011). The OIB-like lavas are characterized by absence of the Nb-Ta trough, a feature typical of intraplate but not subduction zone lavas (for comparison Chiar Kkollu alkali basalt from Davidson & De Silva, 1995, Figure 12).

The involvement of the shoshonite-type end-member in the CVZ volcanic arc lavas, identified by PVA, indicates that this kind of enriched magmas is not limited to the back arc. High-K calc-alkaline lavas show similar distribution: they occur in the volcanic arc and in the back arc. In contrast to the shoshonite and high-K calc-alkaline magma series, the high-Al calc-alkaline (CAB) suite and the OIB-like magmas are limited to the volcanic arc and back arc, respectively.

Accocella et al. (2011) observed differences in the composition of Quaternary shoshonite lavas across the back arc in the Central Puna Plateau and Eastern Cordillera (24°S). The shoshonites in the Central Puna show a moderate degree of differentiation (4-7 wt% MgO, Cr>100 ppm) in contrast to more primitive shoshonites from the Eastern Cordillera (7-9 wt% MgO, Cr>400 ppm). Our study corroborates the westward trend of increasing intracrustal interactions of the shoshonite magmas in the CVZ: in the Western Cordillera, the shoshonites are recognized only as component of the high-K calc-alkaline lavas.

6.7. PETROLOGICAL EVIDENCE FOR RDEM BASED ON Fe IN PLAGIOCLASE

Taapaca dacites contain two plagioclase populations characterized by distinct Fe contents (see Chapter 3). Low-Fe plagioclase population found in the dacites and as inclusions in sanidine megacrysts forms nearly horizontal trend in Fe-An space (Figure 20, Chapter 3), in a compositional range of An22-49 and 900-2000 ppm Fe. This plagioclase population is presumed to crystallize from the rhyodacitic end-member, from the RDEM. As presented in the section 7.1.2.2, Chapter 3, the highest measured Fe concentration in this plagioclase population reaches ~2000 ppm Fe. Using Fe partition coefficient D^{Fe}(pl)=0.09, a value adopted from Ginibre et al. (2002), this Fe contents in plagioclase requires ~2.9 wt% FeO in the melt. This value is in accordance with 2.7 wt% FeO obtained from the preferred PVA model (25e-8p) for the RDEM.

6.8. PETROLOGICAL EVIDENCE FOR BEM AND AEM BASED ON OLIVINE COMPOSITIONS

Forsterite (Fo)(3) content in olivine is a reliable measure of the degree of fractional crystallization and allows an estimation of the parental melt composition from which the olivine crystallized, due to the generally constant $Kd^{Fe\text{-}Mg}$(olivine)0.3 ±0.03 at pressure <20-30 kbar, recognized in many experimental studies e.g. Roeder & Emslie (1970) and Putirka (2007, 2008) and references therein. In this study, olivine compositions found in low- and high-Sr basaltic andesite lavas form Parinacota have been examined to trace the early magmatic evolution of the parental magmas and to validate the BEM and AEM magmatic end-member compositions obtained from the PVA.

Generally, olivine is a rare phase in the CVZ lavas. Owing to this, there is a scarcity of olivine analysis obtained from the CVZ lavas. A study by Wittenbrink et al. (1997) presents olivine compositions from Cerro Overo in a range Fo88-80 and by Mattioli et al. (2006) from SC2 basaltic andesite lavas at Ollagüe volcano in a range Fo82-74(4). Olivine compositions from Parinacota lavas, obtained in this study, are reported in Electronic Supplementary Data.

As mentioned in section 6.5.2, a few Fo-rich (89-95)(2) olivine inclusions in amphiboles are reported from Parinacota andesite pre-collapse lava (PAR 82) by Entenmann (1994). These high-Fo olivines may be connected to fractionation processes assumed for the evolution of the mantle-derived AEM end-member and support the mantle-derivative nature of the AEM-type melts involved in the petrogenesis of Parinacota lavas.

Figure 16 illustrates Ni vs. forsterite contents of Parinacota olivines in comparison to several olivines found in andesites of Lascar volcano (CVZ, 23°S, own data) and olivines found in the mantle-derived basaltic and andesitic magmas from the subduction-related Quaternary volcanos of Central Mexican Volcanic Belt (MVB), presented by Straub et al. (2008, 2011). Parinacota olivines are characterized by significantly lower Fo contents and higher Ni concentrations at a given Fo content, compared to olivines from MVB. They reveal an upper *threshold value* at Fo contents of 81 mol% and 2500 ppm Ni, while MVB olivines start at ~Fo92 at ~4600 ppm Ni. Furthermore, there are two separate trace element(5)-forsterite trends corresponding to two geochemically distinct, high-Sr (unit a3) and low-Sr (unit a2 and OCba) basaltic andesite lavas. These two distinct olivine trends found in the Parinacota most mafic and geochemically contrasting lavas suggest connection to two mafic end-members, enriched shoshonitic BEM and high-Al calk-alkaline AEM, obtained from the PVA for Taapaca volcano. I use this observation to prove the correctness of the statistical results.

---

[3] Fo is defined as molar ratio of $Mg/[Mg+Fe^{2+}]$ in olivine.

[4] These analyses do not include Ni contents and cannot be placed in the Ni-Fo space (Figure 16) for comparison.

[5] Trace elements in olivine: Ni, Ca and Mn.

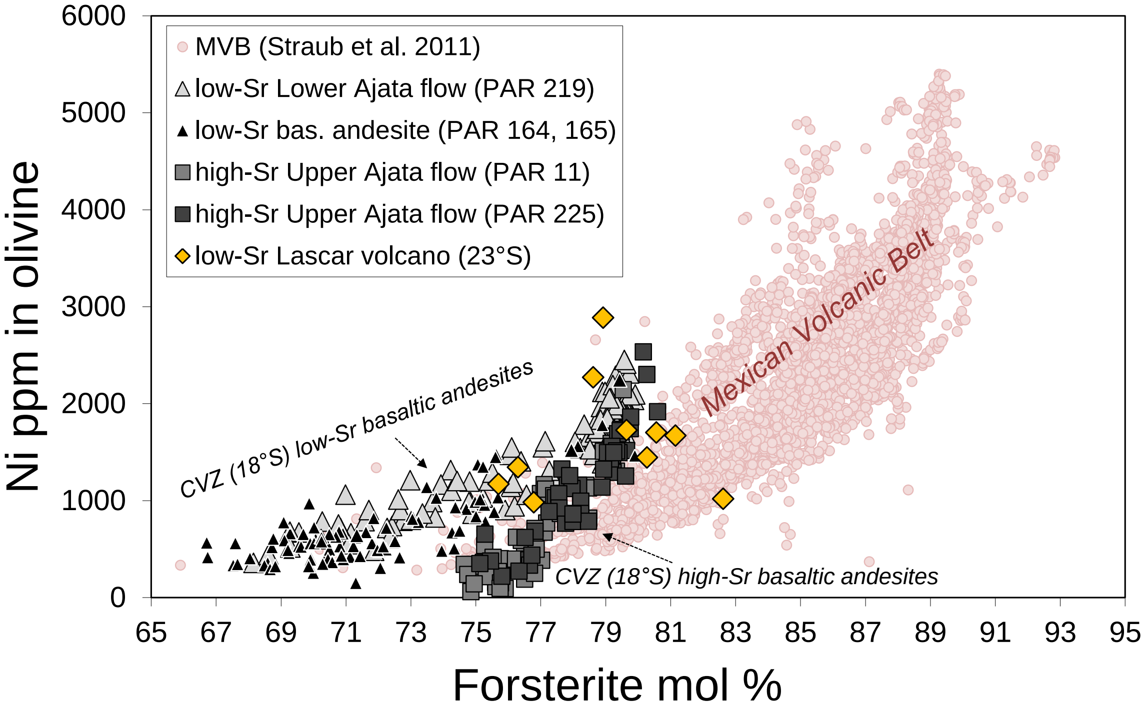

Figure 16. *Ni vs. forsterite (Fo) contents in the Parinacota olivines compared to olivines presented by Straub et al. (2011) comprising olivine from basaltic and andesitic magmas from Quaternary volcanic centers in the Central Mexican Volcanic Belt (MVB). At Ni ~2500 ppm, Parinacota olivines show a shift to lower Fo in comparison to the MVB olivines. Low Fo reflects low Mg#*$_{melt}$ *in Fe-enriched shoshonite magmas (see 6.8.1 for explanation). Parinacota olivines form two distinct trends corresponding to two geochemically distinct low- and high-Sr parental magmas, which occur at 18°S of the CVZ. Both types of lavas carry large olivine phenocrysts of Fo81-78. Nearly continuous trend of olivines in high-Sr lavas indicates fractionation in a chemically closed system. Low-Sr basaltic andesites show a turning point in the trend at Fo78, which marks a change in the trend course suggesting mixed character of these lavas.*

6.8.1. RELATIONSHIP BETWEEN FO81 THRESHOLD-VALUE AND ALKALINE (SHOSHONITIC) AFFINITY OF THE PARENTAL MAGMA

The surprisingly low initial forsterite content of Fo81 in the most magnesian olivines from Parinacota volcano suggests equilibrium with more evolved melts than typical primary mantle-derived liquids, which would crystallize Fo>87 (Sobolev et al., 2007; Straub et al., 2011). However, tiny Cr-spinel inclusions found in the most magnesian (Fo78-81) cores (Figure 18b, c, h) emphasize their relatively primitive character. The relatively low, maximal Fo-contents in Parinacota olivines is therefore assumed as evidence for low-Mg#$_{melt}$ in the primary melt form which the olivines started to crystallize.

The most mafic, BEM (47 wt% SiO_2) shoshonitic end-member, obtained from the PVA, reveals low MgO, Ni and high FeO contents (6.5-6.8 wt% MgO, 9.8-11.5 wt% FeO, 55-78 ppm Ni, Table 3) relatively to the most mafic CVZ natural basaltic andesites, e.g. San Francisco-Incahuasi lava (9.4 wt% MgO, 7.2 wt% FeO, 197 ppm Ni) and modeled mantle-derived basalt composition (10.9 wt% MgO, 8.72 wt% FeO, 229 ppm Ni) of Kay et al. (1996a, 1999). As presented in the Figure 4, the whole rock composition of the BEM reveals alkaline affinity, associated with Fe-enrichment, expressed by its relative low Mg#$_{melt}$=55, (Table 5, section 6.8.3). This Mg-number corresponds to Fo80 ±2 equilibrium olivine composition, calculated form BEM composition of the (25e-8p) PVA model, using $Kd^{Fe\text{-}Mg}$(olivine)=0.3 ±0.03, (Roeder & Emslie, 1970). The threshold value (Fo81) of Parinacota olivine requires 56 $Mg\#_{melt}$-values in the host magma at $Kd^{Fe\text{-}Mg}$(olivine)=0.3. Exactly this $Mg\#_{melt}$-value is, in fact observed in the olivine-free, high-Sr basaltic andesitic enclave CAL-138B, (Table 5), the most mafic composition from Taapaca volcano.

The low $Mg\#_{melt}$ of the shoshonitic BEM end-member overlaps with Mg-numbers in the range from 55 to 65, measured in olivine-bearing alkaline magmas from Mexican Volcanic Belt (MVB), presented by Straub et al. (2008). The olivines from the MVB alkali basalts range from Fo78 to Fo87, whereas olivines found in the MVB calc-alkaline lavas reach Fo90. Such high Fo-values require higher $Mg\#_{melt}$= ~70, which correspond exactly to the mentioned Incahuasi lavas in the range of 68 to 70, where high-Fo olivine would be expected (data not available).

In view of that, the $Mg\#_{melt}$=55 of the statistically obtained BEM composition is in accordance with the observed initial Fo81 forsterite content found in Parinacota olivines. With regard to this finding, the compositions of the natural olivines have been examined with the statistically calculated BEM and AEM compositions.

6.8.2. CONNECTION BETWEEN OLIVINE COMPOSITIONS AND TEXTURES IN BASALTIC ANDESITES FROM PARINACOTA

Two separate trends in low- and high-Sr Parinacota lavas show connection to distinct textural features observed in olivines. Figure 18 demonstrates olivine textures of representative olivine crystals in backscattered electron (BSE) images. The composition of these selected crystals is presented in Fo-Ni plot (Figure 17), in colors used accordingly to the colored BSE images.

Both olivine trends start at the same Fo81-79, measured in cores of large olivine phenocrysts (>300 µm). The main crystal parts of these large phenocrysts, presented in Figure 18 in green, occur in both type of the basaltic andesites and form a separate compositional group (Figure 17).

Olivines from the high-Sr lavas show a nearly continuous trend characterized by a steep decrease of Ni concentrations from 2533 to 61 pm between Fo81 and Fo74. The most magnesian “green cores” phenocrysts of the high-Sr lavas show a continuous decrease of Ni and Fo contents toward rim and form a continuous trend together with euhedral olivine microcrysts and microlites (Figure 18a).

In contrast, a textural variability of olivine found in low-Sr lavas (Figure 18b-h) is reflected by a turning point at Fo77 and small sub-trends. The “green cores” phenocrysts in low-Sr lavas demonstrate a sharp change of Ni and Fo contents at rims, showing Ni<1500 ppm and Fo<76, plotting behind the turning point of Fo77 (pink rims in Figure 18b, g, h). The compositions of the “pink rims” overlap in part with fine-grained olivine agglomerate (Figure 18c, d) which form disequilibrium coronas on some of the “green cores”, after orthopyroxene overgrowth; however, the “pink rims” show higher Ni contents. The agglomerate, olivine microcrysts and microlites (red crystals in Figure 18c, e, f, g, h) form a continuous trend (Fo72-65), and are also enclosed by orthopyroxenes. Anhedral olivine inclusions in orthopyroxene and olivine remnants included in orthopyroxene, further overgrown by clinopyroxene (violet areas in Figure 18e, f) plot between

Fo76 and Fo72. These inclusions constitute a kind of second threshold value at Fo76, marked by a nearly vertical Ni-Fo trend (Figure 17).

The compositional gap found in all low-Sr lavas divides these olivine compositions into two groups forming 1) a steep Ni-Fo trend (Fo81-78) represented by the "green cores" of the large phenocrysts and 2) flat trends (Fo≤76) represented by phenocrystic rims, microcrysts, microlites, olivine remnants and inclusions in pyroxenes.

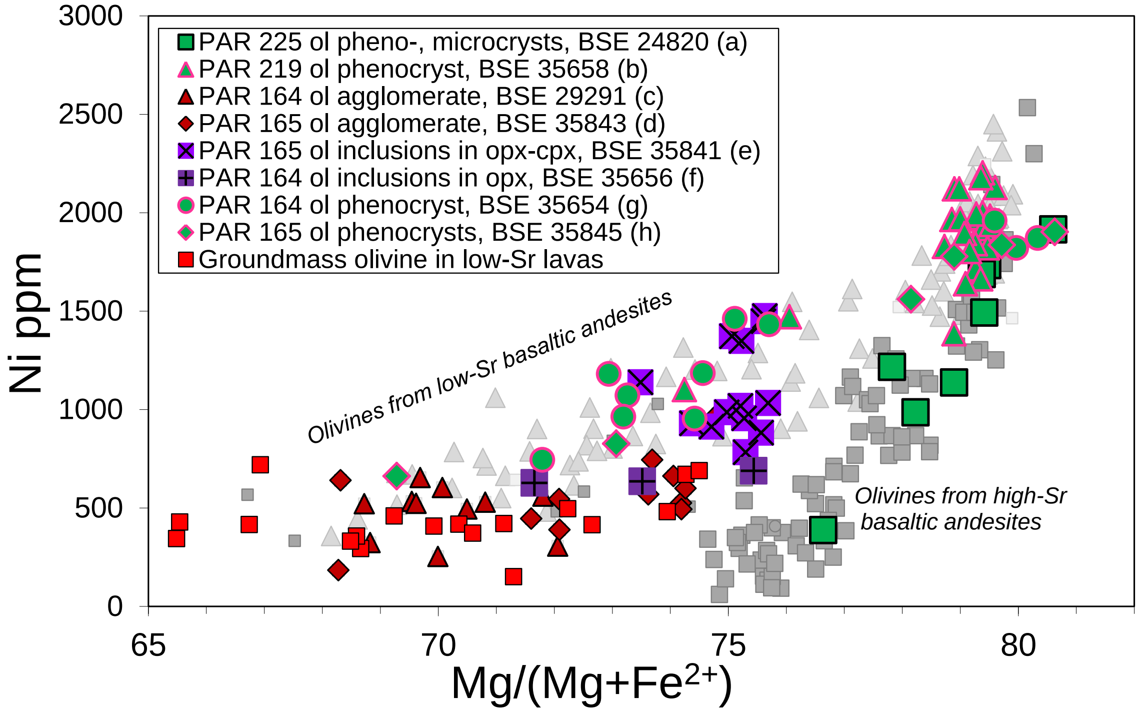

Figure 17. *Ni vs. forsterite presents relationship between compositions and textures of olivines presented in BSE images in Figure 18. Colors of points in the diagram correspond to colors used in the BSE images.*

Figure 18. ***Next page:*** *Backscatter electron (BSE) images of olivine found in Parinacota high-Sr Upper Ajata (a3) and low-Sr Old Cone (OCba) and Lower Ajata (A2) lavas. Compositions of these olivine crystals are presented in Ni-Fo space, Figure 17. High-Sr and low-Sr specify the geochemical affinity of lavas, as used in the text, in which olivines are hosted. Crystal colors demonstrate distinct textural-compositional groups: green cores (a, b, c, g, h) show Fo81-78 and 2533-1291 Ni ppm. Yellowish color (a) represents fractionation toward Fo74 and 60 ppm Ni. Pink (b, g, h) mark rims (Fo<76 and 1970-600 ppm Ni) compositionally distinct from the cores; violet represents olivine inclusions and remnants in pyroxene (Fo<76 and 1060-184 ppm Ni); groundmass olivine in red (Fo<74 and 720-150 ppm Ni). Olivine from high-Sr Upper Ajata lavas (a3) in:* ***a)*** *micro- and phenocrysts from (a3) representing fractionation trend in a narrow Fo range. Olivine from low-Sr Lower Ajata lavas (a2) in:* ***b)*** *skeletal green core phenocryst with more evolved rim. Olivine from low-Sr Old Cone basaltic andesite lavas in:* ***c)*** *high-Fo-Ni core with disequilibrium corona composed of orthopyroxene Ti-magnetite and next olivine generation, forming olivine agglomerate of Fo69-74;* ***d)*** *olivine agglomerate on opx;* ***e)*** *olivine remnant preserved as inclusion in cpx preceded by peritectic reaction to opx;* ***f)*** *olivine remnant preserved as inclusion in opx;* ***g)*** *skeletal phenocrysts;* ***h)*** *high-Ni-Fo euhedral phenocrysts existing beside groundmass olivine, the rims of the phenocrysts show higher Ni contents.*

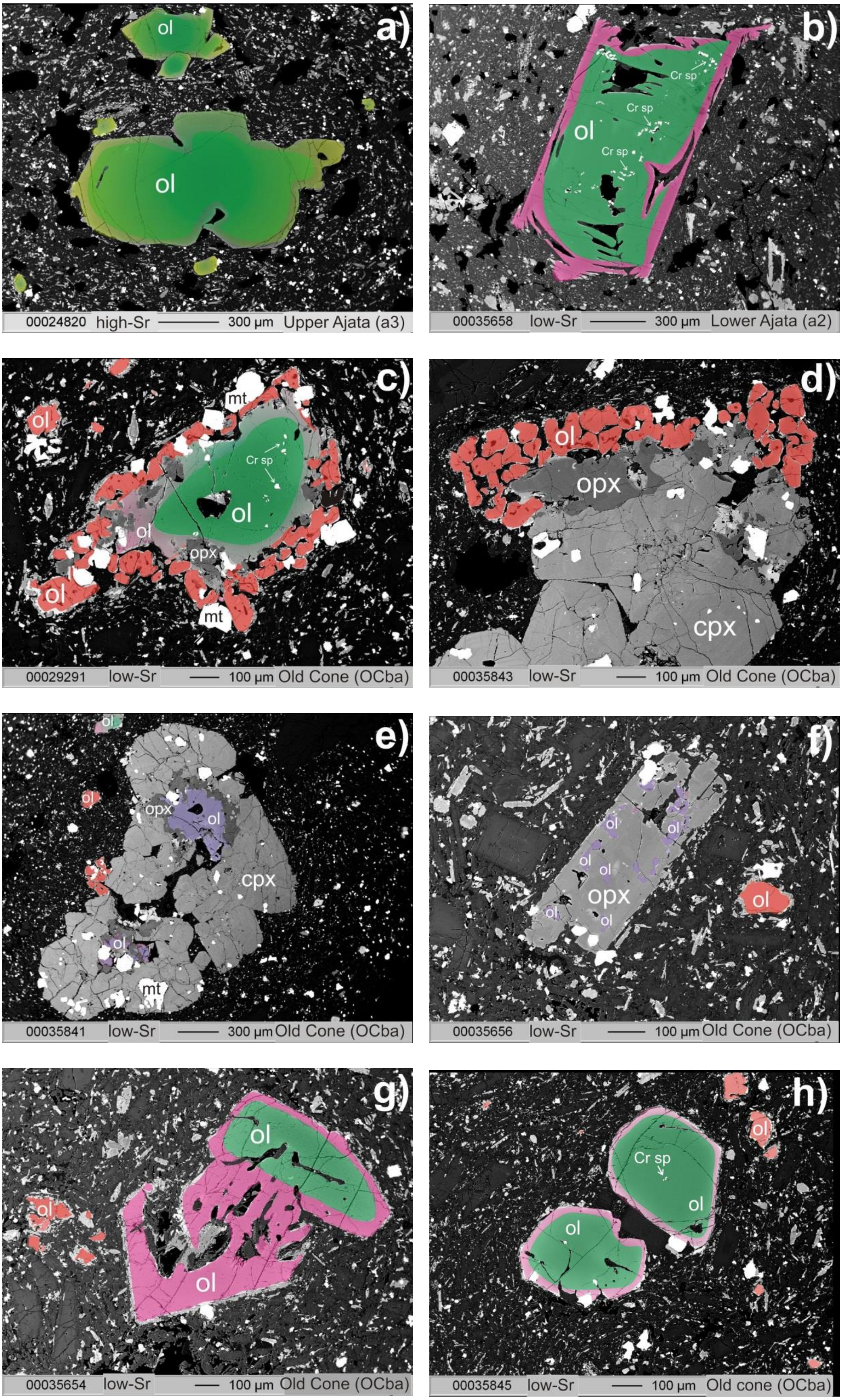
a)
ol
ol
00024820 high-Sr 300 µm Upper Ajata (a3)
b)
Cr sp
Cr sp
ol
Cr sp
00035658 low-Sr 300 µm Lower Ajata (a2)
c)
mt
ol
Cr sp
ol
ol
opx
ol
mt
00029291 low-Sr 100 µm Old Cone (OCba)
d)
ol
opx
cpx
00035843 low-Sr 100 µm Old Cone (OCba)
e)
ol
ol
opx
ol
cpx
ol
mt
00035841 low-Sr 300 µm Old Cone (OCba)
f)
ol
ol
ol
ol
opx
ol
ol
ol
00035656 low-Sr 100 µm Old Cone (OCba)
g)
ol
ol
ol
00035654 low-Sr 100 µm Old Cone (OCba)
h)
ol
Cr sp
ol
ol
00035845 low-Sr 100 µm Old cone (OCba)

6.8.3. EXAMINATION OF FO AND NI CONTENTS IN NATURAL OLIVINES WITH BEM AND AEM PVA COMPOSITIONS

Table 5 comprises measured and calculated MgO, FeO^{TOT} and Ni concentrations in magma, and mafic PVA end-members, Fo and Ni contents in olivines from Parinacota, and Mg#$_{melt}$-values from Parinacota lavas, Taapaca mafic enclave, PVA end-members, and calculated from olivine compositions. These values are used for examination of the consistency of the olivine compositions with the statistical PVA end-members.

6.8.3.1. Examination of Fo contents in Parinacota olivines with Mg-numbers of the BEM and AEM statistical end-members

The highest Mg#$_{melt}$=57 in natural whole rock have been found in the sample CAL-138, the high-Sr mafic enclave of Taapaca volcano. Basaltic andesite lavas from Parinacota show lower values than expected for the most magnesian olivines. These lower observed Mg# whole rock may result from mixing of the BEM with AEM having lower Mg#, influence of shallow assimilation/oxidation or overestimating Fe-values based on assumption that all analyzed Fe=FeO^{TOT}.

Table 5. *Relevant chemical characteristics of selected olivine-bearing, low- and high-Sr Parinacota lavas, olivines hosted in these lavas, and calculated PVA end-members. (OCba) represents pre-collapse low-Sr basaltic andesite lavas; (a2), (a3) post-collapse low- and high-Sr lavas; TAP m. encl. is the most mafic Taapaca enclave; BEM and AEM are PVA end-member obtained from (43-36) and (25-8p) models. (+)denotes: Mg#$_{melt}$ based on whole rock MgO and FeO^{TOT}; (++): Mg#$_{melt}$ calculated from olivine compositions using Kd$^{Fe\text{-}Mg}$=0.3 (Roeder & Emslie, 1970); (*): calculated Fo mol%=Mg# in olivine in equilibrium with the magma MgO and FeO^{TOT} using Kd$^{Fe\text{-}Mg}$=0.3; (**): D^{Ni} – the highest values dependent on MgO-contents, taken from Beattie et al. (1991); (***): predicted Ni ppm in olivine from magma composition.*

		Magma					Olivine		
Sample	Unit	MgO wt%	FeO^{TOT}wt%	Ni ppm	Mg#$_{melt}$$^{(+)}$	Mg#$_{melt}$$^{(++)}$	Fo mol%	Ni ppm	DNi $^{(**)}$
PAR 164	(Ocba) low-Sr	4,3	7,2	39	52	36 - 55	65 - 80	254 - 2245	
PAR 165	(Ocba) low-Sr	4,2	7,2	38	51	35 - 56	64 - 81	150 - 1903	
PAR 219	(a2) low-Sr	4,1	7,5	44	49	37 - 55	66 - 81	358 - 2451	
PAR 225	(a3) high-Sr	5,1	7,9	53	53	41 - 56	70 - 81	61 - 2533	
CAL-138	TAP m.encl.	6,4	8,8	83	57		81 $^{(*)}$	2075 $^{(***)}$	25
BEM (43-36)	PVA	6,5	11,1	60	51		78 $^{(*)}$	1500 $^{(***)}$	25
BEM (25-8p)	PVA	6,6	9,8	78	55		80 $^{(*)}$	1950 $^{(***)}$	25
AEM (43-36)	PVA	3,6	7,8	16	45		73 $^{(*)}$	800 $^{(***)}$	50
AEM (25-8p)	PVA	4,3	8,2	0	48		76 $^{(*)}$	-	-

To find a consistency between statistical end-members and natural olivines we compare: 1) Mg#$_{melt}$$^{(+)}$ of the BEM and AEM with the highest Mg#$_{melt}$$^{(++)}$ calculated from the natural olivines, and 2) the highest Fo contents found in the natural olivine with values calculated form the BEM and AEM PVA end-members.

1) The Mg#$_{melt}$$^{(++)}$ calculated from the most magnesian "green core" olivine compositions require equilibrium values of 55-56 at Kd$^{Fe\text{-}Mg}$=0.3. These values are represented by BEM end-member obtained from the calculation model (25-8p). The AEM end-member from the same PVA model reveals Mg#$_{melt}$$^{(+)}$ of 48, which corresponds to Fo76 of olivine inclusions in

pyroxenes, forming the second threshold value at Fo76, as mentioned in the previous section 6.8.2.

2) The Fo81 and Fo76 threshold values of the “green cores” and olivine inclusions in pyroxene (violet areas), respectively, correspond well to the Fo80 and Fo76, olivine compositions which would be in equilibrium with the BEM and AEM, statistically obtained end-members (Figure 19). Both BEM PVA end-members presented from the model (43-36) and (25-8p) yield slightly lower values of calculated equilibrium contents of Fo79-80, most likely resulting from an overestimation of FeO^{TOT} concentrations from the PVA due to the specification of all Fe as Fe^{2+}.

The Mg#$_{melt}$ and Fo contents obtained for BEM and AEM from the PVA model (25-8p) show the best approximation of the equilibrium values to the natural olivines.

The consistence of the observed Fo-threshold values of 81 and 76 with the Fo contents calculated from the PVA end-members suggests that these Fo values are initial olivine compositions in magmas representing shoshonite und high-Al calc-alkaline end-members, respectively, involved in the petrogenesis of the baseline lavas in the CVZ (Figure 17 and Figure 19).

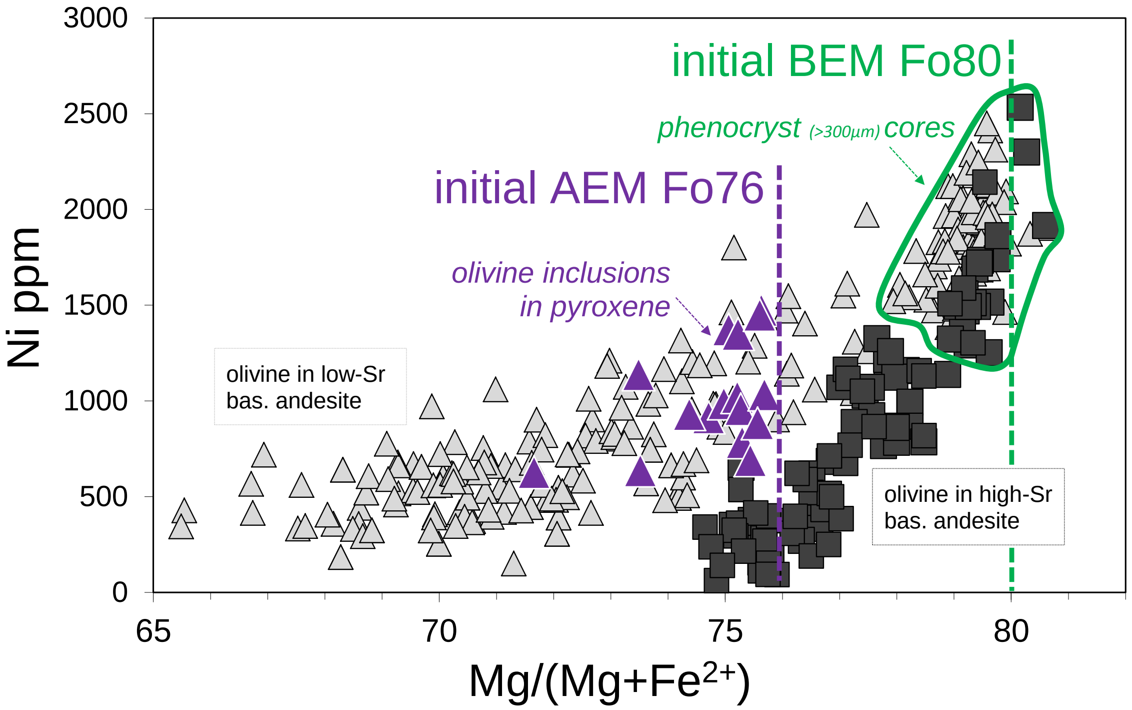

Figure 19. *Ni vs. forsterite in olivines from high-Sr (dark grey) and low-Sr (light grey) Parinacota basaltic andesites. Vertical lines mark calculated initial Fo contents in equilibrium with the PVA shoshonitic BEM and high-Al calc-alkaline AEM end-members. Large phenocrysts (>300 µm) occur in both types of basaltic andesites.*

6.8.3.2. Examination of Ni concentrations in Parinacota olivines with BEM and AEM statistical end-members

Similar to Mg and Fe, Ni content in olivine is controlled by relative proportions of all these elements in the melts and not by their abundances (Hart & Davis, 1978; Kinzler et al., 1990; Beattie et al., 1991). Consequently, the D^{Ni} follows an exponentially increasing curve with decreasing MgO contents in the melt (Beattie et al. 1991). In the melts of MgO<10 wt% the D^{Ni} increases significantly and can reach values D^{Ni}>50 at MgO<4.0 wt%.

Table 5 presents a range of Ni concentration measured in the Parinacota olivines and expected Ni concentration (marked as “(***)”) in olivines which would crystallize from the melt equal to the compositions represented by CAL-138 and the BEM and AEM end-members. The calculated Ni concentrations resulting from D^{Ni}(olivine)=25 for 6 wt% MgO in BEM and D^{Ni}(olivine)=50 for 4 wt% MgO in AEM reveal lower Ni concentrations as these found in the natural olivines representing the threshold Fo-values, presented in e.g. Figure 19. These generally ~20-45 % lower estimated Ni contents than observed in natural olivines may result from: 1) too low D^{Ni} values, which are poorly constrained for MgO<5 wt%, or from 2) underestimated Ni contents in the BEM and AEM PVA end-members. Considering higher Ni contents determined for the Taapaca mafic enclave (sample CAL-138) than determined by the PVA for the Taapaca end-members, the underestimation of Ni by the PVA gives more likely explanation for the observed discrepancies. However, the examination of the Ni concentrations confirms relative differences between BEM and AEM compositions.

6.8.4. MAGMA MIXING RECORDED IN OLIVINE TRENDS FORM PARINACOTA

The initial Fo81 BEM-type olivines have been found in both, low- and high-Sr basaltic andesites from Parinacota. The occurrence of BEM-type olivines in the AEM-dominated, low-Sr lavas gives evidence for magma mixing between BEM and AEM. In contrast to the BEM-type olivines, the initial Fo(76) AEM-type olivines occur only in low-Sr basaltic andesites from Parinacota. This suggests that the BEM, shoshonite magmas, can reach the higher crustal levels without mixing with the AEM, high-Al calc-alkaline basalts. The AEM-type magmas do involve the BEM component during ascent in the Parinacota volcanic system. A far-reaching interpretation of these observations supports deeper generation depth of the AEM end-member in comparison to the BEM and confirms the possible sources of these end-members in the mantle wedge and lithospheric mantle, as discussed in section 6.5. Furthermore, two distinct types of olivines present in the baseline lavas, which are represented by the low- and high-Sr Parinacota basaltic andesites, is in accordance with the observation that basaltic andesites of the CVZ, lying on the magma mixing line between BEM and AEM, as discussed in section 6.3 and presented in Figure 10, must be hybrid compositions. Therefore, mixing between arc basalts and enriched shoshonite component may be an essential process generating baseline mafic compositions in the CVZ.

7. CONCLUSIONS

The hybrid dacites of Taapaca volcano are appropriate rocks for application of the multivariate statistical method, the Polytopic Vector Analysis, especially designed for mixed geological systems. The results of the PVA reveal the number of magmatic end-members, their compositions and relative mixing proportions involved in the petrogenesis of the Taapaca rocks. In this way, the PVA describes the mixed system completely.

The PVA resolves the Taapaca dacites into three magmatic end-members: a basaltic, a basaltic andesitic and a rhyodacitic component. Besides the clear differences in the major element compositions, these end-members show three different REE patterns. The basalt (BEM) is extremely enriched in incompatible elements showing fractionation in the HREE, high LILE/HFSE and MREE/HREE ratios. The basaltic andesite (AEM) shows LILE-enrichment and Nb-Ta anomaly, typical for arc magmas; however, in comparison to the BEM this composition seems to be mostly depleted in incompatible elements, resulting in significantly lower LILE contents, lower LILE/HFSE and nearly unfractionated REE pattern. The rhyodacite (RDEM) is characterized by lower concentrations of the incompatible elements in comparison to the BEM but its strong, spoon-like depletion in the HREE results in MREE/HREE similar to the BEM. Furthermore, the LILE/HFSE ratio of the RDEM overlaps with the BEM too. The geochemical characteristics of the PVA magma compositions allow classifying BEM, AEM and RDEM as end-members representing shoshonite, high-Al calc-alkaline and high-K calc-alkaline series, respectively. The overlapping trace element signatures of the geochemically quite distinct BEM and RDEM have not been identified as two distinct components in the CVZ lavas before. This finding can be regarded as one of the most important observations in this study.

Detection of three distinct magmatic series involved in the petrogenesis of Taapaca rocks gives a new insight into petrogenesis of the Quaternary volcanoes in the entire Central Andean Volcanic Zone. In contrast to previous petrogenetic models of the CVZ magmas based on one main magma source in the mantle wedge, the petrogenetic model presented here proposes three different magmatic sources for the three different magmatic series. They represent three main environments of the subduction zones: the enriched lithospheric mantle, mantle wedge and the crust, respectively. Consequently, the pronounced compositional variability of the Quaternary CVZ lavas may rather result from variable contribution of the three components than be evolved from sole mantle wedge magmas, modified by MASH and AFC processes at the base and/or within the crust at different crustal levels.

Petrological evidence confirms the reliability of the end-member compositions obtained by multivariate statistical method. Olivine compositions found in the geochemically contrasting low- and high-Sr (likewise low- and high-LILE/HFSE and -MREE/HREE) lavas from neighboring Parinacota volcano, form two distinct Fo vs. trace element tends. In connection to textural features of the Parinacota olivines, there are two initial olivine compositions showing Fo81, (BEM-type) and Fo76, (AEM-type), which correspond to equilibrium olivine compositions calculated from BEM and

AEM end-members. The RDEM composition is confirmed by the highest Fe concentrations of low-Fe plagioclase population found in Taapaca dacites corresponding to FeO concentration in the RDEM end-member.

The simultaneous presence of both olivine-types in basaltic andesite lavas from Parinacota suggests magma mixing between high-Al calc-alkaline and shoshonitic components. This process may be responsible for a generation of the baseline, most mafic lavas found in the Quaternary CVZ volcanic arc systems. These variable compositions act as parental magmas and are responsible for the pronounced compositional variability of the CVZ Quaternary lavas. Furthermore, the PVA end-members, which do not erupt as clear components or are very rare, demonstrate a kind of threshold compositions limited by their physical properties such density and viscosity.

The PVA results suggest that shoshonite, which so far has been only found in the back arc volcanic centers, is also present in the volcanic arc, however only as a component. The presence of high-Al calc-alkaline basalts, which occur in the SVZ as clear lavas, shows that this type of magma may be present in entire Andean volcanic arc and may constitute a persisting magmatic component and is limited to the volcanic arc.

These PVA results are a geochemical basis for the geochemical and petrological investigation and description of the distinct differentiation regimes, which occur in the Central Andean volcanic arc.

With regard to Taapaca volcanic system, the PVA results explain the characteristic compositional scatter of the mineralogically uniform dacites. The PVA reveals two-stage magma mixing processes. The first stage involves only the mafic components forming a series of hybrid mafic magmas consisting of high-Al calc-alkaline and enriched shoshonitic components (BEM+AEM), which must take place before interaction with the silicic end-member. These basaltic andesitic magmas are an input into the rhyodacitic (RDEM) reservoir. The second stage generates the dacites and the basaltic andesitic to andesitic enclaves. The mixing proportions obtained from the PVA reveal generally significantly lower amount of the shoshonitic component in the “subgroup” dacites and lower contents of the rhyodacitic component in the low-Sr mafic enclaves in comparison to the main dacite group and high-Sr mafic enclaves. Taking onto account statistical parameters, three components are required and sufficient to explain the whole variability of Taapaca hybrid dacites.

The PVA reveal for the first time major and trace element compositions of the CVZ end-member magmas. Furthermore, it yields relative proportions of the end-members that are a contribution of the different magmatic sources in the Taapaca rocks. An extensive application of this method in the geochemical research of the Andean volcanic systems would reveal the relative role of the magmatic sources on a global scale in the Andean Central Volcanic Zone.

8. REFERENCES

Acocella, V., Gioncada, A., Omarini, R., Riller, U., Mazzuoli, R. & Vezzoli, L. (2011). Tectonomagmatic characteristics of the back arc portion of the Calama - Olacapato - El Toro Fault Zone, Central Andes. *Tectonics* **30**, TC3005.

Adam, J., Green, T. H., Sie, S. H. & Ryan, C. G. (1997). Trace element partitioning between aqueous fluids, silicate melts and minerals. *European Journal of Mineralogy* **9**, 569-584.

Allmendinger, R. W., Jordan, T. E., Kay, S. M. & Isacks, B. (1997). The evolution of the Altiplano-Puna plateau of the Central Andes. *Annual Reviews of Earth and Planetary Sciences* **25**, 139-174.

Alonso-Perez, R., Müntener, O. & Ulmer, P. (2009). Igneous garnet and amphibole fractionation in the roots of island arcs: experimental constraints on andesitic liquids. *Contributions to Mineralogy and Petrology* **157**, 541-558.

Annen, C., Blundy, J. D. & Sparks, R. S. J. (2006). The Genesis of Intermediate and Silicic Magmas in Deep Crustal Hot Zones. *Journal of Petrology* **47**, 505-539.

Annen, C., Blundy, J. D. & Sparks, R. S. J. (2008). The sources of granitic melt in Deep Hot Zones. *Transactions of the Royal Society of Edinburgh: Earth Sciences* **97**, 297-309.

Armstrong, J. T. (1995). A package of correction programs for the quantitative electron microbeam X-ray analysis of thick polished materials, thin films and particles. *Microbeam Analysis* **4**, 177-200.

Babeyko, A. Y., Sobolev, S. V., Trumbull, R. B., Oncken, O. & Lavier, L. L. (2002). Numerical models of crustal scale convection and partial melting beneath the Altiplano-Puna plateau. *Earth and Planetary Science Letters* **199**, 373-388.

Bach, P., Smith, I. E. M. & Malpas, J. G. (2012). The Origin of Garnets in Andesitic Rocks from the Northland Arc, New Zealand, and their Implication for Sub-arc Processes. *Journal of Petrology* **53**, 1169-1195 .

Bachmann, O., Dungan, M. A. & Lipman, P. W. (2002). The Fish Canyon magma body, San Juan volcanic field, Colorado: Rejuvenation and eruption of an upper crustal batholith. *Journal of Petrology* **43**, 1469-1503.

Bachmann, O. & Bergantz, G. W. (2006). Gas percolation in upper-crustal silicic crystal mushes as a mechanism for upward heat advection and rejuvenation of near-solidus magma bodies. *Journal of Volcanology and Geothermal Research* **149**, 85-102.

Baker, M. B., Grove, T. L. & Price, R. C. (1994). Primitive basalts and andesites from the Mt. Shasta region, N. California: Products of varying melt fraction and water content. *Contributions to Mineralogy and Petrology* **118**, 111-129.

Banaszak, M. (2007). Kristallisationsbedingungen und Barium-Zonierung von Sanidinen in Magmen des Taapaca Vulkans, Nord Chile. *Diploma Thesis, University of Göttingen*.

Barboni, M., Bussy, F. & Chiaradia, M. (2011). Origin of Early Carboniferous pseudo-adakites in northern Brittany (France) through massive amphibole fractionation from hydrous basalt. *Terra Nova* **23**, 1-10.

Beattie, P., Ford, C. & Russell, D. (1991). Partition coefficients for olivine-melt and orthopyroxene-melt systems. *Contributions to Mineralogy and Petrology* **109**, 212-224.

Beck, S. L. & Zandt, G. (2002). The nature of orogenic crust in the central Andes. *Journal of Geophysical Research* **107**, B10, 2230, ESE 7-1–ESE 7-16.

Blundy, J. & Wood, B. (2003). Partitioning of trace elements between crystals and melts. *Earth and Planetary Science Letters* **210**, 383-397.

Bourdon, B., Wörner, G. & Zindler, A. (2000). U-series evidence for crustal involvement and magma residence times in the petrogenesis of Parinacota volcano, Chile. *Contributions to Mineralogy and Petrology* **139**, 458-469.

Bouvet de Maisonneuve, C., Dungan, M. A., Bachmann, O., Burgisser, A. (2013). Petrological Insights into Shifts in Eruptive Styles at Volcán Llaima (Chile). *Journal of Petrology* **54**, 393-420.

Brenan, J. M., Shaw, H. F., Ryerson, F. J. & Phinney, D. L. (1995). Mineral–aqueous fluid partitioning of trace elements at 900°C and 2.0 GPa: constraints on the trace element chemistry of mantle and deep crustal fluids. *Geochimica Cosmochimica Acta* **59**, 3331-3350.

Brophy, J. G. & Marsh, B. D. (1986). On the Origin of High-Alumina Arc Basalt and the Mechanics of Melt Extraction. *Journal of Petrology* **27**, 763-789.

Brown, M. (1994). The generation, segregation, ascent, and emplacement of granite magma: the migmatite-to-crustally-derived granite connection in thickened orogens. *Earth Science Reviews* **36**, 83-130.

Brown, M. (2001a). Crustal melting and granite magmatism: key issues. *Physics and Chemistry of the Earth* **26**, 201-212.

Brown, M. (2004). The mechanism of melt extraction from lower continental crust of orogens. *Transactions of the Royal Society of Edinburgh: Earth Sciences* **95**, 35-48.

Brown, M. & Rushmer, T. E. (2006). Evolution and differentiation of the Continental Crust. *Cambridge University Press, Cambridge*.

Brown, M. (2007). Crustal melting and melt extraction, ascent and emplacement in orogens: mechanisms and consequences. *Journal of Geological Society* **164**, 709-730.

Browne, B. L., Eichelberger, J. C., Patino, L. C., Vogel, T. A., Dehn, J., Uto, K., Hoshizumi, H. (2006). Generation of porphyritic and equigranular mafic enclaves during magma recharge events at Unzen Volcano, Japan. *Journal of Petrology* **47**, 301-328.

Carlier, G., Lorand, J. P., Bonhomme, M. & Carlotto, V. (1996). A reappraisal of the Cenozoic inner arc magmatism in Sothern Peru: Consequences for the evolution of the Central Andes for the past 50 Ma. *Third ISAG, St Malo (France), 17-19/9/1996*.

Carlier, G., Lorand, J. P., Liégeois, J. P., Fornari, M., Soler, P., V., C. & Cárdenas, J. (2005). Potassic-ultrapotassic mafic rocks delineate two lithospheric mantle blocks beneath the southern Peruvian Altiplano. *Geology* **33**, 601-604.

Carmichael, I. S. E., Lange, R. A. & Luhr, J. F. (1996). Quaternary minettes and associated volcanic rocks of Mascota, western Mexico: a consequence of plate extension above a subduction modified mantle. *Contributions to Mineralogy and Petrology* **124**, 302-333.

Carmichael, I. S. E. (2002). The andesite aqueduct: perspectives on the evolution of intermediate magmatism in west-central (105-99°W) Mexico. *Contributions to Mineralogy and Petrology* **143**, 641-663.

Castillo, P. R., Janney, P. E. & Solidum, R. (1999). Petrology and geochemistry of Camiguin Island, southern Philippines: insights into the source of adakite and other lavas in a complex arc tectonic setting. *Contributions to Mineralogy and Petrology* **134**, 33-51.

Chang, Y.-H. (2008). O-Isotopes as Tracer for Assimilation Processes in Different Magmatic Regimes (El Misti, Southern Peru and Taapaca, Northern Chile) *Diploma Thesis*, *University of Göttingen*.

Chappell, B. W. (2004). Towards a unified model for granite genesis. *Transactions of the Royal Society of Edinburgh: Earth Sciences* **95**, 1-10.

Chiaradia, M., Müntener, O., Beate, B. & Fontignie, D. (2009). Adakite-like volcanism of Ecuador: lower crust magmatic evolution and recycling. *Contributions to Mineralogy and Petrology* **158**, 563-588.

Chmielowski, J., Zandt, G. & Haberland, C. (1999). The central Andean Altiplano-Puna magma body. *Geophysical Research Letters* **26**, 783-786.

Clark, C., Fitzsimons, I. C. W., Healy, D. & Harley, S. L. (2011). How Does the Continental Crust Get Really Hot? *Elements* **7**, 235-240.

Clavero, J. E. (2002). Evolution of Parinacota Volcano and Taapaca Volcanic Complex, Central Andes of Northern Chile. *PhD Thesis*, *University of Bristol*.

Clavero, J. E., Sparks, R. S. J., Pringle, M. S., Polanco, E. & Gardeweg, M. C. (2004). Evolution and volcanic hazards of Taapaca Volcanic Complex, central Andes of northern Chile. *Journal of Geological Society* **161**, 603-618.

Coira, B. & Kay, S. M. (1993). Implications of Quaternary volcanism at Cerro Tuzgle for crustal and mantle evolution of the Puna Plateau, Central Andes, Argentina. *Contributions to Mineralogy and Petrology* **113**, 40-58.

Conrey, R. M., Sherrod, D. R., Hooper, P. R. & Swanson, D. A. (1997). Diverse primitive magmas in the Cascade Arc, Northern Oregon and Southern Washington. *The Canadian Mineralogist* **35**, 367-396.

Conrey, R. M., Hooper, P. R., Larson, P. B., Chesley, J. & Ruiz, J. (2001). Trace element and isotopic evidence for two types of crustal melting beneath a High Cascade volcanic center, Mt. Jefferson, Oregon. *Contributions to Mineralogy and Petrology* **141**, 710-732.

Crawford, A. J., Falloon, T. J. & Eggins, S. (1987). The origin of island arc high-alumina basalts. *Contributions to Mineralogy and Petrology* **97**, 417-430.

Davidson, J. P., McMillan, N. J., Moorbath, S., Wörner, G., Harmon, R. S. & Lopez-Escobar, L. (1990). The Nevados de Payachata volcanic region (18°S 69°W, N Chile) II. Evidence for widespread crustal involvement in Andean magmatism. *Contributions to Mineralogy and Petrology* **105**, 412-432.

Davidson, J. P., Harmon, R. S. & Wörner, G. (1991). The source of the Central Andes magmas: some considerations. *Geological Society of America Special Paper* **265**, 233-244.

Davidson, J. R. & de Silva, S. L. (1995). Late Cenozoic magmatism of the Bolivian Altiplano. *Contributions to Mineralogy and Petrology* **119**, 387-408.

Davidson, J., Turner, S., Handley, H., Macpherson, C. & Dosseto, A. (2007). Amphibole "sponge" in arc crust? *Geology* **35**, 787-790.

de Silva, S. L. (1989a). Altiplano-Puna volcanic complex of the Central Andes. *Geology* **17**, 1102-1106.

de Silva, S. L. (1989b). Geochronology and stratigraphy of the ignimbrites from the 21°30'S to the 23°30'S portion of the Central Andes of N. Chile. *Journal of Volcanology and Geothermal Research* **37**, 93-131.

Deering, C. D., Cole, J. W. & Vogel, T. A. (2008). A Rhyolite Compositional Continuum Governed by Lower Crustal Source Conditions in the Taupo Volcanic Zone, New Zealand. *Journal of Petrology* **49**, 2245-2276.

Defant, M. J. & Drummond, M. S. (1990). Derivation of some modern arc magmas by melting of young subducted lithosphere. *Nature* **347**, 622-665.

DePaolo, D. J. (1981). Trace element and isotopic effects of combined wallrock assimilation and fractional crystallization. *Earth and Planetary Science Letters* **53**, 189-202.

Déruelle, B. (1991). Petrology of Quaternary shoshonitic lavas of northwestern Argentina. In: R.S.Harmon and C.W. Rapela (eds)," Andean magmatism and its tectonic setting". *Geological Society of America Special Paper*, 201-216.

Déruelle, B. (1994). Volcan Puntas Negras and Cordón Puntas Negras (northern Chile): petrology and geochemistry of minor eruptive centers. *Congr. Geol. Chileno, Concepción, Univ. Concepción*, 1029-1033.

Déruelle, B., Figueroa, A. & Moorbath, S. (1996). Basalts of the Chilean Altiplano, South-Central Andes. *Third ISAG, St Malo (France), 17-19/9/1996*.

Dudás, F. O., Carlson, R. W. & Eggler, D. H. (1987). Regional middle Proterozoic enrichment of the subcontinental mantle source of igneous rocks from central Montana. *Geology* **15**, 22-25.

Ehrlich, R. & Full, W. E. (1987). Sorting out geology - unmixing mixtures *in Size, W.B., ed., "Use and Abuse of Statistical Methods in the Earth Sciences", Oxford University Press, New York*, 43-46.

Eichelberger, J. C. (1978). Andesitic volcanism and crustal evolution. *Nature* **275**, 21-27.

Entenmann, J. (1994). Magmatic evolution of the Nevados de Payachata Complex and the petrogenesis of basaltic andesites in the Central Volcanic Zone of northern Chile. *PhD Thesis, University of Mainz*.

Francis, P. W., Sparks, R. J. S., Hawkesworth, C. J., Thorpe, R. S., Pyle, D. M., Tais, S. R., Mantovani, M. S. & McDermott, F. (1989). Petrology and geochemistry of volcanic rocks of the Cerro Galán caldera, north west Argentina. *Geological Magazine* **126**, 515-547.

Freymuth, H. (2006). Crystal Size Distribution in megacrystic dacites from Taapaca Volcano, Northern Chile (18.10°S - 69.50°W). *Bachelor Thesis, University of Göttingen*.

Full, W. E., Ehrlich, R. & Klovan, J. E. (1981). EXTENDED QMODEL-Objective definition of external end members in the analysis of mixtures. *Journal of the International Association for Mathematical Geology* **13**, 331-344.

Full, W. E., Ehrlich, R. & Bezdek, J. C. (1982). FUZZY QMODEL—A new approach for linear unmixing. *Journal of the International Association for Mathematical Geology* **14**, 259-270.

Gaetani, G. A., Grove, T. L. & Bryan, W. B. (1993). The influence of water in the petrogenesis of subduction - related igneous rocks. *Nature* **365**, 332-334.

Gaetani, G. A. & Grove, T. L. (1998). The influence of water on melting of mantle peridotite. *Contributions to Mineralogy and Petrology* **131**, 323-346.

Gaetani, G. A. & Grove, T. L. (2003). Experimental constraints on melt generation within the mantle wedge. *in : "Geophysical Monograph 138: Inside the Subduction Factory", J. M. Eiler (ed.)*, 107-134, American Geophysical Union, Washington, D. C., 2003.

Gaetani, G. A., Kent, A. J. R., Grove, T. L., Hutcheon, I. D. & Stolper, E. M. (2003). Mineral/melt partitioning of trace elements during hydrous peridotite partial melting. *Contributions to Mineralogy and Petrology* **145**, 391-405.

Garrido, C. J., Bodinier, J.-L., Burg, J.-P., Zeilinger, G., Hussain, S. S., Dawood, H., Chaudhry, M. N. & Gervilla, F. (2006). Petrogenesis of Mafic Garnet Granulite in the Lower Crust of the Kohistan Paleo-arc Complex (Northern Pakistan): implications for Intra-crustal Differentiation of Island Arcs and Generation of Continental Crust. *Journal of Petrology* **47**, 1873-1914.

Garrison, J. M. & Davidson, J. P. (2003). Dubious case for slab melting in the Northern Volcanic Zone of the Andes. *Geology* **31**, 565-568.

Gill, J. (1981). Orogenic andesites and plate tectonics. *Springer Verlag, Berlin*. 390 p.

Ginibre, C., Wörner, G. & Kronz, A. (2002). Minor- and trace-element zoning in plagioclase: implications for magma chamber processes at Parinacota volcano, northern Chile. *Contributions to Mineralogy and Petrology* **143**, 300-315.

Ginibre, C. & Wörner, G. (2007). Variable parent magmas and recharge regimes of the Parinacota magma system (N. Chile) revealed by Fe, Mg and Sr zoning in plagioclase. *Lithos* **98**, 118-140.

Goss, A. R., Kay, S. M. & Mpodozis, C. (2011). The geochemistry of a dying continental arc: the Incapillo Caldera and Dome Complex of the southernmost Central Andean Volcanic Zone (~28°S). *Contributions to Mineralogy and Petrology* **161**, 101-128.

Green, T. H. & Adam, J. (2003). Experimentally-determined trace element characteristics of aqueous fluid from partially dehydrated mafic oceanic crust. *European Journal of Mineralogy* **15**, 815-830.

Griffin, W. L. & O´Reilly, S. Y. (1986). The lower crust in eastern Australia: xenolith evidence. *In: Dawson J. B. et al. (eds) "The Nature of the Lower Continental Crust"* Geological Society of London, Special Publication **24**, 363-374.

Grove, T. L., Parman, S. W., Bowring, S. A., Price, R. C. & Baker, M. B. (2002). The role of an H_2O-rich fluid component in the generation of primitive basaltic andesites and andesites from the Mt. Shasta region, N. California. *Contributions to Mineralogy and Petrology* **142**, 375-396.

Grove, T. L., Elkins-Tanton, L. T., Parman, S. W., Müntener, O. & Gaetani, G. A. (2003). Fractional crystallization and mantle melting controls on calc-alkaline differentiation trends. *Contributions to Mineralogy and Petrology* **145**, 515-533.

Grove, T. L., Baker, M. B., Price, R. C., Parman, S. W., Elkins-Tanton, L. T., Chatterjee, N. & Müntener, O. (2005). Magnesian andesite and dacite lavas from Mt. Shasta, northern California: products of fractional crystallization of H_2O-rich mantle melts. *Contributions to Mineralogy and Petrology* **148**, 542-565.

Grove, T. L., Chatterjee, N., Parman, S. W. & Medard, E. (2006). The influence of H_2O on mantle wedge melting. *Earth and Planetary Science Letters* **249**, 74-89.

Guzmán, S. R., Petrinovic, I. A. & Brod, J. A. (2006). Pleistocene mafic volcanoes in the Puna-Cordillera Oriental boundary, NW-Argentina. *Journal of Volcanology and Geothermal Research* **158**, 51-69.

Haberland, C., Rietbrock, A., Schurr, B. & Brasse, H. (2003). Coincident anomalies of seismic attenuation and electrical resistivity beneath the southern Bolivian Altiplano Plateau. *Geophysical Research Letters* **30**, 1923.

Halliday, A. N., Stephens, E., Hunter, R. H., Menzies, M. A., Dicken, A. P. & Hamilton, P. J. (1985). Isotopic and chemical constraints on the building of the deep Scottish lithosphere. *Scottish Journal of Geology* **21**, 465-491.

Hart, S. R. & Davis, K. E. (1978). Nickel Partitioning between Olivine and Silicate Melt. *Earth and Planetary Science Letters* **40**, 203-219.

Haschke, M., Siebel, W., Günther, A. & Scheuber, E. (2002). Repeated crustal thickening and recycling during the Andean orogeny in north Chile (21°-26°S). *Journal of Geophysical Research* **107**, B1, pages ECV 6-1–ECV 6-18.

Haschke, M. & Günther, A. (2003). Balancing crustal thickening in arcs by tectonic vs. magmatic means. *Geology* **31**, 933-936.

Hawkesworth, C. J. & Vollmer, R. (1979). Crustal Contamination Versus Enriched Mantle: $^{143}Nd/^{144}Nd$ and $^{87}Sr/^{86}Sr$ Evidence from the Italian Volcanics. *Contributions to Mineralogy and Petrology* **69**, 151-165.

Hawkesworth, C. J., Norry, M. J., Roddick, J. C., Baker, P. E., Francis, P. W. & Thorpe, R. S. (1979). ^{143}Nd/^{144}Nd, ^{87}Sr/^{86}Sr, and incompatible element variations in calc-alkaline andesites and plateau lavas from South America *Earth and Planetary Science Letters* **42**, 45-57.

Hawkesworth, C. J., Rogers, N. W., van Calstren, P. W. C. & Menzies, M. A. (1984). Mantle enrichment processes. *Nature* **311**, 331-335.

Hermann, J., Spandler, C., Hack, A. & Korsakov, A. V. (2006). Aqueous fluids and hydrous melts in high-pressure and ultra-high pressure rocks: Implications for element transfer in subduction zones. *Lithos* **399**, 399-417.

Hesse, M. & Grove, T. L. (2003). Absarokites from the western Mexican Volcanic Belt: constraints on mantle wedge conditions. *Contributions to Mineralogy and Petrology* **146**, 10-27.

Hildreth, W. (1981). Gradients in silicic magma chambers: implications for lithospheric magmatism. *Journal of Geophysical Research* **86**, 10153-10191.

Hildreth, W. & Moorbath, S. (1988). Crustal contribution to arc magmatism in the Andes of Central Chile. *Contributions to Mineralogy and Petrology* **98**, 455-489.

Hildreth, W. (2004). Volcanological perspectives on Long Valley, Mammoth Mountain, and Mono Craters: several contiguous but discrete systems. *Journal of Volcanology and Geothermal Research* **136**, 169-198.

Hildreth, W. (2007). Quaternary Magmatism in the Cascades - Geologic Perspectives. *U.S. Geological Survey Professional Paper* **1744**.

Hora, J. M., Singer, B. S. & Wörner, G. (2007). Volcano evolution and eruptive flux on the thick crust of the Andean Central Volcanic Zone; ^{40}Ar/^{39}Ar constraints from Volcán Parinacota, Chile. *Geological Society of America Bulletin* **119**, 343-362.

Hora, J. M., Singer, B. S., Wörner, G., Beard, B. L., Jicha, B. R. & Johnson, C. M. (2009). Shallow and deep crustal control on differentiation of calc-alkaline and tholeiitic magma. *Earth and Planetary Science Letters* **285**, 75-86.

Huber, C., Bachmann, O. & Manga, M. (2009). Homogenization processes in silicic magma chambers by stirring and latent heat buffering. *Earth and Planetary Science Letters* **283**, 38-47.

Huber, C., Bachmann, O. & Dufek, J. (2010a). The limitations of melting on the reactivation of silicic mushes. *Journal of Volcanology and Geothermal Research* **195**, 97-105.

Huber, C., Bachmann, O. & Manga, M. (2010b). Two competing effects of volatiles on heat transfer in crystal-rich magmas: Thermal insulation vs defrosting. *Journal of Petrology* **51**, 847-867.

Huber, C., Bachmann, O. & Dufek, J. (2011). Thermo-mechanical reactivation of locked crystal mushes: Melting-induced internal fracturing and assimilation processes in magmas. *Earth and Planetary Science Letters* **304**, 443-454.

Huber, C., Bachmann, O. & Dufek, J. (2012). Crystal-poor versus crystal-rich ignimbrites: A competition between stirring and reactivation. *Geology* **40**, 115-118.

Imbrie, J. (1963). Factor and vector analysis programs for analyzing geologic data. *p. 83, Off. of Naval Res., Washington, D. C.*

Irvine, T. N. & Baragar, W. R. A. (1971). A guide to the chemical classification of the common volcanic rocks. *Canadian Journal of Earth Sciences* **8**, 523-548.

Isacks, B. L. (1988). Uplift of the central Andean plateau and bending of the Bolivian orocline. *Journal of Geophysical Research* **93**, 3211-3231.

James, D. E. (1971a). Andean crustal and upper mantle structure. *Journal of Geophysical Research* **76**, 3246-3271.

Jamieson, R. A., Unsworth, M. J., Harris, N. B. W., Rosenberg, C. L. & Schulmann, K. (2011). Crustal Melting and the Flow of Mountains. *Elements* **7**, 253-260.

Johannes, W. & Holtz, F. (1991). Formation and ascent of granitic magmas. *Geologische Rundschau* **80**, 225-231.

Johannes, W. & Holtz, F. (1996). Petrogenesis and Experimental Petrology of Granitic Rocks. *Minerals and Rocks Series V. 22, Springer Verlag, Berlin*.

Johnson, G. W. (2002). Principal components analysis and receptor models in environmental forensics, in: "An Introduction to Environmental Forensics", edited by B. L. Murphy and R.D. Morrison. *Academic, San Diego, California*, 461-515.

Kay, R. W. (1978). Aleutian Magnesian Andesites: Melts from Subducted Pacific Ocean Crust. *Journal of Volcanology and Geothermal Research* **4**, 117-182.

Kay, S. M., Coira, B. & Viramonte, J. (1994). Young mafic back-ark volcanic rocks as guides to lithospheric delamination beneath the Argentine Puna Plateau, Central Andes. *Journal of Geophysical Research* **99**, 24323-24339.

Kay, S. M., Mpodozis, C. & Coira, B. (1996a). Central Andean mantle-derived basalts and Neogene mantle enrichment beneath the Puna plateau. *Colloques et Seminares ORSTOM, Symposium International III, "Geodynamique Andine", St Malo*, 583-586.

Kay, S. M., Mpodozis, C. & Coira, B. (1999). Neogene Magmatism, Tectonism, and Mineral Deposits of the Central Andes (22° to 33° S Latitude). *Geology and Ore Deposits of the Central Andes* Society of Economic Geology, Special Publications, 27-59.

Kay, S. M. & Mpodozis, C. (2001). Central Andean Ore Deposits Linked to Evolving Shallow Subduction Systems and Thickening Crust. *GSA Today* **11**, 4-9.

Kay, S. M., Godoy, E. & Kurtz, A. (2005). Episodic arc migration, crustal thickening, subduction erosion, and magmatism in the south-central Andes. *Geological Society of America Bulletin* **117**, 67-88.

Kiebala, A. (2008). Magmatic processes by U-Th disequilibria method. Comparison of two Andean systems: El Misti Volcano (S. Peru) and Taapaca Volcanic Center (N. Chile). *PhD Thesis, University of Göttingen*.

Kinzler, R. J., Grove, T. L. & Recca, S. I. (1990). An experimental study on the effect of temperature and melt composition on the partitioning of nickel between olivine and silicate melt. *Geochimica et Cosmochimica Acta* **54**, 1255-1265.

Klovan, J. E. & Imbrie, J. (1971). An algorithm and FORTRAN-IV program for large-scale Q-mode factor analysis and calculation of factor scores. *Journal of the International Association for Mathematical Geology* **3**, 61-77.

Klovan, J. E. & Miesch, A. T. (1976). EXTENDED CABFAC and QMODEL, computer programs for Q-mode factor analysis of compositional data. *Computers & Geosciences* **1**, 161-178.

Knesel, K. M. & Davidson, J. P. (2002). Insights into Collisional Magmatism from Isotopic Fingerprints of Melting Reactions. *Science* **296**, 2206-2208.

Kohlbach, I. (1999). Spatial and temporal variations in magma geochemistry along W-E traverse at 18°-19°S, North Chile. *Diploma Thesis, University of Göttingen*.

Kohlbach, I. & Lohnert, E. (1999). Geological Map of Taapaca Volcano and adjacent areas, North Chile. *Diploma Mapping Report, University of Göttingen*.

Kulakov, I., Sobolev, S. V. & Asch, G. (2006). P- and S-velocity images of the lithosphere–asthenosphere system in the Central Andes from local-source tomographic inversion. *Geophysical Journal Inernational* **167**, 106-126.

Lopez-Escobar, L., Frey, F. A. & Vergara, M. (1977). Andesites and High-Alumina Basalts from the Central-South Chile High Andes: Geochemical Evidence Bearing on Their Petrogenesis. *Contributions to Mineralogy and Petrology* **63**, 199-228.

Luhr, J. F. (1997). Extensional tectonics and the diverse primitive volcanic rocks in the western Mexican Volcanic Belt *Canadian Mineralogist* **35**, 473-500.

Macpherson, C. G., Dreher, S. T. & Thirlwall, M. F. (2006). Adakites without slab melting: High pressure differentiation of island arc magma, Mindanao, the Philippines. *Earth and Planetary Science Letters* **243**, 581-593.

Mamani, M. I. (2006). Variation in magma composition in time and space along the Central Andes (13°S-28°S). *PhD Thesis, University of Göttingen*.

Mamani, M., Tassara, A. & Wörner, G. (2008). Composition and structural control of crustal domains in the central Andes. *Geochemistry Geophysics Geosystems* **9**, Issue 3.

Mamani, M., Wörner, G. & Sempere, T. (2010). Geochemical variations in igneous rocks of the Central Andean orocline (13°S to 18°S): Tracking crustal thickening and magma generation through time and space. *GSA Bulletin* **122**, 162-182.

Marsh, B. D. (1979a). Island-arc volcanism. *American Scientist* **67**, 161-172.

Marsh, B. D. (1979b). Island arc development: some observations, experiments, and speculation *Journal of Geology* **87**, 687-714.

Matteini, M., Mazzuoli, R., Omarini, R., Cas, R. & Maas, R. (2002). Geodynamical evolution of Central Andes at 24°S as inferred by magma composition along the Calama-Olacapato-El Toro transversal volcanic belt. *Journal of Volcanology and Geothermal Research* **118**, 205-228.

Mattioli, M., Renzulli, A., Menna, M. & Holm, P. M. (2006). Rapid ascent and contamination of magmas through the thick crust of the CVZ (Andes, Ollagüe region): evidence from a nearly aphyric high-K andesite with skeletal olivines. *Journal of Volcanology and Geothermal Research* **158**, 87-105.

McLeod, C. L., Davidson, J. P., Nowell, G. M., de Silva, S. L., Schmitt, A. K. (2013). Characterizing the continental basement of the Central Andes: Constraints from Bolivian crustal xenoliths. *GSA Bulletin* **125**, 985-997.

McMillan, N., Davidson, J., Wörner, G., Harmon, R. S., Moorbath, S. & Lopez-Escobar, L. (1993). Influence of crustal thickening on arc magmatism: Nevados de Payachata volcanic region, northern Chile. *Geology* **21**, 467-470.

Menzies, M. A. e. & Hawkesworth, C. J. e. (1987). "Mantle Metasomatism". *Academic Press geology series, London; Orlando*.

Middlemost, E. A. K. (1975). The basalt clan. *Earth Science Reviews* **11**, 337-364.

Miesch, A. T. (1976). Q-mode factor analysis of compositional data. *Computers & Geosciences* **1**, 147-159.

Miesch, A. T. (1976). Q-Mode Factor Analysis of Geochemical and Petrologic Data Matrices with Constant Row-Sums. *Geological Survey Professional Paper 574-G*.

Morrison, G. W. (1980). Characteristics and tectonic setting of the shoshonite rock association. *Lithos* **13**, 97-108.

Müntener, O., Kelemen, P. B. & Grove, T. L. (2001). The role of H_2O during crystallization of primitive arc magmas under uppermost mantle conditions and genesis of igneous pyroxenites: an experimental study. *Contributions to Mineralogy and Petrology* **141**, 643–658.

Myers, J. D., Angevine, C. L. & Frost, C. D. (1986). Mass balance calculations with end member compositional variability: applications to petrologic problems. *Earth and Planetary Science Letters* **81**, 212-220.

Myers, S. C., Beck, S., Zandt, G. & Wallace, T. (1998). Lithospheric-scale structure across the Bolivian Andes from tomographic images of velocity and attenuation for P and S waves. *Journal of Geophysical Research* **103**, 21233-21252.

Nelson, D. R., McCulloch, M. T. & Sun, S.-S. (1986). The origin of ultrapotassic rocks as inferred from Sr, Nd and Pb isotopes. *Geochimica Cosmochimica Acta* **50**, 231-245.

Ocola, L. C. & Meyer, R. P. (1972). Crustal low-velocity zones under the Peru-Bolivia Altiplano. *Geophysical Journal of the Royal Astronomical Society*. **30**, 199-209.

Pearce, J. A. & Cann, J. R. (1973). Tectonic setting of basaltic volcanic rocks determined using trace element analyses: arc, within-plate, and ocean floor basalts. *Earth and Planetary Science Letters* **19**, 290-300.

Petford, N. & Atherton, M. (1996). Na-rich Partial Melts from Newly Underplated Basaltic Crust: the Cordillera Blanca Batholith, Peru. *Journal of Petrology* **37**, 1491-1521.

Petford, N., Cruden, A. R., McCaffrey, K. J. W. & Vigneresse, J.-L. (2000). Granite magma formation, transport and emplacement in the Earth's crust. *Nature* **408**, 669-673.

Petford, N. & Gallagher, K. (2001). Partial melting of mafic (amphibolitic) lower crust by periodic influx of basaltic magma. *Earth and Planetary Science Letters* **193**, 483-499.

Petrinovic, I. A., Riller, U., Brod, J. A., Alvarado, G. & M., A. (2006). Bimodal volcanism in tectonic transfer zone: Evidence for tectonically controlled magmatism in the southern Central Andes, NW Argentina. *Journal of Volcanology and Geothermal Research* **152**, 240-252.

Prezzi, C. B., Götze, H.-J. & Schmidt, S. (2009). 3D density model of the Central Andes. *Physics of the Earth and Planetary Interiors* **177**, 217-234.

Prezzi, C. B., Götze, H.-J. & Schmidt, S. (2011). The Central Andes lithospheric structure from 3D gravity modeling. *In "Cenozoic Geology of the central Andes of Argentina"* Editors: Salfity, J. A. and Marquillas, R. A., 395-410.

Putirka, K. D., Perfit, M., Ryerson, F. J. & Jackson, M. G. (2007). Ambient and excess mantle temperatures, olivine thermometry, and active vs. passive upwelling. *Chemical Geology* **241**, 177-206.

Putirka, K. (2008). Excess temperatures at ocean islands: Implications for mantle layering and convection. *Geology* **31**, 283-286.

Reubi, O. & Blundy, J. (2009). A dearth of intermediate melts at subduction zone volcanoes and the petrogenesis of arc andesites. *Nature* **461**, 1269-1272.

Rickwood, P. C. (1989). Boundary lines within petrologic diagrams which use oxides of major and minor elements. *Lithos* **22**, 247-263.

Rodriguez, C., Sellés, D., Dungan, M., Langmuir, C. & Leeman, W. (2007). Adakitic Dacites Formed by Intracrustal Crystal Fractionation of Water-rich Parent Magmas at Nevado de Longaví Volcano (36.2°S; Andean Southern Volcanic Zone, Central Chile). *Journal of Petrology* **48**, 2033-2061.

Roeder, P. L. & Emslie, R. F. (1970). Olivine-Liquid Equilibrium. *Contributions to Mineralogy and Petrology* **29**, 275-289.

Rogers, G. & Hawkesworth, C. J. (1989). A geochemical traverse across the North Chilean Andes: evidence for crust generation from the mantle wedge. *Earth and Planetary Science Letters* **91**, 271-285.

Rollinson, H. R. (1993). "Using geochemical data: evaluation, presentation, interpretation". *Longman, Scientific & Technical, UK.*

Rudnick, R. L., Barth, M., Horn, I. & McDonough, W. F. (2000). Rutile-Bearing Refractory Eclogites: Missing Link between Continents and Depleted Mantle. *Science* **287**, 278-281.

Ruprecht, P., Bergantz, G., Cooper, K. & Hildreth, W. (2012). The crustal magma storage system of Volcán Quizapu, Chile, and the effects of magma mixing on magma diversity. *Journal of Petrology* **53**, 801-840.

Samaniego, P., Martin, H., Monzier, M., Robin, C., Fornari, M., Eissen, J.-P. & Cotten, P. (2005). Temporal Evolution of Magmatism in the Northern Volcanic Zone of the Andes: The Geology and Petrology of Cayambe Volcanic Complex (Ecuador). *Journal of Petrology* **46**, 2225-2252.

Sawyer, E. W., Cesare, B. & Brown, B. (2011). When the Continental Crust Melts. *Elements* **7**, 229-233.

Scaillet, B., Holtz, F. & Pichavant, M. (1998). Phase equilibrium constraints on the viscosity of silicic magmas. 1. Volcanic-plutonic comparison. *Journal of Geophysical Research* **103**, 27257-27266.

Scambelluri, M. & Philippot, P. (2001). Deep fluids in subduction zones. *Lithos* **55**, 213-277.

Schurr, B., Asch, G., Rietbrock, A., Trumbull, R. & Haberland, C. (2003). Complex patterns of fluid and melt transport in the central Andean subduction zone revealed by attenuation tomography. *Earth and Planetary Science Letters* **215**, 105-119.

Schurr, B., Rietbrock, A., Asch, G., Kind, R. & Oncken, O. (2006). Evidence for lithospheric detachment in the central Andes from local earthquake tomography. *Tectonophysics* **415**, 203-223.

Sisson, T. W. & Grove, T. L. (1993a). Temperatures and H_2O contents of low-Mg high-alumina basalts. *Contributions to Mineralogy and Petrology* **113**, 167-184.

Sisson, T. W. & Grove, T. L. (1993b). Experimental investigations of the role of H_2O in calc-alkaline differentiation and subduction zone magmatism. *Contributions to Mineralogy and Petrology* **113**, 143-166.

Sobolev, A. V., Hofmann, A. W., Kuzmin, D. V., Yaxley, G. M., Arndt, N. T., Chung, S.-L., Danyushevsky, L. V., Elliott, T., Frey, F. A., Garcia, M. O., Gurenko, A. A., Kamenetsky, V. S., Kerr, A. C., Krivolutskaya, N. A., Matvienkov, V. V., Nikogosian, I. K., Rocholl, A., Sigurdsson, I. A., Sushchevskaya, N. M. & Teklay, M. (2007). The Amount of Recycled Crust in Sources of Mantle-Derived Melts. *Science* **316**, 412-417.

Solano, J. M. S., Jackson, M. D., Sparks, R. S. J., Blundy, J. D. & Annen, C. (2012). Melt Segregation in Deep Crustal Hot Zones: a Mechanism for Chemical differentiation, Crustal Assimilation and the Formation of Evolved Magmas. *Journal of Petrology* **53**, 1999-2026.

Solar, G. S., Pressley, R. A., Brown, M. & Tucker, R. D. (1998). Granite ascent in convergent oceanic belts: Testing a model. *Geology* **26**, 711-714.

Stern, C. R. (1991). Role of subduction erosion in the generation of Andean magmas. *Geology* **19**, 79-81.

Stern, C. R., Moreno, H., Lopez-Escobar, L., (coordinators), Clavero, J. E., Lara, L. E., Naranjo, J. A., Parada, M. A. & Skewes, M. A. (2004). Chilean volcanoes. In: Moreno T, Gibbons W (eds) The Geology of Chile, Geological Society of London, Chapter 5, pp 149-180.

Straub, S. M., LaGatta, A. B., Martin-Del Pozzo, A. L. & Langmuir, C. H. (2008). Evidence from high-Ni olivines for a hybridized peridotite/pyroxenite source for orogenic andesites from the central Mexican Volcanic Belt. *Geochemistry Geophysics Geosystems* **9**, Q03007.

Straub, S. M., Gomez-Tuena, A., Stuart, F. M., Zellmer, G. F., Espinasa-Perena, R., Cai, Y. & Iizuka, Y. (2011). Formation of hybrid arc andesites beneath thick continental crust. *Earth and Planetary Science Letters* **303**, 337-347.

Straub, S. M., Gómez-Tuena, A., Zellmer, G. F., Espinasa-Perena, R., Stuart, F. M., Cai, Y., Langmuir, C. H., Martin-Del Pozzo, A. L. & Mesko, G. T. (2013). The Processes of Melt Differentiation in Arc Volcanic Rocks: Insight from OIB-type Arc Magmas in the Central Mexican Volcanic Belt. *Journal of Petrology* **54**, 665-701.

Tatsumi, Y., Sakuyama, M., Fukuyama, H. & Kushiro, I. (1983). Generation of arc basalt magmas and thermal structure of the mantle wedge in subduction zones. *Journal of Geophysical Research* **88**, 5815-5825.

Tatsumi, Y. (1986). Formation of the volcanic front in subduction zones. *Geophysical Research Letters* **13**, 717-720.

Tatsumi, Y., Hamilton, D. L. & Nesbitt, R. W. (1986). Chemical characteristics of fluid phase released from a subducted lithosphere and origin of arc magmas: evidence from high-pressure experiments and natural rocks. *Journal of Volcanology and Geothermal Research* **29**, 293-309.

Tatsumi, Y. (1989). Migration of fluid phases and genesis of basalt magmas in subduction zones. *Journal of Geophysical Research* **94**, 4697-4707.

Tatsumi, Y. & Eggins, S. (1995). "Subduction zone magmatism". *Blackwell, Boston, 1995*.

Tatsumi, Y. (2003). Some Constraints on Arc Magma Genesis. *Inside the Subduction Factory, Geophysical Monograph 138* American Geophysical Union 277-292.

Tefend, K. S., Vogel, T. A., Flood, T. P. & Ehrlich, R. (2007). Identifying relationships among silicic magma batches by polytopic vector analysis: A study of the Topopah Spring and Pah Canyon ash-flow sheets of the southwest Nevada volcanic field. *Journal of Volcanology and Geothermal Research* **167**, 198-211.

Thorpe, R. S., Francis, P. W. & Harmon, R. S. (1981). Andean andesites and continental growth. *Phil. Trans. R. Soc. Lond.* **301**, 305-320.

Thorpe, R. S., Francis, P. W., Hamill, M. & Baker, M. C. W. (1982). The Andes: in "Andesites: orogenic andesites and related rocks". *R.S. Thorpe (ed.), Chichester: Wiley*, 187-205.

Thorpe, R. S., Francis, P. W., O'Callaghan, L., Hutchison, R. & Turner, J. S. (1984). Relative Roles of Source Composition, Fractional Crystallization and Crustal Contamination in the Petrogenesis of Andean Volcanic Rocks *Philosophical Transactions of the Royal Society London* **310**, 675-692.

Tiepolo, M., Vannucci, R., Oberti, R., Foley, S. F., Bottazzi, P. & Zanetti, A. (2000). Nb and Ta incorporation and fractionation in titanian pargasite and kaersutite: crystal-chemical constraints and implications for natural systems. *Earth and Planetary Science Letters* **176**, 185-201.

Topuz, G., Altherr, R., H., S. W., Siebel, W., Satır, M. & Dokuz, A. (2005). Post-collisional plutonism with adakite-like signatures: the Eocene Saraycık granodiorite (Eastern Pontides, Turkey). *Contributions to Mineralogy and Petrology* **150**, 441-455.

Vigneresse, J.-L. & Clemens, J. D. (2000). Granitic magma ascent and emplacement: neither diapirism nor neutral buoyancy. *Geological Society, London, Special Publications* **174**, 1-19.

Vigneresse, J.-L. (2004). A new paradigm for granite generation. *Transactions of the Royal Society of Edinburgh: Earth Sciences* **95**, 11-22.

Vogel, T. A., Hidalgo, P. J., Patino, L., Tefend, T. S. & Ehrlich, R. (2008). Evaluation of magma mixing and fractional crystallization using whole-rock chemical analyses: Polytopic vector analyses. *Geochemistry Geophysics Geosystems* **9**.

Wagner, T. P., Donnelly-Nolan, J. M. & Grove, T. L. (1995). Evidence of hydrous differentiation and crystal accumulation in the low-Mg, high-Al_2O_3 Lake Basalt from Medicine Lake volcano, California. *Contributions to Mineralogy and Petrology* **121**, 201-216.

Watts, R. B., de Silva, S. L., Jimenez de Rios, G. & Croudace, I. (1999). Effusive eruption of viscous silicic magma triggered and driven by recharge: a case study of the Cerro Chascon-Runtu Jarita Dome Complex in Southwest Bolivia. *Bulletin of Volcanology* **61**, 241-264.

Whitman, D., Isacks, B., Chatelain, J.-L., Chiu, J.-M. & Perez, A. (1992). Attenuation of high-frequency seismic waves beneath the central Andean plateau. *Journal of Geophysical Research* **97**, 19929-19947.

Wigger, P. J. e. a. (1994). Variation of the crustal structure of the southern Central Andes deduced from seismic refraction investigations, in "Tectonics of the Southern Central Andes" eds. Reutter, K.-J., Scheuber, E. & Wigger, P. *Springer Verlag, Berlin*, 23-48.

Wilson, M. B. (First edition 1989). "Igneous Petrogenesis, A Global Tectonic Approach". *Chapman & Hall*.

Wittenbrink, R. (1997). Zeitliche Variationen der Magmengenese miozäner bis quartärer Vulkanite im südlichen Bereich der Zentralen Vulkanischen Zone der Anden. *PhD Thesis, Free University Berlin*.

Wolff, J. A. & Gardner, J. N. (1995). Is the Valles caldera entering a new cycle of activity? *Geology* **23**, 411-414.

Wörner, G., Harmon, R. S., Davidson, J., Moorbath, S., Turner, D. L., Mcmillan, N., Nye, C., Lopez-Escobar, L. & Moreno, H. (1988). The Nevados de Payachata volcanic region (18°S/69°W, N. Chile) I. Geological, geochemical, and isotopic observations. *Bulletin of Volcanology* **50**, 287-303.

Wörner, G., Moorbath, S. & Harmon, R. S. (1992). Andean Cenozoic volcanic centers reflect basement isotopic domains. *Geology* **20**, 1103-1106.

Wörner, G., Hammerschmidt, K., Hemjes-Kunst, F., Lezaun, J. & Wilke, H. (2000). Geochronology (^{40}Ar-^{39}Ar-, K-Ar-, and He-exposure-) ages of Cenozoic magmatic rocks from Northern Chile (18°- 22°S). Implications for magmatism and tectonic evolution of the central Andes. *Revista Geológica de Chile* **27**, 205-240.

Wyllie, P. J. (1982). Subduction products according to experimental prediction. *GSA Bulletin* **93**, 468-476.

Yagodzinski, G. M., Kay, R. W., Volynets, O. N., Koloskov, A. V. & Kay, S. M. (1995). Magnesian andesite in western Aleutian Komandorsky region: implications for slab melting and processes in the mantle wedge. *GSA Bulletin* **107**, 505-519.

Yamamoto, H. & Yoshino, T. (1998). Superposition of replacements in the mafic granulites of the Jijal complex of the Kohistan arc, northern Pakistan: dehydration and rehydration within deep arc crust. *Lithos* **43**, 219-234.

Yoshino, T., Yamamoto, H., Okudaira, T. & Toriumi, M. (1998). Crustal thickening of the lower crust of the Kohistan arc (N. Pakistan) deduced from Al-zoning in clinopyroxene and plagioclase. *Journal of Metamorphic Geology* **16**, 729-748.

Yuan, X., Sobolev, S. V., Kind, R., Oncken, O., Bock, G., Asch, G., Schurr, B., Graeber, F., Rudloff, A., Hanka, W., Wylegalla, K., Tibi, R., Haberland, C., Rietbrock, A., Giese, P., Wigger, P., Röwer, P., Zandt, G., Beck, S., Wallace, T., Pardo, M. & Comte, D. (2000). Subduction and collision processes in the Central Andes constrained by converted seismic phases. *Nature* **408**, 958-961.

Zandt, G., Leidig, M., Chmielowski, J., Baumont, D. & Yuan, X. (2003). Seismic Detection and Characterization of the Altiplano-Puna Magma Body, Central Andes. *Pure and Applied Geophysics* **160**, 789-807.

Zellmer, G. F. (2009). Petrogenesis of Sr-rich adakitic rocks at volcanic arcs: insights from global variations of eruptive style with plate convergence rates and surface heat flux. *Journal of the Geological Society, London* **166**, 725-734.

APPENDIX

Table A. *Major and trace element compositions of rock from Taapaca Volcanic Centre used for PVA modelling, ordered due to increasing Sr concentrations.*

Table A.

	Mafic enclaves																	
Samples	TAP-97-37-1	TAP 97-37/1	TAP 97-36/1	TAP 97-36	CAL-147	TAP 97-25/1	TAP 97-8	TAP 97-27/1	TAP 97-29/1	TAP 97-38/1	CAL-148A	TAP-003	CAL-138B	CAL-116B	TAP 07-05	TAP 07-04 M	TAP-002	TAP-02-02-b
Major and elements analysed by XRF (wt%)																		
SiO2	53.2	52.9	52.1	52.4	53.7	53.8	55.3	54.7	55.5	54.6	58.9	53.4	52.2	54.6	55.7	55.4	54.7	56.8
TiO2	1.0	1.0	1.3	1.2	1.2	1.8	1.6	1.5	1.5	1.5	1.3	1.8	1.8	1.6	1.4	1.4	1.8	1.4
Al2O3	17.8	17.5	16.8	16.9	17.6	16.0	16.6	16.6	16.7	16.2	16.3	16.7	16.3	16.6	16.1	16.0	17.0	15.9
Fe2O3	8.9	8.8	9.3	9.2	6.3	8.8	8.2	8.2	7.7	7.9	4.8	8.4	5.8	5.7	7.4	7.4	8.2	7.1
FeO					2.4						1.7		3.5	2.2				
MnO	0.15	0.15	0.13	0.14	0.13	0.10	0.09	0.10	0.08	0.10	0.08	0.09	0.10	0.09	0.09	0.10	0.09	0.09
MgO	4.5	4.4	4.9	5.0	4.6	4.0	3.5	4.0	3.6	3.6	3.0	4.3	6.4	4.3	3.5	3.5	3.6	3.5
CaO	7.9	7.8	7.7	7.8	7.6	6.5	6.3	6.7	6.4	6.0	5.3	6.9	7.3	6.9	5.8	5.8	6.5	5.9
Na2O	3.22	3.25	3.35	3.23	3.38	3.94	4.35	4.00	4.06	4.07	4.29	4.23	3.86	3.91	4.01	3.99	4.30	3.98
K2O	1.74	1.75	1.57	1.56	1.80	2.00	2.14	2.11	2.27	2.25	2.83	2.26	2.00	2.73	2.91	2.91	2.37	3.18
P2O5	0.25	0.26	0.36	0.32	0.28	0.64	0.56	0.52	0.53	0.62	0.37	0.75	0.46	0.51	0.57	0.57	0.74	0.59
total	98.6	97.7	97.6	97.7	99.0	97.7	98.6	98.4	98.4	96.9	99.0	98.8	99.6	99.1	97.5	97.0	99.3	98.3
Trace elements analysed by XRF (ppm)																		
Nb	6.0	5.3	5.9	5.6	6.0	8.5	7.6	7.1	7.0	8.4	9.0	14.0	10.0	12.0	6.5	6.8	17.0	11.0
Zr	126	126	142	142	163	184	201	192	211	186	222	243	184	100	223	225	266	245
Y	22.0	23.7	20.4	22.9	20.0	14.8	13.9	15.9	13.0	18.0	13.0	17.0	15.0	15.0	18.9	19.2	17.0	15.0
Sr	647	643	755	762	880	967	1058	1076	1101	1163	1200	1213	1300	1300	1322	1327	1430	1439
Rb	59	52	33	33	36	41	40	47	45	63	53	42	37	52	60	60	40	71
Zn	103	108	97	90	91	126	127	119	111	136	106	111	130	122	107	110	113	104
Ni	9	10	24	23	15	45	33	37	31	51	19	45	83	36	20	22	28	24
Co	21	25	29	28	22	29	25	25	23	25	15	33	28	20	20	21	27	25
Cr	35	36	54	54	48	51	52	73	46	80	46	77	225	81	11	14	45	24
V	139	134	232	224	224	204	197	198	195	136	173	186	238	194	170	169	170	165
Ba	581	594	625	614	675	858	1042	1052	1104	1044	1400	1286	1200	1100	1509	1520	1380	1534
Sc	24	28	21	24	22	12	13	14	15	16	10		16	12	13	16		19
Li	21								38			26					21	36
Trace elements analysed by ICPMS (ppm)																		
Cs	3								6			2					2	2
La	17	22	22	24	26	32	38	42	31	48	46	48	39	46	56	56	42	54
Ce	40	46	44	46	52	68	77	72	64	92	93	107	81	90	109	106	97	125
Pr	5.2								7.8			13.5					11.9	14.2
Nd	20.2	24.0	23.0	25.0	28.0	37.0	41.0	39.0	29.9	46.0	41.0	53.2	51.0	50.0	55.0	54.0	48.4	56.0
Sm	4.1	5.7	5.2	5.4		8.0	8.0	7.5	5.0	9.4		9.8			9.8	10.1	9.0	9.1
Eu	1.28								1.27			2.98					2.98	2.43
Gd	4.2								3.3			8.1					7.5	8.0
Tb	0.62								0.38			1.01					0.92	0.82
Dy	3.75								1.88			3.94					3.70	3.53
Ho	0.69								0.29			0.56					0.56	0.62
Er	2.23								0.71			1.45					1.45	1.67
Tm	0.28								0.09			0.14					0.17	0.20
Yb	2.04	2.10	2.10	2.00		1.70	1.60	1.90	0.56	1.90		0.84			1.80	2.20	0.96	1.23
Lu	0.28								0.08			0.11					0.14	0.19
Hf	3.2	3.5	3.4	3.9		4.3	4.9	4.6	3.5	4.4		5.2			5.8	5.4	6.5	5.9
Ta	0.30								0.43			0.67					0.71	0.34
Pb	13								18			11					9	15
Th	4.1	4.7	2.5	2.0		4.4	3.1	3.5	7.0	7.4		11.3			6.9	5.6	4.1	5.1
U	0.4	1.2	0.7	0.6		1.2	1.0	0.8	3.0	2.1		1.1			1.8	1.5	1.0	0.9

Table A.- continued

	Dacite																		
Samples	TAP-007	TAP 97-37	TAP 97-02	TAP-97-37	TAP 97-39	TAP-97-10	TAP-006	CAL-141	TAP 97-35	CAL-117	TAP 97-30	TAP 97-11	TAP-97-34	CAL-136	TAP 97-34	CAL-147A	CAL-124E	TAP-97-01	TAP 97-43
Major and elements analysed by XRF (wt%)																			
SiO2	62.1	61.9	61.6	62.5	65.3	62.8	62.1	62.7	63.4	65.5	66.0	62.8	65.5	64.5	65.2	62.1	65.5	65.3	61.6
TiO2	0.8	0.6	0.7	0.6	0.6	0.7	0.7	0.7	0.6	0.6	0.6	0.8	0.7	0.6	0.7	0.8	0.7	0.7	0.9
Al2O3	16.9	16.8	16.7	17.1	16.4	17.7	17.3	16.5	15.3	16.4	16.1	16.3	15.8	16.0	15.8	15.9	16.2	16.0	16.5
Fe2O3	5.3	5.1	5.1	5.1	4.0	3.8	4.9	3.2	3.4	2.0	3.7	4.4	3.7	2.5	3.7	3.5	4.0	3.7	5.3
FeO						0.5		1.8		1.3				1.2		2.0	0.1		
MnO	0.08	0.09	0.09	0.09	0.06	0.03	0.07	0.06	0.05	0.05	0.06	0.06	0.06	0.06	0.06	0.09	0.06	0.05	0.08
MgO	2.4	1.8	2.4	1.9	1.6	0.6	2.2	2.4	1.3	1.3	1.4	1.5	1.5	1.8	1.4	2.8	1.9	1.5	2.4
CaO	4.9	4.0	5.0	4.0	3.5	2.8	5.0	4.8	3.3	3.3	3.6	3.7	3.5	4.1	3.4	4.9	3.8	3.6	4.7
Na2O	3.33	3.71	3.68	3.97	4.46	3.49	2.99	3.80	4.47	4.29	4.43	4.50	4.40	4.29	4.40	3.88	3.66	4.57	4.38
K2O	3.49	2.61	2.78	2.61	2.90	2.94	3.51	3.19	3.06	3.26	3.30	2.94	3.11	3.23	3.16	2.79	3.39	3.10	2.52
P2O5	0.20	0.16	0.20	0.17	0.18	0.20	0.21	0.17	0.21	0.13	0.23	0.27	0.23	0.14	0.24	0.18	0.18	0.24	0.29
total	99.5	96.8	98.3	98.1	99.0	95.5	99.0	99.3	95.1	98.1	99.4	97.3	98.4	98.4	98.1	99.0	99.5	98.6	98.7
Trace elements analysed by XRF (ppm)																			
Nb	6.0	6.9	7.0	7.0	8.0	9.0	7.0	6.0	6.0	6.0	5.0	0.0	6.0	5.0	8.0	7.0	6.0	7.0	9.0
Zr	150	133	146	128	136	153	157	156	163	123	147	144	166	128	171	152	155	164	155
Y	12.0	13.0	11.5	12.0	10.0	17.0	12.0	10.0	4.0	7.0	10.0	1.0	5.0	8.0	8.0	12.0	9.0	9.0	10.0
Sr	536	566	564	559	581	592	593	596	615	637	639	647	662	664	673	677	682	686	688
Rb	101	91	88	95	105	96	119	97	92	98	102	87	96	84	96	75	94	88	68
Zn	75	67	77	63	68	93	79	92	68	62	67	81	67	69	74	74	74	74	83
Ni	9	4	13	4	26	8	7	10	7	8	13	17	9	9	13	10	14	9	18
Co	27	11	17	13	14	15	26	12	7	7	4	12	10	9	6	13	11	9	14
Cr	11	18	22	22	39	17	11	20	8	17	18	12	12	23	8	105	33	11	32
V	113	92	126	98	73	93	102	130	80	80	70	80	87	97	80	139	86	87	97
Ba	913	757	839	729	818	982	1016	965	886	861	940	800	936	900	936	790	879	959	781
Sc		13	12	15	8	10		10	4	5	7	6	8	7	6	12	7	10	13
Li			11	15		7			43		36	33	29		41			27	
Trace elements analysed by ICPMS (ppm)																			
Cs			7	6		4			7		7	6	6		7			6	
La		18	29	13		18		32	25	28	19	22	25	27	24	25	34	23	
Ce		39	59	30		41		54	50	48	40	45	51	46	48	48	61	48	
Pr			6.3	3.1		4.3			5.8		4.7	5.5	5.7		5.7			5.2	
Nd		18.0	23.0	12.3		15.4		25.0	22.2	25.0	18.2	22.2	19.9	22.0	22.1	23.0	26.0	19.6	
Sm		3.8	3.9	2.4		3.4			3.6		3.0	3.9	3.5		3.6			3.5	
Eu			0.80	0.67		0.94			0.92		0.78	1.01	0.95		0.92			0.92	
Gd			5.4	2.4		3.0			2.7		2.3	2.9	2.8		2.7			2.8	
Tb			0.40	0.31		0.46			0.28		0.24	0.30	0.32		0.27			0.31	
Dy			2.00	1.80		2.24			1.39		1.25	1.48	1.21		1.37			1.15	
Ho			0.40	0.35		0.46			0.23		0.21	0.24	0.24		0.23			0.23	
Er			1.10	1.01		1.35			0.51		0.48	0.51	0.59		0.51			0.51	
Tm			0.10	0.14		0.17			0.07		0.07	0.07	0.07		0.07			0.06	
Yb		1.80	0.90	0.95		1.26			0.47		0.46	0.45	0.47		0.46			0.41	
Lu			0.10	0.15		0.19			0.07		0.07	0.06	0.08		0.07			0.07	
Hf		3.5	1.3	2.5		3.3			3.0		2.7	3.6	3.4		3.1			3.2	
Ta			3.30	0.46		0.39			0.30		0.42	0.43	0.29		0.41			0.29	
Pb			18	17		17			19		18	18	19		18			19	
Th		7.5	13.2	5.8		10.0			5.2		5.0	4.8	6.1		4.9			4.6	
U		1.8	3.5	2.0		1.8			2.2		1.8	2.2	2.1		1.9			1.7	

Table A.- continued

	Dacite																		
Samples	TAP 97-01	CAL-149	CAL-150	TAP-97-06	CAL-124C	CAL-128C	TAP 97-07	CAL-13	TAP-97-29	CAL-143	AP 87-002	TAP 97-29	AP-87-002	CAL-152	TAP-001	CAL-139	TAP-004	TAP-97-22	TAP-97-28
Major and elements analysed by XRF (wt%)																			
SiO2	64.5	66.2	66.9	61.5	64.3	65.6	63.8	65.2	64.1	65.7	64.9	63.6	64.8	65.9	65.0	63.7	62.9	62.4	65.2
TiO2	0.7	0.7	0.7	1.1	0.9	0.7	0.7	0.7	0.8	0.8	0.8	0.8	0.8	0.8	0.9	1.0	1.0	0.9	0.7
Al2O3	15.9	15.5	15.5	16.1	16.0	15.7	15.9	16.0	16.0	15.5	16.2	15.9	16.1	15.3	16.4	16.0	16.2	16.1	15.9
Fe2O3	3.7	3.0	3.5	2.5	2.5	2.7	4.1	2.1	2.1	2.6	4.2	4.5	4.2	2.3	4.5	2.5	5.2	5.1	3.4
FeO		0.8	0.3	3.0	1.9	1.0		1.4	2.1	1.4				1.6		2.0			0.4
MnO	0.05	0.05	0.05	0.08	0.06	0.05	0.06	0.05	0.06	0.05	0.06	0.06	0.06	0.05	0.06	0.05	0.07	0.07	0.06
MgO	1.4	1.5	1.5	2.6	2.0	1.5	1.8	1.5	1.8	1.7	1.7	1.8	1.7	1.8	1.9	1.8	2.5	2.5	1.7
CaO	3.5	3.3	3.3	4.9	4.0	3.4	3.8	3.8	4.0	3.8	3.9	4.0	3.9	3.7	4.1	3.8	4.6	4.6	3.7
Na2O	4.49	4.31	4.41	4.34	4.41	4.32	4.37	4.54	4.42	4.41	4.46	4.42	4.64	4.34	4.38	4.15	4.28	4.39	4.53
K2O	3.15	3.60	3.63	2.60	3.31	3.46	3.05	3.41	3.03	3.31	3.13	3.07	3.03	3.46	3.24	3.43	2.96	2.82	3.21
P2O5	0.24	0.17	0.17	0.33	0.22	0.17	0.27	0.28	0.28	0.21	0.27	0.29	0.27	0.20	0.28	0.24	0.34	0.31	0.26
total	97.6	99.1	99.8	98.9	99.4	98.6	97.9	98.9	98.8	99.5	99.5	98.5	99.5	99.6	100.6	98.5	100.0	99.2	99.0
Trace elements analysed by XRF (ppm)																			
Nb	4.0	7.0	7.0	7.5	6.0	5.0	5.0	5.0	6.0	7.0	4.0	6.0	8.0	7.0	8.0	7.0	8.0	9.0	7.0
Zr	154	179	173	160	163	166	164	168	170	175	175	166	180	170	173	169	162	155	150
Y	9.0	8.0	8.0	10.0	9.0	7.0	9.0	7.0	9.0	8.0	10.0	9.0	12.0	9.0	8.0	8.0	10.0	10.0	10.0
Sr	697	706	708	719	724	725	726	728	742	744	748	751	751	751	752	753	763	768	775
Rb	80	95	99	74	86	92	92	98	86	89	85	88	85	92	85	84	84	79	95
Zn	73	74	77	85	78	80	79	69	85	74	72	79	74	77	69	81	72	79	65
Ni	9	5	6	24	12	7	14	3	14	9	14	16	13	10	12	13	24	28	10
Co	12	8	8	18	11	9	10	8	12	10	11	15	13	10	23	10	29	14	11
Cr	11	20	38	41	28	19	32	20	23	23	15	20	18	23	16	23	65	58	11
V	82	88	72	140	117	92	89	85	108	97	94	101	98	102	92	115	111	124	85
Ba	965	1100	1000	862	1000	1000	866	1300	1051	1000	1050	1055	1060	1100	1231	1000	1002	949	1072
Sc	7	6	5	13	6	5	7	5	10	6	7	6	5	6		6		6	8
Li	40			32			39		37		33	37	21		37			19	39
Trace elements analysed by ICPMS (ppm)																			
Cs	6			5			7		6		4	6	4		5			4	7
La	24	35	40	25	31	35	30	31	29	33	27	30	24	34	40	33		26	31
Ce	50	63	67	53	59	56	59	60	59	64	56	62	50	64	87	59		54	66
Pr	5.8			6.8			6.8		7.1		6.5	7.2	6.1		9.4			6.9	7.7
Nd	22.8	27.0	31.0	27.4	26.0	25.0	26.0	25.0	26.4	28.0	25.5	28.4	21.8	29.0	33.6	31.0		27.3	28.8
Sm	3.8			5.1			4.2		4.6		4.2	4.7	3.7		5.4			4.5	4.7
Eu	0.94			1.35			1.09		1.17		1.11	1.23	1.11		1.77			1.32	1.21
Gd	2.6			3.5			3.1		3.1		3.3	3.6	3.1		4.7			4.3	3.3
Tb	0.27			0.42			0.33		0.36		0.34	0.37	0.36		0.54			0.45	0.37
Dy	1.36			2.10			1.63		1.79		1.75	1.87	1.51		2.19			2.12	1.86
Ho	0.23			0.32			0.27		0.28		0.28	0.31	0.26		0.30			0.35	0.30
Er	0.48			0.80			0.60		0.69		0.62	0.67	0.69		0.76			0.92	0.76
Tm	0.07			0.10			0.09		0.09		0.09	0.09	0.07		0.11			0.11	0.10
Yb	0.43			0.59			0.54		0.52		0.53	0.58	0.53		0.55			0.68	0.62
Lu	0.06			0.08			0.08		0.08		0.08	0.08	0.08		0.10			0.11	0.09
Hf	3.2			3.6			3.6		3.4		3.1	3.5	3.4		3.3			3.4	3.1
Ta	0.47			0.16			0.47		0.29		0.40	0.48	0.25		0.44			0.40	0.35
Pb	19			16			18		18		18	18	17		17			16	18
Th	4.8			5.8			6.0		6.6		5.2	5.6	6.6		16.5			5.6	7.0
U	2.1			2.6			2.5		2.7		2.2	2.5	2.2		4.7			2.2	2.8

Table A.- continued

	Dacite																		
Samples	TAP 97-28	CAL-148	TAP-005	TAP-02-03	CAL-140	TAP-97-48	CAL-142	TAP-97-45	CAL-124A	CAL-131	CAL-138A	AP-02-02-a	TAP 97-45	CAL-116A	TAP-97-18	TAP-97-13	TAP 97-18	TAP 97-41	TAP-97-17
Major and elements analysed by XRF (wt%)																			
SiO2	64.9	65.7	64.9	63.5	64.0	64.5	63.3	64.8	65.8	62.9	64.0	64.6	64.4	63.2	64.1	64.5	63.1	62.0	63.6
TiO2	0.7	0.8	0.7	0.9	0.9	0.7	0.8	0.8	0.8	0.9	0.9	0.8	0.8	1.0	0.8	0.7	0.8	0.8	0.8
Al2O3	15.8	15.4	16.5	16.2	16.0	15.7	15.8	15.9	16.0	16.2	15.7	16.0	16.0	16.4	16.0	16.1	15.9	16.9	16.2
Fe2O3	3.9	2.9	4.1	4.6	2.5	4.1	3.6	4.2	2.4	3.0	3.0	4.3	4.2	3.0	4.3	3.8	4.3	4.7	4.4
FeO		1.1			1.8		0.3		1.4	1.7	1.6			1.6				0.2	
MnO	0.06	0.05	0.05	0.06	0.06	0.06	0.04	0.06	0.05	0.06	0.06	0.06	0.06	0.06	0.07	0.06	0.07	0.07	0.06
MgO	1.6	1.7	1.6	1.8	1.8	1.7	0.8	1.9	1.7	2.1	2.4	1.7	1.8	2.0	2.0	1.5	1.9	1.2	1.6
CaO	3.7	3.7	3.9	4.3	3.9	3.7	2.3	3.9	3.7	4.4	4.3	4.0	4.0	4.4	4.2	3.7	4.1	4.0	3.9
Na2O	4.43	4.39	4.38	4.49	4.31	4.32	3.78	4.57	4.44	4.35	4.31	4.44	4.46	4.46	4.50	4.71	4.46	4.62	4.58
K2O	3.31	3.39	3.26	2.86	3.43	3.18	3.37	3.16	3.46	3.07	3.12	3.05	3.20	3.18	3.10	3.19	3.16	2.77	3.21
P2O5	0.27	0.20	0.23	0.30	0.24	0.29	0.19	0.28	0.22	0.25	0.23	0.27	0.30	0.31	0.29	0.28	0.30	0.33	0.36
total	98.6	99.3	99.7	99.0	98.9	98.3	94.3	99.5	99.9	99.0	99.7	99.2	99.2	99.5	99.2	98.5	98.0	97.7	98.7
Trace elements analysed by XRF (ppm)																			
Nb	6.0	7.0	7.0	9.0	7.0	7.0	6.0	8.0	6.0	6.0	7.0	9.0	6.0	8.0	6.0	6.0	5.0	6.0	7.0
Zr	165	182	158	176	176	162	167	165	149	168	158	180	172	168	156	171	161	157	194
Y	11.0	8.0	7.0	12.0	8.0	8.0	5.0	9.0	9.0	9.0	9.0	12.0	11.0	9.0	8.0	9.0	11.0	8.0	10.0
Sr	779	784	786	790	794	803	805	805	810	816	833	845	849	861	878	880	890	911	980
Rb	99	89	89	81	85	95	131	94	93	80	84	96	91	88	89	93	89	79	86
Zn	71	94	66	78	88	70	45	97	88	82	80	72	71	84	70	68	70	79	78
Ni	12	10	9	15	10	10	3	10	7	13	20	10	14	14	16	11	20	22	14
Co	8	11	24	13	11	10	3	13	8	11	11	6	6	11	15	8	12	16	9
Cr	8	40	23	25	23	17	22	13	23	29	61	11	11	36	28	11	22	42	14
V	88	101	79	108	112	97	96	103	95	125	117	98	93	117	90	90	82	81	126
Ba	1104	1100	1099	970	1100	1039	1100	1040	1100	1100	965	1116	1002	939	1124	1138	1129	1056	1252
Sc	5	6		6	6	8	6	7	6	7	7	9	3	7	8	6	3	6	13
Li	40			25		24		23				20	34		24	21	32	17	19
Trace elements analysed by ICPMS (ppm)																			
Cs	7			5		7		5				5	6		6	7	6		5
La	28	34		29	34	28	35	27	37	34	35	26	37	37	33	32	37	34	34
Ce	58	65		59	61	59	62	57	69	62	65	55	73	63	65	63	67	70	69
Pr	7.0			7.0		7.3		6.4				6.7	8.6		7.4	7.5	8.4	8.6	8.7
Nd	27.3	28.0		28.1	31.0	26.8	25.0	22.2	30.0	30.0	32.0	23.5	32.9	31.0	27.8	28.9	32.2	32.7	33.3
Sm	4.5			4.8		4.1		3.9				4.0	5.2		4.9	4.7	5.1	5.5	5.1
Eu	1.11			1.33		1.21		1.12				1.20	1.33		1.30	1.28	1.32	1.00	1.48
Gd	3.3			4.2		3.6		3.1				3.4	3.9		4.0	4.1	3.8	4.1	4.6
Tb	0.35			0.44		0.39		0.38				0.38	0.40		0.44	0.42	0.39	0.40	0.45
Dy	1.77			1.87		1.74		1.46				1.60	2.01		1.80	1.74	1.96	1.90	1.95
Ho	0.30			0.32		0.29		0.28				0.27	0.34		0.34	0.31	0.33	0.30	0.32
Er	0.68			0.78		0.81		0.72				0.75	0.75		0.82	0.76	0.72	0.90	0.85
Tm	0.10			0.09		0.09		0.08				0.08	0.11		0.10	0.10	0.10	0.10	0.10
Yb	0.60			0.57		0.62		0.57				0.55	0.67		0.64	0.60	0.64	0.70	0.63
Lu	0.09			0.09		0.10		0.09				0.08	0.10		0.11	0.11	0.09	0.10	0.10
Hf	3.0			3.4		3.5		3.5				3.4	3.2		3.3	3.1	2.8	0.8	4.1
Ta	0.44			0.32		0.33		0.29				0.33	0.44		0.34	0.41	0.52	1.80	0.40
Pb	18			19		13		18				17	17		19	19	18	14	18
Th	5.5			5.3		6.7		6.6				6.5	6.4		5.9	6.6	5.8	5.6	7.1
U	2.2			2.2		2.5		2.1				2.2	2.6		1.8	2.7	2.2	1.3	2.6

Taapaca Volcanic Complex

Central Volcanic Zone (18°S), Northern Chile

Photo: Gerhard Wörner

CHAPTER 3

Differentiation regime of Taapaca dacitic complex, Central Volcanic Zone, N. Chile

ABSTRACT

Taapaca Volcanic Complex, located at 18°S in the Andean Central Volcanic Zone, erupted monotonous (62-67 wt% SiO_2), porphyric dacites during its main ~1 Ma eruptive history. Taapaca dacites show a textural and mineralogical kinship to granodioritic batholiths, large-volume Monotonous Intermediate, and to porphyric dacite eruptions in volcanic arcs characterized by an “adakitic” signature. A presence of sanidine megacrysts alongside basaltic andesitic microphyric enclaves and two amphibole and plagioclase populations in all of the Taapaca dacites is an indication of their hybrid nature.

The petrogenesis of the Taapaca dacites results from two-stage magma mixing between low-Mg high-Al mid-K calc-alkaline basaltic andesite and shoshonitic basalt in the first stage, forming an array of compositionally different mafic recharge magmas. These hybrid mafic magmas mix with high-K calc-alkaline rhyodacite magma, finally forming the monotonous dacites, characterized by a small compositional scatter. Mixing proportions between mafic and silicic components vary slightly, depending on the composition of the mafic recharge. The Taapaca dacites consist of ~60-70 % of the silicic, and ~30-40 % of the mafic component. These values remain constant through the entire eruptive history of Taapaca.

An application of geothermo-oxy-barometry (GTOB) methods based on amphibole compositions in connection with an experimental approach provides an evaluation of the GTOB formulations suitable to two distinct Ca-amphibole populations present in the Taapaca dacites. According to the experimental results, low-Al-Ti magnesiohornblende could be reproduced from a dacitic starting material, high-Al-Ti magnesiohastingsite from a basaltic andesitic. The connection between amphibole and whole rock chemistry allows an assignment of the amphibole species and their crystallization conditions to the certain end-member magmas involved in the generation of the dacites. Crystallization pressures of magnesiohornblende and magnesiohastingsite yield consistent range of ~1.0-3.0 and ~1.9-3.0 kbar, respectively; however, P-values from magnesiohornblende are determined with Al^{TOT}-in-Hbl barometer of Johnson & Rutherford (1989), and from magnesiohastingsite with barometer formulation of Ridolfi & Renzulli (2011, Equation 1e). Amphibole crystallization temperatures reveal ~750-840°C for the rhyodacitic, and ~900-1000°C for the basaltic andesitic mixing end-members. The oxygen fugacity varies between NNO+1-NNO+2 in the rhyodacitic, and NNO-NNO+3.5 in the mafic magmas. Rhyodacite contains higher melt water contents of 6.0-8.5 wt% obtained from magnesiohornblende, in comparison to 3.0-4.5 wt% obtained from magnesiohastingsite.

Crystallization temperatures from amphibole rim - plagioclase rim pairs show significantly lower values of ~690-740°C for low-Al-Ti amphibole and low-An plagioclase, and ~760-850°C for high-Al-Ti amphibole and high-An plagioclase. Fe-Ti oxide temperatures range from ~780 to ~900°C obtained from Fe-Ti oxide thermometer of Andersen & Lindsley, (1985). These T-values are between two T-ranges obtained from amphibole compositions and may reflect the last pre-eruptive thermal conditions, due to fast compositional reequilibration of the Fe-Ti oxide.

The differentiation regime forming monotonous Taapaca dacite links plutonic and volcanic realms. The silicic and mafic magmas did not erupt as single eruptions. The silicic magmas most probably attain the rheological lock-up point in the shallow crust; the mafic magmas are too dense to erupt.

Obviously, the rejuvenation of the cold and water-rich, highly porphyric silicic magma by intrusion of the hot mafic magma makes both magmas eruptible, however as intermediate, hybrid lavas. Obviously, a clash of silicic and mafic magmas, followed by rejuvenation and remobilization processes, play a key role in formation of stratovolcanoes in the subduction zones.

1. INTRODUCTION

Taapaca Volcanic Complex (TVC) is a Quaternary dome cluster volcano located in the Andean Central Volcanic Zone at 18°S. After an initial andesitic phase, Taapaca generated remarkably uniform high-K dacitic lavas during its main eruptive history since Early Pleistocene. The highly-porphyritic Taapaca dacites share textural, mineralogical, and chemical similarity with *monotonous intermediates* (MIs) recognized by Hildreth (1981) in the study of the highly voluminous (>1000 km³) ash-flow deposits. The MI rocks have a limited compositional range from silicic andesite to rhyodacite (62-69 wt% SiO_2), which represents complete eruption volumes. They are characterized by high crystal content (>25 vol%), where the phenocryst assemblage is dominated by plagioclase and amphibole with subordinate biotite, titanite, apatite, Fe-Ti oxide, quartz, zircon, ±sanidine, ±pyroxene and sulfide minerals, as well presence of mafic enclaves and bimodal phenocryst populations. This type of uniform and crystal-rich dacite constitutes not only 1) large volume ignimbrite deposits (e.g. Fish Canyon Tuff, Colorado, Bachmann et al., 2002; Lund Tuff, Indian Peak caldera, Maughan et al., 2001; Cerro Galan caldera, Central Andes, Francis et al., 1989; Wright et al. 2011; Folkes et al., 2011; Atana ignimbrite, La Pacana caldera, Central Andes, Lindsay et al., 2001), but also: 2) dome-building volcanic centers (e.g. Cayambe, NVZ, Samaniego et al., 2005; Yanacocha, CVZ, Chambefort et al., 2009; Aucanquilcha, CVZ, Klemetti & Grunder, 2008, Walker et al., 2010; Incapillo Complex, CVZ, Goss et al., 2010; Longavi, SVZ, Rodríguez et al., 2007), 3) single dacitic lava flows or domes of relatively high volume compared to the total volcano volume found in the stratovolcanoes (Parinacota volcano, CVZ, Border Dacite unit, Wörner et al., 1988; Hora et al., 2007), 4) composite coulées (Cerro Chao, CVZ, de Silva et al., AGU Abstract), or 5) pyroclastic deposits (Pagosa Peak Dacite, Colorado, Bachmann et al., 2000). All of them represent calc-alkaline arc volcanism.

The significant chemical and textural similarities observed in the eruptive products of small dacitic dome centers and large ignimbrite sheets suggests that there is no fundamental difference in the magma genesis of MIs despite differences in eruption volume (Caffe et al., 2002; Goss et al., 2010). Commonly, the MIs are related to the granodioritic batholiths due to observed resemblance of the compositional homogeneity, typical plutonic near-solidus mineral assemblage, which is rare in crystal-poor volcanic rocks, and the volume dimensions (Bachmann et al., 2007). This shows petrogenetic relation between silicic volcanism and shallow granitoid plutons (Glazner et al., 2004; Lipman, 2007; Bachmann et al. 2007 and references therein). Observed disequilibrium textures, bimodal phenocryst populations, and presence of mafic enclaves in the monotonous intermediate magmas reflect interactions between silicic and mafic magmas. Therefore, the crystal-rich intermediate volcanic deposits have recently been interpreted as a product of remobilized plutons by intrusion of hot mafic magma (e.g. Keller, 1969; Mahood, 1990; Stimac & Pearce, 1992; Watts et al., 1999; Murphy et al., 2000; Couch et al., 2002; Bachmann et al., 2002; Zellmer & Turner, 2006; Kent et al., 2010; Zellmer et al., 2011; Cooper & Kent, 2014). These types of highly porphyritic dacites represent pre-eruptive mixtures of mafic and silicic magmas, which yield notable homogeneity at both magma chamber and millimeter scale. This implies generation in a highly dynamic system (Bachmann et al., 2002). The reactivation of shallow crustal magma reservoirs involves thermo-mechanical processes inducing “defrosting” of the rheologically locked crystal mushes (Mahood, 1990; Bachmann & Berganz, 2006; Huber et al. 2010) which offer a plausible explanation for reactivation of the mature, near-solidus, crystal-rich magma bodies that erupt with average crystallinities higher than 40 vol% (Huber et al., 2011).

The porphyritic lava dome complexes represent highly the viscous end-member morphology of effusive styles arc volcanism. Dome-building eruption style is linked to low magma flux rates providing rapid magma cooling and long residence times (Zellmer, 2009). Accordingly, volcano morphology and erupted compositional range reflect the constitution of the magma plumbing and storage system, which set up a particular magma differentiation regime, governed by magmatic physical conditions.

In spite of the fact that the well-known Andean dacitic dome complexes share diverse features such as: an initial andesitic phase, bimodal mineral populations, presence of the mafic enclaves, high Sr/Y ratios and depletion in HREE related to “adakite-like” magmas(6), somewhat different magma differentiation paths have been recognized for the generation of the porphyritic dacites. Focusing on the coeval Andean examples, mixing between adakite-like and mantle-derived magmas is proposed as a principal mechanism generating the dacites of Cayambe Volcanic Complex, NVZ, Equador, by Samaniego et al. (2005). In contrast, Rodríguez et al. (2007) suggest polybaric, two-stage fractional crystallization from mafic enclaves to the dacites composition at Nevado de Longaví adakitic dacites, SVZ, Chile. Another petrogenetic model involves low-pressure fractional crystallization and upper crustal assimilation altering the composition of parental melts generated in the lower crust (Incapillo, CVZ, Goss et al., 2010). However, none of the studies identifies the composition of the primary magma(s) involved in the petrogenesis.

Taapaca dacitic complex represents an outstanding example of a volcanic system characterized by a long-lasting incremental extrusion of texturally and mineralogically uniform lavas, showing petrological evidence for magma mixing. Hence, the whole rock dataset of Taapaca rocks constitutes an appropriate basis for application of Polytopic Vector Analysis (PVA), a multivariate statistical technique designed exclusively for mixed geological systems including magmatic systems (Johnson et al., 2002 and references therein). PVA consists of numerous mathematical algorithms, which allow a determination of a number of magmatic end-members, major- and trace-element compositions of the end-members, and their mixing proportions - all the parameters required for complete characterization of a compositionally mixed system.

---

6 „adakite-like“ or „adakitic“ magmas or rocks are terms used for rocks with chemical characteristics nearly identical to true adakite but are produced by other petrogenetic processes (e.g. Castillo, 2006)

The statistical-geochemical PVA study of Taapaca dacites and basaltic andesitic enclaves hosted in the dacites, presented in Chapter 2, reveals three end-member magmas of basaltic, basaltic andesitic and rhyolitic composition with respect to silica contents, involved in the petrogenesis of Taapaca rocks. These end-members show distinct major and trace element characteristics, which reveal their geochemical affinity connected to shoshonitic, high-Al calc-alkaline and high-K calc-alkaline magmatic series, respectively. Furthermore, the mixing proportions of the end-members yield two magma mixing stages. The first stage comprises hybridization of the shoshonitic and high-Al calc-alkaline most mafic components, which originate in lithospheric and asthenospheric mantle, respectively. These hybrid magmas form a mafic recharge intruding into a rhyodacitic reservoir representing silicic crustal melts, and induce the second magma mixing stage, resulting in the generation of dacites and basaltic andesitic enclaves.

The PVA study is groundwork that gives the unique possibility to create a holistic petrogenetic picture of a volcanic system. Most studies carried out on volcanic rocks investigate geochemical properties and/or petrological observations to find the nature of primary magmas. In this case, the compositions of the (near) primary magmas have been determined. The challenge of this study is to integrate all previous findings (Chapter 2) and results of geothermo-oxy-barometry into a complete image of the Taapaca volcanic system.

This study started with detailed petrography, determination of mineral chemistry and estimation of the intensive parameters of crystallization in Taapaca lavas. An experimental approach by Botcharnikov et al. (in prep.) has expanded the findings about the crystallization conditions in Taapaca magmas. The PVA study was conducted during the final stage of preparation of this Chapter. Therefore, the work would have been carried out somewhat differently if the PVA results had already been known at the beginning of this study.

The study presented here describes an extreme example of a magmatic differentiation regime, which occurs in the modern CVZ volcanic arc. The Taapaca volcanic system involves simultaneously three main primary magmas generated in the Central Andean subduction zone.

2. VOLCANOLOGICAL BACKGROUND

2.1. GEOLOGICAL SETTING

Taapaca Volcanic Complex (TVC, 18°S, 69°W), also known as Nevados de Putre is located in an active volcanic chain developed in the central Andes, on the western margin of the South American continent. The Andes represent the largest recent magmatic continental arc in the world, and result from subduction of the Nazca and Antarctic oceanic plates beneath the South American continental lithosphere. The Quaternary Andean volcanic activity occurs in four segments, the Northern, Central, Southern and Austral volcanic zones, which are separated by volcanic gaps. The TVC is a part of the Andean Central Volcanic Zone (CVZ) extending between latitudes 14° and 28°S (Figure 1).

The TVC is a part of the Western Cordillera, which borders the western margin of the Altiplano

Plateau, the largest non-collisional plateau on the Earth (Isaacks, 1988). The Western Cordillera comprises the Quaternary volcanic chain aligned NW-SE to the border between Chile and Bolivia, characterized by high topography with numerous active volcanoes exceeding elevation of 6000 m asl. Taapaca lies about 30 km to the west from the main volcanic chain forming the central part of the CVZ, the Altiplano-segment (15-23°S)(7). At 23°S, the volcanic chain changes to the N-S alignment including volcanic centers of the Puna region (23-28°S).

Volcanism in the CVZ occurred since about 300 Ma (e.g. Scheuber et al., 1994). The CVZ is underlain by subducting slab, descending at a relatively steep angle of ~25° (Cahill and Isaacks, 1992) at a current convergence rate of 75-80 mm/a (Samoza, 1998). The volcanic front of the CVZ lies approximately 120-150 km above the subducted slab and remarkably thick continental crust exceeding 70 km below the Altiplano region (James, 1971; Zandt et al., 1994; Allmendinger et al. 1997; Scheuber & Giese, 1999; Yuan et al., 2002; Tassara et al., 2006).

The crust below the Altiplano consists of Palaeoproterozoic (2.0-1.8 Ga) Arequipa terrane represented by metamorphic and igneous rocks exposed in southern Peru. Proterozoic amphibolites and gneisses of metamorphic Belen Complex as well granulites and charnockites of Cerro Uyarani, exposed in northernmost Chile, on the western Altiplano and along the Chilean Precordillera have been reported by Wörner et al. (2000) and are assumed to underlie significant portions of the CVZ in northern Chile.

2.2. ORIGIN OF THE CVZ QUATERNARY MAGMAS

The predominantly mafic composition and old age of the Arequipa crustal domain is reflected by the specific isotopic and trace element composition of the Quaternary magmas erupted in the Altiplano region, characterized by low $^{206}Pb/^{204}Pb$ and $^{143}Nd/^{144}Nd$, elevated $^{87}Sr/^{86}Sr$ and high Sr/Y (e.g. Mamani et al., 2010 and references therein). The adakite-like signature (Sr/Y>40) found in the Central Andean magmas since Miocene time is commonly assumed to result from an involvement of garnet and/or amphibole in partial melting of thickened lower crust, high pressure fractional crystallization of mantle-derived magmas, and assimilation of crustal rocks into mantle-derived magmas (Mamani et al., 2010 and references therein). It is broadly accepted that these processes can occur simultaneously and set up the “baseline” chemical and isotopic features of erupted magmas, in the MASH (melting, assimilation, storage, and homogenization) zones at the mantle-crust transition (Hildreth & Moorbath, 1988; Davidson et al., 1990, 1991).

Magmas erupted at Quaternary volcanic centers near 18°S yield two kind of parental mafic magmas characterized by different baseline geochemical features. These baseline magmas contrast in Ti, Cr, Sr- and Ba-contents, and HREE patterns, which suggest interactions at different MASH-levels in the upper crust (Ginibre & Wörner, 2007; Hora et al., 2009; Mamani et al., 2008). They emphasize the role of a more mafic composition of the Arequipa domain in generation of the adakite-like signature in the CVZ, which does not occur in the Puna region that is also characterized

---

[7] 23° is the geographic boundary between Altiplano and Puna Plateau presented by e.g. Stern et al. (2004). Based on paleogeographic features, Allmendinger et al. (1997) set the boundary across the volcanic arc at ~20°S.

by relatively thick crust (>65 km). Minor variations in isotopic composition within a wide range of SiO_2-contents in magmas erupted at 18°S (Davidson et al., 1990) imply generation of intermediate and silicic magmas in deep-seated baseline MASH zones, as suggested by Ginibre & Wörner (2007) for Parinacota volcano (CVZ: 18°S), and Goss et al. (2010) for Incapillo Caldera and Dome Complex (CVZ: 28°S). These data are in agreement with the deep hot zones differentiation model of Annen et al. (2006).

In contrast to the broadly accepted MASH-based explanation of the geochemical properties of the Neogene CVZ lavas, a multivariate statistical modeling using Polytopic Vector Analysis (PVA), presented in Chapter 2 of this work, has detected three distinct magmatic components involved in the petrogenesis of the recent Central Andean lavas. These (near) primary magma compositions represent shoshonitic, high-Al calc-alkaline and high-K calc-alkaline magmatic series. Two-stage magma mixing between these three end-member magmas with minor contribution of assimilation and fractional crystallization may be responsible for the entire compositional variability of the Quaternary CVZ lavas.

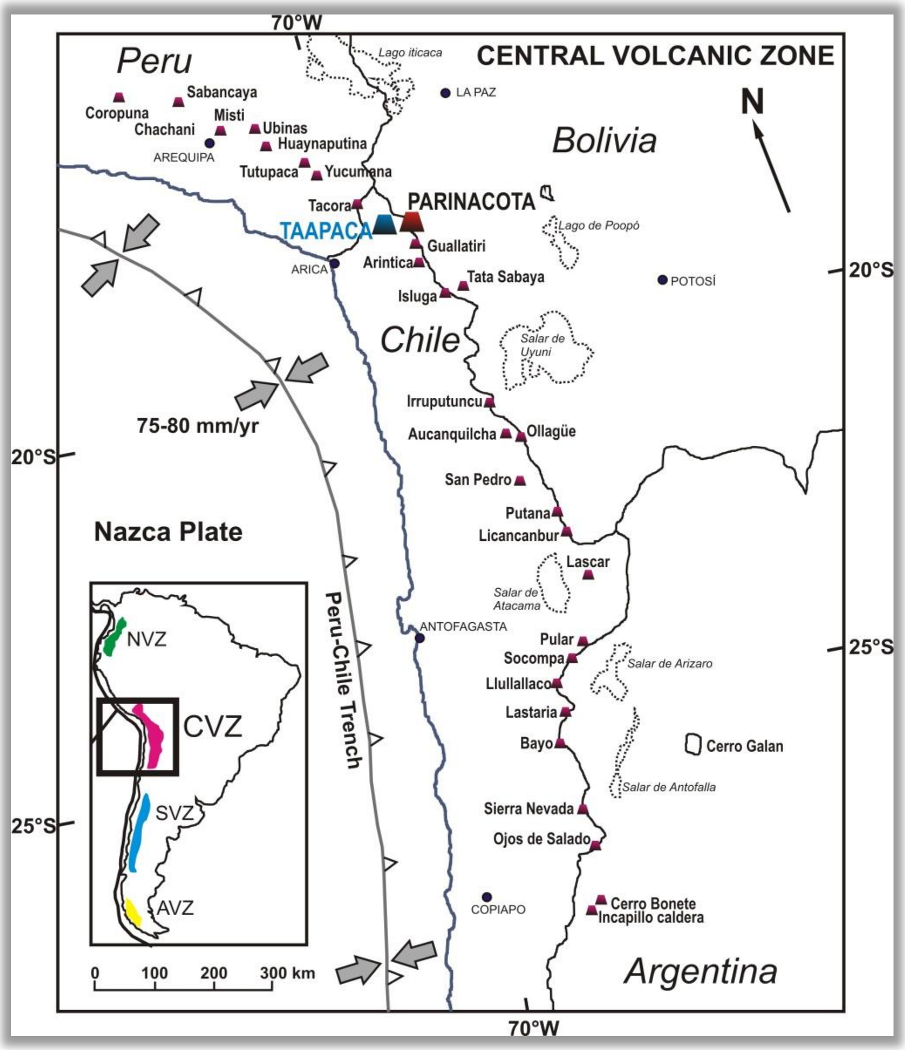

Figure 1. *Schematic map of the Andean Central Volcanic Zone (CVZ) modified from Stern (2004), illustrating location of Taapaca volcano and other volcanic centers in the CVZ. Inset shows the position of the CVZ in relation to the Northern (NVZ), Southern (SVZ), and Austral (AVZ) Volcanic Zones. Nazca Plate convergence rate of 75-80 mm is taken from Samoza (1998).*

2.3. ERUPTIVE HISTORY OF TAAPACA VOLCANIC COMPLEX

The eruptive history of the TVC, previously described by Kohlbach & Lohnert (1999), have been refined and presented in detail by Clavero et al. (2004), who recognized four evolutionary stages based on geochronological and morphological criteria, including migration of the main vent system. A geological map modified from Clavero et al. (2004) is presented in Figure 3.

The volcanic edifice of Taapaca is constructed atop three main uppermost basement units: Upper Oligocene - Lower Miocene Lupica Formation, Miocene andesitic volcanic deposits, and Upper Pliocene rhyolitic Lauca Ignimbrite. The Taapaca edifice consists of elongated dome clusters with three exposed summit domes of which the highest reaches 5850 m asl. The main edifice volume is estimated to be 35 km³; the eruptive products of Taapaca cover an area of 250 km² (Clavero et al., 2004).

The initial eruptive stage I formed a shield-like stratocone consisting of moderately porphyritic two-pyroxene andesitic lava flows containing small amounts of sanidine and hornblende. Stage I is estimated to be older than 1.5 Ma; the oldest $^{40}Ar/^{39}Ar$ age from earliest dacitic stage II samples from Taapaca is 1.46 ±0.07 Ma (Clavero et al., 2004). This stage formed the main volume of TVC between 1.5 and 0.5 Ma. It consists of viscous dacitic lava flows, which formed a stratovolcano with steeply dipping flanks. A major collapse event is documented by a voluminous debris avalanche/lahar, dated at 1.27 ±0.04 Ma by Wörner et al. (2000). The dacites of stage II contain sanidine megacrysts, plagioclase, amphibole and biotite phenocrysts, rare quartz and titanite, and very rare, small anhedral clinopyroxene. Stage III consists of small volume lava domes and block-and-ash flow deposits concentrated mainly in the central part of the dome complex erupted during a short period between 0.5 and 0.47 Ma. The eruptive products differ from stage II only by higher amounts of sanidine megacrysts and mafic enclaves. Partial collapse of the southern part of ancestral stage II edifice and stage III domes marks the start of the youngest and morphologically most complex stage IV. The dacites generated during Late-Pleistocene – Holocene eruptive activity of TVC are petrographically undistinguishable from those of unit III. Clavero et al. (2004) observed higher amounts of mafic enclaves comprising up to 6 vol% of the juvenile material and increasing sizes and abundance of sanidine megacrysts. Stage IV form the main edifice of TVC, characterized by extrusion of voluminous domes and associated block-and-ash flows, blasts, tephra fallout, pyroclastic flows, debris avalanche, and lahars. The pyroclastic flows, surges, and tephra fallout are associated with dome growth-collapse explosions.

Numerous debris avalanche deposits are evidence for frequent edifice collapse events at TVC. Clavero et al. (2004) recognize two types of debris avalanche at Taapaca. First, debris avalanches that are a consequence of extensive hydrothermal alteration causing edifice weakening, and second, by intrusion of a cryptodome causing deformation and instability of the edifice. The latter collapse triggering mechanism is evidenced by blast deposits integrated in the debris avalanche, which result from a rapid decompression after abrupt mass unloading. Despite the catastrophic mass unload events observed at TVC, a change in the composition and mineralogy of erupting products after edifice collapses, as documented for Parinacota volcano (Wörner et al, 1988; Hora et al., 2007; Chapter 4 of this work) has not been observed.

2.4. GEOCHEMICAL CHARACTERISTICS OF TAAPACA LAVAS

2.4.1. TAAPACA HYBRID DACITES

According to the classification of Le Maitre et al. (1989), Taapaca rocks plot in the transition zone between andesite-dacite and trachyandesite-trachyte fields (Figure 2a). The prefix “trachy”-denotes genetic link to the alkaline intra-plate volcanism, which cannot be used for classification here, otherwise as suggested by Higgins (2011) due to the high alkali contents in Taapaca rocks. Using the division of Irvine & Baragar (1971), Taapaca rocks are subalkaline and classify as high-K calc-alkaline andesite and dacite, due to the subdivision of Rickwood (1989), (Figure 2b).

Previous studies of the Taapaca whole rock chemistry (Kohlbach, 1999; Clavero et al., 2004; Higgins, 2011) report a limited range in silica content through all eruptive stages I-IV (60-68 SiO_2 wt%) characterized by a strong (linear) correlation of the most major and trace elements. Moreover, the dacites show a compositional dispersion, which is greater than an analytical error in each data point. Considerable compositional scatter of Taapaca dacites, reported also in Chapter 2 (section 4.2.1, Figure 2, 4, 5) does not follow any spatial or temporal trends. The variable modal percentage of sanidine megacrysts may be considered as one reason for data scatter. However, an influence of sanidine megacrysts on the whole rock composition is small due to their small amount (<5 vol%) and similar composition to the host dacites (Higgins, 2011). Nonetheless, two main compositional trends can be extracted from the scatter in the Taapaca dacites, forming a “main-group” dacites and “subtrend” dacite, previously recognized by Kohlbach (1999) as well.

These two trends are also known from other Andean volcanic centers. Two distinct calc-alkaline trends of different Na_2O, K_2O, TiO_2, P_2O_5, LILE and HREE have been defined by Davidson et al. (1990) for Nevados de Payachata twin volcanoes, Parinacota and Pomerape (Figure 2c). The younger trend (<1 Ma), called PP-trend shows an enrichment in incompatible elements in contrast to an older, Neogene (>1 Ma) trend, called N-trend, from the same Nevados de Payachata region. Both trends converge at ~68-70 wt% SiO_2. The main group of Taapaca dacite overlaps the PP-trend; the subgroup overlaps the N-trend (Figure 2c).

An involvement of whole rock compositions of the mafic enclaves into a geochemical examination of Taapaca magmas reveals a wide range of different compositions of the mafic input magmas. The compositions of the Taapaca mafic enclaves span contrasting both, major and trace element characteristics, e.g. low- and high- TiO_2 contents (1.0-1.9 wt%), low- and high-LILE contents (647-1439 ppm Sr), low- and high-LILE/HFSE and -LREE/HREE ratios (e.g. $27<Sr/Y<161$, $2.0<Sm/Yb<11.7$, respectively). Such distinct geochemical signatures imply different petrogenetic processes generating the parental magmas forming the mafic enclaves.

Thus, the compositional variability of the mafic recharge magma is responsible for the compositional scatter observed in the Taapaca dacites. The minor compositional differences occurring in the dacites resemble the significant compositional differences in the mafic enclaves, most apparent for Sr contents illustrated in Figure 2c.

2.4.2. COMPARISON TO OTHER ANDEAN DACITIC COMPLEXES

Figure 2 presents Taapaca rocks with selected, morphologically and compositionally similar Andean volcanic centers. A narrow compositional gap between ~60 to ~61 wt% SiO_2 between the dacites and more mafic compositions found at this volcanoes can be observed in all presented examples. Due to the results obtained from multivariate statistical Polytopic Vector Analysis (PVA, Chapter 2), the geochemical characteristics of Taapaca rocks, result from two-stage magma mixing between three magmatic end-member magmas, representing shoshonitic (BEM) basaltic magmas, low-Mg high-Al calc-alkaline (AEM) basaltic andesite magma, and high-K calc-alkaline (RDEM) rhyodacite magma. It is strongly suggested, that the selected dacitic centers, showing similar petrological characteristics to Taapaca samples, may originate via the same differentiation processes, and furthermore, contain a silicic end-member generated in the thick crust, as argued for RDEM in Chapter 2.

A crucial geochemical signature leading to the above mentioned conclusion is the high Sr/Y ratio found in Taapaca (27-161), Haunyaputina (50-94) Irruputuncu (32-57), as well as Cayambe (32-79) and Longaví (14-81). Sr/Y ratios >30 are connected to the “adakitic” signature, as mentioned in section 1, and connected to the magma interactions with an exceptionally thick crust in the CVZ, with garnet as a residual phase. Although the two latter volcanoes Cayambe and Longaví are located in the NVZ and SVZ, respectively, characterized by a significantly lower thickness of the underlying crust (e.g. Tassara, & Yanez, 2003; Tassara, 2005), they also show high Sr/Y ratios. In contrast to the mainly high-K calc-alkaline CVZ dacites, they plot in medium-K calc-alkaline field. They do not contain high-K - high-Sr/Y shoshonitic component, as observed for the CVZ magmas. The origin of the adakitic signature in these highly porphyritic dacites must result from high Sr/Y ratios in the RDEM-type silicic magmas, due to presented issue in section 6.6.1, Figure 15 in Chapter 2.

Figure 2. ***Next page: a)*** *Total Alkali vs. Silica (TAS) diagram according to Le Maitre et al. (1989) with alkaline/subalkaline division of Irvine & Baragar (1971), showing Taapaca and selected Quaternary Andean dacitic volcanic centers.* ***b)*** *K_2O vs. Silica subdivision of Rickwood (1989) presenting the subalkaline lavas from a).* ***c)*** *Sr vs. Silica plot presents Taapaca rocks in comparison to two main compositional trends occurring in the CVZ, defined by Davidson et al. (1990). Main Taapaca dacite group overlaps with the highly in incompatible elements enriched PP-trend; the Taapaca subgroup dacites overlaps with the Neogene trend. Abbr.: BEM-basaltic shoshonitic, AEM-high-Al basaltic andesitic calc-alkaline, RDEM-high-K calc alkaline PVA end-members.*

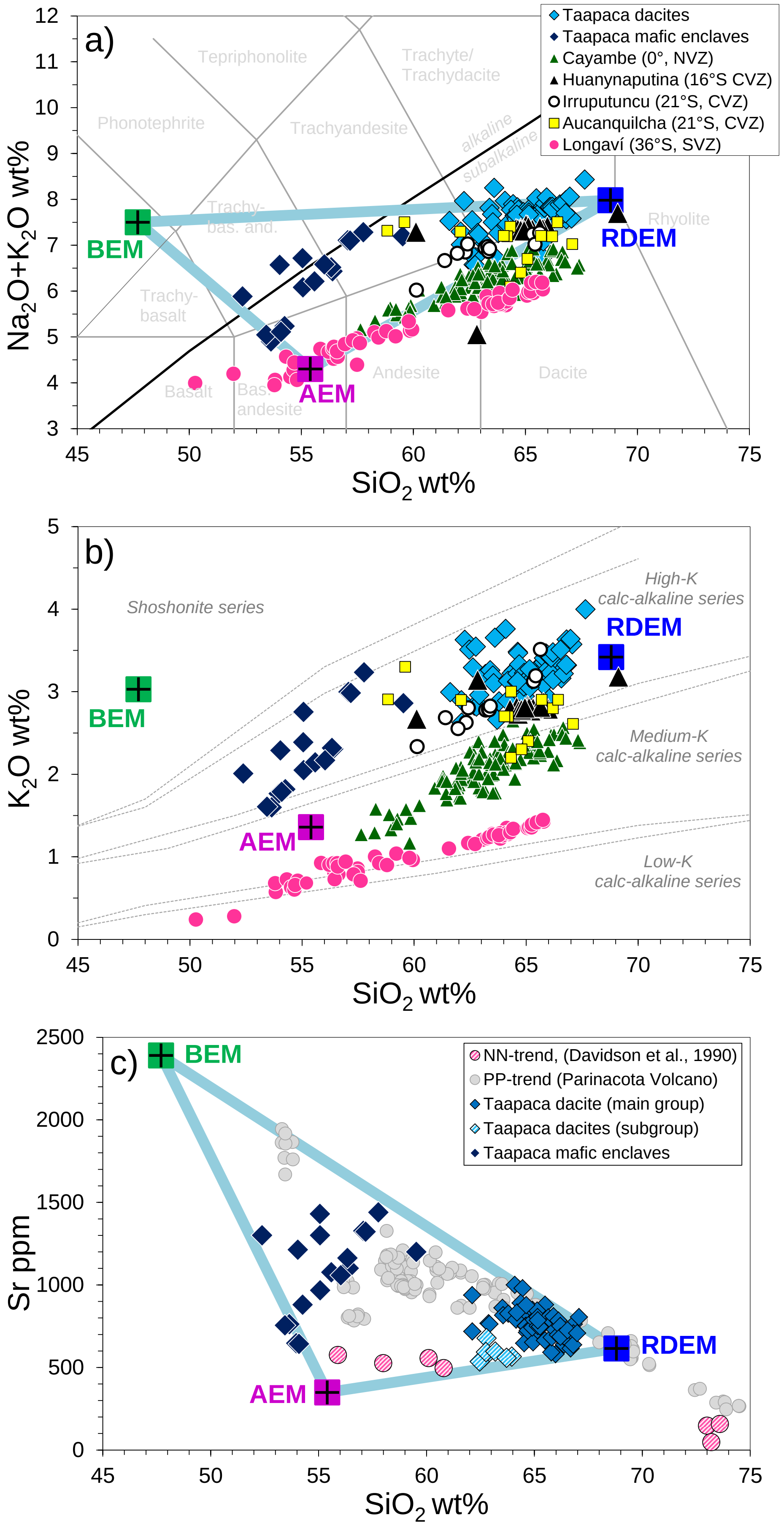
a)
Taapaca dacites
Taapaca mafic enclaves
Cayambe (0°, NVZ)
Huanynaputina (16°S CVZ)
Irruputuncu (21°S, CVZ)
Aucanquilcha (21°S, CVZ)
Longaví (36°S, SVZ)
Tepriphonolite
Trachyte/
Trachydacite
Phonotephrite
Trachyandesite
alkaline
subalkaline
Trachy-
bas. and.
Trachy-
basalt
Basalt
Bas.
andesite
Andesite
Dacite
Rhyolite
BEM
AEM
RDEM
Na_2O+K_2O wt%
SiO_2 wt%
b)
Shoshonite series
High-K
calc-alkaline series
Medium-K
calc-alkaline series
Low-K
calc-alkaline series
BEM
AEM
RDEM
K_2O wt%
SiO_2 wt%
c)
NN-trend, (Davidson et al., 1990)
PP-trend (Parinacota Volcano)
Taapaca dacite (main group)
Taapaca dacites (subgroup)
Taapaca mafic enclaves
BEM
AEM
RDEM
Sr ppm
SiO_2 wt%

2.5. PREVIOUS WORK

The first reconnaissance mapping and geochemical studies presented by Kohlbach & Lohnert (1999) and Kohlbach (1999) show that Taapaca dacitic complex experienced multistage evolution resulting with remarkably uniform chemical and mineralogical composition of its eruptive products. Further studies based on $^{40}Ar/^{39}Ar$ dating (Wörner et al., 2004; Clavero et al., 2004) reveal Taapaca, previously declared as extinct (Gonzales, 1995), as a long-lived and still active magmatic system. In the last decade Taapaca became famous for the occurrence of the largest known volcanic sanidine megacrysts in intermediate volcanic rocks, presented by Zellmer & Clavero (2006) and Higgins (2011), investigated previously also by Lohnert (1999), Wegner (2005), and Banaszak (2007). Pronounced Ba-zoning found in the sanidines has been used as an archive of the evolution of the Taapaca magmatic system. These several geochemical and petrological studies reveal inconsistent results with respect to the chemical crystallization environment of the sanidines. A study by Banaszak (2007) demonstrates uniform trace element and $\delta^{18}O$ composition in low- and high-Ba zones, indicating crystallization in a chemically closed system. Ba zoning has been explained as a result of small-scale movement of the megacrysts in the Taapaca magma reservoir as well as temperature fluctuations caused by repeated rejuvenation processes. The magmatic times scales of Taapaca volcanic system have been investigated by U-Th isotope geochronology (Kiebala, 2008), which yield magma storage times exceeding 105 key In contrast, Ba-diffusion in sanidine megacrysts (Wegner, 2005) yields timescales shorter than 105 yr. Using $\delta^{18}O$ and $^{87}Sr/^{86}Sr$ data, Chang, 2007 shows an isotopic evolution of Taapaca magmas, which are interpreted to reflect magma source contamination and subsequent crustal contribution. The study of plagioclase Crystal Size Distribution presented by Freymuth (2006) reveals indistinguishable CSD patterns in Taapaca samples from all dacitic stages. This finding confirms the macroscopically observed textural uniformity of Taapaca rocks.

3. METHODS

3.1. SAMPLE SELECTION

The whole rock and isotopic database of Taapaca volcano used in this study comprises 27 dacite and three mafic enclaves analyzed by Wörner et al. (2004), Kohlbach (1999) and Kiebala (2008). Additionally for this study, 10 mafic enclaves found in the previously investigated dacitic samples were analyzed by XRF for major and selected trace elements. The studied samples are a part of the sample collection of the Geochemistry Department, University of Göttingen. A set of 12 samples, representing all Taapaca dacitic stages was selected for petrographic study, mineral chemistry, and geothermobarometry. This study involves the sample set used for sanidine analysis by Banaszak (2007) as well as CSD-method by Freymuth (2006). For the most of the analyzed samples, sample location and $^{40}Ar/^{39}Ar$ ages are available from Kohlbach (1999) and Wörner et al. (2004), respectively. The whole rock data of Clavero et al., (2004) is included in presented diagrams. All whole rock data are presented in Chapter 2, Appendix, Table A, and in Electronic Suppl. Data.

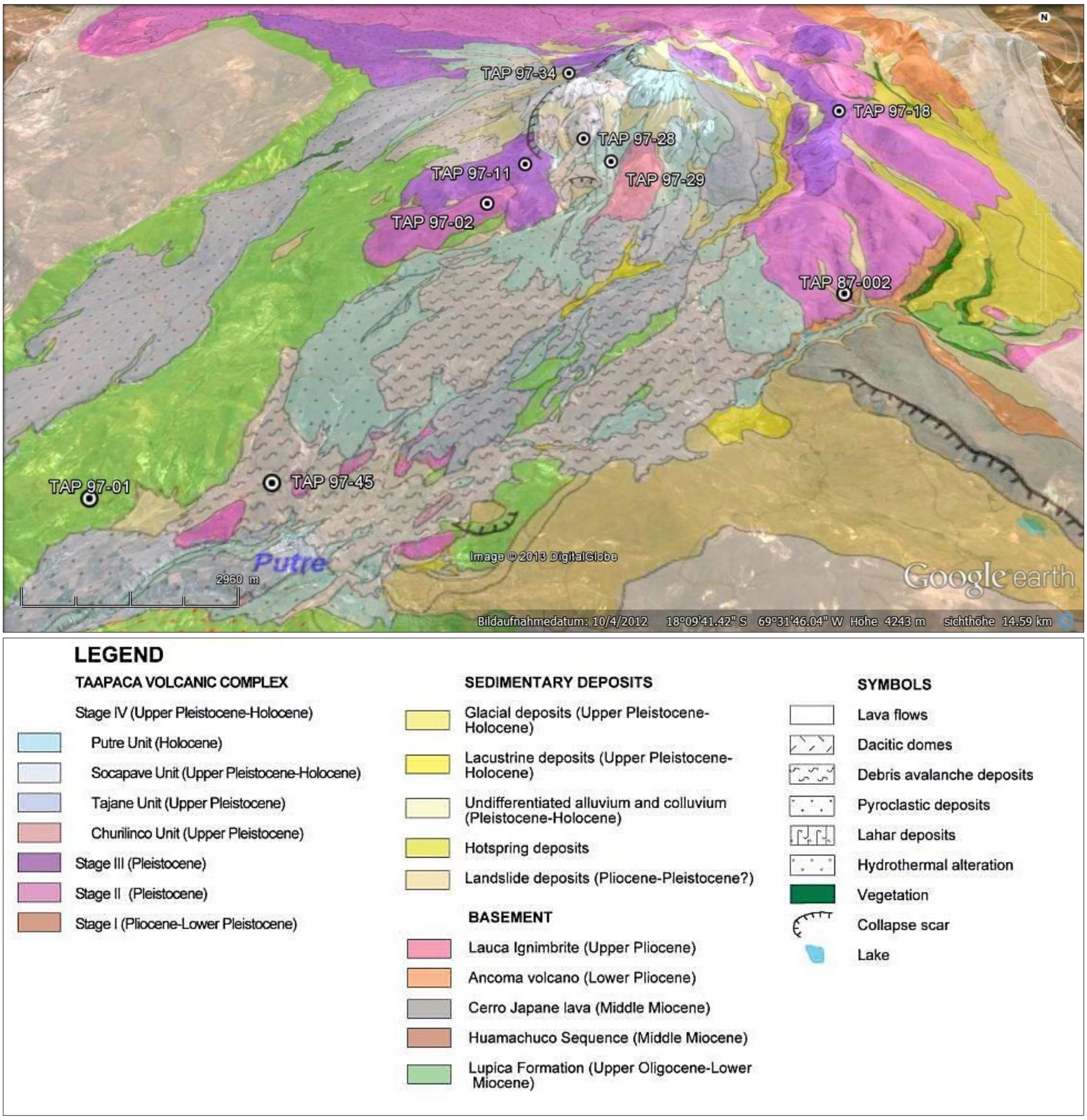

Figure 3. *Location of 9 of 11 samples selected for geothermo-oxy-barometry study presented using Geological Map of Taapaca Volcanic Complex of Clavero et al. (2004) as overlay in Google Earth ©2012 Google Inc.(00008.00015.00010.02656).*

3.2. ANALYTICAL METHODS

The major and trace element analyses were obtained by X-ray fluorescence (XRF) and ICPMS at the Geoscience Centre Göttingen. The measurements of Kohlbach (1999) were conducted with a Philips-PW 1480 X-ray fluorescence spectrometer; further measurements were carried out on PANalytical AXIOS X-ray fluorescence spectrometer. Both measurement sessions proceeded on fused glass discs fused automatically form a mixing of sample powder (<65 µm grain size) and $Li_2B_4O_7$ by a Schoeps SGE 20 automatic fusion machine. Repeated measurement by Banaszak (2007) of a few selected samples of Kohlbach (1999) reproduces the composition obtained by the second XRF spectrometer within analytical error.

Trace elements were analyzed by inductively coupled plasma mass spectrometry (ICP-MS) using Fissons VG PQ2+ (Kohlbach, 1999) and Perkin Elmer SCIEX Elan DRC II (this study). Dissolution of whole rock powders was done using a mixture of HF and $HClO_4$ followed by re-dissolution with HNO_3 after evaporation in Teflon beakers, method modified after Heinrichs and Herrmann (1990). Internal standards of Ge, Rh, In and Re were added to diluted sample solutions. The international standards JB3 (basalt) and JA2 (andesite) were analyzed continuously together with samples. The estimate analytical error yields ±5% 2σ for REE, <10% for Li, Be, Cu, Rb, Y, Cs, Hf, Tl, Pb, Th and U, <20% for Nb and Ta.

Quantitative analyses of mineral phases were determined by a JEOL JXA 8900RL electron microprobe on polished thin sections at the Geosciences Centre Göttingen using the wavelength dispersive method. The operating conditions for silicate minerals were 15 kV accelerating voltage, 15 nA beam current and 5-15 µm beam diameter, depending on the grain sizes. Oxide minerals were measured using 20 kV and 20 nA in focused spot beam due to the small grain sizes. Peak counting times were usually 15 s and 5 s for the background. For the trace elements in oxide minerals (Si, Al, Mg) 30 s for peak and 15 s for the background were applied. Matrix corrections for both measurement programs were performed automatically using the Phi-rho-Z procedure of Armstrong (1995). The analytical error is typically <1%.

3.3. GEOTHERMO-OXY-BAROMETRY

Geo-**T**hermo-**O**xy-**B**arometry calculation methods (further referred to as GTOB) used in this study comprise calculations of intensive crystallization parameters derived from single mineral and mineral-mineral thermometer and barometer, commonly applied to the volcanic systems. A petrographic examination of melt inclusions hosted in phenocrysts yields a large textural variety and do not satisfy common petrographic criteria and measurable sizes, which exclude application of mineral-melt methods.

3.3.1. GEOTHERMOMETER

The geothermometer of Holland & Blundy (1994) was used for estimation of crystallization temperatures recorded by amphibole-plagioclase pairs. The thermometer formulation based on exchange vector of albite-anorthite $(NaSi)(CaAl)_{-1}$ and edenite-richterite $(NaSi)_{-1}(CaAl)$ components requires molar fraction of albite (X_{ab}) and anorthite (X_{an}) in plagioclase and molar fraction of particular elements on T, M2, M4 and A crystallographic sites in amphibole. Cation values per formula unit (a.p.f.u), used for calculations of molar fractions (X_{Si}^{T1}, X_{Al}^{T1}, X_{Al}^{M2}, X_{Na}^{M4}, X_{Na}^{A} and X_{Ca}^{M4}), were determined using the recommended calculation procedure of Holland & Blundy (1994). The compositions of Taapaca amphibole and plagioclase meet the thermometer conditions defined by $X_{Na}^{M4}>0.03$, $Al^{VI}<1.8$, Si range of 6.0-7.7 p.f.u for amphibole and $0.1<X_{an}<0.9$ for plagioclase. Both thermometer formulations, “Thermometer A”, referred as T(A), for mineral assemblages with quartz and “Thermometer B”, referred as T(B), for mineral assemblages without quartz were used depending on Fe contents in plagioclase and Al, Ti contents in amphibole hosted in the Taapaca dacite. Low-Fe plagioclase and low-Al, Ti amphibole pairs, found as inclusions in the sanidine megacrysts as well as in the host dacite, are assumed to have crystallized from rhyodacitic end-member, allow application of both, T(A) and T(B). High-Fe plagioclase and high-Al, Ti amphibole population which occur in the mafic enclaves and host dacite only allow application of T(B).

The T(A) estimates temperatures with ±28°C uncertainty, T(B) with ±32°C, which comprise different error sources. However, testing a dataset of 294 experimental amphibole-plagioclase pairs, Blundy & Cashman (2008) found that the average absolute deviation (aad) between experimental and calculated T°C is aad=6°C. This value is robust to the typical errors in microprobe analysis ($\sigma=1\%$). Due to pressure insensibility of the thermometer in the range of 2-3 kbar (Blundy & Cashman, 2008), the temperature variations resulting from different pressure values used for the calculations reveal differences up to 17°C. It is worth to noting, that a lack of a chemical equilibrium-test for amphibole, and textural indications of reliable amphibole-plagioclase pairs, the possible combinations of the plagioclase-amphibole produce significant variations and uncertainties of the determined temperatures and expand the estimated temperature range.

Crystallization temperatures of amphibole are also estimated using thermometer of Féménias et al. (2006), (referred to as Fetal2006), based on Ti content in amphibole. This thermometer is applicable for T>700°C, for Ti-saturated calc-alkaline magmas. Estimated temperatures from experimental amphibole compositions are well correlated with the experimental results of Botcharnikov et al. (in prep.) carried out for Taapaca dacite. The maximum thermometer error is ±55°C for temperatures ranging from 600 to 1000°C. The error of microprobe analysis induces ±10°C for 1 wt% TiO_2 and are included in the error estimation (Féménias et al., 2006). The determination of Ti p.f.u in amphibole is based on Holland & Blundy (1994), according to the IMA classification and Fe^{3+} determination of Leake et al. (1997) used by Féménias et al. (2006) for calibration.

3.3.2. *GEOTHERMO-OXY-BAROMETER*

The temperature and oxygen-fugacity sensitive reactions between cubic magnetite$_{ss}$ and rhombohedral ilmenite$_{ss}$(8) are widely used in geothermo-oxy-barometry formulations (e.g Andersen & Lindsley, 1988; Ghiorso & Sack, 1991; Sauerzapf et al., 2008). The exchange reaction involving Fe^{2+}+Ti – $2Fe^{3+}$:

$$^{cubic}\,Fe^{2+}(Fe^{2+},Ti)_2O_4 + {}^{rhombohedral}\,(Fe^{3+},Fe^{3+})_2O_3 = {}^{cubic}\,Fe^{3+}(Fe^{2+},Fe^{3+})_2O_4 + {}^{rhombohedral}\,(Fe^{2+},Ti)_2O_3$$

is used for geothermometer formulation and determination of equilibrium temperature. The redox equilibrium, defined by reaction involving Fe-phases:

$4Fe_3O_4 + O_2 = 6\,Fe_2O_3$ (Andersen & Lindsley, 1988)

or a reaction involving Ti-phases:

$6FeTiO_3 + 2\,Fe_3O_4 = 6Fe_2TiO_4 + O_2$ (Sauerzapf et al., 2008) are used for oxy-barometer formulations and estimation of fO_2. The exchange- and redox-reactions are combined in

---

[8] Solid solutions magnetite$_{ss}$: magnetite (Fe_3O_4) – ulvöspinel (Fe_2TiO_4); ilmenite$_{ss}$: ilmenite ($FeTiO_3$) – hematite (Fe_2O_3)

thermodynamic models to construct the geothermo-oxy-barometer.

Among numerous geothermo-oxy-barometer formulations (Andersen & Lindsley, 1985; Ghiorso & Evans, 2008; Andersen et al., 1993) tested for their reliability by Blundy & Cashman (2008), the smallest average absolute deviation between experimental and calculated temperatures of aad=33°C yields the formulation of Andersen & Lindsley (1985), in combination with procedure of Stormer (1983) for calculation of molecular fractions of ulvöspinel and ilmenite. This calculation algorithm is also recommended as the most consistent with experimental approaches by Venezky & Rutherford (1999) for Unzen dacites, Devine et al. (2003) for Soufrière Hills andesites, and Palister et al. (2008) for Mount St Helens dacites. It should be noted, that this algorithm tends to overestimation for <860°C and underestimation for >860°C, as presented by Blundy & Cashman, (2008), their Fig. 13b.

Temperatures and oxygen fugacity were determined using ILMAT Excel worksheet of LePage (2003), which includes oxygen-fugacity and temperature (fO_2-T) results from multiple solution models for the Fe-Ti exchange geothermo-oxy-barometer. Due to the study of Blundy & Cashman (2008) and to facilitate comparison with other dacitic systems (e.g. Mount St. Helens, Palister et al. 2008), the fO_2-T data presented in this study comes from geothermo-oxy-barometer of Andersen & Lindsley (1985) and oxide formula calculation of Stormer (1983). Magnetite-ilmenite pairs were tested for chemical equilibrium using Mg/Mn atomic ratios in both Fe-Ti phases (Bacon & Hirshmann, 1988). Additionally, textural features of the Fe-Ti oxides were examined.

3.3.3. AMPHIBOLE BAROMETRY

Al-in hornblende barometer of Johnson & Rutherford (1989) (further referred to as J&R89) was applied to estimate equilibration pressures of amphibole, only to the low-Al amphibole population (magnesiohornblende) found in Taapaca dacites and sanidine megacrysts, which compositionally overlap with low-Al amphibole compositions synthetized at pressure up to 3 kbar, used for the verification of the calibration. The calibration conditions (T<760°C, NNO+2, starting whole rock composition of 64.4 wt% SiO_2 and mineral assemblage consisting of pl, bi, qz, san, mt, il, sp) match the whole rock composition of Taapaca dacite, its mineral assemblage as well as a part of temperature and oxygen fugacity conditions obtained from other GTOB methods. The linear regression of the J&R89 based on Al-total (Al^{TOT}) content, calculated using 15 cations normalization method for the experimental amphibole were recalculated to the Al^{TOT} determined by amphibole formula calculation of Ridolfi et al. (2010) based 13eCNK normalization recommended by International Mineralogical Association (IMA) (Leake et al. 1997). The updated equations is $P=4.2707(Al^{TOT})-3.4013$ ($r^2=0.99$). The recalculated Al^{TOT} values do not exceed 2.7% difference in Al^{TOT} p.f.u determined by J&R89 and the new equation yields pressures somewhat higher in the range of 3.3 and 0.7 kbar.

3.3.4. SEMIQUANTITATIVE AMPHIBOLE THERMOBAROMETER

Ernst & Liu (1998), (referred as E&L98), present Al_2O_3 and TiO_2 contents of Ca-amphibole in dependence on pressure and temperature conditions, in form of Al_2O_3 and TiO_2 isopleths in a P-T space. In this study, the graph has been transformed in the way, that P- and T-values are fixed as points according to their Al_2O_3 and TiO_2 concentrations in the Al_2O_3-TiO_2 space. Such transformation allows a fast estimation of the P-T conditions of a large number of amphibole analyses.

The semiquantitative thermobarometer of E&L98 is based on Ca-amphiboles, synthetized from mid-ocean ridge basalts (MORB), recommended for metabasalts in the pressure range up to ~1.2 GPa and subsolidus temperatures. The isopleths reach P up to 2.5 GPa and T up to 1000°C. Although the thermobarometer of E&L98 is not suitable for all Taapaca amphiboles, this method used before the other GTOB have been available (e.g. R&R2011), gave indications of lower crystallization pressure of high-Al amphiboles than expected from Al-in Hbl barometer.

3.3.5. AMPHIBOLE COMBI-P-T-fO_2-H_2O_{MELT}-METER

Empirical thermobarometric formulations of Ridolfi & Renzulli (2011), (further referred to as R&R2011), were used for a reconstruction of amphibole crystallization conditions. The calculation algorithm is based on thermobarometric and chemometric equations for P, T, ΔNNO, H_2O_{melt}, as well SiO_2, TiO_2, Al_2O_3, FeO, MgO, CaO, and K_2O contents in the melt, which require only amphibole composition as total atom per formula unit (a.p.f.u) of Si, Ti, Al, Fe, Mg, Ca, Na and K, calculated on the basis of the 13eCNK normalization procedure. The list of constant values and coefficients for each element in each equation were taken from R&R2011. The calibrations (multivariate least-squares regression analyses) are based on experimental Ca-amphibole synthesized in the P-T ranges of 130-2200 MPa and 800-1130°C, respectively. Although the compositions of all Taapaca amphiboles meet the condition of $Mg/(Mg+Fe^{2+})>0.5$ represented by the experimental amphiboles used for R&R2011 calibrations, the low-Al population of Taapaca amphibole do not match the selected experimental amphiboles. The combi-P-T-fO_2-H_2O_{melt}-meter of R&R2011 gives uncertainties of ±11.5% for P, T ±23.5°C, ΔNNO ±0.37 and H_2Omelt ±0.78 wt% for the above- mentioned P-T range, with the exception of ΔNNO, which validate for P up to 500 MPa.

4. PETROGRAPHY AND MINERAL CHEMISTRY OF THE TVC

4.1. PETROGRAPHY

Monotonous whole rock composition of Taapaca dacites is reflected by a uniform petrography generated consistently during all dacitic stages. The eruptive products of Taapaca are volumetrically dominated by gray plagioclase-amphibole porphyric dacite with up to 30 vol% phenocrysts, 1-5 vol% mafic enclaves and 1-3 vol% sanidine megacrysts (Clavero et al., 2004). Older samples show light to dark brownish-red colors, due to modification of the mineral assemblage by hydrothermal alteration and oxidation reactions, producing e.g. sericite, hematite, jarosite, limonite, and goethite in the groundmass.

For crystal size description, following convention is used: megacrysts >15 mm, phenocrysts 15-0.3 mm, microcrysts 0.3-0.03 mm and microlite <0.03mm.

4.1.1. DACITES

All Taapaca dacites contain the same mineral assemblage consisting of, in order of decreasing abundance, plagioclase, amphibole, biotite, Fe-Ti oxide, apatite, titanite, sanidine, zircon, quartz, ±clinopyroxene. The invariable phenocrysts assemblage is accompanied by minor differences between single eruptions in phenocrysts proportions as well as crystal and groundmass textures, which occur also within individual samples.

Figure 4 presents Ca distribution maps of Taapaca dacites, which reveal different proportions of plagioclase microlite and amphibole pheno- and microcrysts, in samples representing dacitic units II to IV. Phenocrysts and microcrysts are mostly euhedral to subhedral, disequilibrium textures and broken crystals are common. Matrix characteristics vary from vesicular to compact (Figure 4c, d); textures vary from trachytic, with microcrysts and microlite aligned due to lava flowage (Figure 4d, f), to pilotaxitic, with randomly oriented crystals (Figure 4a, e). These textures vary also within one sample. The microlites are commonly embedded in fresh matrix glass, however some samples show extensive matrix crystallization with feldspar crypto-crystals and interstitial subhedral to anhedral tridimite.

4.1.2. MAFIC ENCLAVES

Mafic enclaves (52-60 wt% SiO_2) constitute 1 to 5 vol% of the Taapaca dacite with increasing proportion in the youngest units (Clavero et al., 2004). The enclaves range in size from 3 to 15 cm in diameter and reach maximum up to 50 cm, reported by Clavero et al. (2004). Spherical to ellipsoidal shapes are accentuated by macroscopically sharp chilled contacts. Microscopic pictures (Figure 5a, c) show adjoining and rather interlocking contact between mafic enclaves and dacite host. The enclaves differ in average crystal sizes and range from very fine- to fine-grained (Figure 5b, d).

All investigated mafic enclaves are mineralogically uniform and contain three main phases: plagioclase, amphibole, and magnetite, as well as minor phases: clinopyroxene, sanidine microlite and interstitial tridimite (Figure 5f). Plagioclase and amphibole display dixytaxitic texture characterized by randomly oriented elongated crystals forming interlocked frameworks (Figure 5). Skeletal-dendritic plagioclase growth is also observed (Figure 5e), giving evidence for a large magma undercooling (Lofgren, 1974; Kirkpatrick, 1975).

The enclaves differ in proportions of incorporated xenocrystic material crystallized from silicic magma. These mingled phases reveal commonly disequilibrium structures such clinopyroxene coronas on quartz, amphibole coronas on clinopyroxene, resorption and dissolution in feldspars, and breakdown of amphibole followed by renewed homogenous crystal growth. Xenocrystic plagioclase and amphibole in the mafic enclaves can be identified by larger crystal sizes compared to host enclave phenocrysts, and by sieve-textured or breakdown cores and euhedral regrowth rims.

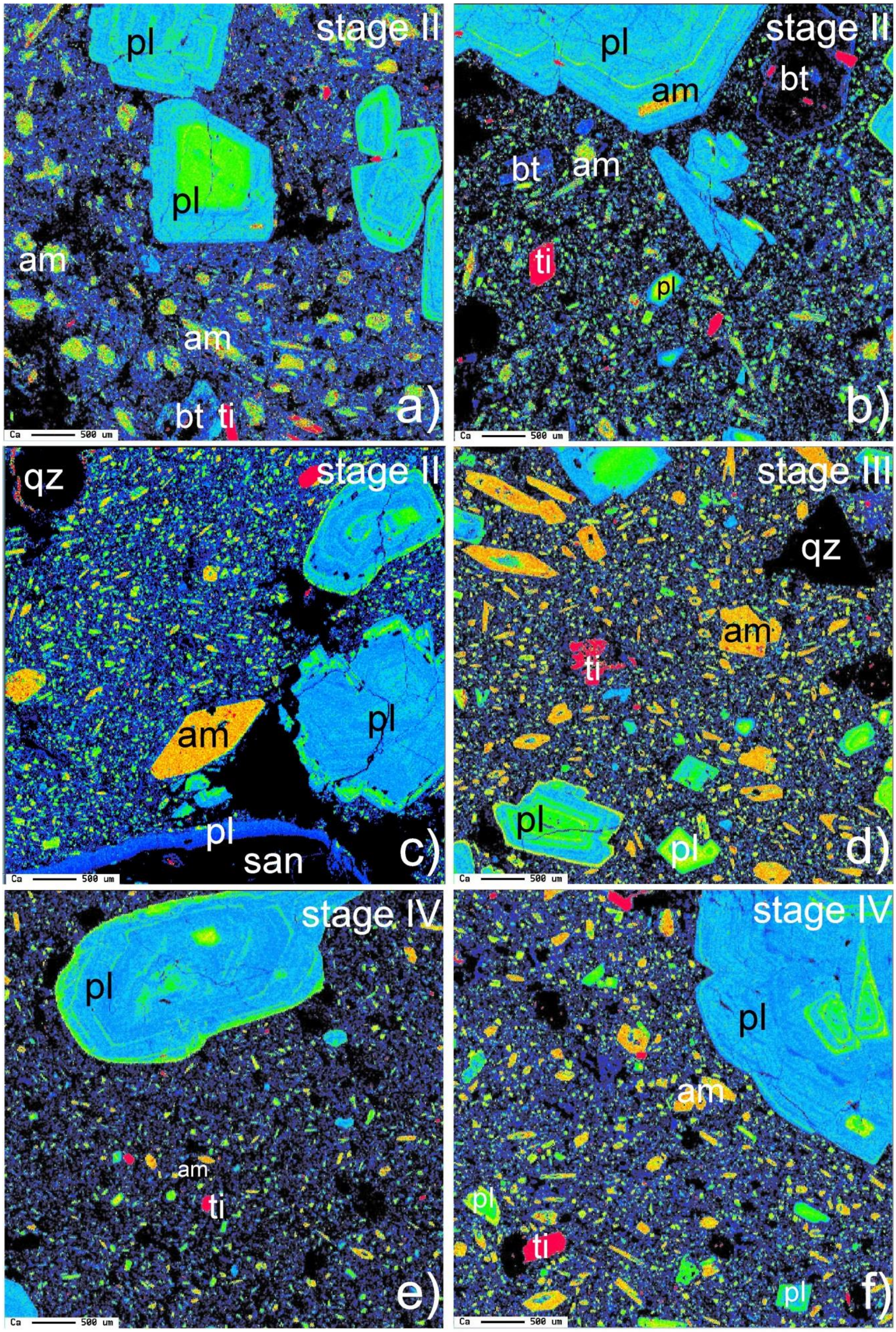

Figure 4. *Ca mapping of Taapaca dacites from Banaszak (2007). All samples show the same mineral assemblage and phenocrysts textures but slightly variable textures within one eruption unit, and even within one sample. In **a)** and **b)** the oldest samples from stage II, **c)** stage III, **d)** –**f)** stage IV.*

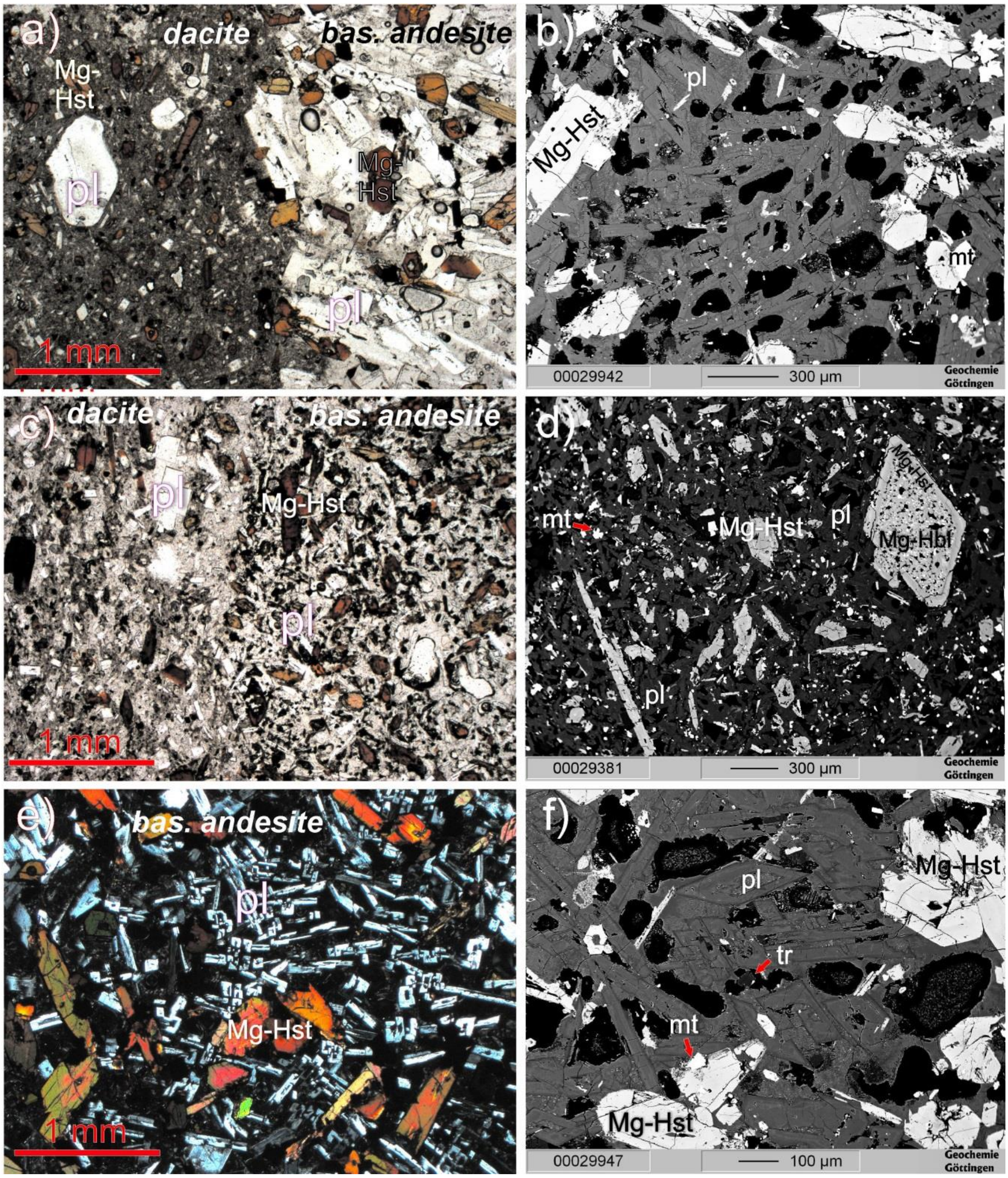

Figure 5. *Representative microscopic pictures of mafic enclaves showing:* ***a)*** *a sharp boundary between coarse-grained mafic enclave and a dacite host;* ***b)*** *BSE image of a coarse grained mafic enclave;* ***c)*** *well-defined boundary between fine grained mafic enclave and a dacite;* ***d)*** *BSE image of a fine-grained enclave;* ***e)*** *skeletal (spiral) plagioclase growth in a mafic enclave TAP 28;* ***f)*** *interstitial tridimite in the mafic enclave TAP 28. Abbr.: pl – plagioclase, Mg-Hst – magnesiohastingsite, mt – magnetite, tr – tridimite.*

4.2. MINERAL TEXTURES AND CHEMISTRY

Mineral compositions of 11 samples were analyzed representatively for dacitic stages II-IV. The microprobe analyses are given in Electronic Supplementary Data.

4.2.1. PLAGIOCLASE

4.2.1.1. Textures

Plagioclase is the most abundant mineral phase in Taapaca dacites (10-20 vol%). Crystal sizes range from microlite <0.03 to 15 mm large phenocrysts. They demonstrate wide diversity of morphologies. Based on the crystal size and textures, three main types can be identified in all dacite samples. 1) Euhedral to rounded, often fragmented, 1-15 mm large plagioclase phenocrysts and synneusis clusters(9) display sieve-textured cores or rings, strong resorption zones with following regrowth rims, amphibole and apatite inclusions are common. 2) Euhedral to subhedral, oscillatory zoned small phenocrysts and microcrysts (0.03-0.5 mm) are equant or tabular. 3) Unzoned microcrysts and microlite (<100 µm) have euhedral shapes.

Crystal size distribution (CSD) study of plagioclase in Taapaca dacites, presented by Freymuth (2006), reveals four distinct crystal size-ranges in all samples. There are two different slopes in the range of 0.02 to 0.1 mm. The CSD slopes and intercepts decrease with increasing crystal sizes. The size-ranges show linear tends separated by sharp bends. The highest diversity between plagioclase in the different samples occurs for micro- and phenocrysts in a range of 0.2-1.0 mm, recognized optically as one group. Microlite and large crystals overlap well in their CSD characteristics in different samples.

Plagioclase inclusions in sanidine megacrysts show two different morphologies: 1) up to 1 mm large euhedral crystals, and 2) <0.5 mm anhedral, strongly resorbed crystals arranged in the high-Ba sanidine growth zones.

Normally zoned plagioclase is the most abundant phase in the mafic enclaves and occurs as euhedral prismatic, tabular or skeletal phenocrysts and microcrysts.

4.2.1.2. Classification and occurrence

The compositions of Taapaca plagioclase ranges from oligoclase to labradorite (anorthite content between An18 and An56 mol%). However, a majority of Taapaca plagioclase have a more limited compositional range - oligoclase to andesine (An22-48). There is a characteristic threshold value of An55-56 for plagioclase composition in both, dacites and mafic enclaves; however, plagioclase inclusions in sanidine do not exceed An50.

Three distinct compositional plagioclase groups have been recognized based on Fe content in Taapaca rocks (see section 7.1.2.2, Figure 20). First, plagioclase inclusions in sanidine reveal two groups, calcic andesine cores (An40-52) and oligoclase (An23-34) rims and small grains; Fe content is limited to 1900 ppm and forms a horizontal trend in the Fe-An space (Figure 20). Second, mafic enclaves contain continuously, normal zoned plagioclase in a range of An30-56, and matrix crystals of An18-30. Both groups have high-Fe contents ranging between 1600 and 4000 ppm. Third, plagioclase compositions found in the dacite host are related to their morphology: 1) high-An40-55 and low-Fe (1000 ppm) phenocrystic cores, 2) high-An38-55 and high-Fe (1500-4200 ppm) phenocrystic rims and microlite, and 3) a compact compositional group of phenocrysts and microcrysts in a range of An23-35 and Fe of 900-2000 ppm.

---

[9] Crystals clustered in a twinned orientation formed by attachment in energetically favorable orientation of two crystals of the same mineral phase (Vance , 1969)

4.2.2. AMPHIBOLE

Amphibole is a dominant ferromagnesian phase in Taapaca rocks, reaching up to 6 vol% in dacites and up to 30 vol% in mafic enclaves.

4.2.2.1. Textures

Microscopic observations reveal three textural amphibole groups in the dacites: 1) euhedral to subhedral, often broken 0.3-2 mm large, elongated crystals, commonly with biotite and zircon inclusions or attached biotite, 2) euhedral to subhedral <0.3 mm microcrysts with skeletal shapes or hollow cores, 3) euhedral microlite. Only microcrysts show pronounced zoning with rounded resorption zones followed by euhedral re-growth (Figure 6). Taapaca amphiboles vary from entirely intact to crystals where breakdown reactions have proceeded to varying extent: Amphibole breakdown occurs as 1) thin (<100 µm) opacitic fine-grained reaction rims, 2) fine-grained reaction products in the inner parts of crystals, and 3) crystals completely replaced by fine or coarse-grained plagioclase-pyroxene-Fe-Ti oxide clusters, within preserved euhedral crystal shapes. Complete amphibole breakdown is observed mostly in the oldest samples from stage II (Figure 4a). In younger samples, the reaction rims and breakdown reaction features within single crystals are not uniform.

In the mafic enclaves, zoned amphibole is a principal mafic phase. It occurs as euhedral, tabular to acicular crystals, ranging from microlite to 1.5 mm large phenocrysts in the length axis. Amphiboles in enclaves show variable breakdown characteristics, from intact to entirely reacted crystals in diverse samples. In contrast to the dacite, they show uniform breakdown reactions within single samples.

4.2.2.2. Classification and occurrence

Two different compositional groups of amphibole, both characterized by ~11 wt% CaO content are present in Taapaca rocks. The differences between these populations are mainly based on Al, Ti and Na content. According to the amphibole nomenclature of the International Mineralogical Association (IMA) presented by Leake et al. (1997), Ca_B>1.5 classify them to calcic amphibole group. Low-Al and Ti amphiboles (5-9 Al_2O_3 wt % and TiO_2<1 wt%) have 6.5-7.5 Si p.f.u., and $(Na+K)_A$<0.5. They classify as magnesiohornblende (Mg-Hbl). High-Al and Ti amphiboles (8-14 Al_2O_3 wt% and 1.5-4 TiO_2 wt%) have consequently lower Si contents (5.5-6.5 p.f.u.), higher $(Na+K)_A \geq 0.5$, and they meet $^{VI}Al<Fe^{3+}$, classifying them as magnesiohastingsite (Mg-Hst). Both populations occur in every single dacite sample.

Mg-Hbl occurs as large internally unzoned phenocrysts (>300 µm) or as rims on smaller (<300 µm) Mg-Hst crystals (Figure 6a). Mg-Hbl is present as the only one amphibole population found as inclusions in sanidine megacrysts.

Mg-Hst forms microcrysts, microlite and thin rims on Mg-Hbl crystals in the dacite samples (Figure 6b). Moreover, this amphibole composition occurs as a single population in the mafic enclaves. Large Mg-Hbl crystals incorporated in mafic enclaves show complete breakdown and Mg-Hst rims. Pronounced internal zoning is ubiquitous in Mg-Hst (Figure 6c) and is observable both in BSE images and optically. This compositional zoning involves Mg, Fe, Al and Ti (see next section).

Because of zoning, Mg-Hst reveals much higher compositional variability in comparison to Mg-Hbl. There are slight compositional differences between Mg-Hst found in different mafic enclaves; their Mg-Hst compositions overlay with Mg-Hst found in the dacites hosting the enclaves.

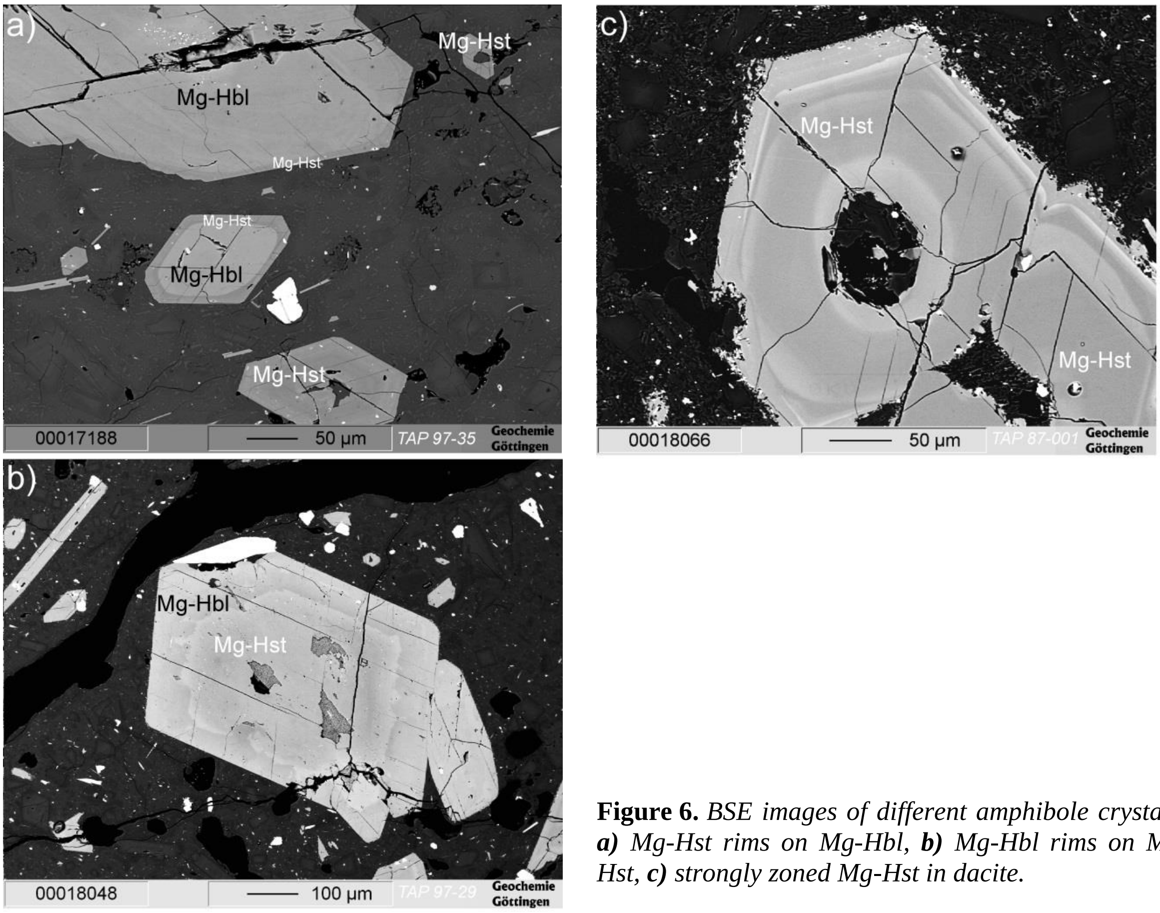

Figure 6. *BSE images of different amphibole crystals:* ***a)*** *Mg-Hst rims on Mg-Hbl,* ***b)*** *Mg-Hbl rims on Mg-Hst,* ***c)*** *strongly zoned Mg-Hst in dacite.*

4.2.2.3. The cation variation diagrams

Cation-substitution mechanisms in amphibole are responsible for the compositional variability and the large number of amphibole end-member compositions. These mechanisms involve 1) a coupling of cations of different valence states to maintain a charge balance and/or 2) simple exchange between cations of the same valence state. An analysis of bivariate cation variation diagrams gives an insight into these mechanisms. Correlations between certain cations yield substitution vectors that are governed by physico-chemical parameter of crystallization (e.g. Helz, 1979; Spear, 1981; Blundy & Holland, 1990; Ernst & Liu, 1998; Almeev et al., 2002; Simakin et al., 2009; Ridolfi et al., 2010). Therefore, an identification of the prevailing substitution vectors may reveal important information with respect to geothermo-oxy-barometry methods used in this study. Figure 7 presents a number of cation variations (per formula unit) in Mg-Hbl and Mg-Hst selected from correlation matrices (not presented here), representing bivariate combinations of cations contents, determined using 13eCNK structural formula calculation. The aim of this analysis is to test which of the possible substitutions based on P-T-fO_2 changes are consistent with the cation trends observed in Taapaca amphiboles.

Crystal cores of Mg-Hst show two different compositional groups in Taapaca mafic enclaves depending on the whole rock composition of the enclaves. Samples TAP 97-28 and TAP 02-02b represent the same dome eruption and their mineral compositional ranges overlap. Therefore, both samples are presented together as TAP 28. This eruption differs from TAP 97-25 and -29 by significantly higher proportions of BEM-type, shoshonitic end-member, relatively to AEM (high-Al calc-alkaline) and RDEM (high-K calc-alkaline), (Table 4, Chapter 2). The cores of Mg-Hst found in the dacites correspond to the core compositions from the mafic enclaves. In contrast, cores of the Mg-Hbl overlap in each sample and do not reveal any correlation with the whole rock of the dacites.

The substitution mechanisms in calcic amphibole have been discussed in numerous studies, e.g. Helz (1979), Spear (1981), Blundy & Holland (1990), Ernst & Liu (1998), Almeev et al. (2002), Simakin et al. (2009), Ridolfi et al (2010). Commonly, the substitution equations are related to a compositionally simplest *tremolite* end-member formula $\square Ca_2Mg_5Si_8O_{22}(OH)_2$. As presented by IMA (Leake et al., 1997) *magnesiohornblende* and *magnesiohastingsite* end-member formulas are: $\square Ca_2(\boldsymbol{L}_4\boldsymbol{M})Si_7AlO_{22}(OH)_2$ and $NaCa_2(\boldsymbol{L}_4\boldsymbol{M})Si_6Al_2O_{22}(OH)_2$, respectively, where $\square$=vacancy, $\boldsymbol{L}$=Mg, Fe^{2+},Mn, and $\boldsymbol{M}={}^{[6]}Al$, Fe^{3+}.

In Tschermakite substitution, Mg and Si can be coupled with $^{[4]}Al$ substitution involving $^{[6]}Al$, Ti, or Fe^{3+}. The correlation between Si and Mg is clearly defined in Mg-Hbl, whereas in Mg-Hst high variations of Mg are observed in a narrow range of Si (Figure 7a). However, Mg-Hst compositions in cores, in three different mafic enclaves, form a parallel trend to the Mg-Hbl (black solid lines in Figure 7a). Compositions of Mg-Hst from cores toward rims define also slight positive Mg-Si correlation. The Mg vs. Si correlation may be over-interpreted as Tschermakite substitution due to a fractionation effect reflected in $Mg\leftrightarrow Fe^{2+}$ substitution (Figure 7c), the strongest cation correlation observed simultaneously in Mg-Hbl and Mg-Hst.

Al-Tschermakite substitution ($2^{[4]}Si+2^{[6]}Mg=2^{[4]}Al+2^{[6]}Al$) would require 1:1 correlation between $^{[4]}Al$ and $^{[6]}Al$. A plot (Figure 7b) of tetrahedral vs. octahedral Al reveals rather a cluster of points in Mg-Hbl, whereas Mg-Hst extend from zero values in several Mg-Hst cores to 0.45 p.f.u. of $^{[6]}Al$ at unchanged $^{[4]}Al$.

Ti-Tschermakite substitution ($2^{[4]}Si+^{[6]}Mg=2^{[4]}Al+^{[6]}Ti$) should reveal a 2:1 correlation between $^{[4]}Al$ and Ti. Figure 7d demonstrates two different slopes of $^{[4]}Al$ and Ti, far from expected 2:1 ratio. This means, the substitution, if occurs, is not independent. Again, a correlation is observed for Mg-Hst cores but not for Mg-Hst within single samples.

Fe-Tschermakite ($2^{[4]}Si+2^{[6]}Mg=2^{[4]}Al+2^{[6]}Fe^{3+}$) is not represented in Taapaca amphiboles due to lack of any correlation between Fe^{3+} and other elements involved in this substitution (e.g. Mg vs. Fe^{3+}, Figure 7e). Ferric iron shows strongest correlation with $^{[6]}Al$ (Figure 7f) and slight with $^{[A]}Na$, Fe^{2+} and Ca, and not with expected $^{[4]}Al$ and Mg (Figure 7e).

Correlation of Fe^{3+} and $^{[6]}Al$ suggests strong dependence between both three-valent cations that may be of particular importance for interpretation of the geothermobarometry data. Figure 7f presents several regression lines in the selected Taapaca Mg-Hst and Mg-Hbl groups.

Edenite substitution ($^{[A]}\square+^{[4]}Si=^{[A]}Na+^{[4]}Al$) occurs in Mg-Hbl, identified by strong correlation between $^{[A]}Na$ and $^{[4]}Al$ (Figure 7g). In contrast, Mg-Hst shows weak correlation rather between $^{[A]}Na$ and $^{[6]}Al$ (Figure 7g, h). $^{[A]}Na$ shares the A-site with $^{[A]}K$. The A-site occupancy by $^{[A]}K$ shows positive trend with $^{[4]}Al$ and $^{[A]}Na$ in Mg-Hbl but negative in Mg-Hst and again only between core compositions. Occupancy of the A site by Na and K reveals also opposite tendency for Mg-Hbl and Mg-Hst (Figure 7i, j).

4.2.3. BIOTITE

Biotite occurs as euhedral to subhedral phenocrysts - commonly fragmented or deformed - that comprise up to 3 vol% of Taapaca dacite. They contain plagioclase, titanite and zircon inclusions. In some samples, biotite crystals have a thin opacite rim. In older lavas from stage II, biotite shows complete breakdown reactions to Fe-oxide and silicate phases faintly oriented to the crystal cleavage, different to the randomly distributed amphibole breakdown products. Biotite is the second most common ferromagnesian phase in the Taapaca dacites but is absent in the mafic enclaves and in the initial stage I. They occur as unzoned phenocrysts and inclusions in amphibole, both are compositionally indistinguishable. The Mg-number of biotite remains constant in the range of 0.58-0.66. The compositions remain in a very narrow compositional range for major elements and show uniform chemistry through all dacitic units.

4.2.4. Fe-TI OXIDE

Fe-Ti oxides reach up to 5 vol% and represent wide range of textural characteristics due to exsolution/oxidation reactions. Titanomagnetite occurs as up to 300 µm large euhedral to subhedral microcrysts, which display typical high temperature oxidation textures. Various microtextures in the titanomagnetite occur due to distinct oxidation stages (Haggerty, 1991) and display 1) trellis types exsolution, ilmenite intergrowths along {111} planes of titanomagnetite, pleonaste exsolution (very fine black spinel rods), sandwich types, thick ilmenite-hematite lamellae. The titanomagnetite host crystals itself oxidize to titanohematite in most dome samples. A second group of titanomagnetite occur as <30 µm subhedral to anhedral microlites, forming individual grains or composite types, characterized by internal or external ilmenite inclusions, where ilmenite can form primary grains or oxidation-exsolution products (Haggerty, 1991). The microlite fraction shows exsolution ilmenite lamellae in the most oxidized oldest Taapaca samples. The composition obtained from homogenous small fraction of composite and single microlite grains ranges from 10 to 38 mol% Usp (most common value of 18 mol%) and constant values for MgO and Al_2O_3 contents.

Ilmenite occurs rarely as single, <50 µm subhedral to anhedral microlite grains or more commonly as composite grains with titanomagnetite. Skeletal ilmenite is common and coexists with euhedral grains. Some ilmenite crystals show parallel hematite lamellae, hematite rims, or form irregular shapes along holes or fractures. The composition of homogenous ilmenite ranges from 56 to 79 mol%, obtained from different samples. Secondary formation as oxidation product of titanite is common.

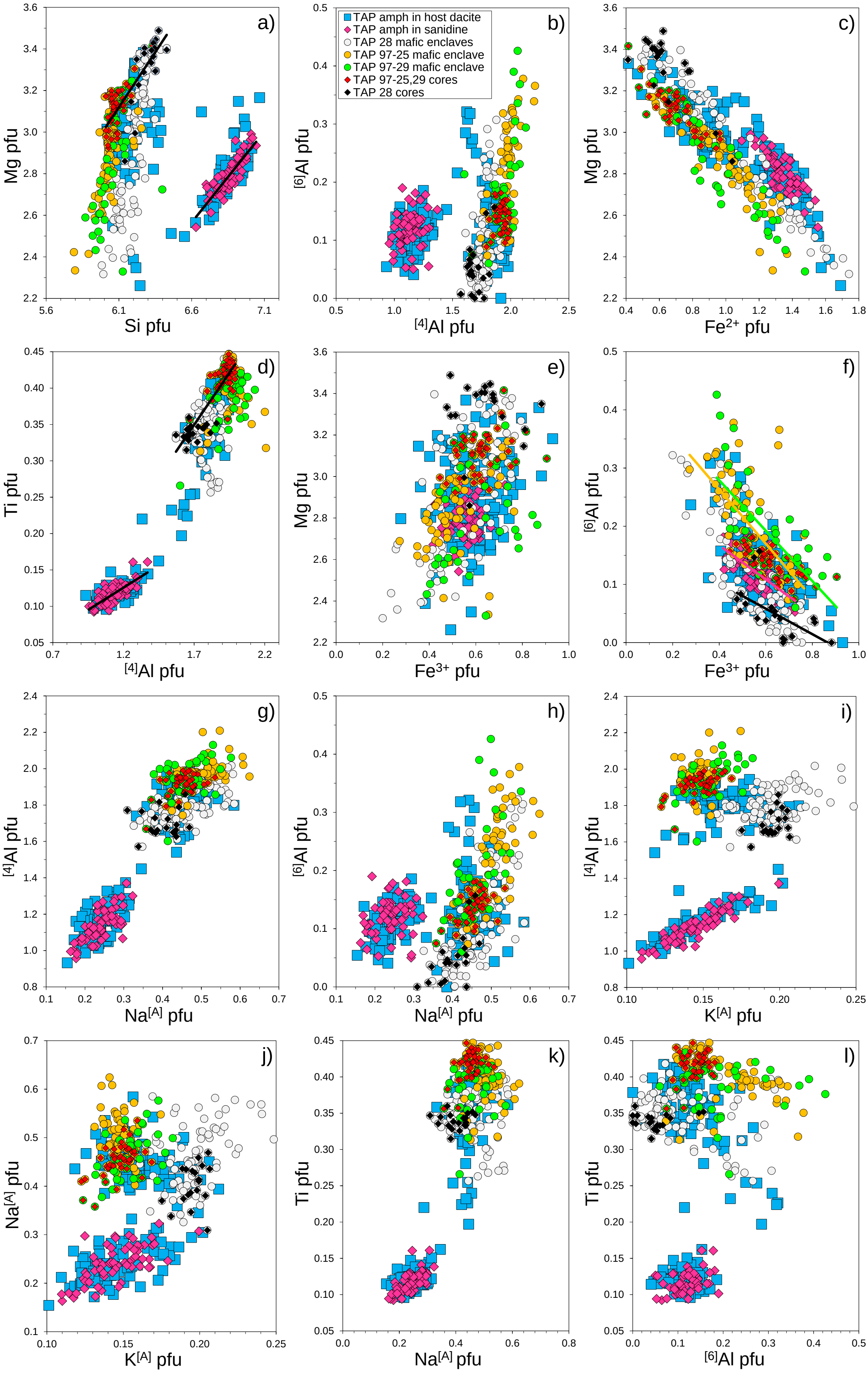

Figure 7. *Variations in cation site occupancy in Taapaca amphiboles. See section 4.2.2.3 for explanation. Presented lines highlight in* ***a)*** *and* ***d)*** *a correlation formed by Mg-Hst crystal cores from mafic enclaves, the second line is correlation formed by Mg-Hbl; in f) parallel trends can be defined in different samples.*

4.2.5. ACCESSORY MINERALS

Quartz occurs as rounded, strongly resorbed, fractured, or fragmented, <25 mm phenocrysts and does not exceed <2 vol% of the dacite. Some crystals have acicular clinopyroxene coronas.

Titanite is an accessory phase (<1 vol%) and forms up to 1 mm large euhedral crystals, some with thin opacite rims. Some crystals show advanced oxidation reaction, fringed or are completely replaced by ilmenite needles associated with crystallization of zircon, Ca-silicate, and pyrite.

Other minor accessory phases comprise apatite (>1 vol%) which occurs as euhedral, up to 200 µm large microphenocrysts or as inclusions in plagioclase or biotite; zircon <0.05 µm small euhedral crystal are mostly observed as inclusions in ferromagnesian phases.

4.2.6. PYROXENE

Clinopyroxene is rare in Taapaca dacites. It forms subhedral to anhedral microcrysts or in corona structures on quartz. Some rounded grains have amphibole coronas. Very small sizes (<15 µm) of clinopyroxene grains in Taapaca dacites do not allow extensive determination of their composition by microprobe analysis. Three reliable analysis show that clinopyroxene may be restricted to augite. Clavero et al. 2004 presents three different compositional groups of pyroxene in the andesitic stage I (augite, ferroaugite and hypersthene), one analysis from stage II showing the same augite composition as clinopyroxene from stage IV. They form an array from the composition of stage I towards FeO richer compositions (decreasing Mg-number).

Small orthopyroxene microlite (<10 µm) have been identified in several samples.

4.2.7. SANIDINE

Sanidine constitutes 1-7 vol% of the dacite, and increases in abundance in younger lavas (Clavero et al., 2004). The euhedral, locally moderately resorbed crystals range from 15 to 120 mm in long axis. Sanidine crystals <15 mm have not been found in Taapaca dacites. They contain large amounts of euhedral mineral inclusions such as plagioclase, amphibole, Fe-Ti oxide, titanite and rare biotite and apatite. Inclusions are mostly concentrated in re-growth zones, associated with strong resorption, glassy channels and holes and high-Ba content. These chemical and macro-textural features characterize the zoning of the megacrysts. Some crystals, mostly these representing older lavas from stage II, show poikilitic-like growth with randomly oriented mineral inclusions. Generally, sanidine megacrysts show decreasing amounts of mineral inclusions in the stage III and IV in comparison to inclusion-rich crystals from stage II. Smaller sanidines (15-20 mm) embedded in the dacite matrix show epitaxial anorthite-rich plagioclase growth, known as rapakivi structure.

High-Ba zones are characterized by patchy chemical zoning, resulting from probably fast re-growth after strong resorption events. In contrast, low-Ba zones are more homogenous, oscillatory zoned and generally do not include other mineral phases. Amphibole inclusions in the sanidines show variable breakdown reactions, which mostly correspond to the amphibole breakdown in the host dacite. However, several samples reveal a discrepancy between amphibole breakdown in the sanidine and in the host, showing more advanced breakdown of amphibole inclusions in the sanidine.

The composition of the megacrysts varies within the range of Or65-80 (8.8-13.0 K_2O wt%) and Ab20-35 (2.5-4.9 Na_2O wt%), throughout the entire eruptive history of Taapaca. The variations of K_2O correlate negatively with BaO, which varies from 0.3 up to 2.5 wt% BaO in Ba-rich zones. Elevated Ba concentrations occur during crystal re-growth after resorption, showing correlation between intensity of the resorption and Ba contents in the re-growth zones. After stepwise increase, Ba contents always decrease toward the crystal rim and correlate strongly with Ca and Sr in the sanidine. Concentrations of transition elements (Cr, Ni, Co) in sanidine are close to the limit of detection and do not increase in association with increasing Ba concentrations. This observation indicates that Ba-jumps are not linked to Ba-rich mafic recharge. Measured concentrations of Mg in high- and low-Ba zones vary between 1.5 and 8 ppm, independently of Ba content. Similar patterns are observed for Rb contents, suggesting that increases in Ba concentration are not connected to movements toward Ba-rich - highly differentiated magma. $^{87}Sr/^{86}Sr$ ratios and $\delta^{18}O$ values obtained from low- and high-Ba zones yield invariable isotopic compositions of 0.706728-0.706795 (±6) (Kiebala & Wegner, unpublished data) and 7.0 -7.5 ‰ (±0.2 ‰), respectively, and are consistent with values of Taapaca whole rocks.

Plagioclase and amphibole inclusions in sanidine represent one of the two populations, which are present in the dacite host. Anorthite contents in plagioclase vary between 23 and 50 mol% An within a limited range of Fe (1000-1800 ppm), (Figure 20). Low-Al and -Ti Mg-Hbl inclusions in sanidines cover with the compositional array of Mg-Hbl found in the host dacites (Figure 7).

5. CONSTRAINTS ON CRYSTALLIZATION CONDITIONS

The uniform mineral assemblage and mineral chemistry observed in all dacitic stages of Taapaca indicate constant pre-eruptive crystallization conditions. Amphibole is a basic mineral phase that enables estimation of intensive crystallization parameters (P-T-fO_2) as well water contents in Taapaca magmas. However, its complex mineral chemistry and substitution mechanisms lead to large compositional variability, which make the estimation of pre-eruptive physical parameter difficult.

A validity of different geothermometer and geobarometer, based on amphibole compositions (e.g. Johnson & Rutherford, 1989; Blundy & Holland, 1990; Holland & Blundy, 1994; Ernst & Liu, 1998; Féménias et al., 2005; Ridolfi et al., 2010; Ridolfi & Renzulli, 2011) has been tested with experimental studies carried out directly on the Taapaca dacite (Botcharnikov et al., in prep.; Blum-Oeste, 2014). These empirical and experimental results can be compared with studies carried out on volcanics, compositionally comparable to the Taapaca dacites (e.g. Mount St Helens: Rutherford & Devine, 1988; Fish Canyon: Johnson & Rutherford, 1989; Pinatubo: Scaillet & Evans, 1999; Unzen: Sato et al., 1999, 2005; Soufriere Hill: Rutherford & Devine, 2003).

5.1. COMPOSITIONS OF NATURAL AND EXPERIMENTAL AMPHIBOLE

Experimental amphibole compositions are presented for comparison with natural Taapaca amphibole compositions using an Al_2O_3 vs. TiO_2 plot (Figure 8), adapted from the study of Ernst & Liu (1998). According to this study, conducted on MORB as a starting material (49-52 SiO_2 wt%), Al_2O_3 contents of experimental Ca-amphibole increase with both P and T; TiO_2 contents increase almost exclusively with increasing T. Therefore, both oxides give a first view into P-T relations in Taapaca magmas from amphibole composition. Figure 8 includes experimental studies performed on dacite as starting materials at temperature range from 725 to 1033°C and pressure 1.5 to 3.9 kbar.

The experimental studies of Botcharnikov et al. (in prep.), and Blum-Oeste (2014) were carried out on a representative crystal-rich dacite sample TAP 87-002 from stage IV. This sample has an average silica content of 65 wt% SiO_2, and mineral assemblage typical for stages II to IV. Experimental conditions were chosen according to crystallization conditions obtained previously from natural amphiboles (Banaszak, 2007 and this study). The geothermobarometry data indicate the most likely temperature and pressure conditions for Taapaca dacite at 700-850°C and 850-1000°C at 1-3 kbar (presented in next sections). The fO_2 was varied from NNO to NNO+1. Because the whole rock composition of Taapaca mafic enclaves correspond to the basaltic andesite lavas from Parinacota volcano, amphibole compositions from crystallization experiments with natural basaltic andesite from Parinacota volcano, sample PAR 11 (Botcharnikov et al., in prep.), conducted at 900-1000°C and 3 kbar are included in this study.

A comparison of the natural Taapaca and experimental amphiboles reveals three essential findings that play a crucial role in evaluating pre-eruptive crystallization conditions and verification of GTOB methods applicable for Taapaca dacite.

1) Two amphibole populations found in Taapaca dacites, the Mg-Hbl and Mg-Hst crystallized from different magma compositions. The results of the experimental approach of Botcharnikov et al. (in prep.) confirm the observations from natural systems. Referring to Al and Ti contents in Ca-amphibole, Féménias et al. (2006) describe decreasing Ti contents in amphiboles with increasing differentiation. Ridolfi et al. (2010) emphasize the role of decreasing alumina/silica ratios in calc-alkaline magmas leading to decreasing Al_2O_3 contents in amphibole with increasing SiO_2 contents of magma from which the amphiboles crystallized. The Mg-Hst in Taapaca experiments crystallized only from basaltic andesite starting material. Mg-Hbl crystallized only form dacite starting material. Other experimental studies, e.g. Johnson & Rutherford (1989) and Rutherford & Devine (2008) did not synthetize Mg-Hst from dacite starting material, even at temperatures of 920-1033°C or pressures of 8 kbar. Although the amphiboles from the latter studies reach Al_2O_3 contents comparable with Mg-Hst from Parinacota basaltic andesite experiments (~10-13 wt%), they are characterized by significantly lower TiO_2 contents (Figure 8).

2) Crystallization conditions of Mg-Hbl can be restricted to relatively low temperatures according to the experimental range of 725-780°C, because the best compositional fit to the natural Mg-Hbl is represented by amphibole synthesized at T<760°C (Johnson & Rutherford, 1989; Scaillet & Evans,

1999; Botcharnikov et al., in prep.). It is worth to noting, that an increase in experimental P or T conditions does not reproduce the Mg-Hst compositions from the dacitic starting material. This observation is based on the experimental studies presented in Figure 8.

3) Compositions of Mg-Hbl and Mg-Hst can be reproduced from different magma composition at the same pressure conditions ranging between 2 and 3 kbar. Therefore, the crystallization pressures, in spite of their different Al-contents may overlap for both amphibole populations.

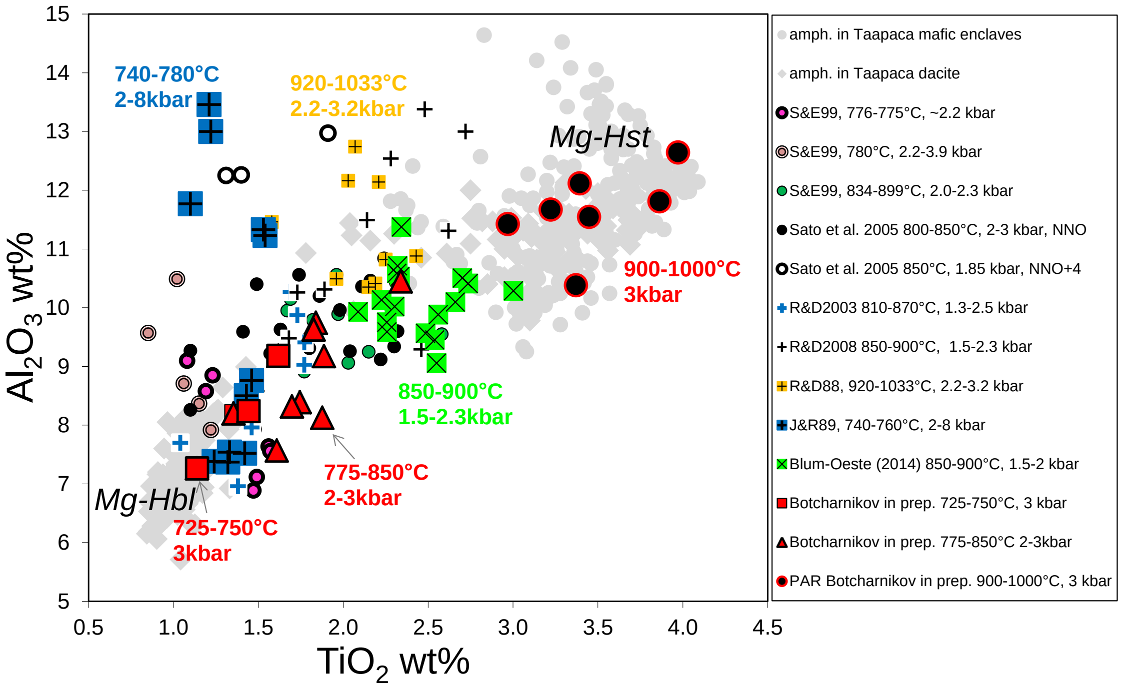

Figure 8. *Al_2O_3 and TiO_2 contents of natural Taapaca and experimental amphibole generated from dacite starting material in a pressure range of 1.3-3.9 kbar and different temperatures from studies of: Blum-Oeste (2014) and Botcharnikov et al. (in prep.) for Taapaca; Johnson & Rutherford, 1989, (J&R89) for Fish Canyon; Scaillet & Evans, 1999, (S&E99) for Pinatubo; Sato et al. (2005) for Unzen; Rutherford & Devine, 2003 (R&D2003) for Soufriere Hill; Rutherford & Devine, 2008 (R&D2008) for Mount St Helens. Only amphibole generated at low temperatures (<760 °C) match the trend of magnesiohornblende (Mg-Hbl) found in Taapaca rocks. Due to the results of Botcharnikov et al. (in prep.), high-Al-Ti magnesiohastingsite (Mg-Hst) could be reproduced only from basaltic andesite starting material of Parinacota volcano at 900-1000°C at the same pressure values as Mg-Hbl.*

5.2. AL-IN-HORNBLENDE GEOBAROMETRY

Al-in-Hornblende (Al-in-Hbl) barometer of Johnson & Rutherford (1989) was applied exclusively to the Taapaca magnesiohornblende. Three criteria allow an application of the Al-in Hbl (J&R89) barometer to the Taapaca Mg-Hbl. First, consistent experimental and natural whole rock compositions; however, the results of PVA study presented in Chapter 2 reveal more silica-rich and MgO-poor rhyodacitic composition (RDEM end-member), than the composition used in the experimental studies, from which most probably Taapaca Mg-Hbl crystallized. Secondly, an identical mineral assemblage obtained by the calibration experiments of J&R89 and this found in natural Taapaca samples. Third, nearly equal natural and experimental low-Al amphibole compositions - experimental amphiboles synthesized at 2-3 kbar and T<760°C correspond most closely to the composition of Taapaca Mg-Hbl (Figure 8). Slightly higher MgO contents in the experimental amphibole (~12.5-14.5 wt% MgO, not presented here) in comparison to natural Mg-Hbl (~11.3-13.5 wt% MgO) may reflect: 1) higher log fO_2 compared with the natural conditions or 2) compositional differences between the experimental dacite and rhyodacitic RDEM end-member from which Taapaca Mg-Hbl originate.

Following numerous publications presenting different formulations of Al^{TOT}-in Hbl barometers (Hammarstrom & Zen, 1986; Hollister et al., 1987; Johnson & Rutherford, 1989), Blundy & Holland (1990) showed a strong dependence of $^{[4]}Al$ contents in Ca-amphibole on temperature. For that reason, the authors concluded that Al^{TOT}-in Hbl barometers yield a considerable uncertainty. Figure 9 shows variations of $^{[4]}Al$ vs. $^{[6]}Al$ in experimental amphiboles of Botcharnikov et al. (in prep.), Blum-Oeste (2014), and Stechern et al. (in prep.), in terms of temperature and pressure. The amphiboles of Stechern et al. (in prep.) comprise tschermakite(10) synthetized from mafic andesite composition from Lascar volcano. They show Al^{TOT} similar to Mg-Hst and similar $(Na+K)_A<0.5$ and Ti contents to Mg-Hbl.

The tetrahedral $^{[4]}Al$ shows clearly strong T-dependence (Figure 9a) and lacking correlation with P. The octahedral $^{[6]}Al$ reveals higher contents in amphibole synthetized at both, low temperature experiments at 300 MPa (725-775°C, blue points, Figure 9b) and higher temperatures at 150-200 MPa (825-900°C, green points) in comparison to amphiboles synthetized at 200 MPa and intermediate temperature range of 775-850°C. This observation suggests an influence of other intensive variables on $^{[6]}Al$ in two presented experimental studies carried out on the same starting whole rock composition. Although the Mg-Hbl and tschermakite show a positive $^{[6]}Al$-pressure correlation from the experiments of Botcharnikov et al. (in prep.) and Stechern et al. (in prep.), the amphiboles of Blum-Oeste (2014) do not fall along this trend. These observations point out that Al^{TOT} in Hbl is not only governed by P and T. $^{[6]}Al$ depends also on fO_2 (Simakin et al., 2009); additionally, Sisson & Grove (1993) found out, that Al/Si in synthetized amphibole correlates linearly with Al/Si in the melt. Therefore, the Al^{TOT}-in Hbl barometry includes a substantial error in pressure estimations for natural systems.

Figure 9a and d confirms the results of Blundy & Holland (1990) showing general dependence of $^{[4]}Al$ on temperature and $^{[6]}Al$ on pressure. However, the $^{[4]}Al$ shows correlation with T in a much narrower range in comparison to $^{[6]}Al$, showing a wide range of contents increasing with P. This observation suggests that amphibole documents higher T-sensibility and may give results that are more reliable for T than for P.

---

[10] Tschermakite is a third compositional group of amphibole occurring in CVZ magmas, therefore the comparison may be useful for further studies.

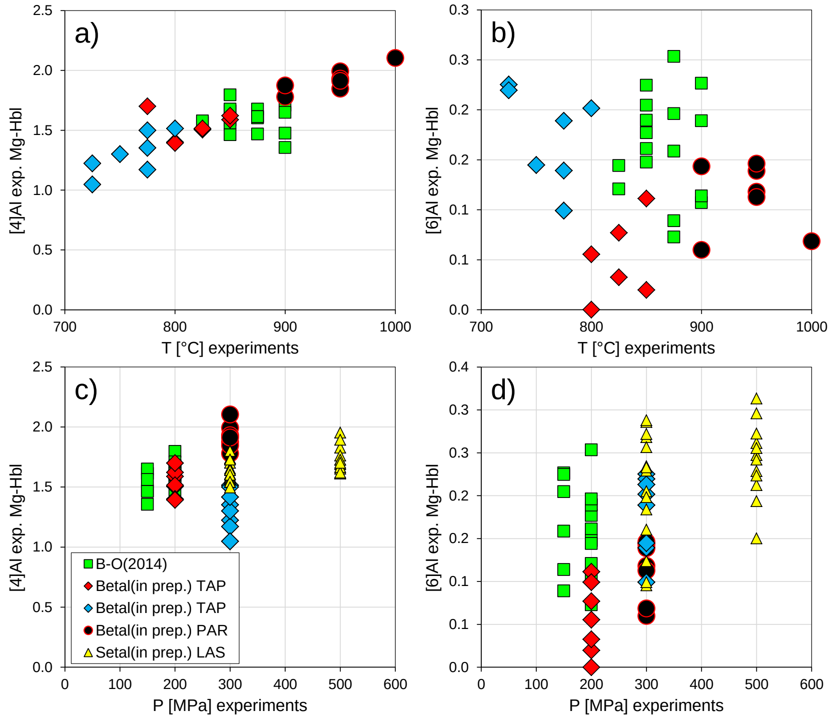

Figure 9. *Variations of $^{[4]}$Al and $^{[6]}$Al depending on **a)** and **b)** temperature and **c)** and **d)** pressure in experimental amphibole of Botcharnikov et al. (in prep.), abbr. Betal(in prep.), Blum-Oeste (2014), abbr. B-O(2014), and Stechern et al. (in prep.), abbr. Setal(in prep.), synthetized from Taapaca dacite starting material. Red points: 775-850°C, 200 MPa; Blue points 725-775°C; 300 MPa, green pints 825-900°C, 150-200 MPa. Black points represent high-Al Mg-Hst synthetized from Parinacota basaltic andesite, and yellow triangles represent tschermakite synthetized from Lascar mafic andesite as starting composition, presented for comparison. TAP=Taapaca, PAR=Parinacota, LAS=Lascar.*

Al^{TOT} of experimental Mg-Hbl of Botcharnikov et al. (in prep.) presented in Figure 10a, yields the widest range between 1.3 and 1.7 p.f.u. in comparison to the Mg-Hbl synthetized by J&R89 at 2-3 kbar, due to higher temperatures (up to 850°C) used in their experiments. The experimental calibration of J&R89 was carried out at 740-780°C. This temperature range overlaps with temperatures obtained from hornblende-plagioclase thermometer of Holland & Blundy (1994), (section 5.4.2). Furthermore, Taapaca Mg-Hbl and J&R89 synthetic Mg-Hbl show consistent Al_2O_3-TiO_2 composition for pressure up to 3 kbar (Figure 8). Therefore, the Al^{TOT}-in Hbl barometer calibration of J&R89 can be applied to Taapaca Mg-Hbl, to reconstruct approximately crystallization pressure.

Pressure values obtained from Mg-Hbl (Figure 10b) using the equation presented in Figure 10a, overlap in the range of 1.2-2.8 ±0.5 kbar for Mg-Hbl from the dacite samples and inclusions in sanidine megacrysts, with extreme values of 0.76 and 3.4 kbar. The cores of large Mg-Hbl phenocrysts yield 1.3-3.4 kbar and overlap with pressure values determined at the other crystal parts. Regarding possible T-fluctuations and the simultaneous dependence of Al^{TOT}-in-Hbl on P, T, fO_2 conditions as well as magma composition, these results demonstrate an approximation of pressure conditions in the Taapaca rhyodacite reservoir.

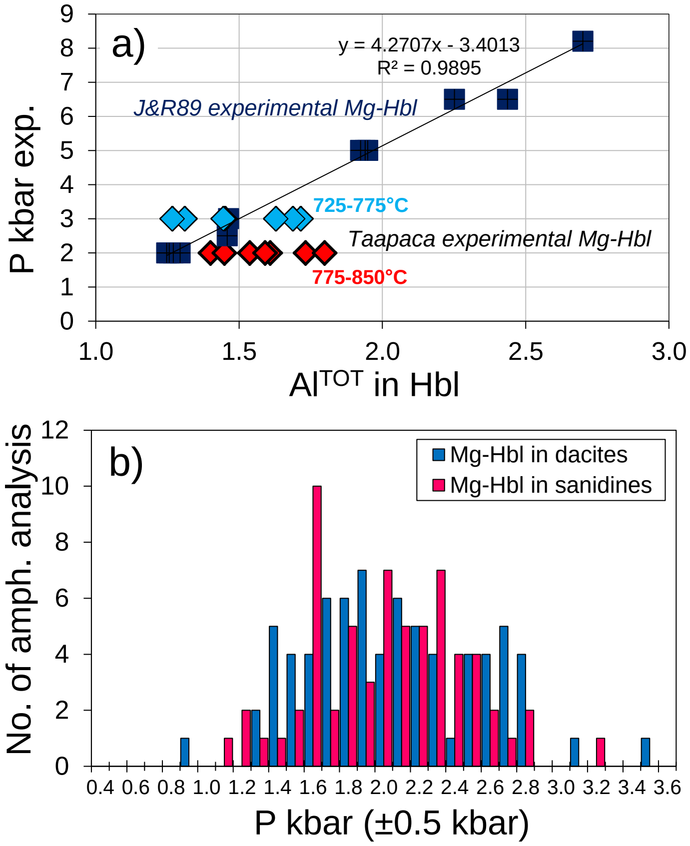

Figure 10. ***a)*** *Crystallization pressure and total Al-contents (Al^{TOT}) in experimental Mg-Hbl of Botcharnikov et al. in prep., (red points) and Johnson & Rutherford (1989), (blue points). The equation represents P-Al^{TOT} correlation based on 13eCNK normalization of amphibole cation-site occupancy.* ***b)*** *Pressure values obtained from Mg-Hbl in Taapaca lavas obtained form Al^{TOT}-in-Hbl geobarometer using calibration of Johnson & Rutherford (1989) presented in a).*

5.3. AMPHIBOLE THERMO-OXY-BAROMETER

Results of P-T-fO$_2$-H$_2$O$_{melt}$ obtained from a thermobarometric formulation of Ridolfi & Renzulli (2011), (further referred as R&R2011), are presented in Figure 11 and Figure 13. In their previous study, Ridolfi et al. (2010) divided the experimental and natural amphibole into "consistent" and "inconsistent" amphibole using Al-number Al#=$^{[6]}$Al/Al^{TOT}. Consistent experimental amphiboles (Al#<0.21) represent compositions synthetized in equilibrium with melts which meet the main Al$_2$O$_3$ vs. SiO$_2$ trend of volcanic rocks and glasses, in equilibrium with typical crystallization conditions of calc-alkaline magmas: melt water contents H$_2$O$_{melt}$ of 3.7 to 8.2 wt% (average 5.9 wt%) and fO$_2$ in a range of -1<ΔNNO<+2.7. Inconsistent amphibole (Al#>0.21) refer to crustal (high-P) compositions and experimental pargasites, crystallized in equilibrium with melts characterized by high water contents (>4.5-13 wt%, average 8.3 wt%) and a broad range of fO$_2$ (-3<ΔNNO<+4.8). All Taapaca amphiboles show Al#<0.21 and classify as "consistent" (0.04<Al#<0.15 for Mg-Hbl inclusions in sanidine; Al#<0.17 for Mg-Hst from mafic inclusions).

The P-T and T-H$_2$O$_{melt}$ diagrams include the maximal and lower "thermal stability curve" defined by Ridolfi et al. (2010) for consistent amphiboles. These curves constrain a narrow crystallization conditions range estimated based on experimental amphiboles selected in the mentioned study.

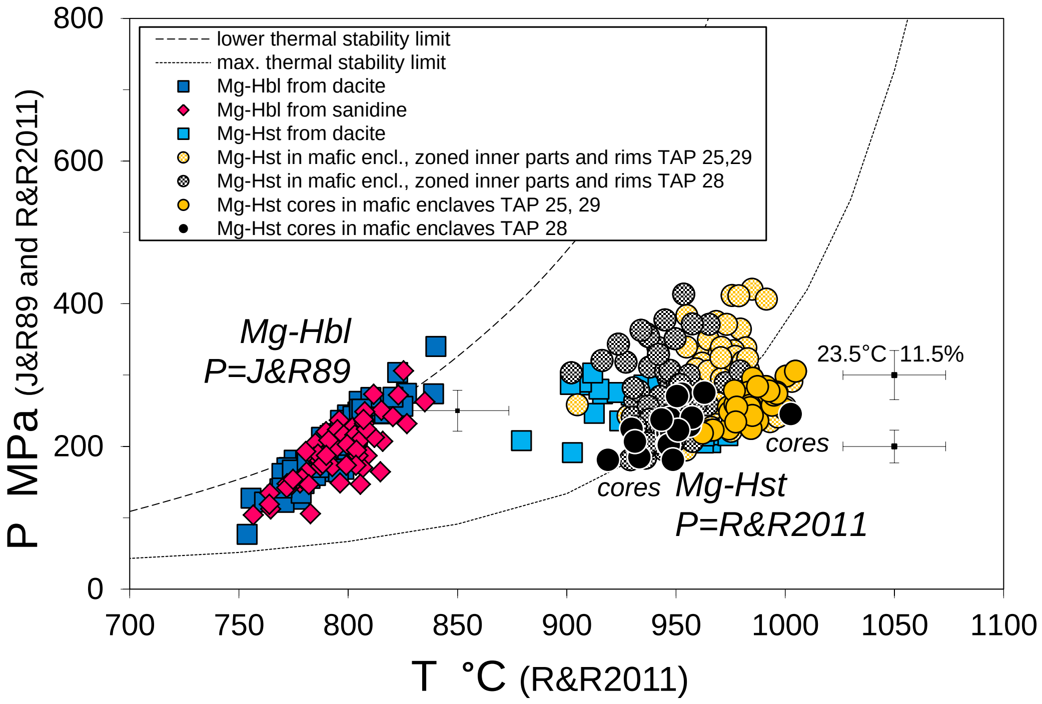

Figure 11. *P-T crystallization conditions of Taapaca amphiboles. Pressure values of low-Al-Ti Mg-Hbl are calculated using* Al^{TOT}*-in Hbl formulation of Johnson & Rutherford (1989) due to the best consistency of calibration conditions with Taapaca natural Mg-Hbl (section 5.2 and 5.3.1 for explanation). Pressure values of high-Al-Ti Mg-Hst are obtained from Eq. 1e presented by Ridolfi & Renzulli (2011) due to the best fit of experimental Mg-Hst (Figure 12e, section 5.3.1). Crystallization temperatures of both amphibole populations presented in this diagram results from R&R2011 calculated with appropriate pressures used in the T-formula. Dashed lines show lower and maximal stability limits of amphibole defined by Ridolfi et al. (2010). The error bars represent values for model uncertainties specified by R&R2011.*

5.3.1. PRESSURE

R&R2011 present five different coefficient-sets for pressure calculation (equations for P: 1a-1e), valid for different pressure ranges (Eq.1a: 130/2200 MPa; Eq.1b: 130/500 MPa; Eq.1c. 300/500 MPa; Eq.1d: 400/1500 MPa; Eq.1e: 930/2200 MPa). An empirical procedure recommended by R&R2011 confines a selection of reliable equations, giving a “P2”, indicated as a final and reliable pressure value. The “P2” is an equivalent of P(1b), (1c), (1d), and (1e) depending on pressure values calculated from the equations 1a-1e, or is an average pressure value obtained from equations 1b, 1c, and 1e. Pressures calculated with Eq.1d, using Taapaca experimental and natural Ca-amphibole compositions, show negative values and are not reasonable.

Figure 12 (a-f) shows correlations between experimental and calculated P using formulation of Ridolfi et al (2010) and equations (1a), (1b), (1c), (1e), and “P2” (average of 1b, 1c, and 1e) of R&R2011 for experimental Taapaca amphiboles of Botcharnikov et al. (in prep.), Blum-Oeste (2014), Stechern et al. (in prep.) and J&R89 for comparison.

The negative trend of experimental vs. calculated P-values formed by Mg-Hbl, synthesized from dacite starting material (red and blue diamonds, Figure 12), results from differences in temperature-sensitive Al and Ti in amphibole. These elements show lower contents and consequently lower pressures for experiments conducted at 3 kbar and 725-775°C, in comparison to experiments at 2 kbar and higher temperatures of 775-850°C (problem discussed in section 5.2). The experimental study by Blum-Oeste (2014) confirms this observation also by the R&R2011 formulations: lower experimental pressures (150-200 MPa) and higher temperatures (800-900°C) shift the results also to higher calculated pressures. However, as presented in Figure 9b, $^{[6]}$Al in synthetic amphibole of the latter study suggest an influence of other parameters than pressure, most probably fO_2 and/or H_2O_{melt}, because amphiboles of Botcharnikov et al. (in prep.), synthetized at similar equilibrium pressures and temperatures show significantly lower $^{[6]}$Al contents.

Considering correlations between experimental and calculated pressure values using R&R2011-equations (Figure 12b-f), the best fit can be achieved from R&R2011 Eq. 1e, only for Mg-Hst (Figure 12e). This fit, however, comprises only experimental result conducted at 300 MPa. Further, it is clear from Figure 12, that R&R2011 underestimate significantly pressure calculated from Mg-Hbl, which crystallized at experimental temperatures <775°C. Generally, the R&R2011 formulation for pressure underestimate P obtained from amphibole synthetized at P>500 MPa (Mg-Hbl and tschermakite). For this reason, we can accept the barometer of Johnson & Rutherford (1989) for Mg-Hbl in Taapaca dacites as more reliable than R&R2011.

Figure 11 presents in this study preferred P conditions obtained from two amphibole populations found in Taapaca rocks. Crystallization pressures of Mg-Hbl results from Al^{TOT}-in Hbl barometer of J&R89 in a range of 106 to 306 MPa, limited by extreme values of 76 to 340 MPa (section 5.2). In contrast to nearly horizontal P-T path obtained from Mg-Hbl using Eq. 1b {or 1e} of R&R2011 (92-158 MPa {or 96-165}and 766-835°C, not presented graphically), these pressure values follow the maximum thermal stability limit defined by Ridolfi et al. (2010) for “consistent” amphiboles. Crystallization pressures calculated from Eq.1e of R&R2011 for Mg-Hst range from 191 to 302 MPa (±21 and ±35 MPa, respectively, for the lowest and highest P value) in crystals found in dacite hosts; 181-305 MPa ((±21 and ±35 MPa) in crystal-cores found in mafic enclaves, and up to 420 MPa (±48 MPa) at rims of Mg-Hst found in mafic enclaves.

The cores of Mg-Hst reveal pressures equal to the highest and most frequent P-values obtained from Mg-Hbl. In contrast to Mg-Hbl, pressure-values obtained from Mg-Hst cores follow the maximal thermal stability-limit defined by Ridolfi et al. (2010); however, the Mg-Hst cores from mafic enclaves TAP 97-25 and 29 exceed the limit, moving to higher temperatures at pressure equal to the mafic enclaves TAP 28. As mentioned in section 4.2.2, these samples differ in the proportions of the mafic end-members BEM and AEM, defined in Chapter 2. Furthermore, inner parts and rims of Mg-Hst crystals, mostly in mafic enclaves, show higher P-values in comparison to their cores. An explanation of this phenomenon is discussed in context of fluctuations of the physic-chemical parameters taking place during magmas mixing and mingling (section 7.2.2).

The cores of Mg-Hst exceed the lower P-T stability limit defined by Ridolfi et al. (2010) for “consistent” amphiboles. It must be noted, that Ridolfi et al. (2010) used a limited amount of experimental amphibole compositions and the curves results from only rough estimations of the limits. Therefore, this study suggests, these limit-curves are not meaningful for analysis of extreme natural systems.

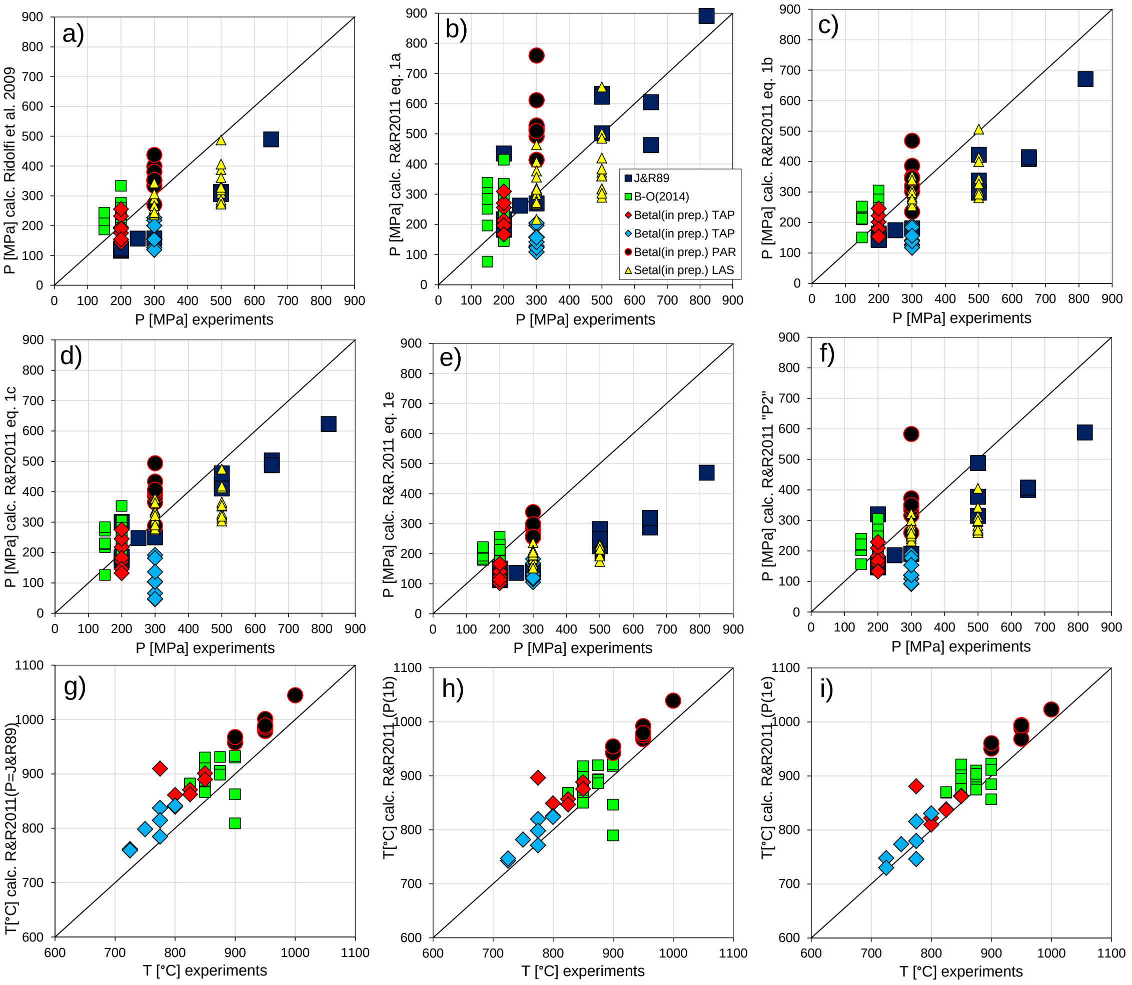

Figure 12. *Experimental vs. calculated pressures (a-f) and temperatures (g-i) from experimental amphibole of Botcharnikov et al. (in prep.), abbr. Betal (in prep.); Blum-Oeste (2014), abbr. B-O(2014); Stechern et al. (in prep.), abbr. Setal(in prep.); Johnson & Rutherford (1989), abbr. J&R89 using formulations of Ridolfi et al. (2010) and (2011), abbr.: R&R2011. Plots* ***(a-f)*** *present different equations used for pressure calculation presented by Ridolfi et al. (2010) and R&R2011. "Betal(in prep.) TAP" represents Mg-Hbl synthesized from Taapaca dacite starting material at 2 kbar and 775-850°C, and at 3 kbar and 725-775°C; "Betal(in prep.) PAR" represents Mg-Hst generated from basaltic andesite starting material from neighboring Parinacota volcano at 3 kbar and 900-1000°C. Plots* ***(h-i)*** *show temperatures calculated using pressure values obtained from* ***h)*** *Eq. 1b in and* ***i)*** *Eq. 1e. TAP=Taapaca, PAR=Parinacota, LAS=Lascar.*

5.3.2. TEMPERATURE

Due to the temperature calculations using algorithm of R&R2011, which includes pressure as a variable, different P equations (1a-1e, P2) and P obtained from J&R89 have been tested in the T-formula for experimental amphibole (Figure 12). According to the best fit between calculated and experimental T, Figure 12h-i presents temperatures of experimental amphiboles calculated with Eq. 1b and 1e. Pressure "P2" results in a correlation very similar to P1b. The absolute average deviation (aad) between experimental and calculated temperatures are: 45°C for calculation using P=JR89, 35°C with P=R&R2011(1b), and 31°C with P=R&R2011(1e). Pressure values of J&R89 show stronger temperature overestimation than other R&R2011 solutions. Although the pressure values obtained from J&R89 are preferred in this study for Mg-Hbl, crystallization temperatures of Mg-Hbl resulting from Eq. 1e for P may present values that are more reliable.

Generally, R&R2011 formulation overestimates crystallization temperatures, reaching up to 121°C differences between experimental and calculated values using Eq. 1b for P, and 106°C using Eq. 1e for P (Figure 12h, i). An underestimation of crystallization temperatures from several amphiboles give also the temperature-formula using Eq. 1b, reaching up to 110°C lower calculated than experimental equilibration T. An average overestimation for T estimation from Mg-Hbl and Mg-Hst is 46°C using P(J&R89), 33°C using P(1b), and 31°C using P(1e). The best correlations therefore, can be obtained using Eq. 1e for pressure in T-formula.

Crystallization temperature of Mg-Hbl in Taapaca dacites ranges from 740-825°C (calculated with P(1b)) and 754-840°C (with P(1e)); Mg-Hbl inclusions in sanidine megacrysts reveal 743-863°C and 756-835°C, respectively. Mg-Hst from Taapaca dacites yields 864-993°C (with P(1b)) and 879-981°C (with P (1e)); Mg-Hst from mafic enclaves shows 893-1020°C and 902-1005°C, respectively. The uncertainty of the thermometer is ±23.5°C.

Summarizing, the most reliable temperature values obtained from R&R2011 range from 754 to 840°C for Mg-Hbl crystallized from silicic RDEM Taapaca end-member and from 879 to 1005°C for Mg-Hst crystallized from the mafic (hybrid) end-member magmas.

5.3.3. OXYGEN FUGACITY

The R&R2011 calculation algorithm for redox conditions in the melt depends only on amphibole composition and does not require P as variable in the equation. Figure 13a presents log$f$O$_2$-T conditions obtained from Taapaca amphiboles.

Mg-Hbl yields a compact trend of decreasing temperature with decreasing log$f$O$_2$ in a range of -14.4 to -11.5 ±0.37 log units (NNO+0.8 to NNO+2.0). These values form an inverse log$f$O$_2$-T trend in comparison to the results obtained from Fe-Ti oxides presented also in Figure 13a. Mg-Hst from different dacite host and mafic enclave samples reveals a broad range of log$f$O$_2$ values, and accordingly various log$f$O$_2$-T trends for different samples. Mg-Hst spans a fO$_2$-range between -10.8 and -6.3 -±0.37 log units (NNO+0.2 to NNO+3.9) from mafic enclaves, and between -11.7 and -7.6 ±0.37 log units (NNO+0.4 to NNO+3.4) from dacite hosts.

Amphibole from the mafic enclaves TAP 28 and dacite host sample TAP 97-28, which show nearly the highest Mg, K and the lowest $^{[6]}$Al contents (Figure 7), yield more oxidized conditions, above NNO+2, than all other investigated samples. The cores of Mg-Hst reveal significantly more oxidized conditions than their rims. The lowest NNO values determined from Mg-Hst meet the conditions recorded in a few magnetite-ilmenite pairs showing temperatures of 900 to 950°C at NNO to NNO+1. These trends, moving toward more reduced condition below NNO+2 during crystallization is in contrary to the typical observed differentiation conditions and requires explanation in a context of the magma mixing of Taapaca magmas.

5.3.4. MELT WATER-CONTENTS H_2O_{MELT}

The R&R2011 hygrometer algorithm for calculation of water contents in the melt from amphibole composition is P-sensitive and, as tested by Ridolfi & Renzulli (2011), in agreement with most volatile solubility models showing realistic H_2O_{melt}-values, consistent with experimental values. Figure 13b, and c present H_2O_{melt} vs. T and red-ox conditions (ΔNNO buffer values). The uncertainty of the hygrometer is ±0.78 wt%.

Due to compositional differences of two amphibole populations, the Mg-Hst, which crystallized from the mafic input magma of Taapaca, reveal significantly lower melt water contents in comparison to the rhyodacite magma. Mg-Hbl form a compact trend of decreasing H_2O_{melt} with slightly decreasing T and P, and yields 8.5-6.0 wt% H_2O_{melt} at 840-756°C and 340-76 MPa. In contrast, Mg-Hst shows generally a smooth trend of increasing H_2O_{melt} with decreasing T, and yields values of 3.0 to 4.3 wt% obtained from cores, and up to 6.8 wt% from the rims. There are noticeable differences between two Mg-Hst crystal-core groups in mafic enclaves. Mg-Hst cores of the sample TAP 28, which contain higher proportions of the BEM Taapaca mafic end-member, yield slightly higher melt water contents at lower P-T conditions in a range of 3.0 to 4.3 wt% at 963-919°C and 275-181 MPa. Samples TAP 97-25 and 29, characterized by higher proportions of the AEM mafic end-member contain Mg-Hst, which reveal 3 to 3.9 wt% H_2O_{melt} at 1004-962°C and 305-218 MPa. Similarly to the P-T variations, both amphibole populations exceed the stability limits in the H_2O_{melt} –T space, estimated by Ridolfi et al. (2010), (dashed, and pointed curves, Figure 13b). As mentioned before, this observation probably results from limited amount of experimental amphibole compositions considered in the estimation.

To test the correlation between changes in water contents of the melt and oxygen fugacity, Figure 13c presents H_2O_{melt} vs. ΔNNO. Mg-Hbl shows a week tendency to more reduced conditions at slightly higher H_2O_{melt}. Mg-Hst demonstrates variable ΔNNO values, from nearly NNO to NNO+4 at the same melt water contents of 3.0-4.3 wt%. The rims of Mg-Hst do not reveal consistent tendency to more oxidized or reduced conditions with increasing H_2O_{melt}.

Figure 13. ***Next page: a)*** *Thermo-oxy-barometric results obtained from Taapaca amphibole using formulation of Ridolfi & Renzulli (2011) and from Fe-Ti oxide using oxy-barometer of Andersen & Lindsley, (1985). Generally, fO_2 from Taapaca amphibole shows more reduced conditions with decreasing T. This tendency is different to the results obtained from magnetite and ilmenite.* ***b)*** *T-H_2O_{melt} results for the amphibole data set used in the previous plots. Dashed lines show lower and maximal stability limits of amphibole defined by Ridolfi et al. (2010).* ***c)*** *ΔNNO-$H_2O_{melt.}$ The error bars represent values for model uncertainties specified by R&R2011. Symbols are as in Figure 11. The oxygen buffer curves are calculated from Frost (1991): MH, magnetite-hematite, NNO, nickel-nickel oxide, FMQ, fayalite-magnetite-quartz.*

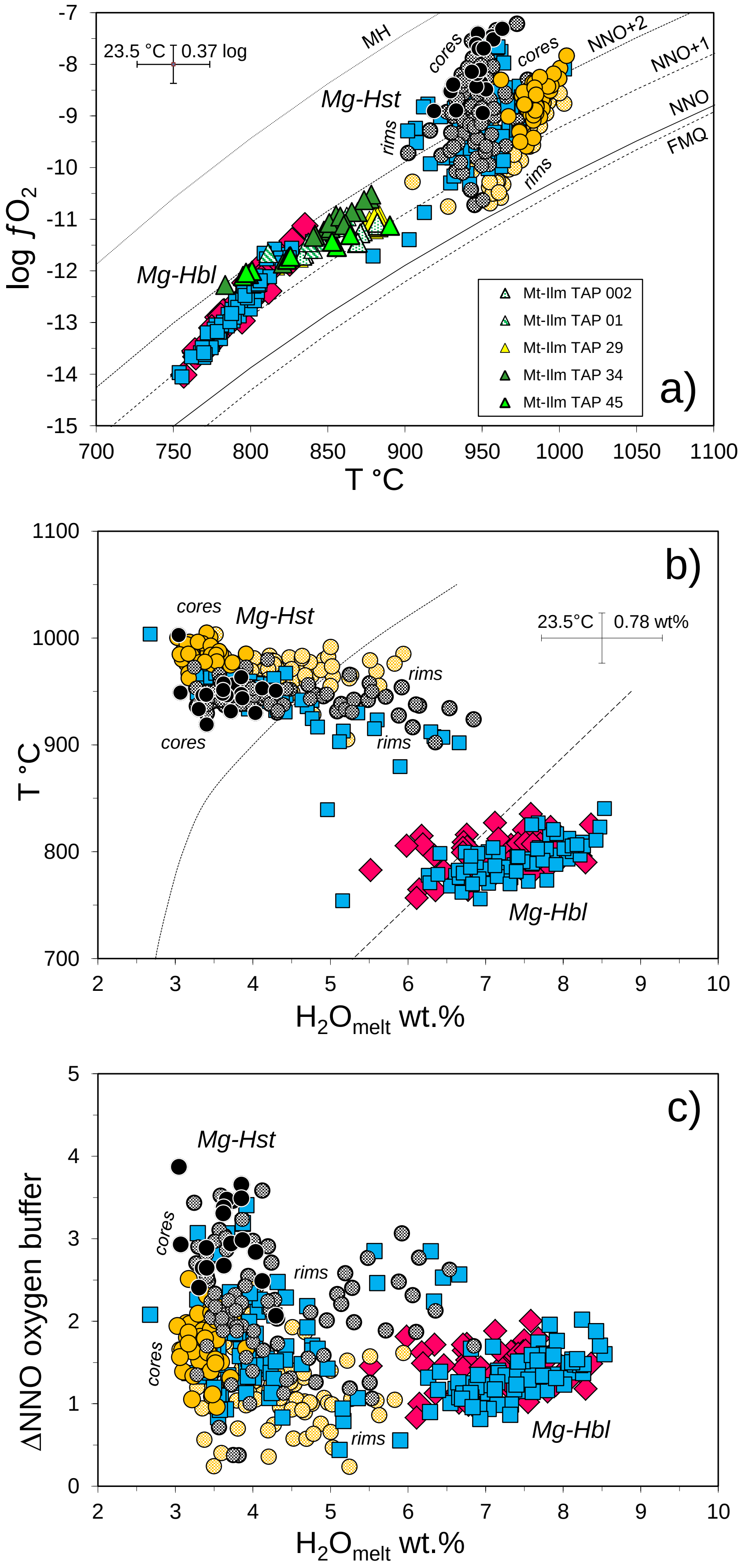
log fO_2
-7
-8
-9
-10
-11
-12
-13
-14
-15
700
750
800
850
900
950
1000
1050
1100
T °C
23.5 °C
0.37 log
MH
NNO+2
NNO+1
NNO
FMQ
Mg-Hst
Mg-Hbl
cores
rims
cores
rims
△ Mt-Ilm TAP 002
△ Mt-Ilm TAP 01
△ Mt-Ilm TAP 29
▲ Mt-Ilm TAP 34
▲ Mt-Ilm TAP 45
a)
T °C
1100
1000
900
800
700
2
3
4
5
6
7
8
9
10
H_2O_{melt} wt.%
23.5°C
0.78 wt%
cores
Mg-Hst
rims
cores
rims
Mg-Hbl
b)
ΔNNO oxygen buffer
5
4
3
2
1
0
2
3
4
5
6
7
8
9
10
H_2O_{melt} wt.%
Mg-Hst
cores
rims
cores
rims
Mg-Hbl
c)

5.4. AMPHIBOLE-PLAGIOCLASE THERMOMETRY

The thermometer of Holland & Blundy (1994) was applied to coexisting amphibole and plagioclase in Taapaca rocks (Figure 14). Thermometer A, referred as T(A), is appropriate only for Mg-Hbl and low-Fe plagioclase, which represent rhyodacitic, quartz-bearing Taapaca end-member magma. Thermometer B, referred as T(B), is applicable for assemblages with or without quartz, therefore uses for both amphibole populations. The pressure values used in calculations and presented in Figure 14 are taken from J&R89 geobarometer for Mg-Hbl and R&R2011 (P1e) for Mg-Hst.

5.4.1. SELECTION OF AMPHIBOLE-PLAGIOCLASE PAIRS

There is a lack of a general chemical equilibrium-test between amphibole and plagioclase crystals, and obvious textural indications for amphibole-plagioclase pairs in Taapaca rocks. Therefore, a potential range of crystallization temperatures can be determined using following pair-selection procedure: 1) in the dacites, amphibole compositions are paired with plagioclase analysis showing the highest and lowest An-contents found in single samples. An additional chemical condition considers Fe-concentrations of plagioclase. Mg-Hbl were coupled only with the low-Fe and Mg-Hst with the high-Fe (>2000 ppm) plagioclase population. A distinction between core and rim compositions does not reveal any systematic trends for both, amphibole and plagioclase. 2) Temperatures obtained from amphibole and plagioclase inclusions in sanidine results also from combination of the highest and the lowest An contents in plagioclase with all Mg-Hbl measured in the single sanidine crystals. 3) Temperatures obtained from mafic enclaves result from core-core and rim-rim compositions, which have been coupled under the assumption of simultaneous crystallization in a closed system. Therefore, the presented P-T groups in Figure 14 define the lowest and highest temperatures, considered as possible values.

5.4.2. AMPHIBOLE-PLAGIOCLASE CRYSTALLIZATION TEMPERATURES OF TAAPACA ROCKS

Considerable discrepancy between temperatures calculated with T(A) and T(B) from Mg-Hbl and low-Fe plagioclase, compositions assumed to crystallize from silicic Taapaca end-member, are observed. The T-values from T(A), using P=J&R89, range from 719 to 845°C for Mg-Hbl coupled with low-An plagioclase, and 724 to 854°C coupled with high-An plagioclase. The T-values from T(B) ranges from 688 to 788°C and 709 to 805°C, respectively. Despite of the presence of quartz in the Taapaca dacites (in fact originating from the rhyodacitic end-member), indicating $a_{SiO2}=1$, temperatures calculated using T(A) for Mg-Hbl and low-Fe plagioclase show consistently higher values than the results obtained from T(B). As recommended by Holland & Blundy (1994), in such a case, the T(B)-temperatures represent the equilibrium conditions. T(A) shows a temperature-offset due to probably lower silica activity $a_{SiO2}<1$ than assumed by the T(A) formulation. This evidence indicates that amphibole and plagioclase crystallized before appearance of quartz. Crystallization temperatures of Mg-Hbl obtained by T (B), using the amphibole-plagioclase coupling method described in section 5.4.1 reveals 702 to 807°C for the low-Fe plagioclase of the highest anorthite contents (An26-49) and 677 to 788°C for the lowest anorthite contents (An23-28). Consequently, a probable crystallization temperature range of Mg-Hbl in Taapaca rhyodacite end-member magma spans from 677 to 807°C.

Mg-Hst coupled with high-Fe plagioclase yield a wide range of temperatures obtained with T(B), as a result of noticeable variations in anorthite content in high-Fe plagioclase. The temperature range obtained from T(B) for Mg-Hst and plagioclase found in mafic enclaves span an interval of 188°C, between 747 and 935°C. In detail: Mg-Hst and plagioclase (An43-45) crystal core-pairs reveal 840 to 935°C; Mg-Hst and plagioclase (An20-28) crystal rim-pairs reveal 747 to 850°C. The temperature range for Mg-Hst and plagioclase found in the dacite samples span results from combination of amphibole with the highest and lowest An-content of high-Fe plagioclase found in a single sample and span an interval of 152°C, between 814 and 966°C. In detail: Mg-Hst and low-An plagioclase (An38-54) reveal 834 to 966°C; Mg-Hst and high-An plagioclase (An31-45) reveal 814 to 918°C. The temperature values obtained from rim-rim compositions of Mg-Hst and plagioclase from mafic enclaves overlap partially with the highest temperatures obtained from Mg-Hbl and plagioclase representing the rhyodacite magma.

5.4.3. COMPARISON OF TEMPERATURE RESULTS FROM H&B94 AND R&R2011

A comparison of two-phase geothermometer of H&B94 and single-phase geothermometer of R&R2011 reveals a substantial difference in crystallization temperatures of amphibole, which cannot only result from different range of uncertainty of both geothermometers. An involvement of the second mineral phase detects broadest range of pre-eruptive temperatures recorded in Taapaca lavas.

Starting with Mg-Hbl: 1) the T(A) roughly resembles crystallization temperatures obtained from R&R2011 (719-854°C and 754-840°C, respectively). 2) The highest temperatures obtained by T(B) from Mg-Hbl in combination with a low-Fe plagioclase of a highest anorthite content (An47) found in a dacite sample TAP 28 is 807°C; in combination with the lowest An content, plagioclase of An24, T(B) yields 720°C; R&R2011 (with P(1e)) yields 800°C for the same amphibole analysis. Mg-Hbl rims with the lowest An-contents in a single sample show temperatures even <700°C (Figure 14b). Whereas R&R2011 shows T>754°C for Mg-Hbl, the lowest temperature range obtained from Mg-Hbl and low-An plagioclase using T(B) spans mainly between 690-740°C.

Similarly to the Mg-Hbl, the T(B) reveals significantly lower temperatures from Mg-Hst, which have not been detected using R&R2011. There is a general shift of the highest temperatures obtained from the two geothermometers, from 1005°C detected by R&R2011 to 966°C detected by T(B). The highest temperature of T=1005°C (R&R2011) found in the Mg-Hst core in a mafic enclave is 70°C higher than the highest temperature of T=935°C obtained by T(B) from the same sample. The most surprising result show the Mg-Hst rims, coupled with plagioclase rims found in the mafic enclaves. They yield a range of 747 to 850°C, whereas the same amphibole analysis used in R&R2011 yield 902 to 1003°C, the same temperatures as found in the amphibole cores. Regarding the cooling processes, which take place during mixing/mingling of an input of hot mafic magma into relatively cold (subsolidus temperatures) rhyodacite magma, the cooling scenario detected by H&B94 T(B) may be closer to the real conditions.

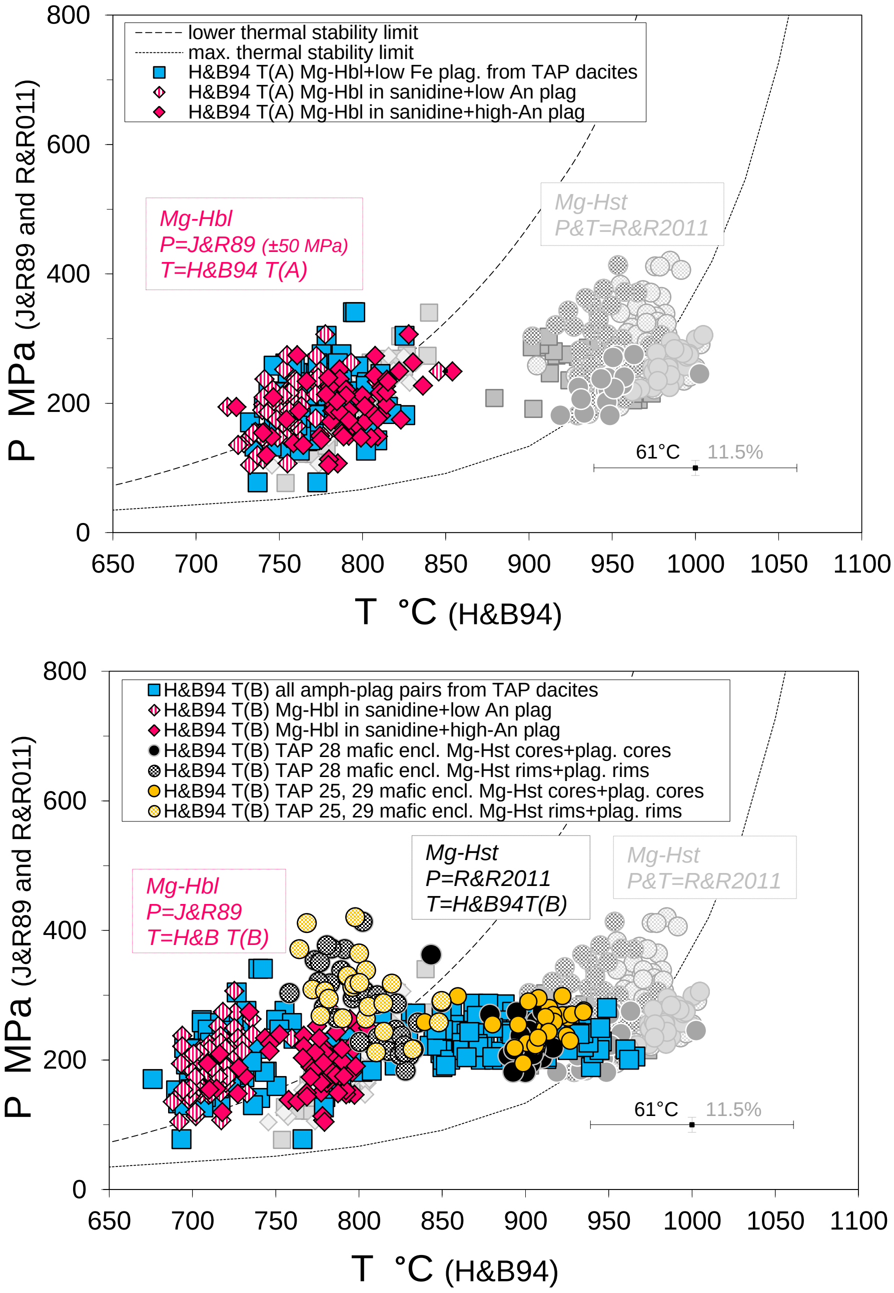

Figure 14. *Amphibole-plagioclase crystallization temperatures calculated using thermometer of Holland & Blundy (1994) and pressure from Al-in-Hbl barometer of Johnson & Rutherford for Mg-Hbl, and Ridolfi & Renzulli (2011) for Mg-Hst. Note that higher Mg-Hst pressures obtained from Mg-Hst rims may not represent reliable values, a problem discussed in the section 7.2.2. P-T space in* ***a)*** *presents temperatures obtained from Thermometer A, T(A), and* ***b)*** *from Thermometer, T(B). Due to lacking chemical tests and textural indications for amphibole-plagioclase pairs in equilibrium, presented P-T groups define the highest and lowest possible temperature ranges obtained from combination of amphibole compositions with the highest and lowest anorthite contents in plagioclase found in the individual sanidine crystals. For mafic enclaves, core-core and rim-rim compositions were chosen, due to assumed simultaneous crystallization in a closed system. For comparison, grey points show P-T conditions presented in Figure 11 representing the results of GTOB of R&R2011.*

On one hand side, the determination of temperature from amphibole using R&R2011 show a good correlation with the experimental results and may be regarded as more reliable than H&B94. The latter underestimates experimental temperatures significantly, in average 61°C as presented by Blundy & Cashman (2008). On the second hand side, the results obtained from amphibole-plagioclase are more acceptable with respect to the expected thermal equilibration of the mafic input magma, forming the mafic enclaves.

Figure 15a shows an example of a zoned amphibole and several adjacent plagioclase crystals with compositional variations of both phases illustrated in Figure 15b and c. Table 1 reports the crystallization conditions obtained for the example-crystals in Figure 15, using H&B94 and R&R2011. The Mg-Hst (crystal am 4) shows pronounced compositional variations from core to rim without any continuous trend. These variations account for a significant scatter of the physical-chemical parameter during crystallization as obtained from the single-phase GTOB of R&R2011; for instance, the lowest P and T conditions are recorded in the core of “am 4”, not at the rim (Table 1). Despite the compositional differences between core and rim in the amphibole, composition of the plagioclases reveals significantly lower An-contents at the rims (Figure 15c), leading inevitably to lower crystallization temperatures obtained from the amphibole + plagioclase rims, representing the latest crystallization stage.

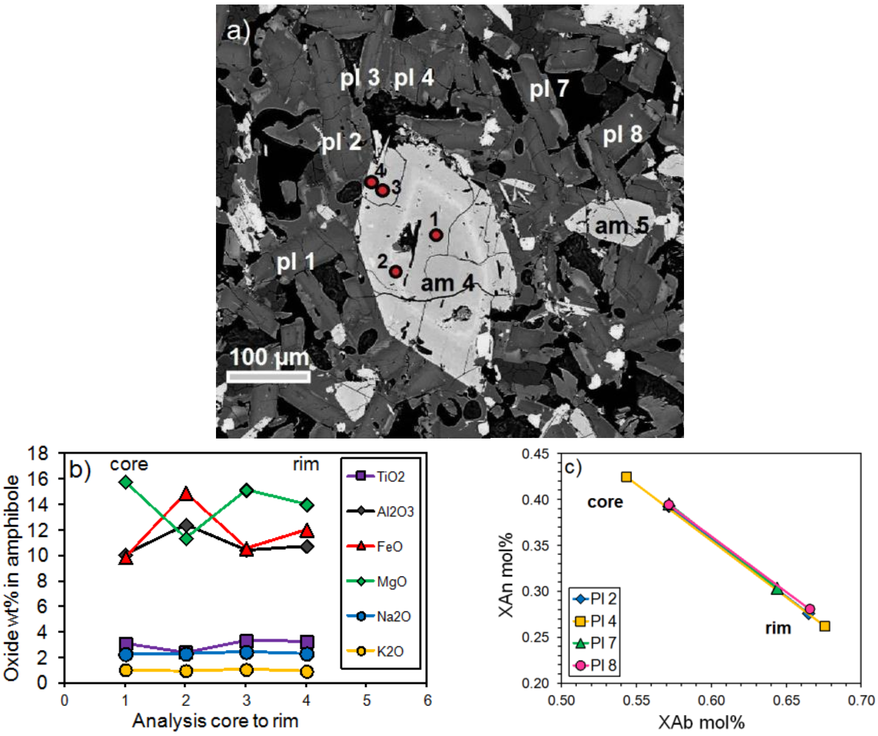

Figure 15. *Morphology and compositional features of amphibole and plagioclase in Taapaca mafic enclave TAP 28/1: **a)** BSE-image presents zoning in Mg-Hst and plagioclase. Red points represent analysis of Mg-Hst presented in plot **b)**. Light-grey zone in am 4 corresponds to higher Fe-contents (analysis point No. 2). Darker plagioclase rims correspond to lower An contents as presented in **c)** for four selected plagioclase around the amphibole “am 4”. Resulting P-T conditions are presented in Table 1 (see text for details).*

Table 1. *Crystallization conditions obtained from an example of Mg-Hst (am 4) and adjacent plagioclase grains (pl1-4, 7, 8), displayed in Figure 15, using R&R2011and H&B94.*

Mafic enclave TAP 28	No. pl	An-contents core, rim	am 4 point 1 core	am 4 point 2	am 4 point 3	am 4 point 4 rim
P [Mpa] (R&R2011, Eq. 1e)			206	343	233	214
T [°C] (R&R2011)			**931**	923	957	**946**
ΔNNO (R&R2011)			2.9	1.7	2.9	1.9
H_2O_{melt} [wt%](R&R2011)			3.7	6.8	3.7	4
T [°C] (H&B94, T(B))	pl 1	An40, An36	**878**			**857**
T [°C] (H&B94, T(B))	pl 2	An39, An28	**877**			**824**
T [°C] (H&B94, T(B))	pl 4	An42, An26	**890**			**818**
T [°C] (H&B94, T(B))	pl 7	An40, An30	**878**			**835**
T [°C] (H&B94, T(B))	pl 8	An39, An28	**877**			**825**

5.5. AMPHIBOLE TI-THERMOMETER

Due to corresponding calc-alkaline whole rock and Ca-amphibole compositions used for the calibration, geothermometer of Féménias et al. (2006), (referred as Fetal2006) appears to be suitable for Taapaca amphiboles. The Fetal2006 Ti-in amphibole geothermometer is based solely on Ti-contents in amphiboles. Figure 16a presents correlation between experimental and from Fetal2006 calculated crystallization temperatures of experimental amphiboles presented in Figure 12. The formulation of Fetal2006 does not require pressure values, due to pressure independency of Ti-contents in Ca-amphibole in the temperature range of 600-1000°C, at pressures <2.5 GPa. Amphibole synthetized from dacite whole rock (Betal in prep., and B-O2014) show a good correlation between experimental and calculated values, even closer to 1:1 correlation line than geothermometer of R&R2011. The aad (average absolute deviation) for Mg-Hbl is 15°C and Mg-Hst is 44°C. Generally, aad for both populations is 20°C. The maximum overestimated value is 77°C. The experimental amphiboles reveal lower aad between experimental and calculated values with Fetal2006 than with the formulation of R&R2011.

Figure 16b presents crystallization temperatures of natural Taapaca amphibole using the Ti-in amphibole geothermometer. Mg-Hbl shows temperatures between 638 and 740°C. Mg-Hst ranges from ~890 to 1040°C. In comparison to R&R2011 and H&B94, the Fetal2006 geobarometer extends crystallization temperatures of Mg-Hbl to significantly lower values and Mg-Hst to higher values.

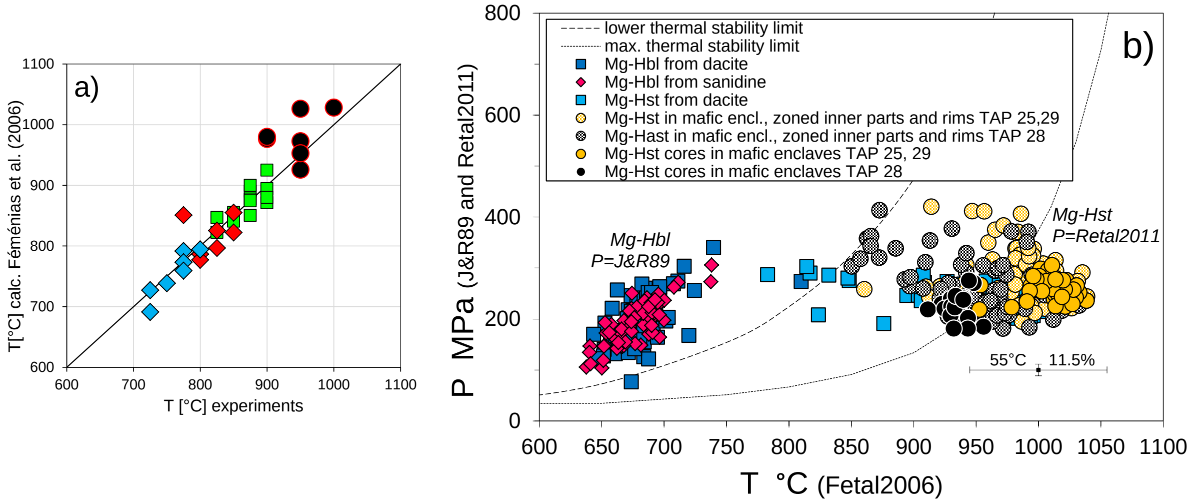

Figure 16. *Amphibole thermometer of Féménias et al (2006).* ***a)*** *Correlation between experimental and with Fetal2006 calculated crystallization temperatures.* ***b)*** *P-T conditions of Taapaca amphibole, alternative to results presented in Figure 11 and Figure 14. Pressure values represents J&R89 for Mg-Hbl and R&R2011(1e) for Mg-Hst.*

5.6. CA-AMPHIBOLE SEMI-QUANTITATIVE THERMOBAROMETRY

Application of semi-quantitative Ca-amphibole thermobarometer of Ernst & Liu (1998) (referred as E&L1998), based on contents of Al_2O_3 and TiO_2 wt% in amphibole (Figure 17), admittedly calibrated for basaltic rocks, reveals P-T consistency with results for Mg-Hst obtained from P-T calculation algorithm of R&R2011. The semi-quantitative thermobarometric formulation allows estimation of P-T ranges, not exact numbers.

Crystallization temperatures of amphibole obtained from E&L98 show values consistent with Fetal2006, according to used T-dependency of Ti-contents in amphibole in both geothermometers. Temperatures for Mg-Hst show ~850 to ~890°C for several rim analyses and range mainly from ~930 to ~1000°C. The main temperature range overlaps roughly also with R&R2011 (Figure 11). In contrast to temperature, pressure determined, based mainly on Al^{TOT} cannot be accepted to represent reliable values. As mentioned in previous sections, Al shows strong dependence on magma composition from which amphibole crystallizes as well as temperature and oxygen fugacity. However, this semiquantitative approximation shows, that both, low-Al Mg-Hbl and high-Al Mg-Hst can crystallize at similar pressure at ~3 kbar.

Regardless of the Mg-Hbl compositions <7 wt% Al_2O_3 and <1.5 wt% TiO_2, which are not included in the thermobarometric approximation, as well as substantial differences between the whole rock and amphibole compositions used for calibration, the Mg-Hbl show good agreement with P-T results obtained from Fetal2006 for temperatures and J&R89 for pressure.

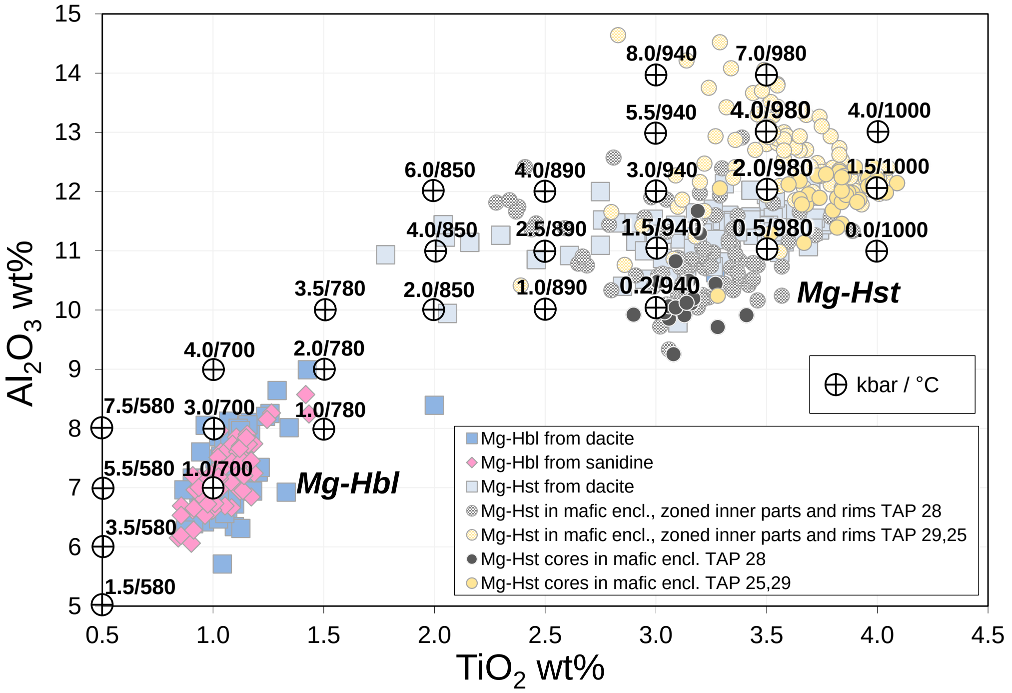

Figure 17. *Semiquantitative thermobarometer of Ernst& Liu (1998) converted from P-T space with Al_2O_3 and TiO_2 isopleths to Al_2O_3-TiO_2 space, with denoted P-T conditions for specific Al_2O_3 and TiO_2 contents in amphibole.*

5.7. GEOTHERMO-OXY-BAROMETRY BASED ON Fe-Ti OXIDE

Determination of fO_2-T conditions in Taapaca rocks from Fe-Ti oxide is possible only from five youngest dacite samples, (stage IV). These samples carry only a small amount of homogenous magnetite and ilmenite in contact with melt, which can be texturally recognized as individual crystals, not affected by exsolution/oxidation processes. Older dacite samples as well as all Fe-Ti oxide inclusions in sanidine megacrysts show advanced exsolution/oxidation of Fe-Ti oxide. Ilmenite is very rare and mostly occurs as a secondary product of titanite oxidation. Mafic enclaves contain only magnetite. Composition of magnetite and ilmenite used for geothermo-oxybarometer of Andersen & Lindsley (1985) and molecular fractions of ulvöspinel (X_{usp}) and ilmenite (X_{ilm}) calculated using method of Stormer (1983). Magnetite compositions used in the geothermo-oxybarometer range from 11 to 29% X_{usp}; a magnetite inclusion in amphibole shows lower Ti-content, reaching 9.7% X_{usp}. Ilmenite shows 57 to 77% X_{ilm}. All magnetite-ilmenite pairs meet the empirical Mg/Mn partitioning test of Bacon & Hirschmann (1988).

The results of GTOB are presented in Figure 13a, together with fO_2-T obtained from the single-phase amphibole GTOB of R&R2011. All samples reveal a uniform temperature range between 799 and 890°C (average 850°C). The lowest temperature value of 784°C has been obtained from Fe-Ti oxide inclusions in Mg-Hbl. Oxygen fugacity ranges from -12.3 to -10.5 log units, comprising ΔNNO+0.9 to +2.0 at the equilibrium temperatures. The redox conditions obtained from magnetite-ilmenite pairs are also nearly uniform in all samples and show only slightly higher ΔNNO+1.5 to +1.8 in one sample in comparison to main values of ΔNNO+0.9 to +1.3 at higher temperatures (850-

890°C). At temperatures <850°C, magnetite-ilmenite pairs reveal slightly more oxidized conditions.

Generally, the Fe-Ti oxides form Taapaca dacites yield redox conditions consistent with results obtained from Mg-Hbl using R&R2011 (Figure 13a). The temperature range overlaps partially with Mg-Hbl. A single temperature value obtained from Fe-Ti oxide inclusions in Mg-Hbl is consistent with other geothermometer. The temperature range of 850-890°C, above values representing crystallization conditions of Mg-Hbl, may be considered as the last magma equilibration conditions before ascent. Based on experimental studies on Fe-Ti oxides, Venezky & Rutherford (1999), and references therein) show that the oxides reequilibrate by diffusion or by crystallization within a few days to weeks under magmatic conditions. Taking into account the calculated temperature range in Taapaca dacites and the grain sizes (<50 µm) of magnetite-ilmenite pairs used for GTOB, the reequilibration of whole grains may be assumed because zoned magnetite or ilmenite crystals have not been found. Due to small amount of the homogenous magnetite and ilmenite crystals and their small grain sizes as well as large amount of Fe-Ti oxide showing pronounced exolution/oxidation textures, the magnetite-ilmenite pairs used in GTOB represent rather last crystallization phases.

It is worth mentioning, that geothermo-oxybarometry conducted on magnetite-ilmenite pairs from Parinacota dacite, rhyodacite, and rhyolite samples reveal two T-NNO groups connected to the SiO_2 contents of the whole rock composition (Figure 14, Chapter 4). In comparison to dacite, rhyodacite and rhyolite show lower T<830°C and slightly higher NNO around +1.9, in comparison to the dacite ~T>840°C and NNO between +1 and +1.8 (several rhyodacitic T-fO_2 also occur in the dacite). Parinacota rocks define these two groups, which are represented in single dacite samples of Taapaca. This observation suggests that the T-fO_2 conditions from the RDEM end-member magma are still preserved in the Fe-Ti oxide from Taapaca dacites. Therefore, a range of 780 to 830°C and NNO+1.5 to NNO+2.1 may represent conditions in the RDEM silicic magma.

6. SIMPLE MAGMA MIXING MODELING

Connecting the mafic enclaves with their host dacites in the Sr-SiO_2 space, the connecting lines form an array of distinct mixing lines converging to one rhyodacitic end-member of ~68-70 wt% SiO_2 (Figure 18). Assuming that the dacite compositions are mixtures between the mafic end-members, represented by the compositions of mafic enclaves and silicic end-members, the mixtures (dacites) can be expressed in terms of mixing proportions *X* and concentrations *C* of elements, as oxide in wt% or trace elements in ppm by the mass balance equation of Myers et al. (1987):

$$C_{\text{dacite}} = X\, C_{\text{silicic end-member}} + (1-X)\, C_{\text{mafic enclave}}$$

This equation represents a line connecting the mafic enclaves and the silicic end-member. The results show that the mixing proportions between silicic and mafic end-members are nearly constant and yield a mixing ratio ranging between 6:4 and 7:3, respectively, (Figure 18b). This estimation is consistent with the mixing proportions obtained using multivariate statistical technique, the Polytopic Vector Analysis (PVA), presented in Chapter 2 of this work. The PVA gives the exact proportions of each end-member in each single sample used in the modeling (section 5.3, Chapter 2) and these values are preferred in this study.

The simplest way to calculate the whole rock composition of the silicic end-member results from the linear dependence of the binary magma mixing between two components. Modeled compositions of the silicic end-member presented in this study are based on linear regressions between the oxide/elements and SiO_2 contents. Using the method of ordinary least squares (solution that minimizes the sum of the squares of the difference between observed and fitted concentrations) for each linear equation representing oxide/element vs. SiO_2, the equation parameters allow calculation of the predicted oxide/element contents in the silicic end-member. Table 2 presents the whole rock compositions of the silicic end-member modeled by simple mixing for assumed SiO_2 values.

Additionally, Table 2 provides compositions of the silicic end-member obtained from the PVA, a technique that do not need any mathematical assumptions. The results of simple mixing modeling show quite consistent results with the PVA model-compositions, at the equivalent SiO_2 values and similar database used in the PVA models. Especially, models based on selected eight dacites and their mafic enclaves reveal very good agreement. The consistency between the compositions of the silicic end-member obtained from the PVA and the simple mixing modeling results from the mathematical basis of both methods, extracting end-member compositions that minimize the variance of the resulting solutions.

Table 2. *Major and trace element composition of silicic end-member obtained from mass balance modeling based on an assumption that the composition. "*" indicates the assumed SiO_2 value in the calculation.*

oxide/ element	Simple mixing modeling 8 dacite-mafic enclaves pairs			Simple mixing modeling 79 samples					PVA model (25-8p) 25 analyte 8 mafic silicic pairs	PVA model (43-36) 43 analyte 36 samples
	rhyodacite end-member			rhyodacite end-member					RDEM	RDEM
SiO_2 wt%	*68**	*69**	*70**	*68**	*69**	*70**	*71**	*72**	69	72
TiO_2	0.59	0.53	0.47	0.58	0.51	0.44	0.37	0.30	0.53	0.23
Al_2O_3	16.1	16.0	15.9	16.1	16.0	15.9	15.8	15.7	16.0	15.9
FeO	2.9	2.5	2.2	2.8	2.4	2.0	1.7	1.3	2.7	1.4
MnO	0.05	0.05	0.04	0.05	0.04	0.04	0.03	0.03	0.05	0.04
MgO	0.92	0.65	0.37	1.01	0.76	0.52	0.27	0.02	0.83	0.17
CaO	3.0	2.7	2.3	3.0	2.7	2.4	2.1	1.8	2.8	1.9
Na_2O	4.6	4.6	4.7	4.5	4.6	4.6	4.7	4.7	4.6	4.8
K_2O	3.4	3.5	3.6	3.6	3.6	3.7	3.8	3.9	3.4	3.6
P_2O_5	0.20	0.19	0.17	0.18	0.15	0.12	0.10	0.07	0.17	0.05
Nb ppm	6.9	6.9	6.8	5.5	5.1	4.8	4.5	4.2	6.8	3.4
Zr	161	161	161	154	151	148	145	142	156	130
Y	7.9	7.1	6.4	6.5	5.7	4.8	4.0	3.1	7.4	4.2
Sr	667	639	610	647	612	576	540	505	615	438
Rb	107	111	115	104	109	113	118	122	109	120
Zn	60	56	52	66	62	59	55	51	61	53
Ni	3	1	-2	6	4	1	-1	-3	3	0
Co	7	5	4	7	6	4	3	2	6	0
Cr	8	3	-1	11	7	3	-1	-5	12	0
V	76	67	59	70	61	52	43	34	67	36
Ba	985	986	986	997	989	981	973	965	976	852
Li	26.5	26.2	26.0	31	31	32	32	33		35
Sc	5.4	4.3	3.2	4.2	3.2	2.1	1.1	0.1	5.0	0
Cu	21.6	20.2	18.8	28.5	27.1	25.7	24.2	22.8		25.5
La	25	25	24	29	29	28	28	27	24	17
Ce	50	48	46	55	53	51	49	47	49	30
Pr	5.2	5.0	4.8	4.7	4.1	3.5	2.9	2.3		3.1
Nd	20.5	19.2	17.9	24.1	22.9	21.8	20.6	19.5	19.8	10.8
Sm	3.2	3.0	2.7	3.2	2.8	2.4	2.1	1.7		1.6
Eu	0.87	0.81	0.75	0.66	0.50	0.35	0.19	0.03		0.30
Gd	2.6	2.4	2.2	2.2	1.8	1.4	1.0	0.6		1.0
Tb	0.27	0.24	0.22	0.22	0.16	0.11	0.06	0.01		0.07
Dy	1.27	1.13	0.98	1.14	0.95	0.76	0.57	0.38		0.43
Ho	0.22	0.20	0.17	0.22	0.19	0.17	0.14	0.12		0.11
Er	0.49	0.39	0.30	0.52	0.45	0.38	0.31	0.25		0.15
Tm	0.07	0.06	0.05	0.07	0.07	0.06	0.05	0.05		0.03
Yb	0.32	0.21	0.10	0.33	0.24	0.15	0.06	-0.03		0.23
Lu	0.07	0.06	0.05	0.08	0.07	0.07	0.07	0.06		0.04
Hf	2.9	2.8	2.7	2.7	2.6	2.4	2.3	2.1		2.3
Ta	0.46	0.47	0.48	0.40	0.37	0.34	0.31	0.28		0.25
Pb	18	18	18	19	20	21	21	22		21
Th	6.2	6.3	6.3	6.6	6.7	6.8	6.8	6.9		5.3
U	2.5	2.6	2.7	2.6	2.7	2.8	2.9	3.0		2.7

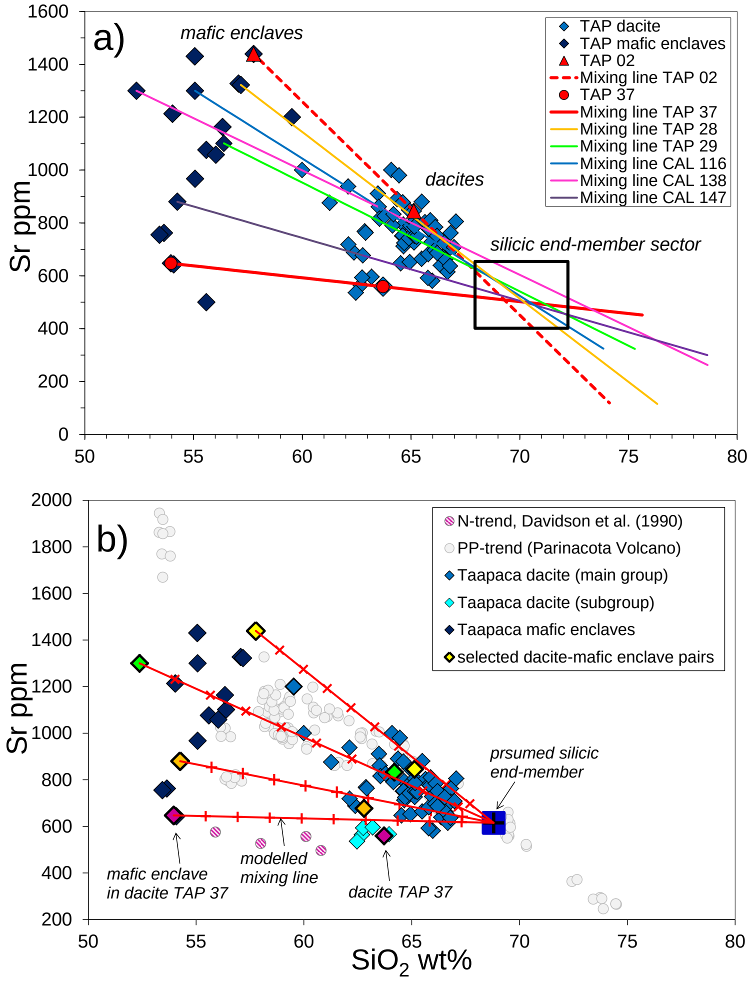

Figure 18. ***a)*** *An array of mixing lines connecting mafic enclaves with their host dacites converges in a sector of a silicic end-member composition (black rectangle) at ~68-73 wt%* SiO_2 *and 400-700 ppm Sr. Two sample-pairs of the lowest an highest Sr contents (highlighted in red) converge to a rhyodacitic composition at 69 wt%* SiO_2 *and 500 ppm Sr. TAP and CAL denote the samples.* ***b)*** *Modeled mixing lines connecting selected mafic enclaves with a assumed silicic end member composition, taken from PVA model (25e-8p) of 68.8 wt%* SiO_2 *and 615 ppm Sr. Mixing proportions labeled on the mixing lines denote nearly constant mixing proportions of the silicic to mafic end-members ranging between 6:4 and 7:3, respectively.*

7. DIFFERENTIATION REGIME OF TVC

The whole rock compositions of Taapaca eruptive products presented in the Harker-diagrams in Chapter 2 and this study show, that the Taapaca subvolcanic system produced remarkably uniform dacites magmas, repeatedly over a >1 Ma history of the TVC. On one side, the Taapaca dacites show a homogeneity manifested by only minor differences in major and trace element compositions; on the other side, there are significant compositional differences demonstrated by the basaltic andesitic mafic enclaves, representing the recharge magmas. The homogeneity extends to the uniform mineral assemblage and mineral chemistry found in all samples, as well as to the nearly uniform mixing proportions between the silicic and the recharge components (Chapter 2 section 5.3).

The long-lasting monotonous eruptive products of Taapaca volcano arise some questions:

- Which factors and processes play a major role in maintaining such a steady-state system?
- What are the physical conditions that rule the system?
- How does the subvolcanic plumbing system work?

Numerous petrographic features present in Taapaca rocks, such as mafic enclaves hosted in the dacites, bimodal amphibole and plagioclase compositions, phenocrysts disequilibrium textures are indisputable evidence for extensive magma mixing. The PVA-technique, designed for mixed magmatic systems, determines the major and trace element compositions, hence the geochemical character of the mixing end-members and defines quantitatively their contribution in the hybrid dacites. The geothermo-oxy-barometry presented in this study, and experimental approach (Botcharnikov et al. in prep.) complete the geochemical-statistical study providing a comprehensive information about the TVC magma mixing regime which may serve for detailed study of the rejuvenation/mobilization processes.

7.1. MAGMA MIXING REGIME

7.1.1. LIQUID LINE OF DESCENT (LLD) OF TAAPACA AND PARINACOTA SUITE

A series of experimental melt compositions of Botcharnikov et al. (in prep.) constrain a liquid line of descent (LLD) of Taapaca and Parinacota suite. Due to the geochemical affinity of Taapaca and Parinacota eruptive products, explained in Chapter 2, it is reasonable to discuss both LLDs together.

Figure 19 illustrates the LLD of Taapaca and Parinacota together with the compositions of the natural rocks, the end-members obtained from PVA (Chapter 2, model 25e-8p), and starting experimental compositions. The latter are: 1) the most mafic basaltic andesite lava from Parinacota volcano, sample PAR 11, characterized by the highest enrichment in LILE found in the Quaternary CVZ volcanics, one of the “baseline” compositions defined by Davidson et al. (1990), and 2) an average dacite composition of Taapaca, sample TAP 87-002.

Davidson et al. (1990) suggest, that due to the small variations in isotopic composition of Parinacota lavas, the differentiation trends for major and trace elements may be well explained through a fractionation in a closed system over the range of basaltic andesite to rhyolite. Concerning the strongly curved trends visible for e.g. Al_2O_3, Sr and Zr, they excluded simple mixing as a main differentiation process. However, based on Ni-Rb composition, Wörner at al. (1988) recognize both, fractionation and magma mixing dominated trends in the intermediate Parinacota lavas. Although the fractionating phases in the experimental study mimic the mineral assemblages found in the natural hybrid rocks (Botcharnikov et al., in prep.), the LLDs do not match the natural Parinacota-Taapaca trend for the major elements. In comparison to the curved LLD lines, indicating fractionation as a continuous process in a closed system under experimental conditions, the natural rocks show straight linear trends characterized by a compositional scatter. Such trends may be generated by extensive magma mixing, however, not a binary mixing, but rather between three components, as presented in Chapter 2 of this work, with a negligible involvement of the AFC processes.

In fact, a nearly curved Al_2O_3 vs. SiO_2 or MgO Parinacota trend, at a closer look shows rather compositional scatter in the range 57-68 wt% SiO_2 (and 1.2 wt% MgO), and a turnover at 68 wt%, which nota bene matches the rhyodacitic mixing end-member (RDEM). The fractionation-dominated sub-trend, identified by Wörner et al. (1988) within Parinacota andesites, represents most likely a fractionation of already hybrid baseline magmas. This sub-trend may be characterized by only a small extend of fractionation because these natural lavas do not reach compositions obtained from the experimental study.

Similar course of the LLD of Taapaca dacite and Parinacota rhyodacite to rhyolite rocks suggest that these magmas may undergo mainly fractional crystallization, most probably from the initial RDEM-like magmas. This implication is supported by the trace element characteristics of these rhyodacitic to rhyolitic lavas (see Chapter 4, section 5.2, Figure 6).

The LLDs of the Taapaca dacite and Parinacota basaltic andesites support the results of the PVA study, explaining the main variability in the Taapaca as well as other Quaternary CVZ volcanic centers through complex magma mixing processes and a minor shallow fractionation of already hybrid magmas.

7.1.2. EVIDENCE FROM MINERAL CHEMISTRY

7.1.2.1. Sanidine megacrysts

An occurrence of sanidine reaching megacrystic size (1.5-12 cm in a long axis) is an exceptional feature of Taapaca volcanic rocks (Johnson & Glazner, 2010). Detailed geochemical and petrological studies of Taapaca sanidines are presented by Wegner (2004), Zellmer & Clavero (2006), Banaszak (2007), and Higgins (2011). The results of Banaszak (2007) contradicts with other studies, and show that the uniform compositions of the low-Al amphibole and low-Fe plagioclase inclusions, and unvarying concentrations of trace elements (Mg, Cr, Ni, Co), oxygen and Sr(11) isotopic compositions determined in the strongly chemically and texturally zoned sanidines indicate crystallization in a chemically closed magmatic system. The sanidines therefore provide important piece of information about a type of a differentiation regime prevailing in the rhyodacitic RDEM end-member magma. Sanidine crystallization proceeded in the rhyodacite crystal mush, which has been only thermally, not chemically affected by repeated underplating of fresh hotter magma. Sanidine re-growth in the hybrid dacites occurs only as calcic plagioclase-overgrowths (rapakivi texture).

---

[11] Kiebala, unpublished data, used by Banaszak (2009)

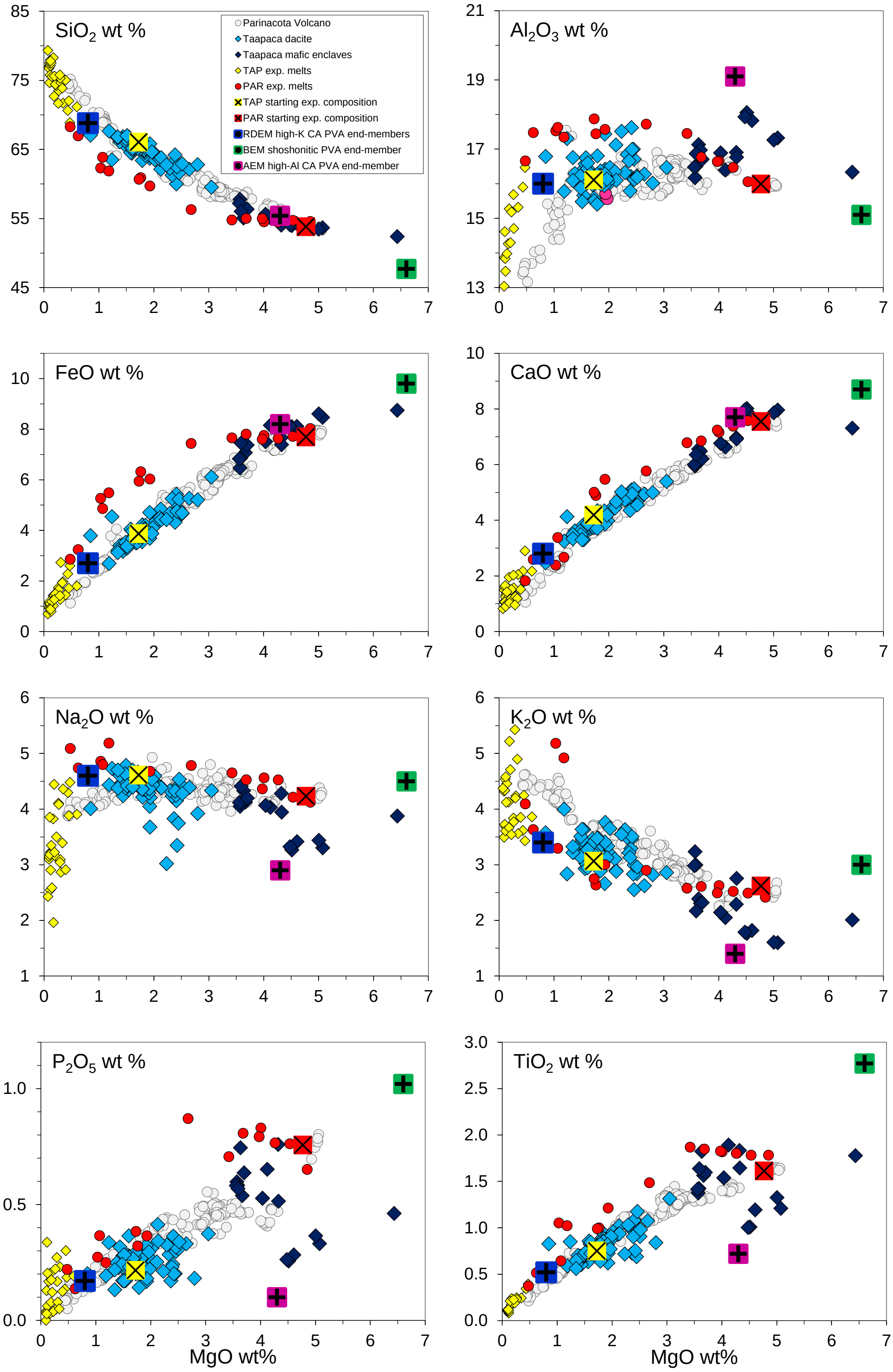

Figure 19. *Natural rocks and liquid lines of descent (LLD) constrained from experimental glass compositions, from equilibrium experiments of Botcharnikov et al. (in prep.) conducted on Taapaca dacite (yellow points) and Parinacota basaltic andesite (red points). Both LLDs meet at the composition close to the rhyodacitic end-member (RDEM) identified for Taapaca but they do not follow the whole rock trends. The magma mixing end-member compositions (crossed points) obtained by PVA (Chapter 2) explain sufficiently both, Taapaca and Parinacota whole rock trends.*

7.1.2.2. Two plagioclase populations

Figure 20 presents plagioclase compositions in Fe-An space from evolutionary stages II-IV, analyzed in Taapaca rocks. Fe-content discriminates the Taapaca plagioclase into two different groups, present either in the sanidine megacrysts or in the mafic enclaves. Both populations occur in the Taapaca dacites.

Concentration of Fe in plagioclase depends on numerous crystallization conditions such temperature, H_2O_{melt}, oxygen fugacity, also on An-content in plagioclase, but mostly on the concentration of the Fe in the melt from which the plagioclase crystallize (Ginibre et al., 2002; Ruprecht & Wörner, 2007; and references therein). The apparent differences in Fe concentrations found in the plagioclase from mafic enclaves and plagioclase inclusions in sanidine megacrysts support the effect of the melt composition on the Fe in plagioclase, which obscure the effect of other factors. The model of Ruprecht & Wörner (2007), which uses Fe-Anorthite patterns recorded in plagioclase, traces the effect of *thermal mixing* and decompression in a closed system versus compositional effect of *chemical mixing* in a chemically open system. Application of this model reveals three distinct differentiation modes from Taapaca plagioclase, plotting in the same An-range. The analysis of the Fe-An patterns in Taapaca plagioclase contributes therefore to the reconstruction of the dynamic of Taapaca magmatic system.

The first mode is represented by a horizontal trend in the Fe-An space ranging from An49-An23 at restricted low-Fe concentrations from 900 to 2000 ppm, represented by the plagioclase inclusions in sanidine megacrysts, together with the low-Fe population in the dacites. The highest anorthite contents of An>35 mol% at low-Fe concentrations are recorded in both, in the phenocryst cores and rims. Because the Fe-contents do not decrease with decreasing An-contents, this magmatic system may be primarily governed by thermal fluctuations, with only negligible contribution of fractional crystallization. Therefore, the horizontal trend suggests crystallization in a chemically closed but thermally variable system. Adopting the Fe partition coefficient value D^{Fe}=0.09 from Ginibre et al. (2002), the concentrations of 900-2000 ppm Fe in plagioclase require 1.3 to 2.9 wt% FeO in the melt. The highest value is consistent with the FeO-contents of the rhyodacitic end-member of 2.9 and 2.7 wt% obtained from simple mixing and PVA modeling.

The second mode, represented by plagioclase from mafic enclaves is defined by two separate groups of cores and crystal growth zones between cores and rims (An56-34), and rims (An38-17). Decreasing Fe concentrations with decreasing An contents reflect crystallization in small closed systems dominated by a compositional effect of fractional crystallization involving Fe-bearing phases (amphibole and magnetite). This effect have not been considered in the model of Ruprecht & Wörner (2007), nonetheless, beside the strong fluctuations of intensive parameters of crystallization evident from zoning of Mg-Hst, fractional crystallization would be the main process governing the Fe-An patterns in the plagioclase from mafic enclaves.

The third mode joins both, the chemical and thermal effects and represents large volume open system. The dacites contain both, the low- and high-Fe plagioclase populations, resulting from mixing between silicic and mafic magmas. Moreover, elevated Fe concentration of microlite and rims of low-Fe plagioclase reflect crystallization in hybrid magma. These drastic changes in Fe and An contents have not been found within the plagioclase phenocrysts. This observation indicates that magma mixing is a process triggering the eruption. Magma mixing takes place repeatedly, due to reproduction of exactly the same Fe-An trends in all Taapaca samples from all dacitic stages. However, each time a new batch of the recharge magma must have remobilized a new part of the silicic reservoir, because high-Fe contents have not been found within low-An plagioclase crystals. This observation is consistent with the invariable concentrations of transition elements in the sanidine megacrysts.

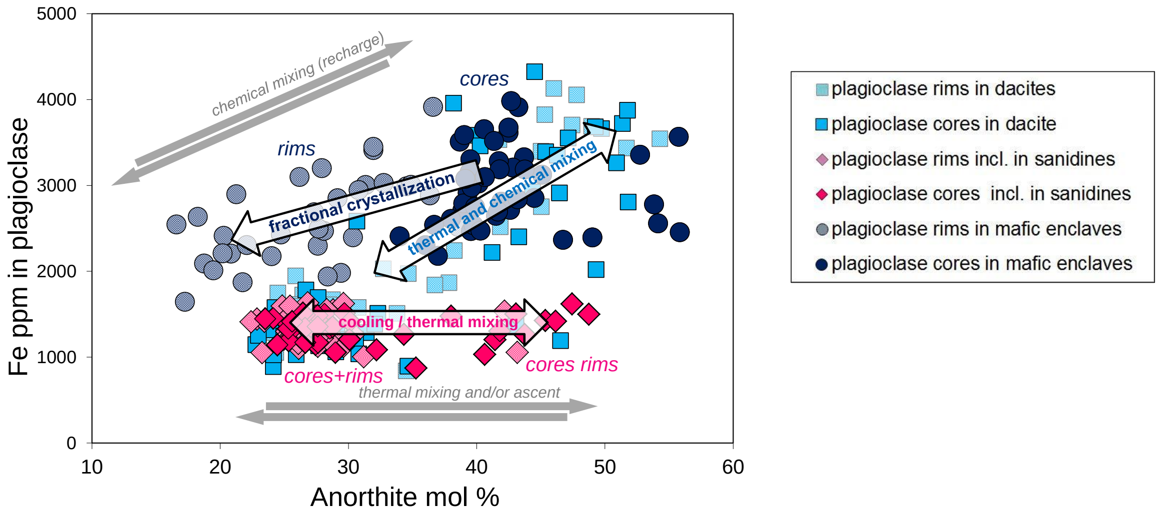

Figure 20. *Fe-An patterns of plagioclase found in Taapaca dacites, as inclusions in sanidine and in mafic enclaves, representing all dacitic stages (II-IV). The arrows indicating differentiation paths recorded in the Fe-An space are adopted from Ruprecht & Wörner (2007).*

7.1.2.3. *Two amphibole populations*

Two amphibole populations are ubiquitous feature in dacite lavas. Coexisting Mg-Hbl and Mg-Hst populations have been found in dacites characterized also by adakitic signature forming dacitic complexes, sharing petrographical similarities with Taapaca volcano (e.g. Longavi, SVZ, Rodriguez et al., 2007; NVZ, Cayambe, NVZ, Samaniego et al., 2006; Unzen, Japan, Sato et al., 1999). The existence of different amphibole species without a compositional passage in amphibole core compositions indicates hybrid character of the magma. However, Rodriguez et al. (2007) propose polybaric fractional crystallization to explain the generation of the Longavi dacites. Considering these two contrasting differentiation paths for generation of the two-amphibole dacites, the REE patterns of the amphibole may provide key information to define the differentiation paths.

The Chondrite-normalized REE contents of Taapaca amphiboles reveal two quite distinct patterns for Mg-Hbl and Mg-Hst (Figure 21). Mg-Hbl shows homogenous patterns in all samples characterized by LREE-enrichment and a continuous depletion from La to Lu with light Eu-anomaly. A spoon-like shape in heavy REE (HREE) mimics the HREE pattern of the rhyodacitic end-member, from which the Mg-Hbl crystallized. The REE patterns of Mg-Hbl inclusions in sanidines overlap with Mg-Hbl from the host dacites.

In contrast to Mg-Hbl, the Mg-Hst shows an increase in LREE from La to Nd, and a sharp decrease from Nd to Lu. This characteristic REE pattern is observed in amphibole (hastingsite and pargasite) and clinopyroxene found in mafic alkaline lavas, as presented by e.g. Shaw & Eyzaguirre, (2000) and Viccaro et al. (2007); and clinopyroxene from other alkaline lavas (Eby et al., 1998; He et al., 2013). Calculated REE patterns of parental magmas, presented in the mentioned studies, from which these amphiboles and clinopyroxenes could crystallize, are strongly fractionated, showing a LREE enrichment and HREE depletion. Such steep REE patterns are comparable with the BEM shoshonitic Taapaca end-member described in Chapter 2, Figure 5. This observation points to the origin of the Mg-Hst rather from the BEM-type end-member composition, characterized by strong alkaline affinity in comparison to other Taapaca end-members.

It must be noted, that amphibole carried in low-Sr mafic enclaves, which are dominated by the high-Al calc-alkaline AEM end-member show overall complete amphibole breakdown. This is also observed in the low-Sr Parinacota basaltic andesite lavas. Thereby, the amphibole composition, which might have crystallized from the AEM end-member or baseline mafic magmas dominated by the AEM cannot be determined. Based on amphibole compositions representing AEM-dominated lavas of Lascar volcano (unpublished own data) and experimental study of Stechern et al. (in prep.), high-Al and low $(Na+K)_A<0.5$ *tschermakite* are presumed to occur in the low-Sr Taapaca mafic enclaves, hence also low-Sr Parinacota lavas.

In view of the *alkaline-type* REE pattern found in the Mg-Hst in high-K calc-alkaline Taapaca lavas, further investigations are required to find out, if an occurrence of two distinct amphibole populations may occur via fractionation. The melt composition from which the amphibole crystallizes, is in this study regarded as a first-order factor governing the amphibole composition, see section 7.2.1. Therefore, the REE patterns of the amphiboles could serve as magmatic fingerprints, showing a geochemical character of magmas involved in the petrogenesis.

An occurrence of Mg-Hst rims on Mg-Hbl and vice versa (Figure 6a, b), suggests that the first stage of magma mixing may represent rather mingling, which forms compositional magma domains, where the amphibole rims crystallize. The amphibole rims representing the other population than the cores, occur in both, in the dacites and the mafic enclaves; however the Mg-Hbl transferred from the rhyodacite host into the mafic enclaves show complete breakdown and coherent Mg-Hst rims, and can be recognized due to their crystal sizes >300 µm (Figure 5d).

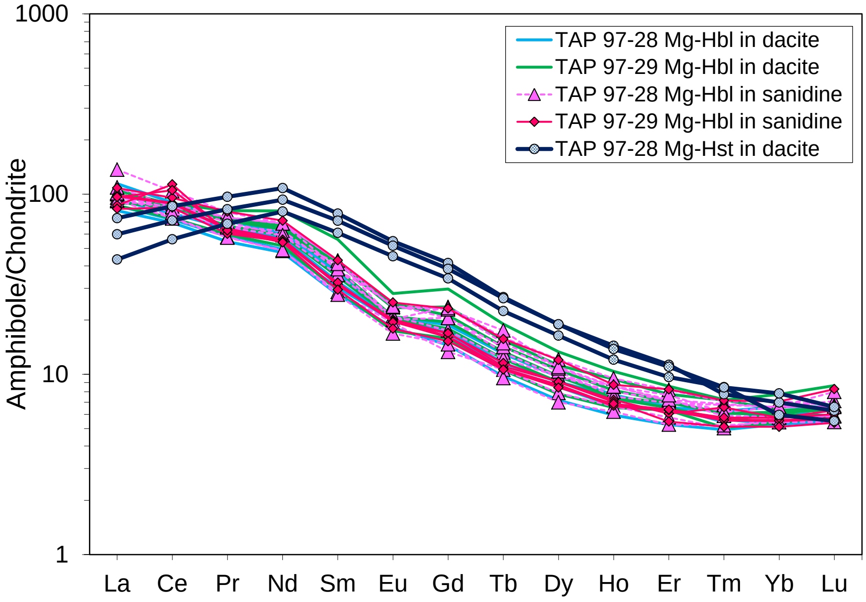

Figure 21. *Rare-earth-element (REE) patterns of magnesiohornblende (Mg-Hbl) phenocrysts in two selected dacites and sanidine megacrysts found in these dacites, and magnesiohastingsite (Mg-Hst) microcrysts in dacite (normalized to chondrite 1 of Sun & McDonough, 1989). Small crystal sizes of Mg-Hst account for low number of reliable analysis obtained by Laser-Ablation ICPMS.*

7.1.3. PETROLOGY OF MAGMA MIXING PROPORTIONS OBTAINED FROM THE PVA STUDY

Section 5.3 of Chapter 2 presents mixing proportions of the three end-member magmas in Taapaca rocks. Invariable geochemical signatures determined in sanidine megacrysts indicating crystallization and stagnation in a chemically closed system, and a uniform composition of several mafic enclaves found in one lava dome give evidence that single mafic magma inputs intruding into silicic reservoir, produced the monotonous Taapaca dacites. Among three PVA models based on different number of variables and samples used in the calculations, model (25e-8p) including only dacite-mafic enclave pairs, is consistent with petrographical and geochemical observations (Figure 8b of Chapter 2). The end-member proportions in the single Taapaca samples, presented in the mixing triangle, define two-stage magma mixing, which explains the binary petrographical and geochemical features in three end-member system of the Taapaca dacites.

As recognized in the Chapter 2, the first stage comprises shoshonitic, high-Sr (BEM) and high-Al calc-alkaline, low-Sr (AEM) end-members, forming hybrid mafic recharge magmas (BEM+AEM); the second stage is a commingling of the mafic, already mixed (BEM+AEM) component and the silicic, high-K calc-alkaline (RDEM) component. The existence of the mafic enclaves in the dacites reflects a complex process of magma commingling (mingling + mixing), forming two definite products, the basaltic andesite to mafic andesite enclaves, and the dacite simultaneously. These both components, however, consist of chemically and petrographically homogenous mixtures of the three end-members. Thus, the magma mingling and magma mixing are two overlapping processes.

7.1.3.1. Thermal differences of the mafic end-member magmas

To examine thermal differences between BEM and AEM magmas, prior to the first magma mixing stage, the olivine-liquid thermometer of Putirka (2008) and graphical approach of the olivine liquidus by Roeder & Emslie (1970) and Putirka et al. (2007, 2008b) can be applied. We use the olivines found in the high- and low-Sr Parinacota lavas, in connection with MgO-FeO mol fractions of the BEM and AEM Taapaca end-members. However, a strong pressure-dependence of these thermometers does not provide substantial results, due to the unknown pressure and depth of olivine crystallization. Nonetheless, a rough approach by the graphical thermometer of Roeder & Emslie (1970) reveals crystallization temperatures slightly above 1200°C for Fo81 from the high-Sr BEM magma and slightly below 1100°C for Fo76 from the low-Sr AEM magma at 3 kbar. At 10 kbar both approximations move toward ~20°C higher T. Using thermometer of Putirka (2007), (included in Putirka 2008), the crystallization temperatures are: 1210° and 1116°C at 3 kbar; 1248° and 1153°C at 10 kbar, respectively. This approximation suggests that the AEM-type may be ~100°C colder than the BEM-type magmas entering the volcanic plumbing system.

Unfortunately, differences in crystallization conditions of high- and low-Sr mafic enclaves are not possible to determine directly because all investigated low-Sr mafic enclaves show complete amphibole breakdown; moreover, the absence of ilmenite in the mafic enclaves precludes the application of Fe-Ti oxide geothermo-oxy-barometry. Indirectly, there is an indication for the intensive parameter of the AEM-dominated magmas: as mentioned in section 7.1.2.3, experimental study of Stechern et al. (in prep.) in connection with the PVA results and amphibole chemistry of Lascar volcano (own data) suggests, that tschermakite may be an amphibole species crystallizing from the AEM-type end-member magmas. These amphiboles show crystallization temperatures in a range of 870 to 962°C from the R&R2011 method (own data), temperatures slightly lower than that obtained from the cores of Mg-Hst in Taapaca rocks.

7.1.3.2. Two commingling courses in monotonous Taapaca magmas

There are two separate groups of mafic enclaves defined by the distinct proportions of the BEM (high-Sr) and AEM (low-Sr) end-members as well as incorporated silicic material. Using the term of high- and low-Sr mafic enclaves from section 4.2.1 in Chapter 2, the high-Sr MEs contain higher proportions of the silicic (RDEM) component, reaching 1 to 50%, than the low-Sr MEs containing 0.5 to 6.1% of the RDEM. Likewise, the dacites hosting the high-Sr enclaves show higher proportions of the silicic component reaching up to 86% in comparison to maximally 64% determined in the dacites hosting low-Sr enclaves. Based on the major and trace element composition, the latter dacites have been defined as the *subgroup dacites* and show slightly lower SiO_2 contents (~62 to 64 wt %) in comparison to the *main dacite group*.

Generally, the mafic enclaves dominated by the low-Sr AEM end-member show shift toward less silicic composition of the basaltic andesite - dacite system relatively to the high-Sr BEM dominated recharge, forming two different commingling courses. This observation indicates differences in the physical conditions governing the magma mixing/mingling processes involving BEM or AEM dominated recharge. A simplest interpretation suggests that the high-Sr dominated mafic input requires lower proportions to rejuvenate the rhyodacite reservoir. This may result from differences in the initial temperature and volatile content of the recharge magma, two major factors governing the mixing processes (e.g. Huppert et al. 1982; Sparks & Marshall, 1986) besides the crystallinity (e.g. Marsh, 1981). The crystallization temperatures of olivine reveal a difference of ~100°C between the hotter high-Sr BEM and colder low-Sr AEM end-member magmas. Differences in the H_2O_{melt} content between BEM and AEM may be roughly estimated form amphibole using R&R2011 method. The tschermakites from AEM-dominated lavas of Lascar volcano yield 4-6 wt% H_2O_{melt}, higher than the BEM-dominated magmas showing 3-4 wt% H_2O_{melt}, values obtained from amphibole hygrometer of R&R2011.

Summarizing, the results of the mixing proportions in connection with the GTOB data show that higher amounts of the colder and wetter mafic input are required to rejuvenate and remobilize the stagnating silicic magma, compared to the hotter and drier mafic input. The hotter and drier input involves more silicic magma during magma mixing than the colder and wetter magma and indicates more efficient mixing course.

7.2. GEOTHERMO-OXY-BAROMETRY OF TVC MAGMAS

7.2.1. WHAT DOES GOVERN AMPHIBOLE COMPOSITIONS

Amphibole is a main mineral phase that allows estimation of the pre-eruptive intensive parameter in Taapaca magmas. The strong compositional variability of amphibole, even within one population arise questions about the reliability of the P-T-fO_2-H_2O_{melt} results.

7.2.1.1. Magma composition – primary factor influencing amphibole composition

The results of this study show that the chemistry of calcic amphibole in calc-alkaline magmas primarily depends on magma composition from which the amphibole crystallized. Spear (1981) and Sisson & Groove (1993) note, that Al content in amphibole is controlled by whole rock composition. Féménias et al. (2006) link different Ca-amphibole species to the calc-alkaline magmatic series, due to the magmatic differentiation from basalt to rhyolite, in order kaersutite→ Ti-pargasite→ pargasite→ Ti-magnesiohastingsite→ magnesiohastingsite→ edenite→ tschermakite→ magnesiohornblende. Ridolfi et al. (2010) present three main amphibole-species in calc-alkaline magmas for variable magma compositions in terms of SiO_2 contents: magnesiohastingsite (Mg-Hst) in a range of 52-64 wt% SiO_2, tschermakite ~54-70, and magnesiohornblende (Mg-Hbl) >70. The experimental Mg-Hst and Mg-Hbl, species relevant for this study, selected for the thermo-oxy-barometric formulations by Ridolfi & Renzulli (2011), have been synthesized in equilibrium with basaltic andesites or dacite-rhyolite glasses, respectively.

There are lines of evidence summarized below, which suggest a link between the three main Ca-amphibole species and a type of the three end-member magmas, which occur in the CVZ.

A) Natural amphibole compositions

1) Taapaca high-Sr mafic enclaves and Parinacota lavas, dominated by the BEM-type magma, contain the high-Al-Ti magnesiohastingsite (Mg-Hst). 2) The most silicic Taapaca and Parinacota rocks representing the RDEM-type end-member magmas contain low-Al-Ti magnesiohornblende (Mg-Hbl). 3) High-Al and low-Ti tschermakite are present in rocks of Lascar volcano, representing the prevailing AEM-type end-member. The amphiboles found in the low-Sr mafic enclaves of Taapaca, as well as low-Sr Parinacota lavas, dominated by AEM-type end-member show complete breakdown that prevent the determination of the amphibole composition. This finding suggests that this amphibole may represent tschermakite, which may not be stable during mixing with the hotter and drier BEM type magma, or it undergoes breakdown during magma ascent, due to decreasing pressure.

B) Experimental amphibole compositions

1) The experimental amphiboles synthetized from BEM-type basaltic andesite (Parinacota) by Botcharnikov et al. (in prep.) are Mg-Hst. 2) Mg-Hbl could be reproduced by Botcharnikov et al. (in prep.) from RDEM-dominated Taapaca dacite. 3) The experimental amphiboles synthetized by Stechern et al. (in prep.) from AEM-type basaltic andesite (Lascar) at the same P-T-fO_2 as at Parinacota experiments, are tschermakite.

C) Differences between single mafic enclaves

The cation-site variations in Taapaca amphiboles (Figure 7) reveal compositional differences in composition of Mg-Hst cores from different mafic enclaves. These differences correlate with other proportions of two mafic end-members involved in the petrogenesis of these mafic enclaves. For instance, Mg-Hst from samples characterized by higher proportions of the high-Al AEM end-member show higher Al^{TOT} in the amphibole and lower K contents than Mg-Hst from mafic enclave dominated by the shoshonitic BEM end-member.

The observations A, B, and C require a detailed examination in connection with REE patterns of amphibole. The occurrence of these three amphibole species could be used as a fingerprint of the end-member type magmas involved in the petrogenesis. Furthermore, it could be a basis for a verification and improvement of the GTOB-formulations based on the amphibole compositions, which are perhaps more affected by relations between different major elements in the melt, for example Al/Si ratio or Na_2O contents mentioned by Sisson & Groove (1993), than the intensive parameter of crystallization. Thus, the relative P-T-fO_2-H_2O_{melt} variations may rather reflect the differences in the melt compositions and not necessarily the intensive parameter of crystallization.

7.2.1.2. Intensive parameter - cation substitutions used in the GTOB

It is well known, that compositional differences within one amphibole species are caused by a general ability of introduction of a large number of cations, governed by variable, coupled iso- and heterovalent substitution mechanisms, demanding charge balance (Hawthorne, 1983; Leake et al.

1997). The variations in cation sites occupancy are connected to changes in the intensive magmatic parameters (e.g. Spear, 1981; Blundy & Holland, 1990; Ernst & Liu, 1998; and references therein), which influence the introduction of single components in the amphibole structure, depending on valence and ion radius.

In an isochemical system, changes in amphibole composition caused by changes in intensive parameter involve numerous cations simultaneously. Furthermore, the same cations are sensible for more than one parameter. 1) Ti, Na, K, Al^{TOT}($^{[4]}Al$) increase, and Si decreases with increasing temperature; Al^{TOT}($^{[6]}Al$) increases with increasing pressure; Si, Mg, Fe^{3+} and Mn increase and Al^{TOT}($^{[6]}Al$), Fe^{2+}, Ti, Na, K decrease with increasing fO_2 (Spear 1981; Blundy & Holland, 1990; Ernst & Liu, 1998; Ridolfi et al., 2010, Ridolfi & Renzulli, 2011 and references therein). The natural geological processes are characterized by simultaneous changes of the intensive parameter of crystallization. Hence, the effects of changes of the physico-chemical parameters on the amphibole composition overlap. The prominent example is the Al^{TOT} content. Successive studies have shown that Al^{TOT} depends not only on pressure but also temperature (e.g. Holland & Blundy, 1994), oxygen fugacity (Simakin et al., 2009) as well as magma composition (e.g. Spear, 1981; Sisson & Grove, 1993).

The most frequently discussed substitution vectors defined on the basis of the idealized tremolite formula comprise pressure-dependent $Mg_{-1}Si_{-1}{}^{[4]}Al^{[6]}Al$ tschermakite vector, with participation of Mg^{2+} and tetrahedrally and octahedrally coordinated Al^{3+}. This substitution mechanism is a basis for geobarometer formulations based on Al total (Al^{TOT}) content in amphibole (e.g. Hammarstrom & Zen, 1986; Johnson & Rutherford, 1989). However, when Al^{TOT} from different amphibole species is used, it does not produce reliable results. As broadly discussed (e.g. Blundy & Holland, 1990; Anderson & Smith, 1995; Ridolfi et al. 2008, 2010; Ridolfi & Renzulli, 2011), Al^{TOT} content in amphibole therefore cannot be directly related to differences in crystallization pressure, because of strong coupled T-, fO_2- and Al_2O_{3melt}-dependence of Al^{TOT} in amphibole. Temperature and oxygen-fugacity sensitive Ti-tschermakite ($Mg_{-1}Si_{-1}TiAl$) and ferri-tschermakite ($Mg_{-1}Si_{-1}Fe^{3+}Al$) substitutions involve also Mg and Al, masking the effect of single intensive parameter (P, T and fO_2) on amphibole chemistry. Additionally, Blundy & Holland (1990), And Holland & Blundy (1994) explain the changes in Al^{TOT} in amphibole by edenitic exchange ($Na^{[4]}Al\square_{-1}Si_{-1}$) in reactions participating plagioclase. Well defined correlation between $Na^{(A)}$ and $K^{(A)}$ vs. $^{[4]}Al$ in the Mg-Hbl of Taapaca (Figure 7g, i) corresponds to the strongly temperature-dependent edenite exchange (Blundy & Holland, 1990). Therefore, higher crystallization temperatures are inevitably expected from the Mg-Hst defined by $(Na+K)_A>0.5$.

The cation-variation diagrams presented in Figure 7 display a large variability of the cation-site occupancy in the Mg-Hst, reflected as pronounced textural-chemical zoning of the Mg-Hst, in comparison to rather strictly defined trends in relatively homogenous the Mg-Hbl. A considerable chemical zoning in the Mg-Hst (Figure 6c) is a typical feature of Mg-Hst, reported by e.g. Sato et al. (2005), and Féménias et al. (2006). The Mg-Hst displays therefore an amphibole species that is very sensible to any changes during crystallization, in any magmatic systems. To establish which factors play a major role, and how they influence the GTOB results, further studies are required.

7.2.2. *DIFFERENTIATION REGIME REFLECTED BY INTENSIVE PARAMETER OF CRYSTALLIZATION*

An application of different GTOB methods requires an integration of the obtained P-T-fO_2-H_2O_{melt} data to create a consistent picture of the differentiation regime of the Taapaca magmas. In terms of temperature, this study presents geothermobarometry data obtained from the single-phase amphibole thermometry, amphibole-plagioclase and magnetite-ilmenite equilibrium crystallization. The discrepancy between the crystallization temperatures obtained from different geothermometers may reveal different crystallization intervals or reflect uncertainty of the thermometers.

Summarizing the T-results from all methods for rhyodacite reservoir, this magma represents a cold upper crustal silicic magma body, which stagnate at most probable temperature interval, in the average, of 700-800°C, an overlapping range estimated from all applied geothermometer. Such thermal conditions at shallow crustal level, in connection with high H_2O_{melt} of 6-8.5 wt%, promote suppression of the liquidus, thereby extensive crystallization leading to the “viscous death”. High crystallinity and magma viscosity hinder fractionation (different forms of crystal-liquid separation) and hinder vertical zonation of the magma reservoir. This leads to formation of a uniform mineral assemblage and mineral chemistry, showing consistent fractional crystallization trends of amphibole and plagioclase through all dacitic stages of Taapaca magmas.

The temperatures estimated from Fe-Ti oxide embedded in the dacite matrix (ilmenite is absent in the mafic enclaves) show temperatures between 780 and 900°C (mainly 840-900°C), a range between the temperatures obtained from two amphibole populations. Due to fast equilibration of Fe-Ti oxide within a few days to weeks (Venezky & Rutherford, 1999), these temperatures probably represent the latest pre-eruptive conditions of the dacites, resulting from magma mixing between hot mafic and cold silicic magmas.

The highest crystallization pressure of 250-300 MPa, obtained from Mg-Hst crystal cores representing the mafic recharge magmas corresponds to the highest P-values obtained from Mg-Hbl, representing the rhyodacite reservoir (Figure 11). Assuming the crystallization pressure equals the lithostatic pressure, the pressure of 250-300 MPa correspond to 9.4 and 11.3 km depth(12). The maximal depth most probably represents the lower limit of the silicic magma reservoir. This geobarometry result, showing nearly equal P-values for two different amphibole populations, characterized by quite different Al^{TOT} contents, suggests that the mafic recharge starts to crystalize just in the shallow crust. According to Hora et al. (2009), showing evidence for a fast crustal transit times of the mafic magma in Parinacota subvolcanic system, we can assume a fast transit of the mafic input in the Taapaca subvolcanic system. At the depth of ~11 km started the accumulation and mafic underplating of the rhyodacitic reservoir followed by magma mixing. The crystallization of the Mg-Hst, and thus an extensive crystallization of the mafic recharge magma started at the contact

---

[12] Depth calculation based on the crust density of 2700 kg/m³ (Lucassen et al. 2001)

of the mafic magma with the rhyodacite reservoir. By contact with the silicic magma reservoir, the mafic recharge cools rapidly (e.g. Bachmann & Berganz, 2006; Huber et al., 2011) to the amphibole liquidus. Simultaneously, it incorporates silicic material during magma commingling, omitting the olivine liquidus. This mixing scenario may cause the absence of olivine in the basaltic andesitic enclaves, which are, in contrast, present in the geochemically related basaltic andesites of Parinacota volcano, reaching the surface as olivine-bearing lavas (see also Chapter 4, section 7.2.2).

Outside the crystal cores, in Mg-Hst crystal mantles and rims, the pressure values exceed the range obtained from the cores, showing up to 420 MPa. Simultaneously, the same analysis of Mg-Hst showing the highest P, reveals increasing H_2O_{melt}, and a tendency to more reduced conditions in comparison to the cores (Figure 13). It must be noted, that the pressure values exceeding 300 MPa are only recorded in the Mg-Hst from the mafic enclaves and have not been found in the dacites. This observation suggests several explanations, which may cause such remarkable compositional variability of Mg-Hst, and consequently the strong variability in P-T-fO_2 conditions in the mafic enclaves: 1) extensive changes of the magma composition during magma mixing in the small-volume system, 2) strong variability of T, fO_2 and H_2O_{melt}, leading to persistent disequilibrium conditions, which are not considered in the GTOB formulation, and 3) increasing pressure (overpressure) during magma mixing caused by i.a. volatile exsolution. The development of the overpressure conditions during magma mixing depends on the thermal equilibration condition of both magmas, as well as volatile content in the residual and recharge magma, their solubility, volume fraction and crystallinity (Folch & Martí, 1998). Although Huber et al. (2011) quantify the overpressure in a reactivated mush in connection with the intrusion of mafic magma in the silicic reservoir to values of $\Delta P \sim 10^7$ Pa(13), the mafic enclaves may undergo another overpressurization history than the silicic reservoir. However, the relatively low ΔP during reactivation of the mush suggest that rather other factors overwhelm the pressure effects.

Physical conditions in mafic enclaves tend to an equilibration with the conditions prevailing in the rhyodacite reservoir. This tendency may explain the simultaneous increase of H_2O_{melt} recorded at the Mg-Hst rims and decrease of oxygen fugacity toward lower ΔNNO values. Generally, water acts as an oxidation agent and relatively high water contents of the magma are accompanied by higher ΔNNO, as observed i.a. for water-richer andesites of Lascar volcano in comparison to drier andesites of Parinacota volcano (Lascar unpublished data). However, Burkhard (2005) find out, that degassing and oxidation of magma are not related directly. Moreover, as discussed by e.g. Kelley & Cottrell (2009), H_2O requires efficient dissociation and removal of H_2 to induce magmatic oxidation. This process may be prevented in the small-volume magmatic enclaves of increasing viscosity during proceeding crystallization. The large-volume rhyodacitic reservoir dominates the equilibration path of the mafic enclaves. The fO_2 obtained from magnetite-ilmenite pairs show red-ox conditions overlapping with the fO_2 of Mg-Hbl. During magma mixing, the T- fO_2 and H_2O_{melt}, apparently tend to achieve equilibrium, dominated by the large-volume rhyodacite magma.

---

[13] Critical melting-induced threshold ΔP value at which fracturing of mush reservoir starts.

Strong fluctuations of the intensive parameters of crystallization observed in the amphibole crystallized in the mafic enclaves result most probably from rapid cooling of the mafic enclaves and equilibration processes between mafic input-magma and the rhyodacitic reservoir. Such unstable conditions are indicated by a large range of cation-site occupancy illustrated in Figure 7, found in Mg-Hst. They do not define clearly any substitution vectors as visible for Mg-Hbl. Because fluctuations of T, H_2O_{melt}, fO_2, and melt composition in the mafic enclaves probably dominate over pressure changes during magma mixing and mingling, higher pressure-values obtained from the barometer may reveal a byeffect on the Mg-Hst composition.

8. LINK BETWEEN TVC AND PLUTONIC REALM

"The link between plutonic and volcanic rocks is the key to understanding the formation and evolution of magmatic systems" (Reubi & Blundy, 2009) and "integration of plutonic and volcanic data sets is a step toward better understanding of the processes that lead to the observed petrologic diversity on our planet" (Bachmann et al., 2007).

8.1. COMPOSITIONAL LINK BETWEEN VOLCANIC AND PLUTONIC REALM RECOGNIZED IN TAAPACA (AND PARINACOTA)

The compositional binary system of Taapaca includes the silicic end-member of ~69 wt% SiO_2 and hybrid mafic end-member of ~53 wt% SiO_2. These two compositions represent "peak compositions" of arc-plutonic and arc-volcanic whole rock compositions in terms of the silica content, respectively, as presented by a global whole rock data compilation of Reubi & Blundy (2009). The authors emphasize that both silicic and basaltic magmas ascent into the shallow crustal levels to produce intermediate, mostly andesite rocks via commingling processes and these effective mixing/mingling processes obscure the role of the silicic magmas in the petrogenesis of intermediate volcanoes.

With regard to petrography, mineral assemblage, major element, and mineral chemistry Taapaca dacites represent monotonous intermediate magmas comparable with the large-volume *Monotonous Intermediates* (MIs), (Hildreth, 1981; Bachmann et al., 2002, 2007) ignimbrites and granodioritic plutons. Bachmann et al. (2007) emphasize the textural and mineralogical similarities of the large volume MIs magmas to the granodioritic plutons and refer the small-volume crystal-rich volcanic units, corresponding to Taapaca rhyodacite, as remobilized proto-plutons.

Whereas Taapaca volcano consists solely of the hybrid dacites, one large-volume unit of the neighboring Parinacota volcano consists of the same type of the hybrid dacites (unit: Border Dacite, Hora et al., 2007), compositionally and petrographically directly comparable with the Taapaca rocks. Such similarities suggest that the same magma differentiation as well as accumulation, rejuvenation, and mobilization processes may be involved in the petrogenesis of the Parinacota dacites (and silicic andesites), and a presence of a proto-pluton below the stratovolcano as well. This observation implies that the link between volcanic and plutonic realm is not limited to the large volume events and may occur even within a stratovolcanic activity. This supports the hypothesis presented in numerous studies, e.g. Glazner et al. (2004), Bachmann et al. (2007 and references therein), Reubi & Blundy (2009).

8.2. SANIDINE MEGACRYSTS FIRST-ORDER LINK TO PLUTONIC REALM

K-feldspar megacrysts are a characteristic feature of many granitic and granodioritic rocks, they commonly lack in volcanic rocks (Vernon, 1986). Taapaca is only one worldwide documented volcano, which contain sanidine of megacrystic sizes hosted in the dacites (Johnson & Glazner, 2010). However, there are other known examples of dacite eruptions from the CVZ, where sanidines, significantly larger than other phenocrysts in the dacites, have also been found: Sara-Sara volcano (Wörner pers. communication), the “Border Dacite” unit of Parinacota volcano.

K-feldspar megacrysts represent late plutonic magmatic stage (Swanson, 1977; Vernon, 1986; Vernon & Patterson, 2008; Johnson & Glazner, 2010; Higgins, 2011) giving a first-order similarity of Taapaca dacites to the plutonic realm in the granodiorite, the plutonic chemical counterpart of the dacite. Among different hypotheses about early vs. late crystallization of the megacrysts (Mehnert & Buesch, 1981; Vernon & Paterson, 2008), a crystal size distribution (CSD) study of microcline of the Cathedral Peak granodiorite by Higgins (1999), showing concave-downward CSD curves (lack of the smallest crystals), suggests that a crystal coarsening caused by thermal cycling forms the megacrysts. Simakin & Bindeman (2008) show that concave-downward CSDs result from a sequence of dissolution and crystallization events caused by temperature fluctuations in the natural magmatic open-systems. Such dissolution and regrowth zones are typical feature of Taapaca sanidine (Wegner, 2004; Banaszak, 2007). Johnson & Glazner (2010) explain the existence of K-feldspar megacrysts in Tuolumne Intrusive Suite (granodiorite pluton) by a late-stage textural coarsening(14) during thermal cycling. Supported by experimental evidence of crystal coarsening in an oscillating temperature field, Mills et al. (2011) emphasize the role of this process driven by external temperature oscillations that are common in the natural systems. Moreover, small amounts of large sanidine coexist with large amounts of small plagioclase in the Taapaca dacites. This suggests thermal conditions providing euhedral megacrystic sanidine growth from a melt at temperatures around sanidine liquidus. Such thermal conditions induce a small nucleation density and high growth rates, which produce large crystals (Swanson, 1977).

Higgins (2011) proposes the textural coarsening as a process generating sanidine megacrysts in the Taapaca dacite. This explanation is consistent with the observations described in the study of Banaszak (2007), which recognizes three types of Ba-zoning in Taapaca sanidine connected to temperature fluctuations, however, in a chemically closed system. Such crystallization environment contradicts with the crystallization model of Higgins (2011) assuming frequent mafic input into the silicic reservoir responsible for the reheating of the magma. Nevertheless, Higgins (2011) refers to the uniform Sr and O isotopic data of Banaszak (2009) emphasizing that the magma mixing was not an important process in the generation of the sanidine megacrysts.

---

[14] The textural coarsening caused by dissolution-crystallization cycle differ from the Ostwald ripening occurring at constant temperatures, this subject is discussed by Simakin & Bindeman (2008) and Mills et al. (2011).

Temperature fluctuations inducing the crystal coarsening in Taapaca reservoir must have oscillated around a K-feldspar liquidus. The three textural types of sanidine zoning, showing different dissolution and regrowth patterns indicate variable amplitude of the temperature variations. Mafic underplating is considered as a principal heat source inducing a source of reheat and partial re-melting as well as a conductive instability at the base of magma reservoir (e.g. Bachmann et al., 2002; Bachmann & Berganz, 2006; Huber et al., 2009). Episodic underplating events of a hot mafic magma may allow the cyclic thermal fluctuations around the K-feldspar liquidus. However, this scenario would require numerous mafic underplating events, to produce multiple resorption-regrowth zones observed in the sanidine megacrysts, which do not intrude into the silicic magma. There is a second potential heat source, which may cause low-amplitude thermal fluctuations during the stagnation of the rhyodacitic magma in the shallow crust, recorded as weak resorption events, in form of fine scale oscillatory zoning: an incremental input and amalgamation of silicic magma pulses.

An incremental input of the silicic magma is supported by the results of crystal residence times obtained from Ba diffusion profiles in sanidine, found in different eruptions (Banaszak, 2007). The sanidine residence times(15) obtained from Ba-diffusion profiles at 800°C do not yield increasing values with time and form a nearly horizontal trend and are comparable in all investigated samples. The longest crystal residence times are approximately 50 ka, recorded in the sanidine erupted between 800 and 10 ka ago. If the sanidine crystals from the youngest eruptions would have crystallized simultaneously with the crystals erupted earlier, they should record longer residence times, additionally affected by succeeding thermal fluctuations, “accelerating” the diffusion and “extending” the residence times .

It needs a separate investigation, if the thermo-rheological conditions during the amalgamation of the rhyodacite magma batches may allow complete or at least an incomplete mixing between fresh silicic inputs and stagnating older batches, and heating the sanidine-bearing reservoir to the temperatures oscillating around the sanidine liquidus.

8.3. INCREMENTAL MAGMA EMPLACEMENT AND EXTRUSION

An incremental intrusion and amalgamation of nearly monotonous, only subtly geochemically distinguishable batches of the silicic magma has been documented from, for instance the sanidine-bearing Tuolumne granodioritic intrusion (Coleman et al., 2004) and proposed for the formation of the large-volume monotonous intermediate Fish Canyon magma (Huber et al., 2009). An incremental growth of the large-volume silicic magmatic systems is postulated in numerous studies (e.g. Petford, 1996; Petford et al., 2000; Glazner et al., 2004) as a common process. Also small-volume, crystal-rich silicic volcanic systems sharing textural and geochemical features with Taapaca dacites has been interpreted as “proto-plutons” (Bachmann et al., 2007 and references therein). Thus, an incremental addition of silicic magma from the deep crust to a growing Taapaca silicic reservoir

---

[15] The oldest residence times measured in the representative sanidine crystals do not show the real residence times of the crystals due to: 1) dissolution processes destroying the earliest Ba-jumps in the crystals, 2) temperature fluctuations affecting the diffusion, hence the residence times determined for one definite T-value, and 3) availability of measureable profiles.

via dykes (Petford, 1996) may act as a heat source during stagnation of the silicic magma in the upper crust.

The subvolcanic system of Taapaca may represent small-volume and steady injections of the silicic crustal melt into the shallow crust, succeeding over 1 Mio years. Lipman (2007) infers from a rapid emplacement of the silicic magmas forming large-volume volcanic eruptions and incrementally emplaced plutons, that the volcanic and plutonic realms involve fundamentally different evolutionary processes. The example of Taapaca volcano shows a third possible scenario resulting from a slow and continuous silicic input accompanied by a sufficient large but sporadic mafic input, which hinder a formation of a pluton. Therefore, the critical factor affecting and governing the plutonic formation vs. volcanic activity is perhaps connected to the input rates of the mafic recharge magmas at the same location and their ability to rejuvenate and remobilize the proto-plutons, which reached the rheological lock-up point. Hence, the incremental emplacement accompanied by an incremental extrusion of the crystal-rich silicic magmas provides an insight into the evolution and differentiation processes of shallow crustal reservoirs, linking the plutonic and volcanic realms.

8.4. REJUVENATION, COMMINGLING AND MOBILIZATION OF THE SILICIC TAAPACA MAGMAS

The magma commingling scenario of Taapaca rocks illustrate a “classic case” of two magmas, contrasting in composition and rheology. The two mafic end-member magmas are slightly variable in terms of the composition and intensive parameter described in previous sections. The physical conditions of the silicic mixing end-member show low-temperature <850°, even <700°C (amphibole-plagioclase equilibrium temperatures), high H_2O_{melt} ranging between 6 and 8.5 wt% during Mg-Hbl crystallization. Such silicic crystal-melt mixture (crystal mush) reach a rheological lock-up point (e.g. Scaillet et al. 1998, Bachmann & Berganz, 2006) because of cooling, crystallization, exsolution of the volatile phase (Bachmann & Berganz, 2006, and references therein), and degassing in the shallow crust (at pressure 1-4 kbar).

The commingling mechanism between mafic magmas and silicic crystal mushes has been investigated and discussed in numerous publications. For instance, Sparks & Marshall (1986) present the *crossover* of the viscosity, a point at specific proportions of two magmas, from which the viscosity of the initially high-viscous silicic magma is lower than that of the mafic magma. These proportions have been quantified for Taapaca rocks by the PVA study, presented in Table 4, Chapter 2, and contradict the thesis of Spark & Marshal (1986) that large proportions of mafic magmas, exceeding 50% are required to produce “complete hybrid” magmas. Taapaca dacites show that <40% of the mafic input is sufficient to remobilize the silicic magma and produce homogenous intermediate magmas.

The rejuvenation and remobilization of the crystal mushes and generation conditions of the hybrid intermediate magmas have been broadly investigated and presented in a series of papers: e.g. Scaillet et al. (1998, 2000), Bachmann & Berganz (2006), Huber et al. (2009, 2010a, 2010b, 2011, 2012), Burgisser & Berganz (2011). The complex thermo-mechanical processes investigated with regard to large-volume Monotonous Intermediate (ignimbrite), for instance latent heat buffering of silicic magmas, defrosting(16), overpressurization, convective stirring, are processes certainly also running during reactivation of the Taapaca rhyodacite reservoir.

The generation of such uniform eruptive products as observed for >1 Ma of the eruptive history of Taapaca results most probably from the constant chemical and physical conditions of the end-member magmas. These specific conditions limit the proportions of the silicic and mafic end-members and determine the mixing ratios between mafic and silicic, from 3:7 to 4:6, resulting in the specific, dacitic composition. The detailed analysis of the processes proceeding during the generation of the monotonous dacites is above the scope of this study. Further studies could utilize the nearly complete dataset of compositions, mixing proportions and intensive parameter of the end-members involved in the generation of the monotonous Taapaca dacites, necessary for the thermo-mechanical modeling.

Based on numerical model, Bachmann & Berganz (2006) found out, that depending on the remobilized volume, in a case of remobilization of small-volume silicic mush, a single injection of mafic magma might rejuvenate the completely erupted volume. This finding is consistent with the results of this study, suggesting that one single and compositionally uniform input of mafic magma may trigger an eruption.

The mafic input rejuvenates and remobilizes a definite part of a complex of the Taapaca rhyodacite sills and evacuates the whole hybrid volume. There is evidence from sanidine zoning patterns that one rhyodacite magma batch may feed more than one single eruption. Banaszak (2007) presents two sanidine megacrysts from two separate eruptions showing perfectly overlapping crystal cores and crystal mantles, in terms of the crystal size and Ba-zoning patterns. One of the megacrysts shows further growth zones, suggesting longer residence and growth in the rhyodacite reservoir.

Cold (T< 850°C) and highly crystalline, thus highly viscous rhyodacite crystal mush undergoes thermal reactivation caused by an underplating and intrusion of the hotter mafic magma. Simultaneously, a cooling of the hot mafic recharge at Taapaca, ranging from ~950-1000°C recorded in amphibole cores, to ~750-850°C recorded in Fe-Ti oxides and equilibrium temperatures of amphibole-plagioclase pairs (Figure 14), causes nearly complete crystallization of the mafic magma and increases its viscosity, which stops the mixing, preserving the mafic enclaves. Moreover, significantly higher H_2O_{melt} contents of the rhyodacite magma in comparison to mafic magma may contribute to a rapid rejuvenation and remobilization of the silicic end-member. So far, numerous studies assumed rather higher volatile contents in the mafic recharge magmas than the silicic, remobilized crystal mushes (e.g. Huber et al., 2010).

Both, the PVA and geothermobarometry study of Taapaca rocks provide essential information required for a detailed study of the magma mixing and rejuvenation processes generating the homogenous intermediate magmas.

---

[16] Melting of the crystalline framework of a mush (Huber et al., 2010)

9. PLUMBING SYSTEM OF TAAPACA VOLCANIC COMPLEX

Besides the three distinct magmatic suites involved in the petrogenesis of Taapaca magmas, a fundamental control on the magma differentiation path and generation of the monotonous dacite magmas may have the architecture of the plumbing and storage system.

As presented in the Chapter 2, the deep feeding system of Taapaca volcano comprises three different magmatic-tectonic environments. Three end-member magmas involved in the petrogenesis of Taapaca rocks are the low-Mg high-Al calc-alkaline magma form the mantle wedge, the shoshonitic magma from lithospheric mantle and the high-K calc-alkaline from the lower to middle crust. The mafic, nearly primary mantle magmas mix on the way to the upper crust forming a hybrid mafic input into a silicic, in the deep crust produced melt, accumulating then in the shallow crust. The localization of the first mixing stage is not possible in the scope of this study.

This study focuses on the shallow differentiation processes, proceeding in the uppermost crust. Referring to the geochemical and petrological features of Taapaca rocks linking the Taapaca volcanic system to the plutonic realm, the emplacement mechanism and the geometry of the silicic reservoir are connected to the pluton-forming processes. The transport and emplacement of the granitic magma in the upper crust is controlled by mechanical interactions and density effect of arising melt with its surroundings (e.g. Hutton, 1988; reference in Petford 2000). Field observations and geophysical data from other studies reveal that the majority of plutons are flat-lying, sheet-like to open funnel-shaped structures with central or marginal located feeder zones (e.g. Petford et al., 2000). These findings and petrological observations on Taapaca rocks suggest that silicic reservoir of the Taapaca subvolcanic system may most probably consist of sill-like ephemeral silicic magma bodies, where large-scale fractionation in the silicic reservoir is hindered.

Commonly, crystal-liquid separation is regarded to be the main process driving the magmatic differentiation in the magma reservoirs leading to a magma fractionation, consequently to a chemical zoning in the magma reservoirs (de Silva & Wolff, 1995 and references therein). Bachmann et al. (2007) summarize various forms of fractionation depending on the crystallinity of the magma (crystal settling, compaction, filter-pressing), and suggest that the fractionation is a common process, however depending on melt density, viscosity, and convective movements in the reservoir. Moreover, de Silva & Wolff (1995) and Maughan et al. (2001) emphasize the effect of the magma reservoir shape as an important factor controlling fractionation. The slab-shaped or sill-like reservoirs inhibit the separation of the crystals from the melt and chemical zonation of the magma. Therefore, the occurrence of the monotonous dacite at Taapaca volcano may indicate the stagnation of the rhyodacite end-member in sill-like reservoirs. A long-lasting generation of the silicic magma in the Taapaca subvolcanic system is not a result of a shallow fractionation. This process cannot generate the strong HREE depletion, as observed for RDEM-type Taapaca end-member.

However, as discussed by Christiansen (2005), mainly high crystallinity of the stagnated dacite magmas, induced by low temperatures and high water content hinder the fractionation, which can well precede for hot and crystal-poor rhyolite magmas stalling in the sill-like reservoirs. The GTOB data obtained from Taapaca amphibole and plagioclase yield low crystallization temperatures (<850°C) and high water contents (6-8.5 wt %) of the Taapaca rhyodacitic end-member magmas. These factors lead to a high crystallinity caused by subsidence of the liquidus temperatures. Christiansen (2005) proved that although the intermediate magmas are water-enriched, the low temperatures and high crystallinity makes the crystal fractionation inefficient.

An indication for a flat-shaped silicic reservoir below Taapaca may be also the fact, that the rejuvenation, mobilization, and evacuation of the Taapaca rhyodacitic magma is evidently initiated by one single mafic recharge event. Due to the study by Burgisser & Berganz (2011), the temperature of the intrusion, viscosity of crystal mush, and the thickness of the remobilized mush mostly affect the remobilization of the crustal mush-reservoirs, reheated from below by a hot, mafic intrusion. Moreover, the mentioned study shows that only a very small amount of intrusive material is needed for a rapid remobilization of highly viscous crystal-rich mushes. If the thickness of the rhyodacitic mush layer would remain nearly constant through the entire eruptive history of Taapaca, caused, for instance, by a specific crustal architecture below Taapaca, a repeated remobilization events would result in the nearly constant proportions between the silicic and mafic magmas. The mobilized volume may be simply limited by the thickness of the crystal mush. This could explain the negligible variations in the magma mixing proportions and small compositional variability of the Taapaca dacites.

Figure 22 illustrate schematically the Taapaca plumbing system and generation stages of the monotonous, sanidine-bearing dacites. This model is consistent with petrographical observations, geochemical modeling and petrological study of the Taapaca dacites, and in the dacites hosted basaltic andesitic enclaves.

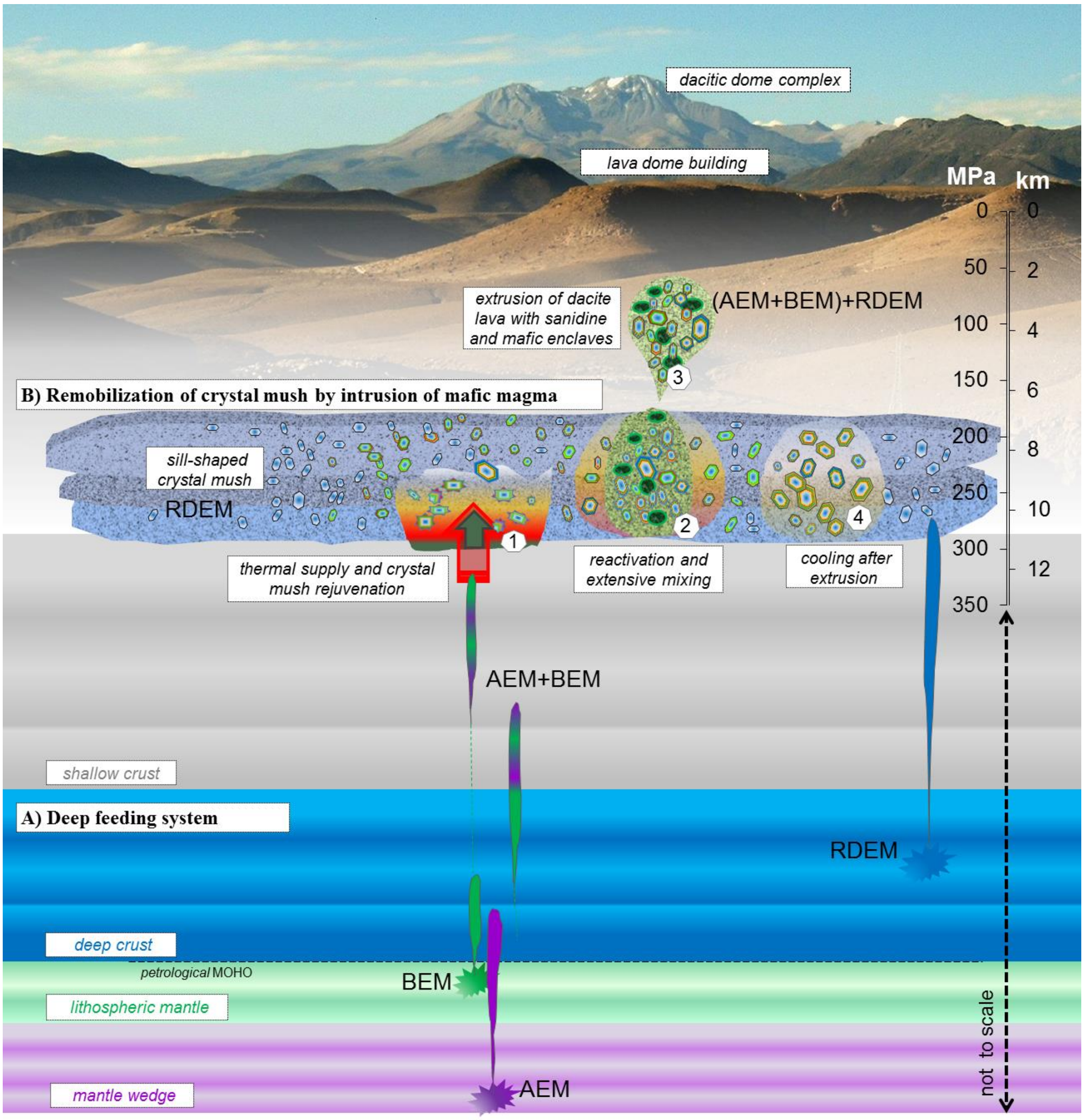

Figure 22. *A cartoon of the Taapaca plumbing system showing* ***A)*** *simplified deep feeding system, discussed in Chapter 2 of this work.* ***B)*** *Shallow stagnation level of the rhyodacitic crustal magmas in form of sill-complexes and stages of the remobilization of the rhyodacite crystal mush: (1) reheating by underplating mafic recharge, partial sanidine dissolution, thermo-mechanical reactivation processes of the rheologically locked crystal mush; (2) intrusion of mafic magma into "defrosted" crystal mush, mobilization of a rhyodacite volume limited in size by the mush thickness; (3) extrusion of a whole volume of the hybrid dacite magma hosting sanidine and mafic enclaves; and (4) cooling of a thermally influenced part of crystal mush, further sanidine growth in thermally affected parts of the crystal mush.*

10. SUMMARY AND CONCLUDING REMARKS

This petrological study, in connection with the experimental approach (Botcharnikov et al. in prep.) and the multivariate statistical study (Polytopic Vector Analysis, Chapter 2) provides a complete characterization of the differentiation regime generating the monotonous dacite magmas of the Taapaca Volcanic Complex.

1. Taapaca dacites are produced by two-stage magma mixing involving three end-member magmas, generated in three main subduction zone magmatic environments: 1) the typical arc basalts (low-Mg high-Al calc-alkaline suite) derived from mantle wedge and differentiated to more evolved basaltic andesitic composition, 2) the LILE- and HFSE-enriched shoshonitic magmas, originating from the fertile and garnet-bearing lithospheric mantle, and 3) the rhyodacitic high-K calc-alkaline magmas, produced in the deep, garnet- and amphibole-bearing crust. The first-stage magma mixing involves the low-Mg high-Al basaltic andesite and shoshonitic basalt, generating a mafic hybrid input into a rhyodacitic reservoir. Distinct mixing proportions of the mantle and lithospheric mantle magmas are responsible for a wide compositional range of the mafic "baseline" recharge magmas entering the Taapaca plumbing system.
2. An application of geothermo-oxy-barometry formulations based on amphibole compositions, and their evaluation in connection with the results of the experimental approach, reveals consistent results for P-T crystallization conditions of two compositionally different Ca-amphibole species. A comparison of Taapaca amphibole chemistry with those used for P-T calibrations in available amphibole-geothermometers and -geobarometers allows application of the Al^{TOT}-in Hbl barometer of Johnson & Rutherford (1989) for low-Al-Ti magnesiohornblende (Mg-Hbl), and barometer formulation of Ridolfi & Renzulli (2011, Equation 1e) for high-Al-Ti magnesiohastingsite (Mg-Hst). Both, the low- and high-Al-Ti Ca-amphibole yield nearly equal maximal P-values, limited to ~3 kbar, by crystallization at different thermal and compositional conditions. According to the hybrid history of Taapaca dacites, we have recognized two T-fO_2-H_2O_{melt} ranges, corresponding to cold and water-rich silicic, as well as hotter and direr mafic mixing end-member magmas. The oxidation conditions show stronger variations in the mafic end-member, due to equilibration with the silicic magmas during rejuvenation and magma mixing processes.
3. The major element amphibole chemistry in Taapaca rocks and in the experimental studies conducted on the staring compositions from Taapaca, Parinacota and Lascar volcanoes show a noticeable connection to the whole rock composition of the melt, form which the amphibole crystallized, independently on the experimental P-T conditions.
4. A comparison of the liquid line of descent (LLD) of a Taapaca dacite and a basaltic andesite of Parinacota volcano, compositionally related to the basaltic andesitic mafic enclaves hosted in Taapaca dacite, indicates that magma mixing is a main petrogenetic mechanism, generating the Taapaca (as well as Parinacota) differentiation trend.

5. Mineral assemblage, chemistry, and phenocrystic zoning patterns in the dacites and their mafic enclaves, in connection to the uniform compositions of the mafic enclaves in one eruption, give evidence for only one magma mixing event responsible for rejuvenation and extrusion of a thermally and mechanically remobilized part of the silicic reservoir. Uniform maximal residence times of sanidine megacrysts obtained from Ba-diffusion profiles in the strongly zoned crystals hosted in the dacites of distinct ages (10-800 ka) suggest a permanent silicic magma supply in the Taapaca plumbing system.
6. Taapaca subvolcanic system involves continuously varying undercooling. The presence of sanidine megacrysts requires thermal cycles, which oscillate around K-feldspar liquidus. Such conditions may be connected to temperature fluctuations caused by 1) an incremental amalgamation of the rhyodacite melts in the upper crust, which can cause small temperature variations around the K-feldspar liquidus, and 2) also a much hotter mafic underplating immediately before eruption, which causes more pronounced dissolution and regrowth of sanidine in form of plagioclase rims (rapakivi texture). Textural coarsening, as observed by Taapaca dacite is a typical phenomenon for plutonic realm (Bachmann et al., 2007).
7. The differentiation regime of Taapaca magmas connects the plutonic and volcanic realms. According to the geochemical, physical and mineralogical criteria, the RDEM-type silicic Taapaca component presents a kinship to granodioritic plutons. The differentiation and eruption mode reflects an involvement of remarkably constant silicic to mafic magma ratio, which is assumed to result from the architecture of the Taapaca plumbing and storage system, and constant chemical and physical properties of the Taapaca end-member magmas. Small differences of the silicic to mafic magma mixing ratios are connected to small compositional difference of the recharge magmas.

11. REFERENCES

Allmendinger, R. W., Jordan, T. E., Kay, S. M. & Isacks, B. (1997). The evolution of the Altiplano-Puna plateau of the Central Andes. *Annual Reviews of Earth and Planetary Sciences* **25**, 139-174.

Almeev, R. R., Ariskin, A. A., Kimura, J.-I. & Barmina, G. S. (2013). The role of polybaric crystallization in genesis of andesitic magmas: Phase equilibria simulations of the Bezymianny volcanic subseries. *Journal of Volcanology and Geothermal Research* **263**, 182–192.

Almeev, R. R., Ariskin, A. A., Ozerov, A. Y. & Kononkova, N. N. (2002). Problems of the Stoichiometry and Thermobarometry of Magmatic Amphiboles: An Example of Hornblende from the Andesites of Bezymyannyi Volcano, Eastern Kamchatka. *Geokhimiya* **40**, 803-819.

Andersen, D. J. & Lindsley, D. H. (1985). New (and final!) models for the Ti-magnetite/ilmenite geothermometer and oxygen barometer. *Abstract AGU 1985 Spring Meeting Eos Transactions. American Geophysical Union* **66**, 416.

Andersen, D. J. & Lindsley, D. H. (1988). Internally consistent solution models for Fe-Mg-Mn-Ti oxides: Fe-Ti oxides. *American Mineralogist* **73**, 714-726.

Andersen, D. J., Lindsley, D. H. & Davidson, P. M. (1993). QUILF: A Pascal program to assess equilibria among Fe-Mg-Mn-Ti oxides, pyroxenes, olivine and quartz. *Computers & Geosciences* **19**, 1333-1350.

Anderson, J. L. & Smith, D. R. (1995). The effects of temperature and fO_2 on the Al-in-hornblende barometer. *American Mineralogist* **80**, 549-559.

Armstrong, J. T. (1995). A package of correction programs for the quantitative electron microbeam X-ray analysis of thick polished materials, thin films and particles. *Microbeam Analysis* **4**, 177-200.

Bachmann, O. & Bergantz, G. (2003). Rejuvenation of the Fish Canyon magma body: a window into the evolution of large-volume silicic magma systems. *Geology* **31**, 789-792.

Bachmann, O. & Bergantz, G. W. (2006). Gas percolation in upper-crustal silicic crystal mushes as a mechanism for upward heat advection and rejuvenation of near-solidus magma bodies. *Journal of Volcanology and Geothermal Research* **149**, 85-102.

Bachmann, O., Dungan, M. A. & Lipman, P. W. (2000). Voluminous lava-like precursor to a major ash-flow tuff: low-column pyroclastic eruption of the Pagosa Peak Dacite, San Juan Volcanic field, Colorado. *Journal of Volcanology and Geothermal Research* **98**, 153-172.

Bachmann, O., Dungan, M. A. & Lipman, P. W. (2002). The Fish Canyon magma body, San Juan volcanic field, Colorado: Rejuvenation and eruption of an upper crustal batholith. *Journal of Petrology* **43**, 1469-1503.

Bachmann, O., Miller, C. F. & De Silva, S. L. (2007). The plutonic-volcanic connection as a stage for understanding crustal magmatism. *Journal of Volcanology and Geothermal Research* **167**, 1-23.

Bacon, C. R. & Hirschmann, M. M. (1988). Mg/Mn partitioning as a test for equilibrium between coexisting Fe-Ti oxides. *American Mineralogist* 73, 57-61.

Banaszak, M. (2007). Kristallisationsbedingungen und Barium-Zonierung von Sanidinen in Magmen des Taapaca Vulkans, Nord Chile. *Diploma Thesis, University of Göttingen*.

Banaszak, M., Wegner, W., Simon, K. & Wörner, G. (2009). Zoned sanidine in Taapaca dacites (I): textural and chemical characteristics of zoning patterns: *In: Mineralogical Society Annual Meeting, Edinburgh, UK.*

Blum-Oeste, N. (2014). Entgasung und Kristallisation beim Aufstieg dazitischer Magmen zur Erdoberfläche. *PhD Thesis, University of Göttingen*.

Blundy, J. & Cashman, K. (2008). Petrologic Reconstruction of Magmatic System Variables and Processes. *Reviews in Mineralogy and Geochemistry* **69**, 179-239.

Blundy, J. & Holland, T. (1990). Calcic amphibole equilibria and a new amphibole-plagioclase geothermometer. *Contributions to Mineralogy and Petrology* **104**, 208-224.

Botcharnikov, R., Stechern, A., Banaszak, M., Wörner, G. & Holtz, F. (**in prep.**). Experimental constraints on pre-eruptive conditions of Taapaca and Parinacota volcanoes, Central Andes.

Burgisser, A. & Bergantz, G. (2011). A rapid mechanism to remobilize and homogenize highly crystalline magma bodies. *Nature* **471**, 212-215.

Burkhard, D. J. M. (2005). Crystallization and oxidation during emplacement of lava lobes. *Geological Society of America Special Papers* **396**, 67-80.

Caffe, P. J., Trumbull, R. B., Coira, B. L. & Romer, R. L. (2002). Petrogenesis of Early Neogene Magmatism in the Northern Puna; implications for Magma Genesis and Crustal Processes in the Central Andean Plateau. *Journal of Petrology* **43**, 907-942.

Castillo, P. R. (2006). An overview of adakite petrogenesis. *Chinese Science Bulletin* **51**, 257-268.

Chambefort, I., Dilles, J. H. & Kent, A. J. R. (2008). Anhydrite-bearing andesite and dacite as a source for sulfur in magmatic-hydrothermal mineral deposits. *Geology* **36**, 719-722.

Christiansen, E. (2005). Contrasting processes in silicic magma chambers: evidence from very large volume ignimbrites. *Geological Magazine* **142**, 669-681.

Clark, C., Fitzsimons, I. C. W., Healy, D. & Harley, S. L. (2011). How Does the Continental Crust Get Really Hot? *Elements* **7**, 235-240.

Clavero, J. E., Sparks, R. S. J., Pringle, M. S., Polanco, E. & Gardeweg, M. C. (2004). Evolution and volcanic hazards of Taapaca Volcanic Complex, central Andes of northern Chile. *Journal of Geological Society* **161**, 603-618.

Coleman, D. S., Gray, W. & Glazner, A. F. (2004). Rethinking the emplacement and evolution of zoned plutons: Geochronologic evidence for incremental assembly of the Tuolumne Intrusive Suite, California. *Geology* **32**, 433-436.

Cooper, K. M. & Kent, A. J. R. (2014). Rapid remobilization of magmatic crystals kept in cold storage. *Nature* **506**, 480–483.

Couch, S., Harford, C. L., Sparks, R. J. S. & Carroll, M. R. (2003). Experimental Constraints on the Conditions of Formation of Highly Calcic Plagioclase Microlites at the Soufrière Hills Volcano, Montserrat. *Journal of Petrology* **44**, 1455-1475.

Davidson, J. P., Harmon, R. S. & Wörner, G. (1991). The source of the Central Andes magmas: some considerations. *Geological Society of America Special Paper* **265**, 233-244.

Davidson, J. P., McMillan, N. J., Moorbath, S., Wörner, G., Harmon, R. S. & Lopez-Escobar, L. (1990). The Nevados de Payachata volcanic region (18°S 69°W, N Chile) II. evidence for widespread crustal involvement in Andean magmatism. *Contributions to Mineralogy and Petrology* **105**, 412-432.

de Silva, S. L., Selfe, S., Francis, P. W., Drake, R. E. & Ramirez, C. R. (1994). Effusive silicic volcanism in the Central Andes: The Chao dacite and other young lavas of the Altiplano-Puna Volcanic Complex. *Journal of Geophysical Research* **99**, 17805-817825.

de Silva, S. L. & Wolff, J. A. (1995). Zoned magma chambers; the influence of magma chamber geometry on sidewall convective fractionation. *Journal of Volcanology and Geothermal Research* **65**, 111-118.

Devine, J. D., Rutherford, M. J., Norton, G. E. & Young, S. R. (2003). Magma Storage Region Processes Inferred from Geochemistry of Fe–Ti Oxides in Andesitic Magma, Soufrière Hills Volcano, Montserrat, W.I. *Journal of Petrology* **44**, 1375-1400.

Eby, G. N., Woolley, A. R., Din, V. & Platt, G. (1998). Geochemistry and Petrogenesis of Nepheline Syenites: Kasungu-Chipala, Ilomba, and Ulindi Nepheline Syenite Intrusions; North Nyasa Alkaline Province, Malavi. *Journal of Petrology* **39**, 1405-1424.

Ernst, W. G. & Liu, J. (1998). Experimental phase-equilibrium study of Al- and Ti-contents of calcic amphibole in MORB—A semiquantitative thermobarometer. *American Mineralogist* **83**, 952-969.

Féménias, O., Mercier, J.-C. C., Nkono, C., Diot, H., Berza, T., Tatu, M. & Demaifee, D. (2006). Calcic amphibole growth and compositions in calc-alkaline magmas: Evidence from the Motru Dike Swarm (Southern Carpathians, Romania). *American Mineralogist* **91**, 73-81.

Floch, A. & Martí, J. (1998). The generation of overpressure in felsic magma chambers by replenishment. *Earth and Planetary Science Letters* **163**, 301-314.

Folkes, C. B., Wright, H. M., Cas, R. A. F., de Silva, S., Lesti, C. & Viramonte, J. G. (2011). A re-appraisal of the stratigraphy and volcanology of the Cerro Galán volcanic system, NW Argentina. *Bulletin of Volcanology* **73**, 1427-1454.

Francis, P. W., Sparks, R. J. S., Hawkesworth, C. J., Thorpe, R. S., Pyle, D. M., Tais, S. R., Mantovani, M. S. & McDermott, F. (1989). Petrology and geochemistry of volcanic rocks of the Cerro Galán caldera, north west Argentina. *Geological Magazine* **126**, 515-547.

Freymuth, H. (2006). Crystal Size Distribution in megacrystic dacites from Taapaca Volcano, Northern Chile (18.10°S - 69.50°W). *Bachelor Thesis, University of Göttingen*.

Frost, B. R. (1991). Introduction to oxygen fugacity and its petrologic importance. *Reviews in Mineralogy and Geochemistry* **25**, 1-9.

Ghiorso, M. S. & Evans, B. W. (2008). Thermodynamics of rhombohedral oxide solid solutions and a revision of the Fe-Ti two-oxide geothermometer and oxygen-barometer. *American Journal of Science* **308**, 957-1039.

Ghiorso, M. S. & Sack, O. (1991). Fe-Ti oxide geothermometry: thermodynamic formulation and the estimation of intensive variables in silicic magmas. *Contributions to Mineralogy and Petrology* **108**, 485-510.

Gill, J. (1981). Orogenic andesites and plate tectonics. *Springer Verlag, Berlin*.

Ginibre, C. & Wörner, G. (2007). Variable parent magmas and recharge regimes of the Parinacota magma system (N. Chile) revealed by Fe, Mg and Sr zoning in plagioclase. *Lithos* **98**, 118-140.

Ginibre, C., Wörner, G. & Kronz, A. (2002). Minor- and trace-element zoning in plagioclase: implications for magma chamber processes at Parinacota volcano, northern Chile. *Contributions to Mineralogy and Petrology* **143**, 300-315.

Glazner, A. F., Bartley, J. M., Coleman, D. S., Gray, W. & Taylor, R. Z. (2004). Are plutons assembled over millions of years by amalgamation from small magma chambers? *GSA Today* **14**, 4-11.

Goss, A. R., Kay, S. M. & Mpodozis, C. (2011). The geochemistry of a dying continental arc: the Incapillo Caldera and Dome Complex of the southernmost Central Andean Volcanic Zone (~28°S). *Contributions to Mineralogy and Petrology* **161**, 101-128.

Haggerty, S. E. (1991). Oxide textures-a mini-atlas. In: Lindsley DH (ed) Oxide minerals: petrologic and magnetic significance. *Mineralogical Society of America* **25**.

Hammarstrom, J. M. & Zen, E. (1986). Aluminum in hornblende; an empirical igneous geobarometer. *American Mineralogist* **71**, 1297-1313.

Hawthorne, F. C. (1983). The crystal chemistry of the amphiboles. *Canadian Mineralogist* 21, 173-480.

He, D., Liu, Y., Tong, X., Zong, K., Hu, Z. & Gao, S. (2013). Multiple exsolutions in rare clinopyroxene megacrysts from the Hannuoba basalt, North China: Implications for subducted slab-related crustal thickening and recycling. *Lithos* **177**, 136-147.

Heinrichs, H. & Herrmann, A. G. (1990). Praktikum der analytischen Geochemie. *Springer- Verl., 669 S.*

Helz, R. T. (1979). Alkali exchange between hornblende and melt: a temperature-sensitive reaction. *American Mineralogist* **64**, 953-965.

Higgins, M. (1999). Origin of megacrysts in granitoids by textural coarsening: a crystal size distribution (CSD)study of microcline in the cathedral peak granitoide, Sierra Nevada, California. In: Fernandez C, Castro A (eds) Understanding granites: integrating modern and classical techniques. . *Special Publications, Geological Society of London* **158**, 207-219.

Higgins, M. (2011). Quantitative petrological evidence for the origin of K-feldspar megacrysts in dacites from Taapaca volcano, Chile. *Contributions to Mineralogy and Petrology* **162**, 709-723.

Hildreth, W. (1981). Gradients in silicic magma chambers: implications for lithospheric magmatism. *Journal of Geophysical Research* **86**, 10153-10191.

Hildreth, W. & Moorbath, S. (1988). Crustal contribution to arc magmatism in the Andes of Central Chile. *Contributions to Mineralogy and Petrology* **98**, 455-489.

Holland, T. & Blundy, J. (1994). Non-ideal interactions in calcic amphiboles and their bearing on amphibole-plagioclase thermometry. *Contributions to Mineralogy and Petrology* **116**, 433-447.

Hollister, L. S., Grissom, G. C., Peters, E. K., Stowell, H. H. & Sisson, V. B. (1987). Confirmation of the empirical correlation of Al in hornblende with pressure of solidification of calc-alkaline plutons. *American Mineralogist* **72**, 231-239.

Hora, J. M., Singer, B. S. & Wörner, G. (2007). Volcano evolution and eruptive flux on the thick crust of the Andean Central Volcanic Zone; ^{40}Ar/^{39}Ar constraints from Volcán Parinacota, Chile. *Geological Society of America Bulletin* **119**, 343-362.

Hora, J. M., Singer, B. S., Wörner, G., Beard, B. L., Jicha, B. R. & Johnson, C. M. (2009). Shallow and deep crustal control on differentiation of calc-alkaline and tholeiitic magma. *Earth and Planetary Science Letters* 285, 75-86.

Huber, C., Bachmann, O. & Dufek, J. (2012). Crystal-poor versus crystal-rich ignimbrites: A competition between stirring and reactivation. *Geology* **40**, 115-118.

Huber, C., Bachmann, O. & Dufek, J. (2010a). The limitations of melting on the reactivation of silicic mushes. *Journal of Volcanology and Geothermal Research* **195**, 97-105.

Huber, C., Bachmann, O. & Dufek, J. (2011). Thermo-mechanical reactivation of locked crystal mushes: Melting-induced internal fracturing and assimilation processes in magmas. *Earth and Planetary Science Letters* **304**, 443-454.

Huber, C., Bachmann, O. & Manga, M. (2009). Homogenization processes in silicic magma chambers by stirring and latent heat buffering. *Earth and Planetary Science Letters* **283**, 38-47.

Huber, C., Bachmann, O. & Manga, M. (2010b). Two competing effects of volatiles on heat transfer in crystal-rich magmas: Thermal insulation vs defrosting. *Journal of Petrology* **51**, 847-867.

Huppert, H. E., Turner, J. S. & Sparks, R. S. J. (1982). Replenished magma chambers: effects of compositional zonation and input rates. *Earth and Planetary Science Letters* **57**, 345-357.

Hutton, D. H. W. (1988). Granite emplacement mechanisms and tectonic controls: inferences from deformation studies. *Transactions of the Royal Society of Edinburgh: Earth Sciences* **79**, 245-255.

Irvine, T. N. & Baragar, W. R. A. (1971). A guide to the chemical classification of the common volcanic rocks. *Canadian Journal of Earth Sciences* **8**, 523-548.

Isacks, B. L. (1988). Uplift of the central Andean plateau and bending of the Bolivian orocline. *Journal of Geophysical Research* **93**, 3211-3231.

James, D. E. (1971). Andean crustal and upper mantle structure. *Journal of Geophysical Research* **76**, 3246-3271.

Johnson, B. R. & Glazner, A. F. (2010). Formation of K-feldspar megacrysts in granodioritic plutons by thermal cycling and late-stage textural coarsening. *Contributions to Mineralogy and Petrology* **159**, 599-619.

Johnson, G. W. (2002). Principal components analysis and receptor models in environmental forensics, in: "An Introduction to Environmental Forensics", edited by B. L. Murphy and R.D. Morrison. *Academic, San Diego, California*, 461-515.

Johnson, M. C. & Rutherford, M. J. (1989). Experimental calibration of the aluminum-in-hornblende geobarometer with application to Long Valley caldera (California). *Geology* **17**, 837-841.

Keller, J. (1969). Origin of rhyolites by anatectic melting of granitic crustal rocks: The example of rhyolitic pumice from the island of Kos (Aegean Sea). *Bulletin Volcanologique* **33**, 942-959.

Kelley, K. A. & Cottrell, E. (2009). Water and the Oxidation State of Subduction Zone Magmas. *Science* **325**, 605-607.

Kent, A. J. R., Darr, C., Koleszar, A. M., Salisbury, M. J. & Cooper, K. M. (2010). Preferential eruption of andesitic magmas through recharge filtering. *Nature Geoscience* **3**, 631-636.

Kiebala, A. (2008). Magmatic processes by U-Th disequilibria method. Comparison of two Andean systems: El Misti Volcano (S. Peru) and Taapaca Volcanic Center (N. Chile). *PhD Thesis, University of Göttingen*.

Kirkpatrick, R. J. (1975). Crystal Growth from the Melt: A Review. *American Mineralogist* **60**, 798-814.

Klemetti, E. W. & Grunder, A. L. (2008). Volcanic evolution of Volcan Aucanquilcha: a long-lived dacite volcano in the Central Andes of northern Chile. *Bulletin of Volcanology* **70**, 633-650.

Kohlbach, I. (1999). Spatial and temporal variations in magma geochemistry along W-E traverse at 18°-19°S, North Chile. *Diploma Thesis, University of Göttingen*.

Kohlbach, I. & Lohnert, E. (1999). Geological Map of Taapaca Volcano and adjacent areas, North Chile. *Diploma Mapping Report, University of Göttingen*.

Le Maitre, R. W., Bateman, P., Dudek, A., Keller, J., Lameyre, J., Le Bas, M. J., Sabine, P. A., Schmid, R., Sorensen, H., Streckeisen, A., Woolley, A. R. & Zanettin, B. (1989). A Classification of Igneous Rocks and Glossary of terms: Recommendations of the International Union of Geological Sciences Subcommission on the Systematics of Igneous Rocks. *Blackwell Scientific Publications, Oxford, U.K.*

Leake, B. E., Woolley, A. R., Arps, C. E. S., Birch, W. D., Gilbert, M. C., Grice, J. D., Hawthorne, F. C., Katio, A., Kisch, H. J., Krivovichev, V. G., Linthout, K., Laird, J., Mandarino, J. A., Maresch, W. V., Nickel, E. H., Schumacher, J. C., Smith, D. C., Stephenson, N. C. N., Ungaretti, L., Whittaker, E. J. W. & Youzhi, G. (1997). Nomenclature of amphiboles: report of the subcommittee on amphiboles of the International Mineralogical Association, Commission on new minerals and mineral names. *Canadian Mineralogist* **35**, 219-246.

LePage, L. D. (2003). ILMAT: an excel worksheet for ilmenitemagnetite geothermometry and barometry. *Computers & Geosciences* **29**, 673-678.

Lindsay, J. M., de Silva, S., Trumbull, R., Emmermann, R. & Wemmer, K. (2001). La Pacana caldera, N. Chile: a re-evaluation of the stratigraphy and volcanology of one of the world's largest resurgent calderas. *Journal of Volcanology and Geothermal Research* **106**, 145-173.

Lipman, P. W. (2007). Consolidation of Cordilleran magma chambers: Evidence from the Southern Rocky Mountain volcanic field. *Geosphere* **3**, 42-70.

Lofgren, G. (1974). An experimental study of plagioclase morphology. *American Journal of Science* **273**, 243-273.

Lohnert, E. (1999). Chemical variations of sanidine megacryst and its implications on the pre-eruptive evolution of the Taapaca volcano in North Chile: electron microprobe and Sr-isotope studies. *Diploma Thesis, University of Göttingen*, Germany.

Lucassen, F., Becchio, R., Harmon, R., Kasemann, S., Franz, G., Trumbull, R., Wilke, H.-G., Romer, R. L. & Dulski, P. (2001). Composition and density model of the continental crust at an active continental margin - the Central Andes between 21° and 27°S. *Tectonophysics* **341**, 195-223.

Mahood, G. A. (1990). Second reply to comment of R.S.J. Sparks, H.E. Huppert, and C.J.N. Wilson on "Evidence for long residence times of rhyolitic magma in the Long Valley magmatic system: the isotopic record in postcaldera lavas of Glass Mountain" *Earth and Planetary Science Letters* **99**, 395-399.

Mamani, M., Tassara, A. & Wörner, G. (2008). Composition and structural control of crustal domains in the central Andes. *Geochemistry Geophysics Geosystems* **9**.

Mamani, M., Wörner, G. & Sempere, T. (2010). Geochemical variations in igneous rocks of the Central Andean orocline (13°S to 18°S): Tracking crustal thickening and magma generation through time and space. *GSA Bulletin* **122**, 162-182.

Marsh, B. D. (1981). On the crystallinity, probability of occurrence, and rheology of lava and magma. *Contributions to Mineralogy and Petrology* **78**, 85-98.

Maughan, L., Christiansen, E. H., Best, M. G., Gromme, C. S., Deino, A. L. & Tingey, D. G. (2001). The Oligocene Lund Tuff, Great Basin, USA: a very large volume monotonous intermediate. *Journal of Volcanology and Geothermal Research* **113**, 129-157.

Mehnert, K. R. & Büsch, W. (1981). The formation of K-Feldspar megacrysts in granites, migmatites and augengneisses. *N. Jb. Miner.Abh.* **140**, 221-252.

Mills, R. D., Ratner, J. J. & Glazner, A. F. (2011). Experimental evidence for crystal coarsening and fabric development during temperature cycling. *Geology* **39**, 1139-1142.

Murphy, M. D., Sparks, R. J. S., Barclay, J., Carroll, M. R. & Brewer, T. S. (2000). Remobilization of Andesite Magma by Intrusion of Mafic Magma at the Soufriere Hills Volcano, Montserrat, West Indies. *Journal of Petrology* **41**, 21-42.

Myers, J. D., Angevine, C. L. & Frost, C. D. (1987). Mass balance calculations with end member compositional variability: applications to petrologic problems. *Earth and Planetary Science Letters* **81**, 212-220.

Pallister, J. S., Thornber, C. R., Cashman, K. V., Clynne, M. A., Lowers, H. A., Mandeville, C. W., Brownfield, I. K. & Meeker, G. P. (2008). Petrology of the 2004–2006 Mount St. Helens lava dome—implications for magmatic plumbing and eruption triggering. *chap. 30 of Sherrod, D.R., Scott, W.E., and Stauffer, P.H., eds., A volcano rekindled; the renewed eruption of Mount St. Helens, 2004–2006* U.S. Geological Survey Professional Paper **1750**.

Petford, N. & Atherton, M. (1996). Na-rich Partial Melts from Newly Underplated Basaltic Crust: the Cordillera Blanca Batholith, Peru. *Journal of Petrology* **37**, 1491-1521.

Petford, N., Cruden, A. R., McCaffrey, K. J. W. & Vigneresse, J.-L. (2000). Granite magma formation, transport and emplacement in the Earth's crust. *Nature* **408**, 669-673.

Putirka, K. (2008b). Excess temperatures at ocean islands: Implications for mantle layering and convection. *Geology* **31**, 283-286.

Putirka, K. (2008). Thermometers and Barometers for Volcanic Systems. *Reviews in Mineralogy and Geochemistry* **69**, 61-120.

Putirka, K. D., Perfit, M., Ryerson, F. J. & Jackson, M. G. (2007). Ambient and excess mantle temperatures, olivine thermometry, and active vs. passive upwelling. *Chemical Geology* **241**, 177-206.

Reubi, O. & Blundy, J. (2009). A dearth of intermediate melts at subduction zone volcanoes and the petrogenesis of arc andesites. *Nature* **461**, 1269-1272.

Rickwood, P. C. (1989). Boundary lines within petrologic diagrams which use oxides of major and minor elements. *Lithos* **22**, 247-263.

Ridolfi, F., Puerini, M., Renzulli, A., Menna, M. & Toulkeridis, T. (2008). The magmatic feeding system of El Reventador volcano (Sub-Andean zone, Ecuador) constrained by texture, mineralogy and thermobarometry of the 2002 erupted products. *Journal of Volcanology and Geothermal Research* **176**, 94-106.

Ridolfi, F. & Renzulli, A. (2011*online). Calcic amphiboles in calc-alkaline and alkaline magmas: thermobarometric and chemometric empirical equations valid up to 1,130°C and 2.2 GPa. *Contributions to Mineralogy and Petrology* 163, 877-895.

Ridolfi, F., Renzulli, A. & Puerini, M. (2010). Stability and chemical equilibrium of amphibole in calc-alkaline magmas: an overview, new thermobarometric formulations and application to subduction-related volcanoes. *Contributions to Mineralogy and Petrology* 160, 45-66.

Rodriguez, C., Selle, D., Dungan, M., Langmuir, C. & Leeman, W. (2007). Adakitic Dacites Formed by Intracrustal Crystal Fractionation of Water-rich Parent Magmas at Nevado de Longaví Volcano (36,2°S; Andean Southern Volcanic Zone, Central Chile). *Journal of Petrology* 48, 2033-2061.

Roeder, P. L. & Emslie, R. F. (1970). Olivine-Liquid Equilibrium. *Contributions to Mineralogy and Petrology* **29**, 275-289.

Ruprecht, P. & Wörner, G. (2007). Variable regimes in magma systems documented in plagioclase zoning patterns: El Misti stratovolcano and Andahua monogenetic cones. *Journal of Volcanology and Geothermal Research* **165**, 142-162.

Rutherford, M. J. & Devine, J. D. (1988). The May 18, 1980, eruption of Mount St. Helens, III; stability and chemistry of amphibole in the magma chamber. *Journal of Geophysical Research* **93**, 11,949-11959.

Rutherford, M. J. & Devine, J. D. (2003). Magmatic conditions and magma ascent as indicated by hornblende phase equilibria and reactions in the 1995–2002 Soufrière Hills magma. *Journal of Petrology* **44**, 1433-1454.

Samaniego, P., Martin, H., Monzier, M., Robin, C., Fornari, M., Eissen, J.-P. & Cotten, P. (2005). Temporal Evolution of Magmatism in the Northern Volcanic Zone of the Andes: The Geology and Petrology of Cayambe Volcanic Complex (Ecuador). *Journal of Petrology* **46**, 2225-2252.

Samoza, R. (1998). Updated Nazca (Farallon)-South America relative motions during the last 40 My: implications for mountain building in the central Andean region. *Journal of South American Earth Science* **11**, 211-215.

Sato, H., Holtz, F., Behrens, H., Botcharnikov, R. & Nakada, S. (2005). Experimental Petrology of the 1991-1995 Unzen Dacite, Japan. Part II: Cl/Oh Partitioning between Hornblende and Melt and its Implications for the Origin of Oscillatory Zoning of Hornblende Phenocrysts. *Journal of Petrology* **46**, 339-354.

Sato, H., Nakada, S., Fujii, T., Nakamura, M. & Suzuki-Kamata, K. (1999). Groundmass pargasite in the 1991–1995 dacite of Unzen volcano: phase stability experiments and volcanological implications. *Journal of Volcanology and Geothermal Research* **89**, 197-212.

Sauerzapf, U., Lettard, D., Burchard, M. & Engelmann, R. (2008). The Titanomagnetite-Ilmenite Equilibrium: New Experimental Data and thermooxybarometric Application to the Crystallization of Basic to Intermediate Rocks. *Journal of Petrology* **49**, 1161-1185.

Scaillet, B. & Evans, B. W. (1999). The June 15, 1991 eruption of Mount Pinatubo. I. Phase equilibria and pre-eruption P-T-fO2-fH2O conditions of the dacite magma. *Journal of Petrology* **40**, 381-411.

Scaillet, B., Holtz, F. & Pichavant, M. (1998). Phase equilibrium constraints on the viscosity of silicic magmas 1. Volcanic-plutonic comparison. *Journal of Geophysical Research* **103**, 27257-27266.

Scaillet, B., Whittington, A., Martel, C., Pichavant, B. & Holtz, F. (2000). Phase equilibrium constraints on the viscosity of silicic magmas with implications for mafic-silicic mixing processes. *Transactions of the Royal Society of Edinburgh: Earth Sciences* **91**, 61-72.

Scheuber, E., Bogdanic, T., Jensen, A. & Reutter, K.-J. (1994). Tectonic development of the North Chilean Andes in relation to plate convergence and magmatism since the Jurassic. *In: Reutter, K.-J., Scheuber, E. & Wigger, P. (Herausgeber): Tectonics of the Southern Central Andes, S. 121-139, Springer.*

Scheuber, E. & Giese, P. (1999). Architecture of the Central Andes a compilation of geoscientific data along a transect at 21°S. *Journal of South American Earth Sciences* 12, 103-107.

Shaw, C. J. & Eyzaguirre, J. (2000). Origin of megacrysts in the mafic alkaline lavas of the West Eifel volcanic field, Germany. *Lithos* **50**, 75-95.

Simakin, A. G. & Bindeman, I. N. (2008). Evolution of crystal sizes in the series of dissolution and precipitation events in open magma systems. *Journal of Volcanology and Geothermal Research* **177**, 997-1010.

Simakin, A. G., Salova, T. P. & Babansky, A. D. (2009). Amphibole Crystallization from a Water-Saturated Andesite Melt: Experimental Data at P = 2 kbar. *Petrology* **17**, 591-605.

Sisson, T. W. & Grove, T. L. (1993b). Experimental investigations of the role of H_2O in calc-alkaline differentiation and subduction zone magmatism. *Contributions to Mineralogy and Petrology* **113**, 143-166.

Sisson, T. W. & Grove, T. L. (1993a). Temperatures and H_2O contents of low-Mg high-alumina basalts. *Contributions to Mineralogy and Petrology* **113**, 167-184.

Sparks, R. J. S. & Marshall, L. A. (1986). Thermal and mechanical constraints on mixing between mafic and silicic magmas. *Journal of Volcanology and Geothermal Research* **29**, 99-124.

Spear, F. S. (1981). Amphibole-plagioclase equilibria: An empirical model for the relation albite+tremolite=edenite+4 quartz. *Contributions to Mineralogy and Petrology* **77**, 355-364.

Stechern, A., Banaszak, M., Botcharnikov, R., Holtz, F. & Wörner, G. (**in prep.**). Petrological and experimental constraints on the pre-eruptive conditions of 1993 Lascar andesites and the evolution of calc-alkaline intermediate lavas.

Stern, R. C. (2004). Active Andean volcanism: its geologic and tectonic setting. *Revista Geológica de Chile* **31**, 161-206.

Stimac, J. A. & Pearce, T. H. (1992). Textural evidence of mafic-felsic magma interaction in dacite lavas, Clear Lake, California. *American Mineralogist* **77**, 795-809.

Stormer, J. C. (1983). The effects of recalculation on estimates of temperature and oxygen fugacity from analyses of multicomponent iron-titanium oxides. *American Mineralogist* **68**, 586-594.

Swanson, S. E. (1977). Relation of nucleation and crystal-growth rate to the development of granitic textures. *American Mineralogist* **62**, 966-978.

Tassara, A. (2005). Interaction between the Nazca and South American plates and formation of the Altiplano–Puna plateau: Review of a flexural analysis along the Andean margin (15°–34°S). *Tectonophysics* **399**, 39-57.

Tassara, A., Götze, H. J., Schmidt, S. & Hackney, R. (2006). Three-dimensional density model of the Nazca plate and the Andean continental margin. *Journal of Geophysical Research: Solid Earth* **111**, 1978-2012.

Tassara, A. & Yanez, G. (2003). Relacion entre el espesor elastico de la litosfera y la segmentacion tectonica del margen andino (15–47°S). *Revista Geológica de Chile* **30**, 159-186.

Vance, J. A. (1969). On synneusis. *Contributions to Mineralogy and Petrology* **24**, 7-29.

Venezky, D. Y. & Rutherford, M. J. (1999). Petrology and Fe-Ti oxide reequilibration of the 1991 Mount Unzen mixed magma. *Journal of Volcanology and Geothermal Research* 89, 213-230.

Vernon, R. H. (1986). K-feldspar megacrysts in granites; phenocrysts, not porphyroblasts. *Earth Sci. Rev.* **23**, 1-63.

Vernon, R. H. & Paterson, S. R. (2008). How late are K-feldspar megacrysts in granites? *Lithos* **104**, 327-336.

Viccaro, M., Ferlito, C. & Cristofolini, R. (2007). Amphibole crystallization n in the Etnean feeding system: mineral chemistry and trace element partitioning mineral chemistry and trace element partitioning. *European Journal of Mineralogy* **19**, 499-511.

Walker, B. A., Grunder, A. L. & Wooden, J. L. (2010). Organization and thermal maturation of long-lived arc systems: evidence from zircons at the Aucanquilcha volcanic cluster, northern Chile. *Geology* **38**, 841–844.

Walker, B. A. J., Klemetti, E. W., Grunder, A. L., Dilles, J. H., Tepley, F. J. & Giles, D. (2013). Crystal reaming during the assembly, maturation, and waning of an eleven-million-year crustal magma cycle: thermobarometry of the Aucanquilcha Volcanic Cluster. *Contributions to Mineralogy and Petrology* **165**, 663-683.

Watts, R. B., de Silva, S. L., Jimenez de Rios, G. & Croudace, I. (1999). Effusive eruption of viscous silicic magma triggered and driven by recharge: a case study of the Cerro Chascon-Runtu Jarita Dome Complex in Southwest Bolivia. *Bulletin of Volcanology* **61**, 241-264.

Wegner, W. (2004). Growth history of sanidine crystals in Taapaca Dacites (Northern Chile). *Diploma Thesis University of Göttingen*, Germany.

Wegner, W., Wörner, G. & Kronz, A. (2005). Evolution of Taapaca Volcano, N. Chile: evidence from major and trace elements, Sr-,Nd-, Pb-isotopes, age dating and chemical zoning in sanidine megacrysts. *In: 6th International symposium on Andean geodynamics, Barcelona*, 795-798.

Wörner, G., Hammerschmidt, K., Hemjes-Kunst, F., Lezaun, J. & Wilke, H. (2000). Geochronology (^{40}Ar-^{39}Ar-, K-Ar-, and He-exposure-) ages of Cenozoic magmatic rocks from Northern Chile (18°- 22°S). Implications for magmatism and tectonic evolution of the central Andes. *Revista Geológica de Chile* 27, 205-240.

Wörner, G., Harmon, R. S., Davidson, J., Moorbath, S., Turner, D. L., McMillan, N., Nye, C., Lopez-Escobar, L. & Moreno, H. (1988). The Nevados de Payachata volcanic region (18°S/69°W, N. Chile) I. Geological, geochemical, and isotopic observations. *Bulletin of Volcanology* **50**, 287-303.

Wörner, G., Moorbath, S. & Harmon, R. S. (1992). Andean Cenozoic volcanic centers reflect basement isotopic domains. *Geology* **20**, 1103-1106.

Wörner, G., Wegner, W., Kiebala, A., Singer, B. S., Heumann, A., Kronz, A. & Hora, J. M. (2004). Evolution of Taapaca volcano, N. Chile, evidence from major and trace element, Sr-, Nd-, Pb-, and U-series isotopes, age dating and chemical zoning in sanidine megacrysts. *IAVCEI General Assembly, Volcanism and its impact on society, Pucon, Chile*.

Wright, H. M. N., Folkes, C. B., Cas, R. A. F. & Cashman, K. V. (2011). Heterogeneous pumice populations in the 2.08 Ma Cerro Galán Ignimbrite: implications for magma recharge and ascent preceding a large volume silicic eruption. *Bulletin of Volcanology* **73**, 1513-1533.

Yuan, X., Sobolev, S. V. & Kind, R. (2002). Moho topography in the Central Andes and its geodynamic implications. *Earth and Planetary Science Letters* **199**, 389-402.

Yuan, X., Sobolev, S. V., Kind, R., Oncken, O., Bock, G., Asch, G., Schurr, B., Graeber, F., Rudloff, A., Hanka, W., Wylegalla, K., Tibi, R., Haberland, C., Rietbrock, A., Giese, P., Wigger, P., RoÈwer, P., Zandt, G., Beck, S., Wallace, T., Pardo, M. & Comte, D. (2000). Subduction and collision processes in the Central Andes constrained by converted seismic phases. *Nature* **408**, 958-961.

Zandt, G., Velasco, A. A. & Beck, S. (1994). Composition and thickness of the southern Altiplano crust, Bolivia. *Geology* **22**, 1003-1006.

Zellmer, G. F. (2009). Petrogenesis of Sr-rich adakitic rocks at volcanic arcs: insights from global variations of eruptive style with plate convergence rates and surface heat flux. *Journal of the Geological Society, London* **166**, 725-734.

Zellmer, G. F. & Clavero, J. E. (2006). Using trace element correlation patterns to decipher a sanidine crystal growth chronology: An example from Taapaca volcano, Central Andes. *Journal of Volcanology and Geothermal Research* **156**, 291-301.

Zellmer, G. F., Sheth, H. C., Iizuka, Y. & Lai, Y.-J. (2012). Remobilization of granitoid rocks through mafic recharge: evidence from basalt-trachyte mingling and hybridization in the Manori–Gorai area, Mumbai, Deccan Traps. *Bulletin of Volcanology* **74**, 47-66.

Zellmer, G. F. & Turner, S. P. (2007). Arc dacite genesis pathways: evidence from mafic enclaves and their hosts in Aegean lavas. *Lithos* **95**, 346-362.

Parinacota Volcano

Central Volcanic Zone (18°S), Northern Chile

Photo: Nils Blum-Oeste

CHAPTER 4

Petrological and geochemical changes in magmas of Parinacota Volcano, N. Chile, accompanied by edifice sector collapse

ABSTRACT

Parinacota is a stratovolcano located in the Andean Central Volcanic Zone (18°S/69°W). It experienced a sector collapse that punctuates petrological and geochemical changes in the erupted lavas. The pre-collapse lavas comprise a broad compositional range reaching from basaltic andesites to rhyolites, whereas the post-collapse lavas are of basaltic andesitic to andesitic composition.

On the basis of a statistical geochemical modelling (Polytopic Vector Analysis, PVA), conducted on hybrid dacites of the neighboring Taapaca volcano, the geochemical variability of the Parinacota lavas may be explained by two-stage magma mixing of three end-member magmas involved in the petrogenesis of the Quaternary volcanic rocks in the CVZ. The first stage produces hybrid baseline magmas consisting of low-Mg high-Al calc-alkaline basaltic andesite (AEM) and incompatible trace elements enriched basalt (BEM). The second stage represents shallow crustal magma mixing between already mixed, mafic (AEM+BEM) and a silicic component, the latter identified as high-K calc-alkaline rhyodacite (RDEM), enriched in LILE and depleted in HREE. The trend toward more mafic magma compositions erupted after sector collapse suggests a "cleaning" of the plumbing system from the silicic magmas. Many lines of evidence suggest that this process is not related to the edifice sector collapse but to an increased mafic magma input into slowly recharged silicic magmas.

The sector collapse marks also changes in the mineralogy of Fe-Mg phases in the intermediate Parinacota magmas. Amphibole and titanomagnetite are present in the pre-collapse andesites to dacites that show mineral chemical and petrographical evidence for mixing with large proportions of the silicic RDEM magmas. Post-collapse lavas have ±olivine, clinopyroxene, orthopyroxene, titanomagnetite and ilmenite, while amphibole is very rare.

The availability of the RDEM magmas in subvolcanic systems determines also the mineralogy of the Fe-Mg phases in the intermediate magmas. Volcanic rocks from neighboring Taapaca and Parinacota volcanoes show that amphibole and titanomagnetite are present in basaltic andesites, andesites and dacites that show geochemical evidence for mixing with a large proportion of the silicic RDEM magma. Other basaltic andesites and andesites of very similar major element composition have ±olivine, pyroxene, titanomagnetite and ilmenite, while amphibole is absent. During magma mixing, a drop in temperature, an increase in the water content, and changes in the redox conditions of the (AEM+BEM) component destabilize olivine, pyroxene and ilmenite and promote amphibole + titanomagnetite crystallization in the hybrid magmas. Amphibole-bearing rocks thus form primarily by RDEM-AEM-BEM hybridization whereas pyroxene-bearing rocks are differentiation products of dominantly AEM-BEM hybrids with minor RDEM admixture.

1. INTRODUCTION

Parinacota is a Late Pleistocene-Holocene active composite volcano located in the Andean Central Volcanic Zone (CVZ). A perfect conical shape of the Parinacota stratocone represents a rapid edifice-rebuilding phase after sector collapse (Hora et al., 2007, 2009). Accompanied by increased eruption rates after collapse, Parinacota changed petrological and geochemical characteristics of erupted lavas indicating a rearrangement of its plumbing system and a change in magma evolution regime. The rock compositions vary from mainly andesite to rhyolite in the pre-collapse stages and basaltic andesite to andesite in the cone-rebuilding and flank eruptions period. The time of collapse punctuates also changes in the mineralogy of Fe-Mg-bearing silicate phases in Parinacota lavas, from dominantly amphibole-bearing pre-collapse lavas to two-pyroxene-bearing post-collapse lavas (Wörner et al., 1988); moreover, ilmenite is not stable in amphibole-bearing rocks. Chemical and textural changes in plagioclase zoning patterns (Ginibre & Wörner, 2007), decreasing (^{230}Th/^{232}Th) activity ratios, and increasing Th-excess (Burdon et al., 2000; Hora et al., 2009) are also observed. Hora et al. (2009) show a conversion of magma affinity from calk-alkaline toward tholeiitic.

Volcanic edifice collapse is recognized as an ubiquitous phenomenon defining volcanic life-cycles recorded at both, composite and oceanic shield volcanoes (e.g. Siebert et al., 1984, 1987, 1995; Bogoyavlenkaya et al., 1985; McGuire 1996, 2003, Carracedo, 1999). Since the lateral blast of Mount St. Helens on 18 May 1980 eruption, the failure of volcanic cones has drawn an increased attention to the studies of volcanic hazard and its role in the evolution of volcanic systems. Based on textural and morphological characteristics of debris avalanche deposits Siebert (1984) recognized high frequency of volcanic edifice collapse on the global scale. Detailed study of volcanic regions in the Central Andes (Francis & Wells, 1988) and Japan (Inokuchi, 1988) revealed debris avalanche as a common volcanic product beside lavas and pyroclastic flows generated during evolution of composite volcanoes.

Regarding high hazard potential of a volcanic edifice collapse most studies focus on endo- and exogenetic mechanisms triggering edifice instability (Siebert et al., 1987; Siebert et al., 1992; Francis & Wells, 1988; Voight & Elsworth, 1997; McGuire, 1996; Van Wyk de Vries & Borgia, 1996; Carracedo, 1999; Vidal & Merle, 2000; Reid et al., 2001; Tibaldi, 2001; Tibaldi et al., 2006; Reid et al., 2010) and monitoring of edifice deformation and landmass displacement (Lipman et al., 1981; Voight et al., 1983; Siebert, 1996), contributing to assessment of risk areas. From a mechanical standpoint, numerous experimental studies and numerical models have examined the effects of volcanic edifice load on magma reservoir behavior and magma ascent beneath volcanoes (Pinel & Jaupart, 2000, 2003, 2004; Pinel & Albino, 2013; Pinel et al., 2010; Hurwitz et al., 2009; Kervyn et al., 2009). Discussing a range of internal and external collapse triggers, McGuire (2004) emphasized leading role of magmatic intrusions destabilizing volcanic edifices and triggering sector collapse as in the prominent cases of Mount St Helens and Bezymianny volcanoes. Designated as Bezymianny-type eruptions (Siebert et al., 1987), growth of an intra-crater lava dome is typical for the immediate post-collapse volcano activity. Furthermore, frequent association of edifice failure with phreatic and phreatomagamatic eruptions indicates that decompression of the magmatic plumbing systems and magma reservoirs in connection with volcanic hydrothermal system demonstrate high potential triggering volcanic eruptions (Bandaian-type eruptions, Siebert et al., 1987), e.g. Mauna Loa, Lipman et al. (1991), Stromboli, Petrone et al. (2009).

The reduction of edifice load induces changes in volcano's local stress field. The likelihood of an eruption caused by collapse depends on edifice dimensions and magma reservoir size (Pinel & Jaupart, 2005). The amplitude of decompression depends on volume of collapsed flank, additionally the ratio between initial and final load and radius of the initial cone control the pressure changes at depth (Manconi et al., 2009). Stress perturbations, evaluated by Pinel & Jaupart, (2005), become negligible at the depth greater than three times the edifice radius, therefore decreasing mass of volcanic edifice must affect shallow plumbing system components. However, Presley et al. (1997) suggest possible effects of mass-wasting events even on magma production in the mantle and degree of magma differentiation. Numerical simulations of Manconi et al. (2009) show that the collapse induced pressure gradient decreases exponentially with depth, which results with very low decompression values at the regions of magma source, therefore edifice collapse cannot affect magma production. Pinel et al. (2010) incorporated in their analytical model the input rate of magma from the deep magma source into reservoir providing the insight into long-term relationships between edifice growth-destruction phases, eruption rates, and magma composition. They argue that changes in eruption rates and magma compositions do not require changes in magma supply rates from the source. This is supported by notably higher eruption rates (5 km^3/ka) observed directly after flank collapse at Tahiti-Nui Island compared to pre-collapse shield phases (2 km^3/ka), as well later post collapse activity characterized by diminishing magma supply (0,5 km^3/ka) due to increasing edifice load, as suggested by Hildebrandt et al. (2004).

According to Pinel & Jaupart (2000), edifice load operates as density filter for erupted products. Changes in magma composition toward denser and less evolved lavas after edifice destruction were recorded, besides Parinacota, at numerous other volcanoes (Mount S. Helens, Gardner et al., 1995, Pinel et al., 2010; Ubinas, Thouret et al., 2005; Bezymianny, Bogoyavlenskaya et al., 1985, Turner et al., 2013; Tungurahua, Hall et al., 1999; El Hierro, Manconi et al., 2009). However, many volcanic systems, which experienced an edifice collapse, show an opposite behavior, due to eruptions of silicic post-collapse lavas (e.g. Ollagüe, Feeley et al., 1993; Llullaillaco, Richards & Villeneuve, 2001; Pichincha, Samaniego et al., 2010).

Volcanic mass load affects the equilibrium pressure within the magma reservoir and may affect the depth of magma storage, geometry, and size of magma reservoir (Hurwitz et al., 2009, Pinel et al. 2010). Correlation between magma composition and stagnation depth has been observed at Mount St Helens, where more evolved magmas are connected to higher petrological pressure (Pinel et al., 2010). Thus, the reduction of edifice mass through a landslide or explosive eruption is expected to rearrange subvolcanic plumbing and magma storage conditions, and influences magma differentiation regime and volcanic activity. Though, as mentioned before, numerous volcanoes do not yield compositional changes with regard to the edifice collapse and erupt intermediate and silicic magmas as well in edifice-rebuilding phases (Pitons du Carbet, Soufrière Volcanic Centre, Boudon et al., 2013; Ollagüe 21°S, CVZ, Feeley et al., 1993; Tungurahua, NVZ, Hall et al., 1999; Llullaillaco, CVZ, Richards & Villeneuve, 2001; Pichincha, NVZ, Samaniego et al., 2010). Differing response modes of the volcanic system to the edifice destruction pose questions about key factors, which determine chemical and mineralogical composition of the subsequently to collapse erupted lavas.

We observe long-lasting changes in the dynamic of Parinacota subvolcanic system associated with the sector collapse. Increased eruption rates correlate to faster magma transfer through the crust, shorter magma residence times and, in consequence, an alteration of predominant magma differentiation processes, which overprint the base geochemical signatures (Wörner et al., 1988; Hora et al., 2007, 2009). The readjustment of the Parinacota volcanic system results in general absence of amphibole replaced by two pyroxenes, and presence of the ilmenite in the post collapse lavas. This suggests a crucial role of thermodynamic parameters controlling evolution of magmatic systems (e.g. Sisson & Grove, 1993; Martel et al., 1999). The methods of geothermo-oxy-barometry adopted und applied to Taapaca volcano, presented in Chapter 3, are also applied to Parinacota volcano, extended on geothermobarometer of Putirka (2008), according to available two-pyroxene andesites.

A shift in the whole rock composition toward more mafic magmas after Parinacota edifice collapse has been related to changes in the subvolcanic plumbing system, which may have included changes in intensive parameters controlling the differentiation or an injection of a new magma batch (Wörner et al., 1988; Ginibre & Wörner, 2007).

The objective of this study is to constrain the mechanisms and physical conditions, which lead to the geochemical and petrological changes in Parinacota lavas accompanied by the edifice sector collapse. The key questions of this study are:

- Is the sector collapse the reason for an abrupt switch in the differentiation regime of Parinacota?
- Is the sector collapse rather a consequence of an edifice overload and/or oversteepening, a common and widespread phenomenon?

Taking into account other geochemical and petrological studies on the effect of the sector collapse on the magma evolution, the exact causes of the switch from one differentiation regime to another has commonly not been explained yet (Thouret et al., 2005). This study of the Parinacota volcanic system in terms of whole rock compositions, mineral chemistry, and intensive parameter of crystallization obtained from the selected pre-and post-collapse Parinacota lavas give a new insight into the mechanisms, which may be responsible for such changes.

2. VOLCANOLOGICAL BACKGROUND

2.1. PREVIOUS STUDIES

The eruptive history of Parinacota was initially divided into five stages by Katusi & Gonzales-Ferran, (1968), which integrated debris avalanche as an eruption unit. The edifice collapse event and its role in the evolution of Parinacota were firstly recognized by Wörner et al. (1988) and Francis and Wells (1988). Wörner et al. (1988) distinguished five stages comprised 1) initial andesitic lava flows, 2) rhyolitic Dome Plateau, 3) Old Cone andesitic lavas, 4) Healing Flows after edifice collapse, and 5) flank eruptions. The changes in magma chemistry and eruption rates after volcano collapse were related to an input of a new magma into deep plumbing system (Wörner et al., 1988) and abrupt changes from sluggish to rapid differentiation regime (Bourdon et al., 2000). Small variations in isotopic composition over broad compositional range from basalt andesitic to rhyolitic lavas at Parinacota indicate that the “baseline” isotopic composition (Davidson et al., 1991) is established by deep crust interactions and subsequently differentiated in the upper crustal magma reservoirs (Davidson et al., 1990).

Further investigations of the edifice morphology and its environment in connection with ^{40}Ar-^{39}Ar dating presented by Clavero (2002), refined by Hora et al. (2007) resulted in a detailed geological map based on age defined eruptive units, and estimated time of edifice collapse. These studies revealed overlapping eruption stages of Dome Plateau and Old Cone units as well Young Cone and flank eruptions simplifying Parinacota evolution to main pre- and post-collapse stages.

Ginibre & Wörner (2007) present a geochemical record of the Parinacota plumbing and storage system related to the sector collapse. Changes recognized in textural and chemical characteristics of plagioclase zoning in pre- and post-collapse lavas as well the nature of Parinacota source magmas (Entenmann, 1994) give evidence of two parental magmas stagnating at distinct MASH (mixing-assimilation-storage-homogenization)-zone levels, feeding simultaneously the shallow storage system. The reconfiguration of the plumbing-storage system after cone collapse is expressed by 1) shallower storage depth, 2) increasing recharge rate and 3) smaller reservoir volumes. The complementary model of Hora et al. (2009) improved temporal and spatial configuration of the subvolcanic system emphasizing that volcano collapse is a temporally related to increased magma flux and recharge frequency and may have contributed to reorganization of a magma system that was already primed for change.

2.2. GEOLOGICAL SETTING

The Central Andes is a part of an Andean orogeny resulting from the subduction of the oceanic Nazca Plate beneath the continental South American Plate since Jurassic time, and a formation of the world largest plateau, the Altiplano-Puna Plateau (e.g. Barazangi and Isacks, 1976; Coira et al., 1982; Isacks, 1988; Baby et al., 1992, Gubbels et al., 1993; Wigger et al., 1994; Allmendinger et al., 1997). The Altiplano-Puna Plateau formed in Cenozoic time since 20 Ma is the central morpho-tectonic segment of the Central Andes which span the western margin of the South American Plate between 13 and 27°S (Allmendinger et al., 1997), with an average elevation of 3.65 km (Isacks, 1988). It is subdivided into Altiplano (15-23 °S) and Puna region (23-28°S) (Stern et al., 2007) and shows a change from NW-SE to N-S alignment of the Quaternary volcanic chain at 23°S. Subduction related volcanism started before plateau formation, and is characterized by a progressive migration from the western position by about 150 km to the east (Coira et al., 1982; Scheuber et al., 1994). The recent volcanic front is concentrated on the western plateau border where it forms an active magmatic arc in the Western Cordillera, the Central Volcanic Zone (e.g. Thorpe et al. 1984, Ramos, 1999, Kley et al., 1999; Stern, 2004).

Parinacota volcano is located at 18°S/69°W, at the north-west edge of the Altiplano plateau, in Arica elbow, where the obliquity of the convergence angle is 0° (Stern et al., 2007) and the Altiplano-Puna reaches a maximum width of 400 km. The Altiplano is underlain by a subducting slab descending at a relatively steep angle of ~25° (Cahill & Isaacks, 1992) at convergence velocity of 7-9 cm/a (DeMets et al., 1990; Samoza, 1998). The volcanic front of the CVZ lies approximately 120-150 km above the subducted slab and a remarkably thick continental crust exceeding 70 km below the Altiplano region (James, 1971; Zandt et al., 1994; Allmendinger et al. 1997; Scheuber & Giese, 1999; Yuan et al., 2000, 2002; Tassara et al., 2006). The extraordinary thick crust below the Altiplano Plateau is considered to be formed by mostly crustal shortening of the South American plate and lower crustal flow (Isacks, 1988; Allmendinger et al., 1997; Babeyko &Sobolev, 2005). Furthermore, tectonic underplating of material removed by subduction erosion (Schmitz, 1994; Baby et al., 1997), magmatic additions to the crust (Thorpe et al., 1981; Petford et al., 1996; Lamb et al., 1997) as well climate controlled sediment starvation (Lamb & Davis, 2003) are also considered processes contributed to the creation of an unusually thick crust below the CVZ.

Parinacota forms together with Pomerape volcanic twins, known as the Nevados de Payachata located in the Central Andes, in the north-east Chile on the border with Bolivia. The recent morphology of Parinacota is characterized by a nearly perfect conical shaped stratovolcano (6350 m asl) covered by a permanent ice cup and includes three flank eruption centers on the south side of the volcano. The cone is formed by andesitic lava and pyroclastic flows and sits on an earlier andesitic to rhyolitic lava dome complex. The estimated total erupted volume for Parinacota reaches ~46 km^3 (Hora et al, 2007). A sector collapse at Parinacota volcano has been recognized from debris avalanche deposit by remote sensing study (Francis & Wells, 1988) and detailed field work (Wörner et al., 1988). The debris avalanche extends on the western side of the volcano surrounding area to >25 km distance with more than 140 km^2 and an estimated volume of 6 km^3 (Wörner at al., 1988; Clavero, 2002). Significant changes in eruption rates are linked to edifice collapse and reach from 0.5-0.8 km^3/ka for the pre-collapse phase and 0.7-1.2 km^3/ka for the post-collapse phase (estimated eruption rates intervals are based on minimum and maximum eruptive volumes depending on assumed hidden volcano morphology, Hora et al., 2007).

The basement underlying Parinacota volcano is built of the Proterozoic Arequipa terrain (Tosdal, 1996; Wörner et al., 2000; Loewy et al., 2004), characterized by low unradiogenic Pb and εNd values with high $^{87}Sr/^{86}Sr$ ratios and Sr/Y ratios observed in magmas that traverse the Arequipa crustal domain (Mamani et al., 2008). The crust below the Altiplano is felsic to the depth of 50-55 km and has a more mafic composition below this depth (Yuan et al., 2002; Tassara, 2005). The upper crust simulates granitic composition whereas lower crust most probably consists of garnet-pyroxene granulite (Mamani et al., 2008). The lithologies below Parinacota likely comprise: 1) the Proterozoic amphibolites and gneisses of metamorphic Belen Complex in the northernmost Chile and granulites and charnokites of Cerro Uyarani exposed in western Bolivia (Wörner et al., 2000); 2) late Oligocene to middle Miocene volcanoclastic and lacustrine Lupica Formation, 3) Miocene volcaniclastic Oxaya Formation, 4) Late Miocene to Pleistocene Lauca Formation dominated by Ignimbrite layers and lacustrine sediments (Kött et al., 1995; Gaupp et al., 1999; Wörner et al., 2000).

2.3. EVOLUTIONARY STAGES

Detailed study of the eruptive history of Parinacota, the relationships in morphology and stratigraphy including geochronology and geochemistry provides a first insight into evolution of subvolcanic system. A brief stratigraphic overview presented here (Figure 1) is based on compositional units and $^{40}Ar/^{39}Ar$ ages determined from groundmass or sanidine crystals by Hora et al. (2007). The whole rock data set consists of new and published analyses of Wörner et al. (1988), Clavero et al. (2004), and Hora et al. (2007).

2.3.1. INITIAL ERUPTIONS CHUNGARÁ ANDESITES (ca)

The initial andesitic stage dated at 163-117 ka forms southward-directed lava flows close to the shore of Chungará Lake. The restricted composition (58-60 wt% SiO_2) is reflected by uniform porphyric amphibole andesites with up to 20% phenocrysts by volume. A hiatus of 65 ka between effusion of Chungará andesites and further pre-collapse Parinacota eruptions as well as similar K-Ar-ages of adjacent small volcanic centers indicates that these early Chungará flows may be temporally rather related to the small andesite centers of Chucullo and Caquena and the older Pomerape volcano than represent Parinacota volcanic system.

2.3.2. PRE-COLLAPSE UNITS OF OLD CONE (OC) AND RHYODACITE DOME PLATEAU (dp)

The main part of the pre-collapse flows forms the debris avalanche deposits to the west of the edifice surrounding area. Debris avalanche lithologies consist of chemically variable lavas reflected also in a broad textural range, characterized by occurrence of amphibole phenocrysts as prevailing Fe-phase. In situ Old Cone outcrops occur in the northern and southern part of the Parinacota edifice and reveal complex eruptive sequences from temporal and spatial separated centers (Hora et al., 2009).

The Old Cone andesite-dacite lavas span an eruption interval from 52 to 20 ka. The beginning of Old Cone growth is preserved in two North flank units which have been distinguished on the basis of different textures and mineralogy, (*ocl1* 52-39 ka) and (*ocl2* 38-20 ka), the composition range from silicic andesite to dacite lavas (62.6-66.1 wt% SiO_2). Hora et al. (2009) joined both isotopically uniform units (*ocl1* and *ocl2*) to (*oc1*), characterized by low $^{87}Sr/^{86}Sr$ ratios, and suggested the eruptions from a northerly located magma reservoir. Coeval to (*oc1*) lavas, the andesite group (*occ*) with the highest $^{87}Sr/^{86}Sr$ ratios was produced from a separate reservoir, located below the edifice. The (*occ*) unit shows ages older than 28 ka and is only represented in the debris avalanche material.

Simultaneous emplacement of rhyodacitic to rhyolitic domes in a short time interval between 47 and 40 ka occurred to the south and south-west of the stratocone, forming the Dome Plateau (*dp*). The compositions show two cluster of rhyodacitic (67-70 wt% SiO_2) and more evolved rhyolitic suite (72-74.5 wt% SiO_2). The chemical and textural features of the rhyodacites sampled from debris avalanche correspond to in-situ samples and overlap the same age range.

The second eruptive sequence during Old Cone stage comprises two coeval distinct magma batches, northern andesitic (58-63 wt% SiO_2) lava flows (*oc1a*) dated at 32-28 ka and a large voluminous dacitic coulees (63-65 wt% SiO_2) extending along the border between Chile and Bolivia, called "Border Dacite" (*ocb*) by Wörner at al. (1988). Border dacites extruded from southerly vents in a short time interval from 31 to 28 ka represent about 3 km³ lavas (~7% of total eruption volume) of uniform composition and textures. Hora et al. (2007) describe this early Old Cone stage as an intermediate to silicic dome and flow complex.

The youngest Old Cone lavas (*oc2*) erupted from 28 to 20 ka show a notable scatter in chemical and isotopic compositions within andesitic and dacitic compositions, suggesting already increased recharge frequency prior to collapse. Beside andesites and dacites, there have also been found two-pyroxene- and olivine-bearing basaltic andesitic lavas (*OCba*) at the NW part of the edifice (undated). They show the lowest silica content found among the Old Cone (56 wt% SiO_2). This unit is considered as a beginning of the reconfiguration of the plumbing system and coalescence of three main magma reservoirs below Parinacota that had existed during Old Cone stage (Hora et al., 2009).

2.3.3. Edifice collapse and Debris Avalanche (dbf)

The destruction of the ancestral Parinacota edifice has been recognized as a single catastrophic sector collapse event that produced ~6 km³ of debris avalanche deposit generating hummocky topography to the west of the present stratocone (Francis & Wells, 1988; Wörner at al., 1988; Clavero, 2002). The relation between collapse volume and estimated volcano volume before collapse (22.8- 39.6 km³, Hora et al., 2007) exceeds the average 5-10 % known from other examples of stratovolcano collapse (Siebert at al. 1995). The debris avalanche deposit consists mainly of the rhyodacite and amphibole-andesite representing the geochemical and mineralogical features of Dome Plateau and Old Cone lavas. The absence of juvenile magmatic component excludes a laterally directed and magmatically driven explosion, such as occurred at Mount St Helens.

Several factors have been considered for being responsible for development of edifice instability and emplacement of the large sector of the Parinacota western flank. The failure of the water-saturated substrate, overloaded by the dense ancestral edifice, is considered as a primary cause for the edifice collapse (Clavero et al., 2002). Changes in the hydrologic system of Parinacota caused by rapid glacial retreat, accompanied by fast edifice growth during the latest Old Cone period probably also contributed to edifice failure (Hora et al., 2007). An intrusion of a cryptodome buried by further post-collapse eruptions might have finally triggered the edifice failure as suggested by Clavero (2002). Wörner et al. (1988) reported rare dacitic deposits associated with the collapse event. They interpreted the presence of fresh prismatically joined dacitic bombs, found on top of avalanche deposit as juvenile magmatic component. Moreover, the oldest Chungará Lake sedimentary unit shows 2 cm thin glass shards dominated tephra layer (Sáez et al., 2007) that can represent both, a juvenile material or a fine ash fall associated with the edifice collapse.

The time of the sector collapse were derived from different estimations/observations, which confine the time interval for this event. Radiocarbon dating of pre-avalanche sediments from the Cotacotani Lake, created within the avalanche hummocky topography, reveals a minimum age of 13.5 ka (Francis & Wells, 1988). The Chungara Lake, generated by avalanche damming of the westward drainage of Pre-Lauca River (Francis & Wells, 1988; Wörner et al., 1988; Sáez et al., 2007), yields ~15 ka by Moreno et al. (2006) and ~16 ka by Sáez et al. (2007) from ^{14}C-dating of the oldest, lacustrine sediment unit. The ^{3}He-exposure age dating obtained from fresh columnar joined block exposed on the top debris avalanche gives slightly older age of 18.2 ±0.7 ka (Wörner at al., 2000). The same age of Parinacota edifice collapse has been bracketed by ^{40}Ar/^{39}Ar dating of the youngest pre-collapse (*oc2*) andesite, which reveals 20 ±4 ka (Hora et al., 2007) and the exact oldest age can thus not be obtained from the ^{40}Ar/^{39}Ar technique due to inaccessible earliest post-collapse eruptions, as suggested by Hora et al. (2007). Strong glacial erosion of the Old Cone with numerous moraines and glacio-fluvial deposits related to the pre-collapse eruptions (Hora et al., 2007) are correlated with the local glaciation events (Thompson et al., 1998), and the global Late-Pleistocene Last Glacial Maximum in the Andes around 18 ka (Lowell et al. 1995; Lamy et al., 1999; Kaplan et al., 2004). The age of the oldest lacustrine sediments from Chungara Lake correlate with the palynological studies from Chiloé Island indicating rapid warming after the final glaciation between ca. 17.6 and 16.4 ka and cold-wet conditions for the interval 21.5-16.5 ka in the Southern Andes (Lamy et al., 1999). Concluding, the upper and lower time limit of Parinacota edifice collapse is formerly constrained to 18 and 15 ka and may be closely related in true to ice retreat, following the last glacial maximum at ~18 ka.

2.3.4. POST-COLLAPSE UNITS OF YOUNG CONE (YC) AND FLANK ERUPTIONS – AJATA FLOWS (a)

The post-collapse activity of Parinacota volcano results in the rapid construction of a new cone accompanied by flank vents eruptions on the south side of the edifice. The emission of Young Cone lava flows (*ycl*) and pyroclastic material (*ycp*) proceeded from one central summit vent in all directions with tephra fallout to the east of the cone according to the dominant wind direction. One central crater and the symmetrical stratocone of the Young Cone suggest a focused subvolcanic plumbing and development of a unified magma reservoir system. The oldest accessible Young Cone lava yields age of 8.1 ±1.8 ka, the most recent eruption sourced from central vent shows ^{40}Ar/^{39}Ar ages of 0.5 ±0.3. The large majority of post-collapse lavas forming the Young Cone are limited to a very narrow range of andesitic composition (57.9-59.3 wt% SiO_2). Several samples found on the east side of the cone form more evolved trend (60-64 wt% SiO_2). Isotopic characteristics of Young Cone show features corresponding to the coeval flank Ajata eruptions.

Flank vents located in the southwestern part of the Parinacota stratocone have been connected to a local NNE lineament comprising Cerro Condorini, Pomerape and Parinacota (Clavero et al., 2004). These most mafic Parinacota eruptions formed monogenetic scoria cones and aa lava flows representing three compositionally distinct magma batches. The Ajata flows are situated at a minimum linear distance of 3.5 km from the main crater. They consist of two lava flows, the oldest flank lava of the Middle Ajata (*a1*) dated at 9.9 ±2.1 ka and 5.4 ±2.7 ka, and the youngest high-elevation flank eruption of the High Ajata (*a4*) dated at 2.6 ±1.3 ka. These adjacent flank eruptions show major-element chemistry, mineral compositions, and petrography similar to the Young Cone lavas. The southern Ajata centers are located about 5.5 km linear distance from the Parinacota central summit crater. It comprises two nested scoria cones placed between three rhyolitic Dome Plateau units. It produced Lower (*a2*) and Upper (*a3*) basalt andesitic lava flows. The (*a2*) and (*a3*) Ajata eruptions have poorly constrained $^{40}Ar/^{39}Ar$ ages of 5.8 ±7.4 ka and 4.8 ±4.0 ka, respectively. Both microphyric lavas show contrasting geochemical and isotopic signatures. The Upper Ajata has the most mafic composition erupted at Parinacota (53.3 wt% SiO_2) with the highest Sr and Ba contents (1650-1950 ppm) known from the Central Andes. In contrast, the Lower Ajata (56.7 wt% SiO_2) yields the lowest Sr and Ba (~800 ppm) concentrations within all mafic Parinacota lavas. The Lower and Upper Ajata flows represent to two distinct baseline magmas entering the Parinacota volcanic system.

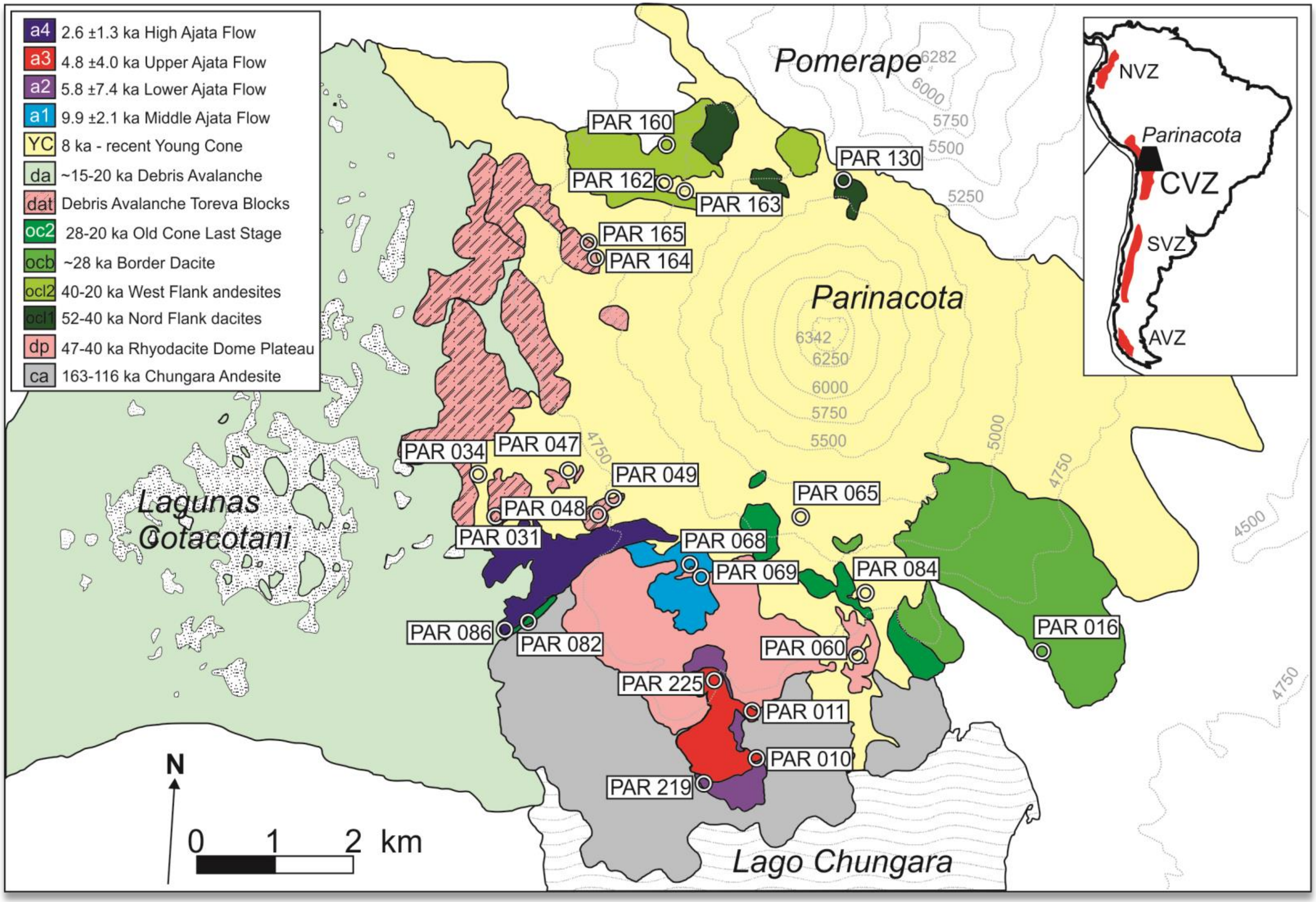

Figure 1. *Schematic geological map of Parinacota volcano modified from Hora et al. (2007) and Hora et al. (2009), presenting location of samples used for geothermo-oxy-barometry study. Inset shows location of Parinacota in the Central Volcanic Zone (CVZ). NVZ – Northern, SVZ – Southern, AVZ – Austral Volcanic Zones. Colors of the stratigraphic units are used in the mineral chemistry and geothermo-oxy-barometry plots. Sample locations are indicated with small circles.*

3. METHODS

3.1. SAMPLING

Referring to different petrographical features, 23 samples were selected from the sample set of Wörner et al. (1988) and Entenmann (1994) for the **g**eo**t**hermo-**o**xy-**b**arometry (GTOB) methods. The samples represent all five stratigraphical and compositional units of Parinacota. Sample locations are presented in Figure 1. Main sample characteristics and relation to Parinacota units of Hora et al. (2007), (2009) are presented in Table 1. Additionally, we present here new complementary bulk chemistry data covering whole sample set collected since 1986 field work (Wörner et al., 1988; Hora et al., 2007), (Electronic Supplementary Data).

3.2. ANALYTICAL METHODS

Are Analyses of 10 major and 28 trace elements were performed on fused glass discs using X-ray fluorescence (XRF) on a PANalytical AXIOS sequential spectrometer equipped with rhodium target tube and seven laterally curved monochromators at the Geosciences Centre Göttingen. The automated glass fusion technique SGE 21 (Schoeps) from rock powder was used. The instrument calibration was based on the international geochemical reference samples from e.g. US Geological Survey, the International Working Group “Analytical standards of mineral, ores and rocks”. The UA-G and UA-U standards were measured together with the samples. Applied routine measurement method performed with the SuperQ 4 spectrometer software and interference corrections results in accuracy and precision better than 1-2 % for major elements and 2-5% for trace elements as indicates by analyses of international reference materials.

Trace elements data were obtained by inductively coupled plasma mass spectrometry (ICP-MS) using Perkin Elmer SCIEX Elan DRC II at Geoscience Centre Göttingen. The dissolution of whole rock powders was prepared with the mixture of HF and $HClO_4$ followed by re-dissolution with HNO_3 after evaporation in Teflon beakers, method modified after Heinrichs and Herrmann (1990). Internal standards of Ge, Rh, In and Re were added to diluted sample solutions. The international standards JB3 (basalt) and JA2 (andesite) were analyzed attendant. The estimate analytical error yields ±5% 2σ for REE, <10% for Li, Be, Cu, Rb, Y, Cs, Hf, Tl, Pb, Th and U, <20% for Nb and Ta.

Mineral major element compositions were determined by electron microprobe (EMS) analysis carried out at the Geoscience Center Göttingen on five-spectrometer microprobe JEOL JXA 8900 RL. The measurements were performed separately for different mineral phases using appropriate measurement and standard conditions. BSE images of measured mineral grains were taken additionally using a COMPO-mode beam scan for proving the textural information to asses equilibrium conditions of the mineral pairs used for GTOB calculations.

Because of small oxide grain sizes, Fe-Ti oxide compositions, analyzed with the “spinel program” with a focused beam at 20 keV accelerating voltage, and 20 nA beam current. Peak counting times varied for the major elements (Fe, Ti) and trace elements (Si, Al, Mg) between 15 and 30 s on the peak and 5 and 15 s for the background, respectively. The Ti peak overlap correction was set for V, Cr, Ni and Zn. Silicate minerals were analyzed using 15 keV accelerating voltage and 15 nA beam current, a defocused beam (5-15 µm) as applied depending on grain sizes. Peak counting times were usually 15 s and 5 s for the background. Natural and synthetic oxides and silicate were used as standards. For both, oxides and silicate x-ray intensities corrections for matrix effects were made automatically using the Phi-rho-Z procedure of Armstrong, 1995. The analytical uncertainty is typically <1%.

3.3. GEOTHERMO-OXY-BAROMETRY METHODS (GTOB)

Geothermo-oxy-barometry methods applied in this study comprise methods described in Chapter 3, section 3.3, extended to two-pyroxene thermobarometer. A series of available geothermobarometer based on mineral-liquid equilibria (Putirka, 2008), commonly used for volcanic rocks are not applicable for Parinacota rocks due to an absence of primary silicate-melt inclusions in olivine, pyroxene and feldspars.

3.3.1. TWO-PYROXENE THERMOMETER AND BAROMETER

Crystallization temperatures and pressures of clinopyroxene-orthopyroxene pairs were calculated by applying formulations of Putirka (2008), based on revised calibrations by Brey & Köhler (1990) for two-pyroxene (2px) thermometer and by Mercier et al. (1984) for two-pyroxene barometer. Due to a P-sensitivity of the 2px-thermometer and T-sensitivity of the 2px barometer, P-T calculations were conducted using iterative calculation spreadsheet of Putirka (2008), including a default P-T input for iterative calculations, which solve the equations for T (eq. 37), and for P (eq. 39) simultaneously. The P-T estimations have a standard error of ±3.2 kbar, ±60°C, however higher precision is given for cpx with Mg#>75(17) (±2.8 kbar, ±38°C).

Equilibrium conditions between clinopyroxene and orthopyroxene were tested by comparing the observed and experimentally determined Fe-Mg exchange coefficient, which yield $Kd^{Fe\text{-}Mg}$(cpx-opx) = $(X_{Fe}^{cpx}/X_{Mg}^{cpx})/(X_{Fe}^{opx}/X_{Mg}^{opx})=1.09 \pm 0.14$ by Putirka (2008). The $Kd^{Fe\text{-}Mg}$ of the cpx-opx pairs in Parinacota lavas show systematically lower values, in average 0.94 (σ±0.14) from all coupled cpx-opx pairs. Similar offset have been found for cpx-opx pairs from Lascar lavas, showing an average of (0.84 σ±0.17). This finding suggests that the offset may be connected to the calc-alkaline magmas investigated in this work, differing geochemically from these used by Putirka (2008), resulting in the value of 1.09. For this reason, the empirical value of $Kd^{Fe\text{-}Mg}$(cpx-opx)=0.94 ±0.14, obtained from Parinacota cpx-opx pairs have been used instead of that presented by Putirka (2008). This problem will be discussed in section 6.1.2.

A selection of the cpx-opx pairs has been a major challenge in the thermobarometry study of Parinacota rocks. Pronounced zoning, very rare occurrence of touching cpx-opx crystals, as well as presence of different pyroxene populations in single samples hinders unambiguous choice of the pair-analysis. The cpx-opx pairs have therefore been selected in connection with the textural features

---

[17] $Mg\#=[Mg/(Mg+Fe^{2+})]*100$

documented with BSE-images and general chemistry additionally, finally reduced by the chemical test ($0.802<Kd^{Fe\text{-}Mg}$(cpx-opx)<1.076). Generally, cpx-opx phenocrystic core analyses and rim analyses were coupled, phenocryst rims with microcrysts, or cpx-opx microcrysts. Some analyses were coupled repeatedly with different analyses of the other pyroxene species. Therefore, the two-pyroxene thermobarometry represents a range of possible P-T conditions.

4. WHOLE ROCK CHEMISTRY

The whole rock data set used in this study includes four data sets published by Wörner et al. (1988), Entenmann (1998), Clavero et al. (2004), and Hora et al. (2007), supplemented by 25 new analyses of samples collected since the 1986-campaign of Wörner et al. (1988). These additional analyses were prepared to provide a statistically representative data set. It has to be noted, that the number of analyses presented for the particular evolutionary stages does not necessarily correlate with the volume and eruption frequency of the individual stratigraphic units. This is mainly true for multiple analyses of the single Ajata lava flows, which represent significantly lower volumes (0.1-0.2 km³) compared to Old Cone (17-27 km³) and Young Cone (11-19 km³) lavas (volume estimations from Hora et al., 2007). Around one third of the samples are dated by $^{40}Ar/^{39}Ar$ and some by K-Ar, He-exposure (Wörner et al., 1988, 2000; Hora et al., 2007). This provides a precise evaluation of the edifice evolution in connection to the temporarily changing differentiation regime of Parinacota volcano. The complete data set is documented in Electronic Supplementary Data.

Parinacota rocks display a broad subalkaline compositional range from basaltic andesite to rhyolite (53-75 SiO_2 wt%) lying in the high-K calc-alkaline field (subdivision of Rickwood, 1989). According to the geochemical statistical modelling using Polytopic Vector Analysis (PVA), presented in Chapter 2, the petrogenesis of Parinacota lavas is based on two-stage magma mixing, comprising three distinct magmatic series present in Quaternary Central Andean magmas. Three end-member magma compositions are defined for their major and trace element compositions: 1) a basaltic BEM end-member (47.7 wt% SiO_2, 6.5 wt% MgO, 2390 ppm Sr) of shoshonitic affinity, 2) a mid-K calc-alkaline basaltic andesite AEM end-member (55.4 wt% SiO_2, 4.3 wt% MgO, 349 ppm Sr), representing low-Mg and high-Al arc magmas, and rhyodacite RDEM end-member (68.8 wt% SiO_2, 0.8 wt% MgO, 615 ppm Sr), which classifies as high-K calc-alkaline composition.

The two mafic BEM and AEM end-members, which are involved in the first magma mixing stage, for an array of “baseline” mafic compositions, which occur in the modern CVZ arc. They show contrasting LILE/HFSE and LREE/HREE. Their contrasting LILE contents are well defined by Sr contents. Among all Parinacota lavas, the basaltic andesites of the Lower Ajata (*a2*) and Upper Ajata (*a3*) represent magma compositions most similar to the AEM and BEM end-member compositions, respectively. The terms “low-Sr” and “high-Sr" are therefore here used, according to previous studies of Parinacota by Ginibre & Wörner (2007), and PVA study in Chapter 2.

A precise determination of end-member magma compositions involved directly in Parinacota, and their proportions in each sample, requires a separate PVA modelling. Young Cone lavas are assumed to be stronger overprinted by fractional crystallization, compared to magma mixing dominated Old Cone lavas (Wörner et al., 1988). For this reason, a careful selection of samples for the PVA modelling is required as well as an evaluation of effects by fractional crystallization in the PVA modeling, which is above a scope of this study.

We can simplify this study by adopting of the PVA end-members obtained from the Taapaca rocks. The whole rock trends of Parinacota rocks overlap for nearly whole major and trace elements with Taapaca. The most mafic high-Sr (*a3*) samples lies in Sr-SiO_2 space exactly on a mixing line between BEM and RDEM end-members obtained from Taapaca (Figure 11, Chapter 3 and Figure 18b section 7.2, this Chapter). Moreover, forsterite contents in olivines from Parinacota lavas are consistent with the Mg# of the PVA Taapaca end-members (Chapter 2, section 6.8). These observations justify the application of the Taapaca PVA results directly in the Parinacota study.

The PVA modeling on the hybrid Taapaca rocks shows that the magma mixing of the PVA end-member compositions explains the compositional variability of the Quaternary volcanics in the CVZ. Parinacota whole rock, which form very similar differentiation trend compared to Taapaca, were apparently also generated via two-stage magma mixing. Magma mixing as a main petrogenetic process is supported by the experimental study of Botcharnikov et al. (in prep.) conducted on Taapaca dacite and Parinacota basaltic andesite. Experimental fractionation trends differ significantly from the trend formed by natural compositions (Chapter 3, Figure 19), suggesting the petrogenesis of the Parinacota results from two-stage magma mixing PVA model. The whole rock compositions of Parinacota lavas in Figure 2 to Figure 5 are presented together with the PVA end-members.

Figure 2 and Figure 3 illustrate temporal changes in major and trace element chemistry of Parinacota rocks based on $^{40}Ar/^{39}Ar$ dating of Hora et al. (2009), thus, these plots comprise compositions of only dated samples from the data set of Hora et al. (2007, 2009). A series of Harker diagrams for major and selected trace element compositions, including all available whole rock data, are presented in Figure 4 and Figure 5.

A crucial difference in the whole rock compositions between pre- and post-collapse lavas is a significant compositional variability observed in pre-collapse lavas. They comprise compositions from 56 to 75 wt% SiO_2 in contrast to the post-collapse lavas, which span 53 to 64 wt% SiO_2.

The temporal evolution of major element compositions lead to more focused magmatic system in the post-collapse stage producing mainly andesites (Figure 2). However, trace elements of the post-collapse lavas show stronger variability in comparison to the major elements. This observation indicates variable proportions of both, geochemically contrasting mafic, and the silicic end-members magmas in the pre- and post-collapse magmas.

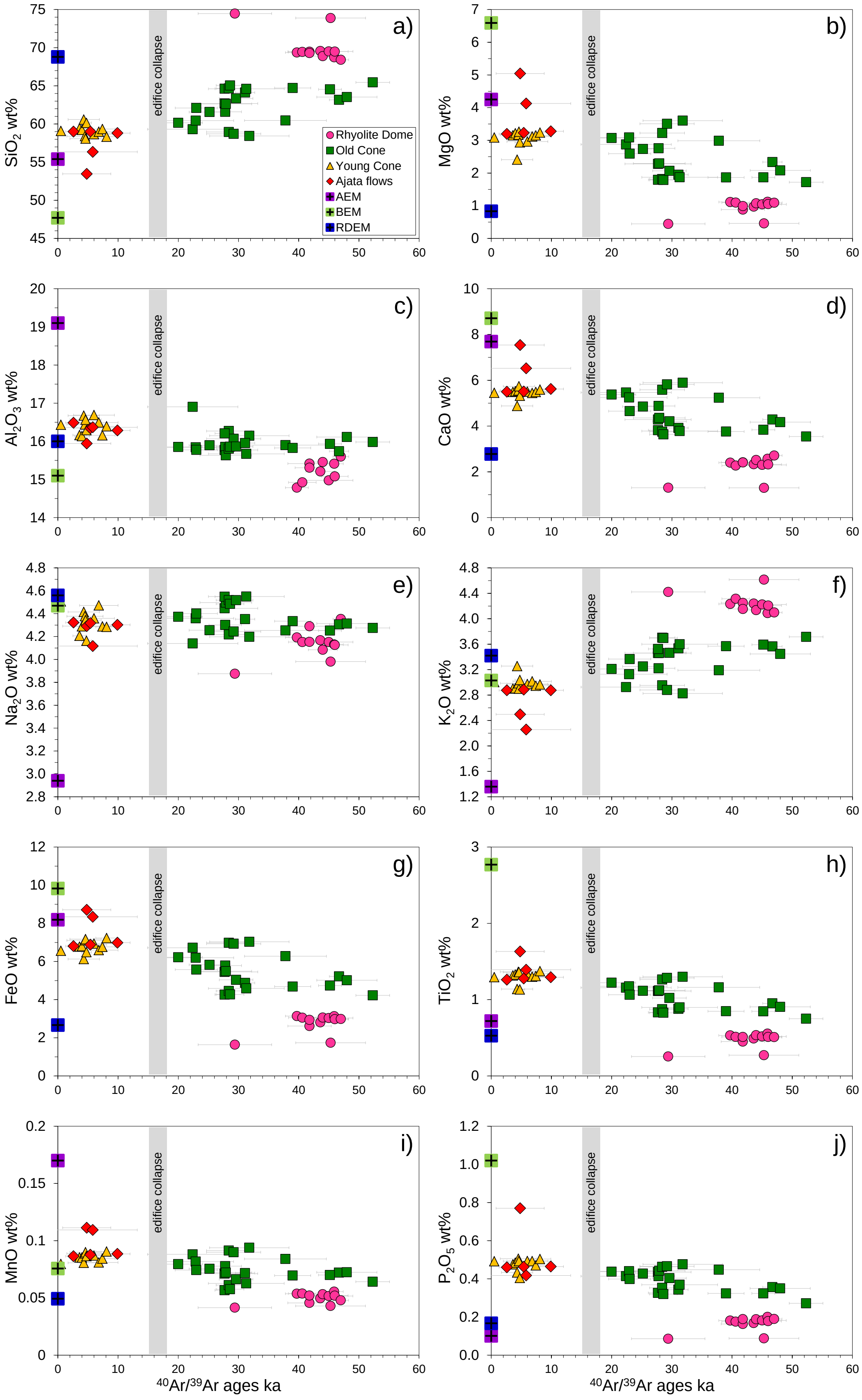

Figure 2. *Major element concentrations of pre- and post-collapse Parinacota lavas. The compositions of PVA end-member magmas (model 25-8p, Chapter 2) are presented for comparison at "zero age". Whole rock analysis and* $^{40}Ar/^{39}Ar$*-ages of Parinacota samples are taken from Hora et al. (2009). The timing of the sector collapse is marked as a time-interval between 15 and 18 ka (see 2.3.3 for explanation).*

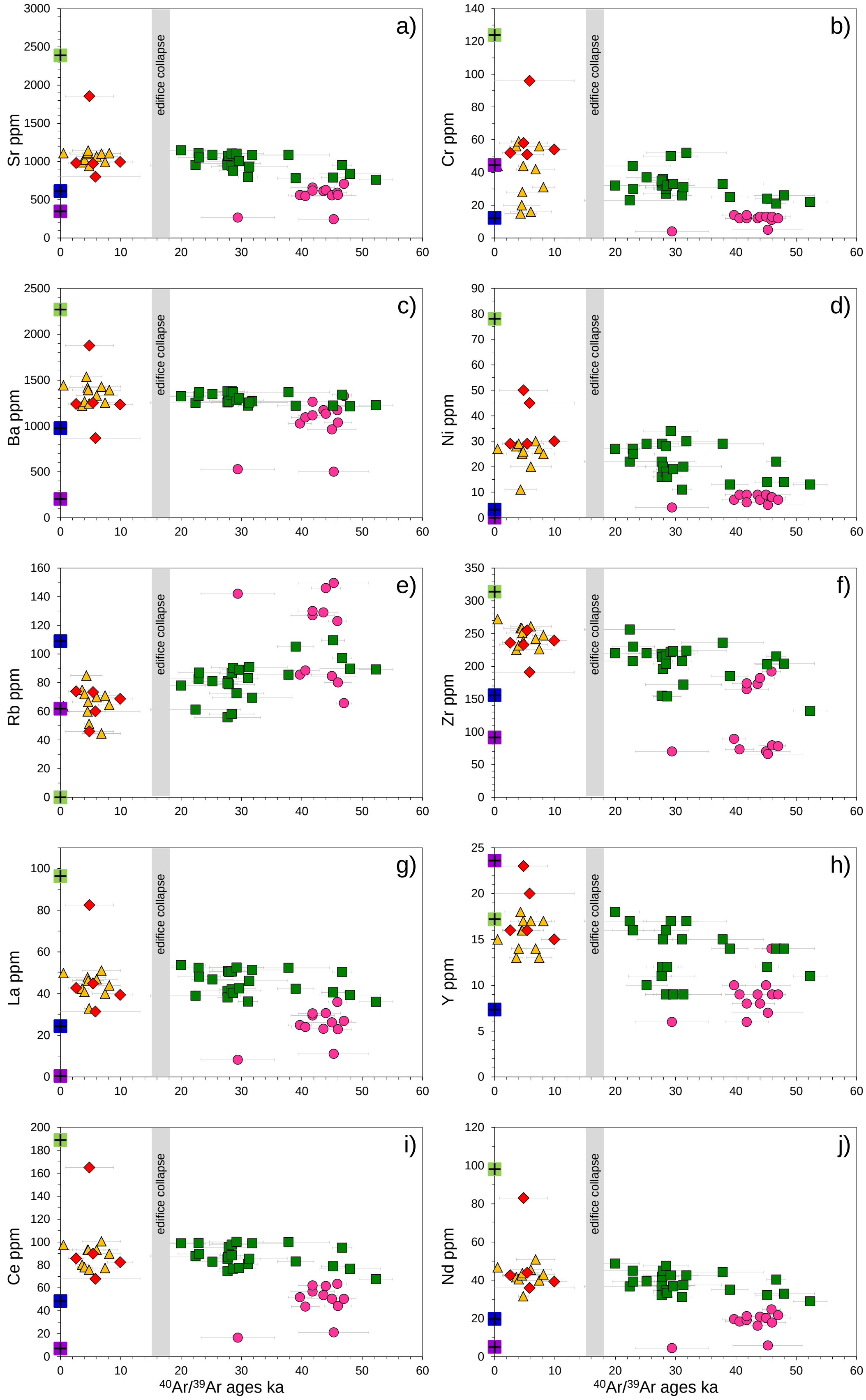

Figure 3. *Selected trace element concentrations of pre- and post-collapse lavas. The samples, database and symbols are the same as used in Figure 2.*

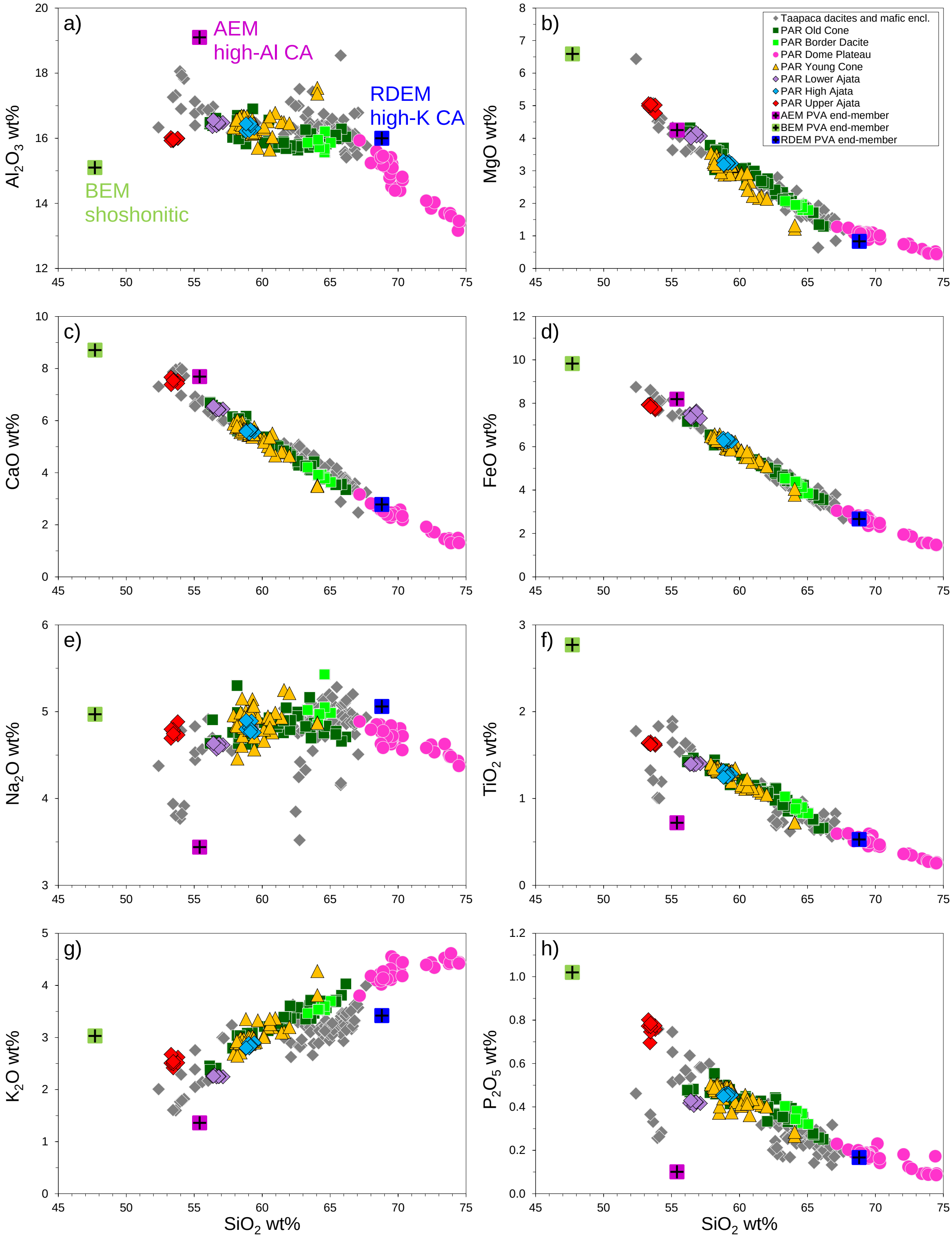

Figure 4. *Variations of major element in Parinacota lavas explained in relation to the PVA end-members. Taapaca samples are shown for comparison.*

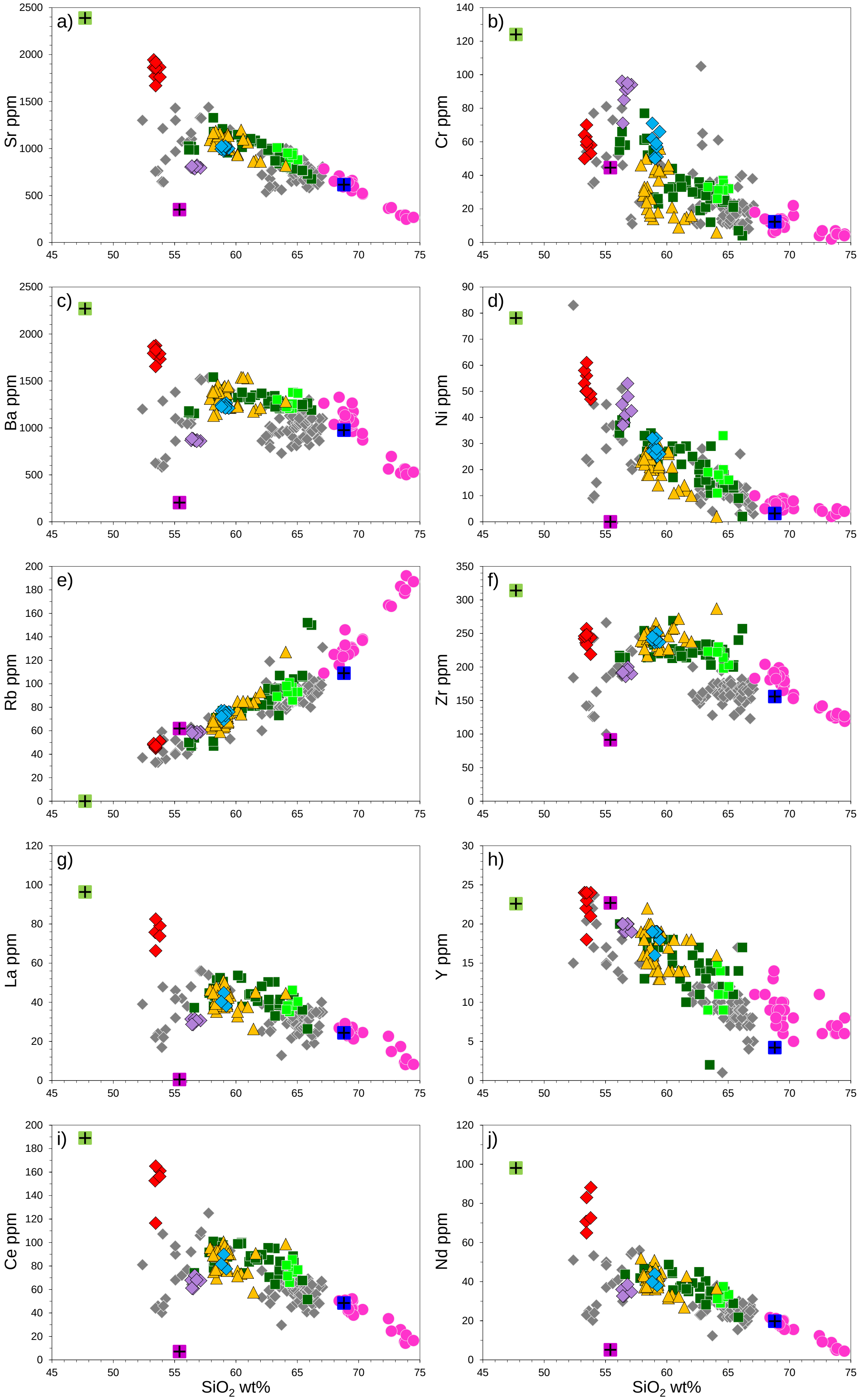

Figure 5. *Selected trace element compositions in Parinacota lavas explained in relation to the PVA end-members. Taapaca samples are shown for comparison. Symbols are the same as used in Figure 4.*

5. PETROGRAPHY AND MINERAL CHEMISTRY

5.1. PETROGRAPHY

The main petrographic characteristics of the samples selected for geothermo-oxy-barometry presented in this study are summarized in the Table 1. Differences between pre- and post-collapse encompass several features: 1) a change in the mineralogy of prevailing Fe-Mg phases in the intermediate lavas, 2) generally smaller phenocrysts sizes in the post-collapse lavas, 3) more continuous crystal size distribution (CSD) observed for plagioclase and Fe-phases in the post-collapse andesites (seriate textured) in comparison to rather bimodal CSD’s of the pre-collapse andesites (porphyritic), 4) a change in the morphology of plagioclase and their zoning patterns (Ginibre & Wörner, 2007), and 5) more diverse textural and chemical disequilibrium features observed in the pre-collapse lavas, strongly indicating mixing between mafic and silicic magmas.

5.1.1. PRE-COLLAPSE UNITS

Petrographic features found in the Old Cone lavas demonstrate unique characteristics related to their temporal and spatial distribution. Photomicrographs of selected samples representing pre- and post-collapse are presented in Figure 6. Except for basaltic andesite (OCba), all Old Cone samples contain: 1) rounded, entirely sieve-textured plagioclase phenocrysts with oscillatory-zoned overgrowth, besides euhedral normal and oscillatory-zoned phenocrysts, 2) xenocrysts of rhyolitic origin, and 3) Ti-magnetite phenocrysts as a stable Fe-Ti phase. In all Old Cone samples ilmenite is absent as micro- or phenocrysts. Its occurrence is restricted to composite grains with Ti-magnetite in the basaltic andesites and several andesites. The composite grains comprise ilmenite inclusions or ilmenite grains in contact to Ti-magnetite, which can represent both, primary grains or oxidation-exsolution (Haggerty, 1991).

The oldest unit (*ocl1*) is represented by porphyric andesite sample (PAR 130 in Figure 6a), analyzed extensively for plagioclase zoning by Ginibre et al. (2002). Evidence for magma mixing or assimilation processes is expressed by the occurrence of rhyolitic mineral phases in the andesite sample (rounded quartz, sanidine, biotite and amphibole), which result in the determined dacitic whole rock composition. Only a small amount of subhedral amphibole (~1 vol%) with fine-grained and thin breakdown rims have been found. Pyroxenes are a main Fe-phase and occur as single, commonly zoned, up to 5 mm large phenocrysts or in cpx-opx-pl-mt glomerocrysts. The pyroxenes rims as well as some small crystals show the lowest Mg-number and Ti contents as well as the highest Fe and Mn contents among all Parinacota samples. Ilmenite occurs rare and only as a composite type. Despite this, the plagioclase zoning patterns are relatively simple and suggest that mixing did not affected much plagioclase phenocrysts during their growth (Ginibre et al., 2002).

Unit (*ocl2*) is represented here by a porphyric amphibole-andesite (PAR 160 in Figure 6b), which contains euhedral to subhedral amphibole pheno- and microcrysts bordered by thin (<5 µm) reaction rims. Moreover, the amphiboles display both, hollow or fine- to coarse-grained cores, which often extend to large parts of the crystals. The grains are composed of typical amphibole breakdown assemblage, pyroxene, plagioclase, and magnetite. Beside rare sieve textured phenocrysts, plagioclase dominates as a groundmass phase; magnetite forms single grains or aggregates. Rounded biotite and euhedral cpx microcrysts are rare.

The most voluminous Old Cone unit consists of a highly porphyric dacite (*ocb*), the Border Dacite (PAR 16 in Figure 6c), which hosts up to 1 cm large plagioclase and amphibole crystals. A characteristic feature is the occurrence of sanidine megacrysts (<1 vol%). Strong petrographic evidence for magma mixing have been recognized by the presence of fine-grained, equigranular mafic enclaves, extensive disequilibrium structures such cpx coronas on resorbed quartz, amphibole coronas on cpx, sieve textured inner parts and rims of plagioclase, sanidine rapakivi rims. The phenocrysts assemblage consists of two compositionally and texturally distinct plagioclase, amphibole and magnetite populations (Figure 7 and Figure 8). Large amphiboles (>300 µm) are magnesiohornblende, which belong to the rhyolitic mineral assemblage, together with the sanidine, quartz, biotite, titanite, and zircon. Andesitic assemblage is represented by a second amphibole species, the magnesiohastingsite and plagioclase microcrysts, phases found also in the mafic enclaves. In general, the Border dacite mimics the dacites of Taapaca volcano, described in Chapter 3.

The youngest unit (*oc2*) comprises in this study two petrographically identical porphyric amphibole andesite PAR 49 and PAR 82, (Figure 6d). Amphibole phenocrysts and microcrysts show coarse-grained breakdown products (px, pl, mt), forming extensive, irregularly distributed areas within the crystals. Moreover, all amphiboles have variably and up to 100 µm thick, fine-grained (opaque) reaction rims. Hollow cores, zoning, co-growth with cpx and olivine inclusions (Entenmann, 1994) are common. Cpx occurs associated with amphibole or it forms glomerocrysts with magnetite; oscillatory and sector zoning is common. Opx is very rare and occurs as anhedral inclusions in cpx or as groundmass microlite. Strong evidence for magma mixing or assimilation processes are evidenced by subhedral sanidine and completely reacted biotite (biotite breakdown) as well as in “rhyolitic” (An<40) plagioclase compositions and cpx compositional modes (Figures Figure 7, Figure 8, and Figure 9).

A single Old Cone basaltic andesite (OCba) lava flow (PAR 164, PAR 165) is amphibole-free and reveals extensive disequilibrium features of the Fe-Mg silicates. It hosts texturally diverse olivine, cpx, and opx populations. Normally zoned olivine phenocrysts are rare and show extensive peritectic replacement by opx and magnetite. Small (<100 µm) groundmass relatively Fe-rich olivine with opx-magnetite overgrowth dominates. Slightly corroded cpx and opx phenocrysts and oscillatory-zoned cpx with opx inclusions or attached subhedral crystals have been identified as compositionally different populations (Figure 9). The finely zoned cpxs include rarely preserved rounded Fe-Mn-rich cores. Moreover, the opx are also mantled by coarse-grained olivine. Glomerophyric aggregates are common and consist of either cpx and magnetite or plagioclase phenocrysts. Plagioclase occurs mainly as lath-shaped and oscillatory zoned crystals and display seriate CSD. Sieve-textured inner zones are common. The entirely sieve-textured plagioclase phenocrysts, which occur in all other OC samples, are absent. Ilmenite is also rare and occurs only as composite grains together with Ti-magnetite.

The rhyodacite (*rd*), (sample PAR 48) and rhyolite (PAR 31) of the Dome Plateau usually contains up to 30 vol% phenocrysts of plagioclase, sanidine, quartz, amphibole, biotite, titanite, magnetite and zircon; ilmenite is rare. This unit comprises a large textural variety of porphyric hypohyaline perlitic-, spherulitic- and felsitic- or fabric-textured, often vesicular rocks.

5.1.2. POST-COLLAPSE UNITS

Post-collapse lavas change generally toward more mafic, compositionally and petrographically more uniform lavas. The andesite of the Young Cone (*yc*), (PAR 34 in Figure 6e, PAR 47, PAR 60, PAR 65, PAR 162, and PAR 163), as well as Middle (PAR 68, PAR 69 in Figure 6f) and High (PAR 86) Ajata flows consist of plagioclase, cpx and opx, and Ti-magnetite, ilmenite, apatite, and rare olivine-remnants. Plagioclases occur in most samples in a seriate crystal size distribution between pheno- to microcrysts and microlite. They reach up to 2 mm and show coarse sieve textures in the inner parts of the crystals, associated with extensive resorption surfaces and followed patchy zoning. Numerous resorption zones in the plagioclase phenocrysts, described by Ginibre & Wörner (2007), are associated with more sodic plagioclase composition. Glomeroporphyritic clusters of pyroxene, plagioclase and Fe-Ti oxides are frequent. Amphibole is rare, characterized by thick oxidized breakdown rims and composition matching Old Cone amphibole compositions.

The fine-grained basaltic andesite Ajata flank lavas differ petrographically from the basaltic andesites of the Old Cone by simpler porphyritic texture and general absence of plagioclase phenocrysts. The Lower Ajata (*a2*), (PAR 219 in Figure 6g) contains olivine, cpx and opx phenocrysts and amphibole “crystal clots” (term adopted from Stewart, 1975), coexisting with resorbed plagioclase and rare quartz xenocrysts, giving evidence for an overprint by underlying rhyodacitic material, erupted in the pre-collapse phase. Amphibole clots are common. They show complete breakdown with well-preserved euhedral shape. Olivine phenocrysts are skeletal with Cr-spinel inclusions; olivine microcrysts are surrounded by lath-shaped micro-opx. Both pyroxene and titanomagnetite reveal compositionally distinct groups (Figure 9 and Figure 10). Ilmenite is very rare and occurs as composite grains with Ti-magnetite. The Upper Ajata (*a3*) flow (PAR 10, PAR 11 in Figure 6h, and PAR 225) contains olivine and cpx phenocrysts; orthopyroxene is absent. Plagioclase occurs only as microcrysts and microlites characterized by the highest Sr contents among all Parinacota samples (Figure 7). The Upper Ajata, the most mafic Parinacota lava flow shows variations in mineral assemblage at constant bulk rock composition, observed in three different thin sections. Lower amounts of ilmenite observed in PAR 11 compared to PAR 10, is accompanied by a larger number of amphibole microcrysts. Only PAR 225 contains abundant amphibole microcrysts with fine-grained reaction rims; ilmenite is absent in this sample. Thus, in the Upper Ajata lava flow a remarkable change from small groundmass amphibole, completely affected by breakdown reaction to large partially preserved grains is observed.

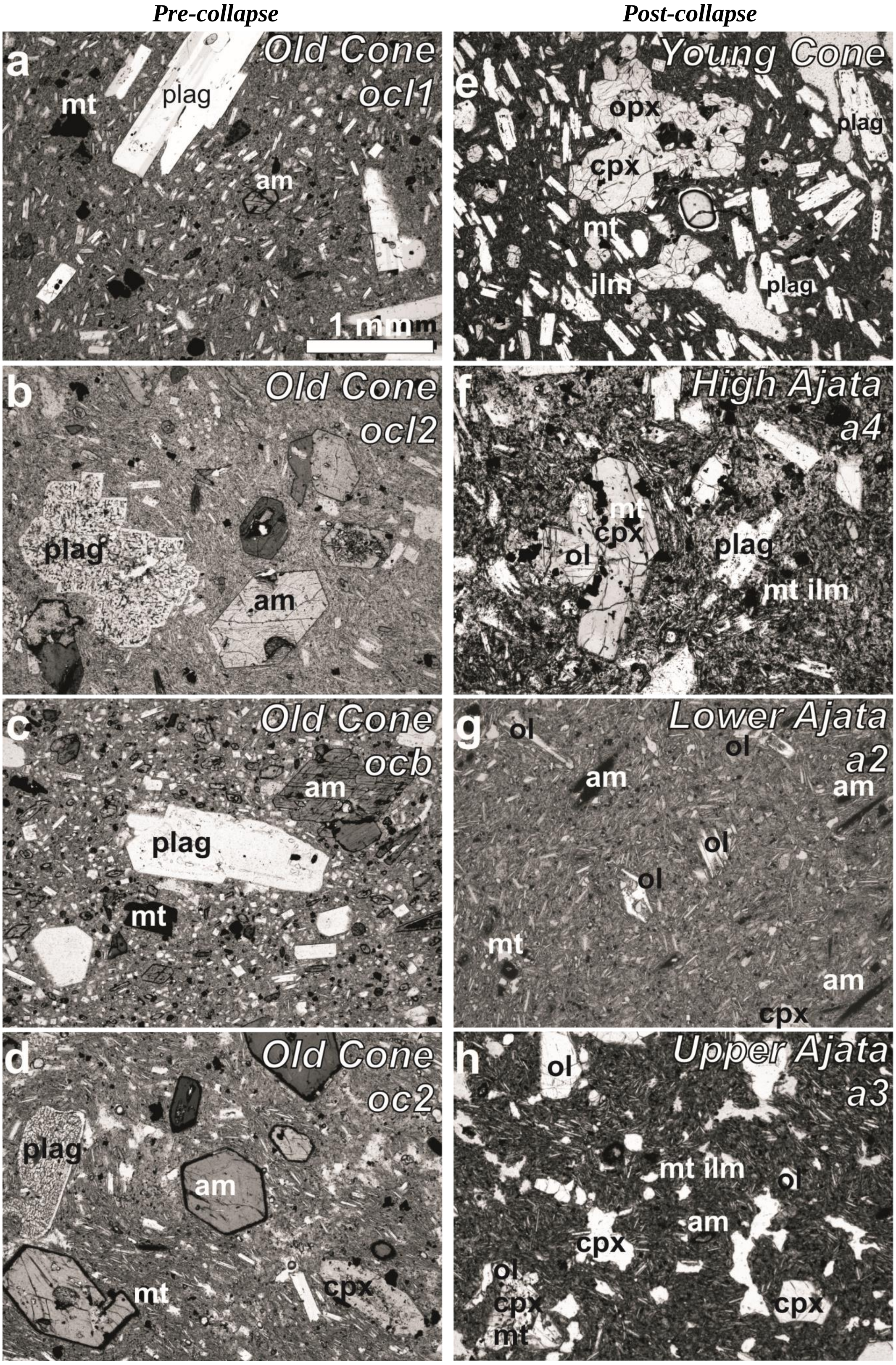

Figure 6. *Petrographic features of pre- and post-collapse Parinacota lavas. Pictures **a)-d)** represent pre-collapse Old Cone with mainly am-pl-mt assemblages with exception to basaltic andesite lava flows (OCba-not presented) which contain ol-pl-cpx-opx-mt. Picture **e)** shows typical Young Cone andesite, petrographically indistinguishable from the Middle (a1), and High Ajata (a4) flows presented in **f)**. Low- and high-Sr basaltic andesite Lower and Upper Ajata are presented in **g)** and **h)**. Both contain olivine in a broad crystal-size range, from micro- to phenocrysts (>300 µm), (see also Figure 18, Chapter 2). Plagioclases occur mainly as microlite and xenocrysts in the Lower Ajata. Amphibole microcrysts occur in different proportions and vary locally within the flows. Lower Ajata amphiboles show complete breakdown. Post-collapse lavas contain ilmenite in contrast to pre-collapse lavas, where ilmenite is not stable phase.*

Table 1. *Petrography of pre- and post-collapse Parinacota rocks selected for this study.*

Sample	stage	SiO_2 wt%$^{o*)}$	rock type	mineral assemblage
I. Pre-collapse units				
			Rhyolite Dome Plateau (47-40 ka)	
PAR 031	*rd*	73.4	coarse-grained pl-am rhyolite	san=qz>pl>bio>hb>ox
PAR 048	*rd*	69.5	medium-grained pl-am-bio phyric rhyodacite	pl>san=qz=bio>hb>ox>tit>cpx
			Old Cone (52-20 ka)	
PAR 130	*ocl1*	65.8	coarse-grained pl-am phyric andesite	pl>cpx=opx>ox>am=bio=san=qz
PAR 160	*ocl2*	62.6	medium-grained pl-am phyric andesite	pl>am>ox>cpx=bio>(opx)
PAR 016	*ocb*	64.6	coarse-grained pl-am phyric dacite with san megacrysts	pl>am>bio>ox>tit=ap=san=qz>cpx>(opx)
PAR 049	*oc2*	61.2	medium-grained pl-am phyric andesite	pl>am>ox>cpx=opx=bio
PAR 082	*oc2*	60.2	medium-grained pl-am phyric px-glomerophyric andesite	pl>am>ox>cpx>san>qz>ol>(opx)
PAR 164	*OCba*	56.4	fine-grined pl-ol-px seiate glomerophyric basaltic andesite	pl>ox=cpx>opx=ol
PAR 165	*OCba*	56.6	fine-grined pl-ol-px seiate glomerophyric basaltic andesite	pl>ox=cpx>opx=ol
II. Post-colllapse units				
			Young Cone (> 8 ka - recent)	
PAR 034	*yc*	57.9	fine-grined pl-px seiate glomerophyric andesite	pl>cpx=opx=ox>qp>ol relict
PAR 047	*yc*	59.3	vesicular fine-grained pl seriate glomerophyric andesite	pl>opx>cpx>ox>ap>am xeno(?)
PAR 060	*yc*	59.4	vesicular fine-grained pl-px seriate glomerophyric andesite	pl>cpx=opx>ox>ap
PAR 065	*yc*	58.7	fine-grained pl-px seriate glomerophyric andesite	pl>cpx=opx>ox>ap
PAR 084	*yc*	58.1	vesicular medium-grained pl-px seriate glomerophyric andesite	pl>cpx>opx=ox>ap
PAR 162	*yc*	61.6	fine-grained pl-px seriate andesite	pl>cpx=opx>ox>am
PAR 163	*yc*	59.5	fine-grained pl-px seriate andesite	pl>cpx>opx>ox>am
			Ajata Flows (10-3 ka)	
PAR 068	*a1*	59.2	fine-grained pl-px seriate andesite	pl>cpx=opx>ox>am
PAR 069	*a1*	58.8	fine-grained pl-px seriate andesite	pl>cpx=opx>ox>am>ol relict
PAR 219	*a2*	56.4	fine-grained pl-ol-px phyric basaltic andesite	pl>cpx=am(bd)>ox>ol>opx xeno
PAR 010	*a3*	53.4	vesicular fine-grained ol-cpx phyric basaltic andesite	ol=cpx>ox; pl only microlite
PAR 011	*a3*	53.8	vesicular fine-grained ol-cpx phyric basaltic andesite	ol=cpx>ox>am and pl only microlite
PAR 225	*a3*	53.3	vesicular fine-grained ol-cpx phyric basaltic andesite	cpx>ox>ol>am; pl only microlite
PAR 086	*a4*	58.8	fine-grained pl-px seriate glomerophyric andesite	pl>cpx=opx>ox>am

5.2. MINERAL CHEMISTRY

Different compositional and textural populations within a group of phenocrysts need to be correctly evaluated prior to an application of geothermo-oxy-barometers. In this study, mineral populations have been discriminated based on textural characteristics and binary plots (Figure 7-10), more effective than usual classifications. An exact examination of mineral chemistry from different samples provides a tool for identification of the magma type from which the minerals may have crystallized, also for a magnitude of magma mixing and/or AFC processes. The most useful discrimination for mafic phases is based on Mg, Ti and Al, complementary with Mn (per formula unit). The estimations of Fe^{3+} in ferromagnesian silicates from microprobe analyses were done using formula of Droop (1987) for pyroxene and amphibole, and with calculation scheme of Carmichael (1967) for Fe-Ti oxide. Chemical differences in plagioclase are illustrated using variations in Fe and Sr concentrations vs. anorthite contents.

A comprehensive mineral database comprising phenocrysts and microcrysts from all Parinacota units (included in Electronic Supplementary Data) displays generally well-defined mineral compositional trends and/or groups in each sub-unit in the pre-collapse lavas. In contrast, the mineral compositions in the post-collapse lavas show a scatter within a definite range, in accordance with the uniform whole rock compositions and petrographic characteristics. Two or more populations of one mineral phase as well as considerable compositional zoning usually occur in the Old Cone. Extreme compositions of outliers found in the post-collapse lavas, are considered to be of xenocrystic in origin.

5.2.1. PLAGIOCLASE

Figure 7 presents plagioclase analyses from the pre- and post-collapse Parinacota eruptive units, which comprise microlites and representative core to rim areas of phenocrysts. The detailed investigations of the plagioclase zoning of Ginibre et al. (2002) and Ginibre & Wörner (2007), as well as our own new data, which additionally include groundmass plagioclase from the mafic flank eruptions, do not reveal anorthite contents higher than 63 mol% in Parinacota lavas. This observation is consistent with plagioclase chemistry of Taapaca plagioclases described in Chapter 3.

Three compositionally distinct plagioclase groups occur in the pre-collapse lavas (Figure 7a, b): 1) A "rhyolitic" group, forming a coherent group in a narrow range of An20-30 and Fe<2000 ppm. Several analyses fall outside the An-interval that may be connected to a fractionation trend similar to Taapaca plagioclases (Chapter 3, section 7.1.2.2.). 2) An "intermediate" group, characterized by a nearly horizontal Fe-An trend in a range of An20-60 and 2500<Fe<5000 ppm, formed by plagioclase found in andesite and dacite samples. 3) A "mafic" group characterized by increasing Fe (3900-10200 ppm) with decreasing An (62-32 mol%) contents, found in "low-Sr" basaltic andesites and one andesite sample (PAR 82) from the youngest (*oc2*) eruptive unit. Sr concentrations of the pre-collapse plagioclase show a strong variability. The rhyolitic plagioclases contain up to 3000 ppm Sr, and the intermediate and mafic plagioclase show 540-5400 ppm Sr in An30-62 range. It is worth to noting, that the Sr concentrations in plagioclase from the andesite and dacite lavas show slightly higher Sr contents in comparison to the plagioclase from the low-Sr (OCba) lavas. In the rhyodacite samples, some high-calcic cores with elevated Fe and Sr concentrations have been found. Furthermore, beside the basaltic andesite, all pre-collapse samples contain the rhyolitic plagioclase. These characteristic rhyolitic plagioclase compositions (Fe<2000 ppm), which have been connected to the rhyodacitic end-member (RDEM) involved in the petrogenesis of Taapaca dacites do not occur in Parinacota post-collapse lavas.

After collapse, plagioclases show rather compositional scatter in comparison to the defined groups in the pre-collapse lavas. They show indistinguishable chemical characteristics in the andesites of the Young Cone, Middle and High Ajata units (Figure 7). Individual phenocrysts show a general fractionation trend of decreasing An and Fe contents. In addition, they record mafic magma inputs of a various recharge composition, limited to 8000 ppm Fe-contents and 3500 ppm Sr. Most plagioclase compositions form a coherent group of An30-62 within 2000-6000 ppm Fe, and Sr<3500 ppm. In the Fe-An space a separate group of plagioclase showing Fe>4000 ppm is recognized. This group represents crystal-rim compositions as well as small crystals crystalizing from the mafic recharge magmas. The highest Fe contents reaching 10000 ppm and moderate An35-50 and Sr (3000-5000 ppm) occur in plagioclase inclusions in orthopyroxene or enclosed in glomerophyric clusters of cpx and opx.

Plagioclases from the low- and high-Sr basaltic andesites of the Lower (*a2* unit) and Upper (*a3* unit) Ajata flows erupted from the flank vent after edifice collapse forms two separate compositional groups defined by distinct Fe and Sr within An48-62. Plagioclases from the high-Sr (*a3*) lavas show the highest Sr contents recorded in Parinacota plagioclases, reaching up to 7554 ppm; however, despite their high Fe concentrations (up to 1 wt%), An content is anyway limited to 63 mol%. Plagioclases from the low-Sr (*a2*) show the lowest Sr contents in plagioclase of the highest An contents, whereas Fe contents are similar to the large part of the plagioclase from (*a3*). Noticeable differences in Sr contents in the plagioclase in the An-range between 50 and 60 mol% from the basaltic andesitic pre-collapse (OCba), and post-collapse Lower (*a2*) and Upper (*a3*) Ajata lavas correlate with the differences in the Sr whole rock concentrations, forming positive trend between the maximal Sr contents measured in the plagioclase and in whole rock.

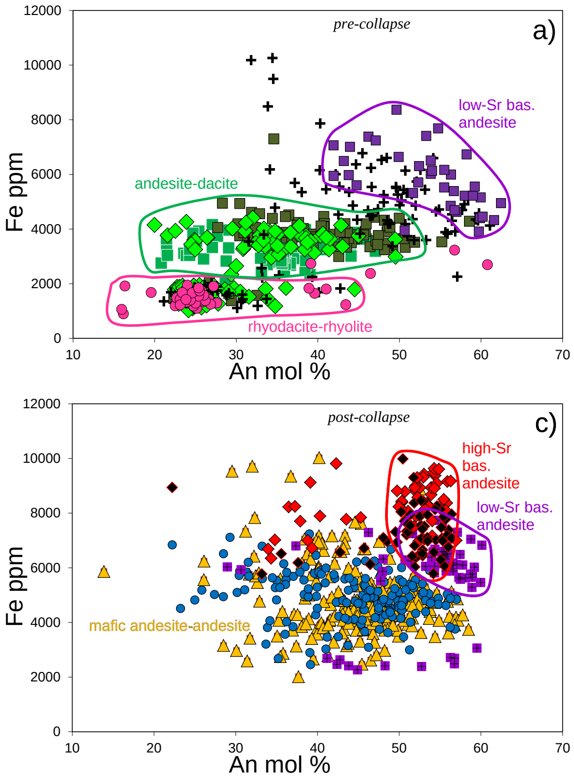

Figure 7. ***a)**, **c)** Fe-An, and **b)**, **d)** Sr-An space defined by plagioclase from pre-collapse (upper diagrams), and post-collapse (lower diagrams) Parinacota lavas.*

5.2.2. AMPHIBOLE

The classification of amphibole is based on 13eCNK calculation procedure favored by IMA (Leake et al., 1997). Calcic amphiboles (~11 wt% CaO) in Parinacota lavas show two separate populations due to differences in $(Na+K)_A$ within a Mg-number of 0.63-0.88 and Al_2O_3, TiO_2, and MnO contents. Amphibole characterized by low Al_2O_3 (5-10 wt%), TiO_2 (0.8-2.0 wt %, Ti<0.25 p.f.u.) and $(Na+K)_A<0.5$ p.f.u. are classified as magnesiohornblende (Mg-Hbl) with high MnO (2000-6000 ppm) and FeO (12.5-16.6 wt%) concentrations. High Al_2O_3 (10-13 wt%) and TiO_2 (2.5-4.3 wt%, 0.25-0.47 p.f.u.) amphibole classifies as (titanian)- magnesiohastingsite (Mg-Hst), which have $(Na+K)_A>0.5$ p.f.u., MnO<2000 ppm and FeO<12 wt %; they meet the criterion of $Fe^{3+}>^{[6]}Al$ for the hastingsite.

Although Mg-Hbl crystallizes from more evolved magma composition than the Mg-Hst (see Chapter 3, section 7.2.1), its Mg-number and MgO content overlap with those of Mg-Hst. In Figure 8 both amphiboles species are separated by their distinct Al_2O_3 contents. Plot of Al_2O_3 vs. MgO in Parinacota amphiboles reveals a noticeable connection between their chemistry and the major element compositions of the host rocks. It suggests that the magma composition may be a first-order factor controlling the amphibole chemistry, diminishing the role of the physical parameters of crystallization, as discussed in Chapter 3.

Mg-Hbl analyses from rhyodacite and rhyolite from Parinacota show that MgO content of the Mg-Hbl increases with increasing SiO_2 wt% of the host rock. A negative trend between Al and Mg in Mg-Hbl indicates Al-Tschermakite substitution ($Mg_{-1}Si_{-1}{}^{[4]}Al^{[6]}Al$), which incorporates more Mg and Si instead of Al in Mg-Hbl during differentiation. This compositional evolution toward higher MgO is consistent with an Mg-Fe-Ca amphibole (cummingtonite) found in silicic volcanic rocks, stable at low-T and high H_2O_{melt}, and high oxygen fugacity (<800°C, 6.4 wt%, >NNO+1.9, Mount St. Helens, Geschwind & Rutherford, 1992).

In contrast to the Mg-Hbl, the Mg-hastingsites form in the Al_2O_3-MgO space a series of subparallel trends of increasing Al_2O_3 with decreasing MgO in the basaltic andesite→ andesite→ dacite sequence of lavas from pre- and post-collapse Parinacota rocks. Notable is the opposite direction of decreasing SiO_2 contents of the host rocks for increasing MgO contents in amphibole, in comparison to the Mg-Hbl trend. The most mafic Mg-Hst from basaltic andesite (*a3*) and from mafic andesite (*a4*) overlaps with the core compositions of Mg-Hst found in the Taapaca basaltic andesitic enclaves (Figure 8a).

TiO_2 contents in amphibole shows generally positive correlation with Al_2O_3 (Figure 8b). Mg-Hbl from Parinacota rocks shows slightly higher TiO_2 contents at a given Al_2O_3 compared to Mg-Hbl from Taapaca dacites, whereas Mg-Hst overlap with those from Taapaca. Similar to Mg-Hst from Taapaca rocks, also Parinacota high-Al-Ti amphibole forms rather cluster of Mg-Hst from different samples superimposed on the general Al-Ti trend.

Amphibole chemistry from the post-collapse samples examined in the Al_2O_3-MgO and TiO_2 space states that these amphiboles may have crystallized from the post-collapse magmas and are not xenocrysts from the pre-collapse magmas. Moreover, the amphibole compositions found in the post-collapse lavas are limited to the Mg-Hst; the Mg-Hbl occurs in the pre-collapse lavas exclusively.

The study of amphibole compositions presented in Chapter 3 shows evidence for basaltic andesitic magma composition required for crystallization of the Mg-Hst. This amphibole population found in the andesites and dacites may indicate an origin of the Mg-Hst from compositionally variable mafic magmas. As shown in Chapter 2, the most mafic magmas in the Quaternary CVZ form an array of the high-Al basaltic andesite and shoshonitic basalt magma.

Amphiboles in Parinacota lavas reveal a noticeable link between their compositions and the major element chemistry of the host rock. As presented in Chapter 3 of this work, the Mg-Hbl crystalizes from the rhyodacitic magmas; the Mg-Hst crystalizes from the basaltic andesite magmas.

However, the large compositional variability of the Parinacota lavas reveals more clearly compositional differences within one amphibole species, depending on the whole rock. Such dependence has also been observed in Mg-Hst core compositions from the different basaltic andesitic enclaves from Taapaca rock, described in Chapter 3, section 4.2.2.3. Figure 8 shows Al_2O_3 vs. MgO and TiO_2 contents in Parinacota amphiboles. Al_2O_3 and MgO contents in Mg-Hst form a series of subparallel trends of increasing Al_2O_3 with decreasing MgO for the dacite-andesite-basaltic andesite sequence. The MgO contents decrease also with increasing SiO_2 wt% of the whole rock. The trend formed by Mg-hastingsites from Parinacota basaltic andesites overlap with the Mg-hastingsites from Taapaca basaltic andesitic enclaves. While the compositional differences of the basaltic andesite enclaves and their Mg-Hst from Taapaca have been connected to different proportions of the AEM (high-Al calc-alkaline) and BEM (shoshonitic) end-members, the Mg-Hst trends in Parinacota can be rather connected to different proportions of the RDEM-type silicic end-member admixed to the hybrid (AEM+BEM) magmas.

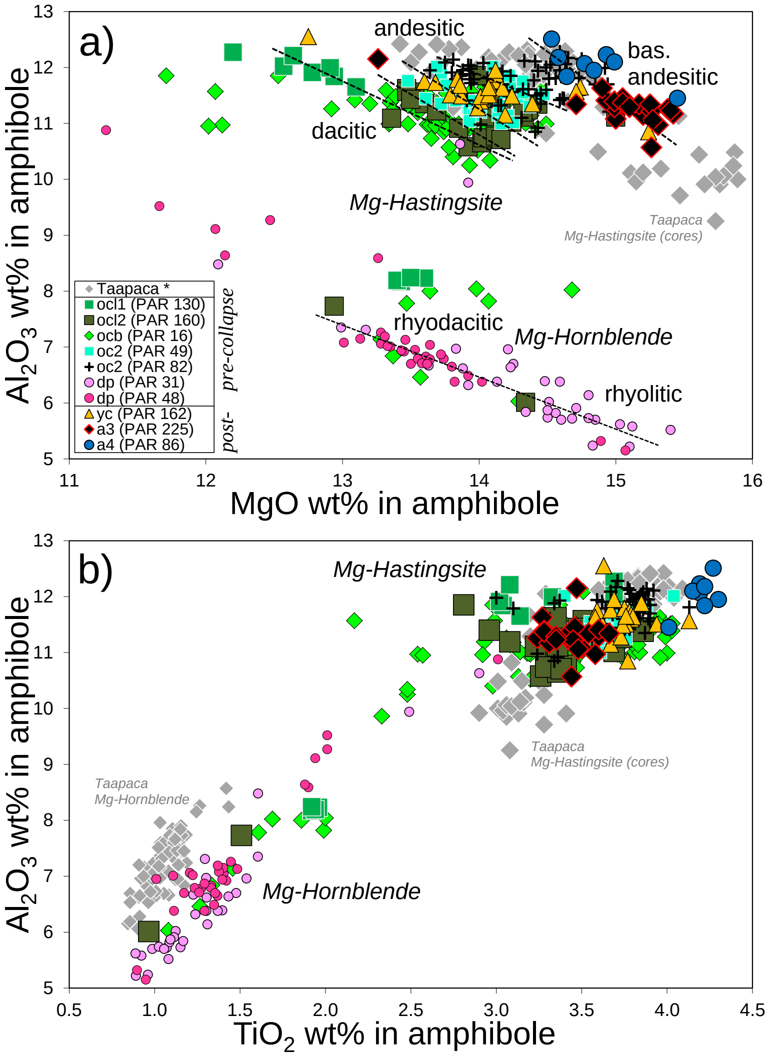

Figure 8. ***a)*** *Al_2O_3 vs. MgO, and* ***b)*** *TiO_2 contents in magnesiohornblende and magnesiohastingsite from basaltic andesitic to rhyolitic samples from pre- and post-collapse Parinacota lavas. For comparison, "Taapaca *" comprises in a) only crystal-cores compositions of magnesiohastingsite from Taapaca basaltic andesitic enclaves, in b) additionally magnesiohornblende.*

5.2.3. *PYROXENE*

Pyroxenes are defined on a basis of the relative amounts of Wo-En-Fs quadrilateral of Morimoto et al. (1988) where the composition is normalized to $Ca+Mg+(Fe^{2+}+Fe^{3+}+Mn)=100$. Figure 9 presents Ai/Ti vs. Mg/Mn ratios in clinopyroxene (cpx) and orthopyroxene (opx) from pre-collapse Old Cone lavas (Figure 9a, b) and post-collapse Young Cone lavas (Figure 9c, d) and separately from Ajata flows (Figure 9e, f). The Al/Ti ratio in cpx has been used by Le Bas (1962) to discriminate different mafic magma series and is used in this study to discriminate pyroxene populations. According to Loucks, (1990), crystallization of cpx having a high $CaTiAl_2O_6$(18)/$CaMgSi_2O_6$ ratio is favored by low silica activity relative to Ti and Al in the melt. Thus, the Al/Ti ratios are likely decoupled from physical parameter of crystallization and point to chemical properties of the melt. The Mg/Mn ratios are used to trace the differences in magma chemistry, due to an equivalent valence of Mg and Mn, and an assumption taken from Bacon & Hirschmann (1988) for Fe-Ti oxides, that Kd^{Mn} in pyroxene is not strongly dependent on whole rock composition and physical parameter of crystallization, therefor reflects the melt composition.

Pre- and post-collapse lavas reveal similar cpx compositions of $Wo_{29-47}En_{35-53}Fs_{10-20}$, which classify as augite, alumino-augite and minor ferric diopside in the most mafic magmas. Cpx is a minor mafic phase in the earliest Old Cone units and is very rare in the Parinacota dacites, where it rather has a xenocrystic character or forms corona structures on quartz. It becomes more frequent in the youngest Old Cone (*oc2*) unit and in the basaltic andesite (OCba). Cpx is then the main mafic phase in the post-collapse lavas and occurs as phenocrysts, microcrysts, in glomeroporphyritic clusters or in corona structures mantling olivine (after orthopyroxene) or quartz. Zoning is ubiquitous in cpx, and is defined by changing of Mg, Ti, Al, reflecting the Ti-Tschermakite exchange, accompanied with noticeable changes of Fe and consequently the Mg-number. Commonly, three parts in the phenocrysts are observed: core, mantle and rim, defined by abrupt compositional changes. The mantle is often characterized by fine oscillatory zoning. Sector zoning is present in the cpx in the mafic lavas of high TiO_2 in the bulk rock contents (1.4-1.6 wt %), and reveal differences up to 1.3 wt % TiO_2 between low and high Ti zones, causing up to 5 wt % changes in MgO, 5.5 wt % in Al_2O_3 and 2,5 wt % in FeO^{TOT}.

In the Old Cone lavas, cpx forms three compositional groups (Figure 9a). The oldest sample of a dacitic composition (*ocl1*) shows one population of cpx characterized by increasing Al/Ti ratios at low Mg/Mn (40-70). These compositions have been found in the cpx phenocrystic mantels and rims; the crystal cores lie on the horizontal trend in the Al/Ti-Mg/Mn space, showing Mg/Mn from 70 to 240, and at uniform Al/Ti ratios between 4 and 7(19). In contrast, younger Old Cone samples show merely the horizontal trend, which is also preserved in the post-collapse lavas (Figure 9c, e). In numerous samples, cpx compositions forms the third separate group of Al/Ti<4, having the lowest $^{[6]}Al$ values, not represented in the post collapse lavas. These compositions represent small (<100 µm) cpx crystals, which often occur as aggregates. Cpxs in the Young Cone samples plot rather as a

---

[18] $CaTiAl_2O_6$ – Ti-Tschermak component

[19] These compositional differences between cores and rims are discussed in section

compositional cluster with some more mafic compositions Mg/Mn>180. The vertical trend in the Al/Ti vs. Mg/Mn diagram recorded in the (*ocl1*) has only been found in the post-collapse basaltic andesite (*a2* unit), suggesting an involvement of cpx xenocrysts. In the Upper Ajata (*a3* unit), cpxs showing the Mg/Mn>180 have also significantly higher Cr contents reaching up to 5700 ppm, compared to other analysis having Cr below the limit of detection. High-Cr cpx were also found in the Young Cone lavas, in the crystal mantles after resorption of the crystal cores, characterized by the lowest Mg-number.

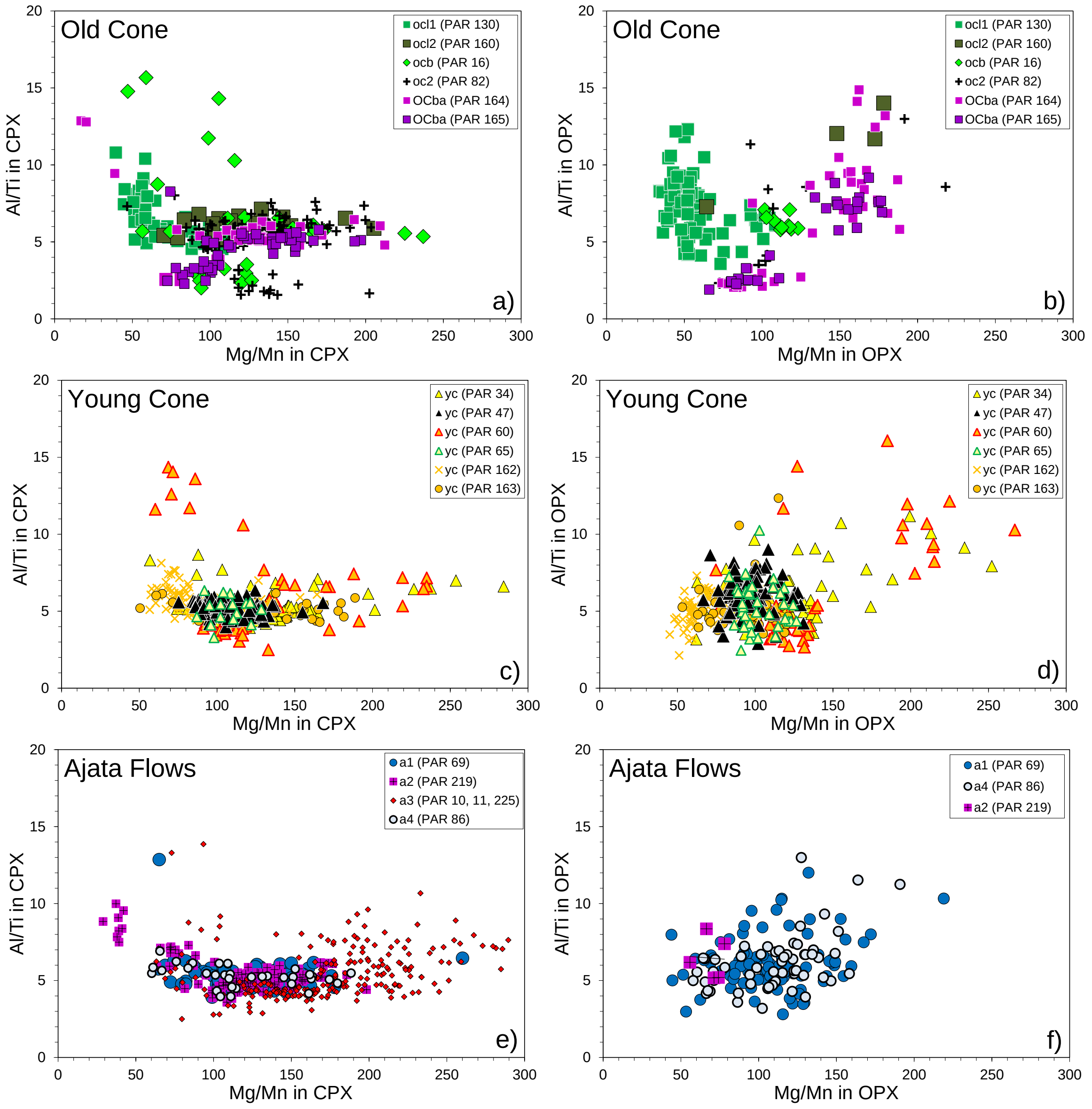

Figure 9. *Ai/Ti vs. Mg/Mn ratios in clinopyroxene and orthopyroxene in* ***a-b)*** *pre- and* ***c-f)*** *post-collapse Parinacota lavas.*

Orthopyroxene occurs as a second main mafic phenocrystic phase in the post-collapse andesites; in basaltic andesites from the Ajata flows the opx is absent, only one opx crystal have been found in this study in the low-Sr (*a2*) unit. Opx composition spans values of $Wo_{1-4}En_{62-78}Fs_{19-35}$, classifying as enstatite. The main analyses show Fs and En components in the range of $En_{70-75}Fs_{20-30}$ corresponding to bronzite; hypersthenes of Fs_{30-35} occurs in the oldest (*ocl1*) Old Cone dacite. The differences in the crystallization history between single lava flows are visible in the crystal zoning and crystal textures, comparable with the cpxs.

In the pre-collapse lavas, opx is a rare phase relatively to cpx. It occurs in the (*ocl1*), (*oc2*) and (OCba) units; in other pre-collapse lavas, opx is of xenocrystic origin or is a minor groundmass phase. Similar to the cpx, three compositional groups of the opx were recognized in the pre-collapse units (Figure 9b). Adequate Mg/Mn ratios to the cpx groups suggest simultaneous crystallization of these pyroxenes from the same magma composition. Post-collapse orthopyroxene in the Young Cone, Middle and High Ajata flows shows compositional uniformity within $Wo_{2-7}En_{65-78}Fs_{19-32}$ and the range of Al/Ti and Mg/Mn ratios (Figure 9d, f). The highest values of the Al/Ti>8 and Mg/Mn>150 are mostly represented in crystal rims or crystal mantles.

The Mg-numbers of the cpx range from 68 to 81 in both, pre- and post-collapse lavas, and reach even 84 in the high-Sr (*a3*) basaltic andesite. Similar Mg# range of 68 to 80 is observed in the opx, however the oldest dacite (*ocl1*) unit contains opx showing Mg#(opx)=65. Changes in the Mg# in pyroxene is connected to the zoning and resorption patterns. Equivalent patterns have been found in both, cpx and opx. The lowest Mg# of 71 to 68 are recorded in crystal cores. An abrupt increase of the Mg#(pyroxene) shows in most lavas Mg#=80, and in (*a3*) even Mg#=84, which occurs at the crystal mantle after resorption. The rims, which exceed often 100 µm, show sharp boundary by change to lower Mg# of ~77, following by slight decrease to ~74. Equivalent patterns have been found in the post-collapse lavas in both, cpx and opx.

5.2.4. OLIVINE

Olivines from Parinacota lavas are presented in connection with the compositions of the mafic end-member magmas involved in the petrogenesis of the Quaternary CVZ magmas in Chapter 2, section 6.8 of this work.

Olivine occurs in all basaltic andesites of Parinacota (units OCba, *a2*, *a3*) as phenocrystic and groundmass phase and forms two distinct compositional trends, starting at undistinguishable phenocrystic (>300 µm) core compositions of Fo79-81 found in both, the high-Sr and the low-Sr type basaltic andesites (Figure 16 and 17, Chapter 2). These core compositions are separated from the phenocrystic rims, microcrysts and groundmass olivine compositions by a small compositional gap (Figure 16, 17 and 19, Chapter 2). The compositional gap indicates a second stage of olivine crystallization, which follows magma mixing between two mafic AEM-type and BEM-type magmas. Olivine from high-Sr lava flow (*a3*) comprises altogether Fo values, which is limited to a range of 81 to 74 mol%; in contrast, the low-Sr lavas (OCba and *a2*) reveal broader range of Fo contents reaching from 80 to 64 mol% within the same range of MnO (0.2-0.7 wt%) and CaO (0.7-

0.4 wt%) contents.

As presented in Chapter 2 (Figure 18, Table 5, section 6.8.3), the phenocrystic cores of Fo79-81 correspond to the $Mg\#_{melt}=56$ of the statistically obtained basaltic-shoshonitic (BEM) PVA end-member magma composition. In the low-Sr lavas, olivine inclusions in pyroxene showing Fo76-74 are consistent with the $Mg\#_{melt}=48$ calculated from the high-Al calc-alkaline (AEM) basaltic andesitic PVA end-member.

Olivine phenocrysts in the Young Cone, Middle and High Ajata lavas are rare and their occurrence indicates an antecrystic or orthocrystic origin. Olivine inclusions in amphibole found in the youngest Old Cone lavas (PAR 82) reveal Fo content of 90-92 mol% (analyses from Entenmann, 1994). Calculated whole rock Mg# ~71-78 for Fo90-92 using Kd values of 0.27-0.33 indicate crystallization in equilibrium with partial melts extracted from peridotitic mantle residue (Baker et al., 1995).

5.2.5. Fe-TI OXIDE

Iron-titanium oxide minerals represent wide variety of petrographic and chemical characteristics in Parinacota lavas. Titanomagnetite (Tmt) and ilmenite (Ilm) occur as pheno- and microcrysts, as inclusions or attached to plagioclase, olivine, pyroxene, amphibole, as breakdown products of amphibole and biotite, and oxidation of titanite. Ti-magnetite occurs as lamellae in ilmenite and vice versa, as a product of oxidation exsolution (e.g. Haggerty, 1991). Ti-magnetite is present in all lavas; by contrast, ilmenite is not stable in the Old Cone lavas and occurs only as composite grains with Ti-magnetite or rare inclusions in pyroxene or amphibole.

Titanomagnetite forms solid solution between magnetite ($Fe^{2+}Fe^{3+}{}_2O_4$) and ulvöspinel ($Ti^{4+}Fe^{2+}{}_2O_4$) with TiO_2 contents between 3.2-16 wt% and considerable amounts of MgO (0.5-5 wt%) and Al_2O_3 (1-4.5 wt. %) as well trace concentrations of MnO (up to 0.7 wt. %), and V_2O_3 (up to 0.6 wt%). Ilmenite occurs as solid solution between ilmenite ($Fe^{2+}TiO_3$) and hematite ($Fe^{3+}{}_2O_3$) containing 23-46 wt% TiO_2, minor contents of MgO (1-5 wt%) and trace contents of Al_2O_3, MnO and V_2O_3, which do not exceed 0.7 wt%. Cr-spinel occurs rare as inclusions in olivine. MgAl-rich magnetite, with MgO and Al_2O_3 concentrations up to 10 wt. % have been found as inclusions in amphibole and pyroxene in the youngest Old Cone (*oc2*) lavas.

Total iron FeO^{TOT} obtained from EMP oxide measurements were recalculated to FeO and Fe_2O_3 using the method of Carmichael (1967) based on ideal stoichiometry and proportions of tetrahedral and octahedral sites occupancy. That is, Fe_2O_3 contents in Ti-magnetite are derived from FeO excess resulting from stoichiometric combination of FeO with TiO_2+SiO_2 and bivalent elements in proportion 2:1 as well trivalent elements in proportion 1:1 forming ulvöspinel fraction ($2FeO*TiO_2$); in Ilm FeO have been combined with TiO_2+SiO_2 and bivalent cations in proportion 1:1, the FeO excess have been recalculated to Fe_2O_3. The average total of oxide analyses after the recalculation is 99.5 wt% in the interval of 98-101 wt%. The recalculated totals show slight dependence on TiO_2 contents.

The chemistry of the Fe-Ti oxides shows noticeable differences in the pre- and post-collapse lavas. Figure 10a presents Ti p.f.u. vs. $Mg/(Mg+Fe^{2+})$ in magnetite, a plot adopted from Martel et al. (1999), presenting the dependence between the magnetite compositions and the oxidation conditions, in a range between NNO and NNO+2 (Ni-NiO buffer), a range of oxygen fugacity comprising Parinacota rocks. This type of diagram serves as a rough approximation of the oxidation conditions, especially for lavas lacking ilmenite and is discussed in section 6.3.

There is a well-defined boundary between pre- and post-collapse Ti-magnetite compositions: variable-in-Ti (0.08<Ti<0.4 p.f.u., equivalent to 8-40 mol% Usp) and low-Mg# (<10) magnetite from Old Cone and Dome Plateau (*rd*) units are separated from high-Ti (0.15<Ti<0.46 p.f.u., equivalent to 15-40 mol% Usp), and high-Mg# (10-24) Ti-magnetite from Young Cone and Ajata flows. However, the compositions from the youngest pre-collapse andesites of the (*oc2*) unit plot in the field of post-collapse lavas, showing 9<Mg#<50 and Ti contents lower (0.10-0.35 p.f.u., equivalent of 8-35 mol% Usp), than the other post-collapse lavas (except for several grains found in the (*a2*) unit). In the basaltic andesite lavas (*a2*) and (*a3*) different Ti-magnetite populations can be identified. It is worth to noting, that in one (*a3*) sample in which amphibole is present (PAR 225), the Ti-magnetite compositions differ significantly from the other samples representing the same lava flow (PAR 10, 11). Furthermore, ilmenite is absent in PAR 225, likewise to other amphibole-bearing rocks, where ilmenite is either absent or occurs only as composite grains with Ti-magnetite. Mn vs. Mg contents (p.f.u.) in ilmenite, presented in Figure 10b, separate the pre- and post-collapse compositions by higher Mn contents in Old Cone and Dome Plateau units and higher Mg contents in Young Cone and Ajatas. Rare ilmenite grains in the (*oc2*) unit plot in the post-collapse ilmenite field.

6. GEOTHERMO-OXY-BAROMETRY (GTOB) - RESULTS

A compilation of crystallization conditions in Parinacota rocks, presented in Table 2, comprises the lowest and the highest values of P, T, NNO-buffer and H_2O_{melt} obtained from four GTOB methods. Figure 11 to Figure 17 illustrate the GTOB results separately for pre- and post-collapse conditions. For comparison, the results of Fe-Ti oxide oxy-barometer of Andersen & Lindsley (1985) included in ILMAT calculation spreadsheet by LePage (2003), and amphibole combi- P-T-fO_2-H_2O_{melt}-meter of Ridolfi & Renzulli (2011) are presented with the conditions determined for Taapaca rocks[20].

---

[20] Two-pyroxene thermobarometer is not applicable to Taapaca rocks due to the absence of clinopyroxene-orthopyroxene bearing rocks.

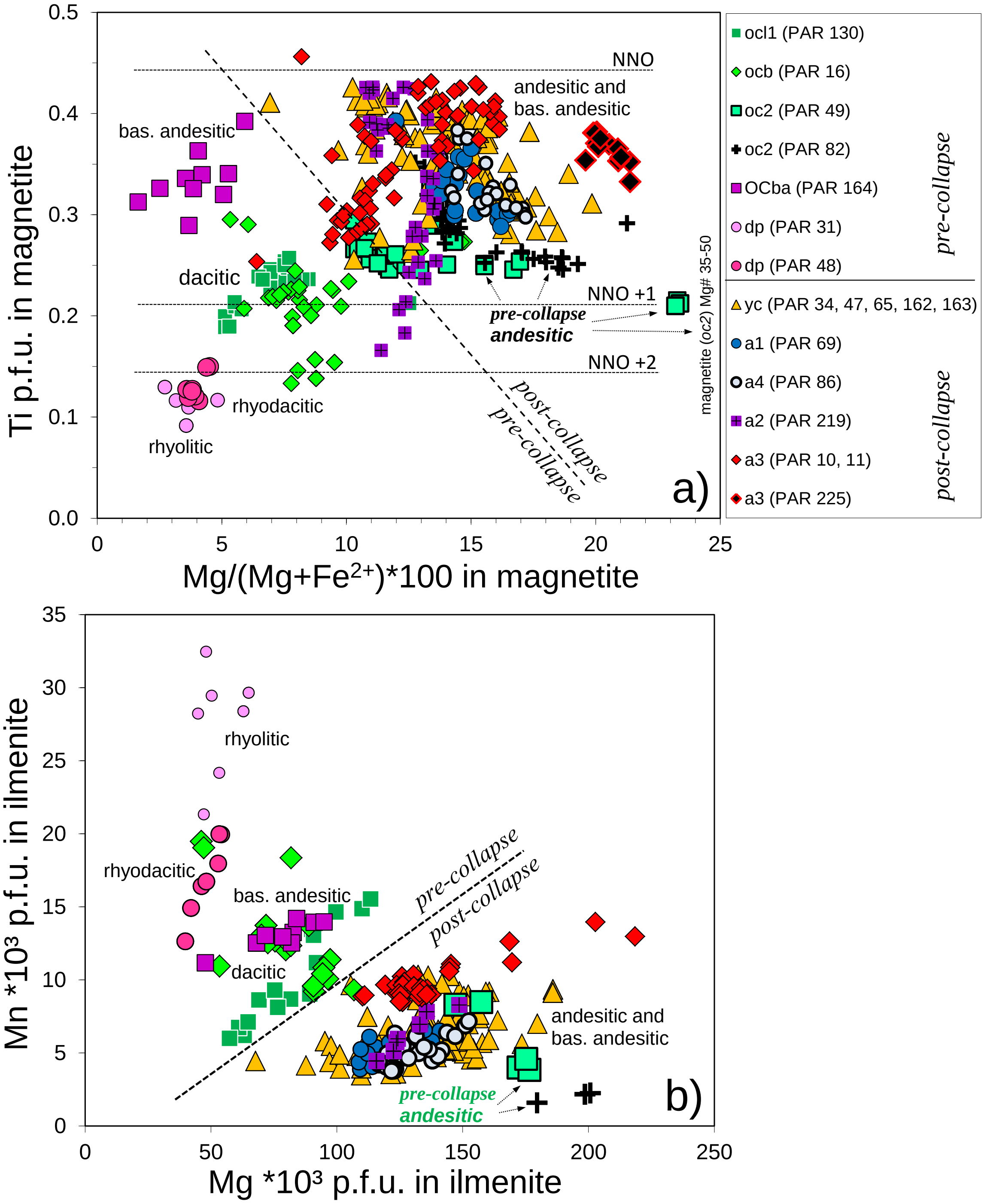

Figure 10. *Chemistry of **a)** titanomagnetite, and **b)** ilmenite in pre- and post-collapse Parinacota lavas. Plot a) presents the redox conditions based of titanomagnetite chemistry, model adopted from Martel et al, (1999).*

Table 2. *Compilation of the GTOB results showing crystallization conditions in pre- and post-collapse Parinacota magmas. Abbr. A&L85,P2008, R&R2011, J&R89, H&B94- see text for explanation. A)-barometer used only for Mg-Hbl; B)-results from several Mg-Hst found in the sample beside the main population of the Mg-Hbl, C) results from tschermakitic Hbl beside the main population of Mg-Hbl, D) results from tschermakitic Hbl beside Mg-Hst, G) results from groundmass pyroxene.*

			thermo-oxy-meter A&L85 mag-ilm pairs (X_{Usp}-X_{Ilm} S83)		thermobarometer P2008 cpx-opx-pairs		thermo-oxy-barometer R&R2011 and barometer J&R89$^{A)}$ amphibole (13eCNK)				thermometer "B" H&B94 amph-plag pairs /rims only
Sample	stage	SiO_2 wt% (norm)	T [°C] ± 40 [°C]	f_{O_2} Ni-NiO buffer	T [°C] ± 60 [°C]	P [MPa] ± 320 [MPa]	T [°C] ± 23.5[°C]	P [MPa] ± 11.5% [MPa]	f_{O_2} Ni-NiO buffer ±0.37 log	H_2O_{melt} [wt%] ±0.78 [wt%]	T [°C] ± 60 [°C]
I. Pre-collapse units											
			Rhyolite Dome Plateau (47-40 ka)								
PAR 031	*rd*	73.4	778-807	NNO+1.6-NNO+2.0	cpx-opx pairs free		746-852 (920)$^{B)}$	35-200 (203)$^{B)}$	NNO+1.6 (1.4)$^{B)}$-NNO+2.4	3.1-6.4	529-850
PAR 048	*rd*	69.5	807-831	NNO+1.6-NNO+2.0	cpx-opx pairs free		715-865 (930)$^{C)}$	27-242	NNO+1.1 (1.0)$^{C)}$-NNO+2.0	3.1-6.7	704-805
			Old Cone (52-20 ka)								
PAR 130	*ocl1*	65.8	826-923	NNO+0.9-NNO+1.6	862-990	330-1380	(878)$^{D)}$ 918-950	234-260	NNO+0.5-NNO+1.7 (2.1)$^{D)}$	3.7-4.4. (5.2)$^{D)}$	839-906
PAR 160	*ocl2*	62.6	ilmenite free		cpx only		(754)$^{D)}$ 925-967(989)$^{B)}$	94-261	NNO+1.2-NNO+2.3	(7.0)$^{D)}$ 3.2-4.3 (4.9)$^{B)}$	843-927
PAR 016	*ocb*	64.6	814-921	NNO+0.6-NNO+1.7	cpx only		(786)$^{D)}$ 910-1005	(104)$^{D)}$ 193-311	NNO+0.8-NNO+2.2	2.7-5.7 (6.3)$^{D)}$	708-949
PAR 049	*oc2*	61.2	900-935	NNO+0.8-NNO+1.6	cpx only		944-978	203-269	NNO+1.1-NNO+1.9	3.3-3.8	823-951
PAR 082	*oc2*	60.2	ilmenite free		989-1073$^{G)}$	160-520 $^{G)}$	947-999	183-288	NNO+1.2-NNO+2.2	2.8-4.2	820-929
PAR 164	*OCba*	56.4	843-874	NNO+0.1-NNO+0.6	969-1061	240-720	amphibole free				amphibole free
PAR 165	*OCba*	56.6	ilmenite free		979-1052	210-440	amphibole free				amphibole free
II. Post-colllapse units											
			Young Cone (> 8 ka - recent)								
PAR 034	*yc*	57.9	928-992	NNO+0.5-NNO+1.1	939-1071	60-700	amphibole free				amphibole free
PAR 047	*yc*	59.3	910-996	NNO+0.4-NNO+0.9	949-1038	170-770	amphibole free				amphibole free
PAR 060	*yc*	59.4	n.d.		967-1052	140-1170	amphibole free				amphibole free
PAR 065	*yc*	58.7	908-1002	NNO+0.3-NNO+1.2	n.d.		amphibole free				amphibole free
PAR 084	*yc*	58.1	n.d.		n.d.		amphibole free				amphibole free
PAR 162	*yc*	61.6	915-986	NNO+0.7-NNO+1.1	n.d.		952-975	201-275	NNO+1.0-NNO+1.8	3.2-4.3	863-969
PAR 163	*yc*	59.5	989-1000	NNO+0.2-NNO+0.6	961-1281	270-960	976-991	211-225	NNO+1.6-NNO+2.0	3.0-3.3	890-981
			Ajata Flows (10-3 ka)								
PAR 068	*a1*	59.2	n.d.		n.d.		amphibole free				amphibole free
PAR 069	*a1*	58.8	910-1009	NNO+0.6-NNO+1.1	907-1048	100-1020	amphibole free				amphibole free
PAR 219	*a2*	56.4	830-1024	NNO+0.5-NNO+1.5	912-933	650-840	amphibole breakdown				amphibole breakdown
PAR 010	*a3*	53.4	896-971	NNO+0.4-NNO+0.9	cpx only		amphibole free				amphibole free
PAR 011	*a3*	53.8	885-983	NNO+0.3-NNO+1.0	cpx only		amphibole breakdown				amphibole breakdown
PAR 225	*a3*	53.3	ilemite free		cpx only		949-986	225-298	NNO+1.8-NNO+3.6	3.4-4.3	817-936
PAR 086	*a4*	58.8	924-992	NNO+0.7-NNO+1.1	n.d.		972-1026	190-245	NNO+1.0-NNO+2.0	2.3-3.1	901-976

6.1. BAROMETRY

Pressure is the most critical parameter to determine using mineral chemistry (e.g. Blundy & Holland, 1990; Putirka, 2008; Anderson et al., 2008; Blundy & Cashman, 2008; Ridolfi & Renzulli, 2011), nonetheless essential for description of the volcanic plumbing system with respect to magma storage and crystallization. Crystallization pressure of Parinacota magmas is determined using amphibole and pyroxene chemistry(21). These two Fe-Mg bearing silicate phases punctuate a change in the differentiation regimes in association with the edifice collapse, by change of the prevailing mineral assemblages from amphibole to pyroxene. The barometry data are therefore expected to reveal a displacement of the magma stagnation depth due to reduction of the edifice load and changes in the local stress field, as suggested by Ginibre & Wörner (2007).

6.1.1. CRYSTALLIZATION PRESSURE OF PARINACOTA AMPHIBOLES

Chapter 3, section 5 presents constraints on pressure for Taapaca magmas, determined from amphibole chemistry, in connection to the experimental results of Botcharnikov et al. (in prep.). This evaluation involves high-Al-Ti magnesiohastingsite (Mg-Hst) synthetized from the whole rock composition of Parinacota high-Sr basaltic andesite (*a3*), according to a consistency of these amphibole compositions found in the rocks of both volcanoes. A comparison of experimental and calculated pressure values using different pressure formulations presented by Ridolfi & Renzulli (2011)(22), suggests the best pressure approximation from Mg-Hst by Eq. 1e of R&R2011 (Figure 12, Chapter 3). Crystallization pressure of low-Al-Ti amphibole magnesiohornblende (Mg-Hbl) is determined using Al-in-Hornblende (Al-in-Hbl) barometer of Johnson & Rutherford (1989)(23) as reasoned in Chapter 3, section 5.2.

Besides the basaltic andesites, amphibole is present as phenocrysts in all pre-collapse lavas, except for (*ocl1*), and it occurs as microcrysts and groundmass phase in post-collapse Young Cone lavas (PAR 162, 163), high-Sr basaltic andesite (*a3*) lava (PAR 225), and low-Sr basaltic andesite (*a2*) lava (PAR 219). However, the latter sample shows complete amphibole breakdown precluding the determination of the amphibole species, also observed in low-Sr basaltic andesitic enclaves from Taapaca. This phenomenon in low-Sr magmas, containing large proportions of the AEM-type PVA end-member, have been interpreted in Chapter 3 to reflect high-Al-low-Ti tschermakitic composition, inferred from exclusive tschermakitic amphibole synthetized from low-Sr AEM-type dominated magmas of Lascar volcano (Stechern et al., in prep.).

Owing to nearly identical amphibole compositions present in the Parinacota and Taapaca rocks, the results of barometer of R&R2011 and J&R89 for Parinacota overlap with crystallization pressures obtained from Taapaca dacites (Figure 11). Parinacota amphiboles form rather P-T cluster than trends, as observed in Mg-Hbl from Taapaca dacitic rocks, however Border Dacite sample from Parinacota (*ocb*), which is very similar to Taapaca dacite, shows also a broad T-range in comparison

---

(21) Primary phenocrystic melt inclusions have not been found.

(22) Abbreviation: R&R2011

(23) Abbreviation: J&R89

to other andesitic and basaltic andesitic samples.

Mg-Hbl hosted in the rhyolite sample yields the lowest pressures <100 MPa, which have not been found in Taapaca, where such high evolved magmas did not erupt. Mg-Hbl shows decreasing P with increasing SiO_2 content of the sample. Because pressure from Mg-Hbl have been determined using A^{TOT}-in Hbl (J&R89), the question arises, if Al-contents are affected by other factors than pressure. Figure 8a shows negative correlation between MgO-Al_2O_3, and Figure 8b shows a strong correlation between Al_2O_3 and TiO_2 in Mg-Hbl with SiO_2 of the sample; Mg correlates negatively with Ti in Mg-Hbl. Analyzing all possible exchange mechanisms in Mg-Hbl, an obvious answer have not been found. For instance, Al^{TOT} correlates strongly with Ti in Mg-Hbl; lower Ti contents could reflect lower crystallization temperatures, but both, rhyolite and rhyodacite show the same crystallization temperatures at ~780°C from R&R2011. There is a consistent negative linear trend between SiO_2 and Al_2O_3 in the Parinacota silicic lavas (67-75 wt% SiO_2 – 16-13 wt% Al_2O_3). This observation strongly supports the dependence of the Al^{TOT} in Mg-Hbl on composition of the melt, suppressing the effect of pressure.

Pressure values obtained from Mg-Hst show a consistent range of 190-260 MPa in pre-collapse and post-collapse andesites. Mg-Hst from the most mafic high-Sr (*a3*) lava, reach even 298 MPa. This value is consistent with the highest P=303 MPa obtained from Taapaca Mg-Hst found in the dacite; P recorded in the Mg-Hst crystal cores from the Taapaca mafic enclaves reach 305 MPa(24). Moreover, in comparison to Mg-Hbl, the Mg-Hst reveals well-defined lower pressure limit at P~200 MPa. It may probably be connected to the amphibole stability limit at temperatures exceeding 900 °C, which means, at lower pressure, during magma movement in the plumbing system, amphibole stops to crystallize, or alternatively, the mafic magma from which the Mg-Hst crystallize is trapped by silicic magmas stagnating in the plumbing system at a defined depth.

---

[24] Pressure values >300 MPa recorded in the Mg-Hst rims from Taapaca mafic enclaves are discussed in section 7.2.2, Chapter 3.

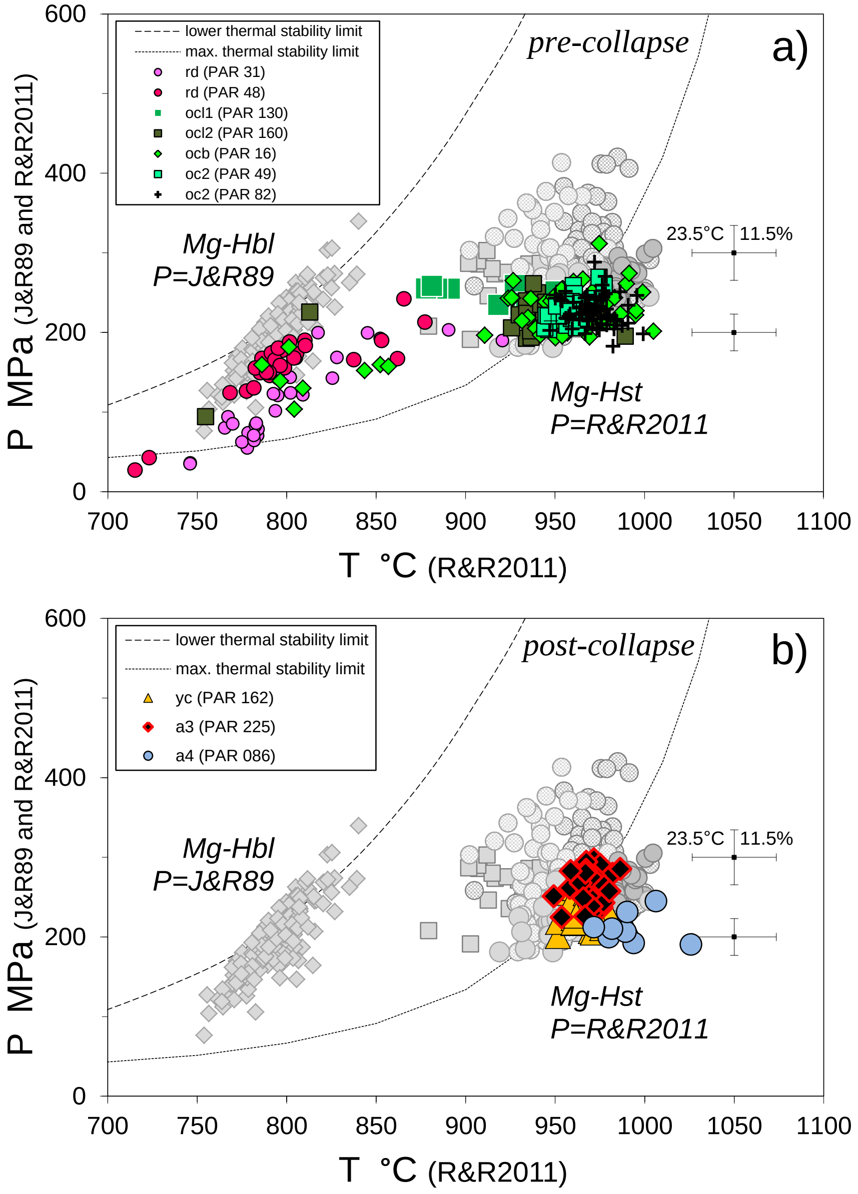

Figure 11. *P-T crystallization conditions of Parinacota amphiboles in:* ***a)*** *pre-collapse;* ***b)*** *post-collapse eruptions. Pressure values of magnesiohornblende are obtained from the modified formulation* Al^{TOT}*-in Hbl of Johnson & Rutherford (1989) presented in Chapter 3 of this work. Pressure values of magnesiohastingsite are calculated using Equation 1e of Ridolfi & Renzulli (2011) as explained in the section 5.3 of Chapter 3. Crystallization temperatures of both amphibole species results from R&R(2011) using appropriate P-values. The results of Taapaca amphiboles (gray points) are presented for comparison.*

6.1.2. CRYSTALLIZATION PRESSURE OF PARINACOTA PYROXENES

The pyroxene pairs presented in this study show a systematic deviation of $Kd^{Fe\text{-}Mg}$(cpx-opx) exchange coefficient to considerably lower values of an average $Kd^{Fe\text{-}Mg}$(cpx-opx) of 0.939 σ±0.137 (median 0.932), relatively to the equilibrium value of 1.09 ±0.14 given by Putirka (2008), (Figure 12). This offset toward lower values occurs in calc-alkaline lavas from Parinacota as well as Lascar (0.84 σ±0.17), (Lascar own data included in Stechern et al., in prep). It may simply reflect differences in equilibrium values of $Kd^{Fe\text{-}Mg}$(cpx-opx) in different magmatic series, because the $Kd^{Fe\text{-}Mg}$(cpx-opx) determined by Putirka (2008) is based on experimental studies conducted on bulk compositions different form calc-alkaline compositions.

Figure 12 presents the $Kd^{Fe\text{-}Mg}$(cpx-opx) values of pyroxene pairs from Parinacota vs. calculated P and T values resulting from these pairs. The average Kd value and its confidence interval of ±σ is postulated here to be a valid $Kd^{Fe\text{-}Mg}$(cpx-opx) range for Parinacota pyroxene. This empirical $Kd^{Fe\text{-}Mg}$(cpx-opx) range encompasses P and T results showing the smallest correlation between the Kd and calculated P and T. It excludes the highest pressure values obtained from cpx-opx rim-rim pairs in touching pyroxene crystals from the oldest Old Cone sample (PAR 130), presented in Figure 13a. It excludes also P-T values above $Kd^{Fe\text{-}Mg}$(cpx-opx)=1.076, which show results consistent with these at lower Kd, but yet these results do not change significantly the P-T range illustrated in Figure 13b for pre- and post-collapse lavas.

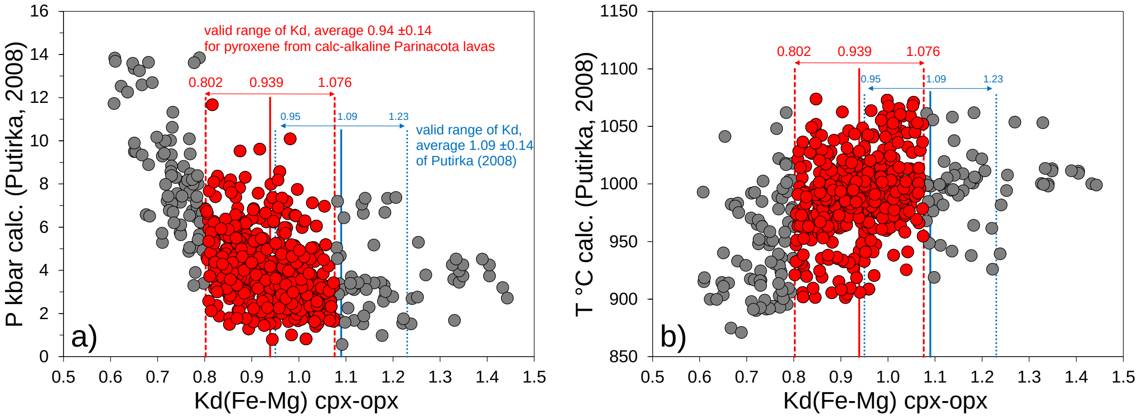

Figure 12. *$Kd^{Fe\text{-}Mg}$-values between cpx-opx pairs from Parinacota lavas and from these pairs calculated **a)** pressures, and **b)** temperatures. Due to an offset to lower Kd values observed in Parinacota (also Lascar) calc-alkaline lavas relatively to the values Kd range (in blue) given by Putirka (2008), an empirical $Kd^{Fe\text{-}Mg}$(cpx-opx) range (in red) is proposed for Parinacota calc-alkaline lavas (see text for explanation). Points marked in red are presented in P-T space in Figure 13.*

A difficulty of the application of the two-pyroxene thermobarometer of Putirka (2008) for calc-alkaline magmas illustrates following example in Figure 13a. Cpx and opx touching crystals, which obviously grown together (yellow points), from the textural perspective are assumed to be suitable to couple the core-core, mantle-mantle, and rim-rim analysis to obtain the P-T history of the crystals. The results yield slightly decreasing P and T (from 550 to 430 MPa, and 980 to 910°C), recorded from crystal cores to crystal mantles, and $Kd^{Fe\text{-}Mg}$(cpx-opx) in the valid range. In contrast, the crystal rim-rim analyses results in implausible high values >9 kbar and $Kd^{Fe\text{-}Mg}$(cpx-opx)<0.8.

Figure 13b presents crystallization pressures of two-pyroxene pairs included in the valid range of $Kd^{Fe\text{-}Mg}$(cpx-opx), as defined in Figure 12. In contrast to crystallization pressures obtained from amphibole (200-300 MPa), each sample reveals a wide P-range of pyroxene crystallization, from maximally 1000 to approximately 100 MPa. However, pressure results obtained from the selected cpx-opx pairs do not show any systematics related to the textural criteria, that is core-core and rim-rim analyses. Table 3 presents P-T results of coupled appropriate core-core, mantle-mantle (if available) and rim-rim analyses of cpx-opx phenocrysts only (not included are microcrysts-

microcrysts, microcrysts-phenocrysts rims.) Based on the colors used for the lowest (blue) and the highest (red) P and T values estimated for these pairs, we can recognize strong variability of P-T conditions represented by different cpx-opx pairs within one sample, and within different cpx-opx pairs toward rim (decreasing P and/or T, increasing P and/or T). Figure 13c highlights the P-T result obtained solely from rim-rim pairs included in Table 3. These results overlap with a nearly whole range of the P-T results calculated using two-pyroxene thermobarometer. Thus, the determination of the latest pre-eruptive P-conditions inferred from crystal rims does not yield consistent results. It is worth to noting, that the cpx-opx phenocrystic pairs, showing a strong P-T variability, show adequate zoning patterns, suggesting similar crystallization conditions.

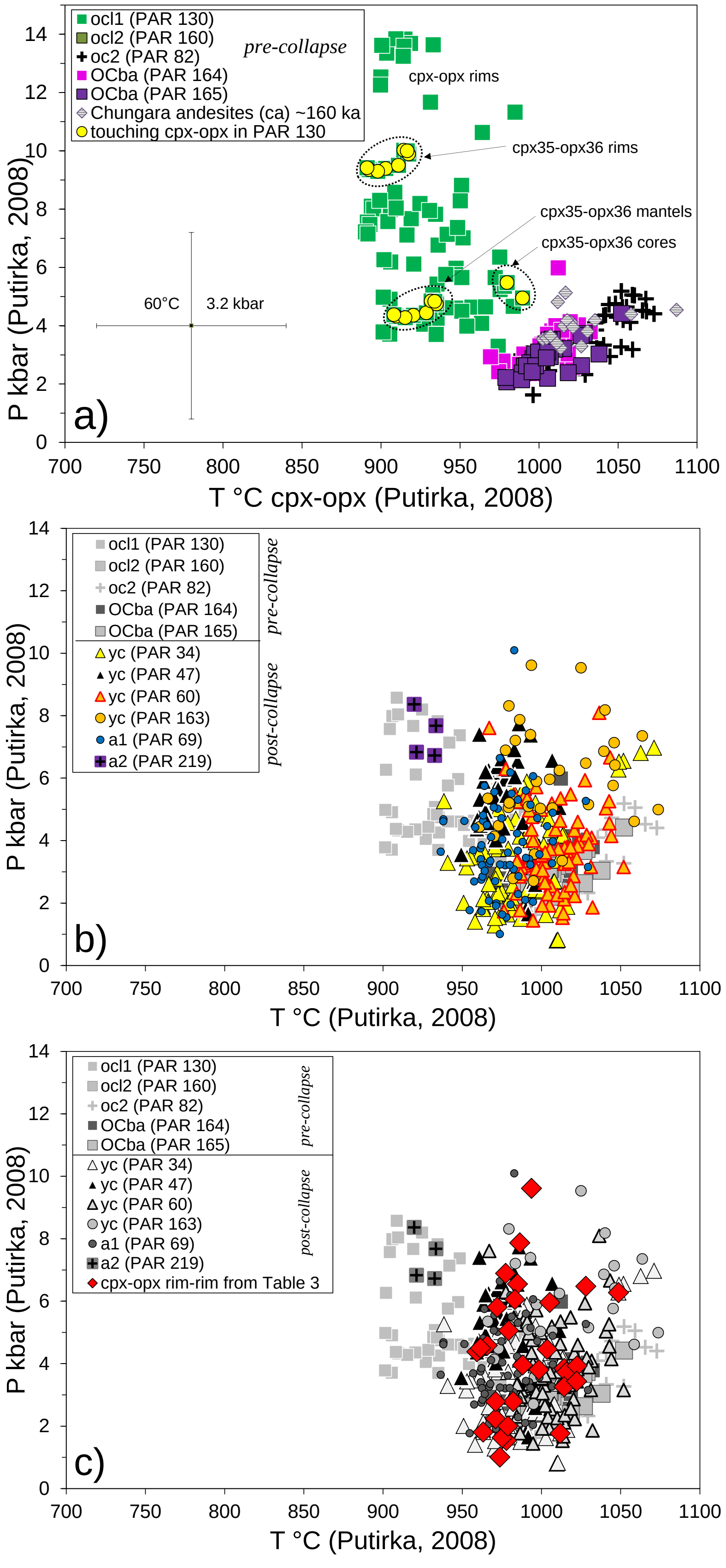

Figure 13. *P-T crystallization conditions obtained from clinopyroxene-orthopyroxene pairs using geothermobarometer of Putirka (2008).* ***a)*** *P-T conditions in pre-collapse lavas representing all coupled cpx-opx pairs showing Kd$^{Fe\text{-}Mg}$ in a range of 0.61 to 1.44. Yellow points illustrate an example found in numerous cpx-opx rim pairs, where pressure values are significantly higher than those from crystal cores and mantles.* ***b)*** *P-T values from pre- and post-collapse lavas, including only cpx-opx pairs with empirical Kd$^{Fe\text{-}Mg}$ in a range of 0.802 to 1.076 postulated for Parinacota calc-alkaline lavas, as explained in section 6.1.2.* ***c)*** *Random distribution of P-T conditions obtained from crystal rims, values from Table 3.*

Table 3. *Selected cpx-opx phenocrysts from different Parinacota lavas showing variation of the calculated P and T within the crystals. Blue T and P cells represent the lowest, red the highest, white the middle values. (-1) or (-1c) term core compositions, higher numbers term the crystal mantles (if available) and rims; "r" terms the rims. Kd$^{Fe\text{-}Mg}$(cpx-opx) values highlighted red denote the values in an empirical Kd$^{Fe\text{-}Mg}$(cpx-opx) range (0.802-1.076) determined for Parinacota.*

Sample-px number-position		Thermobarometer of Putirka (2008)		
Clinopyroxene	Orthopyroxene	T [°C]	P [MPa]	K_d(Fe-Mg)
PAR163-px7-1	PAR163-px8-1	997	311	1.117
PAR163-px7-2r	PAR163-px8-3	1028	647	0.873
PAR163-px5-1c	PAR163-px8-1	982	269	1.240
PAR163-px5-3r	PAR163-px8-2	1039	686	0.904
PAR163-px5-3r	PAR163-px8-3	1005	596	0.818
PAR163-px18-1c	PAR163-px19-1c	1030	515	0.991
PAR163-px18-2r	PAR163-px19-2r	961	443	0.823
PAR163-px18-1c	PAR163-px12-1	1059	461	0.991
PAR163-px18-2r	PAR163-px12-2	982	279	1.048
PAR163-px15-1c	PAR163-px19-1c	1045	576	0.847
PAR163-px15-2r	PAR163-px19-2r	979	506	0.928
PAR163-px15-1c	PAR163-px12-1	1074	499	0.847
PAR163-px15-2r	PAR163-px12-2	1001	332	1.181
PAR163-px15-1c	PAR163-px9-1c	1041	950	0.654
PAR163-px15-2r	PAR163-px9-3r	977	689	0.870
PAR163-px15-2r	PAR163-px9-4r	986	787	0.852
PAR163-px22-1c	PAR163-px25-1c	1025	953	0.875
PAR163-px22-2r	PAR163-px25-2r	994	961	0.917
PAR163-px22-1c	PAR163-px24-1c	979	831	0.886
PAR163-px22-2r	PAR163-px24-2r	994	341	1.160
PAR47-Px57-1	PAR47-Px58-1	979	540	0.820
PAR47-Px57-2	PAR47-Px58-2	966	458	0.865
PAR47-Px25-1	PAR47-Px26-1	967	565	0.789
PAR47-Px25-2	PAR47-Px26-2	985	655	0.950
PAR47-Px29-1	PAR47-Px30-1	963	443	0.872
PAR47-Px29-2	PAR47-Px30-2	972	581	0.839
PAR47-Px53-1	PAR47-Px54-1	961	741	0.823
PAR47-Px53-2	PAR47-Px54-2	959	438	0.862
PAR47-Px52-1	PAR47-Px54-1	965	743	0.722
PAR47-Px52-2	PAR47-Px54-2	961	450	1.000
PAR47-Px57-1	PAR47-Px58-1	979	540	0.820
PAR47-Px57-2	PAR47-Px58-2	966	458	0.865
PAR47-Px57-3	PAR47-Px58-3	983	605	1.037
PAR69-Px6-1	PAR69-Px8-1	963	463	0.873
PAR69-Px6-2	PAR69-Px8-2	988	395	0.872
PAR69-Px2-1	PAR69-Px8-1	958	442	0.951
PAR69-Px2-2	PAR69-Px8-2	993	390	0.780
PAR69-Px37-1	PAR69-Px38-1	983	1009	0.982
PAR69-Px37-2	PAR69-Px38-2	1029	315	0.950
PAR69-Px37-3	PAR69-Px38-3	1004	446	0.981
PAR69-Px51-1	PAR69-Px52-1	924	816	0.773
PAR69-Px51-2	PAR69-Px52-2	978	154	0.950
PAR69-Px51-1	PAR69-Px53-1	907	799	0.775
PAR69-Px51-2	PAR69-Px53-2	974	101	0.984
PAR69-Px51-1	PAR69-Px54-1	929	847	0.770
PAR69-Px51-2	PAR69-Px54-2	975	163	0.978
PAR34-px7-1	PAR34-px6-1c	996	521	0.916
PAR34-px7-2	PAR34-px6-2r	998	380	0.871
PAR34-px4-1c	PAR34-px8-1c	990	229	1.149
PAR34-px4-2	PAR34-px8-2r	1058	664	1.137
PAR34-px4-3r	PAR34-px8-2r	1049	628	0.946
PAR34-px4-1c	PAR34-px9-1c	964	362	1.027
PAR34-px4-2	PAR34-px9-2	971	224	0.999
PAR34-px11-1c	PAR34-px12-1c	968	455	1.082
PAR34-px11-2	PAR34-px12-2	975	236	0.982
PAR34-px11-3r	PAR34-px12-3r	1012	177	0.992
PAR34-px13-1c	PAR34-px14-1c	984	470	0.866
PAR34-px13-2r	PAR34-px14-3r	979	200	0.935
PAR34-px15-1c	PAR34-px14-1c	979	456	0.862
PAR34-px15-2r	PAR34-px14-3r	963	181	0.882
PAR34-px15-1c	PAR34-px19-1c	992	490	0.922
PAR34-px15-2r	PAR34-px19-2r	971	279	0.864
PAR34-px22-1c	PAR34-px23-1c	978	506	0.768
PAR34-px22-2	PAR34-px23-2	938	526	0.820
PAR34-px22-3r	PAR34-px23-3r	959	611	0.749
PAR164-19-1	PAR164-18-1	998	235	1.000
PAR164-19-2	PAR164-18-2	1016	335	1.012
PAR164-47-1	PAR164-48-1	1011	400	0.955
PAR164-47-2	PAR164-48-2	1014	385	0.938
PAR60-4-1	PAR60-1-1	1008	530	1.254
PAR60-4-2	PAR60-1-2	1016	372	0.949
PAR60-6-1	PAR60-1-1	1009	517	1.159
PAR60-6-2	PAR60-1-2	1023	393	1.013
PAR60-4-1	PAR60-2-1	976	643	1.096
PAR60-4-2	PAR60-2-2	1014	326	0.942
PAR60-8-1	PAR60-7-1	1000	320	1.433
PAR60-8-2	PAR60-7-2	1022	343	0.985

6.2. THERMOMETRY

6.2.1. THERMAL CONDITIONS IN PRE-COLLAPSE MAGMAS

Amphibole and Fe-Ti oxide from the most silica-rich pre-collapse eruptions reveal the lowest crystallization temperatures among all Parinacota lavas. T-conditions in these lavas obtained from Mg-Hbl focus in a range from 746 to 818°C. They overlap with the results of Mg-Hbl from Taapaca rhyodacitic end-member (Figure 11). Fe-Ti oxides show slightly higher T in comparison to Mg-Hbl, between 778 and 830°C; however, 807°C defines a boundary between higher temperatures recorded in rhyodacite and lower in rhyolite. These temperature clusters in the rhyolite and rhyodacite overlap perfectly with the lowest temperatures obtained from Fe-Ti oxide found in Taapaca rocks. Crystallization temperatures of Fe-Ti oxide in connection with the oxygen fugacity (Figure 14a) reveal two separate groups marked as rhyolitic-rhyodacitic and dacitic – the silica-richer lavas show a shift to slightly higher oxidized conditions at lower temperatures. These two low-T groups occur in different Parinacota samples, in contrast to Taapaca, where both groups occur simultaneously in single dacitic samples.

Rhyodacitic to dacitic pre-collapse eruptions yield bimodal or even trimodal temperature record from amphibole and Fe-Ti oxide thermometry. These intervals result from different populations preserved in these rocks and used in the GTOB study. Rhyodacite and rhyolite contain rare crystals of the high-Al-Ti amphiboles showing T>850°C, by the way, this “high-T record” is not preserved in the rhyolitic/rhyodacitic Fe-Ti oxides. Samples representing the oldest Old Cone units: (*ocl1*), (*ocl2*), and (*ocb*), show predominantly high temperatures from both, amphiboles (910-1005°C, Figure 11) and Fe-Ti oxides (850-923°C, Figure 14); lower temperatures overlap with those from rhyolite and rhyodacite, represented by mineral phases, which must have originate in the more evolved melts. Characteristic for these oldest units is a wider T-range relatively to these recorded in later lavas.

Two younger andesitic lavas, representing (*oc2*) unit, yield crystallization temperatures from Mg-Hst in a narrow range of 55°C, between 944 and 999°C, and a range of 900 to 935°C recorded in magnetite-ilmenite pairs. Mg-Hbl, and thereby lower recorded temperatures have not been found in these samples, although these samples preserve rhyolitic mineral assemblage (sanidine, quartz, low-An-Fe plagioclase cores). Cpx-opx microcrystic pairs found in one (*oc2*) sample (PAR 82) reveal temperatures which overlap with those from the pre-collapse basaltic andesites (OCba), ranging from 898 to 1073 °C. This T-range is consistent with two-pyroxene thermometry from the pre-collapse basaltic andesites, which also crystallized at the highest temperatures recorded in Parinacota lavas, exceeding 1050°C. These calculated temperatures form an interval of 92°C in a range of 969-1061°C. Composite grains of magnetite-ilmenite from the (OCba) yield temperatures between 843 and 874°C, however at the most reduced conditions at T<900°C, which occur in post-collapse Young Cone lavas.

Due to lacking chemical equilibrium test for amphibole-plagioclase pairs, as well as extremely rare touching amphibole and plagioclase crystals, the results of amphibole-plagioclase thermometer of Holland & Blundy, (1994), (abbr. H&B94) are restricted to amphibole rim - plagioclase rim temperatures. By combination of amphibole analyses with different plagioclase crystal-rims, the results presented in Figure 17 illustrate a possible T-range obtainable from this thermometer. Similar to crystallization conditions obtained from H&B94 thermometer, presented in Chapter 3 for Taapaca rocks, the results for Parinacota (Figure 17) also yield significantly lower crystallization temperatures in comparison to the single-phase amphibole thermometer of R&R2011. This trend suggests magma cooling at isobaric conditions. A difference between the highest temperature calculated from H&B94 (949°C) and R&R2011(1005°C) is 56°C(25).

6.2.2. *THERMAL CONDITIONS IN POST-COLLAPSE MAGMAS*

Post-collapse lavas yield generally crystallization temperatures >900°C from all used thermometers, with exception to several xenocrystic pyroxene and Fe-Ti oxide grains found in low-Sr basaltic andesite (*a2*) lava, involved in the temperature calculations. In contrast to pre-collapse samples, Mg-Hst does not reveal temperatures T<950°C (Figure 11b). This fact pleads against the xenocrystic character of the post-collapse amphiboles and an origin in colder Old Cone magmas. Moreover, these results suggest generally higher temperatures prevailing in the Parinacota plumbing system after collapse, reproduced by thermometry based on Fe-Ti oxide pairs and cpx-opx pairs. The Young Cone, Middle (*a1*) and High Ajata (*a4*) lavas reveal a consistent T-range from titanomagnetite-ilmenite pairs, between 908 and 1002°C. Single temperature value form (*a1*) forms together with several temperature results from the low-Sr (*a2*) Lower Ajata a small group, showing 1010-1024°C, the highest preserved T from Fe-Ti oxides. Other results from Ajata lavas concentrate between 920 and 992°C. An exception is the basaltic andesitic (*a3*) lava, which shows a trend of decreasing T from 983 to 885°C at increasing oxygen fugacity from NNO+0.3 to NNO+1. It should be noted, that this wide T-range relatively to other post-collapse lavas results from calculations using two titanomagnetite populations identified in Figure 10a, and one ilmenite population (Figure 10b) found in (*a3*) high-Sr basaltic andesite(26). This one ilmenite population appears to be in equilibrium with both titanomagnetite populations, and meets the Mg/Mn ratio equilibrium values of Bacon & Hirschmann (1988). The lowest T (830, 842°C) recorded in the low-Sr basaltic andesite (*a2*) results form a few titanomagnetite grains showing lower Ti (p.f.u.) contents (Figure 10a). This finding is in accordance with the pyroxene xenocrysts found in this lava, showing significantly lower T (920-932°C) in comparison to the post collapse lavas, and which overlap with the T recorded in the cpx-opx pairs from (*ocl1*). These low temperatures represent therefore thermal conditions of an admixed colder component in the (*a2*). Clinopyroxene-orthopyroxene pairs (Figure 13b) yield temperatures ranging mainly from 950 to 1020°C. There are slight differences in the crystallization temperatures between PAR 34, 47, and 69 (main interval: 950-1100°C), and PAR 60 and 163 (main interval: 980-1030°C). T>1010°C are also recorded in Old Cone lavas. A separate temperature cluster occurs in a range of 1040-1071°C, which was found in certain pre- and post-collapse samples.

---

[25] From the same amphibole analysis (PAR16-Am58)

[26] A third titanomagnetite population has been identified in (a3) basaltic andesite lava in the ilmenite-free sample PAR 225. Therefore, this population is not used in the Fe-Ti thermo-oxy-barometry.

6.3. OXYGEN BAROMETRY

Martel et al. (1999) show that titanomagnetite composition is a sensitive indicator of $ƒO_2$. They present the NNO-buffer boundaries in a range of NNO to NNO+2, relevant in the intermediate calc-alkaline magmas. This method is very useful, if ilmenite is unstable phase. Figure 10a shows therefore the first approximation of the redox conditions conducted solely from titanomagnetite composition. Titanomagnetite forms compositional cluster, similarly to amphibole, depending on the SiO_2 whole rock content. Generally, pre-collapse magmas reveal more oxidized conditions in comparison to post-collapse magmas. Rhyolitic, rhyodacitic and several dacitic titanomagnetite yield the most oxidized conditions above NNO+2. Dacitic titanomagnetite plot around NNO+1. These conditions occur in the oldest Old Cone lavas, whereas the youngest (*oc2* and OCba) plot clearly above NNO+1, and adjust toward redox conditions in the post-collapse lavas.

Oxygen fugacity obtained from magnetite-ilmenite thermo-oxy-barometer of Andersen & Lindsley (1985)(27) show a good agreement with the redox conditions presented in the simple projection of the Ni-NiO buffer in Ti-Mg# space of titanomagnetite, adopted from Martel et al. (1999). It is worth to noting, that ilmenite compositions representing magnetite-ilmenite composite grains(28) coupled with magnetite in the T-$ƒO_2$ calculations using A&L85 method, yield consistent results with the approximation of Martel et al. (1999). The difference is that titanomagnetite in the Ti-Mg# plot shows a small shift toward more reduced conditions in dacite-andesite, and toward more oxidized conditions rhyolite-rhyodacite.

Using the oxy-barometer of R&R2011, the overall range of oxygen fugacity from amphibole is NNO+1 to NNO+2.3 in pre-collapse lavas and NNO+1 to NNO+3.6 in post-collapse lavas. Amphiboles do not record oxygen fugacity in the range of NNO to NNO+1, which is a dominant range in the post-collapse. The redox conditions obtained from Mg-Hbl in rhyolite and rhyodacite overlap with those from Mg-Hst in other samples. Mg-Hbl from rhyolite shows minor tendency toward higher NNO+2, compared to Mg-Hbl from rhyodacite. The most oxidized conditions are recorded in the Mg-Hst from high-Sr basaltic andesite (*a3*), NNO+1.8 to NNO+3.6 at 949 to 986°C. Comparable values of NNO+2.1 to NNO+3.9 show Mg-Hst cores from high-Sr basaltic andesitic mafic enclave from Taapaca, at slightly lower temperatures of 919 to 963°C (Figure 13a, Chapter 3).

6.4. MELT WATER CONTENTS

The amphibole hygrometer of R&R2011 provides an exclusive estimation method for melt water contents in Parinacota magmas; therefore, the results reflect only amphibole crystallization conditions.

Mg-Hbl from rhyodacite show considerably higher H_2O_{melt} contents of 5.7 to 6.7 wt% compared to 3.5 to 6.4 wt% in rhyolite, at the same temperature range (Figure 16a). Water contents higher than 7 wt%, as obtained from Mg-Hbl from Taapaca, do not occur. Several amphibole analyses from the dacitic to rhyolitic samples reveal 4.8 to 6.4 wt% H_2O_{melt} at ~850°C. Mg-Hst crystallized at lower

---

[27] Abbreviation A&L85

[28] Ilmenite is unstable in Old Cone rocks and occur almost exclusively as composite grains with magnetite (see section 5.2.5)

H_2O_{melt}<5.0 wt%, mainly between 2.8 to 4.2 wt% in the pre-collapse lavas (Figure 16a), and 2.3 to 4.3 wt% in the post collapse lavas (Figure 16b). Similar to the crystallization temperatures obtained from amphibole chemistry, H_2O_{melt} show broad wt% ranges from amphibole from the oldest pre-collapse lavas, exceeding a range of 2 wt%, whereas the youngest pre-collapse amphibole-bearing (*oc2*) and post –collapse (*yc*, *a3*, *a4*) form more focused cluster.

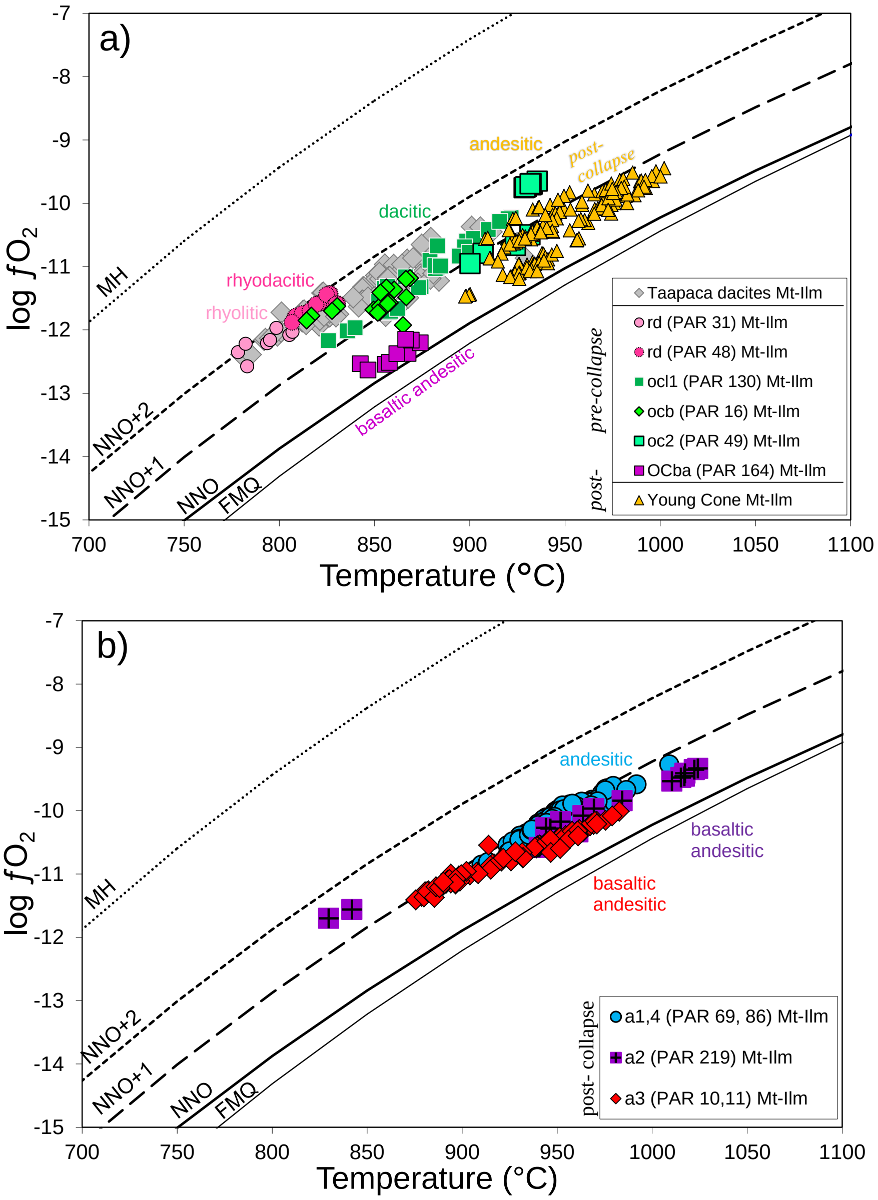

Figure 14. *T-fO_2 conditions calculated from magnetite-ilmenite pairs in:* ***a)*** *pre-and post-collapse andesites to rhyolites;* ***b)*** *pre- and post-collapse basaltic andesites. The oxygen buffer curves are calculated from Frost (1991): MH, magnetite-hematite, NNO, nickel-nickel oxide, FMQ, fayalite-magnetite-quartz.*

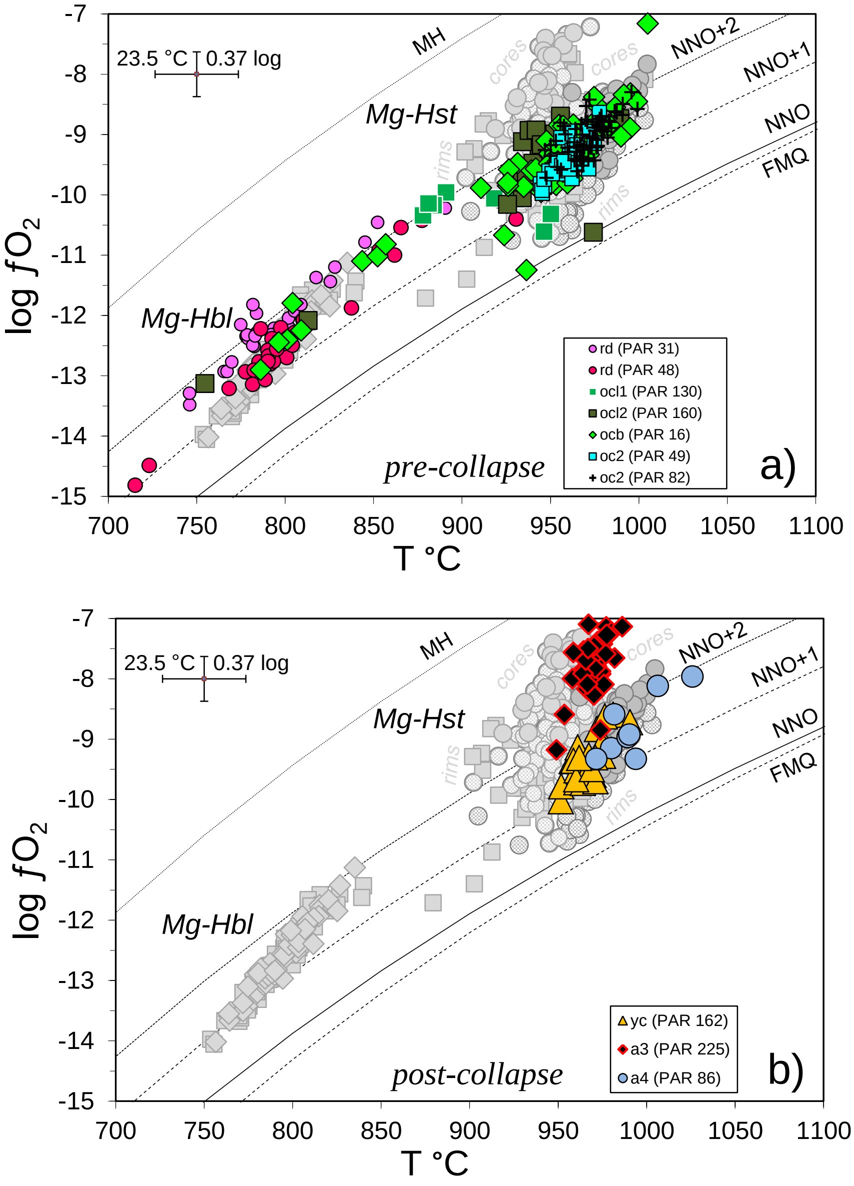

Figure 15. *T-fO_2 conditions calculated from magnesiohornblende and magnesiohastingsite using formulation of Ridolfi & Renzulli (2011):* ***a)*** *pre-collapse;* ***b)*** *post-collapse. The results obtained from Taapaca rocks, presented in Chapter 3(gray points) are presented for comparison. The oxygen buffer curves are calculated from Frost (1991): MH, magnetite-hematite, NNO, nickel-nickel oxide, FMQ, fayalite-magnetite-quartz.*

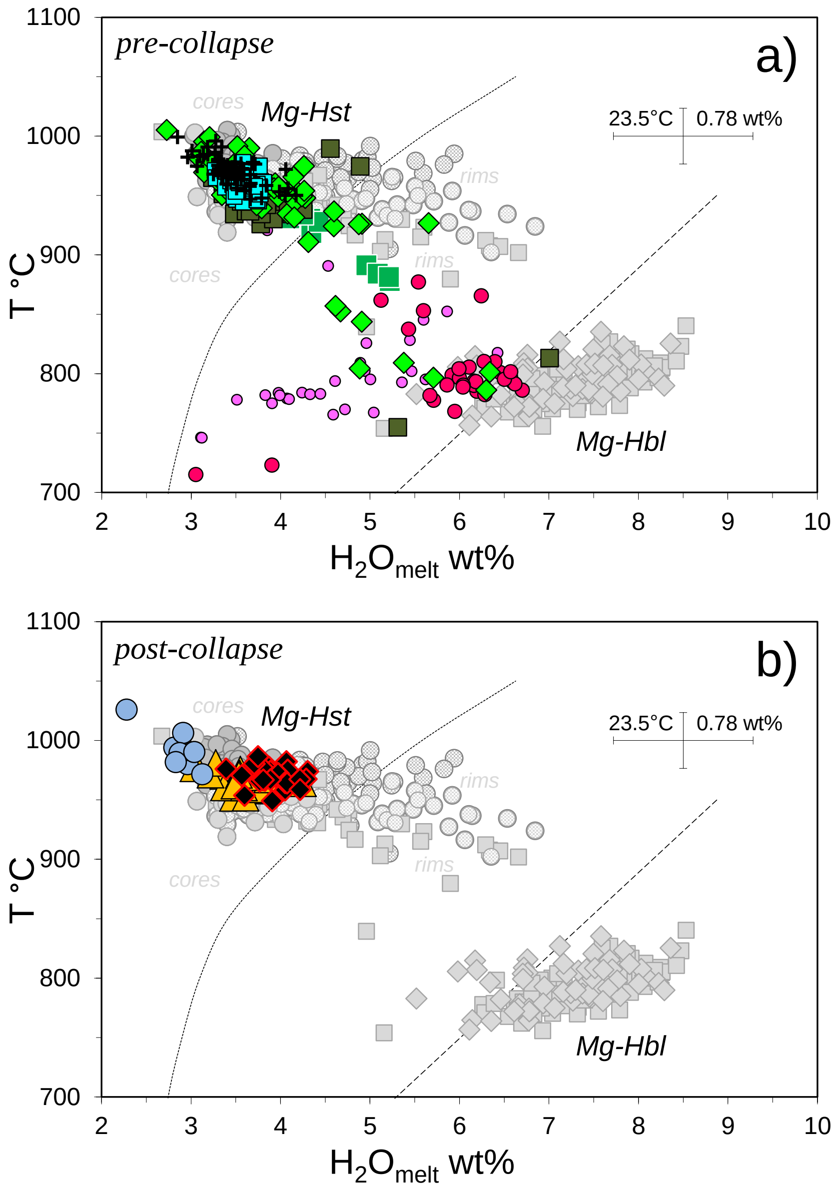

Figure 16. *Melt-water contents H_2O_{melt} in Parinacota lavas obtained from amphibole compositions using hygrometer formulation of R&R2011.*

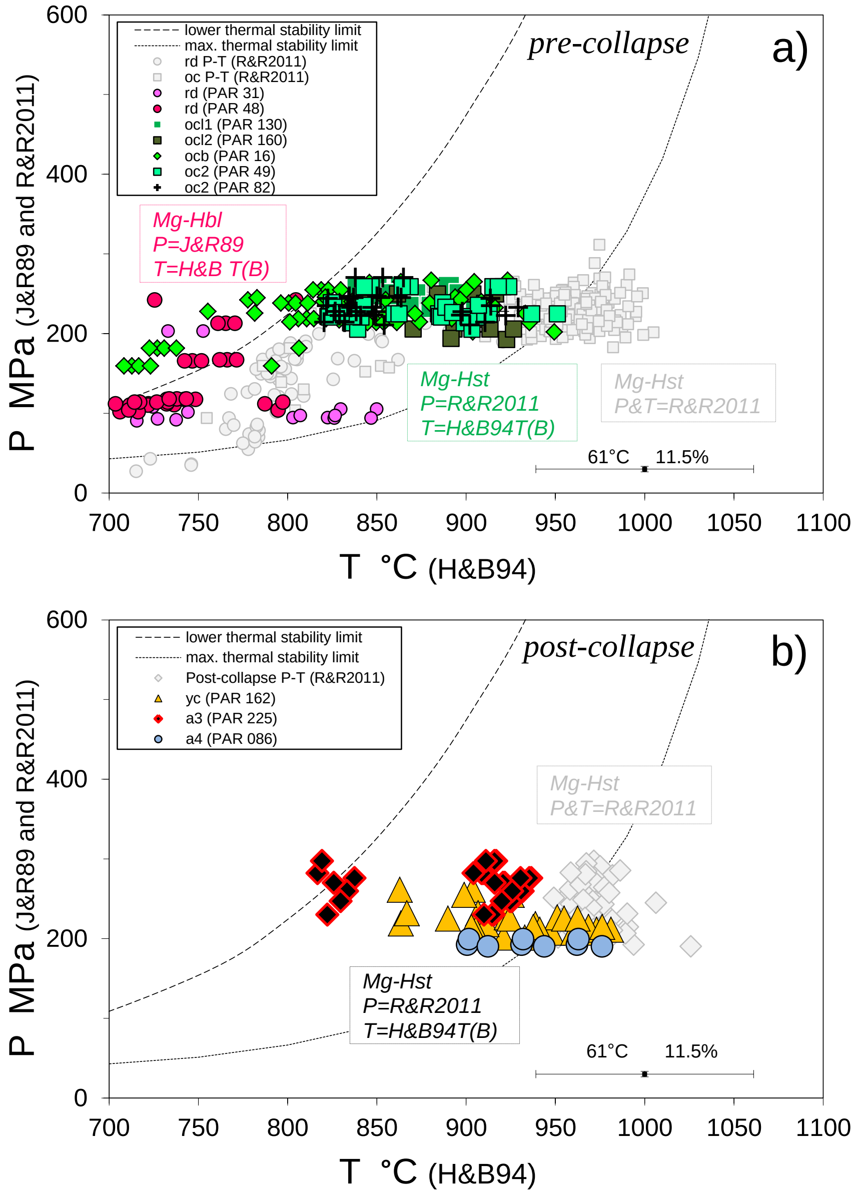

Figure 17. *Amphibole-plagioclase crystallization temperatures obtained from thermometer of Holland & Blundy (1994) using P-values calculated from* Al^{TOT}*-in Hbl of J&R89 for magnesiohornblende and R&R2011 for magnesiohastingsite.*

7. DIFFERENTIATION REGIMES OF PARINACOTA VOLCANO

7.1. DIFFERENTIATION REGIMES REFLECTED BY DIFFERENT VOLCANO MORPHOLOGIES AND MINERAL ASSEMBLAGES

Two characteristic effusive end-member types of arc volcanism, distinctive in the morphology, have been recognized among composite stratovolcanoes (e.g. Thorpe, 1982; Thouret et al., 2005; Hora et al., 2009; Zellmer, 2009): 1) Long-lived (>0.5 Ma) dome complexes, characterized by a monotonous dacitic magma composition, high-crystallinity, and low magma eruption rates. Petrological constraints suggest that these intermediate magmas stagnate in the shallow crust as granodioritic to granitic proto-plutons, undergo the rejuvenation and remobilization by the mafic recharge, and erupt as intermediate porphyritic, highly viscous lavas; 2) Short-lived (<0.3 Ma) symmetrical stratocones, consisting of mainly andesite lavas erupted from a central vent. Periods of high eruption rates separated by an edifice sector collapse are common and often punctuate changes in geochemical signatures of the erupted magmas.

The first end-member type is represented by the Taapaca volcano described in Chapter 2 and 3. Although the eruptive history of Parinacota is <60 ka, this volcano consists of both morphological types. Until ca. 28 ka, the volcano morphology is supposed to be likely a dome complex of intermediate and silicic magmas (Hora et al., 2007, 2009). After edifice sector collapse, a rapid rebuilding to the symmetrical cone occurred, forming clearly the second end-member type, accompanied by compositional and petrological changes.

Worldwide, calc-alkaline basaltic andesite and andesite comprise a diversity of phenocrysts suites at very similar whole rock compositions. A variety of prevailing ferromagnesian (Fe-Mg) silicate phases alone in andesites show two common end-member mineral assemblages: amphibole-bearing or two-pyroxene-bearing rocks. An occurrence of hydrous and anhydrous Fe-Mg phases indicates different conditions of magma storage and phenocrysts crystallization, consequently, two distinct differentiation regimes.

Analogue to bimodal morphology of Parinacota volcano, we observe also bimodal mineral assemblage in Parinacota andesites, related in previous Parinacota studies to the edifice collapse. With regard to the study of Taapaca volcano in Chapter 2 and 3, we have recognized a mechanism generating petrographically and geochemically similar dacitic magmas in two-stage magma mixing regime. The most part of pre-collapse Parinacota lavas overlap in terms of the whole rock compositions, mineral assemblage with amphibole as an essential Fe-Mg silicate phase, mineral chemistry, and intensive parameter of crystallization directly with the Taapaca volcanic system. A rapid change from “Taapaca regime” to more dynamic and generally more mafic and mineralogically different stratocone system with prevailing two-pyroxene mineralogy, is here of particular interest.

7.2. EVOLUTION OF MAGMA COMPOSITIONS ASSOCIATED WITH SECTOR COLLAPSE

7.2.1. PARINACOTA

Beside a reduction of amphibole abundance in post-collapse andesitic lavas, the shift to less silicic magmas is the most prominent manifestation of the changes in the Parinacota subvolcanic system after sector collapse.

"Ariadne's thread" of this study is the assumption, that the compositional variability of Parinacota lavas - according to the PVA study presented in Chapter 2 - results mainly from two-stage magma mixing between the shoshonitic (BEM), the high-Al calc-alkaline (AEM), and the high-K calc-alkaline silicic (RDEM) magmas (see section 4). Adopting the petrogenetic model of Taapaca to Parinacota, there are high-Sr basaltic andesite (*a3*), most similar to the BEM; low-Sr basaltic andesite (*a2*, OCba), similar to the AEM; silicic magmas (*rd*), an equivalent of the RDEM. The link between these compositions is justified by trace element characteristics and REE patterns (Chapter 2, Figure 6). Besides the rhyolites, all of these magmas are enclosed in the mixing triangle, presented in Figure 18c, using Sr vs. SiO_2 plot. This suggests that all the compositions enclosed in the mixing triangle, result generally from magma mixing, and may be additionally, to a lesser degree, overprinted by fractional crystallization and crustal assimilation, as suggested by e.g. Pb-isotopic composition of Taapaca and Parinacota magmas (Wörner et al. 1988; Wörner et al., 1992; Mamani et al., 2008).

Figure 18a presents Parinacota rocks in $FeO^{TOT}/MgO-SiO_2$ space, showing a degree of iron enrichment at a given silica content. Although this plot is commonly used for discrimination between calc-alkaline and tholeiitic magma series (Miyashiro, 1974), and according to the results obtained from the PVA study, tholeiitic magmas are not involved in the petrogenesis of the Quaternary Central Andean magmas, this geochemical signature separates clearly compositions erupted before and after collapse. According to e.g. Tatsumi (2005) and Blatter et al. (2013), tholeiitic andesites result from crystallization-differentiation of arc basalts, whereas calc-alkaline andesites result from mixing or assimilation of evolved crustal material into basalt. This separation in Parinacota lavas may be explained by a remaining overprint by early crystallization-differentiation of the AEM end-member in the Young Cone magmas, in comparison to more magma mixing affected Old Cone magmas. Hora et al. (2009) defined a CA/TH-index(29) illustrated in form of lines with different slopes corresponding to the iron enrichment (the higher the CA/TH-number, the lower relative Fe-enrichment of the magma and stronger calc-alkaline affinity). Samples selected for the GTOB are highlighted to facilitate the connection between whole rock, mineral chemistry, and the results of GTOB presented in Figure 7 to Figure 17.

A crucial feature of the whole rock compositions of Parinacota is an occurrence of rhyolite-rhyodacite-dacite within a certain period before edifice collapse. Such silicic magmas have not been erupted after collapse. Since 28 ka, a continuous decrease of maximal SiO_2 contents in the

---

[29] CA/TH index= (wt% SiO_2-42.8)/(6.4*FeO^{TOT}/MgO) from Hora et al. (2009), based on Miyashiro (1974)

intermediate magmas, from 65 to 60 wt% SiO_2 is observed (Figure 2a); however the Old Cone basaltic andesite (OCba, 56.5 wt% SiO_2) have not been dated and are not included in Figure 2. It must also be noted, that more mafic andesites (~58 wt% SiO_2) erupted also from 32 ka before collapse. Figure 18a reveals that a part of the Old Cone andesites already plot in the trend formed mainly by the younger post-collapse Young Cone lavas. Unfortunately, the mineralogy of these samples has not been determined. Thus, the Old Cone lavas show a pronounced variability but a majority of them forms a continuous and consistent trend from rhyodacite to andesite, up to 60.2 wt% $SiO_{2,}$ in a range of 1.4 and 1.6 CA/TH-index, representing a set of Parinacota compositions, characteristic only to the pre-collapse phase.

After collapse, the andesites show less compositional variability relatively to the Old Cone and focus at 58 to 60 wt% SiO_2 at lower CA/TH-index ranging from 1.2 to 1.4. Minor part of the Young Cone lavas has higher silica contents, reaching up to 63 wt% SiO_2. These samples represent mainly the east cone deposit, less available for sampling, therefore underrepresented in the data set. These eruptions follow a separate trend toward the oldest in this study investigated dacite (*ocl1*, PAR 130), and an amphibole-bearing white pumice, showing the highest SiO_2 content (64 wt%) among all post-collapse eruptions. This Young Cone trend is also represented by several Old Cone samples.

Figure 18b shows ASI-SiO_2 relation of the Parinacota magmas (ASI=Al/(2Ca+Na+K), molar), relation used by Blatter et al. (2013) to identify the role of clinopyroxene and plagioclase fractionation in generation of the andesite magmas. This signature, similarly to the CA/TH diagram reveals similar picture of Parinacota magmas. The ASI vs. SiO_2 trend presented together with the PVA end-member magmas reveal two nearly parallel linear trends for the OC and YC lavas. The OC trend extends from high-Sr (*a3*), the YC extends from low-Sr (*a2*) basaltic andesites. Furthermore, the YC and (*a1*, *a4*) compositions form also a compositional cluster without clear effects of plagioclase or clinopyroxene fractionation from the basaltic andesite “baseline” magmas.

There is no doubt, that the basaltic magmas which originate in the mantle wedge undergo fractionation to low-Mg high-Al calc-alkaline basaltic andesitic composition (e.g. Blatter et al., 2013, and references therein). The characteristic low MgO, Ni, and high Al_2O_3 contents of the PVA AEM end-member indicate an extensive fractionation of Fe-Mg silicates, as argued in Chapter 2, section 6.5.2. The evaluation of the AFC effects on the AEM component from the whole rock compositions is hampered by the unmixed shoshonitic component. These slightly evolved, mantle wedge derived AEM magmas, involved in the petrogenesis of Parinacota magmas, hybridize in different proportions with the shoshonitic, more mafic component produced in the lithospheric mantle. This mixing stage is evidenced by e.g lower Mg# found in pyroxene cores as well as lower Fo76 contents in olivine inclusions enclosed in pyroxene in AEM-type basaltic andesites of Parinacota (Chapter 2, section 6.8).

The temporal-compositional variations of the Old Cone, in connection with petrography and mineral chemistry suggest that the OC dacitic to andesitic lavas were generated by magma mixing between the hybrid baseline (AEM+BEM) magmas with decreasing proportions of the silicic

RDEM-type magma. Simple conclusion follows, that lower silica contents of the post-collapse intermediate magmas, within a SiO_2 range between (AEM+BEM) and RDEM, reflect significantly lower contribution of the silicic magmas.

Based on the linear OC and curved YC trend in Ni-Rb space, Wörner et al. (1988) suggest that both magma mixing and crystal fractionation operated in the shallow Parinacota subvolcanic system, respectively. A detailed study of the Young Cone whole rock compositions supports rather mixing dominated regime with an early fractionation overprint connected to the formation of the AEM basaltic andesite from the arc basalt. The compositions of YC andesite show stronger affinity to the AEM-type end-member. The Young Cone compositions do not form a strictly curved trend but rather compositional clusters. Moreover, other major and trace elements do not reveal consistent fractionation trends caused by shallow crystallization of plagioclase and/or pyroxene, the main mineral phases in the YC lavas. Furthermore, the Young Cone andesites do not match the LLD, as demonstrated from the experimental study of Botcharnikov et al. (in prep.) in Chapter 3, (Figure 19). A comparison to other geochemical studies of major and trace element compositions of magmas from similar stratovolcanoes in the CVZ e.g. Ollagüe and Ubinas (Feeley et al., 1993; Thorpe et al., 2005) shows, that simple differentiation by fractional crystallization cannot explain the compositional variability. Andesites and dacites of the CVZ do not exhibit consistent correlations with any index of differentiation (Francis et al., 1977; Feeley et al., 1993). Thus, two-stage magma mixing, consisting of variable mafic-mafic and hybrid mafic-silicic stages, as presented in the PVA study (Chapter 2) provide the most reliable explanation for the variability of Parinacota intermediate magmas.

Accordingly, the shift to the less silicic compositions may be simply connected to a “cleaning” of the subvolcanic plumbing system caused by an increasing magma throughput in the Parinacota plumbing system.

Based on the eruption volumes estimated by Hora et al. (2007) and Th-excesses found in all post-collapse lavas by Hora et al. (2009), the latter study concludes that the change in the geochemical characteristics of Parinacota rocks is connected to an increasing recharge and eruption rates leading to a decrease in transit times from the lower crust to the surface. Hora et al. (2009) emphasize the evolution from calc-alkaline to more tholeiitic affinity of Parinacota magmas and link this observation to the “dirty” calc-alkaline and “clean” tholeiitic differentiation trends introduced by Myers et al. (1985). The study of Myers et al. (1985) suggests that the differentiation trend depends on maturity of the subvolcanic plumbing system. The “dirty” systems producing calc-alkaline magmas reflect not only the magma source but also an assimilation in combination with crystal fractionation during ascent. An explanation for the compositional and phase relation changes suggested in this study modifies slightly the model of Myers et al. (1985). Our observations strongly suggest that the “maturation” of a volcanic system is a consequence of a removal of the silicic magmas stagnating in the volcanic plumbing system by the mafic magmas. Both types of magma are produced independently in the subduction zone (e.g. Reubi & Blundy, 2009) and erupt rarely by themselves due to physical barriers (density, viscosity).

Compositional evolution of Parinacota magmas indicates that the shift to more mafic magmas is not connected to the edifice sector collapse. An availability of the RDEM-type magma, and certainly the proportions of the mafic/silicic magmas in the subvolcanic plumbing system decide about the direction of the differentiation regime. Thus, the sector collapse may probably be a consequence of the increased activity of the volcano, eruption rates, hence, an edifice destabilization by overload. Additional effect of edifice destabilization caused by climatic fluctuations (see section 2.3.3) should also be taken into account.

Figure 18. ***Next page****: Plot of Parinacota samples used in geothermo-oxy-barometry study in* ***a)*** *FeO^{TOT}/MgO vs. SiO_2 space, which strikingly separates the Old Cone from Young Come andesites, and* ***b)*** *Sr vs. SiO_2 used in the PVA study (Chapter 2) to illustrate the magma mixing relations between three end-member magmas. Plot in a) shows tholeiitic (TH) and calc-alkaline (CA) fields of Miyashiro (1974). Dashed lines mark the CA/TH index, defined by Hora et al. (2009). BEM – shoshonitic, AEM – high-Al calc-alkaline, and RDEM – rhyodacitic end-members obtained from the PVA modeling (25-8p). Crosses mark for the GTOB-study selected samples.*

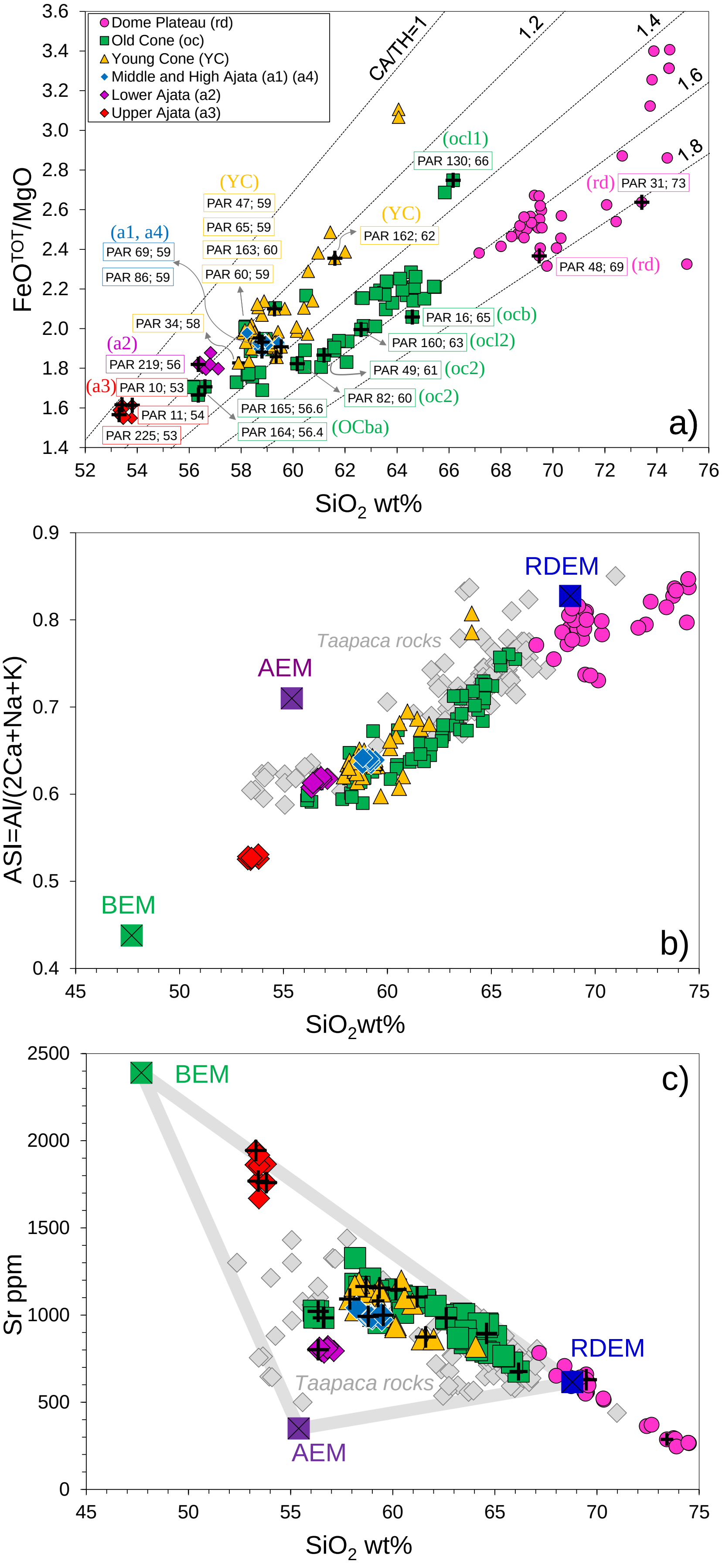
● Dome Plateau (rd)
■ Old Cone (oc)
▲ Young Cone (YC)
◆ Middle and High Ajata (a1) (a4)
◆ Lower Ajata (a2)
◆ Upper Ajata (a3)
CA/TH=1
1.2
1.4
1.6
1.8
(ocl1)
PAR 130; 66
(rd)
PAR 31; 73
(YC)
PAR 47; 59
PAR 65; 59
PAR 163; 60
PAR 60; 59
(YC)
PAR 162; 62
(a1, a4)
PAR 69; 59
PAR 86; 59
PAR 48; 69
(rd)
PAR 34; 58
(a2)
PAR 219; 56
(a3)
PAR 10; 53
PAR 11; 54
PAR 225; 53
PAR 16; 65
(ocb)
PAR 160; 63
(ocl2)
PAR 49; 61
(oc2)
PAR 82; 60
(oc2)
PAR 165; 56.6
PAR 164; 56.4
(OCba)
a)
FeO^{TOT}/MgO
SiO_2 wt%
RDEM
Taapaca rocks
AEM
BEM
b)
ASI=Al/(2Ca+Na+K)
SiO_2wt%
BEM
c)
RDEM
Taapaca rocks
AEM
Sr ppm
SiO_2 wt%

7.2.2. CLUES FROM OTHER ARC VOLCANOES

Arc volcanoes, which experienced edifice collapse, show two different behaviors in terms of magma evolution.

Boudon et al. (2013) recognized opposite compositional trends in magmas from volcanoes of Lesser Antilles Arc and explained both with the effect of decrease in pressure exerted on the magma reservoir after collapse. Montagne Pelée (Martinique) erupted basaltic andesites (52-57 wt% SiO_2) immediately after flank collapse, preceded by andesites (58-63 wt%) erupted before the collapse event. The eruption of the basaltic andesite was continuous at high eruption rates through several thousand years. In contrast, Pitons du Carbet (PdC) and the Soufrière Volcanic Centre (SVC), (St. Lucia) magma compositions changed in an opposite way. PdC produced lavas of 57-60 wt% in the pre-collapse phase followed by 60-67 wt%; SVC produced 53-62 wt% in the pre-collapse phase followed by 61-66.5 wt%.

It is noticeable that, despite of the opposite post-collapse trends, there is no clear overlap of the two, mafic and silicic SiO_2-ranges of the erupted magmas. These three arc volcanic systems suggest that two certain differentiation regimes occur and the availability of the silicic magmas stagnating in subvolcanic arc systems is a key phenomenon of the andesitic stratovolcanoes, as argued by Reubi & Blundy (2009). The compilation of arc volcanic whole rock compositions by Reubi & Blundy (2009) yields two compositional maxima in the ranges of 50-57 wt% and 58-66 wt% SiO_2, adequate to these observed in the mentioned volcanoes.

Two prominent stratovolcanoes located in the Andean Central Volcanic Zone show likewise opposite behavior:

Ubinas (16°S, Thouret et al., 2005) resembles the magmatic evolution of Parinacota. In the first post-flank failure phase, Ubinas erupted andesite (60-62 wt% SiO_2) within a temporal trend of decreasing silica contents, up to 55 wt%. Simultaneously, however, more silicic (63-68 wt%) eruptions were also emitted. The post-collapse activity of Ubinas is, similarly to Parinacota, characterized by high eruption rates. Moreover, the trend of decreasing SiO_2 and increasing MgO of magmas (Thouret at al., 2005; their Fig. 10) started long before the failure event took place. The SiO_2 contents decreased successively form ~70 to ~63 wt% prior to the edifice failure.

Ollagüe (21°S, Feeley et al. 1993) erupted andesites, which span only a narrow range of 60 to 62 wt% SiO_2 subsequent to the collapse event. The post-collapse activity continued by extrusions of highly viscous dacites of 65-66 wt% SiO_2 in form of dome and coulée. Prior to collapse, Ollagüe produced compositionally broad range of rocks between 53 and 67 wt% SiO_2.

Based on a series of mechanical studies concerning volcano sector collapse by Pinel & Jaupart (2000, 2003, 2004, 2005), and Pinel et al. (2010), Pinel & Albino (2013) specify three main modifications regarding the erupted magma after a flank collapse. These are: 1) an increase of eruption rate, 2) a change in magma storage pressure, and 3) a change in erupted magma composition toward less evolved(30) and denser magmas. According to this scheme, a pressure decrease within the underlying magma storage level, caused by relocation of the edifice load must have been responsible for the compositional changes at Parinacota. A numerous examples of intermediate to silicic lavas, erupted subsequently after an edifice collapse, contradict to this theory.

Dacite eruptions after collapse are a common phenomenon, which occurs at arc stratovolcanoes. Beside the SVC and Ollagüe, also Tungurahua (NVZ, Hall et al., 1999), Llullaillaco (CVZ, Richards & Villeneuve, 2001), and Pichincha (NVZ, Samaniego et al., 2010) erupted silicic lavas after edifice destruction. Thus, the dacites after edifice collapse support the concept resulted from present Parinacota study that the availability of the silicic magmas without clear connection to edifice collapse decides about the magma evolution, leading to the differences in the magmatic differentiation regime.

In this context, it must be noted, that the statement of Pinel & Albino (2013) cited in point 3) is based on studies on volcano collapse representing oceanic islands setting, such Manconi et al. (2009), Longpré et al. (2010), and Boulesteix et al. (2012). In this geological setting calc-alkaline silicic RDEM-type magmas are not generated. Therefore, an increasing magma input and eruption rates in oceanic island volcanoes tend rather to an eruption of more mafic magmas.

7.3. OCCURRENCE OF AMPHIBOLE VS. PYROXENE - RELATION TO THE SECTOR COLLAPSE

7.3.1. AMPHIBOLE CRYSTALLIZATION - INSIGHT FROM TAAPACA BASALTIC ANDESITE ENCLAVES

The geochemically variable, low- and high-Sr basaltic andesitic enclaves from Taapaca dacites resemble the whole rock compositions of low- and high-Sr basaltic andesite from Parinacota. Nonetheless, the main Fe-Mg silicate phase in Taapaca enclaves is amphibole (Mg-Hst), in contrast to olivine and cpx bearing Parinacota basaltic andesite lavas. The barometry data obtained from Mg-Hst in Taapaca rocks reveal pressures, which do not exceed 300 MPa, and overlap with the maximal pressure values obtained from the Mg-Hbl crystallized from the silicic magma (Figure 11, and explanation in section 5.3 and 7.4, Chapter 3). This result lead to the interpretation, that amphibole in the mafic recharge magma starts to crystallize, when the ascending magma reaches the silicic reservoir.

A fast heat transfer between a hot mafic magma and a silicic magma reservoir during underplating and rejuvenation (e.g. Bachmann & Berganz, 2006; Huber et al., 2011) causes temperature decrease to slightly above 1000°C in Taapaca and Parinacota rocks, as illustrated for the maximal estimated crystallization temperatures of amphibole in Figure 11 in Chapter 3. A series of experimental studies by Moore & Carmichael (1998), and Blatter & Carmichael (2001) conducted on calc-alkaline basaltic andesite and andesite from Mexican Volcanic Belt show, that under water-saturated conditions, olivine and amphibole phase boundary lines cross at ~310 MPa at 950-1010°C

---

[30] The term "evolved" implies an evolution of the silicic magma via AFC processes from more mafic parental magmas. The PVA study shows that silicic magmas feed the subvolcanic plumbing system similarly to the mafic magmas; therefore "silicic" is preferred in this study.

for basaltic andesitic and andesitic compositions of starting materials. In basaltic andesite both phases can coexist, in the andesite cannot. In the case of Taapaca mafic enclaves, an incorporation of the silicic material during magma mixing eliminates crystallization of olivine and cpx. Furthermore, water concentrations at these P-T conditions are calculated in these studies from experimental residual glass compositions to be 5.5-6.5 wt%. Mg-Hst from Taapaca show, however, lower H_2O_{melt} values in a range of 2.5-4.0 wt% in Taapaca, also 2.5-5.0 wt% in Parinacota rocks, values consistent with other arc basalts (e.g. Almeev et al., 2013; Blatter et al., 2013 and references therein). The relatively low water contents obtained from Mg-Hst using R&R2011 suggest, that rather temperature drop play a key role in amphibole crystallization.

In the preserved droplets of the mafic magmas during hybridization of Taapaca end-member magmas, temperature decreases, and H_2O_{melt} content increases, due to, at least ~200°C lower stagnation temperatures in comparison to the hot mafic recharge, and ~5 wt% higher H_2O_{melt} of the RDEM magmas. In this way, changing conditions are sufficient to destabilize olivine and cpx, and promote amphibole crystallization in basaltic andesite.

This generation scenario of amphibole-bearing basaltic andesite magmas of Taapaca provides a general explanation for amphibole crystallization linked to magma mixing. Insufficient amount of silicic magma admixed into the mafic magmas to cause a sufficient temperature drop to amphibole stability at certain pressure and water contents, supports crystallization of pyroxene in more mafic andesites, compared to more silicic amphibole-bearing andesites.

7.3.2. INSIGHTS FROM PARINACOTA

7.3.2.1. Amphibole occurrence in more silicic andesites

An occurrence of the prevailing Fe-Mg silicate phase, amphibole vs. pyroxene, is a response to a certain differentiation regime, thus, as proposed in this study, to the availability of the silicic magmas in the subvolcanic system. This line of reasoning is based on: 1) the presence of the silicic magmas, 2) mafic-silicic magma mixing dominated whole rock trends, mineral chemistry and textures, 3) and the presence of amphibole as an essential Fe-Mg phase prior to Parinacota sector collapse. It should be noted, that the term “silicic magmas” used here refers to the RDEM-type magmas described geochemically in Chapter 2 and petrologically in Chapter 3.

Parinacota pre- and post-collapse intermediate lavas fall exactly in the more silicic volcanic range of volcanic rocks (58-66 wt% SiO_2) presented by Reubi & Blundy (2009). Within this range, two mineralogically distinct andesite occur, however more precisely, two-pyroxene andesites span from 58 to 60 wt% SiO_2, whereas amphibole-bearing andesites start at 60 wt% SiO_2.

A change from an amphibole-generating to a pyroxene-generating differentiation regime, and vice versa, have been found in numerous stratovolcanoes. An examination of diverse geochemical or petrological studies of the andesites suggests that such mineralogical change is accompanied by a clear change in the whole rock composition in terms of the SiO_2 contents of erupted lavas, independent of a sector collapse. For instance, amphibole occurs in more silicic lavas (>62 wt% SiO_2), which erupted before collapse in Ubinas (Thouret et al., 2005), but after collapse in andesitic to dacitic lavas of Pichincha (Samaniego et al., 2010). One of the recent studies of Kliuchevskoi and Bezymianny volcanoes (Kamchatka) by Almeev et al. (2013) also recognized two separate SiO_2 ranges correlating with different mineral assemblages: two-pyroxene occur in magmas having 55.5-58.5 wt% and amphibole occurs in magmas having 58.5-63 wt% SiO_2.

7.3.2.2. Progressive change from amphibole- to pyroxene-bearing andesite

Detailed petrographical studies of the andesites suggest that rather a progressive alteration from amphibole- to pyroxene-bearing rocks occurs. Parinacota pre-collapse lavas show an increasing pyroxene amounts from the “Border dacite” (PAR 16) to the youngest andesite (PAR 82), beside the prevailing amphibole in these samples. The oldest investigated sample PAR 130, which contains predominantly two populations of pyroxene beside two different amphibole compositions. This sample does not host Mg-Hbl and low-An-Fe plagioclase, which are characteristic to the rhyodacite and rhyolite of the Dome Plateau, found in younger dacite-andesite samples. It suggests that the oldest dacite of Parinacota mixed with other silicic component, differing from the other Old Cone dacite-andesite.

Another example for a documented progressive changes between amphibole and pyroxene in dacite-andesite lavas is observed in Vinta Loma of pre-collapse eruptive unit of volcano Ollagüe (Feeley et al., 1993), consisting of mainly two-pyroxene andesite to dacite. A few of the oldest flows from this unit contain significantly more amphibole relative to pyroxene. Referring to Parinacota Old Cone lavas, this change from amphibole to pyroxene intermediate lavas may reflect progressive removal silicic magmas stagnating in the Ollagüe subvolcanic system at the time.

We can conclude that the occurrence of amphibole vs. pyroxene in andesite lavas does not result from effects of the edifice collapse on the subvolcanic plumbing system connected to pressure changes in the plumbing. This mineralogical effect is strongly related to the presence of silicic magmas stagnating in the subvolcanic system.

7.3.2.3. Information from intensive parameter of crystallization of Parinacota magmas

Similar to Taapaca, amphiboles from Parinacota lavas also show a limited P-range suggesting crystallization in a very narrow shallow depth range. Moreover, Mg-Hst from lavas erupted until 28 ka shows wider T-range compared to younger lavas. The former show similar rage to Mg-Hst from Taapaca dacite and probably reflect the “Taapaca-style” differentiation regime in term of the rejuvenation and remobilization of the silicic magmas. Mg-Hst from other, less silicic magmas reveal more focused T-ranges besides an absence of Mg-Hbl, and preserved pyroxene antecrysts. This observations indicate different mixing regime controlled by prevailing mafic magmas.

An experimental study of Martel et al. (1999) demonstrating the effects of fO_2 and H_2O on andesite (60-61 wt% SiO_2) phase relations between 2 and 4 kbar shows that increasing fO_2 above NNO+1 promotes amphibole stability. Furthermore, more oxidized conditions in amphibole-bearing lavas affect stability of ilmenite. These experimental results are consistent with the mineral assemblage found in Parinacota amphibole-bearing lavas, lacking ilmenite pheno/microcrysts. Thus, variations in composition of Fe-Mg silicates correlate also with oxygen fugacity of the andesitic magmas.

Crystallization temperatures of ~950-1050°C, obtained from two-pyroxene thermometry, suggest that pyroxene phenocrysts in the Old Cone lavas must have originated from the slightly hotter mafic components. Temperature decrease to ~900-1000°C, recorded in Mg-Hst, promoted amphibole crystallization. The pressure range of pyroxene crystallization obtained from two-pyroxene barometry (Putirka, 2008) shows a significant scatter between 1 and 9 kbar, compared to clearly focused P-values of Mg-Hst. Furthermore, the two-pyroxene barometry from the OC lavas shows also a narrow P-range of ~2-5 kbar (Figure 13a). P-values of cpx-opx pairs extend to noticeably lower values in comparison to amphibole; however, we cannot relate it to the decompression effect on the plumbing system caused by sector collapse. The crystallization scenario of amphibole preferred in this study requires silicic magmas, which stagnate at a certain shallow crustal level. The pressure results obtained from Mg-Hbl (~1-3 kbar), representing the silicic magma, indicate the depth of 4-11 km. Consequently, the mafic magmas underplate the silicic reservoir and crystallize compelled to this depth. In contrast, the mafic magmas that are not captured by the silicic magmas can crystallize continuously to until they reach shallower depth.

As known from numerous experimental studies, critical parameters controlling crystallization of amphibole vs. pyroxene in andesite is temperature, oxygen fugacity and water contents. The contact with silicic magmas causes changes in initial T, fO_2, and H_2O_{melt} contents during equilibration, and in bulk composition via mixing. T-decrease and an increase of fO_2, and H_2O_{melt} contents promote amphibole crystallization; if the silicic supplier is not present in the plumbing system in sufficient proportion to the mafic magmas, crystallization of pyroxene continues.

7.4. SUBVOLCANIC SYSTEM OF PARINACOTA VOLCANO

After the edifice sector collapse, the chemically and isotopically variable Parinacota lavas focus to definitely more uniform compositions, as presented by Hora et al. (2009), as well as in Figure 2 and Figure 3 of this study. Based on differences in $^{87}Sr/^{86}Sr$ and $^{230}Th/^{238}U$ isotopic ratios of Parinacota lavas, Hora et al. (2009) postulated a coalescence of small separate magma batches to a single magma reservoir during the evolution of the Parinacota plumbing system, starting already before the edifice sector collapse. Moreover, Wörner et al. (1988) and Ginibre & Wörner (2007) explained the less silicic post-collapse magmas by mafic recharges intruding into successively less differentiated resident magmas. They linked it to changes in the dynamic of magma supply, and increasing recharge rates after volcano collapse recognized from plagioclase zoning patterns. Furthermore, they argue that the patchy zoning of plagioclase observed mainly in the Young Cone andesites, indicates shallower depth of crystallization in comparison to the Old Cone plagioclase, caused by decompression, water saturation and degassing of ascending magma, indicating decreasing depth of magma chamber.

The “cleaning” of the plumbing system, responsible for the differences between pre- and post-collapse andesites, as postulated in this study, describes an alternative model of Parinacota plumbing system. Principally, the Parinacota subvolcanic system reflects those of Taapaca. The crucial difference is the mafic/silicic ratio of magmas, which enter the volcanic plumbing system. Parinacota is characterized by a higher input of the (AEM+BEM) hybrid mafic recharge in comparison to by the predominant RDEM silicic component in the Taapaca plumbing system. The compositional and mineralogical evolution of Parinacota magmas results from a successive removal of the silicic magmas from the plumbing system. Due to low temperatures and high water contents, these magmas crystallize extensively, reach the rheological lock up point, and stagnate at the shallow ~10 km depth. They represent the typical crystal-rich proto-plutons. The mafic recharge overcomes these rheological barriers, and remobilizes the silicic proto-plutons via magma mixing. The mixing proportions of the Taapaca dacite show, that lower proportions of the mafic magmas (~30%), as assumed from different studies, are able to remobilize the silicic magma. The mixing proportions between the mafic/silicic determine also the mineralogy of the erupted magmas, due to the physical and chemical equilibration.

The diversity of the erupted magmas before volcano collapse suggests partially rejuvenated silicic magmas batches, at different mafic/silicic proportions, mainly depending on the availability of the silicic component. The decreasing silica content over time is connected to the increased production of the mafic magmas in the Parinacota subvolcanic system, operating as a “cleaning” agent.

8. SUMMARY AND CONCLUDING REMARKS

1. Parinacota volcanic system integrates the volcanic and plutonic characteristics, similarly to Taapaca. The differentiation regimes operating underneath Parinacota, regarded as “distinct”, are principally the same, based on the magma mixing. “*Distinct*” can be used with regard to the mafic/silicic proportions involved in the petrogenesis. Following numerous recent studies concerning role of (primary) silicic magmas in the formation of andesite volcanoes (e.g. Reubi & Blundy, 2009), mixing and mingling processes between bimodal magmas ascending below stratovolcanoes play a fundamental role beside a negligible contribution of the fractionation-driven magma evolution.
2. Two *distinct* magma differentiation regimes affected the evolution of Parinacota intermediate lavas. The first regime, dominated by the silicic magmas, produced a continuous range of the silicic andesites to rhyodacites (>62 wt% SiO_2), characterized by an occurrence of amphibole as a prevailing Fe-Mg silicate phase. The second regime, dominated by mafic magmas, generated compositionally uniform andesite in a narrow range between 58 to 60 wt% SiO_2 characterized by occurrence of clinopyroxene, orthopyroxene and only negligible abundance of amphibole. The connection between SiO_2 contents and different mineral assemblages suggests a crucial role of the proportions of the silicic component involved in the generation of the intermediate magmas. Thus, the differentiation regimes are defined by a ratio between mafic and silicic magmas present in the volcanic plumbing system.

3. A switch from one regime to another results from changes in mafic/silicic magma proportions feeding the shallow subvolcanic system. These proportions determine the compositions and mineralogy of the erupted magmas, thus the mechanisms and physical conditions that constitute the type of differentiation regime. This study suggests that the changes in the chemistry and mineralogy of the intermediate magmas occur rather progressively in the volcanic shallow plumbing system. The change in the differentiation regime in Parinacota represents a “cleaning” of the plumbing system from the silicic magmas due to a significant increase of the mantle-derived mafic input. The volcano sector collapse occurs as a consequence of an increasing eruptive activity, which lead to the edifice instability.
4. The geobarometry results obtained from amphibole and two-pyroxene chemistry in the pre- and post-collapse lavas do not yield obvious changes in the crystallization pressure caused by decompression of the shallow plumbing system due to mass relocation. Pressure-values obtained from the amphibole, which crystallized from the mafic magmas suggest their crystallization by an underplating of the silicic magma reservoir. After removal of the silicic magma from the plumbing system, the subsequent mafic magmas are not captured in the stagnation zone of the silicic magma and crystallize continuously throughout a wide shallow pressure range.

9. REFERENCES

Allmendinger, R. W., Jordan, T. E., Kay, S. M. & Isacks, B. (1997). The evolution of the Altiplano-Puna plateau of the Central Andes. *Annual Reviews of Earth and Planetary Sciences* **25**, 139-174.

Almeev, R. R., Ariskin, A. A., Kimura, J.-I. & Barmina, G. S. (2013). The role of polybaric crystallization in genesis of andesitic magmas: Phase equilibria simulations of the Bezymianny volcanic subseries. *Journal of Volcanology and Geothermal Research* **263**, 182–192.

Andersen, D. J. & Lindsley, D. H. (1985). New (and final!) models for the Ti-magnetite/ilmenite geothermometer and oxygen barometer. *Abstract AGU 1985 Spring Meeting Eos Transactions. American Geophysical Union* **66**, 416.

Anderson, J. L., Barth, A. P., Wooden, J. L. & Mazdab, F. (2008). Thermometers and Thermobarometers in Granitic Systems. *Reviews in Mineralogy and Geochemistry* **69**, 121-142.

Armstrong, J. T. (1995). A package of correction programs for the quantitative electron microbeam X-ray analysis of thick polished materials, thin films and particles. *Microbeam Analysis* **4**, 177-200.

Babeyko, A. Y. & Sobolev, S. V. (2005). Quantifying different modes of the late Cenozoic shortening in the central Andes. *Geology* **33**, 621-624.

Baby, P., Hérail, G., Salinas, R. & Sempere, T. (1992). Geometry and kinematic evolution of passive roof duplexes deduced from cross section balancing: Example from the foreland thrust system of the southern Bolivian Subandean Zone. *Tectonics* **11**, 523–536.

Baby, P., Rochat, P., Mascle, G. & Herail, G. (1997). Neogene shortening contribution to crustal thickening in the back arc of the Central Andes. *Geology* **25**, 883-886.

Bachmann, O. & Bergantz, G. W. (2006). Gas percolation in upper-crustal silicic crystal mushes as a mechanism for upward heat advection and rejuvenation of near-solidus magma bodies. *Journal of Volcanology and Geothermal Research* **149**, 85-102.

Bachmann, O., Miller, C. F. & De Silva, S. L. (2007). The plutonic-volcanic connection as a stage for understanding crustal magmatism. *Journal of Volcanology and Geothermal Research* **167**, 1-23.

Bacon, C. R. & Hirschmann, M. M. (1988). Mg/Mn partitioning as a test for equilibrium between coexisting Fe-Ti oxides. *American Mineralogist* **73**, 57-61.

Barazangi, M. & Isacks, B. L. (1976). Spatial distribution of earthquakes and subduction of the Nasca plate below South America. *Geology* **4**, 686-692.

Blatter, D. L. & Carmichael, I. S. E. (2001). Hydrous phase equilibria of a Mexican high-silica andesite: a candidate for a mantle origin? *Geochimica Cosmochimica Acta* **65**, 4043-4065.

Blatter, D. L., Sisson, T. W. & Hankins, W. B. (2013). Crystallization of oxidized, moderately hydrous arc basalt at mid- to lower-crustal pressures: implications for andesite genesis. *Contributions to Mineralogy and Petrology* **166**, 861-886.

Blundy, J. & Cashman, K. (2008). Petrologic Reconstruction of Magmatic System Variables and Processes. *Reviews in Mineralogy and Geochemistry* **69**, 179-239.

Blundy, J. & Holland, T. (1990). Calcic amphibole equilibria and a new amphibole-plagioclase geothermometer. *Contributions to Mineralogy and Petrology* **104**, 208-224.

Bogoyavlenskaya, G. E., Braitseva, O. A., Melekestsev, I. V., Kiriyanof, V. Y. & Miller, C. D. (1985). Catastrophic eruptions of the directed-blast type at Mount St. Helens, Bezymianny and Shiveluch volcanoes. *Journal of Geodynamics* **3**, 189-218.

Boudon, G., Villemant, B., Le Friant, A., Paterne, M. & Cortijo, E. (2013). Role of large flank-collapse events on magma evolution of volcanoes. Insights from the Lesser Antilles Arc. *Journal of Volcanology and Geothermal Research* **263**, 224–237.

Boulesteix, T., Hildenbrand, A., Gillot, P.-Y. & Soler, V. (2012). Eruptive response of oceanic islands to giant landslides: new insigths from the geomorphologic evolution of the Teide-Pico Viejo volcanic complex (Tenerife, Canary). *Geomorphology* **138**, 61-73.

Bourdon, B., Wörner, G. & Zindler, A. (2000). U-series evidence for crustal involvement and magma residence times in the petrogenesis of Parinacota volcano, Chile. *Contributions to Mineralogy and Petrology* **139**, 458-469.

Brey, G. P. & Köhler, T. (1990). Geothermobarometry in Four-phase Lherzolites II. New Thermobarometers, and Practical Assessment of Existing Thermobarometers. *Journal of Petrology* **31**, 1353-1378.

Cahill, T., Isacks, B. L. (1992). Seismicity and shape of the subducted Nazca plate. *Journal of Geophysical Research Letters* **97**, 17503-17529.

Carracedo, J. C., Day, S. J., Guillou, H. & Gravestock, P. (1999). The later stages of the volcanic and structural evolution of La Palma, Canary Islands. . *Geological Society of America Bulletin* **111**, 755-768.

Clavero, J. E. (2002). Evolution of Parinacota Volcano and Taapaca Volcanic Complex, Central Andes of Northern Chile. *PhD Thesis, University of Bristol*.

Clavero, J. E., Sparks, R. S. J., Pringle, M. S., Polanco, E. & Gardeweg, M. C. (2004). Evolution and volcanic hazards of Taapaca Volcanic Complex, central Andes of northern Chile. *Journal of Geological Society* **161**, 603-618.

Coira, B., Davidson, J., Mpodozis, C. & Ramos, V. A. (1982). Tectonic and magmatic evolution of the Andes of northern Argentina and Chile. *Earth Sci. Rev.* **18**, 303-332.

Davidson, J. P., Harmon, R. S. & Wörner, G. (1991). The source of the Central Andes magmas: some considerations. *Geological Society of America Special Paper* **265**, 233-244.

Davidson, J. P., McMillan, N. J., Moorbath, S., Wörner, G., Harmon, R. S. & Lopez-Escobar, L. (1990). The Nevados de Payachata volcanic region (18°S 69°W, N Chile) II. evidence for widespread crustal involvement in Andean magmatism. *Contributions to Mineralogy and Petrology* **105**, 412-432.

DeMets, C., Gordon, R., Argus, D. & Stein, S. (1990). Current Plate Motions. *Geophys. J. Int.* **101**, 425–478.

Droop, G. T. R. (1987). A general equation for estimating Fe^{3+} concentrations in ferromagnesian silicates and oxides from microprobe analyses, using stoichiometric criteria. *Mineralogical Magazine* **51**, 431-435.

Entenmann, J. (1994). Magmatic evolution of the Nevados de Payachata Complex and the petrogenesis of basaltic andesites in the Central Volcanic Zone of northern Chile. *PhD Thesis, University of Mainz*.

Feeley, T. C., Davidson, J. P. & Armendia, A. (1993). The volcanic and magmatic evolution of Volcán Ollagüe, a high-K, late quaternary stratovolcano in the Andean Central Volcanic Zone. *Journal of Volcanology and Geothermal Research* **54**, 221-245.

Francis, P. W. & Wells, G. L. (1988). Landsat thematic mapper observations of debris avalanche deposits in the central Andes. *Bulletin of Volcanology* **50**, 258-278.

Frost, B. R. (1991). Introduction to oxygen fugacity and its petrologic importance. *Reviews in Mineralogy and Geochemistry* **25**, 1-9.

Gardner, J. E., Rutherford, M., Carey, S. & Sigurdsson, H. (1995). Experimental constraints on pre-eruptive water contents and changing magma storage prior to explosive eruptions of Mount St Helens volcano. *Bulletin of Volcanology* **57**, 1-17.

Gaupp, R., Kött, A. & Wörner, G. (1999). Paleoclimatic implications of Mio-Pliocene sedimentation in the high-altitude intra-arc Lauca Basin of northern Chile. *Palaeogeography, Palaeoclimatology, Palaeoecology, Special Volume, Vol. 151 'Lacustrine Systems in Convergent Margins'*, 79-101.

Geschwind, C. H. G. & Rutherford, M. J. (1992). Cummingtonite and the evolution of the Mount St. Helens magma system: An experimental study. *Geology* **20**, 1011-1014.

Ginibre, C. & Wörner, G. (2007). Variable parent magmas and recharge regimes of the Parinacota magma system (N. Chile) revealed by Fe, Mg and Sr zoning in plagioclase. *Lithos* **98**, 118-140.

Ginibre, C., Wörner, G. & Kronz, A. (2002b). Minor- and trace-element zoning in plagioclase: implications for magma chamber processes at Parinacota volcano, northern Chile. *Contributions to Mineralogy and Petrology* **143**, 300-315.

Gubbels, T., Isacks, B. & Farrar, E. (1993). High-level surfaces, plateau uplift, and foreland development, Bolivian central Andes. *Geology* **21**, 695-698.

Haggerty, S. E. (1991). Oxide textures-a mini-atlas. In: Lindsley DH (ed) Oxide minerals: petrologic and magnetic significance. *Mineralogical Society of America* **25**.

Hall, M. L., Robin, C., Beate, B., Mothes, P. & Monzier, M. (1999). Tungurahua Volcano, Ecuador: structure, eruptive history and hazards. *Journal of Volcanology and Geothermal Research* **91**, 1-21.

Hildenbrand, A., Gillot, P. & Le Roy, I. (2004). Volcano-tectonic and geochemical evolution of an oceanic intra-plate volcano: Tahiti-Nui (French Polynesia). *Earth and Planetary Science Letters* **217**, 349-365.

Holland, T. & Blundy, J. (1994). Non-ideal interactions in calcic amphiboles and their bearing on amphibole-plagioclase thermometry. *Contributions to Mineralogy and Petrology* **116**, 433-447.

Hora, J. M., Singer, B. S. & Wörner, G. (2007). Volcano evolution and eruptive flux on the thick crust of the Andean Central Volcanic Zone; ^{40}Ar/^{39}Ar constraints from Volcán Parinacota, Chile. *Geological Society of America Bulletin* **119**, 343-362.

Hora, J. M., Singer, B. S., Wörner, G., Beard, B. L., Jicha, B. R. & Johnson, C. M. (2009). Shallow and deep crustal control on differentiation of calc-alkaline and tholeiitic magma. *Earth and Planetary Science Letters* **285**, 75-86.

Huber, C., Bachmann, O. & Dufek, J. (2011). Thermo-mechanical reactivation of locked crystal mushes: Melting-induced internal fracturing and assimilation processes in magmas. *Earth and Planetary Science Letters* **304**, 443-454.

Hurwitz, D. M., Long, S. M. & Grosfils, E. B. (2009). The characteristics of magma reservoir failure beneath a volcanic edifice. *Journal of Volcanology and Geothermal Research* **188**, 379-394.

Inokuchi, T. (1988). Gigantic landslides and debris avalanches on volcanoes in Japan. In: Proceedings of the Kagoshima International Conference on Volcanoes. *In: Proceedings of the Kagoshima International Conference on Volcanoes National Institute for Research Administration, Japan*, 456-459.

Isacks, B. L. (1988). Uplift of the central Andean plateau and bending of the Bolivian orocline. *Journal of Geophysical Research* **93**, 3211-3231.

James, D. E. (1971). Andean crustal and upper mantle structure. *Journal of Geophysical Research* **76**, 3246-3271.

Johnson, M. C. & Rutherford, M. J. (1989). Experimental calibration of the aluminum-in-hornblende geobarometer with application to Long Valley caldera (California). *Geology* **17**, 837-841.

Kaplan, M. R., Ackert, R. P., Singer, B. S., Douglass, D. C. & Kurz, M. D. (2004). Cosmogenic nuclide chronology of millennial-scale glacial advances during O-isotope stage 2 in Patagonia. *Geological Society of America Bulletin* **116**, 308-321.

Katsui, Y. & Gonzalez-Ferran, O. (1968). Geologia del area neovolcanica de los Nevados de Payachata. *Publicacion No. 29, Universidad de Chile, Facultad de Ciencas Fisicas y Matematicas, Departmento Geologia*, 1-61.

Kent, A. J. R., Darr, C., Koleszar, A. M., Salisbury, M. J. & Cooper, K. M. (2010). Preferential eruption of andesitic magmas through recharge filtering. *Nature Geoscience* 3, 631-636.

Kervyn, M., Ernst, G. G. J., van Wyk de Vries, B., Mathieu, L. & Jacobs, P. (2009). Volcano load control on dyke propagation and vent distribution: Insights from analogue modeling. *Journal of Geophysical Research* **114**, Issue B3.

Kley, J., Monaldi, C. & Salfity, J. (1999). Along-strike segmentation of the Andean foreland; causes and consequences. *Tectonophysics* **301**, 75 -94.

Kött, A., Gaupp, R. & Wörner, G. (1995). Miocene to Recent history of the western Altiplano in northern Chile revealed by lacustrine sediments of the Lauca Basin (18°15'-18°40'S/69°30'-69°05'W). *Geologische Rundschau* **84**, 770-780.

Lamb, S. & Davis, P. (2003). Cenozoic climate change as a possible cause for the rise of the Andes. *Nature* **425**, 792-797.

Lamb, S., Hoke, L., Kennan, L. & Dewey, J. (1997). Cenozoic evolution of the Central Andes in Bolivia and northern Chile. *From Burg, J.-P. & Ford, M. (eds), 1997, Orogeny Through Time, Geological Society Special Publication* **121**, 237-264.

Lamy, F., Hebbeln, D. & Wefer, G. (1999). High resolution marine record of climaic change in mid-latitude Chile during last 28,000 years based on terrigenous sediment parameters. *Quaternary Research* **51**, 83-93.

Leake, B. E., Woolley, A. R., Arps, C. E. S., Birch, W. D., Gilbert, M. C., Grice, J. D., Hawthorne, F. C., Katio, A., Kisch, H. J., Krivovichev, V. G., Linthout, K., Laird, J., Mandarino, J. A., Maresch, W. V., Nickel, E. H., Schumacher, J. C., Smith, D. C., Stephenson, N. C. N., Ungaretti, L., Whittaker, E. J. W. & Youzhi, G. (1997). Nomenclature of amphiboles: report of the subcommittee on amphiboles of the International Mineralogical Association, Commission on new minerals and mineral names. *Canadian Mineralogist* **35**, 219-246.

LeBas, M. J. (1962). The role of aluminum in igneous clinopyroxenes with relation to their parentage. *American Journal of Science* **260**, 267-288.

Lindsay, J. M., de Silva, S., Trumbull, R., Emmermann, R. & Wemmer, K. (2001). La Pacana caldera, N. Chile: a re-evaluation of the stratigraphy and volcanology of one of the world's largest resurgent calderas. *Journal of Volcanology and Geothermal Research* **106**, 145-173.

Lipman, P. W. (2007). consolidation of Cordilleran magma chambers: Evidence from the Southern Rocky Mountain volcanic field. *Geosphere* **3**, 42-70.

Lipman, P. W., Moore, J. C. & Swanson, D. A. (1981). Bulging of the north flank before the May 18 eruption: Geodetic data. In: Lipman PW, Mullineaux DR (eds) The 1980 eruptions of Mount St Helens, Washington. *U.S. Geological Survey Professional Paper* **1250**, 143-156.

Loewy, S. L., Connelly, J. N., Dalziel, I. W. D. (2004). An Orphaned Basement Block: The Arequipa-Antofalla Basement of the Central Andean margin of South America. *Geological Society of America Bulletin* **116**, 171-187.

Longpré, M.-A., Troll, V. R., Walter, T. R. & Hansteen, T. H. (2010). Volcanic and geochemical evolution of the Teno massif, Tenerife, Canary Islands: Some repercussions of giant landslides on ocean island magmatism. *Geochemistry Geophysics Geosystems* **10**, Q12017.

Loucks, R. R. (1990). Discrimination of ophiolitic from nonophiolitic ultramafic-mafic allochthons in orogenic belts by the Al/Ti ratio in clinopyroxene. *Geology* **18**, 346-349.

Lowell, T. V., Heusser, C. J., Andersen, B. G., Moreno, P. I., Hauser, A., Heusser, L. E., Schlüchter, C., Marchant, D. R. & Denton, G. H. (1995). Interhemispheric Correlation of Late Pleistocene Glacial Events. *Science* **269**, 1541-1549.

Macpherson, C. G., Dreher, S. T. & Thirlwall, M. F. (2006). Adakites without slab melting: High pressure differentiation of island arc magma, Mindanao, the Philippines. *Earth and Planetary Science Letters* **243**, 581-593.

Mahood, G. A. (1990). Second reply to comment of R.S.J. Sparks, H.E. Huppert, and C.J.N. Wilson on "Evidence for long residence times of rhyolitic magma in the Long Valley magmatic system: the isotopic record in postcaldera lavas of Glass Mountain" *Earth and Planetary Science Letters* **99**, 395-399.

Mamani, M., Tassara, A. & Wörner, G. (2008). Composition and structural control of crustal domains in the central Andes. *Geochemistry Geophysics Geosystems* **9**, No. 3, Q03006

Mamani, M., Wörner, G. & Sempere, T. (2010). Geochemical variations in igneous rocks of the Central Andean orocline (13°S to 18°S): Tracking crustal thickening and magma generation through time and space. *GSA Bulletin* **122**, 162-182.

Manconi, A., Longpré, M.-A., Walter, T. R., Troll, V. R. & Hansteen, T. H. (2009). The effects of flank collapses on volcano plumbing systems. *Geology* **37**, 1099-1102.

Martel, C., Pichavant, M., Holtz, F. & Scaillet, B. (1999). Effects of fO_2 and H_2O on andesite phase relations between 2 and 4 kbar. *Journal of Geophysical Research* **104**, 29453-29470.

McGuire, W. J. (1996). Volcano instability: A review of contemporary themes. *Geological Society of London Special Publications* **110**, 1-23.

McGuire, W. J. (2003). Volcano instability and lateral collapse. *Revista* **1**, 33-45.

Mercier, J.-C. C., Benoit, V. & Girardeau, J. (1984). Equilibrium state of diopside-bearing harzburgites from ophiolites: Geobarometric and geodynamic implications. *Contributions to Mineralogy and Petrology* **85**, 391-403.

Miyashiro, A. (1974). Volcanic rock series in island arcs and active continental margins. *American Journal of Science* **274**, 321–355.

Moore, G. & Carmichael, I. S. E. (1998). The hydrous phase equilibria (to 3 kbar) of an andesite and basaltic andesite from western Mexico: constraints on water content and conditions of phenocryst growth. *Contributions to Mineralogy and Petrology* **130**, 304-319.

Moreno, A., Giralt, S., Valero-Garcés, B., Sáez, A., Bao, R., Prego, R., Pueyo, J. J., González-Sampériz, P. & Taberner, C. (2006). A 14 kyr record of the tropical Andes: The Lago Chungará sequence (18°S, northern Chilean Altiplano). *Quaternary International*. doi:10.1016/j.quaint.2006.10.020.

Morimoto, N., Fabries, J., Ferguson, A. K., Ginzburg, I. V., Ross, M., Seifert, F. A., Zussman, J., Aoki, K. & Gottardi, G. (1988). Nomenclature of pyroxenes. *American Mineralogist* **73**, 1123-1133.

Myers, J. D., Marsh, B. D. & Sinha, A. K. (1985). Strontium isotopic and selected trace-element variations between 2 Aleutian volcanic centers (Adak and Atka) — implications for the development of arc volcanic plumbing systems. *Contributions to Mineralogy and Petrology* **91**, 221–234.

Petford, N. & Atherton, M. (1996). Na-rich Partial Melts from Newly Underplated Basaltic Crust: the Cordillera Blanca Batholith, Peru. *Journal of Petrology* **37**, 1491-1521.

Petrone, C. M., Braschia, E. & Francalancia, L. (2009). Understanding the collapse–eruption link at Stromboli, Italy: A microanalytical study on the products of the recent Secche di Lazzaro phreatomagmatic activity. *Journal of Volcanology and Geothermal Research* **188**, 315–332.

Pinel, V. & Albino, F. (2013). Consequences of volcano sector collapse on magmatic storage zones: Insights from numerical modeling. *Journal of Volcanology and Geothermal Research* **252**, 29-37.

Pinel, V. & Jaupart, C. (2000). The effect of edifice load on magma ascent beneath a volcano. *Philosophical Transactions of the Royal Society* **358**, 1515–1532.

Pinel, V. & Jaupart, C. (2003). Magma chamber behavior beneath a volcanic edifice. *Journal of Geophysical Research* **108**, Issue B2.

Pinel, V. & Jaupart, C. (2004). Magma storage and horizontal dyke injection beneath a volcanic edifice. *Earth and Planetary Science Letters* **221**, 245-262.

Pinel, V. & Jaupart, C. (2005). Some consequences of volcanic edifice destruction for eruption conditions. *Journal of Volcanology and Geothermal Research* **145**, 68-80.

Pinel, V., Jaupart, C. & Albino, F. (2010). On the relationship between cycles of eruptive activity and volcanic edifice growth. *Journal of Volcanology and Geothermal Research* **194**, 150-164.

Presley, T. K., Sinton, J. M. & Pringle, M. (1997). Postshield volcanism and catastrophic mass-wasting of the Waianae volcano, Oahu, Hawaii. *Bulletin of Volcanology* **58**, 597-616.

Putirka, K. (2008). Thermometers and Barometers for Volcanic Systems. *Reviews in Mineralogy and Geochemistry* **69**, 61-120.

Ramos, V. A. (1999). Plate Tectonic Setting of the Andean Cordillera. *Episodes* **22**, 183-190.

Reid, M. E., Keith, T. E. C., Kayen, R. E., Iverson, N. R., Iverson, R. M. & Brien, D. L. (2010). Volcano collapse promoted by progressive strength reduction: new data from Mount St. Helens. *Bulletin of Volcanology* **72**, 761–766.

Reid, M. E., W., S. T. & Brien, D. L. (2001). Volcano collapse promoted by hydrothermal alteration and edifice shape, Mount Rainier, Washington. *Geology* **29**, 779-782.

Reubi, O. & Blundy, J. (2009). A dearth of intermediate melts at subduction zone volcanoes and the petrogenesis of arc andesites. *Nature* **461**, 1269-1272.

Richards, J. P. & Villeneuve, M. (2001). The Llullaillaco Volcano, northwest Argentina: construction by Pleistocene volcanism and destruction by sector collapse. *Journal of Volcanology and Geothermal Research* **132**, 37-365.

Ridolfi, F. & Renzulli, A. (2011*online). Calcic amphiboles in calc-alkaline and alkaline magmas: thermobarometric and chemometric empirical equations valid up to 1,130°C and 2.2 GPa. *Contributions to Mineralogy and Petrology* **163**, 877-895.

Sáez, A., Valero-Garcés, B., Moreno, A., Bao, R., Pueyo, J. J., Gonzalez-Samperiz, P., Gritalt, S., Taberner, C., Herrera, C. & Gilbert, R. O. (2007). Lacustrine sedimentation in active volcanic settings: the Late Quaternary depositional evolution of Lake Chungará (northern Chile). *Sedimentology* **54**, 1191-1222.

Samaniego, P., Robin, C., Chazot, G., Bourdon, E. & Cotten, J. (2010). Evolving metasomatic agent in the Northern Andean subduction zone, deduced from magma composition of the long-lived Pichincha volcanic complex (Ecuador). *Contributions to Mineralogy and Petrology* **160**, 239-260.

Samoza, R. (1998). Updated Nazca (Farallon)-South America relative motions during the last 40 My: implications for mountain building in the central Andean region. *Journal of South American Earth Science* **11**, 211-215.

Scheuber, E. & Giese, P. (1999). Architecture of the Central Andes a compilation of geoscientific data along a transect at 21°S. *Journal of South American Earth Sciences* **12**, 103-107.

Schmitz, M. (1994). A balanced model of the southern Central Andes. *Tectonics* **13**, 484-492.

Siebert, L. (1984). Large volcanic debris avalanches: Characteristics of source areas, deposits, and associated eruptions. *Journal of Volcanology and Geothermal Research* **22**, 163-197.

Siebert, L. (1987). Volcanic hazards from Bezymianny- and Bandai-type eruptions. *Bulletin of Volcanology* **49**, 435-459.

Siebert, L. (1992). Threats from debris avalanches. *Nature* **356**, 658–659.

Siebert, L. (1995). The 1883 and late-prehistoric eruptions of Augustine volcano, Alaska. *Journal of Volcanology and Geothermal Research* **66**, 367–395.

Siebert, L. (1996). Hazards of large volcanic debris avalanches and associated eruptive phenomena. *In: Scarpa T, Tilling R I (eds) Monitoring and Mitigation of Volcanic Hazards. Berlin: Springer Verlag*, 541-572.

Sisson, T. W. & Grove, T. L. (1993). Experimental investigations of the role of H_2O in calc-alkaline differentiation and subduction zone magmatism. *Contributions to Mineralogy and Petrology* **113**, 143-166.

Stern, e. a. (2007). Chilean Volcanoes, In: The Geology of Chile. By Teresa Moreno and Wes Gibbons (eds.) (2007). Geological Society. London (United Kingdom), 147-178.

Stern, R. C. (2004). Active Andean volcanism: its geologic and tectonic setting. *Revista Geológica de Chile* **31**, 161-206.

Tassara, A. (2005). Interaction between the Nazca and South American plates and formation of the Altiplano–Puna plateau: Review of a flexural analysis along the Andean margin (15°–34°S). *Tectonophysics* **399**, 39-57.

Tassara, A., Götze, H. J., Schmidt, S. & Hackney, R. (2006). Three-dimensional density model of the Nazca plate and the Andean continental margin. *Journal of Geophysical Research: Solid Earth* **111**, 1978-2012.

Tatsumi, Y. (1986). Formation of the volcanic front in subduction zones. *Geophysical Research Letters* **13**, 717-720.

Tatsumi, Y. (1989). Migration of fluid phases and genesis of basalt magmas in subduction zones. *Journal of Geophysical Research* **94**, 4697-4707.

Tatsumi, Y. (2003). Some Constraints on Arc Magma Genesis. *Inside the Subduction Factory, Geophysical Monograph 138* American Geophysical Union 277-292.

Tatsumi, Y. (2005). The subduction factory: how it operates in the evolving Earth. *GSA Today* **15**, 4-10.

Thompson, L. G., Davis, M. E., Mosley-Thompson, E., Sowers, T. A., Henderson, K. A., Zagorodnov, V. S., Lin, P. N., Mikhalenko, V. N., Campen, R. K., Bolzan, J. F., Cole-Dai, J. & Francou, B. (1998). A 25,000-year tropical climate history from Bolivian ice cores. *Science* **282**, 858–1864.

Thorpe, R. S., Francis, P. W., Hamill, M. & Baker, M. C. W. (1982). The Andes: in "Andesites: orogenic andesites and related rocks". *R.S. Thorpe (ed.), Chichester: Wiley*, 187-205.

Thorpe, R. S., Francis, P. W. & Harmon, R. S. (1981). Andean andesites and continental growth. *Phil. Trans. R. Soc. Lond.* **301**, 305-320.

Thorpe, R. S., Francis, P. W., O'Callaghan, L., Hutchison, R. & Turner, J. S. (1984). Relative Roles of Source Composition, Fractional Crystallization and Crustal Contamination in the Petrogenesis of Andean Volcanic Rocks *Phil. Trans. R. Soc. Lond.* **310**, 675-692.

Thouret, J.-C., Rivera, M., Wörner, G., Gerbe, M.-C., Finizola, A., Fornari, M. & Gonzales, K. (2005). Ubinas: the evolution of the historically most active volcano in southern Peru. *Bulletin of Volcanology* **67**, 557-589.

Tibaldi, A. (2001). Multiple sector collapses at Stromboli volcano, Italy: how they work. *Bulletin of Volcanology* **63**, 112-125.

Tibaldi, A., Bistacchi, A., Pasquarè, A. F. & Vezzoli, E. (2006). Extensional tectonics and volcano lateral collapses: insights from Ollagüe volcano (Chile-Bolivia) and analogue modelling. *Terra Nova* **18**, 282-289.

Tosdal, R. M. (1996). The Amazon-Laurentian connection as viewed from the Middle Proterozoic rocks in the central Andes, western Bolivia and northern Chile. *Tectonics* **15**, 827-842.

Turner, S. J., Izbekov, P. & Langmuir, C. (2013). The magma plumbing system of Bezymianny Volcano: Insights from a 54 year time series of trace element whole-rock geochemistry and amphibole compositions. *Journal of Volcanology and Geothermal Research* **263**, 108-121.

van Wyk de Vries, B. & Borgia, A. (1996). The role of basement in volcano deformation. In: McGuire, W.J., Jones, A.P., and Neuberg, J., eds., Volcano instability on the Earth and other planets. *Geological Society, London, Special Publications* **110**, 95–110.

Vidal, N. & Merle, O. (2000). Reactivation of basement faults beneath volcanoes; a new model of flank collapse. *Journal of Volcanology and Geothermal Research* **99**, 9-26.

Voight, B. & Elsworth, D. (1997). Failure of volcano slopes. *Geotechnique* **47**, 1-31.

Voight, B., Janda, R. J., Glicken, H. & Douglass, P. M. (1983). Nature and mechanics of the Mount St Helens rockslide-avalanche of 18 May 1981. *Geotechnique* **33**, 243-273

Wigger, P. J. (1994). Variation of the crustal structure of the southern Central Andes deduced from seismic refraction investigations, in "Tectonics of the Southern Central Andes" eds. Reutter, K.-J., Scheuber, E. & Wigger, P. *Springer Verlag, Berlin*, 23-48.

Wörner, G., Hammerschmidt, K., Hemjes-Kunst, F., Lezaun, J. & Wilke, H. (2000). Geochronology (^{40}Ar-^{39}Ar-, K-Ar-, and He-exposure-) ages of Cenozoic magmatic rocks from Northern Chile (18°- 22°S). Implications for magmatismo and tectonic evolution of the central Andes. *Revista Geológica de Chile* **27**, 205-240.

Wörner, G., Harmon, R. S., Davidson, J., Moorbath, S., Turner, D. L., McMillan, N., Nye, C., Lopez-Escobar, L. & Moreno, H. (1988). The Nevados de Payachata volcanic region (18°S/69°W, N. Chile) I. Geological, geochemical, and isotopic observations. *Bulletin of Volcanology* **50**, 287-303.

Wörner, G., Moorbath, S. & Harmon, R. S. (1992). Andean Cenozoic volcanic centers reflect basement isotopic domains. *Geology* **20**, 1103-1106.

Yuan, X., Sobolev, S. V. & Kind, R. (2002). Moho topography in the Central Andes and its geodynamic implications. *Earth and Planetary Science Letters* **199**, 389-402.

Yuan, X., Sobolev, S. V., Kind, R., Oncken, O., Bock, G., Asch, G., Schurr, B., Graeber, F., Rudloff, A., Hanka, W., Wylegalla, K., Tibi, R., Haberland, C., Rietbrock, A., Giese, P., Wigger, P., Rower, P., Zandt, G., Beck, S., Wallace, T., Pardo, M. & Comte, D. (2000). Subduction and collision processes in the Central Andes constrained by converted seismic phases. *Nature* **408**, 958-961.

Zandt, G., Velasco, A. A. & Beck, S. (1994). Composition and thickness of the southern Altiplano crust, Bolivia. *Geology* **22**, 1003-1006.

Zellmer, G. F. (2009). Petrogenesis of Sr-rich adakitic rocks at volcanic arcs: insights from global variations of eruptive style with plate convergence rates and surface heat flux. *Journal of the Geological Society, London* **166**, 725-734.